ANALYSIS OF STEEL BEAMS STRENGTHENED WITH ADHESIVELY – BONDED GFRP PLATES

By

Phe Pham Van

A thesis submitted to the University of Ottawa
in partial fulfillment of the requirements
for the Ph.D. degree in Civil Engineering

Department of Civil Engineering
Faculty of Engineering
University of Ottawa

Acknowledgement

My special thanks go to my supervisor Professor Magdi Mohareb and my co-supervisor Professor Amir Fam for their valuable support, advice, and patience. Their academic excellence, conscientiousness, fun and hard-working characters have inspired me to excel in my research.

Many thanks go to my thesis examining committee including Professor Ashraf El Damatty from Western University, Professor Abhjit Sarkar from Carleton University, and Professors Beatriz Martin-Perez and Martin Noel from the University of Ottawa. Their excellent and discerning comments have contributed to improve the content of my thesis.

My Ph.D. thesis was funded through a full Admission Scholarship and an Excellence Scholarship from University of Ottawa, an Ontario Graduate Scholarship, and additional funding from the Natural and Sciences and Engineering Research Council (NSERC) of Canada from Dr. Magdi Mohareb and Dr. Amir Fam. Their financial support is gratefully acknowledged. Also, I would like to thank to the Department of Civil Engineering at the University of Ottawa for the financial support provided via teaching assistantship positions.

My deep thanks go to my family for their moral support. The patience and sacrifice of my mother, my father, my older brother's small family, and my wife throughout my study are forever in my heart. My deepest thanks go to my seven-year-old son Lam Pham-Thanh and my four-year-old son Phuc Pham-Xuan. I missed them every second of my study abroad. Their smile and innocent words gave me motivation and strength to overcome all difficulties.

Abstract

Glass Fiber-Reinforced Polymer (GFRP) plates offer a light-weight, corrosion-resistant and cost-effective alternative to steel plates for strengthening steel members. Typically, GFRP plates are bonded to steel members through a relatively soft adhesive layer. The large difference between the mechanical properties of the three materials involved is generally associated with relative slip at the steel-GFRP interface and is thus associated with partial interaction between the two materials. Available full interaction models aimed at fully composite systems tend to overestimate the strength of GFRP-strengthened steel beams. Also, quantifying the strength of the resulting steel-adhesive-GFRP composite represents a technical challenge as it involves several potential modes of failure (e.g., local buckling, lateral-torsional buckling, cross-sectional strength, GFRP rupture, adhesive shear failure, adhesive peeling failure, excessive deflections, adhesive loss of strength due to thermal effects). Within the above context, the present research aims at formulating a number of analytical/numerical solutions to quantify the strength of GFRP-strengthened steel beams, and assessing the validity of the models through 3D finite element analyses in commercial software.

Towards this goal, the study contributes to the solution of the problem by developing a series of models that incorporate partial interaction effects between the steel and GFRP. The models are intended to determine: (1) the linear static analysis response, (2) the elastic lateral-torsional buckling capacity, (3) the ultimate moment resistance and propose classification considerations for local buckling, (4) quantifying the detrimental effect of pre-existing load on the added capacity of strengthening GFRP plates, (5) developing an advanced beam theory that captures transverse normal stresses in homogeneous beams (in addition to longitudinal and shear stresses in common beam theories), and (6) generalizing the beam theory to multi-layered beams to model sandwich structures and GFRP-strengthened steel beams.

In contribution 1, a super-convergent finite element formulation is developed for the linear static analysis for steel beams strengthened with a single GFRP plate subjected to general transverse loads. The shear deformation effect is captured in the formulation. The element is shown to circumvent discretization errors in conventional finite elements based on polynomial interpolation functions and to accurately predict displacements and stresses while keeping the number of degrees of freedom to a minimum. The model is then adopted to (a) determine the elastic flexural resistance of strengthened steel beams with class 3 (subcompact) sections based on a first yield mode of failure, (b) quantify deflection limits and (c) conduct the pre-buckling analysis required for subsequent elastic lateral torsional buckling analysis.

In contribution 2, a variational principle and two finite elements are developed for the elastic lateral torsional buckling analysis of steel beams strengthened with a single GFRP plate. The formulation accounts for global and local warping, shear deformation due to bending and twist, partial interaction, and load elevation effects. The study provides a basis to quantify key design information including critical moments, buckling modes, moment gradients, and load elevation effects.

In contribution 3, analytical models are developed to determine the ultimate moment resistance for Class 1 and 2 (compact) sections for steel beams strengthened with a single GFRP plate on the tension side. The models account for the elasto-plastic behaviour of steel, the adhesive shear capacity, and the GFRP tensile strength. Attention is given to relatively strong adhesives (e.g., common adhesives at room temperature) as well as weak adhesives (adhesive at elevated temperatures). Also, a methodology for classifying GFRP-strengthened steel sections is proposed to ensure that local buckling does not occur prior the attainment of the ultimate moment resistance.

In contribution 4, a closed form solution is developed for the linear static analysis of a pre-loaded steel beam strengthened with two GFRP plates bonded to both flanges and then subjected to additional loads. The solution provides means to determine the elastic flexural resistance of strengthened steel beams with class 3 (subcompact) sections based on a first yield mode of failure and to quantify deflection limits.

In contribution 5, a family of higher order beam solutions is developed for the analysis of homogeneous beams with a mono-symmetrical cross-section. The distinctive features of the solution are: (a) it is based on the complementary energy variational principle and thus offers advantages in quantifying stresses when compared to common displacement based formulations, (b) it captures the transverse normal stresses in addition to longitudinal and shear stresses, (c) it is based on a polynomial expansion of the stress fields which enables the analyst to increase the accuracy of the predictions by specifying the order of the polynomial. The governing field equations and boundary conditions are formulated and a closed-form solution scheme is developed. The ability of the theory to capture transverse stresses is key in extending the work to non-homogeneous systems such as GFRP-strengthened steel beams in which the peeling of the adhesive represents a possible mode of failure.

Finally, contribution 6 extends the developments of contribution 5 in two respects: (1) generalizing the solution to multilayer beams, and (2) developing a finite element formulation able to handle general boundary conditions. The solution developed is then applied to a number of applications involving sandwich beams and GFRP-strengthened steel beams where it is shown to capture the peeling stresses at the steel-GFRP interface.

Table of Content

CHAPTER 1: INTRODUCTION

CHAPTER 2: LITERATURE REVIEW

CHAPTER 3: SHEAR DEFORMABLE SUPER-CONVERGENT FINITE ELEMENT FOR STEEL BEAMS STRENGTHENED WITH GFRP PLATES

CHAPTER 4: LATERAL TORSIONAL BUCKLING OF STEEL BEAMS STRENGTHENED WITH GFRP PLATES

CHAPTER 5: ANALYTICAL AND NUMERICAL STUDY FOR ULTIMATE CAPACITY OF STEEL BEAMS STRENGTHENED WITH GFRP PLATES

CHAPTER 7: HIGH-ORDER THEOY FOR THE STATIC ANALYSIS OF BEAMS WITH MONO-SYMMETRIC CROSS-SECTIONS

CHAPTER 8: FINITE ELEMENT FORMULATION FOR THE ANALYSIS OF MULTILAYER BEAMS BASED ON THE PRINCIPLE OF STATIONARY COMPLEMENTARY STRAIN ENERGY

CHAPTER 9 – SUMMARY, CONCLUSIONS AND RECOMMENDATIONS

List of Figures

Introduced in Chapter 1

Introduced in Chapter 2

Introduced in Chapter 3

Introduced in Chapter 4

Introduced in Chapter 5

Introduced in Chapter 6

Introduced in Chapter 7

Introduced in Chapter 8

List of Tables

Introduced in Chapter 7

Introduced in Chapter 8

Introduced in Chapter 9

Chapter 1: Introduction

1.1. Introduction and Motivation

A variety of advanced fiber-reinforced polymer (FRP) plates/sheets are being widely produced nowadays for the strengthening of existing structures. Of the many fiber types (e.g., glass, carbon, aramid, basalt or even wood), Glass and Carbon FRP are gaining momentum in strengthening of steel structures given their advantages; primarily the ease and speed of installation and lightweight compared to welded or bolted steel plates. FRP plates are bonded to the steel surface through a relatively thin layer of adhesive.

The vast majority of past studies focused on the use of carbon-FRP (CFRP) plates given their higher Young modulus which can exceed that of steel (Harries and El Tawil 2008, Shaat and Fam 2009, Ghafoori et al 2012). On the other hand, GFRP plates are considerably lower in cost than CFRP and their lower Young modulus can be compensated for by using thicker plates (El Damatty and Abushagur 2003, El Damatty et al 2003). Thicker GFRP plates also offer an added advantage over thin CFRP sheets when strengthening steel components subjected to compressive stresses, and thus have the potential of increasing local buckling strength of steel plates (Aguilera and Fam 2013, Zaghian 2015). Additionally, when in contact with steel, GFRP plates do not induce galvanic corrosion.

The present thesis focuses on steel beams strengthened with GFRP plates bonded to the compression and/or tension flanges. A number of analytical and numerical models for the behavior and response of steel-adhesive-GFRP systems are developed based on various modes of failure, and their validity are assessed through comparisons with 3D finite element analysis. The models are then used to predict the response and capacity of the strengthened beams (e.g., stresses, deflections, buckling strength, ultimate capacity, etc.). Parametric studies are conducted based on the models developed and, where applicable, simple analytical solutions are developed for design.

A summary of failure modes of GFRP-strengthened steel beams is given in Section 1.2. Section 1.3 surveys the relevant experimental, analytical, and numerical studies on the steel beams strengthened with GFRP plates. Section 1.4 presents a review of multi-layer beams made of other materials. A general outline of the thesis is then presented in Section 1.5.

1.2. Possible modes of failures

1.2.1. Bare steel beams

Possible failure modes for beams with bare steel sections (e.g., CSA-S16 2016) include (1) local buckling occurring in the web or flanges (Figure 1.1a), (2) lateral torsional buckling (Figure 1.1b), and

(3) cross-sectional moment resistances, based either on the first yield or on the fully plastified section (Figure 1.1c). Based on these failure modes, a 4-step design is typically provided to evaluate the moment resistance of the wide flange beam section. The steps according to CSA-S16 are summarized in the following:

Step 1-Classification of the steel section: Section classification is intended to ensure that the occurrence of local buckling in the flange and/or web do not occur before the attainment of cross-sectional failure, either based on first yield, full plastification of the section. Based on sectional dimensions and the yield strength, steel sections are classified into four classes (1 through 4) as shown in Table 1.1 for a wide flange section with a flange width b, a flange thickness t_f, a web clear height h_w, a web thickness t_w and a steel yield strength F_y. Class 1 and 2 sections (also termed as compact in ANSI/AISC 360-16) attain their plastic moment resistance before undergoing local buckling. Class 3 sections (subcompact) attain their elastic moment resistance prior to buckling locally, but do not attain the plastic moment resistance, while Class 4 sections (slender) buckle locally prior to attaining their elastic moment resistance.

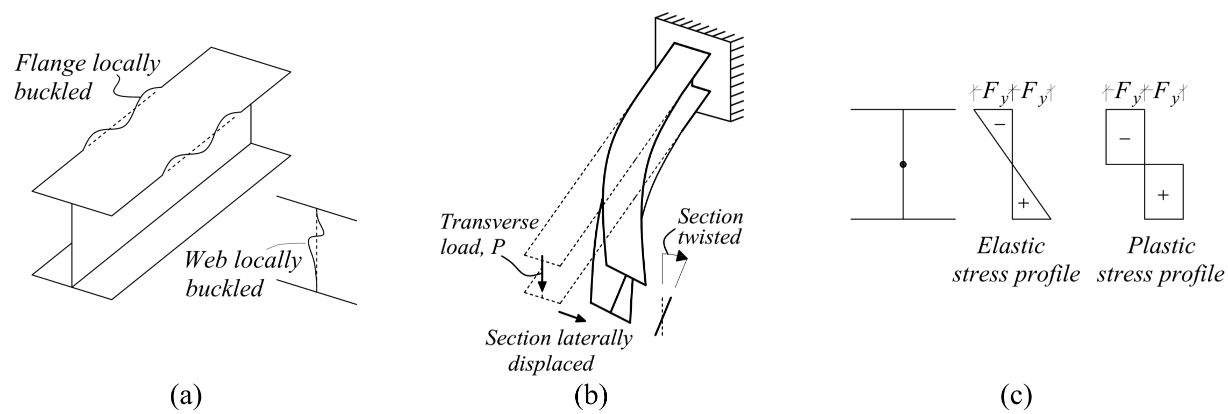

Figure 1.1. Possible failure modes of a wide flange beam (a) local buckling, (b) elastic lateral torsional buckling and (c) sectional moment resistances: elastic stress profile for yielding moment and plastic stress profile for plastic moment

Table 1.1. Section classification limits

Component	Class 1	Class 2	Class 3
Flange	$\frac{b}{2t_f} \le \frac{145}{\sqrt{F_y}}$	$\frac{b}{2t_f} \le \frac{170}{\sqrt{F_y}}$	$\frac{b}{2t_f} \le \frac{200}{\sqrt{F_y}}$
Web	$\frac{h_w}{t_w} \le \frac{1100}{\sqrt{F_y}}\left(1-0.39\frac{C_f}{\phi C_y}\right)$	$\frac{h_w}{t_w} \le \frac{1700}{\sqrt{F_y}}\left(1-0.61\frac{C_f}{\phi C_y}\right)$	$\frac{h_w}{t_w} \le \frac{1900}{\sqrt{F_y}}\left(1-0.65\frac{C_f}{\phi C_y}\right)$

Note: Elements with ratios exceeding Class 3 limits are Class 4 sections, C_f *=compressive force,* C_y *= Flange yield strength, and* ϕ *=resistance factor = 0.9.*

Step 2- Cross-sectional strength: Beams with Class 3 sections are designed based on the first yield of the extreme fibers as depicted in Figure 1.1c and the corresponding yielding moment capacity M_y is given by

$$M_y = S_x.F_y \tag{1.1}$$

where S_x is the elastic section modulus given by $S_x = 2\left[bt_f^3/6 + bt_f\left(h_w + t_f\right)^2/2 + h_w^3 t_w/12\right]/h$ when the fillets are omitted. Beams with section classes 1 and 2, are designed based on the plastic moment capacity corresponding to the full plastification of the cross-section (Figure 1.1c) and the corresponding plastic moment M_p is given by

$$M_p = Z_x.F_y \tag{1.2}$$

where $Z_x = bt_f\left(d - t_f\right) + 0.25t_w\left(d - 2t_f\right)^2$ is the plastic section modulus.

Step3-Elastic lateral torsional buckling: According to CSA S16-14, the elastic buckling resistance M_u is evaluated as

$$M_u = \frac{C_b \pi}{L_u}\sqrt{EI_y GJ + \left(\frac{\pi E}{L_u}\right)^2 I_y I_{\omega\omega}} \tag{1.3}$$

where L_u is the unbraced length of the beam segment, I_y is the moment of inertia about the weak axis, J is Saint Venant torsional constant, $I_{\omega\omega}$ is the warping constant, E is the steel modulus of elasticity and G is the steel shear modulus . C_b is the moment gradient that depends upon on the moment distribution within the unbraced length L_u and is approximated by

$$C_b = \frac{4M_{\max}}{\sqrt{M_{\max}^2 + 4M_a^2 + 7M_b^2 + 4M_c^2}} \leq 2.5 \tag{1.4}$$

where M_a, M_b, M_c are quarter point moments values obtained from the moment diagram (Figure 1.2) and $M_{\max}$ is the peak bending moment value within the span L_u.

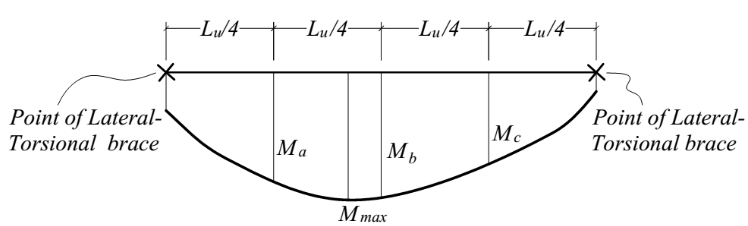

Figure 1.2. Moment diagram

Step 4: Flexural moment resistance: For long unsupported spans L_u, the capacity is governed by the elastic lateral torsional buckling capacity while for short spans, the capacity is governed by cross-sectional strength (either the yield or plastic moment). For intermediate spans, inelastic lateral torsional buckling governs the capacity of the beam and the corresponding resistance is estimated from the cross-sectional strength (as determined from Step 2) and the elastic lateral torsional buckling capacity (as determined from Step 3). Figure 1.3a,b presents the nominal moment M versus unbraced length L_u for class 1 and 2 sections and class 3 sections, respectively.

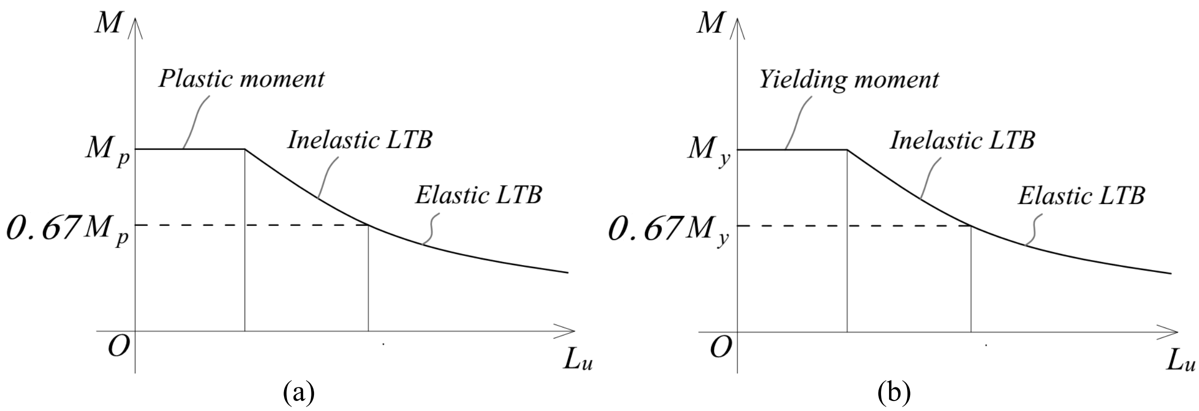

Figure 1.3. Nominal moment resistance against unbraced length for (a) class 1, 2 and (b) class 3

For class 1 and 2 sections, when $M_u < 0.67M_p$ the beam is deemed long and the factored resistance moment is based on the factored elastic lateral torsional buckling strength $M_r = \phi M = \phi M_u$ where $\phi = 0.9$ is the resistance factor. When $M_u \geq 0.67M_p$, the beam is deemed either short or of intermediate length and the factored moment resistance is the lower of the factored plastic moment ϕM_p (short beam) and factored inelastic lateral torsional buckling moment $1.15\phi M_p\left[1-0.28M_p/M_u\right]$ (intermediate beam). A similar procedure is provided for class 3 section by replacing M_p by M_y.

1.2.2. Possible modes of failures for GFRP-strengthened steel beams

The flexural strength of a GFRP-strengthened section is higher than that of the bare steel section (Siddique and El Damatty 2003, Pham and Mohareb 2014, Figure 1.4a). Similar to a bare steel section, a GFRP-strengthened steel section has five modes of failure (Figure 1.1a-c).

(*a*) Local buckling,

(*b*) Elastic lateral-torsional buckling,

(*c*) Inelastic lateral torsional buckling, (*d*) Material flexural strength based on yielding, and

(*e*) Material flexural strength based on plastification.

Additionally, past experimental works by El Damatty and Abushagur (2003) on shear lap splices and by Youssef (2006) on steel beams strengthened with two identical GFRP plates tackled three additional failure modes (Figure 1.4b-d).

(*f*) GFRP plate tension failure,

(*g*) Adhesive shear failure, and

(*h*) Adhesive peeling failure.

Also, Siddique and El Damatty (2013) performed a numerical study on steel beams strengthened with a single GFRP plate bonded to the compressed flange. The model tackled three failure modes: local buckling of the flanges (mode *a*), GFRP plate tension failure (mode *f*), and adhesive shear failure (mode *g*).

Other possible failure modes of the GFRP-strengthened beam may be:

(*i*) Adhesive delamination failure at the steel/adhesive or GFRP/adhesive interfaces (He and Xian 2016): While no experimental studies on GFRP-strengthened-steel beams have reported delamination as possible mode of failure, a number of experimental studies on CFRP-strengthened steel members have observed delamination as a possible mode of failure (Deng and Lee 2007, Stratford and Bisby 2010, Sahin and Dawood 2016).

(*j*) Delamination within the GFRP plate (Yu et al 2012, He and Xian 2016),

(*k*) Cohesive failure within the adhesive layer (Yu et al 2012),

(*m*)Adhesive softening due to thermal effects (Stratford and Bisby 2010, Sahin and Dawood 2016).

(*l*) Fatigue failure (Kamruzzaman et al 2016),

(*n*) Deflection limit states (CSA-S16 2016).

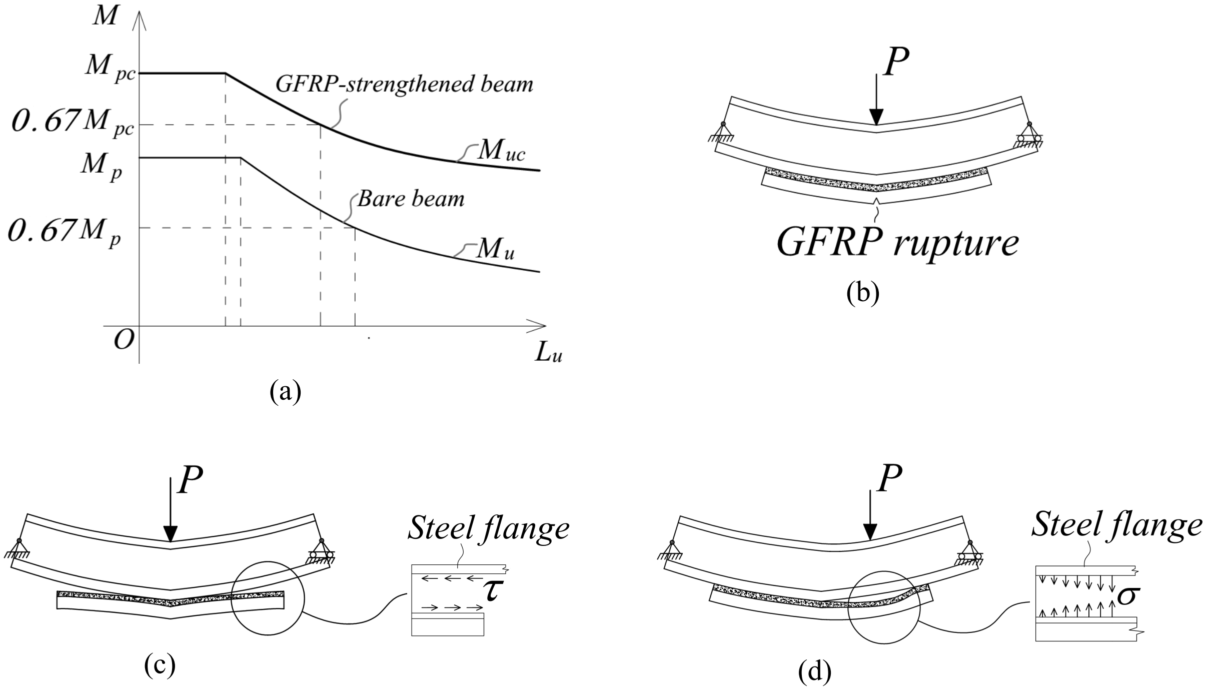

Figure 1.4. (a) Nominal moment resistance against unbraced length for GFRP-strengthened beam and bare beams. Additional failure modes: (b) GFRP plate tension failure, (c) Adhesive shear failure, and (d) Adhesive peel failure

1.3. Scope of present study

Within the above context, the present thesis contributes towards determining the resistance of GFRP-strengthened steel beams based on the following modes of failures:

M1: Local buckling,

M2: Elastic lateral torsional buckling,

M3: Material flexural strength based on yielding,

M4: Material flexural strength based on plastification,

M5: GFRP plate tension failure,

M6: Adhesive shear failure,

M7: Adhesive peeling failure,

M8: Adhesive softening due to thermal effects, and

M9: Deflection limit states.

The approach taken in the present thesis is analogous to that adopted in existing design standards for steel beams where the resistances are quantified based on each of modes M2, M3, and M4 separately, while ensuring that local buckling (mode M1) does not govern the capacity, as by meeting the section classification requirements. Models M1-M4 are equally valid for strengthened steel beams investigated in the present study. The present thesis also develops tools to quantify the resistances based on the additional modes M5-M9 which pertain to GFRP-strengthened steel beams.

1.4. Thesis outline

After the present introductory chapter, Chapter 2 presents a review of the relevant literature. An outline of the contributions of the thesis is provided in the following section. The relevance of each contribution to the above modes of failure is identified where appropriate.

Chapter 3 develops a closed form solution and a finite element formulation for the linear static analysis for steel beams strengthened with a single GFRP plate subjected to general transverse loads. The models capture the partial interaction between the steel and GFRP provided by the relatively soft adhesive layer. The objectives of the study are threefold; (1) conducting the pre-buckling analysis necessary to conduct a lateral torsional buckling analysis (chapter 4), (2) determining the elastic flexural resistance of strengthened steel beams with class 3 (subcompact) sections based on a first yield mode of failure [M3], and (3) quantifying deflection limits [M9].

Chapter 4 then develops a finite element formulation for the elastic lateral torsional buckling analysis of steel beams strengthened with a single GFRP plate [M2]. The model captures the partial interaction between the steel and the GFRP and provides a basis to develop key design information for the design of GFRP-strengthened steel members such as moment gradient effects, load height effect, etc.

Chapter 5 develops analytical procedures to determine the ultimate moment resistance for Class 1 and 2 (compact) sections for steel beams strengthened with a single GFRP plate on the tension side based on full plastification of the steel cross-section [M4]. Consideration is given to tension failure of the GFRP plate [M5], shear failure of the adhesive [M6]. This part of the study is intended to complement chapter 3, which provides a basis to determine the capacity of GFRP-strengthened steel members made of class 3 sections based on a first yield limit state. Attention is given to relatively strong adhesives (e.g., common adhesives at room temperature) as well as weak adhesives (at elevated temperatures) [M8]. The study also proposes a methodology for classifying steel beams strengthened with GFRP plates to ensure that local buckling does not occur prior the attainment of the ultimate moment resistance [M1].

As practical considerations in the field may not enable the designer to fully unload an existing beam prior to strengthening it, it becomes of practical interest to quantify the detrimental effects of pre-existing loads on the strength gained by GFRP strengthening. Towards this goal, Chapter 6 develops a solution that captures this effect for the case of steel beams strengthened with GFRP plates bonded to the tensile and/or compressive flanges. The solution provides means to determine the elastic flexural resistance of strengthened beams with class 3 (subcompact) sections based on a first yield mode of failure [M3], and to quantify deflections for such system, a requirement to satisfy mode of failure [M9].

As identified under section 3, peeling is a possible mode of failure [M7] that may take place when the transverse stresses within the adhesive, at the steel-adhesive interface, or GFRP-adhesive interface exceed a threshold value. Past solutions as well as those presented in chapters 3-6 assume the GFRP and steel beam undergo equal transverse deflections and thus do not provide means to capture the peeling stresses at the interface. A more advanced theory is thus needed to allow the relative transverse displacement between the steel beam and the GFRP plate, thus capturing the peeling stresses. Towards this goal, a higher order beam theory is developed to capture transverse normal stresses (peeling stresses, [M9]) in addition to longitudinal, and shear stresses. A theory is first developed in Chapter 7 to account for transverse stresses for homogeneous beams. The solution provides the governing field equations and develops a closed form solution. The work is then extended in Chapter 8 to develop a finite element analysis formulation for general multi-layer beams. The developments enable the computation of peeling and shearing stresses [M6, M7] at interfacial stresses in steel beams strengthened with GFRP plates, and extends to other applications including sandwich beams.

Chapter 9 then provides a summary of the contributions and provides recommendations for further research. Also presented in chapter 9 is a discussion on design procedures for GFRP strengthened steel sections and how they relate to the developments made in Chapters 3 through 8. Where applicable, recommendations are made for further research needed to complement the contributions of the present study.

1.5. References

[1-1] Aguilera, J. and Fam, A. (2013), Bonded FRP Plates for Strengthening Rectangular Hollow Steel Section T-Joints against Web Buckling Induced by Transverse Compression, Journal of Composites for Construction, ASCE, 17(4), 421-432.

[1-2] ANSI/AISC-360-16, ANSI/AISC 360-16, Specification for structural steel buildings, American Institute of Steel Construction (AISC), Chicago, IL (2016).

[1-3] CSA, Limit states design of steel structures, Standard CAN/CSA-S16-16, Canadian Standards Association, Mississauga, Ontario (2016).

[1-4] Deng, J., Lee., M.M.K., (2007), Behaviour under static loading of metallic beams reinforced with a bonded CFRP plate, Journal of Composite Structures, 78(2), 232-242.

[1-5] El Damatty, A.A. and Abushagur, M. (2003), Testing and modeling of shear and peel behavior for bonded steel/FRP connections, Thin-Walled Structures, 41(11), 987-1003

[1-6] El Damatty, A., Abushagur, M. and Youssef, M. A. (2003), Experimental and analytical investigation of steel beams rehabilitated using GFRP sheets, Journal of Steel & Composite Structures 3(6), 421-438.

[1-7] Ghafoori, E, Motavalli, M., Botsis, J., Herwig, A., Galli, M., (2012), Fatigue strengthening of damaged metallic beams using prestressed unbounded and bonded CFRP plates, International Journal of Fatigue, 44, 303-315.

[1-8] Kamruzzaman, M., Jumaat, M.Z., Sulong, N.H.R., and Islam, B.M.S., (2014), A review on strengthening steel beams using FRP under fatigue, The scientific world journal, 2014, 702537.

[1-9] Stratford, T.J. and Bisby, L.A., (2010), Temperature effects in adhesively bonded FRP strengthening applied to steel beams: Experimental observations, the 5th international conference of FRP composites in civil engineering, Beijing, China.

[1-10] Harries, A.K. and El-Tawil, S. (2008), Steel-FRP composite structural systems, International Conference on Composite Construction in Steel and Concrete 2008, Composite Construction in Steel and Concrete VI, Devil's Thumb Ranch, Tabernash, Colorado, United States, 703-716.

[1-11] He, J., and Xian, G., (2016), Debonding of CFRP-to-steel joints with CFRP delamination, Composite Structures, 153, 12-20.

[1-12] Pham, P.V. and Mohareb, M. (2014), A shear deformable theory for the analysis of steel beams reinforced with GFRP plates, Thin-Walled Structures, 85, 165-182.

[1-13] Sahin, M.U., and Dawood, M., (2016), Experimental investigation of bond between high-modulus CFRP and steel at moderately elevated temperatures, Journal of Composites for Construction ASCE, 20 (6), 04016049.

[1-14] Shaat, A., and Fam, A. (2009). Slender Steel Columns Strengthened Using HighModulus CFRP Plates for Buckling Control. Journal of Composites for Construction, 13(1), 2-12.

[1-15] Siddique, M.A.A. and El Damatty, A.A. (2013), Improvement of local buckling behaviour of steel beams through bonding GFRP plates, Composite Structures, 96(6), 44-56.

[1-16] Youssef, M. (2006), Analytical Prediction of the Linear and Nonlinear Behaviour of Steel Beams Rehabilitated using FRP Sheets. Engineering Structures, 28(6), 903-911.

[1-17] Yu, t., Fernando, D., Teng, J.G., and Zhao, X.L., (2012), Experimental study on CFRP-to-steel bonded interfaces, Composite: Part B, 43, 2279-2289.

[1-18] Zaghian, S. (2015), Buckling analysis of steel plates reinforced with GFRP, Master of Science thesis, University of Ottawa.

Chapter 2: Literature Review

2.1. General

The present chapter reviews the experimental, numerical and analytical studies relevant to the objectives of the research as outlined in Chapter 1. A brief review of experimental studies on GFRP-strengthened steel beams is first presented in Section 2.2. The mechanical properties of GFRP and adhesives used to bond GFRP to steel are reviewed in Section 2.3. Section 2.4 then reviews the linear static analyses for GFRP-strengthened steel beams and relevant methodological aspects in multi-layer beams of other materials, as they relate to the linearly elastic models in Chapters 3 and 6. Next, a review on relevant buckling solutions is presented in Section 2.5 as it provides a foundation for the developments in Chapter 4. Section 2.6 then reviews past studies aimed at determining the ultimate moment capacity for composite beams as they relate to the developments proposed under Chapter 5. Finally, Section 2.7 discusses technical challenges to be addressed in the high-order beam solutions to be developed in Chapters 7 and 8 as observed in past studies along with methodological aspects as identified in relevant past studies.

2.2. Experimental studies on steel beams strengthened with GFRP plates

Most experimental studies focused on investigating the increase in load capacity and local buckling strength attained by GFRP strengthening. Also, failure modes of adhesives connecting the steel to the GFRP have been investigated.

Youssef (2006) reported an increase in ultimate load capacity of 61% for a W150x37 steel beam strengthened by bonding two GFRP plates to the top and bottom flanges. Siddique and El Damatty (2013) reported a load capacity increase of 15% for W150x37 steel beams strengthened with a single GFRP plate bonded to the tension flange. Aguilera and Fam (2013) reported an increase in strength from 9% to 53% for rectangular hollow steel section (HSS) T-joints strengthened with GFRP plates bonded to the face of the HSS.

Several experimental studies have shown that bonding GFRP plates to the compression zone of a steel beam result in a delay of the onset of global buckling. Accord and Earls (2006) strengthened the compression flange of W-section cantilever steel beams with four GFRP plates in order to assess the ability of the strengthening arrangement on reducing deflections. Harries et al. (2009) strengthened the stem of WT compression members by GFRP plates to assess the ability of the strengthened system to delay local buckling and increase the global buckling capacity. Aydin and Aktas (2015) extended the study to cruciform steel plates under compression strengthened with GFRP plates.

The response prediction (i.e., stresses, deflections) of steel beams strengthened with GFRP can be challenging when the adhesive layer provides only partial interaction. This is particularly the case for interfacial stresses at the bonding surfaces. El Damatty and Abushagur (2003) and El Damatty et al. (2005) performed experiments to investigate the mechanical properties and modes of failure of the adhesive layer and showed that the interfacial stresses near the ends were significant due to stress concentration, which can induce delamination failure between adhesive and adjoining materials. Similar conclusions have been observed in the experimental studies of Tavakkolizadeh and Saadatmanesh (2003), Xia and Teng (2005) and Schnerch et al. (2006) for steel beams strengthened with single FRP plates.

2.3. Mechanical properties of GFRP plates and Adhesives

2.3.1. GFRP plates

Several studies investigated the mechanical properties of GFRP plates. The tensile strength of GFRP plates are reported in the work of El Damatty et al. (2003, 2012, 2013), Holloway et al. (2006), Teng and Hu (2007), Shaat and Fam (2008), Correia et al (2011), and Torabizaheh (2013). The compressive strength of GFRP plates were reported in the work of El Damatty et al. (2003), Westover (1998) and Correia et al. (2011). Table 2.1 provides a summary of GFRP properties as reported in key studies. Westover (1998) and Correia et al. (2011) provided a review of the compressive properties of pultruded GFRP composites and indicated that the compressive strength ranges from 20% to 80% of the tensile strength. Also, Correia et al. (2011) suggested that the GFRP modulus of elasticity in compression can be taken as 80% of its tensile modulus (as depicted in Fig. 2.1). A nonlinear behavior of compressed GFRP plates was also observed in their study.

In most studies, GFRP plates/laminates are made by weaving of fibers at $0^0/90^0$ degrees and loads are applied along the longitudinal direction of the fiber. GFRP plates with different weaving angles were also investigated in Holloway et al. (2006), and Mallick (1988). Mallick (1988) suggested that isotropic response in the plane of laminates/plates can be obtained in GFRP plates with random orientation.

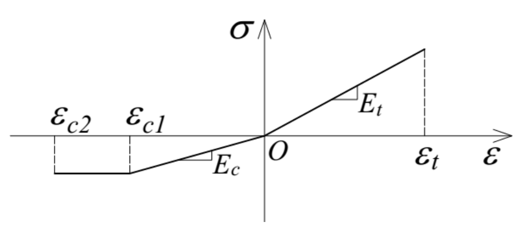

Figure 2.1. Tensile and Compressive behaviour of GFRP material

Table 2.1. Summary of the mechanical properties of GFRP plates

Reference	Tension Response			Poisson's Ratio	Compression Response			
	E_t (GPa)	σ_t (MPa)	ε_t (%)		E_c (GPa)	σ_c (MPa)	ε_{c1} (%)	ε_{c2}
Westover (1998)	Not mentioned			-	19.3	241	1.25	
El Damatty et al (2003)	17.2	930	0.83	0.37	Not mentioned			
Yao et al (2003)	23.0	240	1.04	0.23	23.0	240	1.04	
Holloway et al (2006)*	16.0	215	1.70	0.15	Not mentioned			
Youssef (2006)	12.4	135	1.09	-	12.4	165	1.33	
Teng and Hu (2007)	80.1	1825.5	2.28	-	Not mentioned			
Shaat and Fam (2007a,b)	14.0	269	1.90	-	Not mentioned			
Harris and Tawil (2008)	42.0	896	2.10	-	Not mentioned			
Correia et al (2011)	32.8±0.9	476±25.5	15±1.5	-	26.4±1.9	356±67.9	-	17±2.5
El Damatty et al (2012)	13.8	206.8	1.50	0.31	Not mentioned			
Siddique and El Damatty (2013)	17.2	206.8	1.20	0.33	17.2	206.8	1.20	
Torabizaheh (2013)	23.1	700	3.70	-	23.1	570	0.30	
Liu et al. (2014)	25.0	1324	5.30	-	25.0	330	1.32	
Ascione et al. (2015)	28	240	-	-	28	240	-	-

*Glass fiber direction oriented at $\pm45^0$

In Table 2.1, the mechanical properties of GFRP plates in the studies of El Damatty et al (2003), Youssef (2006), El Damatty et al (2012), Siddique and el Damatty (2013) are based on manufacturers' information while those of other studies are based on material testing.

2.3.2. Adhesives

A comparative summary of adhesive types and properties used for bonding GFRP to steel members is presented in Table 2.2. In these studies, the tensile strength, modulus ratio, Poisson ratio, and ultimate tensile strains were reported. Additional tests on MA 420 adhesive based on shear lap tests were conducted by El Damatty and Abushagur (2003) who found that the maximum shear strength ranged from 20.9 to 34.3 MPa while the maximum peeling stresses ranged from 0.72 to 6.01 MPa.

Table 2.2. Mechanical properties of adhesive materials for bonding GFRP to steel

Authors	Adhesive Type	Tensile strength (MPa)	Young's Modulus (MPa)	Poisson's ratio	Ultimate tensile strain (%)
Miller et al. (2001)	AV8113/HV8113	13.8-17.2	107	-	-
	PlexusMA555	8.6-10.3	-	-	-
Damatty et al. (2003)	MA 420	15.5	-	-	-
Schnerch (2006)	SP Spabond	37.1	3007	0.38	0.0132
	SP spabond 345	34.6	3007	0.38	0.0132
Shaat and Fam (2007)	Typo S	72.4	3180		
Shaat and Fam (2009)	Sikadur-30	33	13000	-	-
Linghoff et al. (2010)	Epoxy 1	25	7000	-	-
	Epoxy 2	30	4500	-	-
Peiris (2011)	SP Spabond 345	34.6	3007	0.38	0.0132

2.4. Linear analysis solutions

Since the models in Chapters 3 and 6 are based on linear analyses, the present section reviews relevant elastic models. Section 2.4.1 reviews linear elastic models for steel beams strengthened with GFRP while Section 2.4.2 presents linear elastic solutions on multilayer beams of other material given the relevance of the underlying methodologies.

2.4.1. Steel beams strengthened with GFRP plates

Since the modulus of elasticity for the adhesive layer is much smaller than those of steel and GFRP, relative slip takes place at the steel-GFRP interface and the adhesive layer provides only partial interaction. As a result, a cross-section for the composite system that is originally plane before deformation may not remain plane after deformation (Ranzi et al. 2006, Pham 2013). Traditional analysis methods based on the plane section assumption (e.g., the transformed section method) will thus under-predict deflections, interfacial shear stresses, or buckling loads (Wenwei and Guo 2006). While a number of experimental studies were conducted for steel beams reinforced with GFRP plates, fewer studies have focused on the formulation of linear elastic models for the analysis of such systems. Elastic analytical models and finite element formulations for the analysis of steel beams strengthened with a single GFRP plate were developed by Pham and Mohareb (2014, 2015a,b) in which non-shear and shear deformable theories were developed for the static analysis of such systems. The longitudinal-transverse and lateral-torsional responses were investigated. Comparisons with 3D FEA modeling indicate that the effect of shear deformation is particularly important to reliably predict the static lateral-torsional response. The finite element solution based on the shear deformable solution for the longitudinal-transverse response was based on conventional Hermitian interpolation shape functions, and thus involved a discretization error, which can be reduced by increasing the number of elements. Within this context, chapter 3 of the thesis aims at developing a general closed form solution for the resulting coupled differential equations of equilibrium and formulating a superior finite element solution that converges to the exact solution while keeping the number of elements to a minimum.

Prior to strengthening a beam with GFRP, it would be ideal to entirely unload the beam. This condition may be difficult to achieve in practice. For instance, while it may be feasible to remove the live loads, it can be impractical to remove the dead loads. In the case where only partial unloading is attainable, the pre-existing deformations and stresses will typically have a detrimental effect on the additional strength gained by GFRP strengthening. There appears to be no studies to capture the detrimental effect of pre-existing loads prior to strengthening on the resistance achievable of the strengthened system. Thus, chapter 6 of the thesis develops an analytical model that accounts for the effect of pre-existing stresses when strengthening steel beams with GFRP plates.

2.4.2. Multilayer beam solutions for other materials

Since Chapters 3 focuses on developing analytical models and finite element formulations for strengthened beams, relevant methodological contributions include the work of Ganapathi et al. (1999), Perel and Palazotto (2001), Frostig et al. (1992), Dall'Asta (2001), Nowzartash and Mohareb (2005), Challamel et al. (2010). These studies capture the partial interaction between different materials but are limited to rectangular sections. Back and Will (2008), Vo and Lee (2009) and Vo and Lee (2013) developed shear deformable finite element formulations for the flexural analysis of layered composite I-beams based on Lagrange shape functions. Formulations involving steel-concrete composite systems include the work of Salari et al. (1998), Ayoub (2001), Ranzi et al. (2006), Ranzi and Zona (2007), and Faella et al. (2010). Nguyen et al. (2011) derived an exact stiffness matrix for a two-layer Timoshenko beam element which captures the effect of partial interaction. Shaat and Fam (2009), Zona and Ranzi (2011), Elchalakani and Fernando (2012), Ritchie et al. (2014), Ghafoori and Motavalli (2013) presented simplified analytical and/or numerical solutions for steel beams strengthened with CFRP laminates. While most previous studies captured partial interaction effects, some of them were intended for sandwich beams with thick cores and are not particularly suited for GFRP plates bonded to steel through rather thin adhesive layers. The concrete-steel composite beams tend to focus on the nonlinear material response of concrete including cracking, which is not representative of that of steel-GFRP systems of interest in the present research. Available models for steel-CFRP strip models tend to postulate full interaction and may not be representative of the partial interaction behavior characteristic of GFRP-steel systems with a relatively low modulus adhesive.

Also, since CFRP strips tend to be thin (typically less than 2 mm) they tend to have a negligible flexural stiffness. In contrast, GFRP plates are typically thick (up to 19 mm or higher) with a considerable flexural stiffness accounted for in the present study.

Chapter 6 develops a model that accounts the pre-existing stresses/strains prior to strengthening. Relevant methodological work includes the work of Ghafoori and Motavalli (2013) who developed analytical models for the analysis of wide flange steel beams strengthened by a single pre-tensioned CFRP plate at the tensile flange, but did not capture the effect of preloading in the steel beam. Also, Wenwei and Guo (2006) and GangaRao et al. (2007) investigated concrete beams strengthened with FRP plates while incorporating the effect of initial stresses/strains. Both studies adopted the transformed section method and are thus limited to the case of full interaction. In this context, the present study develops a solution for the case of partial interaction.

2.5. Buckling Solutions

2.5.1. Steel beams strengthened with GFRP plates

GFRP plates are relatively thick and can withstand compressive stresses and/or bending. Thus, bonding a GFRP plate to the compression flange of a steel beam can delay the occurrence of local buckling. As discussed in Section 1, several experimental studies have shown that bonding GFRP plates to the compression flange of a steel beam delays the onset of global buckling (Accord and Earls 2006, Harries et al. 2009, Aydin and Aktas 2015, Aguilera and Fam 2013). A few studies numerically investigated the advantages of this type of strengthening. This includes the work of Siddique and Damatty (2012, 2013) who developed a finite element formulation and adopted it to investigate the enhancement of the buckling capacity of steel beams strengthened with GFRP plates. The numerical model was based on a 13-node consistent degenerated triangular sub-parametric shear-locking free shell elements. Each layer (GFRP, steel) was modelled by a shell element while the adhesive layer joining them was modelled by two-dimensional distributed springs with zero thickness to represent its shear stiffness and a transverse spring to represent the peeling behavior at the steel-GFRP interface. Zaghian (2015) developed a non-conforming four-node finite shell element for the buckling analysis of steel plates strengthened with GFRP plates. The solutions were observed to underestimate the buckling stresses by around 10-15%. While the above studies have focused on developing models to predict the local buckling strength of steel- adhesive- GFRP systems, no studies have tackled the problem of global buckling of steel beams strengthened with GFRP plates. Within this context, chapter 4 of the present thesis aims at developing a finite element formulation for the lateral-torsional buckling analysis of steel-adhesive- GFRP systems which accounts for the partial interaction provided by the adhesive. The linear static analysis conducted in chapter 3 provides the pre-buckling resultant forces needed prior to the buckling analysis.

2.5.2. Multilayer beam solutions for other materials

Buckling analysis models for composite systems include the work of Girhammar and Pan (2007) who developed an Euler-Bernoulli beam theory for the prediction of buckling loads of two-layer beams with deformable shear connectors. Xu and Wu (2007) developed a Timoshenko beam theory to predict the buckling capacity of two-layer members with partial interaction. Challamel and Girhammar (2012) formulated a non-shear deformable theory for the lateral torsional buckling analysis of layered composite beams with accounting for the effect of partial interaction between the layers. A limitation in the previous models is that they are limited to beam with rectangular sections and hence are not suitable for the analysis of steel beams with I-sections strengthened with GFRP plates sought in the present study. Also, most studies neglected shear deformations effects. Exceptions include the lateral torsional buckling solutions for homogeneous beams (Erkmen and Mohareb 2008, Wu and Mohareb 2011a,b) where it was shown that shear deformation has an detrimental effect for short-span beams. Thus, the present study benefits from past observation by incorporating the effect of shear deformation due to bending and warping in the sought lateral torsional buckling analysis of steel beams strengthened with GFRP.

2.6. Ultimate moment models

2.6.1. GFRP-strengthened steel beams

The ultimate moment capacity for bare steel beams is well established in design standards (e.g., CSA-S16 2016, ANSI/AISC 360-16), while the cross-sectional failure modes of the steel beams strengthened with GFRP plates were observed in numerical and experimental studies. Youssef (2006) conducted an experimental study on a wide flange steel beam strengthened with GFRP plates bonded to the top and bottom flanges. The author also developed an analytical model to estimate the ultimate load capacity of steel beams strengthened with two identical GFRP plates and assumed a constant longitudinal stress across the GFRP plate thickness. Siddique and El Damatty (2013) developed a nonlinear finite element model to predict the moment deformation relations of steel beams strengthened with GFRP plates. The authors identified three possible failure modes that can govern the ultimate moment capacity of the strengthened system (1) local buckling of the flanges, (2) adhesive shear failure and (3) GFRP plate tension failure. Since the study of Youssef (2006) is confined to steel beams strengthened with two identical GFRP plates, chapter 5 develops ultimate moment solutions for a wide flange steel beams strengthened with a single GFRP plate bonded to the tension flange.

2.6.2. Multilayer beam solutions for other materials

Chapter 5 develops simplified design solutions for ultimate load capacity of GFRP-strengthened steel beams. Relevant analytical solutions include the work of Wenwei and Gou (2006), Schnerch et al. (2007) and Skuturna and Valivonis (2014) who developed design equations for ultimate load capacity of concrete beams strengthened with CFRP plates under bending. However, their models assumed a plane strain profile for the entire composite cross-section. Such an assumption led to an overestimation for the beam stiffnesses and an underestimation for the ultimate load capacity (Haghani and Al Emrani 2012a,b). Ghafoori and Motavalli (2013) and Liu and Dawood (2018) presented analytical solutions for interfacial stresses corresponding to the adhesive shear failure mode of steel beams bonded with CFRP plates. Although the partial interaction between steel and CFRP plate was considered, the authors assumed that both steel and CFRP remain elastic until the adhesive failure and while adhesive exhibits an elasto-plastic material behaviour. In this respect, Linghoff et al. (2010) experimentally showed that at failure, the steel undergoes plastic deformation. Also, in Ghafoori and Motavalli (2013) and Liu and Dawood (2018), it is assumed that the adhesive failure takes place prior to the CFRP rupture. While this assumption is likely valid for CFRP owing its relatively high tensile strength, it is not necessarily the case for GFRP with significantly lower tensile strength (El Damatty and Abushagur 2003). Such considerations are accounted for in the models developed in Chapter 5.

2.7. Interfacial shear and peeling stresses

2.7.1. Considerations based on past 3D FEA modelling of GFRP-strengthened steel beams

A possible failure mode of steel beams strengthened with GFRP plates is the delamination of the adhesive (El Damatty et al. 2003, Xia and Teng 2005) due to the high interfacial stresses occurring at the bond interfaces near the ends of the GFRP plate. However, an analytical solution for the interfacial stresses of GFRP-strengthened steel beams is not found in the literature. El Damatty et al (2003) numerically investigated the adhesive shear and peeling stress distributions in a concrete slab-steel girder system adhesively bonded with a GFRP plate at the steel bottom. The steel girder, concrete slab and GFRP plate were modeled by using beam elements with vertical rigid arms and the adhesive layer was modeled using linear springs.

Based on 3D FEA analyses, Pham and Mohareb (2015c, d) showed that transverse shear stresses and peeling stresses are significant at the edges. A schematic distribution of such interfacial stresses in a simply supported steel beam strengthened with a GFRP plate is shown in Figure 2.2. Although 3D FEA models generally provide reliable predictions of stresses in homogeneous continua, when used to predict the shearing and peeling stresses at the bond interfaces they are known to violate the infinitesimal equilibrium conditions at the interface. For example, the shear and peeling stresses along a transverse line of the strengthened flange from Points 1 through 6 (as depicted in Figure 2.3) extracted from a 3D FEA model are presented in Figure 2.4. As observed at the steel-adhesive interface, the interfacial stresses σ_2, τ_2 at Point 2 (as defined in Figure 2.3) are found different from the stresses σ_3, τ_3, at Point 3, as depicted by the stress jumps in Figure 2.4. A similar observation is made for the interfacial stresses σ_4, τ_4 at Point 4 and σ_5, τ_5 at Point 5. The violation of equilibrium condition is a natural outcome of adopting the principle of stationary strain energy. To satisfy the stress equilibrium conditions at interfaces, a beam theory based on the principle of complementary strain energy is appropriate. Wu and Jensen (2011) developed a low order beam theory using the complementary strain energy to approximately predict the interfacial stresses. Stress equilibrium conditions were satisfied at the bond interfaces. However, the theory underestimated the interfacial stresses. The reason was attributed to postulated stress fields with a linear distribution. This may imply that higher order beam theory based on more general stress fields is necessary to provide better predictions for the interfacial stresses. Thus, Chapter 7 in the thesis develops a higher order beam theory that exactly satisfies the stress equilibrium conditions and hence accurately predicts the shear and normal transverse stresses. The implementation of the theory is restricted to homogeneous beams in Chapter 7, and the findings extended to multi-layer beams (such as steel beams strengthened with GFRP) are presented in Chapter 8 where the presence of normal stresses provides a natural way to characterize the peeling stresses within the adhesive.

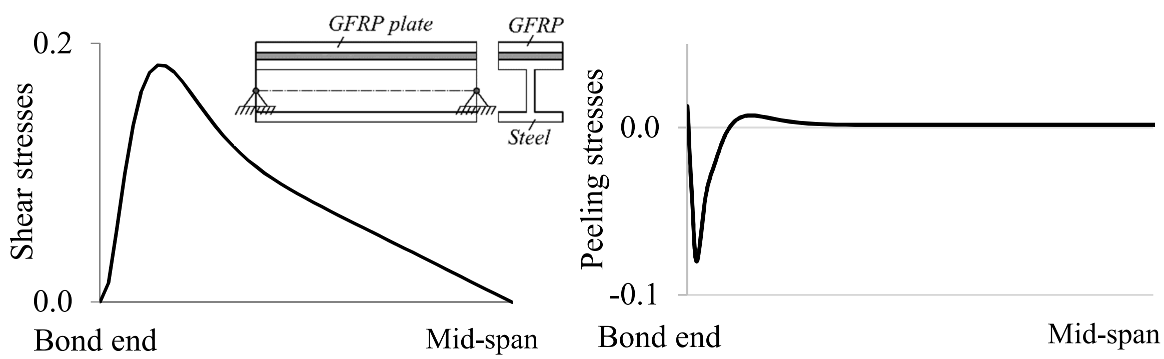

Figure 2.2. Example of interfacial stresses at the adhesive-steel interface

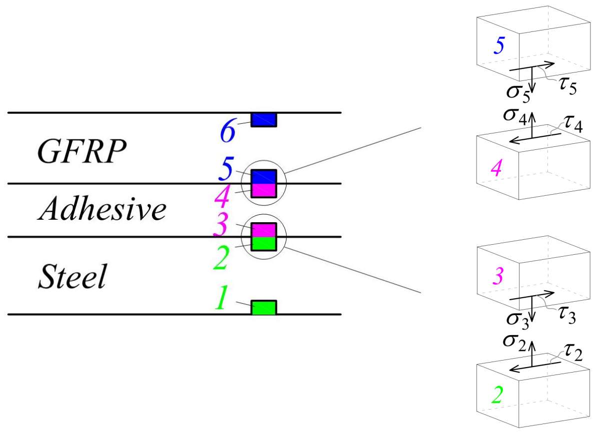

Figure 2.3. Example of stress profile extraction

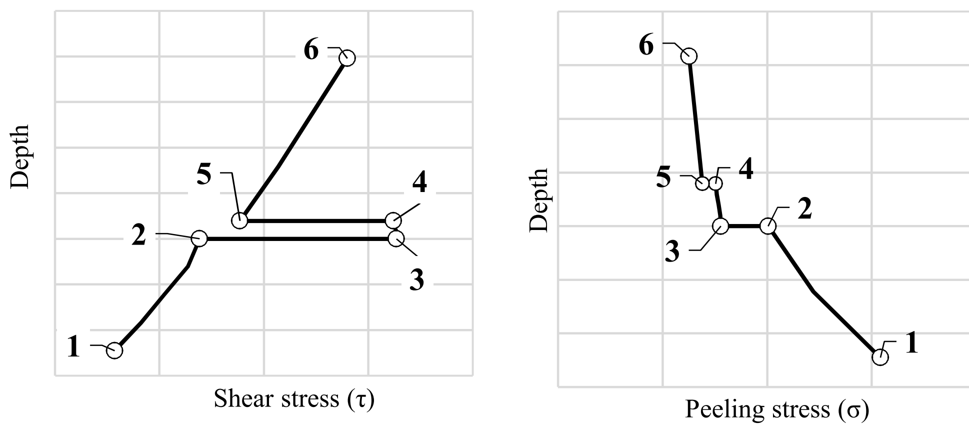

Figure 2.4. Interfacial stress profiles extracted from a 3D FEA solution

2.7.2. Relevant studies

The well-known Euler-Bernoulli and Timoshenko beam theories satisfy equilibrium in an average integral sense, but violate the infinitesimal stress equilibrium condition in the transverse direction since they omit the transverse normal stress. As a result, the Euler-Bernoulli beam theory grossly under-predicts deflections of short span beams, while the Timoshenko beam theory violates the traction equilibrium condition at the extreme fiber and requires the introduction of a shear correction factor to accurately predict deflections. To remedy these problems, more advanced beam theories have been developed. Higher order beam theories were developed by assuming a higher order function for the longitudinal displacement field in conjunction with the conventional principle of minimum potential energy (Figure 2.5a). This includes the work of Stephen and Levinson (1979), Levinson (1981), Reddy (1984), Heyliger and Reddy (1988), Shu and Sun (1994), and Jha et al (2013) who postulated longitudinal displacements with a third order polynomial distribution. These theories are limited to rectangular cross-sections. Another class of solutions based on assuming higher order polynomials for the longitudinal displacements was developed by Carrera (2010), Carrera et al. (2015), Carrera et al. (2015) and Groh and Weaver (2015). Such theories have the advantage of capturing shear deformation and transverse normal stresses without introducing shear modification factors. Irrespective of the kinematic assumptions made, when used in conjunction with the principle of minimum potential energy, such theories lead to approximate differential equations of equilibrium and lead to a stiffer representation of the structure compared to the exact infinitesimal equilibrium conditions based on the theory of elasticity (Figure 2.5b).

In contrast to the conventional treatment, Chapter 7 develops another type of higher order beam theories by postulating a higher order function for the longitudinal stress field in conjunction with the principle of stationary complementary strain energy (Figure 2.5a,b). This treatment is able to (1) naturally capture transverse shear deformations, (2) capture transverse normal stresses, and (3) converge to the exact deflection from above as a complementary energy formulation provides a more flexible representation of the beam.

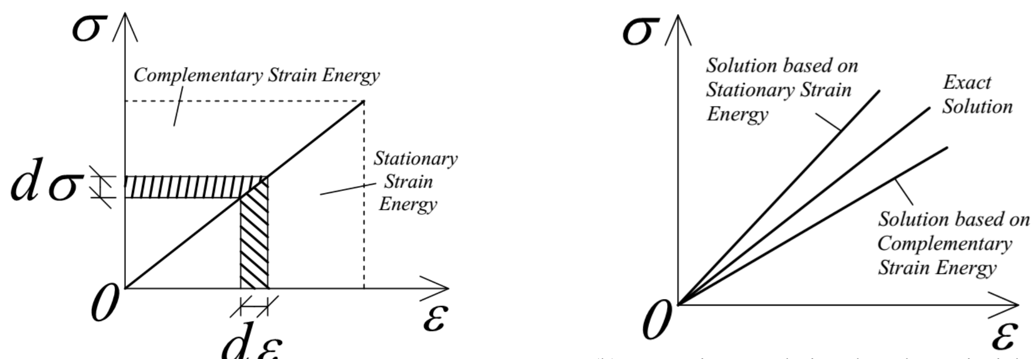

(a) Complementary and Stationary Strain Energies

(b) Approximate Solutions based on principles of stationary complementary strain energy and stationary strain energy

Figure 2.5. General Stress-strain Relationship

In Chapter 8, the developments of Chapter 7 are extended to multi-layer systems. Relevant analytical models include the work of Taljsten (1997), Smith and Teng (2001), Narayanamurthy et al. (2010) who adopted low order beam theories to predict interfacial shear and peeling stresses in rectangular layered beams and validated against older analytical solutions. However, more recent investigations by Wu and Jensen (2011, 2014) who developed similar analytical models based on lower order beam theories have shown that lower order theories considerably underestimate the stresses at the interface when compared to results of 3D FEA solution. The authors concluded that a higher order beam theory is needed for the accurate prediction of interfacial stresses. Carrera (2010), Carrera et al. (2015), and Groh and Weaver (2015) developed higher order beam theories for the prediction of interfacial stresses in layered beams. Their theories were based on the conventional principle of stationary strain energy. Higher order functions were assumed for the longitudinal displacement fields. This treatment provides a stiffer representation of the structure compared to the theory of elasticity (Fig. 2.5b). When applied to layered beams, the conventional treatment based on postulated continuous displacement fields (either linear, cubic, or higher order), while ensures continuity of strains at the interfaces of adjoining materials, leads to discontinuous stresses at the interfaces when such continuous strains are multiplied by significantly different constitutive properties of the adjoining materials. Such stress discontinuities violate the local shear and transverse equilibrium conditions at the interface. Within this context, Chapter 8 contributes to remedying the limitations of the conventional treatment by adopting the principle of complementary total potential energy in conjunction with a higher order stress fields of any order (as chosen by the analyst) to develop a general beam theory applicable to composite beams.

2.8. Summary

The present chapter has summarized the key studies related to each of the contributions in chapters 3 through 8 with an emphasis on the fundamental aspects that need to be treated in the forthcoming solutions. Mechanical properties of GFRP and adhesives were also briefly reviewed. Since the thesis is written in a paper-format, a more detailed literature reviews are provided at the outset of each chapter.

2.9. References

[2-1] Accord, N.B. and Earls, C. J. (2006), Use of Fiber-Reinforced Polymer Composite Elements to Enhance Structural Steel Member Ductility, J. of Composites for Construction, 10(4), 337-344.

[2-2] Aguilera, J. and Fam, A. (2013), Bonded FRP Plates for Strengthening Rectangular Hollow Steel Section T-Joints against Web Buckling Induced by Transverse Compression, Journal of Composites for Construction, ASCE, 17(4), 421-432.

[2-3] Aydin E. and Aktas, M. (2015), Obtaining a permanent repair by using GFRP in steel plates reformed by heat-treatment, Thin-Walled Structures, 94, 13-22.

[2-4] Ayoub, A. (2001), A two-field mixed variational principle for partially connected composite beams, Finite elements in Analysis and Design, 37(11), 929-959.

[2-5] ANSI/AISC-360-16, ANSI/AISC 360-16, Specification for structural steel buildings, American Institute of Steel Construction (AISC), Chicago, IL (2016).

[2-6] Back SY, Will KM (2008). “Shear-flexible thin-walled element for composite I-beams”, Engineering and Structures, 30(5),1447–58.

[2-7] Carrena, E., and Guinta, G., (2010), Refined beam theories based on a unified formulation, International journal of applied mechanics, 2(1), 117-143.

[2-8] Carrena, E., Pagani, A., and Zangallo, F., (2015), Comparison of various 1D, 2D, and 3D models for the analysis of thin-walled box with transverse ribs subjected to load factors, Journal of finite elements in analysis and design, 95(1), 1-11.

[2-9] Challamel, N. (2009), On lateral-torsional vibrations of elastic composite beam with interlayer slip, Journal of Sound and Vibration, 325(4-5), 1012-1022

[2-10] Challamel, N., Bernard, F. and Casandjian, C. (2010), Out-of-plane behavior of partially composite or sandwich beams by exact and finite element methods, Thin-Walled Structures, 48(8), 561-580.

[2-11] Challamel, N. and Girhammar, U.A. (2012), Lateral-torsional buckling of vertically layered composite beams with interlayer slip under uniform moment, Engineering Structures, 34(46), 505-513.

[2-12] Correia, J.R., Branco, F.A., Silva, N.M.F, Camotim, D. and Silvestre, N. (2011), First-order, buckling and post-buckling behaviour of GFRP pultruded beams. Part 1: Experimental study, Computers and Structures, 89(21-22), 2052-2064.

[2-13] CSA, Limit states design of steel structures, Standard CAN/CSA-S16-14, Canadian Standards Association, Mississauga, Ontario (2014).

[2-14] Dall' Asta, A. (2001), Composite beams with weak shear connection, International Journal of Solids and Structures, 38(32-33), 5605-5624.

[2-15] Erkmen, R.E., and Mohareb, M., (2008), Buckling analysis of thin-walled open structures – A finite element formulation, Thin-walled structures, 46, 618-636.

[2-16] El Damatty, A.A. and Abushagur, M. (2003), Testing and modeling of shear and peel behavior for bonded steel/FRP connections, Thin-Walled Structures, 41(11), 987-1003

[2-17] El Damatty, A., Abushagur, M. and Youssef, M. A. (2003), Experimental and analytical investigation of steel beams rehabilitated using GFRP sheets, Journal of Steel & Composite Structures 3(6), 421-438.

[2-18] Elchalakani, M. and Fernando, D. (2012), Plastic mechanism analysis of unstiffened steel I-section beams strengthened with CFRP under 3-point bending, Thin-Walled Structures, 53, 58-71.

[2-19] Faella, C., Martinelli, E., and Nigro, E. (2010), “Steel-concrete composite beams in partial interaction: Closed-form “exact” expression of the stiffness matrix and the vector of equivalent nodal forces”, Engineering Structures, 32(9), 2744-2754.

[2-20] Frostig, Y., and Baruch, M., Vilnay, O., and Sheinman, I. (1992), High-order theory for sandwich-beam behaviour with transversely flexible core, Journal of Engineering Structures, 118(5), 1026-1043.

[2-21] Ganapathi, M., Patel, B.P.m Polit, O., and Touratier, M. (1999), “A C1 finite element including transverse shear and torsion warping for rectangular sandwich beams”, International Journal for Numerical Methods in Engineering, 45(1), 47-75.

[2-22] GangaRao, H.V.S., Taly, N., and Vijay, P.V., (2007), Reinforce Concrete Design, Taylor and Francis Group publisher

[2-23] Ghafoori, E, Motavalli, M., Botsis, J., Herwig, A., Galli, M., (2012), Fatigue strengthening of damaged metallic beams using prestressed unbounded and bonded CFRP plates, International Journal of Fatigue, 44, 303-315.

[2-24] Ghafoori, E, Motavalli, M., (2013), Flexural and interfacial behavior of metallic beams strengthened by prestressed bonded plates, Journal of composite structures, 101, 22-34.

[2-25] Ghafoori, E, Motavalli, M., Zhao, X.L., Nussbaumer, A., Fontana, M. (2015), Fatigue design criteria for strengthening metallic beams with bonded CFRP plates, Engineering Structure, 101, 542-557.

[2-26] Girhammar, U.A. and Pan, D.H. (2007), Exact static analysis of partially composite beams and beam-columns, International Journal of Mechanical Sciences, 49(2), 239-255.

[2-27] Groh, R.,M.,J., and Weaver, P. M., (2015), Static inconsistencies in certain axiomatic higher-order shear deformation theories for beams, plates and shells, Journal of composite structures, 120, 231-245.

[2-28] Haghani, R. and Al Emrani, M. (2012a), A new design model for adhesive joints used to bond FRP laminates to steel beams – Part A: Background and theory, Construction and building Materials, 34, 486-493.

[2-29] Haghani, R. and Al Emrani, M. (2012b), A new design model for adhesive joints used to bond FRP laminates to steel beams – Part B: Experimental verification, Construction and building Materials, 34, 686-694.

[2-30] Harries, K.A., Peck A.J., Abraham, E.J., (2009), Enhancing stability of structural steel sections using FRP, Thin-walled structures, 47, 2092-1101.

[2-31] Heyliger, P. R. and Reddy, J. N., (1988), A higher order beam finite element for bending and vibration problems, Journal of Sound and Vibration, 126(2), 309-326.

[2-32] Hollaway, L.C., Zhang, L., Photiou, N.K., Teng, J.G. and Zhang, S.S. (2006). Advances in Adhesive Joining of Carbon Fibre/Polymer Composites to Steel Members for Repair and Rehabilitation of Bridge Structures. Advances in Structural Engineering, 9(6), 791-803.

[2-33] Jha, D., K., Kant, T., and Singh, R., K., (2013), Stress analysis of transversely loaded functionally graded plates with a higher order shear and normal deformation theory, Journal of engineering mechanics, 139(12), 1663-1680.

[2-34] Levinson, M., (1981), A new rectangular beam theory, J. Sound and Vibration, 74 (1), 81-87.

[2-35] Linghoff, D., Al-Emrani and Kliger, M. R. (2010), Performance of steel beams strengthened with CFRP laminate – Part 1: Laboratory tests, Composites Part B, 41(7), 509-515.

[2-36] Liu, M. and Dawood, M. (2018), A closed-form solution of the interfacial stresses and strains in steel beams strengthened with externally bonded plates using ductile adhesives, Engineering Mechanics, 154, 66-77.

[2-37] Liu, P., Zhao, Q., Li, F, Liu, J, Chen, H., (2014), Research on the Mechanical Properties of a Glass Fiber Reinforced Polymer-Steel Combined Truss Structure, The Scientific World Journal, volume 2014, Article ID 309872, 13 pages.

[2-38] Mallick, P., K., (1988), Fiber Reinforced Composites: Materials, Manufacturing, and Design, Third Edition, Taylor and Francis Group publisher.

[2-39] Miller, C.T., Chajes J.M. and Hastings N.J. (2001), Strengthening of a steel bridge girder using CFRP plates, Journal of Bridge Engineering 6(6), 514-522.

[2-40] Narayanamurthy, V., Chen, J.F., and Cairns, J., (2010), A rigorous solution for interfacial stresses in plated beams, The 5th international conference on FRP composites in Civil Engineering, Beijing, China.

[2-41] Nguyen, Q.H., Martinelli, E., and Hiiaj, M. (2011), Derivation of the exact stiffness matrix for a two-layer Timoshenko beam element with partial interaction, Journal of engineering structures, 33(2), 298-307.

[2-42] Nowzartash, F. and Mohareb, M. (2005), Planar bending of sandwich beams with transverse loads off the centroidal axis, Journal of Structural Engineering, 131(4), 385-396.

[2-43] Peiris, N.A. (2011), Steel Beams Strengthened with ultra High Modulus CFRP Laminates, Doctoral Thesis, College of Engineering, University Kentucky.

[2-44] Perel, V.Y. and Palazotto, A.N. (2001), "Finite element formulation for cylindrical bending of a transversely compressible sandwich plate, based on assumed transverse strains", International Journal of Solids Structures, 38(30-31), 5373-5409.

[2-45] Pham, P.V., (2013), Stress-Deformation Theories for the Analysis of Steel Beams Reinforced with GFRP Plates, Master of Science Thesis, Department of Civil Engineering, University of Ottawa, Ottawa, ON, Canada.

[2-46] Pham, P.V. and Mohareb, M. (2014), A shear deformable theory for the analysis of steel beams reinforced with GFRP plates, Thin-Walled Structures, 85, 165-182.

[2-47] Pham, P.V. and Mohareb, M. (2015a), Finite-Element Formulations for the Spatial Static Response of Steel Beams Bonded to a GFRP Plate, Journal of Engineering Mechanics, ASCE, 141(4), 04014143.

[2-48] Pham, P.V and Mohareb, M. (2015b), Nonshear Deformable Theory for Analysis of Steel Beams Reinforced with GFRP Plate Closed-Form Solution, Journal of Structural Engineering, ASCE, 141(12), 04015063.

[2-49] Ranzi, G., Gara, F., and Ansourian, P. (2006), General method of analysis for composite beams with longitudinal and transverse partial interaction, Computers and Structures, 84(31-32), 2373-2384.

[2-50] Ranzi, G. and Zona, A. (2007), A steel-concrete composite beam model with partial interaction including the shear deformability of the steel component, Engineering Structures 29(11), 3026-3041.

[2-51] Reddy, J. (1984), Energy and variational methods in applied mechanics, John Wiley & Sons.

[2-52] Ritchie, A., Fam, A., and Macdougall, C., (2014), Strengthening long steel columns of S-sections against global buckling around weak axis using CFRP plates of various moduli, Composites and Construction ASCE, 19(4) 0000534.

[2-53] Salari, M.R., Shing, P.B., and Frangopol, D.M. (1998), Nonlinear analysis of composite beams with deformable shear connectors, Journal of Structure Engineering, 124(10), 1148-1158.

[2-54] Skuturna, T. and Valivonis, J., (2014), Design method for calculating load-carrying capacity of reinforced concrete beams strengthened with external FRP, Construction and building Materials, 50, 577-583.

[2-55] Shaat, A., and Fam, A. (2007a), Fiber-Element Model for Slender HSS Columns Retrofitted with Bonded High-Modulus Composites. Journal of Structural Engineering, 133(1), 85-95.

[2-56] Shaat, A., and Fam, A. (2007b). Finite Element Analysis of Slender HSS Columns Strengthened with High Modulus Composites. Steel and Composite Structures, 7(1), 19-34.

[2-57] Shaat, A., and Fam, A. (2008), Repair of cracked steel girders connected to concrete slabs using carbon fiber reinforced polymer sheets, Composites for constructures, ASCE, 12(6), 650-659.

[2-58] Shaat, A., and Fam, A. (2009). Slender Steel Columns Strengthened Using High Modulus CFRP Plates for Buckling Control. Journal of Composites for Construction, 13(1), 2-12.

[2-59] Schnerch, D., Dawood, M., Rizkalla, S., Sumner, E. and Stanford, K. (2006), Bond behavior of CFRP strengthened steel structures, Advances in Structural Engineering, 9(6), 805-817

[2-60] Shnerch, D., Dawood, M., Rizkalla, S., and Sumner, E., (2007), Proposed design guidelines for strengthening of steel bridges with FRP materials, Construction and Building Materials, 21(5), 1001-1010.

[2-61] Shu, X., and Sun, L., (1994), An improved simply higher order theory for laminated composite plates, Journal of computers and Structures, 50(2), 231-236.

[2-62] Smith, S.T. and Teng, J.G., (2001), Interfacial stresses in plated beams, Engineering Structures, 23, 857-871.

[2-63] Siddique, M.A.A. and El Damatty, A.A. (2012), Enhancement of buckling capacity of steel plates strengthened with GFRP plates, Thin-Walled Structures, 60(16), 154-162

[2-64] Siddique, M.A.A. and El Damatty, A.A. (2013), Improvement of local buckling behaviour of steel beams through bonding GFRP plates, Composite Structures, 96(6), 44-56

[2-65] Stephen, N. G. and Levinson, M. (1979), A second order beam theory, Journal of Sound and Vibration, 67 (3), 293-305.

[2-66] Taljsten, B. (1997), Strengthening of beams by plate bonding, Journal of Materials in Civil Engineering, 9(4), 206-212.

[2-67] Tavakkolizadeh, M. and Saadatmanesh, H. (2003), Strengthening of steel-concrete composite girders using carbon fiber reinforced polymers sheets, J. Structural Engineering, 129(1), 30-40.

[2-68] Teng, J.G., and Hu, Y.M. (2007). Behaviour of FRP-jacketed circular steel tubes and cylindrical shells under axial compression. Construction and Building Materials, 21(4), 827-838.

[2-69] Torabizaheh, M.A., (2013), Tensile, compressive and shear properties of unidirectional glass/epoxy composites subjected to mechanical loading and low temperature services, Indian Journal of Engineering & Materials Sciences, 20(4), 299-309.

[2-70] Vo, T.P., and Lee, J. (2009). Flexural-torsional coupled vibration and buckling of thin-walled open section composite beams using shear-deformable beam theory, International Journal of Mechanical Sciences, 51(9-10), 631-641.

[2-71] Vo, T.P., and Lee, J. (2013), Vibration and Buckling of Thin-Walled Composite I-Beams with Arbitrary Lay-Ups under Axial Loads and End Moments, Mechanics of Advanced Materials and Structures, 20(8), 652-665.

[2-72] Wenwei, W. and Guo, L.(2006), Experimental study and analysis of RC beams strengthened with CFRP laminates under sustaining load, Internal journal of solids and structures, 43(6), 1372-1387.

[2-73] Westover, C.M., (1998), The compressive behaviour of Glass Reinforced Composite subjected to local Thermal Loading, Master of Engineering, University of California, Berkeley.

[2-74] Wu, L., and Mohareb, M. (2011a), Buckling of shear deformable thin-walled members — I. Variational principle and analytical solutions. Thin-walled Structures, 49(1), 197 –207.

[2-75] Wu, L., and Mohareb, M. (2011b), Buckling formulation for shear deformable thin-walled members—II. Finite element formulation. Thin-walled Structures, 49(1), 208 –222.

[2-76] Wu, X., F., and Jensen, R. A., (2011), Stress function variational method for stress analysis of bonded joints under mechanical and thermal loads, I. J. of engineering science, 49(3), 279-294.

[2-77] Wu, X., F., and Jensen, R. A., (2014), Semianalytic stress-function variational approach for the interfacial stresses in bonded joints, Journal of Engineering mechanics, 140(11), 1-11.

[2-78] Xia, S.H. and Teng, J.G., 2005, Behaviour of FRP-to-Steel Bonded Joints Proceedings of the International Symposium on Bond Behaviour of FRP in Structures, Hong Kong, 419-426.

[2-79] Xu, R., and Wu Y. (2007), Static, dynamic, and buckling analysis of partial interaction composite members using Timoshenko's beam theory, International journal of mechanical sciences, 49, 1139-1155.

[2-80] Yao, X.F., Kolstein, M.H., Bijlaard, F.S.K, Xu,W., Xu.M., (2003), Tensile strength and fracture of glass fiber-reinforced plastic (GFRP) plate with an eccentrically located circular hole, Journal of Polymer Testing, 22(8), 955-963.

[2-81] Youssef, M. (2006), Analytical Prediction of the Linear and Nonlinear Behaviour of Steel Beams Rehabilitated using FRP Sheets. Engineering Structures, 28(6), 903-911.

[2-82] Zaghian, S. (2015), Buckling analysis of steel plates reinforced with GFRP, Master of Science thesis, University of Ottawa.

[2-83] Zona, A. and Ranzi, G. (2011), Finite element models for nonlinear analysis of steel-concrete composite beams with partial interaction in combined bending and shear, Finite elements in Analysis and Design, 47(2), 98-118.

Chapter 3: Shear Deformable Super-Convergent Finite Element for Steel Beams Strengthened with GFRP Plates

Abstract

The present study develops a super-convergent finite element formulation for steel wide flange beams reinforced with a glass fiber reinforced polymer (GFRP) plate through an adhesive layer. The formulation captures partial interaction and shear deformation effects. Based on a variational principle developed in a recent publication, a general closed form solution is first developed for the governing coupled differential equations of equilibrium. The closed form solution is then used to develop exact shape functions which are subsequently used to develop a super-convergent finite element. The new element is shown to circumvent discretization errors in conventional finite elements based on polynomial interpolation. The element accurately predicts displacements and stresses while keeping the number of degrees of freedom to a minimum. The new element is adopted for the analysis of multi-span continuous beams under transverse loads and investigates shear deformation effects in short-span beams reinforced with GFRP plates. A procedure for the determination of yielding moment for the strengthened beam is proposed. The study also illustrates the importance of shear deformation effects for strengthened beams compared to un-strengthened beams.

Keywords: Steel beams, Glass-fiber reinforced polymer (GFRP), strengthening, exact stiffness matrix, finite element formulation, shear deformation, partial interaction.

3.1. Introduction and Background

GFRP possesses a high strength-to-weight ratio and has a high corrosion resistance. As such, GFRP plates provide a viable alternative for strengthening steel members (Shaat et al. 2004, Harries and El-Tawil 2008). With available plate thicknesses as large as 19mm, GFRP plates can have a significant flexural stiffness and high compressive capacity, when compared to very thin carbon-FRP sheets or plates (Mini et al. 2014, Saribiyik and Caglar 2016). GFRP plates are typically bonded to steel using a thin layer of adhesive with typically low shear modulus thus providing only partial interaction between the steel beam and the GFRP plate. Such systems can be reliably analyzed using 3D finite element modeling. However, such models typically involve a significant effort to build and involve a high computational effort. As such, an effective design of GFRP-strengthened steel members necessitates the development of analytical and 1-D finite element models that are both accurate and simple. Within this context, the present study aims at developing a super-convergent finite element that captures shear deformation effects and models the partial interaction between steel beam and FRP plate, while avoiding mesh discretization errors common in other finite elements and providing accurate predictions of the deformations and stresses.

Analytical models for the analysis of composite beams were developed in various studies including Ditaranto (1973), Gara et al. (2006), Kousawa and Daya (2007), Pham and Mohareb (2015a), and Bai and Davidson (2016). These studies neglected transverse shear deformation effects and thus may overestimate the stiffness for short-span composite beams. To overcome this limitation, shear deformable theories were developed in Akhras and Li (2007), Ranzi and Zona (2007), Back and Will (2008), Dalir and Shooshtari (2015), Pham and Mohareb (2015b), Daouadji et al. (2016), and Ecsedo amd Baksa (2016). While closed form solutions developed in these studies are applicable to single span beams, their extension to systems with multiple spans, and/or general loading becomes impractical. In this respect, finite element solutions offer a practical alternative. Ganapathi et al. (1999) developed a three-noded C1 finite element for rectangular sandwich beams based on Hermittian shape functions. Perel and Palazotto (2001) formulated an element for cylindrical bending of transversely compressible sandwich plates with thick faces and transversely thick cores. Desai and Ramtekkar (2002) proposed a 6-node 2D mixed finite element for analysis of laminated beams. Dall'Asta and Zona (2004) developed a mixed three-field finite element for the non-linear longitudinal-transverse response of steel-concrete beams based on fifth order shape functions. Ranzi et al. (2006) and Ranzi and Zona (2007) developed a 14-degree-of-freedom element. Back and Will (2008) developed a shear deformable finite element formulation for the flexural and buckling analysis of composite I-beams. Their solution was based on two, three, and four-noded elements in which each node possessed 7 degrees of freedom. Lagrangian interpolation shape functions were used. Based on Hermitian cubic and linear interpolation functions, Challamel et al. (2010) developed a 10- and 12- degree-of-freedom elements for the out-of-plane behavior of partially composite or sandwich beams. Pham and Mohareb (2015b) developed a finite element formulation to capture the longitudinal-transverse response of a steel beam strengthened with a GFRP plate through an adhesive layer. Both non-shear and shear deformable elements were included in the study. A common feature in the above studies is the fact that they involve mesh discretization errors, which reduce as the number of elements increase. Thus, for such elements, a mesh study is essential to ensure that discretization errors are kept to a minimum.

Super-convergent finite elements provide an alternative approach to eliminate discretization errors in the solution. The main idea for such elements is to develop the governing equilibrium equations of the system, formulate a closed form solution for the equilibrium and then use the closed form solution to develop "exact" shape functions with superior convergence characteristics. Examples of such treatments are provided in Nowzartash and Mohareb (2005) who developed a shear deformable finite element for the analysis of sandwich beams, Faella et al. (2010) and Martinelli et al. (2012) who developed non-shear deformable super-convergent elements. The study in Nguyen et al. (2011) and Keo et al. (2016) developed finite element formulations for multilayered Timoshenko beam columns with partial interaction. Their study captures the partial interaction through the concept of shear bond stiffness to approximate partial interaction between layers. Joao (2013) developed a super-convergent finite element formulation for multilayered composite members with partial interaction. Pham and Mohareb (2015b) developed super-convergent finite element formulations for steel beams reinforced with GFRP plate through an adhesive layer. However, the solution omitted shear deformation effects. Within this context, the present study focuses on (1) providing a closed form solution for a coupled differential equation system governing the equilibrium of the beams bonded with GFRP plates through a thin adhesive layer and (2) developing a super-convergent beam finite element that avoids discretization errors.

3.2. Statement of the Problem

A steel wide flange beam reinforced with a GFRP plate bonded to one of the flanges through a thin layer of adhesive is considered (Fig. 3.1a). The beam has general end supports at A and B and is subjected to tractions $p_z\left(s_b,n_b,z\right)$ and $p_v\left(s_b,n_b,z\right)$ in the longitudinal and transverse directions, respectively, where $\left(s_b,n_b,z\right)$ are the coordinates in a local Cartesian coordinate system (Fig. 3.1b). The objective of the present study is to develop a finite element capturing partial interaction and shear deformation effects, while accurately predicting the stresses and deformations with a minimal number of degrees of freedom.

Three global left-handed coordinate systems $OXYZ$, $O_pX_pY_pZ$ and $O_aX_aY_aZ$ are chosen for cross-sections of the wide flange beam, GFRP plate, and adhesive layer, respectively, where origins O, O_p and O_a are selected to coincide with the centroids/shear center of the beam, GFRP plate, and adhesive layer, (Figs. 3.1b-d). Local left-handed coordinate systems $C_bn_bs_bz$, $C_pn_ps_pz$ and $C_an_as_az$ are defined for the beam, plate, and adhesive in which point C_i ($i=b,p,a$) is a generic point lying on the section contour (or mid-surface), the s_i-direction is tangent to the contour, while the n_i- direction is normal to the contour. The z-axis is parallel to the global Z- axis. The geometric definitions for the composite cross-section are also shown in Fig. 3.1.

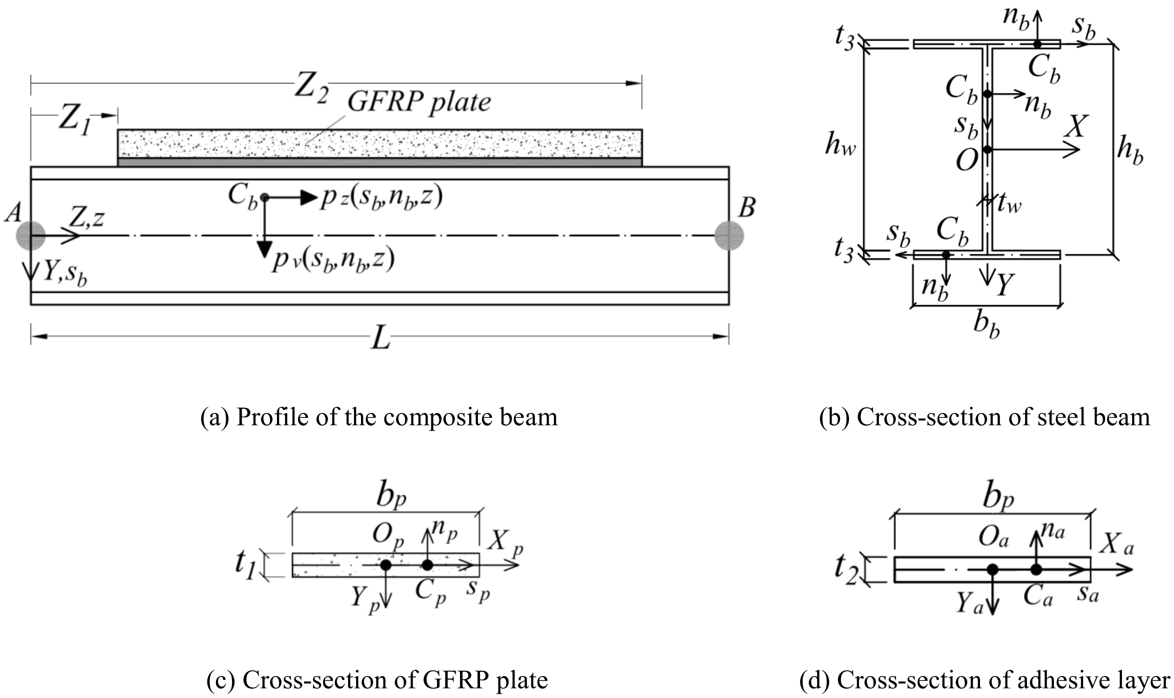

Figure 3.1. Composite beam configuration

3.3. Assumptions

The kinematic model of the present study is based on Pham and Mohareb (2014). As such, the following similar assumptions are adopted in the present study: (i) section contours for the steel beam and GFRP plate are assumed to remain undeformed in their own plane, (ii) perfect bond is assumed at the adhesive-GFRP and adhesive-steel interfaces, and (iii) given that the adhesive layer is thin, the change in transverse displacement within the thickness of the layer is assumed negligible compared to the transverse displacement of the composite system. The present study focuses only on the longitudinal-transverse response and thus the lateral and torsional displacement fields are omitted. The following additional assumptions are introduced for the present study:

(iv) In order to capture shear deformation effects, the wide flange beam is assumed to undergo rotations $\theta_{xb}(z)$ about the $X-$axis of the cross-section which is distinct from the derivatives of the corresponding transverse displacement $V'(z) \neq \theta_{xb}(z)$ in line with the Timoshenko beam assumption (Fig.3.2). Also, for the GFRP plate, rotations $\theta_{xp}(z)$ are assumed to be distinct from the corresponding displacement $V'(z) \neq \theta_{xp}(z)$.

(v) Due to the fact that the adhesive material possesses a very small modulus of elasticity when compared to those of the beam or GFRP, longitudinal normal stresses within the adhesive layer are considered negligible. Also, only the transverse shear stress component is considered to contribute to the longitudinal-transverse response while the other two shear components are negligible.

3.4. Overview of Relevant Previous Work

Given that the change in transverse displacement within the thickness of the layer is assumed negligible (Assumption iii), the transverse displacement $V(z)$ of the beam centroid and the GFRP plate centroid are considered equal. As a matter of convention, the angle of rotation $\theta_{xb}(z)$ about the x-axis follows the sign conventions shown in Fig. 3.2. The longitudinal displacement of the beam centroid is $W_b(z)$ while that of the GFRP plate is $W_p(z)$.

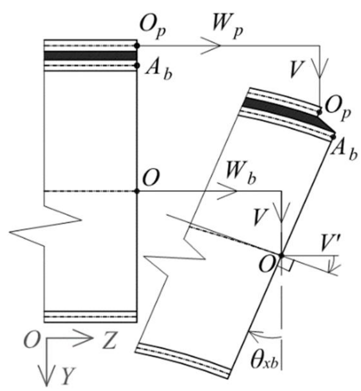

Figure 3.2. Partial interaction for the system of a GFRP plate bonded to a wide flange beam (Elevation View)

The total potential energy π is the sum of internal strain energies stored within the steel beam $\widetilde{U}_b$, the GFRP plate $\widetilde{U}_p$, the adhesive layer $\widetilde{U}_a$ minus the load potential energy loss $\widetilde{V}$ by member tractions forces $p_v(s_b, n_b, z), p_z(s_b, n_b, z)$ acting on the member undergoing displacements v, w, i.e.,

$$\pi = \widetilde{U}_b + \widetilde{U}_p + \widetilde{U}_a - \widetilde{V} \tag{3.1}$$

where

$$\begin{aligned} \widetilde{U}_b &= \frac{1}{2}\int_L \int_{A_b} \left(E_b \varepsilon_{zb}^2 + G_b \gamma_{szb}^2\right) dz, \quad \widetilde{U}_p = \frac{1}{2}\int_L \int_{A_p} E_p \varepsilon_{zp}^2 dz, \\ \widetilde{U}_a &= \frac{1}{2} G_a \int_L \int_{A_a} \gamma_{zna}^2 dz, \qquad \widetilde{V} = \int_z \int_s \left(p_v v + p_z w\right) ds dz \end{aligned} \tag{3.2}$$

From the general strains expressed in Pham and Mohareb (2014), the strains in Eq. (3.2) for the steel beam can be related to displacement fields through:

$$\begin{aligned}\varepsilon_{zb}(z) &= W_b'(z) - y(s_b)\theta_{xb}'(z) + n_b\cos\alpha(s_b)V''(z)\\ \gamma_{szb}(z) &= \left[V'(z) - \theta_{xb}(z)\right]\sin\alpha(s_b)\end{aligned} \tag{3.3}$$

Also, for the GFRP plate, one has:

$$\begin{aligned}\varepsilon_{zp}(z) &= W_p'(z) + n_pV''(z)\\ \gamma_{szp}(z) &= 0\end{aligned} \tag{3.4}$$

The displacement fields within the adhesive layer are linearly interpolated from displacement fields obtained at two interfaces of the steel beam and GFRP plate. Only the transverse shear strain component is considered and is obtained given by:

$$\gamma_{zna}(z) = -c_1W_b(z) + c_1W_p(z) - c_3\theta_{bx}(z) - c_2V'(z) \tag{3.5}$$

in which constants $c_1 = (1/t_2)$, $c_2 = (t_1 + 2t_2 + t_3)/(2t_2)$, $c_3 = h_b/(2t_2)$ are defined, t_1 is the thickness of the GFRP plate, t_2 is that of the adhesive layer, t_3 is the flange thickness and h_b is the effective depth of the steel beam cross-section (Fig. 3.1). Symbols A_b, A_p, A_a are cross-section areas of the wide flange beam, GFRP plate and adhesive layer, respectively, while symbols E_b and E_p denote the elastic moduli of steel and GFRP materials, respectively, and G_b, G_a are shear moduli of steel and adhesive materials. From Eqs. (3.3)-(3.5), by substituting into Eq. (3.2) and then Eq. (3.1), the total potential energy of the system can be obtained as

$$\begin{aligned}\pi = \int_L \Bigg[& \frac{1}{2}E_bA_bW_b'^{\,2} + \frac{1}{2}c_1^2G_aA_aW_b^2 + \frac{1}{2}E_pA_pW_p'^{\,2} + \frac{1}{2}c_1^2G_aA_aW_p^2 + \frac{1}{2}\left(E_bI_{ssbf} + E_pI_{xxp}\right)V''^2\\ & + \frac{1}{2}\left(G_bA_{bw} + c_2^2G_aA_a\right)V'^{\,2} + \frac{1}{2}E_bI_{xxb1}\theta_{xb}'^{\,2} + \frac{1}{2}\left(G_bA_{bw} + c_3^2G_aA_a\right)\theta_{xb}^2 - c_1^2G_aA_aW_bW_p + c_1c_3G_aA_aW_b\theta_{xb}\\ & + c_1c_2G_aA_aW_bV' - c_1c_3G_aA_aW_p\theta_{xb} - c_1c_2G_aA_aW_pV' + \left(c_2c_3G_aA_a - G_bA_{bw}\right)\theta_{xb}V'\Bigg]dz\\ & - \int_L \left[q_{zb}(z)W_b(z) + q_{yb}(z)V(z) + m_{xb}(z)\theta_{xb}(z) + m_{sb1}V'(z)\right]dz\end{aligned} \tag{3.6}$$

in which the following cross-sectional properties are defined:

$$A_b = \sum_{i=1,3} b_it_i;\, A_{bw} = h_wt_w;\, A_p = t_1b_p;\, A_a = t_2b_p;\, I_{xxb1} = t_wh_w^3/12 + 2b_ft_3h_b^2/4;\, I_{ssbf} = b_ft_3^3/6;\, I_{xxp} = b_pt_1^3/12;$$

and the line loads are defined as

$$\begin{Bmatrix} q_{zb}(z) \\ q_{yb}(z) \\ m_{sb1}(z) \\ m_{xb}(z) \end{Bmatrix} = \int_{s_b} \begin{Bmatrix} p_z(s_b, n_b, z) \\ p_v(s_b, n_b, z)\sin\alpha(s_b) \\ p_z(s_b, n_b, z)\, n_b \cos\alpha(s_b) \\ -p_z(s_b, n_b, z)\, y(s_b) \end{Bmatrix} ds_b \tag{3.7}$$

By evoking the stationarity condition of the total potential energy function (Eq. (3.6)) and performing integration by parts (Pham and Mohareb (2014)), one recovers the following coupled systems of equilibrium equations:

$$\begin{bmatrix} \left(-\alpha_b D^2+1\right) & -1 & r_1 D & r_2 \\ -1 & \left(-\alpha_p D^2+1\right) & -r_1 D & -r_2 \\ -r_1 D & r_1 D & \alpha_I D^4-\left(\alpha_s+r_1^2\right)D^2 & \left(\alpha_s-r_1 r_2\right)D \\ r_2 & -r_2 & \left(r_1 r_2-\alpha_s\right)D & -\alpha_J D^2+\left(\alpha_s+r_2^2\right) \end{bmatrix} \begin{Bmatrix} W_b \\ W_p \\ V \\ \theta_{xb} \end{Bmatrix} = \frac{1}{c_1^2 G_a A_a} \begin{Bmatrix} q_{zb}(z) \\ 0 \\ q_{yb}(z) \\ m_{xb}(z) \end{Bmatrix} \tag{3.8}$$

in which the following parameters have been defined:

$$r_1 = c_2/c_1;\, r_2 = c_3/c_1;\, \alpha_a = c_1^2 G_a A_a;\, \alpha_I = \left(E_b I_{ssbf} + E_p I_{xxp}\right)/\alpha_a;\, \alpha_J = E_b I_{xxb1}/\alpha_a;\, \alpha_p = E_p A_p/\alpha_a; \\ \alpha_b = E_b A_b/\alpha_a;\; \alpha_s = G_b A_{bw}/\alpha_a \tag{3.9}$$

3.5. New Closed Form Solution

Equation (3.8) was obtained and solved numerically in Pham and Mohareb (2014). However, no closed form solution was obtained. The present study complements the previous work by providing first a closed form solution for the system (Appendix 3.1), which leads to the following expression:

$$\begin{Bmatrix} W_p(z) \\ W_b(z) \\ V(z) \\ \theta_{xb}(z) \end{Bmatrix} = \begin{bmatrix} 0 & f_1 & 2f_1 z & \left(f_2+f_3 z^2\right) & z & 1 & R_7 e^{m_7 z} & R_8 e^{m_8 z} & R_9 e^{m_9 z} & R_{10} e^{m_{10} z} \\ 0 & 0 & 0 & \left(f_3-3f_1\right)z^2 & z & 1 & S_7 e^{m_7 z} & S_8 e^{m_8 z} & S_9 e^{m_9 z} & S_{10} e^{m_{10} z} \\ 1 & z & z^2 & z^3 & 0 & 0 & e^{m_7 z} & e^{m_8 z} & e^{m_9 z} & e^{m_{10} z} \\ 0 & 1 & 2z & \left(f_4+3z^2\right) & 0 & 0 & T_7 e^{m_7 z} & T_8 e^{m_8 z} & T_9 e^{m_9 z} & T_{10} e^{m_{10} z} \end{bmatrix} \{\mathbf{C}\}_{10\times1} \tag{3.10}$$

in which $\langle \mathbf{C} \rangle_{1\times10}^{\mathbf{T}} = \langle C_1 \quad C_2 \quad C_3 \quad C_4 \quad C_5 \quad C_6 \quad C_7 \quad C_8 \quad C_9 \quad C_{10} \rangle$ is a vector of ten integration constants normally determined from the boundary conditions, and the following constants have been defined.

$$f_1 = r_1 + r_2;\quad f_2 = 6\frac{\alpha_J r_2}{\alpha_s} + 6\frac{(r_1+r_2)(\alpha_s + r_2^2)\alpha_b\alpha_p}{\alpha_s(\alpha_b+\alpha_p)};\quad f_3 = 3\frac{(r_1+r_2)\alpha_b}{(\alpha_b+\alpha_p)};\quad f_4 = 6\frac{\alpha_J}{\alpha_s} + 6\frac{(r_1+r_2)r_2\alpha_b\alpha_p}{\alpha_s(\alpha_b+\alpha_p)};$$

$$R_k = (r_1+r_2)m_i + m_i(1-m_i^2\alpha_b)\frac{\alpha_J}{\alpha_b r_2} + (\beta_2 - \beta_1 m_i^2)\frac{(\alpha_b r_2^2 + \alpha_b\alpha_s + \alpha_J - m_i^2\alpha_b\alpha_J)m_i^2 - \alpha_s}{r_2\alpha_b}m_i;$$

$$S_k = m_i\frac{\alpha_J + (\beta_2 - \beta_1 m_i^2)(m_i^2\alpha_J - \alpha_s)}{r_2\alpha_b};\quad T_k = m_i(1+\beta_2 m_i^2 - \beta_1 m_i^4);\qquad k = 7,\ldots,10$$

The values $m_i, (i = 7,\ldots,10)$ are the root of the equation $-\beta_1 m^4 + (\beta_2 + \beta_4)m^2 + (1-\beta_3) = 0$ where

$$\beta_1 = r_1\alpha_b\alpha_p\alpha_I\alpha_J / \alpha_s\chi;\beta_2 = \left\{r_1\alpha_b\alpha_p(\alpha_s + r_1^2)\alpha_J - \alpha_I\left[r_2(\alpha_s - r_1 r_2)\alpha_b\alpha_p - r_1(\alpha_b+\alpha_p)\alpha_J\right]\right\} / \alpha_s\chi;$$

$$\beta_3 = (r_1+r_2)\alpha_b\alpha_p\alpha_I / \chi;\beta_4 = \left[r_1(\alpha_b+\alpha_p)\alpha_I + (r_1+r_2)(\alpha_s + r_1^2)\alpha_b\alpha_p\right] / \chi;$$

$$\chi = (r_1+r_2)(\alpha_s - r_1 r_2)\alpha_b\alpha_p - r_1(\alpha_b+\alpha_p)\alpha_J$$

3.6. Exact Shape Functions

To relate the displacement fields to the nodal displacement vector, exact shape functions will be developed based on the closed form solution. From the expression in Eqs. (3.10), by substituting into the following displacement vector:

$$\langle \mathbf{\Delta}(z)\rangle_{1\times5}^T = \langle W_p(z)\quad W_b(z)\quad V(z)\quad V'(z)\quad \theta_{xb}(z)\rangle \tag{3.11}$$

one obtains:

$$\{\mathbf{\Delta}(z)\}_{5\times1} = [\mathbf{Z}(z)]_{5\times10}\{\mathbf{C}\}_{10\times1} \tag{3.12}$$

in which matrix $[\mathbf{Z}(z)]_{5\times10}$ is defined as:

$$[\mathbf{Z}(z)]_{5\times10} = \begin{bmatrix} 0 & f_1 & 2f_1 z & (f_2 + f_3 z^2) & z & 1 & R_7 e^{m_7 z} & R_8 e^{m_8 z} & R_9 e^{m_9 z} & R_{10} e^{m_{10} z} \\ 0 & 0 & 0 & (f_3 - 3f_1)z^2 & z & 1 & S_7 e^{m_7 z} & S_8 e^{m_8 z} & S_9 e^{m_9 z} & S_{10} e^{m_{10} z} \\ 1 & z & z^2 & z^3 & 0 & 0 & e^{m_7 z} & e^{m_8 z} & e^{m_9 z} & e^{m_{10} z} \\ 0 & 1 & 2z & 3z^2 & 0 & 0 & m_7 e^{m_7 z} & m_8 e^{m_8 z} & m_9 e^{m_9 z} & m_{10} e^{m_{10} z} \\ 0 & 1 & 2z & (f_4 + 3z^2) & 0 & 0 & T_7 e^{m_7 z} & T_8 e^{m_8 z} & T_9 e^{m_9 z} & T_{10} e^{m_{10} z} \end{bmatrix} \tag{3.13}$$

From Eq. (3.11), by setting $z = 0$ and $z = L$, one obtains:

$$\{\mathbf{\Delta}_N\}_{10\times1} = [\mathbf{L}]_{10\times10}\{\mathbf{C}\}_{10\times1} \tag{3.14}$$

in which $\{\boldsymbol{\Delta}_N\}_{10\times1}$ is the nodal displacement vector of a finite element and is defined as (Fig. 3.3):

$$\langle\boldsymbol{\Delta}_N\rangle^{\mathrm{T}}_{1\times10}=\langle W_p(0)\quad W_b(0)\quad V(0)\quad V'(0)\quad \theta_{xb}(0)\,|\,W_p(L)\quad W_b(L)\quad V(L)\quad V'(L)\quad \theta_{xb}(L)\rangle \tag{3.15}$$

and matrix $[\mathbf{L}]_{10\times10}$ is defined as:

$$[\mathbf{L}]_{10\times10}=\begin{bmatrix}[\mathbf{Z}(0)]_{5\times10}\\ \hdashline [\mathbf{Z}(L)]_{5\times10}\end{bmatrix} \tag{3.16}$$

From Eq. (3.14), one can obtain $\{\mathbf{C}\}_{10\times1}=[\mathbf{L}]^{-1}_{10\times10}\{\boldsymbol{\Delta}_N\}_{10\times1}$. By substituting into Eq.(3.12), one has:

$$\{\boldsymbol{\Delta}(\mathbf{z})\}_{5\times1}=[\mathbf{N}(\mathbf{z})]_{5\times10}\{\boldsymbol{\Delta}_N\}_{10\times1} \tag{3.17}$$

in which $[\mathbf{N}(\mathbf{z})]_{5\times10}$ is a matrix of 50 shape functions and is given by:

$$[\mathbf{N}(\mathbf{z})]_{5\times10}=[\mathbf{Z}(\mathbf{z})]_{5\times10}[\mathbf{L}]^{-1}_{10\times10} \tag{3.18}$$

Figure 3.3. Nodal displacement fields of an element

The displacement fields $W_p(z),W_b(z),V(z),\theta_{xb}(z)$ extracted from Eq. (3.17) by pre-multiplying the right hand side by $\langle\rho_i\rangle^T_{1\times5}\quad i=1,2,3,4$, i.e.,

$$\left[W_p(z),W_b(z),V(z),\theta_{xb}(z)\right]=\left[\langle\rho_1\rangle^T_{1\times5},\langle\rho_2\rangle^T_{1\times5},\langle\rho_3\rangle^T_{1\times5},\langle\rho_4\rangle^T_{1\times5}\right][\mathbf{N}(\mathbf{z})]_{5\times10}\{\boldsymbol{\Delta}_N\}_{10\times1} \tag{3.19}$$

in which $\langle\rho_1\rangle^T_{1\times5}=\langle1\quad0\quad0\quad0\quad0\rangle$; $\langle\rho_2\rangle^T_{1\times5}=\langle0\quad1\quad0\quad0\quad0\rangle$; $\langle\rho_3\rangle^T_{1\times5}=\langle0\quad0\quad1\quad0\quad0\rangle$; and $\langle\rho_4\rangle^T_{1\times5}=\langle0\quad0\quad0\quad0\quad1\rangle$ have been introduced.

3.7. Finite Element Formulation

From Eqs. (3.19), by substituting into the variational principle in Eq.(3.6), one obtains:

$$
\begin{aligned}
\pi = \langle \Delta_{\mathrm{N}} \rangle_{1\times 10}^{T} \Bigg\{ \int_L \Bigg[& \frac{E_b A_b}{2} \left[\mathrm{N}'(\mathrm{z})\right]_{10\times 5}^{T} \{\rho_2\}_{5\times 1} \langle \rho_2 \rangle_{1\times 5}^{T} \left[\mathrm{N}'(\mathrm{z})\right]_{5\times 10} + \frac{E_b I_{ssbf}}{2} \left[\mathrm{N}''(\mathrm{z})\right]_{10\times 5}^{T} \{\rho_3\}_{5\times 1} \langle \rho_3 \rangle_{1\times 5}^{T} \left[\mathrm{N}''(\mathrm{z})\right]_{5\times 10} + \\
& + \frac{E_b I_{xxb1}}{2} \left[\mathrm{N}'(\mathrm{z})\right]_{10\times 5}^{T} \{\rho_4\}_{5\times 1} \langle \rho_4 \rangle_{1\times 5}^{T} \left[\mathrm{N}'(\mathrm{z})\right]_{5\times 10} + \frac{G_b A_{bw}}{2} \left[\mathrm{N}'(\mathrm{z})\right]_{10\times 5}^{T} \{\rho_3\}_{5\times 1} \langle \rho_3 \rangle_{1\times 5}^{T} \left[\mathrm{N}'(\mathrm{z})\right]_{5\times 10} + \\
& + \frac{G_b A_{bw}}{2} \left[\mathrm{N}(\mathrm{z})\right]_{10\times 5}^{T} \{\rho_4\}_{5\times 1} \langle \rho_4 \rangle_{1\times 5}^{T} \mathrm{N}(\mathrm{z})_{5\times 10} - G_b A_{bw} \left[\mathrm{N}(\mathrm{z})\right]_{10\times 5}^{T} \{\rho_4\}_{5\times 1} \langle \rho_3 \rangle_{1\times 5}^{T} \left[\mathrm{N}'(\mathrm{z})\right]_{5\times 10} \Bigg] dz + \\
& + \int_L \left[\frac{E_p A_p}{2} \left[\mathrm{N}'(\mathrm{z})\right]_{10\times 5}^{T} \{\rho_1\}_{5\times 1} \langle \rho_1 \rangle_{1\times 5}^{T} \left[\mathrm{N}'(\mathrm{z})\right]_{5\times 10} + \frac{E_p I_{xxp}}{2} \left[\mathrm{N}''(\mathrm{z})\right]_{10\times 5}^{T} \{\rho_3\}_{5\times 1} \langle \rho_3 \rangle_{1\times 5}^{T} \left[\mathrm{N}''(\mathrm{z})\right]_{5\times 10} \right] dz + \\
& + \int_L \Bigg[\frac{c_1^2 G_a A_a}{2} \left[\mathrm{N}(\mathrm{z})\right]_{10\times 5}^{T} \{\rho_1\}_{5\times 1} \langle \rho_1 \rangle_{1\times 5}^{T} \left[\mathrm{N}(\mathrm{z})\right]_{5\times 10} + \frac{c_1^2 G_a A_a}{2} \left[\mathrm{N}(\mathrm{z})\right]_{10\times 5}^{T} \{\rho_2\}_{5\times 1} \langle \rho_2 \rangle_{1\times 5}^{T} \left[\mathrm{N}(\mathrm{z})\right]_{5\times 10} + \\
& - c_1^2 G_a A_a \left[\mathrm{N}(\mathrm{z})\right]_{10\times 5}^{T} \{\rho_1\}_{5\times 1} \langle \rho_2 \rangle_{1\times 5}^{T} \left[\mathrm{N}(\mathrm{z})\right]_{5\times 10} + c_1 c_3 G_a A_a \left[\mathrm{N}(\mathrm{z})\right]_{10\times 5}^{T} \{\rho_2\}_{5\times 1} \langle \rho_4 \rangle_{1\times 5}^{T} \left[\mathrm{N}(\mathrm{z})\right]_{5\times 10} + \\
& + c_1 c_2 G_a A_a \left[\mathrm{N}(\mathrm{z})\right]_{10\times 5}^{T} \{\rho_2\}_{5\times 1} \langle \rho_3 \rangle_{1\times 5}^{T} \left[\mathrm{N}'(\mathrm{z})\right]_{5\times 10} - c_1 c_3 G_a A_a \left[\mathrm{N}(\mathrm{z})\right]_{10\times 5}^{T} \{\rho_1\}_{5\times 1} \langle \rho_4 \rangle_{1\times 5}^{T} \left[\mathrm{N}(\mathrm{z})\right]_{5\times 10} + \\
& - c_1 c_2 G_a A_a \left[\mathrm{N}(\mathrm{z})\right]_{10\times 5}^{T} \{\rho_1\}_{5\times 1} \langle \rho_3 \rangle_{1\times 5}^{T} \left[\mathrm{N}'(\mathrm{z})\right]_{5\times 10} + \frac{c_2^2 G_a A_a}{2} \left[\mathrm{N}'(\mathrm{z})\right]_{10\times 5}^{T} \{\rho_3\}_{5\times 1} \langle \rho_3 \rangle_{1\times 5}^{T} \left[\mathrm{N}'(\mathrm{z})\right]_{5\times 10} + \\
& + \frac{c_3^2 G_a A_a}{2} \left[\mathrm{N}(\mathrm{z})\right]_{10\times 5}^{T} \{\rho_4\}_{5\times 1} \langle \rho_4 \rangle_{1\times 5}^{T} \left[\mathrm{N}(\mathrm{z})\right]_{5\times 10} + c_2 c_3 G_a A_a \left[\mathrm{N}(\mathrm{z})\right]_{10\times 5}^{T} \{\rho_4\}_{5\times 1} \langle \rho_3 \rangle_{1\times 5}^{T} \left[\mathrm{N}'(\mathrm{z})\right]_{5\times 10} \Bigg] dz \Bigg\} \{\Delta_N\}_{10\times 1} \\
& - \langle \Delta_{\mathrm{N}} \rangle_{1\times 5}^{T} \int_L \left\{ \left[\mathrm{N}(\mathrm{z})\right]_{10\times 5}^{T} \left[q_{zb}(z) \{\rho_2\}_{5\times 1} + q_{yb}(z) \{\rho_3\}_{5\times 1} + m_{xb}(z) \{\rho_4\}_{5\times 1} \right] + m_{sb1} \left[\mathrm{N}'(\mathrm{z})\right]_{10\times 5}^{T} \{\rho_3\}_{5\times 1} \right\} dz
\end{aligned}
\tag{3.20}
$$

From Eq. (3.20), by setting the first variation of the total potential energy to zero, one obtains:

$$
\left([\mathrm{K}_{\mathrm{b}}]_{10\times 10} + [\mathrm{K}_{\mathrm{p}}]_{10\times 10} + [\mathrm{K}_{\mathrm{a}}]_{10\times 10} \right) \{\Delta_{\mathrm{N}}\}_{10\times 1} - \{\mathrm{P}\}_{10\times 1} = 0 \tag{3.21}
$$

in which $[\mathrm{K}_{\mathrm{b}}]$ is the stiffness matrix contributed by the wide flange steel beam. It includes the effects of axial deformation, transverse flexural deformation and transverse shear deformations and is defined as:

$$\left[\mathrm{K_b}\right]=\int_L\Big\{E_b\Big[A_b\left[\mathrm{N}'(\mathrm{z})\right]^T_{10\times5}\{\rho_2\}_{5\times1}\langle\rho_2\rangle^T_{1\times5}\left[\mathrm{N}'(\mathrm{z})\right]_{5\times10}+I_{ssbf}\left[\mathrm{N}''(\mathrm{z})\right]^T_{10\times5}\{\rho_3\}_{5\times1}\langle\rho_3\rangle^T_{1\times5}\left[\mathrm{N}''(\mathrm{z})\right]_{5\times10}+$$

$$+I_{xxb1}\left[\mathrm{N}'(\mathrm{z})\right]^T_{10\times5}\{\rho_4\}_{5\times1}\langle\rho_4\rangle^T_{1\times5}\left[\mathrm{N}'(\mathrm{z})\right]_{5\times10}\Big]+G_bA_{bw}\Big[\left[\mathrm{N}'(\mathrm{z})\right]^T_{10\times5}\{\rho_3\}_{5\times1}\langle\rho_3\rangle^T_{1\times5}\left[\mathrm{N}'(\mathrm{z})\right]_{5\times10}+$$

$$+\left[\mathrm{N}(\mathrm{z})\right]^T_{10\times5}\{\rho_4\}_{5\times1}\langle\rho_4\rangle^T_{1\times5}\left[\mathrm{N}(\mathrm{z})\right]_{5\times10}-\left[\mathrm{N}(\mathrm{z})\right]^T_{10\times5}\{\rho_4\}_{5\times1}\langle\rho_3\rangle^T_{1\times5}\left[\mathrm{N}'(\mathrm{z})\right]_{5\times10}$$

$$-\left[\mathrm{N}'(\mathrm{z})\right]^T_{10\times5}\{\rho_3\}_{5\times1}\langle\rho_4\rangle^T_{1\times5}\left[\mathrm{N}(\mathrm{z})\right]_{5\times10}\Big]\Big\}dz$$

while $\left[\mathrm{K_p}\right]$ is the stiffness matrix contributed by the GFRP plate. It includes the effects of axial deformation and transverse flexural deformation and is defined as:

$$\left[\mathrm{K_p}\right]=E_p\int_L\Big\{A_p\left[\mathrm{N}'(z)\right]^T_{10\times5}\{\rho_1\}_{5\times1}\langle\rho_1\rangle^T_{1\times5}\left[\mathrm{N}'(z)\right]_{5\times10}+I_{xxp}\left[\mathrm{N}''(z)\right]^T_{10\times5}\{\rho_3\}_{5\times1}\langle\rho_3\rangle^T_{1\times5}\left[\mathrm{N}''(z)\right]_{5\times10}\Big\}dz$$

Also, $\left[\mathrm{K_a}\right]$ is the stiffness matrix contributed by the transverse shear deformation in the adhesive layer and defined as:

$$\left[\mathrm{K_a}\right]=G_aA_a\int_L\Big\{c_1^2\left[\mathrm{N}(\mathrm{z})\right]^T_{10\times5}\{\rho_1\}_{5\times1}\langle\rho_1\rangle^T_{1\times5}\left[\mathrm{N}(\mathrm{z})\right]_{5\times10}+c_1^2\left[\mathrm{N}(\mathrm{z})\right]^T_{10\times5}\{\rho_2\}_{5\times1}\langle\rho_2\rangle^T_{1\times5}\left[\mathrm{N}(\mathrm{z})\right]_{5\times10}+$$

$$-2c_1^2\left[\mathrm{N}(\mathrm{z})\right]^T_{10\times5}\{\rho_1\}_{5\times1}\langle\rho_2\rangle^T_{1\times5}\left[\mathrm{N}(\mathrm{z})\right]_{5\times10}+2c_1c_3\left[\mathrm{N}(\mathrm{z})\right]^T_{10\times5}\{\rho_2\}_{5\times1}\langle\rho_4\rangle^T_{1\times5}\left[\mathrm{N}(\mathrm{z})\right]_{5\times10}+$$

$$+2c_1c_2\left[\mathrm{N}(\mathrm{z})\right]^T_{10\times5}\{\rho_2\}_{5\times1}\langle\rho_3\rangle^T_{1\times5}\left[\mathrm{N}'(\mathrm{z})\right]_{5\times10}-2c_1c_3\left[\mathrm{N}(\mathrm{z})\right]^T_{10\times5}\{\rho_1\}_{5\times1}\langle\rho_4\rangle^T_{1\times5}\left[\mathrm{N}(\mathrm{z})\right]_{5\times10}+$$

$$-2c_1c_2\left[\mathrm{N}(\mathrm{z})\right]^T_{10\times5}\{\rho_1\}_{5\times1}\langle\rho_3\rangle^T_{1\times5}\left[\mathrm{N}'(\mathrm{z})\right]_{5\times10}+c_2^2\left[\mathrm{N}'(\mathrm{z})\right]^T_{10\times5}\{\rho_3\}_{5\times1}\langle\rho_3\rangle^T_{1\times5}\left[\mathrm{N}'(\mathrm{z})\right]_{5\times10}+$$

$$+c_3^2\left[\mathrm{N}(\mathrm{z})\right]^T_{10\times5}\{\rho_4\}_{5\times1}\langle\rho_4\rangle^T_{1\times5}\left[\mathrm{N}(\mathrm{z})\right]_{5\times10}+2c_2c_3\left[\mathrm{N}(\mathrm{z})\right]^T_{10\times5}\{\rho_4\}_{5\times1}\langle\rho_3\rangle^T_{1\times5}\left[\mathrm{N}'(\mathrm{z})\right]_{5\times10}\Big\}dz$$

In Eq.(3.21), the nodal load vector P is defined as:

$$\{\mathrm{P}\}=\int_L\Big\{\left[\mathrm{N}(\mathrm{z})\right]^T_{10\times5}\left[q_{zb}(z)\{\rho_2\}_{5\times1}+q_{yb}(z)\{\rho_3\}_{5\times1}+m_{xb}(z)\{\rho_4\}_{5\times1}\right]+m_{sb1}\left[\mathrm{N}'(\mathrm{z})\right]^T_{10\times5}\{\rho_3\}_{5\times1}\Big\}dz$$

3.8. Moment Resistance based on First Yield

For given loads (q_{zb}, q_{yb}, m_{sb1}, m_{xb}) the nodal displacements for an elements $\langle\boldsymbol{\Delta}_N\rangle^{\mathrm{T}}_{1\times10}=\langle W_p(0)\quad W_b(0)\quad V(0)\quad V'(0)\quad \theta_{xb}(0)\mid W_p(L)\quad W_b(L)\quad V(L)\quad V'(L)\quad \theta_{xb}(L)\rangle$ are determined from the FEA. Given the stiffness matrices $\mathbf{K_b},\mathbf{K_p},\mathbf{K_a}$ and the load vector $\{\mathbf{P}\}_{10\times1}$, one can determine a nodal force vector

$$\langle \mathbf{Q} \rangle_{1\times10}^{\mathrm{T}} = \langle -N_p(0) \quad -N_b(0) \quad -Q(0) \quad -M_{x1}(0) \quad -M_{x2}(0) \;\vdots\; N_p(L) \quad N_b(L) \quad Q(L) \quad M_{x1}(L) \quad M_{x2}(L) \rangle$$

From the relation

$$\{\mathbf{Q}\}_{10\times1} = \left[\mathbf{K_b} + \mathbf{K_p} + \mathbf{K_a}\right]_{10\times10} \{\mathbf{\Delta_N}\}_{10\times1} - \{\mathbf{P}\}_{10\times1} \tag{3.22}$$

where internal forces $N_p(z_e), N_b(z_e), Q(z_e), M_{x1}(z_e), M_{x2}(z_e)$ with $z_e = 0, L$ follow the beam theory sign convention (Fig. 3.4).

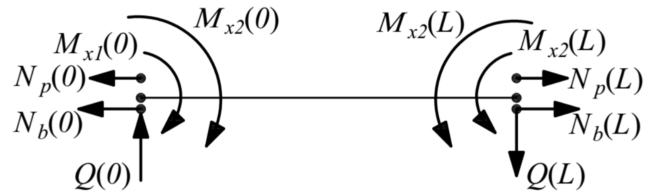

Figure 3.4. Sign convention for nodal forces

Given the internal forces $N_p(z_e), N_b(z_e), M_{x1}(z_e), M_{x2}(z_e)$, the displacement derivatives at the nodes $W_p{}'(z_e)$, $W_b{}'(z_e)$, $V''(z_e)$, $\theta_{xb}{}'(z_e)$ can be given (Pham 2013) from

$$W_p{}'(z_e) = \frac{N_p(z_e)}{E_p A_p}, \quad W_b{}'(z_e) = \frac{N_b(z_e)}{E_b A_b}, \quad V''(z_e) = \frac{M_{x1}(z_e)}{E_b I_{ssbf} + E_p I_{xxp}}, \quad \theta'_{xb}(z_e) = \frac{M_{x2}(z_e)}{E_b I_{xxb1}} \tag{3.23}$$

From Eqs. (3.23), by substituting into Eqs. (3.3)a and (3.4)a, and assuming linear stress-strain relationships $\varepsilon_{zb} = E_b \varepsilon_{zb}$, $\varepsilon_{zp} = E_p \varepsilon_{zp}$, the longitudinal stresses are given as

$$\begin{aligned} \sigma_{zb}(z_e) &= E_b \left[\frac{N_b(z_e)}{E_b A_b} + n_b \cos\alpha(s_b) \frac{M_{x1}(z_e)}{E_b I_{ssbf} + E_p I_{xxp}} - y(s_b) \frac{M_{x2}(z_e)}{E_b I_{xxb1}} \right] \\ \sigma_{zp}(z_e) &= E_p \left[\frac{N_p(z_e)}{E_p A_p} + n_p \frac{M_{x1}(z_e)}{E_b I_{ssbf} + E_p I_{xxp}} \right] \end{aligned} \tag{3.24}$$

The stresses $\sigma_{s,t}, \sigma_{s,b}, \sigma_{g,t}, \sigma_{g,b}$ at the extreme fibers (Fig. 3.5) at the section $z_{\max}$ of maximum moment as evaluated from Eqs. (3.24) are

$$
\begin{aligned}
\sigma_{s,t}\left(z_{\max}\right) &= \frac{N_b\left(z_{\max}\right)}{A_b} + \frac{t_3}{2}\frac{M_{x1}\left(z_{\max}\right)}{I_{ssbf} + \left(E_p/E_b\right)I_{xxp}} + \frac{h_w + t_3}{2}\frac{M_{x2}\left(z_{\max}\right)}{I_{xxb1}} \\
\sigma_{s,b}\left(z_{\max}\right) &= \frac{N_b\left(z_{\max}\right)}{A_b} - \frac{t_3}{2}\frac{M_{x1}\left(z_{\max}\right)}{I_{ssbf} + \left(E_p/E_b\right)I_{xxp}} - \frac{h_w + t_3}{2}\frac{M_{x2}\left(z_{\max}\right)}{I_{xxb1}} \\
\sigma_{g,t}\left(z_{\max}\right) &= \frac{N_p\left(z_{\max}\right)}{A_p} - \frac{t_1}{2}\frac{M_{x1}\left(z_{\max}\right)}{I_{ssbf} + \left(E_p/E_b\right)I_{xxp}} \\
\sigma_{g,b}\left(z_e\right) &= \frac{N_p\left(z_{\max}\right)}{A_p} + \frac{t_1}{2}\frac{M_{x1}\left(z_{\max}\right)}{I_{ssbf} + \left(E_p/E_b\right)I_{xxp}}
\end{aligned}
\tag{3.25}
$$

It is noted that the above stresses correspond to the applied loads $q_{zb}, q_{yb}, m_{sb1},\ m_{xb}$, and thus the peak stress at the top fiber $\sigma_{s,t}$ will differ from the sought yield strength F_y. Thus, the above expressions need to be multiplied by $\lambda = F_y/\sigma_{s,t}$ to recover the stress profile corresponding to the first yield. The location of neutral axis d_{NA} is evaluated through $\sigma_{s,t}\left(z_e\right)$ and $\sigma_{s,b}\left(z_e\right)$ as

$$
d_{NA} = \frac{\sigma_{s,t}}{\sigma_{s,b} + \sigma_{s,t}} h \tag{3.26}
$$

By summing the moments of the stresses about the neutral axis, the internal moment corresponding to the first yield is obtained as

$$
\begin{aligned}
M_y^{PI} = \lambda \Bigg\{ & \sigma_{s,t}\left[\frac{d_{NA}^2 b}{3} - \frac{\left(d_{NA} - t_3\right)^3\left(b - t_w\right)}{3d_{NA}}\right] + \sigma_{s,b}\left[\frac{\left(h - d_{NA}\right)^2 b}{3} - \frac{\left(h - d_{NA} - t_3\right)^3\left(b - t_w\right)}{3\left(h - d_{NA}\right)}\right] \\
& + \frac{1}{2}\sigma_{g,t} b t_1\left(h - d_{NA} + t_2 + \frac{1}{3}t_1\right) + \frac{1}{2}\sigma_{g,b} b t_1\left(h - d_{NA} + t_2 + \frac{2}{3}t_1\right)\Bigg\}
\end{aligned}
\tag{3.27}
$$

where M_y^{PI} accounts for partial interaction effects, and the corresponding effective elastic section modulus of the GFRP-strengthened section is

$$
S_x^{PI} = M_y^{PI}/F_y \tag{3.28}
$$

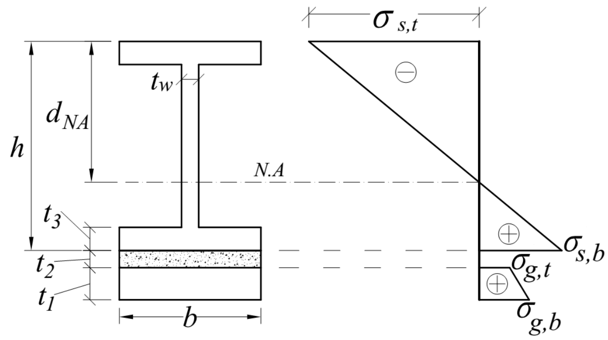

Figure 3.5. Longitudinal normal stress profile of the composite section

3.9. Verification and examples

3.9.1. Example 1 -Verification of Results

A 2-span continuous composite beam (Fig. 3.6) has a W150x13 cross-section and is connected to a GFRP plate with thickness $t_1 = 19mm$ and a width $b_p = 100mm$, through an adhesive of thickness $t_2 = 0.79mm$. The modulus of elasticity of steel is $E_s = 200GPa$, that of GFRP is $E_p = 17.2GPa$ (Abushagur and Damatty (2013)) and that of adhesive is $E_a = 3.18GPa$ (Shaat and Fam (2007)). Poisson's ratio of all three materials is assumed to be 0.3. Both spans of the steel beam are 1.5m long while the length of the GFRP plate is $L_1 = 2.0m$ and is symmetrically placed relative to the intermediate support. Longitudinally, the end $z = 0$ of the beam axis is restrained while at $z = L, 2L$, it is axially free. Both ends of the GFRP plate are longitudinally free. The beam is subjected to a uniform distributed line load $q_y = 15\,kN/m$ applied at the central line of the beam and a concentrated load $P = 5kN$ applied at $z = L/3$ from the left support. It is required to compare the predictions of the present model to that based on a 3D FEA solution. Also, a comparison of these solutions with a classical solution (i.e., Timoshenko beam theory (TB-No Reinforcement) of the non-reinforced steel beams under the same loading and support conditions is also made to clarify the effect of reinforcement.

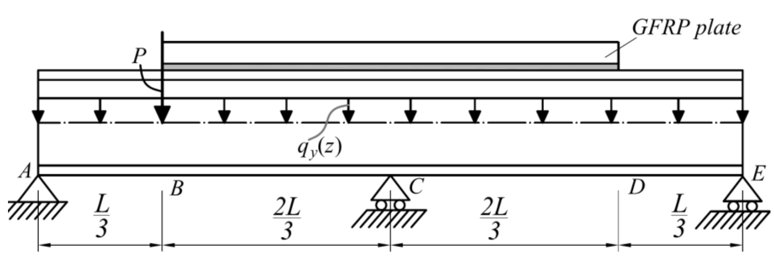

Figure 3.6. Continuous composite beam

Given that the finite element formulation is based on exact shape functions, four elements (AB, BC, CD, DE) are found enough to achieve convergence. Further discretization's are found to not cause any changes in the predicted stresses and displacements. This finding contrasts with the element in (Pham and Mohareb (2015b)). To obtain a suitable number of intermediate reading, 80 elements were selected for the present example where 14 elements are chosen to model the unreinforced segments while 52 elements were selected for the reinforced segment. The 3D FEA analysis is based on the eight-node brick element C3D8R with reduced integration. A mesh study has indicated that displacements and stresses converge when using 20 elements along the flange overhang, 4 elements across the flange thickness, 70 elements along the web height, 4 elements across the web thickness, 4 elements across the adhesive thickness, 8 elements across the GFRP thickness, 500 elements along the GFRP plate length and 1500 elements in the longitudinal direction of the steel beam.

Figure 3.7 depicts the transverse deflection along the span as predicted by the present model and the 3D FEA solution. In both solutions, the maximum transverse deflection takes place at a distance at about 600 mm from the left support. The present model predicts a peak displacement of 0.590 mm. This compares to 0.604mm based on the 3D FEA solution, a 2.3% difference. Also shown on the figure is the deflection obtained from a shear deformable Timoshenko beam solution for the case of no GFRP reinforcement (TB-No Reinforcement). The predicted displacement of 0.66mm occurred at a distance of 638mm from the left support. The GFRP plate reduces the peak deflection by 11.9%.

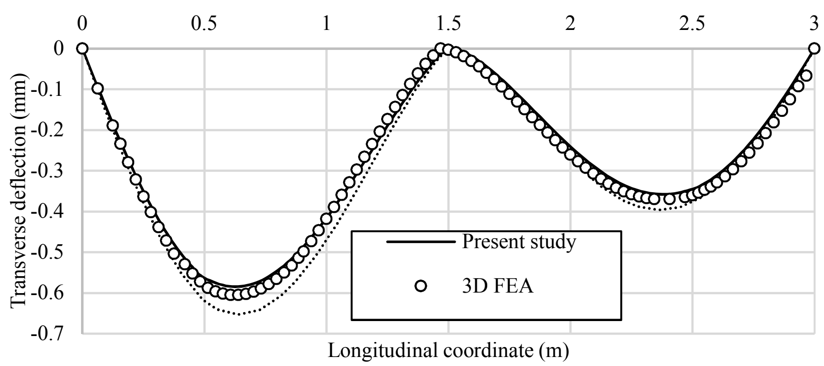

Figure 3.7. Transverse deflection for a two-span continuous beam

Figures 3.8a-b present the longitudinal normal stresses at the bottom flange and that at the top of the GFRP plate, respectively. The stress predictions based on the present study and the 3D FEA solutions are in close agreement (Fig. 3.8a). Based on the present solution, the peak stress is found to be 92.8 MPa. This value compares to 90.6 MPa based on 3D FEA, corresponding to 2.4% difference. This value also compares to a maximum stress of 113.3MPa for the non-reinforced steel beam as predicted by the Timoshenko beam solution (Fig. 3.8a), i.e., the GFRP reinforcement reduces the stresses by 25.1%. Close agreement is observed for the maximum normal stress in the GFRP plate (Fig. 3.8b). The maximum stresses based on the present study is 8.20 MPa. This compares to a stress of 8.41 MPa based on the 3D FEA solution, corresponding to a difference of 2.5%.

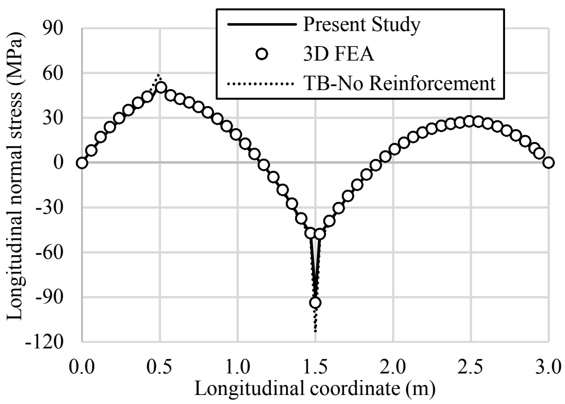

(a)

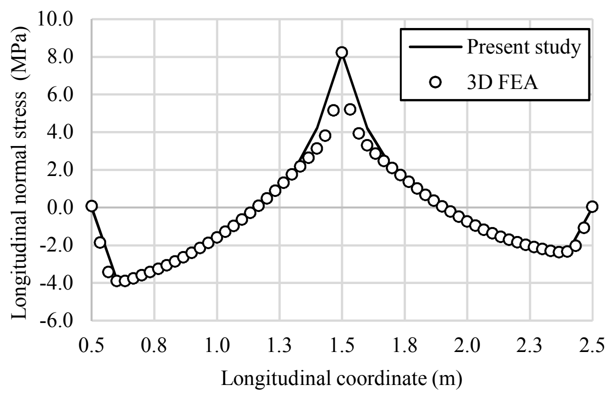

(b)

Figure 3.8. Normal stress distribution for two-span continuous beam at (a) at bottom flange and (b) at top of GFRP plate

3.9.2. Example 2- Convergence characteristics of the element

A 3m-single span composite beam (Fig.3.9a) has a W150x13 cross-section and is strengthened with a GFRP plate of thickness $t_1 = 19mm$ and width $b_p = 100mm$ through an adhesive of thickness $t_2 = 0.79mm$. Material properties are identical to those of the previous example. The GFRP plate is symmetrically placed about the mid-span and has a length L_1 of $2.5m$. End $z = 0$ of the beam is longitudinally restrained, end $z = L$ is free while both ends of the GFRP plate are longitudinally free. The beam is subjected to a uniformly distributed line load $q_y = 10\,kN/m$ applied at the centerline of the beam. It is required to compare the results based on the finite element in Pham and Mohareb (2015b) based on conventional Hermitian polynomials to that based on the present study based on exact shape function.

The problem is solved using 10, 30, 40 and 60 Hermitian elements. In all cases, 4 elements are used to model the unreinforced segments and the remaining elements were used to model the remaining strengthened segment using a uniform discretization. Also, the problem is solved using 4 and 6 “exact” elements. Figures 3.9b-d respectively depict the transverse deflection, the longitudinal normal stresses at the top flange of the steel beam, and that at the bottom fiber of the GFRP plate. The displacements and stresses based on the 40-element mesh is observed to nearly coincide with that based on the 60-element mesh. In contrast, the displacements and the stresses based on the 10-element solution are found to depart from the 40-element mesh. For the 30-element mesh, deflections are found to agree with those based on the 40-element mesh while the stresses are observed to depart from those based on the 40-element mesh, suggesting that a 40-Hermitian element mesh is needed for convergence in the present example. By comparison, the displacements and stress based on the present finite element are found to exactly agree with the converged results whether 4 or 6 elements are used. Further mesh refinements were found to be unnecessary for convergence, indicating that a 4-element solution is enough to achieve convergence. This is a natural outcome of the fact that the present element is based on shape functions which exactly satisfy the equilibrium conditions.

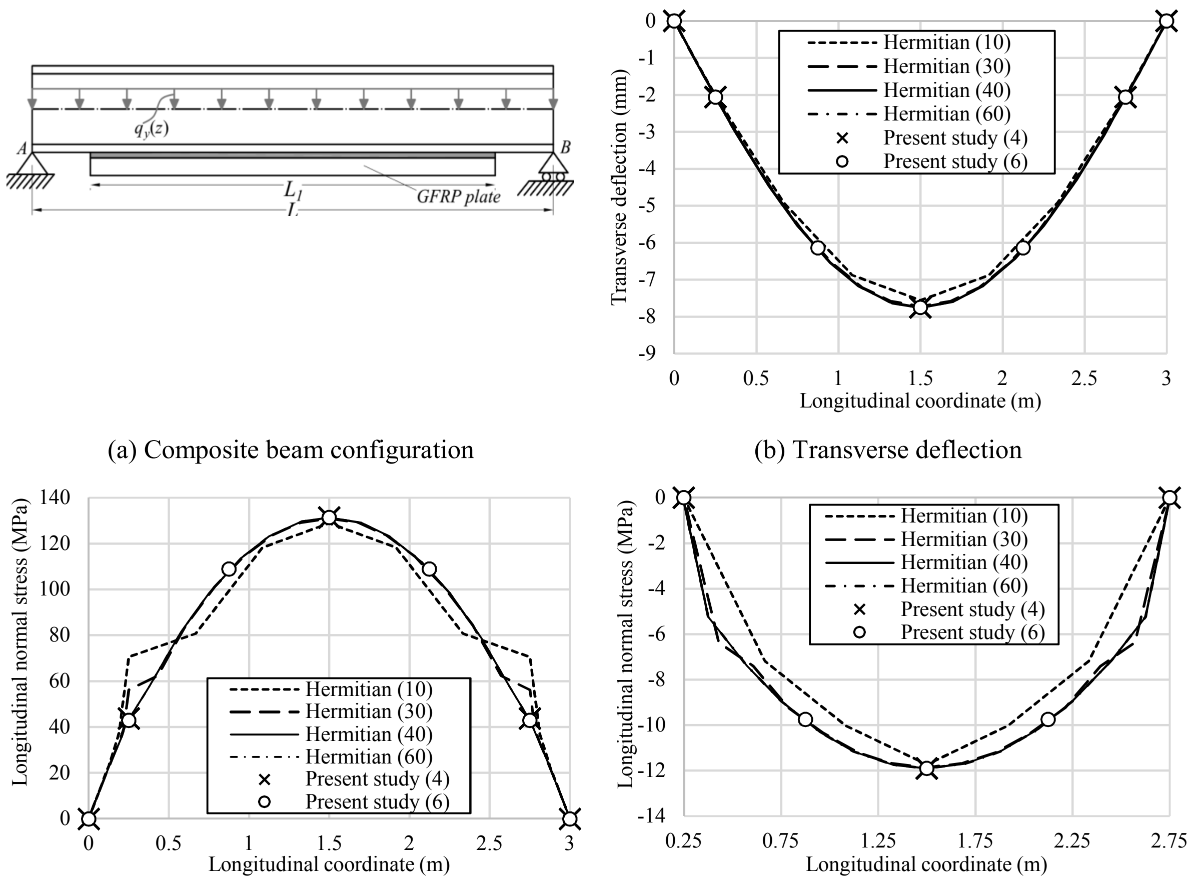

(a) Composite beam configuration

(b) Transverse deflection

(c) at the farthest fibre of the unreinforced flange

(d) at the farthest fibre of the GFRP plate

Figure 3.9. Comparison of the solution convergence between Hermitian element and present study (*bracketed numbers indicate the number of finite element*)

3.9.3. Example 3- First yielding moment for GFRP-strengthened steel beam

It is required to determine the first yield moment for the strengthened beam in Example 2 and compare it to the first yield moment for the bare beam. The steel yielding strength is $F_y = 350\ MPa$. For the bare beam, the elastic section modulus is $S_x = 80.6\times10^3\ mm^3$ and the corresponding first yield moment is $M_y^{bare} = S_x F_y = 28.2\ kNm$.

When the strengthened beam is subjected to $q_y = 10\ kN/m$, the stresses at the extreme fibers of the section of maximum moment are $\sigma_{s,t} = 131.3, \sigma_{s,b} = 116, \sigma_{g,t} = 9.2, \sigma_{g,b} = 11.9\ MPa$ as determined from Equation 25. To attain the point of first yield, the applied load must be magnified by a factor $\lambda = 350/131.3 = 2.67$. The corresponding magnified stresses become $\sigma_{s,t} = 350$, $\sigma_{s,b} = 309.2, \sigma_{g,t} = 24.5, \sigma_{g,b} = 31.7\ MPa$. Distance d_{NA} as determined from Eq. (3.26) is $d_{NA} = 82.2\ mm$ and the first yield moment based on Eq. (3.27) is $M_y^{PI} = 29.9\ kNm$. This value is marginally lower than that based on the transformed section method of $M_y^{TS} = 30.0\ kNm$. Compared to the bare beam, the addition of GFRP-strengthening increased the moment capacity by 6.0% in the present example.

3.9.4. Example 4: Effect of shear deformation-1

A wide flange beam used in the previous examples is re-used in the present example. A W150x13 beam (properties provided in Example 2) is fixed at both ends and is fully reinforced with a GFRP plate with thickness $t_1 = 19mm$, width $b_p = 100mm$ through an adhesive of thickness $t_2 = 0.79mm$. Material properties of steel, GFRP and adhesive are similar to those of Example 2. The beam is subjected to a concentrated transverse load of 15 kN acting at mid-span. It is required to investigate the shear deformation effect by comparing the transverse deflection based on the present shear deformable solution to the non-shear deformable theory (NSDT) developed in Pham and Mohareb (2015b) for various spans.

Figures 3.10a-d depict the distribution of the transverse deflection d along the span length for four spans: *L*=1.0, 2.0, 3.0, and 5.0m. For the shortest span of 1.0m span beam (Fig. 3.10a), with span to depth ratio (L/h) of 6.8, the present solution predicts a peak displacement of 0.13mm in close agreement with that predicted by the 3D FEA solution of 0.14mm at mid-span and, a 3.6% difference. The NSDT solution predicts a peak displacement of 0.06mm, a 59% difference. For the longest span examined, (L=5.0m and L/h of 33.8), the peak displacement predicted by the present study (and the 3D FEA) is 7.38mm while that based on NSDT is 6.97mm, a difference of 5.6% (Fig. 3.10d).

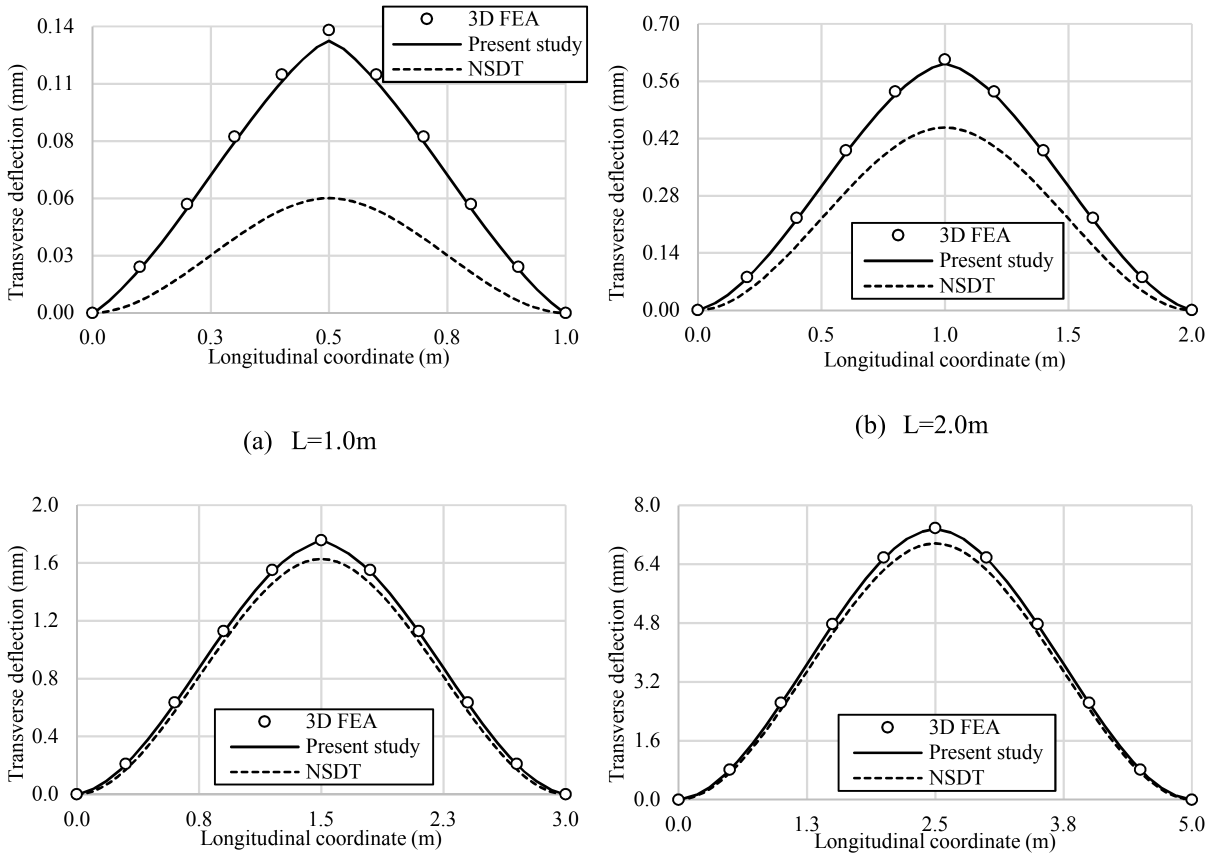

(a) L=1.0m

(b) L=2.0m

(a) L=3.0m

(d) L=5.0m

Figure 3.10. Deflections predicted by the present solution and non-shear deformable study (a) L=1.0m, (b) L=2m, (c) L=3m, and (d) L=4m.

3.9.5. Example 5: Effect of shear deformation-2

To further investigate the contribution of shear deformation a simply supported beam with a W150x13 section subjected to a uniformly distributed line load q=15kN/m is considered. Spans are varied so that the span to depth ratios vary from 3.1 to 41. Two cases are considered: (a) with GFRP-strengthening with $t_1 = 19mm$, width $b_p = 100mm$ and (b) without strengthening. The strengthened beam is solved using the shear deformable element developed in the present study and the non-shear deformable solution (Pham and Mohareb 2015b), and the ratio of the shear deformable solution to the non-shear deformable solution is plotted against the span to depth ratio (Fig. 3.11). For comparison, the un-strengthened beam is solved using Timoshenko beam theory (shear deformable) and the Euler-Bernoulli beam theory (non-shear deformable). A single element is used to model a half of the span. In a manner similar to homogeneous beams, the results show that shear deformation effects tend to be significant for short-span beams, where the ratio of peak deflections significantly exceed unity and tends to approach unity as the span to depth ratio increases. Also, the ratio of the deflection of the fully-reinforced beam is higher than that of the unreinforced beam. This shows that shear deformation is more important in composite beams. When the shear deformation contribution is 5%, i.e., the ratio of peak deflections 1.05, the corresponding span to depth ratio for the strengthened beam is 15.5 which compares to only 8.78 for the non-strengthened, suggesting that shear deformation for strengthened beams is significantly more important than un-strengthened beams.

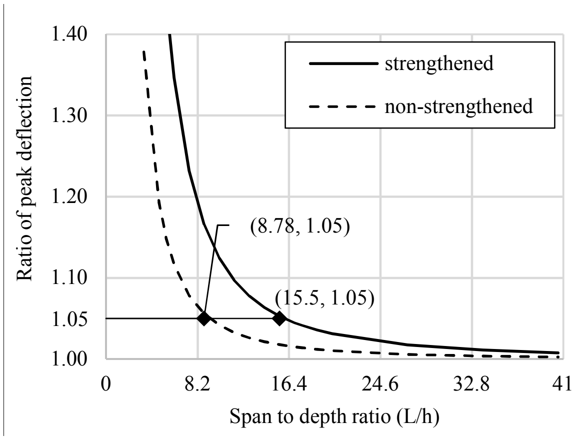

Figure 3.11. Ratios of the deflection based shear deformable solution to that based on non-shear deformable solution for simply supported beam

3.10. Conclusions

- A closed form solution was developed for steel beams strengthened with GFRP plate. The solution captures shear deformation effects and partial interaction between the GFRP and steel section.
- A super-convergent finite element formulation was developed based on the closed form solution. The element eliminates discretization errors common in conventional interpolation techniques and allows the modelling of problems with a minimal number of elements.
- The element was shown to yield results in very close agreement with 3D FEA solutions.
- The present solution proposes a procedure to determine the yielding moment of the GFRP-strengthened steel section taking the effect of partial interaction.
- Shear deformation effects were shown to be significantly more important when predicting deflections for strengthened beams than for the case of homogeneous beams. For example, example 4 shows that the omission of shear deformation effects would under-predict the peak deflection by 5% for a homogeneous beam with span to depth ratio lower than 8.7. By comparison, the span to depth ratio associated with the same error is found to be 15.5 for a strengthened beam.

Appendix 3.1- Closed Form Solution for the Equilibrium Equations

From Eqs. (3.8), by expressing in a non-matrix form, one obtains

$$\begin{aligned}
&-\alpha_b D^2 W_b + W_b - W_p + r_1 DV + r_2 \theta_{xb} = 0 \\
&-W_b - \alpha_p D^2 W_p + W_p - r_1 DV - r_2 \theta_{xb} = 0 \\
&-r_1 DW_b + r_1 DW_p + \alpha_I D^4 V - \left(\alpha_s + r_1^2\right) D^2 V + \left(\alpha_s - r_1 r_2\right) D\theta_{xb} = 0 \\
&r_2 W_b - r_2 W_p + \left(r_1 r_2 - \alpha_s\right) DV - \alpha_J D^2 \theta_{xb} + \left(\alpha_s + r_2^2\right)\theta_{xb} = 0
\end{aligned} \tag{3.29)a-d}$$

Equation (3.29)a yields

$$W_p = -\alpha_b D^2 W_b + W_b + r_1 DV + r_2 \theta_{xb} \tag{3.30}$$

From Eq. (3.30), by substituting into Eqs. (3.29)b-d, one has

$$\begin{aligned}
&\alpha_b \alpha_p D^4 W_b - \left(\alpha_b + \alpha_p\right) D^2 W_b - r_1 \alpha_p D^3 V - r_2 \alpha_p D^2 \theta_{xb} = 0 \\
&-r_1 \alpha_b D^3 W_b + \alpha_I D^4 V - \alpha_s D^2 V + \alpha_s D\theta_{xb} = 0 \\
&+r_2 \alpha_b D^2 W_b - \alpha_s DV - \alpha_J D^2 \theta_{xb} + \alpha_s \theta_{xb} = 0
\end{aligned} \tag{3.31}$$

Equations (3.31)b-c can be re-written as

$$\begin{aligned}
D^3 W_b &= \frac{\alpha_I}{r_1 \alpha_b} D^4 V - \frac{\alpha_s}{r_1 \alpha_b} D^2 V + \frac{\alpha_s}{r_1 \alpha_b} D\theta_{xb} \\
D^2 W_b &= \frac{\alpha_s}{r_2 \alpha_b} DV + \frac{\alpha_J}{r_2 \alpha_b} D^2 \theta_{xb} - \frac{\alpha_s}{r_2 \alpha_b} \theta_{xb}
\end{aligned} \tag{3.32}$$

From Eq. (3.31)c, by differentiating with respect to z and equating to Eq. (3.31)b yields

$$r_1 \alpha_J D^3 \theta_{xb} - \left(r_1 + r_2\right) \alpha_s D\theta_{xb} = r_2 \alpha_I D^4 V - \left(r_1 + r_2\right) \alpha_s D^2 V \tag{3.33}$$

Also, from Eq. (3.31)b, by differentiating with respect to *z* and Eq. (3.31)c , by substitution into Eq. (3.31)a, one obtains

$$\begin{aligned}
&\left[\left(\alpha_s - r_1 r_2\right) r_2 \alpha_b \alpha_p - r_1 \left(\alpha_b + \alpha_p\right) \alpha_J\right] D^2 \theta_{xb} + r_1 \left(\alpha_b + \alpha_p\right) \alpha_s \theta_{xb} = \\
&= -r_2 \alpha_b \alpha_p \alpha_I D^5 V + \left(r_2 \alpha_b \alpha_p \alpha_s + r_1^2 r_2 \alpha_b \alpha_p\right) D^3 V + r_1 \left(\alpha_b + \alpha_p\right) \alpha_s DV
\end{aligned} \tag{3.34}$$

From Eq. (3.34), by differentiating with respect to *z* and combining with Eq. (3.33), one obtains

$$D\theta_{xb} = -\beta_1 D^6 V + \beta_2 D^4 V + D^2 V; \qquad D^3 \theta_{xb} = -\beta_4 D^6 V + \beta_3 D^4 V \tag{3.35}$$

in which the following parameters have been defined

$\beta_1 = r_1 \alpha_b \alpha_p \alpha_I \alpha_J / \alpha_s \chi;$

$\beta_2 = \left\{ r_1 \alpha_b \alpha_p \left(\alpha_s + r_1^2 \right) \alpha_J - \alpha_I \left[r_2 \left(\alpha_s - r_1 r_2 \right) \alpha_b \alpha_p - r_1 \left(\alpha_b + \alpha_p \right) \alpha_J \right] \right\} / \alpha_s \chi;$

$\beta_3 = \left(r_1 + r_2 \right) \alpha_b \alpha_p \alpha_I / \chi;$

$\beta_4 = \left[r_1 \left(\alpha_b + \alpha_p \right) \alpha_I + \left(r_1 + r_2 \right) \left(\alpha_s + r_1^2 \right) \alpha_b \alpha_p \right] / \chi$

$\chi = \left(r_1 + r_2 \right) \left(\alpha_s - r_1 r_2 \right) \alpha_b \alpha_p - r_1 \left(\alpha_b + \alpha_p \right) \alpha_J$

From Eq. (3.35)a, by differentiating twice with respect to *z* and substituting into Eq. (3.35)b, one has

$$-\beta_1 D^8 V + \left(\beta_2 + \beta_4 \right) D^6 V + \left(1 - \beta_3 \right) D^4 V = 0 \tag{3.36}$$

The solution of Eq. (3.36) takes the form

$$V = A_1 + A_2 z + A_3 z^2 + A_4 z^3 + \sum_{i=5}^{8} A_i e^{m_i z} \tag{3.37}$$

where $A_i, (i = 1, \ldots, 10)$ are integration constants and m_i are roots of the characteristic equation

$$-\beta_1 m^4 + \left(\beta_2 + \beta_4 \right) m^2 + \left(1 - \beta_3 \right) = 0 \tag{3.38}$$

From Eq. (3.37), by substituting into Eq. (3.35)a and integrating with respect to *z*, one obtains

$$\theta_{xb} = A_9 + 2 z A_3 + 3 A_4 z^2 + \sum_{i=5}^{8} A_i m_i \left(1 + \beta_2 m_i^2 - \beta_1 m_i^4 \right) e^{m_i z} \tag{3.39}$$

From Eqs. (3.37) and (3.39), by substituting into Eq. (3.32)b and integrating twice with respect to *z* twice, one obtains

$$W_b = A_{11} + A_{10} z + \frac{\alpha_s z^2}{2 r_2 \alpha_b} A_2 + 3 \frac{\alpha_J z^2}{r_2 \alpha_b} A_4 + \sum_{i=5}^{8} m_i \frac{\alpha_J + \left(\beta_2 - \beta_1 m_i^2 \right) \left(m_i^2 \alpha_J - \alpha_s \right)}{r_2 \alpha_b} A_i e^{m_i z} - \frac{\alpha_s z^2}{2 r_2 \alpha_b} A_9 \tag{3.40}$$

Finally, by substituting Eqs. (3.37)-(3.40) into Eq. (3.30), the longitudinal displacement is obtained as

$$\begin{aligned} W_p = {} & \left(\frac{r_1 r_2 - \alpha_s}{r_2} + \frac{\alpha_s}{2 r_2 \alpha_b} z^2 \right) A_2 + 2 \left(r_1 + r_2 \right) z A_3 + 3 \left(-2 \frac{\alpha_J}{r_2} + \frac{\alpha_J + \left(r_1 + r_2 \right) r_2 \alpha_b}{r_2 \alpha_b} z^2 \right) A_4 \\ & + \sum_{i=5}^{8} \left[\left(r_1 + r_2 \right) m_i + m_i \left(1 - m_i^2 \alpha_b \right) \frac{\alpha_J}{\alpha_b r_2} + \left(\beta_2 - \beta_1 m_i^2 \right) \frac{\left(\alpha_b r_2^2 + \alpha_b \alpha_s + \alpha_J - m_i^2 \alpha_b \alpha_J \right) m_i^2 - \alpha_s}{r_2 \alpha_b} m_i \right] A_i e^{m_i z} \\ & + \left(\frac{\alpha_s + r_2^2}{r_2} - \frac{\alpha_s}{2 r_2 \alpha_b} z^2 \right) A_9 + A_{10} z + A_{11} \end{aligned} \tag{3.41}$$

There are 11 constants $C_i \left(i=1,...,11\right)$ in the solution given by (3.37), (3.39), (3.40), and (3.41) but only 10 boundary conditions, indicating that one of the constants is redundant and can be expressed in terms of the other constant. The extra constant arose from differentiating Eq. (3.31)c to obtains Eqs. (3.33). To find dependent constants, the closed from solutions are substituted back to the equilibrium equations (3.29), yielding

$$A_9 = A_2 + 6\left[\frac{\alpha_J}{\alpha_s} + \frac{\left(r_1+r_2\right)r_2\alpha_b\alpha_p}{\alpha_s\left(\alpha_b+\alpha_p\right)}\right]A_4 \tag{3.42}$$

From Eq. (3.42), by substituting into Eqs. (3.37), (3.39), (3.40), and (3.41) and introducing new symbols by substituting $A_1,...,A_4$ as $C_1,...,C_4$; A_{10}, A_{11} as C_5, C_6; and $A_5,\ldots,A_8$ as $C_7,\ldots,C_{10}$, the closed form solution given by Eqs. (3.10) is recovered.

References

[3-1] Akhras, G., and Li, W. (2007), Stability and vibration analysis of composite plates using spline strips with higher-order shear deformation, Journal of Structural Engineering and Mechanics, 27(1), 1-16.

[3-2] Back SY, Will KM (2008). Shear-flexible thin-walled element for composite I-beams, Engineering and Structures, 30(5),1447–58.

[3-3] Bai. F. and Davidson, J.S., (2016), Theory for composite sandwich structures with unsymmetrical wythes and transverse interaction, Engineering Structures, 116, 178-191.

[3-4] Challamel, N., Bernard, F. and Casandjian, C. (2010), Out-of-plane behavior of partially composite or sandwich beams by exact and finite element methods, Thin-Walled Structures, 48(8), 561-580.

[3-5] Dall'Asta, A.D. and Zona, A. (2004), Comparison and validation of displacement and mixed elements for the non-linear analysis of continuous composite beams, Computers & Structures, 82(23-26), 2117-2130.

[3-6] Dalir, M.A. and Shooshtari, A. (2015), Exact mathematical solution for free vibration of thick laminated plates, Journal of Structural Engineering and Mechanics, 56(5), 835-854.

[3-7] Daouadji, T.H., Hadji, L., Meziane, M., and Bekki, H. (2016), Elastic analysis effect of adhesive layer characteristics in steel beams strengthened with a fiber-reinforced polymer plates, J. Structural Engineering and Mechanics, 59(1), 80-100.

[3-8] Desai, Y.M. and Ramtekkar G.S. (2002), Mixed finite element model for laminated composite beams, Journal of Structural Engineering and Mechanics, 13(3), 261-276.

[3-9] Ditaranto R.A., (1973), Static analysis of a laminated beam. J. Manuf. Sci. Eng., 95(3), 755–61.

[3-10] Ecsedi, I. and Baska, A. (2016), Analytical solution for layered composite beams with partial shear interaction based on Timoshenko beam theory, Engineering Structures, 115, 107-117.

[3-11] Faella, C., Martinelli, E., and Nigro, E. (2010), Steel-concrete composite beams in partial interaction: Closed-form "exact" expression of the stiffness matrix and the vector of equivalent nodal forces, Engineering Structures, 32(9), 2744-2754.

[3-12] Ganapathi, M., Patel, B.P.m Polit, O., and Touratier, M. (1999), A C1 finite element including transverse shear and torsion warping for rectangular sandwich beams, International Journal for Numerical Methods in Engineering, 45(1), 47-75.

[3-13] Gara, F., Ranzi, G. and Leoni, G. (2006), Displacement-based formulations for composite beams with longitudinal slip and vertical uplift, International Journal for Numerical Methods in Engineering, 65(8), 1197-1220.

[3-14] Joao, B.M.S.J. (2013), Exact finite elements for multilayered composite beam-columns with partial interaction, Computers & Structures, 123, 48-57.

[3-15] Keo, P., Nguyen, Q.,H., Sobja, H., and Hjiaj, M., Exact finite element formulation for an elastic hybrid beam-column in partial interaction with shear-deformable encasing component, Engineering Structures, 125, 494-503.

[3-16] Koutsawa, Y., and Daya, E.M. (2007), Static and free vibration analysis of laminated glass beam on viscoelastic supports, International Journal of Solids and Structures, 44(25-26), 8735-8750.

[3-17] Martinelli, E., Faella, C., and Palma, G.D. (2012), Shear-flexural steel-concrete composite beams in partial interaction: Closed-form "exact" expression of the stiffness matrix, Journal of engineering mechanics, 138(2), 151-163.

[3-18] Mini, K.M., Alapatt, R.J, David, A.E., Radhakrishnan, A., Cyriac, M.M., and Ramakrishnan, R. (2014), Experimental study on strengthening of R.C beam using glass fibre reinforced composite, Journal of Structural Engineering and Mechanics, 50(3), 275-286.

[3-19] Nguyen, Q.H., Martinelli, E., and Hiiaj, M. (2011), Derivation of the exact stiffness matrix for a two-layer Timoshenko beam element with partial interaction, Journal of engineering structures, 33(2), 298-307.

[3-20] Nowzartash, F. and Mohareb, M. (2005), Planar bending of sandwich beams with transverse loads off the centroidal axis, Journal of Structural Engineering, 131(4), 385-396.

[3-21] Perel, V.Y. and Palazotto, A.N. (2001), Finite element formulation for cylindrical bending of a transversely compressible sandwich plate, based on assumed transverse strains, International Journal of Solids Structures, 38(30-31), 5373-5409.

[3-22] Pham, P.V., (2013), Stress-deformation theories for the analysis of steel beams reinforced with GFRP plates, Master of Science Thesis, University of Ottawa.

[3-23] Pham, P.V. and Mohareb, M. (2014), A shear deformable theory for the analysis of steel beams reinforced with GFRP plates, Thin-Walled Structures, 85, 165-182.

[3-24] Pham, P.V and Mohareb, M. (2015a), Non-shear Deformable Theory for Analysis of Steel Beams Reinforced with GFRP Plate Closed-Form Solution, Journal of Structural Engineering, ASCE, 141(12), 04015063.

[3-25] Pham, P.V. and Mohareb, M. (2015b), Finite-Element Formulations for the Spatial Static Response of Steel Beams Bonded to a GFRP Plate, Journal of Engineering Mechanics, ASCE, 141(4), 04014143.

[3-26] Ranzi, G., Gara, F., and Ansourian, P. (2006), General method of analysis for composite beams with longitudinal and transverse partial interaction, Computers and Structures, 84(31-32), 2373-2384.

[3-27] Ranzi, G. and Zona, A. (2007), A steel-concrete composite beam model with partial interaction including the shear deformability of the steel component, Engineering Structures 29(11), 3026-3041.

[3-28] Salari, M.R., Shing, P.B., and Frangopol, D.M. (1998), Nonlinear analysis of composite beams with deformable shear connectors, Journal of Structure Engineering, 124(10), 1148-1158.

[3-29] Sarabiyik, A., and Caglar, N. (2016), Flexural strengthening of RC Beams with low-strength concrete using GFRP and CFRP, Journal of Structural Engineering and Mechanics, 58(5), 825-845.

[3-30] Harries, A.K. and El-Tawil, S. (2008), Steel-FRP composite structural systems, International Conference on Composite Construction in Steel and Concrete 2008, Composite Construction in Steel and Concrete VI, Colorado, United States, July.

Chapter 4: Lateral Torsional Buckling of Steel beams strengthened with GFRP plate

Abstract

The present study investigates the lateral-torsional buckling of wide flange steel members strengthened by a Glass Fiber Reinforced Polymer (GFRP) plate bonded to one of the flanges through an adhesive layer. A variational formulation and two finite elements are developed for the problem. The formulation captures global and local warping effects, shear deformation due to bending and twist, and partial interaction between the steel and GFRP provided by the flexible layer of adhesive. The destabilizing effects due to strong axis bending, axial force and load height effect are incorporated into the formulation. The first element involves two nodes and 16 buckling degrees of freedom (DOFs) while the second element involves three nodes and 14 DOFs. Comparisons of the present model results against those based on 3D finite element analysis based on solid elements demonstrate the ability of the present models to accurately predict the buckling loads and mode shapes at a fraction of the modelling and computational efforts. Practical examples quantify the gain in elastic buckling strength achieved by GFRP strengthening, and characterize the moment gradient factors and load height effects. Elastic buckling interaction diagrams are developed for beam-columns and comparisons are provided to interaction diagrams of un-strengthened beams.

Keywords: Lateral torsional buckling, flexural torsional buckling, GFRP strengthening, wide flange beam, three node element, finite element analysis, shear deformation

---

4.1. Introduction

GFRP is a lightweight, durable, and economic material that can be formed into thick plates capable of resisting tensile, shear and compression stresses (El Damatty et al 2003). Strengthening existing steel structures using adhesively bonded GFRP plates has become a viable option in recent years given the advantages it offers; when compared to traditional strengthening methods using either welded- or bolted-steel plates (Liu and Gannon 2009), GFRP installation is relatively easier and faster. When compared to bonded carbon-FRP (CFRP) plates with relatively high elasticity modulus (Miller et al 2001, Shaat and Fam 2009), GFRP plates possess a lower stiffness. However, this drawback can be compensated for by using thicker plates (El Damatty et al 2003). This provides the added advantage of achieving a higher flexural stiffness compared to stiffer but thinner CFRP plates and thus can be advantageous when strengthening thin compression flanges to increase their local and global buckling strengths (Accord and Earls 2006, Aguilera and Fam 2013). Additionally, when in contact with steel, GFRP does not induce galvanic corrosion.

Strengthening applications involving GFRP plates were investigated in a number of studies. El Damatty et al. (2003) conducted an experimental study for W-shaped steel beams strengthened with GFRP plate bonded to the tensile flange to increase the ultimate load capacity of the system. Youssef (2006) experimentally investigated the ultimate load capacity of W-steel beams strengthened with two GFRP plates bonded to the compressive and tensile steel flanges. Accord and Earls (2006) numerically investigated the enhancement of local buckling capacity and ductility of W-section cantilever steel beams with four GFRP plates bonded to the compression flange. Harries et al. (2009) conducted experiments on WT steel columns strengthened with GFRP plates bonded to the web to delay local buckling. Other GFRP strengthening arrangements were investigated on members with cruciform cross-sections (Aydin and Aktas 2015). Aguilera and Fam (2013) reported an experimental study on T-joints made of hollow steel sections strengthened with GFRP plates. Siddique and El Damatty (2013) developed a finite element technique to characterize the enhancement in local buckling capacity for steel beams strengthened with GFRP plate bonded to the compression flange. The model was based on a 13-node consistent degenerated triangular sub-parametric shear-locking free shell elements. Each layer (GFRP, steel) was modelled by a shell element while the adhesive layer joining them was idealized as 2D distributed springs with zero thickness to represent the shear stiffness and a distributed transverse spring to represent its compressibility. Zaghian (2015) developed a non-conforming four-node finite shell element for the buckling analysis of steel plates strengthened with GFRP plates. While the above studies focused on developing models for predicting the local buckling strength or ultimate load capacity of steel-adhesive-GFRP systems, none of them tackled their lateral torsional buckling strength.

Buckling solutions for composite systems in general include the work of Girhammar and Pan (2007) who developed an Euler-Bernoulli buckling theory for two-layer members with deformable shear connectors. Xu and Wu (2007) developed a shear deformable buckling theory for two-layer members with partial interaction. Challamel and Girhammar (2012) formulated a non-shear deformable theory for the lateral torsional buckling analysis of layered composite beams that captures the effect of partial interaction between the layers. Zaghian (2015) developed a non-conforming four-node finite shell element for the buckling analysis of steel plates symmetrically strengthened with GFRP plates. The previous models are limited to members with rectangular sections, and thus do not incorporate warping effects which are significant in beams of wide flange cross-sections of interest in the present study. Also, most studies neglected shear deformations in their formulations. Shear deformation effects were shown to influence lateral torsional buckling predictions in short span beams with homogeneous materials (Erkmen and Mohareb 2008, Wu and Mohareb 2011a,b, Sahraei et al 2015, Sahraei and Mohareb 2016).

Pham and Mohareb (2015b) developed a non-shear deformable theory for the static analysis of steel beams strengthened with GFRP plates and formulated a closed solution. A shear deformable theory was developed in (2014) and the field equations were solved using the finite difference technique. Finite element formulations based on shear and non-shear deformable theories were developed in Pham and Mohareb (2015a). A common theme in the studies in Pham and Mohareb (2014, 2015a, 2015b) is that they are limited to linear static analysis and has not tackled buckling problems. In this respect, the present study complements past work by developing a lateral torsional buckling solution. The work of static analyses in Pham and Mohareb (2014, 2015b) has shown that shear deformation effects be more important than in homogeneous beams. As such, the present study benefits from past knowledge by incorporating the effect of shear deformation due to bending and warping into the lateral torsional buckling analysis formulation sought.

Additionally, because the modulus of elasticity of adhesives is orders of magnitude lower than those of steel or GFRP, it may provide only partial interaction between both materials. As a result, throughout pre-buckling bending, a plane cross-section for the system before deformation may not remain plane after deformation (Gara et al. 2006, Challamel and Girhammar 2012). Traditional analysis methods based on the plane section assumption (e.g., the transformed section method) are thus expected to under-predict the displacement response (Wenwei and Guo 2006). Hence, the present formulation incorporates the effect of partial interaction by relaxing the plane section assumption, both throughout pre-buckling and buckling. Also, global and local warping effects are included in the present formulation owing to their importance in buckling analysis of beams with open sections.

In summary, the present study develops finite element formulations for the lateral-torsional buckling analysis of beams with wide flange steel sections strengthened with a single GFRP plate adhesively bonded to one of the flanges. Distinctive features of the theory include: (1) it is based on a 1D beam solution, (2) it captures partial interaction between steel beam and GFRP plate, (3) it includes the contribution of shear strains within the adhesive layer, and (4) it includes the effect of shear deformations due to bending and warping.

4.2. Statement of the problem

A wide flange steel beam with a doubly symmetric cross-section is strengthened with a GFRP plate bonded to one of the flanges through a thin adhesive layer (Figure 4.1). The beam is subjected to general transversely distributed load $q_y\left(z,y\right)$ acting along the curve $y_{qy}\left(z\right)$ within the web middle surface and/or a longitudinally distributed load $q_z\left(z,y\right)$ acting along $y_{qz}\left(z\right)$. The loads are increased to $\lambda q_y\left(z,y\right)$ and/or $\lambda q_z\left(z,y\right)$ at which the member is assumed to buckle in a lateral torsional mode. It is required to determine the buckling load level λ and the corresponding buckling mode by developing one-dimensional finite element formulation.

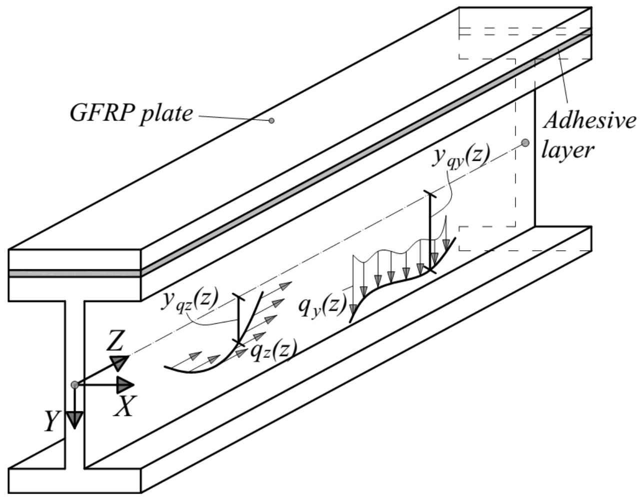

Figure 4.1. A GFRP-reinforced steel beam under the application of distributed loads

4.3. Assumptions

The assumptions of the present theory are an extension of those adopted under Vlasov (1961) and Gjelsvik (1981) beams to the composite beam, i.e.,

(i) In line with Vlasov theory, the section contours for the beam and the GFRP plate are assumed to remain un-deformed in their own plane,

(ii) The displacement fields are expressed according to the Gjelsvik beam theory (1981) which captures global and local warping effects,

(iii) The steel beam and the GFRP plate are assumed to act as Timoshenko beams, i.e., their rotations about the x, y axes are considered distinct from the derivatives of the transverse and lateral displacements. The assumption is further extended to warping which is assumed to be distinct from the derivative of the angle of twist.

The following additional kinematic assumptions are also made:

(iv) Perfect bond is assumed at interfaces between the adhesive-GFRP and adhesive-steel interfaces,

(v) The adhesive is assumed to act as a flexible elastic material with a small modulus of elasticity relative to those of the beam or GFRP. As a result, the adhesive internal strain energy due to longitudinal normal stresses is considered negligible compared to that of the GFRP and steel,

(vi) The compressibility of the adhesive layer in the transverse direction is assumed negligible compared to the transverse displacements of the GFRP and the steel section, i.e., the transverse displacement of the steel beam and the GFRP can be assumed to be nearly equal,

(vii) The displacement fields within the adhesive are assumed to have a linear variation across the thickness,

(viii) Within the steel and GFRP, only the longitudinal normal stresses and the shear stresses in the tangential plane are assumed to contribute to the internal strain energy while contributions of all other stress components are assumed to be comparatively negligible.

Finally, the following assumptions are made regarding the materials and buckling configurations

(ix) The steel, GFRP and adhesive are assumed to be characterized by two material constants; Young modulus and the shear modulus in a manner akin to linearly elastic isotropic materials. The time-dependent properties of the adhesive are omitted in the present pre-buckling analysis. If such properties are known, proper modifications can be made to the pre-buckling analysis while the present buckling analysis remains applicable to assess the stability of the system at any point on the equilibrium path.

The two-constant constitutive model adopted for the GFRP is applicable for isotropic GFRP plates made of chopped random fibers, and for orthotropic GFRP plates with fibers oriented in the longitudinal direction. Past 3D FEA analyses (Xiao et al. 2014) have shown that the critical loads are sensitive only to the Young modulus E_z in longitudinal direction z (Fig. 4.1) and the shear moduli G_{yz}, G_{xz} for stresses acting on the transverse plane and insensitive to remaining properties. In such cases, it was possible to accurately predict the buckling loads for orthotropic beams using an isotropic-like two-constant models (e.g., Du and Mohareb 2016, Hu and Mohareb 2017). Other GFRP constitutive representations such as anisotropic or orthotropic materials where the fibers are not oriented longitudinally, are outside the scope of the present model.

(x) The member buckles in an inextensional mode. This means that during buckling, the centroidal strain and the curvature in the principal *yz*-plane remain unchanged, so that the member buckles under constant axial force and bending moments (Wu and Mohareb 2011a,b, Trahair 1993), and

(xi) Pre-buckling deformation, distortion and P-delta effects are neglected.

4.4. Kinematics

Figures 4.2a and 4.2b present four configurations which describe the strengthened beam starting from an un-deformed state (Configuration 1) to a lateral-torsional buckling state (configuration 4). Under the application of transversely distributed load $q_y(z)$ and longitudinally distributed load $q_z(z)$, the beam is displaced from Configuration 1 to 2. The displacement fields throughout this step are shown in Fig. 4.2b, in which $w_{1p}(z)$ is the longitudinal displacement at the wide flange beam centroid, $w_{3p}(z)$ is that of the GFRP plate centroid, $v_p(z)$ is the transverse deflection for the entire system (the beam, the GFRP plate and the adhesive), and $\theta_{xp}(z)$ is the rotation angle about the strong bending axis (X) for the GFRP plate and the steel section. Subscript p is used to imply that displacements take place in the pre-buckling state.

The applied reference loads are increased to $\lambda q_y(z)$, $\lambda q_z(z)$ until the system attains the point of onset of buckling (Configuration 3), in which the unknown load multiplier λ is to be determined from the buckling analysis. As a result, the associated pre-buckling displacements are assumed to linearly increase with the reference loads (Assumption x) and the corresponding displacements become $\lambda w_{1p}(z), \lambda w_{3p}(z)$, $\lambda v_p(z)$ and $\lambda \theta_{xp}(z)$.

Throughout buckling (from Configuration 3 to 4), the applied loads $\lambda q_y(z)$, $\lambda q_z(z)$ are assumed to remain constant in direction and magnitude while the steel beam and the GFRP plate centroids undergo lateral displacements $u_{1b}(z)$ and $u_{3b}(z)$, respectively. In Configuration 4, the steel beam and GFRP plate undergo weak axis rotation $\theta_{y1b}(z)$ and $\theta_{y3b}(z)$, respectively, while the entire strengthened cross-section is assumed to undergo a twisting angle $\theta_{zb}(z)$. The global warping deformation of the steel beam is $\psi_{1b}(z)$ while that of the GFRP plate is denoted as $\psi_{3b}(z)$. Global warping deformation of the GFRP plate vanishes. The local warping deformations for both the GFRP plate and the steel beam are assumed to be linearly proportional to $\theta_{zb}'(z)$ in a manner that is consistent with the Gjelsvik theory.

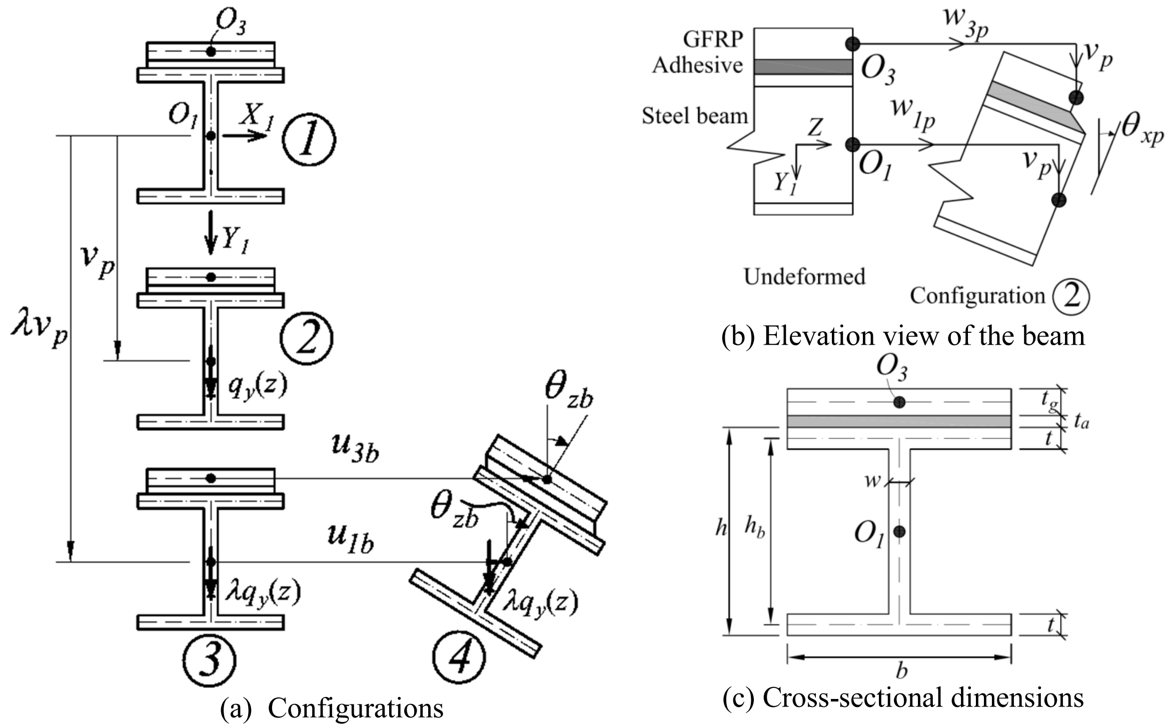

Figure 4.2. Beam configurations (a, b) and cross-sectional dimensions (c)

As a matter of convention, rotations θ_{xp}, $\theta_{y1b}(z)$ and $\theta_{y3b}(z)$ are assumed positive when rotating in the same direction as $v'_p(z)$, $u'_{1b}(z)$ and $u'_{3b}(z)$, respectively, while twisting angle $\theta_{zb}(z)$ is assumed positive when rotating clockwise (Pham and Mohareb 2014). The sign convention for other displacement fields are shown in Figs. 4.2a,b. Also, all field variables with a subscript p denote fields (displacements, strains, stresses, or stress resultants) arising during the pre-buckling stage (from Configuration 1 to 2) and variables with a subscript b denote fields arising during buckling (from Configuration 3 to 4). Total fields arising in going from Configuration 1 to 4 are denoted by the superscript *, while fields with no subscripts p,b nor a superscript * are generic and are considered valid for pre-buckling, buckling, or total responses.

Figure 4.2c shows the geometric parameters for the cross-section. The steel beam has a total depth h, an centerline depth h_b, web thickness w, flange thickness t, and flange width b, while the thickness of the adhesive layer is t_a and that of GFRP plate is t_g. Material elasticity and shear moduli of steel are denoted as E_s and G_s, respectively while those of GFRP are E_g and G_g. The shear modulus of adhesive is assumed as G_a.

4.5. Coordinate systems and displacements at an arbitrary point lying on sections

Three global coordinate systems $O_iX_iY_iZ$ ($i = 1,2,3$) are defined for the wide flange steel beam, adhesive layer and GFRP plate, respectively, in which O_i are centroids of each material (Fig. 4.3a) and subscripts $i = 1,2,3$ respectively denote the steel section, the adhesive, and the GFRP plate.

In a manner consistent with the Gjelsvik thin walled beam theory, the local coordinates of a point A_i offset from the section contour (Fig. 4.3b) are determined by three local coordinates $\left(s_i, n_i, z\right)$ in which s_i is a curvilinear contour coordinate measured from Origin O_i while n_i is the normal distance measured from the contour line. As a matter of sign convention, positive signs of n_i, z and the contour tangent follows a right-handed coordinate system. Angle $\alpha\left(s_i\right)$ between the positive directions of the tangent to the contour at the point of interest and global $X-$direction is taken positive in the clockwise direction from the $X-$axis. When the beam deforms under the application of loads, a Point A_i undergoes displacements $\left(\xi_i, \eta_i, \zeta_i\right)$ along the tangent, normal, and longitudinal directions, respectively.

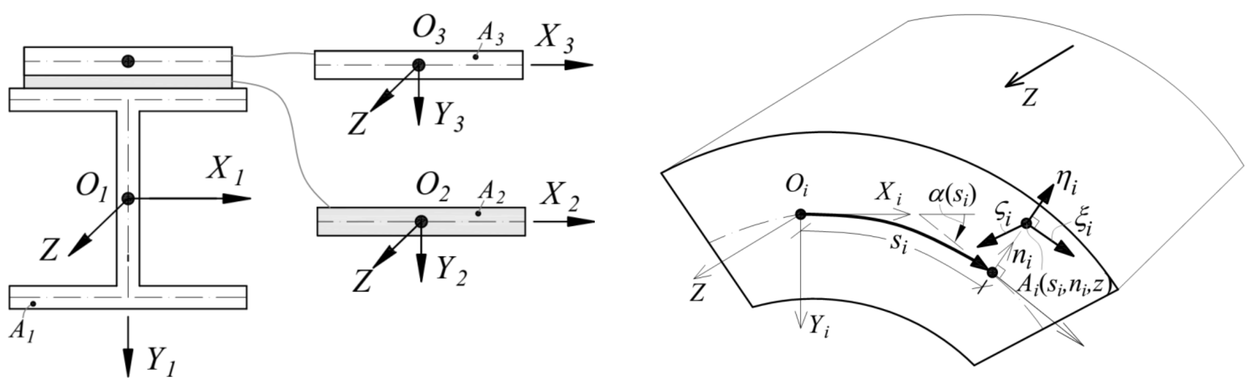

(a) Global coordinate systems for steel beam, adhesive layer, and GFRP plate

(b) Displacement fields of a Point A_i offset from the section contour

Figure 4.3. Coordinate systems and local displacement fields

4.6. Pre-buckling displacement fields

Based on Gjelsvik (1981), the expression of the pre-bucking displacements $\left(\xi_{ip}, \eta_{ip}, \zeta_{ip}\right)$ of Point $A_i\left(s_i, n_i, z\right)$ along the local directions (Figs.4.3a,b) can be related to the global displacement fields

$w_{1p}(z)$, $w_{3p}(z)$, $v_p(z)$ and $\theta_{xp}(z)$. For the steel beam ($i=1$), the displacements of $A_1(s_1,n_1,z)$ are given by

$$\begin{Bmatrix} \xi_{1p}(s_1,n_1,z) \\ \eta_{1p}(s_1,n_1,z) \\ \zeta_{1p}(s_1,n_1,z) \end{Bmatrix} = \begin{bmatrix} 0 & \sin\alpha(s_1) & 0 \\ 0 & -\cos\alpha(s_1) & 0 \\ 1 & n_1\cos\alpha(s_1)D & -y_1(s_1) \end{bmatrix} \begin{Bmatrix} w_{1p}(z) \\ v_p(z) \\ \theta_{xp}(z) \end{Bmatrix} \tag{4.1}$$

where $\alpha_1(s)=0^o$ for the flanges, $\alpha_1(s)=90^o$ for the web and D denotes the derivative operator $\partial/\partial z$. Also, for the pre-buckling displacement fields of Point A_3 within the GFRP plate and noting that $\alpha(s_3)=0$, one obtains $\xi_{3p}=0$ and

$$\begin{Bmatrix} \eta_{3p}(s_3,n_3,z) \\ \zeta_{3p}(s_3,n_3,z) \end{Bmatrix} = \begin{Bmatrix} 0 & -1 & 0 \\ 1 & n_3 D & y_3(s_3) \end{Bmatrix} \begin{Bmatrix} w_{3p}(z) \\ v_p(z) \\ \theta_{xp}(z) \end{Bmatrix} \tag{4.2}$$

For the adhesive layer, the displacement fields of a point A_2 are linearly interpolated from the displacements at the top surface of steel flange and the bottom surface of the GFRP plate (Assumption vii), i.e.,

$$\begin{Bmatrix} \xi_{2p}(s_2,n_2,z) \\ \eta_{2p}(s_2,n_2,z) \\ \zeta_{2p}(s_2,n_2,z) \end{Bmatrix} = \left(\frac{1}{2}+\frac{n_2}{t_a}\right) \begin{Bmatrix} \xi_{3p}(s_3,-t_g/2,z) \\ \eta_{3p}(s_3,-t_g/2,z) \\ \zeta_{3p}(s_3,-t_g/2,z) \end{Bmatrix} + \left(\frac{1}{2}-\frac{n_2}{t_a}\right) \begin{Bmatrix} \xi_{1p}(s_1,t/2,z) \\ \eta_{1p}(s_1,t/2,z) \\ \zeta_{1p}(s_1,t/2,z) \end{Bmatrix} \tag{4.3}$$

By noting that $\alpha(s_1)=0$ for the top flange, Eq. (4.3) simplifies to $\xi_{2p}=0$ and

$$\begin{Bmatrix} \eta_{2p}(s_2,n_2,z) \\ \zeta_{2p}(s_2,n_2,z) \end{Bmatrix} = \begin{Bmatrix} 0 & 0 & -1 & 0 \\ \left(\frac{1}{2}-\frac{n_2}{t_a}\right) & \left(\frac{1}{2}+\frac{n_2}{t_a}\right) & \left[\left(\frac{1}{2}-\frac{n_2}{t_a}\right)\frac{t}{2}-\left(\frac{1}{2}+\frac{n_2}{t_a}\right)\frac{t_g}{2}\right]D & \left(\frac{1}{2}-\frac{n_2}{t_a}\right)\frac{h_b}{2} \end{Bmatrix} \begin{Bmatrix} w_{1p} \\ w_{3p} \\ v_p \\ \theta_{xp} \end{Bmatrix} \tag{4.4}$$

4.7. Total displacement fields

Under the application of loads $\lambda q_y(z)$ and $\lambda q_z(z)$, the strengthened beam deforms from Configuration 1 to 4. The associated total displacement fields $(\xi_i^*,\eta_i^*,\zeta_i^*)$ of Point $A_i(s_i,n_i,z)$ (Figs. 4.3a,b), where $i=1,2,3$ respectively, denotes steel, adhesive, and GFRP, can be expressed in terms of displacements $\lambda w_{1p}(z), \lambda w_{3p}(z), \lambda v_p(z)$, $\lambda\theta_{xp}(z)$ and $u_{1b}(z)$, $u_{3b}(z)$, $\theta_{y1b}(z)$, $\theta_{y3b}(z)$, $\theta_{zb}(z)$, $\psi_{1b}(z)$. For the steel beam, one can express the displacements of point A_1 as:

$$\begin{aligned}
\xi_1^*(s_1,n_1,z) &= \sin\alpha(s_1)\lambda v_p(z) + \cos\alpha(s_1)u_{1b}(z) + \left[r(s_1) + n_1 q'(s_1)\right]\theta_{zb}(z) \\
\eta_1^*(s_1,n_1,z) &= -\cos\alpha(s_1)\lambda v_p(z) + \sin\alpha(s_1)u_{1b}(z) - q(s_1)\theta_{zb}(z) \\
\zeta_1^*(s_1,n_1,z) &= \left[\lambda w_{1p}(z) + n_1\cos\alpha(s_1)\lambda v_p'(z) - y_1(s_1)\lambda\theta_{xp}(z)\right] - n_1\sin\alpha(s_1)u_{1b}'(z) \\
&\quad - x(s_1)\theta_{y1b}(z) + n_1 q(s_1)\theta_{zb}'(z) - \omega(s_1)\psi_{1b}(z)
\end{aligned} \tag{4.5}$$

in which $q(s_1) = x_1(s_1)\cos\alpha(s_1) + y_1(s)\sin\alpha(s_1)$, $r(s_1) = x(s_1)\sin\alpha(s_1) - y_1(s)\cos\alpha(s_1)$, and $\omega(s_1) = \int_0^{s_1} r(s_1)\,ds_1$ are defined. Also, the displacement components of Point A_3 within the GFRP plate ($\alpha(s_3) = 0$) can be expressed as:

$$\begin{aligned}
\xi_3^*(s_3,n_3,z) &= u_3(z) + n_3\theta_{zb}(z) \\
\eta_3^*(s_3,n_3,z) &= -\lambda v_p(z) - x_3(s_3)\theta_{zb}(z) \\
\zeta_3^*(s_3,n_3,z) &= \lambda w_{3p}(z) + n_3\lambda v_p'(z) + n_3 x_3(s_3)\theta_{zb}'(z) - x_3(s_3)\theta_{y3b}(z)
\end{aligned} \tag{4.6}$$

For the adhesive layer, the displacement fields of point A_2 within this layer are linearly interpolated between the displacements at the top surface of steel flange and the bottom surface of the GFRP plate (Assumption vii), i.e.,

$$\begin{Bmatrix} \xi_2^*(s_2,n_2,z) \\ \eta_2^*(s_2,n_2,z) \\ \zeta_2^*(s_2,n_2,z) \end{Bmatrix} = \left(\frac{1}{2} + \frac{n_2}{t_a}\right) \begin{Bmatrix} \xi_{3b}(s_3,-t_g/2,z) \\ \eta_{3b}(s_3,-t_g/2,z) \\ \zeta_{3b}(s_3,-t_g/2,z) \end{Bmatrix} + \left(\frac{1}{2} - \frac{n_2}{t_a}\right) \begin{Bmatrix} \xi_{1b}(s_1,t/2,z) \\ \eta_{1b}(s_1,t/2,z) \\ \zeta_{1b}(s_1,t/2,z) \end{Bmatrix} \tag{4.7}$$

It is noted that in Eq. (4.7), one has $\alpha(s_1) = 0$ and $y(s) = -h_b/2$ for the top flange and $x_1(s_1) = x_2(s_2) = x_3(s_3) = x(s)$. From Eqs. (4.5) and (4.6), by substituting into Eq.(4.7), one obtains:

$$\xi_2^* = \left(\frac{1}{2} - \frac{n_2}{t_a}\right) u_{1b}(z) + \left(\frac{1}{2} + \frac{n_2}{t_a}\right) u_{3b}(z) + \left(\frac{h-t_g}{4} - \frac{h+t_g}{2t_a} n_2\right) \theta_{zb}(z)$$

$$\eta_2^* = -\lambda v_p(z) - x(s)\theta_{zb}(z)$$

$$\begin{aligned}\zeta_2^* = & \left(\frac{1}{2} - \frac{n_2}{t_a}\right)\lambda w_{1p}(z) + \left(\frac{1}{2} + \frac{n_2}{t_a}\right)\lambda w_{3p}(z) + \left(\frac{t-t_g}{4} - \frac{t+t_g}{2t_a} n_2\right)\lambda v_p'(z) + \frac{h_b}{2}\left(\frac{1}{2} - \frac{n_2}{t_a}\right)\lambda\theta_{xp}(z) \\ & -\left(\frac{1}{2} - \frac{n_2}{t_a}\right) x(s)\theta_{y1b}(z) - \left(\frac{1}{2} + \frac{n_2}{t_a}\right) x(s)\theta_{y3b}(z) + \left(\frac{t-t_g}{4} - \frac{t+t_g}{2t_a} n_2\right) x(s)\theta_{zb}'(z) \\ & -\frac{h_b}{2}\left(\frac{1}{2} - \frac{n_2}{t_a}\right) x(s)\psi_{1b}(z)\end{aligned} \quad \text{(4.8)a-c}$$

4.8. Strain-Displacement Relations

4.8.1. Total strains

The nonlinear strain-displacement terms are retained throughout lateral torsional buckling. For the steel beam ($i = 1$) and the GFRP ($i = 3$), the non-vanishing strains take the form:

$$\begin{aligned}\varepsilon_i^* &= \varepsilon_i^{*L} + \varepsilon_i^{*N} = \frac{\partial \zeta_i^{*\prime}}{\partial z} + \frac{1}{2}\left[\left(\frac{\partial \eta_i^{*\prime}}{\partial z}\right)^2 + \left(\frac{\partial \xi_i^{*\prime}}{\partial z}\right)^2\right] \\ \gamma_i^* &= \gamma_i^{*L} + \gamma_i^{*N} = \frac{\partial \xi_i^*}{\partial z} + \frac{\partial \zeta_i^*}{\partial s_i} + \frac{\partial \xi_i^*}{\partial z}\frac{\partial \xi_i^*}{\partial s_i} + \frac{\partial \zeta_i^*}{\partial s_i}\frac{\partial \zeta_i^*}{\partial z} + \frac{\partial \eta_i^*}{\partial s_i}\frac{\partial \eta_i^*}{\partial z}\end{aligned} \quad \text{(4.9)a-b}$$

in which ε_i^{*L} and ε_i^{*N} are the linear and the non-linear strain components of ε_i^*, and $\gamma_i^{*L}, \gamma_i^{*N}$ are the linear and the non-linear strain components of γ_i^*. From Eqs.(4.5)-(4.6) by substituting into Eqs. (4.9) a-b, and introducing symbols ' and " to respectively denote for derivative operators $\partial/\partial z$ and $\partial^2/\partial z^2$, the linear and non-linear strain components are expressed as

$$\begin{aligned}\varepsilon_1^{*L} = & \lambda w_{1p}{}'(z) + n_1\cos\alpha(s_1)\lambda v_p''(z) - y_1(s_1)\lambda\theta_{xp}'(z) + \frac{1}{2}\left[\lambda v_p'(z)\right]^2 - n_1\sin\alpha(s_1)u_{1b}''(z) \\ & -x_1(s_1)\theta_{y1b}'(z) + \lambda v_p'(z)\left\{x_1(s_1) + n_1 q'(s_1)\sin\alpha(s_1)\right\}\theta_{zb}'(z) + n_1 q(s_1)\theta_{zb}''(z) - \omega(s_1)\psi_{1b}'(z) \\ \varepsilon_1^{*N} = & \frac{1}{2}u_{1b}'^{\,2}(z) + \left[n_1 q'(s_1)\cos\alpha(s_1) - y_1(s_1)\right]u_{1b}'(z)\theta_{zb}'(z) + \frac{1}{2}q^2(s_1)\theta_{zb}'^{\,2}(z) \\ & +\frac{1}{2}\left[r(s_1) + n_b q'(s_1)\right]^2\theta_{zb}'^{\,2}(z)\end{aligned} \quad \text{(4.10)a,b}$$

$$\gamma_1^{*L} = \lambda \sin\alpha(s_1)\left\{v_p'(z) - \theta_{xp}(z) - \left[w_{1p}{}'(z) - y_1(s_1)\lambda\theta_{xp}'(z)\right]\theta_{xp}(z)\right\} + \cos\alpha(s_1)u_{sb}'(z)$$
$$+\lambda\theta_{xp}(z)n_1\sin^2\alpha(s_1)u_{1b}''(z) - \cos\alpha(s_1)\left[1+\lambda w_{1p}{}'(z) + n_1\cos\alpha(s_1)\lambda v_p''(z) - y_1(s_1)\lambda\theta_{xp}'(z)\right]\theta_{y1b}(z)$$
$$+\lambda\theta_{xp}(z)x\sin\alpha(s_1)\theta_{y1b}'(z) + \lambda v_p'(z)q'(s_1)\cos\alpha(s_1)\theta_{zb}(z) - \lambda\theta_{xp}(z)n_1q(s_1)\sin\alpha(s_1)\theta_{zb}''(z)$$
$$+\left\{r(s_1) + 2n_1q'(s_1) + \lambda\left[w_{1p}{}'(z) + n_b\cos\alpha(s_1)v_p''(z) - y_1(s_1)\theta_{xp}'(z)\right]n_1q'(s_1)\right\}\theta_{zb}'(z)$$
$$-\omega'(s_1)\left\{1+\lambda\left[w_{1p}{}'(z) + n_1\cos\alpha(s_1)v_p''(z) - y_1(s_1)\theta_{xp}'(z)\right]\right\}\psi_{1b}(z) + \lambda\theta_{xp}(z)\omega(s_1)\sin\alpha(s_1)\psi_{1b}'(z)$$
$$\gamma_1^{*N} = -q'(s_1)\sin\alpha(s_1)u_{1b}'(z)\theta_{zb}(z) - n_1^2q'(s_1)\sin\alpha(s_1)u_{1b}''(z)\theta_{zb}'(z) + n_1\omega'(s_1)\sin\alpha(s_1)u_{1b}''(z)\psi_{1b}(z)$$
$$+x(s_1)\cos\alpha(s_1)\theta_{y1b}(z)\theta_{y1b}'(z) - n_1q(s_1)\cos\alpha(s_1)\theta_{y1b}(z)\theta_{zb}''(z) + \omega(s_1)\cos\alpha(s_1)\theta_{y1b}(z)\psi_{1b}'(z)$$
$$+q(s_1)q'(s_1)\theta_{zb}(z)\theta_{zb}'(z) - x(s_1)n_1q'(s_1)\theta_{y1b}'(z)\theta_{zb}'(z) + x(s_1)\omega'(s_1)\theta_{y1b}'(z)\psi_{1b}(z)$$
$$+n_1^2q(s_1)q'(s_1)\theta_{zb}'(z)\theta_{zb}''(z) - \omega(s_1)n_1q'(s_1)\theta_{zb}'(z)\psi_{1b}'(z) - \omega'(s_1)n_1q(s_1)\theta_{zb}''(z)\psi_{1b}(z)$$
$$+\omega(s_1)\omega'(s_1)\psi_{1b}'(z)\psi_{1b}(z)$$

(4.11)a,b

$$\varepsilon_3^{*L} = \lambda w_{3p}'(z) + n_3\lambda v_p''(z) + \frac{1}{2}\left(\lambda v_p'(z)\right)^2 - x_3(s_3)\theta_{y3b}'(z) + n_3x_3(s_3)\theta_{zb}''(z) + \lambda x_3(s_3)v_p'(z)\theta_{zb}'(z)$$
$$\varepsilon_3^{*N} = \frac{1}{2}u_{3b}'{}^2(z) + n_3u_{3b}'(z)\theta_{zb}'(z) + \frac{1}{2}n_3^2\theta_{zb}'{}^2(z) + \frac{1}{2}x_3^2(s_3)\theta_{zb}'{}^2(z)$$

(4.12)a,b

and

$$\gamma_3^{*L} = u_{3b}'(z) - \left[1+\lambda w_{3p}'(z) + n_3\lambda v_p''(z)\right]\theta_{y3b}(z) + n_3\left[2+\lambda w_{3p}'(z) + n_3\lambda v_p''(z)\right]\theta_{zb}'(z) + \lambda v_p'(z)\theta_{zb}(z)$$
$$\gamma_3^{*N} = x_2(s_2)\left[\theta_{y3b}'(z)\theta_{y3b}(z) - n_3\theta_{y3b}'(z)\theta_{zb}'(z) - n_3\theta_{y3b}(z)\theta_{zb}''(z) + \theta_{zb}(z)\theta_{zb}'(z) + n_3^2\theta_{zb}'(z)\theta_{zb}''(z)\right]$$

(4.13)a,b

For the adhesive layer, normal strains are neglected (Assumption v) while all three shear strains are retained. The total shear strains are

$$\gamma_{2zn}^* = \gamma_{2zn}^{*L} + \gamma_{2zn}^{*N} = \frac{\partial\eta_2^*}{\partial z} + \frac{\partial\zeta_2^*}{\partial n_2} + \frac{\partial\eta_2^*}{\partial z}\frac{\partial\eta_2^*}{\partial n_2} + \frac{\partial\zeta_2^*}{\partial z}\frac{\partial\zeta_2^*}{\partial n_2} + \frac{\partial\xi_2^*}{\partial z}\frac{\partial\xi_2^*}{\partial n_2};$$
$$\gamma_{2sn}^* = \gamma_{2sn}^{*L} + \gamma_{2sn}^{*N} = \frac{\partial\eta_2^*}{\partial s_2} + \frac{\partial\xi_2^*}{\partial n_2} + \frac{\partial\eta_2^*}{\partial s_2}\frac{\partial\eta_2^*}{\partial n_2} + \frac{\partial\xi_2^*}{\partial s_2}\frac{\partial\xi_2^*}{\partial n_2} + \frac{\partial\zeta_2^*}{\partial s_2}\frac{\partial\zeta_2^*}{\partial n_2}; \qquad (4.14)\text{a-c}$$
$$\gamma_{2sz}^* = \gamma_{2sz}^{*L} + \gamma_{2sz}^{*N} = \frac{\partial\xi_2^*}{\partial z} + \frac{\partial\zeta_2^*}{\partial s_2} + \frac{\partial\xi_2^*}{\partial z}\frac{\partial\xi_2^*}{\partial s_2} + \frac{\partial\zeta_2^*}{\partial z}\frac{\partial\zeta_2^*}{\partial s_2} + \frac{\partial\eta_2^*}{\partial z}\frac{\partial\eta_2^*}{\partial s_2};$$

in which γ_{2zn}^{*L} and γ_{2zn}^{*N} are the linear and non-linear shear strain components of γ_{2zn}^{*}. Also, γ_{2sn}^{*L} and γ_{2sn}^{*N} are those of γ_{2sn}^{*} while γ_{2sz}^{*L} and γ_{2sz}^{*N} are those of γ_{2sz}^{*}. From Eqs. (4.8)a-c, by substituting into Eqs. (4.14)a-c, components for shearing strains are obtained as

$$\begin{aligned}\gamma_{2zn}^{*L} = & -\lambda\left(1+c_6\right)v_p'\left(z\right)-\lambda c_5 w_{1p}\left(z\right)+\lambda c_5 w_{3p}\left(z\right)-\lambda c_5 c_7\theta_{xp}\left(z\right)+\lambda^2 B_{1p}\left(z,n_2\right)B_{2p}\left(z\right)\\ & +\lambda c_5 x\left(s\right)B_{1p}\left(z,n_2\right)\theta_{y1b}\left(z\right)-\lambda c_1\left(n_2\right)x\left(s\right)B_{2p}\left(z\right)\theta_{y1b}{}'\left(z\right)-\lambda c_5 x\left(s\right)B_{1p}\left(z,n_2\right)\theta_{y3b}\left(z\right)\\ & -\lambda c_2\left(n_2\right)x\left(s\right)B_{2p}\left(z\right)\theta_{y3b}{}'\left(z\right)-\lambda c_6 x\left(s\right)B_{1p}\left(z,n_2\right)\theta_{zb}'\left(z\right)+\lambda c_3\left(n_2\right)x\left(s\right)B_{2p}\left(z\right)\theta_{zb}''\left(z\right)\\ & +\lambda c_5 c_7 x\left(s\right)B_{1p}\left(z,n_2\right)\psi_{1b}\left(z\right)-\lambda c_7 c_1\left(n_2\right)x\left(s\right)B_{2p}\left(z\right)\psi_{1b}'\left(z\right)\\ & -x\left(s\right)\theta_{zb}{}'\left(z\right)+c_5 x\left(s\right)\theta_{y1b}\left(z\right)-c_5 x\left(s\right)\theta_{y3b}\left(z\right)-c_6 x\left(s\right)\theta_{zb}'\left(z\right)+c_5 c_7 x\left(s\right)\psi_{1b}\left(z\right)\end{aligned} \tag{4.15}$$

in which

$$B_{1p}\left(z,n_2\right)=\left(\frac{1}{2}-\frac{n_2}{t_a}\right)w_{1p}{}'\left(z\right)+\left(\frac{1}{2}+\frac{n_2}{t_a}\right)w_{3p}{}'\left(z\right)+\left(\frac{t-t_g}{4}-\frac{t+t_g}{2t_a}n_2\right)v_p''\left(z\right)+\frac{h_b}{2}\left(\frac{1}{2}-\frac{n_2}{t_a}\right)\theta_{xp}{}'\left(z\right)$$

$$B_{2p}\left(z\right)=\left(-\frac{1}{t_a}\right)w_{1p}\left(z\right)+\left(\frac{1}{t_a}\right)w_{3p}\left(z\right)+\left(-\frac{t+t_g}{2t_a}\right)v_p'\left(z\right)+\frac{h_b}{2}\left(-\frac{1}{t_a}\right)\theta_{xp}\left(z\right)$$

and

$$\begin{aligned}\gamma_{2zn}^{*N} = & -c_5 c_1\left(n_2\right)x^2\left(s\right)\theta_{y1b}{}'\theta_{y1b}-c_5 c_2\left(n_2\right)x^2\left(s\right)\theta_{y1b}\theta_{y3b}{}'+c_5 c_3\left(n_2\right)x^2\left(s\right)\theta_{zb}''\theta_{y1b}\\ & -c_5 c_7 c_1\left(n_2\right)x^2\left(s\right)\psi_{1b}'\theta_{y1b}+c_5 c_1\left(n_2\right)x^2\left(s\right)\theta_{y1b}{}'\theta_{y3b}+c_5 c_2\left(n_2\right)x^2\left(s\right)\theta_{y3b}{}'\theta_{y3b}\\ & -c_5 c_3\left(n_2\right)x^2\left(s\right)\theta_{zb}''\theta_{y3b}+c_5 c_7 c_1\left(n_2\right)x^2\left(s\right)\psi_{1b}'\theta_{y3b}+c_6 c_1\left(n_2\right)x^2\left(s\right)\theta_{y1b}{}'\theta_{zb}'\\ & +c_6 c_2\left(n_2\right)x^2\left(s\right)\theta_{y3b}{}'\theta_{zb}'-c_6 c_3\left(n_2\right)x^2\left(s\right)\theta_{zb}''\theta_{zb}'+c_6 c_7 c_1\left(n_2\right)x^2\psi_{1b}'\theta_{zb}'\\ & -c_5 c_7 c_1\left(n_2\right)x^2\left(s\right)\theta_{y1b}{}'\psi_{1b}-c_5 c_7 c_2\left(n_2\right)x^2\left(s\right)\theta_{y3b}{}'\psi_{1b}+c_5 c_7 c_3\left(n_2\right)x^2\left(s\right)\theta_{zb}''\psi_{1b}\\ & -c_5 c_7^2 c_1\left(n_2\right)x^2\left(s\right)\psi_{1b}'\psi_{1b}-c_5 c_1\left(n_2\right)u_{1b}u_{1b}{}'-c_5 c_2\left(n_2\right)u_{1b}u_{3b}{}'-c_5 c_4\left(n_2\right)u_{1b}\theta_{zb}{}'\\ & +c_5 c_1\left(n_2\right)u_{1b}{}'u_{3b}+c_5 c_2\left(n_2\right)u_{3b}u_{3b}{}'+c_5 c_4\left(n_2\right)u_{3b}\theta_{zb}{}'-\left(c_6+c_5 c_7\right)c_1\left(n_2\right)u_{1b}{}'\theta_{zb}\\ & -\left(c_6+c_5 c_7\right)c_2\left(n_2\right)u_{3b}{}'\theta_{zb}-\left(c_6+c_5 c_7\right)c_4\left(n_2\right)\theta_{zb}\theta_{zb}{}'\end{aligned} \tag{4.16}$$

in which

$$c_1\left(n_2\right)=\frac{1}{2}-\frac{n_2}{t_a};\qquad c_2\left(n_2\right)=\frac{1}{2}+\frac{n_2}{t_a};\qquad c_3\left(n_2\right)=\frac{t-t_g}{4}-\frac{t+t_g}{2t_a}n_2;\qquad c_4\left(n_2\right)=\frac{h-t_g}{4}-\frac{h+t_g}{2t_a}n_2$$

$$c_5=\frac{1}{t_a};\qquad c_6=\frac{t+t_g}{2t_a};\qquad c_7=\frac{h_b}{2};\qquad c_5 c_7=\frac{h_b}{2t_a};\qquad \left(c_6+c_5 c_7\right)=\frac{h+t_g}{2t_a}$$

Also, one has

$$\gamma_{2sn}^{*L} = -\theta_{zb} - c_5 u_{1b} + c_5 u_{3b} - \left(c_6 + c_5 c_7\right)\theta_{zb} + \lambda B_{2p}\left(z\right)\Big[-c_1\left(n_2\right)\theta_{y1b} - c_2\left(n_2\right)\theta_{y3b} + c_3\left(n_2\right)\theta'_{zb} + \\ -c_7 c_1\left(n_2\right)\psi_{1b}\Big] \tag{4.17}$$

$$\begin{aligned}\gamma_{2sn}^{*N} &= -c_5 c_1\left(n_2\right)x\left(s\right)\theta_{y1b}{}^2 - c_5 c_2\left(n_2\right)x\left(s\right)\theta_{y1b}\theta_{y3b} + c_5 c_3\left(n_2\right)x\left(s\right)\theta_{y1b}\theta'_{zb} - c_5 c_7 c_1\left(n_2\right)x\left(s\right)\theta_{y1b}\psi_{1b} \\ &+ c_5 c_1\left(n_2\right)x\left(s\right)\theta_{y1b}\theta_{y3b} + c_5 c_2\left(n_2\right)x\left(s\right)\theta_{y3b}{}^2 - c_5 c_3\left(n_2\right)x\left(s\right)\theta_{y3b}\theta'_{zb} + c_5 c_7 c_1\left(n_2\right)x\left(s\right)\theta_{y3b}\psi_{1b} \\ &+ c_6 c_1\left(n_2\right)x\left(s\right)\theta_{y1b}\theta'_{zb} + c_6 c_2\left(n_2\right)x\left(s\right)\theta_{y3b}\theta'_{zb} - c_6 c_3\left(n_2\right)x\left(s\right)\theta'^{\,2}_{zb} + c_7 c_6 c_1\left(n_2\right)x\left(s\right)\theta'_{zb}\psi_{1b} \\ &- c_5 c_7 c_1\left(n_2\right)x\left(s\right)\theta_{y1b}\psi_{1b} - c_5 c_7 c_2\left(n_2\right)x\left(s\right)\theta_{y3b}\psi_{1b} + c_5 c_7 c_3\left(n_2\right)x\left(s\right)\theta'_{zb}\psi_{1b} - c_5 c_7^2 c_1\left(n_2\right)x\left(s\right)\psi_{1b}{}^2\end{aligned} \tag{4.18}$$

and

$$\begin{aligned}\gamma_{2sz}^{*L} &= c_1\left(n_2\right)u_{1b}{}' + c_2\left(n_2\right)u_{3b}{}' + c_4\left(n_2\right)\theta_{zb}{}' - c_1\left(n_2\right)\theta_{y1b} - c_2\left(n_2\right)\theta_{y3b} + c_3\left(n_2\right)\theta'_{zb} \\ &- c_7 c_1\left(n_2\right)\psi_{1b} + \lambda B_{1p}\left(z,n_2\right)\left[-c_1\left(n_2\right)\theta_{y1b} - c_2\left(n_2\right)\theta_{y3b} + c_3\left(n_2\right)\theta'_{zb} - c_7 c_1\left(n_2\right)\psi_{1b}\right] \\ &+ \lambda v_p{}'\left(z\right)\theta_{zb}\end{aligned} \tag{4.19}$$

and

$$\begin{aligned}\gamma_{2sz}^{*N} &= c_1^2\left(n_2\right)x\left(s\right)\theta_{y1b}{}'\theta_{y1b} + c_1\left(n_2\right)c_2\left(n_2\right)x\left(s\right)\theta_{y1b}{}'\theta_{y3b} - c_3\left(n_2\right)c_1\left(n_2\right)x\left(s\right)\theta_{y1b}{}'\theta'_{zb} \\ &+ c_7 c_1^2\left(n_2\right)x\left(s\right)\theta_{y1b}{}'\psi_{1b} + c_1\left(n_2\right)c_2\left(n_2\right)x\left(s\right)\theta_{y1b}\theta_{y3b}{}' + c_2^2\left(n_2\right)x\left(s\right)\theta_{y3b}{}'\theta_{y3b} \\ &- c_3\left(n_2\right)c_2\left(n_2\right)x\left(s\right)\theta_{y3b}{}'\theta'_{zb} + c_7 c_1\left(n_2\right)c_2\left(n_2\right)x\left(s\right)\theta_{y3b}{}'\psi_{1b} - c_3\left(n_2\right)c_1\left(n_2\right)x\left(s\right)\theta_{y1b}\theta''_{zb} \\ &- c_3\left(n_2\right)c_2\left(n_2\right)x\left(s\right)\theta_{y3b}\theta''_{zb} + c_3^2\left(n_2\right)x\left(s\right)\theta''_{zb}\theta'_{zb} - c_7 c_3\left(n_2\right)c_1\left(n_2\right)x\left(s\right)\theta''_{zb}\psi_{1b} \\ &+ c_7 c_1^2\left(n_2\right)x\left(s\right)\theta_{y1b}\psi'_{1b} + c_7 c_1\left(n_2\right)c_2\left(n_2\right)x\left(s\right)\theta_{y3b}\psi'_{1b} - c_7 c_3\left(n_2\right)c_1\left(n_2\right)x\left(s\right)\theta'_{zb}\psi'_{1b} \\ &+ c_7^2 c_1^2\left(n_2\right)x\left(s\right)\psi'_{1b}\psi_{1b} + x\left(s\right)\theta_{zb}{}'\theta_{zb}\end{aligned} \tag{4.20}$$

4.8.2. Strain fields throughout Pre-buckling

When the beam is displaced from Configuration 1 to 2, the strains are assumed small and thus only the linear terms are retained. From Eqs. (4.10) through (4.20), by omitting the nonlinear terms and the buckling displacements, and setting $\lambda = 1$, the pre-buckling strains are obtained as

$$\varepsilon_{1p} = w'_{1p}\left(z\right) + n_1\cos\alpha\left(s_1\right)v''_p\left(z\right) - y_1\left(s_1\right)\theta'_{xp}\left(z\right); \qquad \gamma_{1p} = \sin\alpha\left(s_1\right)\left[v'_p\left(z\right) - \theta_{xb}\left(z\right)\right] \quad \text{(4.21)a-b}$$

$$\varepsilon_{3p} = w'_{3p}\left(z\right) + n_3 v''_p\left(z\right); \qquad \gamma_{3p} = 0 \quad \text{(4.22)a-b}$$

$$\gamma_{2szp} = 0; \quad \gamma_{2nsp} = 0; \quad \gamma_{2nzp} = -\frac{1}{t_a}w_{1p}\left(z\right) + \frac{1}{t_a}w_{3p}\left(z\right) - \left(1 + \frac{t + t_g}{2t_a}\right)v'_p\left(z\right) - \frac{h_b}{2t_a}\theta_{xp}\left(z\right) \quad \text{(4.23)a-c}$$

Equations (4.21-4.23) are similar to those reported in Pham and Mohareb (2015a).

4.9. Stress-Strain Relations

All materials are assumed linearly elastic and isotropic (Assumption ix) throughout the pre-buckling and buckling analyses. As a result, the pre-buckling stress-strains at Configuration 2 are $\sigma_{1p} = E_1\varepsilon_{1p}$, $\tau_{1p} = G_1\gamma_{1p}$, $\sigma_{3p} = E_3\varepsilon_{3p}$, $\tau_{3p} = G_3\gamma_{3p}$ and $\tau_{zn2p} = G_2\gamma_{zn2p}$ while those at the end of the buckled state at Configuration 4 are $\sigma_1^* = E_1\varepsilon_1^*$, $\tau_1^* = G_1\gamma_1^*$, $\sigma_3^* = E_3\varepsilon_3^*$, $\tau_3^* = G_3\gamma_3^*$, $\tau_{zn2}^* = G_2\gamma_{zn2}^*$, $\tau_{sn2}^* = G_2\gamma_{sn2}^*$ and $\tau_{sz2}^* = G_2\gamma_{sz2}^*$.

4.10. Pre-buckling Stress Resultants

From Eq. (4.21), the stress fields within the steel beam can be expressed as

$$\sigma_{1p} = E_1\varepsilon_{1p} = E_1\left\langle 1 \;\vdots\; n_1\cos\alpha(s_1) \quad -y_1(s_1)\right\rangle \begin{Bmatrix} w'_{1p}(z) \\ v''_p(z) \\ \theta'_{xp}(z) \end{Bmatrix} \tag{4.24a-b}$$

$$\tau_{1p} = G_1\gamma_{1p} = G_1\left[v'_p(z) - \theta_{xb}(z)\right]\sin\alpha(s_1)$$

The stress resultant-displacement relations (Pham 2013, chapter 3) are $N_{1p}(z) = E_1 A_s w'_{1p}(z)$; $M_{sp}(z) = E_1 I_{ss} v''_p(z)$; and $M_{xp}(z) = E_1 I_{xx}\theta'_{xp}(z)$. From Eqs. (4.24)a, by substituting from the stress resultant-displacement relations for the steel beam, one obtains

$$\sigma_{1p} = \frac{1}{A_s}N_{1p}(z) + \frac{n_1\cos\alpha(s_1)}{I_{ss}}M_{sp}(z) - \frac{y_1(s_1)}{I_{xx}}M_{xp}(z) \tag{4.25}$$

in which $I_{ss} = 2bt^3/12 + bt_g^3/12$; $I_{xx} = t_w h_w^3/12 + 2h_b^2 bt/4$ are defined. The shear stress component in Eq. (4.24)b can be related to the shear force also by integrating over the cross-section area to yield

$$\tau_{1p} = \frac{Q_{1p}}{A_w}\sin\alpha(s_1) \tag{4.26}$$

in which the shear force $Q_{1p} = \int_A \tau_{1p}\,dA = G_1\left[v'_p(z) - \theta_{xb}(z)\right]A_w$ has been defined. Also from Eq. (4.22), the stress functions within the GFRP plate can be obtained as:

$$\sigma_{3p} = E_3\varepsilon_{3p} = E_3\left\langle 1 \quad n_3 \quad -y_3(s_3)\right\rangle \begin{Bmatrix} w'_{3p}(z) \\ v''_p(z) \\ \theta'_{xp}(z) \end{Bmatrix}; \qquad \tau_{3p} = G_3\gamma_{3p} = 0 \tag{4.27a-b}$$

From Eq. (4.27)a, by substituting from stress-resultant displacement relations $N_{3p}(z) = E_3 A_g w'_{3p}(z)$; $M_{sp}(z) = E_3 I_{xxp} \theta'_{xp}(z)$, one obtains

$$\sigma_{3p} = \frac{1}{A_g} N_{3p}(z) + \frac{n_3}{I_{xxp}} M_{sp}(z) \tag{4.28}$$

The pre-buckling shear strain γ_{2znp} can be related to the shear force resultant $Q_{2p}(z)$ for the adhesive by integrating the shear stresses over the adhesive area. From Eq. (4.23)c, by integrating the shear stress $\tau_{2znp} = G\gamma_{2znp}$ within the adhesive over the adhesive cross-section yielding

$$Q_{2p}(z) = \int_{A_a} G_2 \gamma_{2znp}(z) dA_a = A_a \tau_{2znp}(z) \tag{4.29}$$

4.11. Second Variation of Total Buckling Potential Energy

The total potential energy π of the system is the summation of the internal strain energy U and total load potential loss V. The buckling load can be mathematically obtained when the variation of the second variation of the total potential energy vanishes, i.e.,

$$\delta\left(\frac{1}{2}\overline{\overline{\pi}}\right) = \delta\left[\frac{1}{2}\left(\overline{\overline{U}} + \overline{\overline{V}}\right)\right] = 0 \tag{4.30}$$

in which $\overline{(\ )}$ and $\overline{\overline{(\ )}}$ respectively denote the first and second variations with respect to the argument function (e.g., $\overline{U} = \delta U$ and $\overline{\overline{U}} = \delta^2 U$). The total internal strain energy is obtained by summing the contributions of the steel beam, the GFRP plate, the adhesive, i.e.,

$$U = \frac{1}{2}\int_0^L \int_{A_1} \left(\sigma_1^* \varepsilon_1^* + \tau_1^* \gamma_1^*\right) dA_1 dz + \frac{1}{2}\int_0^L \int_{A_3} \left(\sigma_3^* \varepsilon_3^* + \tau_3^* \gamma_3^*\right) dA_3 dz + \frac{1}{2}\int_0^L \int_{A_2} \left(\tau_{zn2}^* \gamma_{zn2}^* + \tau_{sn2}^* \gamma_{sn2}^* + \tau_{sz2}^* \gamma_{sz2}^*\right) dA_2 dz \tag{4.31}$$

The total internal strain energy U contributed by the normal strains and transverse shear strains within the steel beam and GFRP plate, and the shear stresses within the adhesive layer. At buckled configuration (Configuration 4), Eq. (4.31) takes the form:

$$\begin{aligned} U = &\frac{1}{2}\int_0^L \int_{A_1} \left[\left(\sigma_{1b} + \lambda\sigma_{1p}\right)\left(\varepsilon_{1b} + \lambda\varepsilon_{1p}\right) + \left(\tau_{1b} + \lambda\tau_{1p}\right)\left(\gamma_{1b} + \lambda\gamma_{1p}\right)\right] dA_1 dz \\ &+ \frac{1}{2}\int_0^L \int_{A_1} \left[\left(\sigma_{3b} + \lambda\sigma_{3p}\right)\left(\varepsilon_{3b} + \lambda\varepsilon_{3p}\right) + \left(\tau_{3b} + \lambda\tau_{3p}\right)\left(\gamma_{3b} + \lambda\gamma_{3p}\right)\right] dA_1 dz \\ &+ \frac{1}{2}\int_0^L \int_{A_2} \left[\left(\tau_{2znb} + \lambda\tau_{2znp}\right)\left(\gamma_{2znb} + \lambda\gamma_{2znp}\right) + \left(\tau_{2snb} + \lambda\tau_{2snp}\right)\left(\gamma_{2snb} + \lambda\gamma_{2snp}\right)\right. \\ &\qquad \left. + \left(\tau_{2znb} + \lambda\tau_{2znp}\right)\left(\gamma_{2znb} + \lambda\gamma_{2znp}\right)\right] dA_2 dz \end{aligned} \tag{4.32}$$

From Eqs. (4.32), by neglecting all zero pre-buckling strains as indicated in Eqs. (4.22)b and (4.23)a-b, (i.e., $\gamma_{3p} = \gamma_{2snp} = \gamma_{2szp} = 0$), and noting that all materials are linearly elastic isotropic (Assumption ix), the second variation of the total strain energy can be expressed as

$$\begin{aligned}\frac{1}{2}\overline{\overline{U}} &= \frac{1}{2}\int_0^L\int_{A_1} E_1\left[\overline{\varepsilon}_{1b}^2 + \lambda\varepsilon_{1p}\overline{\overline{\varepsilon}}_{1b}\right]dA_1dz + \frac{1}{2}\int_0^L\int_{A_1} G_1\left[\overline{\gamma}_{1b}^2 + \lambda\gamma_{1p}\overline{\overline{\gamma}}_{1b}\right]dA_1dz \\ &+\frac{1}{2}\int_0^L\int_{A_3} E_3\left[\overline{\varepsilon}_{3b}^2 + \lambda\varepsilon_{3p}\overline{\overline{\varepsilon}}_{3b}\right]dA_3dz + \frac{1}{2}\int_0^L\int_{A_3} G_3\overline{\gamma}_{3b}^2 dA_3dz \\ &+\frac{1}{2}\int_0^L\int_{A_2} G_2\left[\overline{\gamma}_{2znb}^2 + \lambda\gamma_{2znp}\overline{\overline{\gamma}}_{2znb}\right]dA_2dz + \frac{1}{2}\int_0^L\int_{A_2} G_2\overline{\gamma}_{2snb}^2 dA_2dz + \frac{1}{2}\int_0^L\int_{A_2} G_2\overline{\gamma}_{2szb}^2 dA_2dz\end{aligned} \tag{4.33}$$

The load potential energy is contributed by transverse and longitudinal distributed loads $\lambda q_y(z)$, $\lambda q_z(z)$ and concentrated loads P_{yi}, P_{zi} applied at both member ends i.e.,

$$\begin{aligned}\frac{1}{2}\overline{\overline{V}} &= -\frac{1}{2}\int_0^L q_y(z)\,y_{q_y}(z)\left(\overline{\theta}_{zb}\right)^2 dz - \frac{1}{2}\sum_{i=0,L} P_{yi}y_i(z)\left[\overline{\theta}_{zb}(z_i)\right]^2 \\ &-\frac{1}{2}\int_0^L q_z(z)\,y_{q_z}(z)\overline{\theta}_{zb}\overline{\theta}_{y1b}dz - \frac{1}{2}\sum_{z_i=0,L} P_{zi}y_i(z)\overline{\theta}_{zb}(z_i)\overline{\theta}_{y1b}(z_i)\end{aligned} \tag{4.34}$$

4.11.1. Expression of the first variation of buckling strains

By omitting pre-buckling deformation effects in line with the classical buckling treatment and omitting the non-linear terms, the first variation of the total strains expressions [Eqs. (4.10)-(4.20)] take the form

$$\begin{aligned}&\overline{\varepsilon}_{1b} \approx -n_1\sin\alpha(s_1)\overline{u}''_{1b} - x_1(s_1)\overline{\theta}'_{y1b} + n_1q(s_1)\overline{\theta}''_{zb} - \omega(s_1)\overline{\psi}'_{1b};\\ &\overline{\gamma}_{1b} \approx \cos\alpha(s_1)\overline{u}'_{1b} - \cos\alpha(s_1)\overline{\theta}_{y1b} + \left\{r(s_1)+2n_1\right\}\overline{\theta}'_{zb} - r(s_1)\overline{\psi}_{1b};\\ &\overline{\varepsilon}_{3b} \approx -x_3(s_3)\overline{\theta}'_{y3b} + n_3x_3(s_3)\overline{\theta}''_{zb};\\ &\overline{\gamma}_{3b} \approx \overline{u}'_{3b} - \overline{\theta}_{y3b} + 2n_3\overline{\theta}'_{zb};\\ &\overline{\gamma}_{2znb} \approx c_5x(s)\overline{\theta}_{y1b} - c_5x(s)\overline{\theta}_{y3b} - (1+c_6)x(s)\overline{\theta}'_{zb} + c_5c_7x(s)\overline{\psi}_{1b};\\ &\overline{\gamma}_{2snb} \approx -c_5\overline{u}_{1b} + c_5\overline{u}_{3b} - (1+c_6+c_5c_7)\overline{\theta}_{zb};\\ &\overline{\gamma}_{2szb} \approx c_1(n_2)\overline{u}'_{1b} - c_1(n_2)\overline{\theta}_{y1b} + c_2(n_2)\overline{u}'_{3b} - c_2(n_2)\overline{\theta}_{y3b} + \left[c_3(n_2)+c_4(n_2)\right]\overline{\theta}'_{zb} - c_7c_1(n_2)\overline{\psi}_{1b}\end{aligned} \tag{4.35}$$

a-g

4.11.2. Second variation of buckling strains

Again, by neglecting pre-buckling terms, the second variation of the buckling strains in Eqs. (4.10) through (4.20) take the form

$$
\begin{aligned}
&\bar{\bar{\varepsilon}}_{1b} \approx \left(\bar{u}'_{1b}\right)^2 + 2\left[n_1 \cos\alpha\left(s_1\right) - y_1\left(s_1\right)\right]\bar{u}'_{1b}\bar{\theta}'_{zb} + \left\{q^2 + r^2 + 2rn_1 + n_1^2\right\}\left(\bar{\theta}'_{zb}\right)^2; \\
&\bar{\bar{\gamma}}_{1b} \approx -2\sin\alpha\left(s_1\right)\bar{u}'_{1b}\bar{\theta}_{zb} - 2n_1^2 \sin\alpha\left(s_1\right)\bar{\bar{u}}''_{1b}\bar{\theta}'_{zb} + 2n_1 r\left(s_1\right)\sin\alpha\left(s_1\right)\bar{\bar{u}}''_{1b}\bar{\psi}_{1b} \\
&\qquad +2x\left(s_1\right)\cos\alpha\left(s_1\right)\bar{\theta}_{y1b}\bar{\theta}'_{y1b} - 2n_1 q\left(s_1\right)\cos\alpha\left(s_1\right)\bar{\theta}_{y1b}\bar{\theta}''_{zb} + 2\omega\left(s_1\right)\cos\alpha\left(s_1\right)\bar{\theta}_{y1b}\bar{\psi}'_{1b} \\
&\qquad +2q\left(s_1\right)\bar{\theta}_{zb}\bar{\theta}'_{zb} - 2x\left(s_1\right)n_1\bar{\theta}'_{y1b}\bar{\theta}'_{zb} + 2x\left(s_1\right)r\left(s_1\right)\bar{\theta}'_{y1b}\bar{\psi}_{1b} + 2n_1^2 q\left(s_1\right)\bar{\theta}'_{zb}\bar{\theta}''_{zb} \\
&\qquad -2\omega\left(s_1\right)n_1\bar{\theta}'_{zb}\bar{\psi}'_{1b} - 2r\left(s_1\right)n_1 q\left(s_1\right)\bar{\theta}''_{zb}\bar{\psi}_{1b} + 2\omega\left(s_1\right)r\left(s_1\right)\bar{\psi}'_{1b}\bar{\psi}_{1b}; \\
&\bar{\bar{\varepsilon}}_{3b} \approx \left(\bar{u}'_{3b}\right)^2 + 2n_3\bar{u}'_{3b}\bar{\theta}'_{zb} + \left[n_3^2 + x_3^2\left(s_3\right)\right]\left(\bar{\theta}'_{zb}\right)^2; \\
&\bar{\bar{\gamma}}_{2znb} \approx -2c_5c_1\left(n_2\right)x^2\left(s\right)\bar{\theta}'_{y1b}\bar{\theta}_{y1b} - 2c_5c_2\left(n_2\right)x^2\left(s\right)\bar{\theta}_{y1b}\bar{\theta}'_{y3b} + 2c_5c_3\left(n_2\right)x^2\left(s\right)\bar{\theta}''_{zb}\bar{\theta}_{y1b} \\
&\qquad -2c_5c_7c_1\left(n_2\right)x^2\left(s\right)\bar{\psi}'_{1b}\bar{\theta}_{y1b} + 2c_5c_1\left(n_2\right)x^2\left(s\right)\bar{\theta}'_{y1b}\bar{\theta}_{y3b} + 2c_5c_2\left(n_2\right)x^2\left(s\right)\bar{\theta}'_{y3b}\bar{\theta}_{y3b} \\
&\qquad -2c_5c_3\left(n_2\right)x^2\left(s\right)\bar{\theta}''_{zb}\bar{\theta}_{y3b} + 2c_5c_7c_1\left(n_2\right)x^2\left(s\right)\bar{\psi}'_{1b}\bar{\theta}_{y3b} + 2c_6c_1\left(n_2\right)x^2\left(s\right)\bar{\theta}'_{y1b}\bar{\theta}'_{zb} \\
&\qquad +2c_6c_2\left(n_2\right)x^2\left(s\right)\bar{\theta}'_{y3b}\bar{\theta}'_{zb} - 2c_6c_3\left(n_2\right)x^2\left(s\right)\bar{\theta}''_{zb}\bar{\theta}'_{zb} + 2c_6c_7c_1\left(n_2\right)x^2\bar{\psi}'_{1b}\bar{\theta}'_{zb} \\
&\qquad -2c_5c_7c_1\left(n_2\right)x^2\left(s\right)\bar{\theta}'_{y1b}\bar{\psi}_{1b} - 2c_5c_7c_2\left(n_2\right)x^2\left(s\right)\bar{\theta}'_{y3b}\bar{\psi}_{1b} + 2c_5c_7c_3\left(n_2\right)x^2\left(s\right)\bar{\theta}''_{zb}\bar{\psi}_{1b} \\
&\qquad -2c_5c_7^2c_1\left(n_2\right)x^2\left(s\right)\bar{\psi}'_{1b}\bar{\psi}_{1b} - 2c_5c_1\left(n_2\right)\bar{u}_{1b}\bar{u}'_{1b} - 2c_5c_2\left(n_2\right)\bar{u}_{1b}\bar{u}'_{3b} - 2c_5c_4\left(n_2\right)\bar{u}_{1b}\bar{\theta}'_{zb} \\
&\qquad +2c_5c_1\left(n_2\right)\bar{u}'_{1b}\bar{u}_{3b} + 2c_5c_2\left(n_2\right)\bar{u}_{3b}\bar{u}'_{3b} + 2c_5c_4\left(n_2\right)\bar{u}_{3b}\bar{\theta}'_{zb} - 2\left(c_6 + c_5c_7\right)c_1\left(n_2\right)\bar{u}'_{1b}\bar{\theta}_{zb} \\
&\qquad -2\left(c_6 + c_5c_7\right)c_2\left(n_2\right)\bar{u}'_{3b}\bar{\theta}_{zb} - 2\left(c_6 + c_5c_7\right)c_4\left(n_2\right)\bar{\theta}_{zb}\bar{\theta}'_{zb}
\end{aligned}
\qquad (4.36)\text{a-d}
$$

4.11.3. Second variation of internal strain energy

From Eqs. (4.25), (4.26), (4.28),(4.29), (4.35)a-g and (4.36)a-d, by substituting into Eq. (4.33), the second variation of the total strain energy can be expressed as

$$
\begin{aligned}
&\frac{1}{2}\bar{\bar{U}}=\frac{1}{2}\int_0^L\int_{A_1}E_1\left[-n_1\sin\alpha(s_1)\bar{u}''_{1b}-x_1(s_1)\bar{\theta}'_{y1b}+n_1q(s_1)\bar{\theta}''_{zb}-\omega(s_1)\bar{\psi}'_{1b}\right]^2 dA_1dz\\
&+\frac{\lambda}{2}\int_0^L\int_{A_1}\left[\frac{N_{1p}(z)}{A_s}+\frac{n_1\cos\alpha(s_1)}{I_{ss}}M_{sp}(z)-\frac{y_1(s_1)}{I_{xx}}M_{xp}(z)\right]\left\{\left(\bar{u}'_{1b}\right)^2+2\left[n_1\cos\alpha(s_1)-y_1(s_1)\right]\bar{u}'_{1b}\bar{\theta}'_{zb}\right.\\
&\left.+\left[q^2(s_1)+r^2(s_1)+2r(s_1)n_1+n_1^2\right]\left(\bar{\theta}'_{zb}\right)^2\right\}dA_1dz\\
&+\frac{1}{2}\int_0^L\int_{A_1}G_1\left\{\cos\alpha(s_1)\bar{u}'_{1b}-\cos\alpha(s_1)\bar{\theta}_{y1b}+\left[r(s_1)+2n_1\right]\bar{\theta}'_{zb}-r(s_1)\bar{\psi}_{1b}\right\}^2 dA_1dz\\
&+\frac{\lambda}{2}\int_0^L\int_{A_1}\frac{Q_{1p}}{A_1}\sin\alpha(s_1)\left\{-2\sin\alpha(s_1)\bar{u}'_{1b}\bar{\theta}_{zb}-2n_1^2\sin\alpha(s_1)\bar{u}''_{1b}\bar{\theta}'_{zb}+2n_1r(s_1)\sin\alpha(s_1)\bar{u}''_{1b}\bar{\psi}_{1b}\right.\\
&+2x(s_1)\cos\alpha(s_1)\bar{\theta}_{y1b}\bar{\theta}'_{y1b}-2n_1q(s_1)\cos\alpha(s_1)\bar{\theta}_{y1b}\bar{\theta}''_{zb}+2\omega(s_1)\cos\alpha(s_1)\bar{\theta}_{y1b}\bar{\psi}'_{1b}+2q(s_1)\bar{\theta}_{zb}\bar{\theta}'_{zb}\\
&-2x(s_1)n_1\bar{\theta}'_{y1b}\bar{\theta}'_{zb}+2x(s_1)r(s_1)\bar{\theta}'_{y1b}\bar{\psi}_{1b}+2n_1^2q(s_1)\bar{\theta}'_{zb}\bar{\theta}''_{zb}-2\omega(s_1)n_1\bar{\theta}'_{zb}\bar{\psi}'_{1b}-2r(s_1)n_1q(s_1)\bar{\theta}''_{zb}\bar{\psi}_{1b}\\
&\left.+2\omega(s_1)r(s_1)\bar{\psi}'_{1b}\bar{\psi}_{1b}\right\}dA_1dz+\frac{1}{2}\int_0^L\int_{A_3}E_3\left[-x_3(s_3)\bar{\theta}'_{y3b}+n_3x_3(s_3)\bar{\theta}''_{zb}\right]^2dA_3dz\\
&+\frac{\lambda}{2}\int_0^L\int_{A_3}\left[\frac{N_{3p}(z)}{A_g}+\frac{n_3}{I_{xxg}}M_{sp}(z)\right]\left[\left(\bar{u}'_{3b}\right)^2+2n_3\bar{u}'_{3b}\bar{\theta}'_{zb}+\left[n_3^2+x_3^2(s_3)\right]\left(\bar{\theta}'_{zb}\right)^2\right]dA_3dz+\frac{1}{2}\int_0^L\int_{A_3}G_3\left(\bar{u}'_{3b}-\bar{\theta}_{y3b}+2n_3\bar{\theta}'_{zb}\right)^2dA_3dz\\
&+\frac{1}{2}\int_0^L\int_{A_2}G_2\left[c_5x(s)\bar{\theta}_{y1b}-c_5x(s)\bar{\theta}_{y3b}-(1+c_6)x(s)\bar{\theta}'_{zb}+c_5c_7x(s)\bar{\psi}_{1b}\right]^2dA_2dz\\
&+\frac{\lambda}{2}\int_0^L\int_{A_2}\frac{Q_{2p}(z)}{A_a}\left\{-2c_5c_1(n_2)x^2(s)\bar{\theta}'_{y1b}\bar{\theta}_{y1b}-2c_5c_2(n_2)x^2(s)\bar{\theta}_{y1b}\bar{\theta}'_{y3b}\right.\\
&+2c_5c_3(n_2)x^2(s)\bar{\theta}''_{zb}\bar{\theta}_{y1b}-2c_5c_7c_1(n_2)x^2(s)\bar{\psi}'_{1b}\bar{\theta}_{y1b}+2c_5c_1(n_2)x^2(s)\bar{\theta}'_{y1b}\bar{\theta}_{y3b}+2c_5c_2(n_2)x^2(s)\bar{\theta}'_{y3b}\bar{\theta}_{y3b}\\
&-2c_5c_3(n_2)x^2(s)\bar{\theta}''_{zb}\bar{\theta}_{y3b}+2c_5c_7c_1(n_2)x^2(s)\bar{\psi}'_{1b}\bar{\theta}_{y3b}+2c_6c_1(n_2)x^2(s)\bar{\theta}'_{y1b}\bar{\theta}'_{zb}\\
&+2c_6c_2(n_2)x^2(s)\bar{\theta}'_{y3b}\bar{\theta}'_{zb}-2c_6c_3(n_2)x^2(s)\bar{\theta}''_{zb}\bar{\theta}'_{zb}+2c_6c_7c_1(n_2)x^2\bar{\psi}'_{1b}\bar{\theta}'_{zb}\\
&-2c_5c_7c_1(n_2)x^2(s)\bar{\theta}'_{y1b}\bar{\psi}_{1b}-2c_5c_7c_2(n_2)x^2(s)\bar{\theta}'_{y3b}\bar{\psi}_{1b}+2c_5c_7c_3(n_2)x^2(s)\bar{\theta}''_{zb}\bar{\psi}_{1b}\\
&-2c_5c_7^2c_1(n_2)x^2(s)\bar{\psi}'_{1b}\bar{\psi}_{1b}-2c_5c_1(n_2)\bar{u}_{1b}\bar{u}'_{1b}-2c_5c_2(n_2)\bar{u}_{1b}\bar{u}'_{3b}-2c_5c_4(n_2)\bar{u}_{1b}\bar{\theta}'_{zb}\\
&+2c_5c_1(n_2)\bar{u}'_{1b}\bar{u}_{3b}+2c_5c_2(n_2)\bar{u}_{3b}\bar{u}'_{3b}+2c_5c_4(n_2)\bar{u}_{3b}\bar{\theta}'_{zb}-2(c_6+c_5c_7)c_1(n_2)\bar{u}'_{1b}\bar{\theta}_{zb}\\
&\left.-2(c_6+c_5c_7)c_2(n_2)\bar{u}'_{3b}\bar{\theta}_{zb}-2(c_6+c_5c_7)c_4(n_2)\bar{\theta}_{zb}\bar{\theta}'_{zb}\right\}dA_2dz\\
&+\frac{1}{2}\int_0^L\int_{A_2}G_2\left[-c_5\bar{u}_{1b}+c_5\bar{u}_{3b}-(1+c_6+c_5c_7)\bar{\theta}_{zb}\right]^2dA_2dz\\
&+\frac{1}{2}\int_0^L\int_{A_2}G_2\left[c_1(n_2)\bar{u}'_{1b}-c_1(n_2)\bar{\theta}_{y1b}+c_2(n_2)\bar{u}'_{3b}-c_2(n_2)\bar{\theta}_{y3b}+\left[c_3(n_2)+c_4(n_2)\right]\bar{\theta}'_{zb}-c_7c_1(n_2)\bar{\psi}_{1b}\right]^2dA_2dz
\end{aligned}
$$

(4.37)

4.11.4. Second variation of total potential energy

From Eqs. (4.34) and (4.37), by substituting into Eq. (4.30), the second variation of the total potential energy of the system can be expressed as

$$\delta\frac{1}{2}\bar{\bar{\pi}}=\delta\frac{1}{2}\left(\bar{\bar{U}}+\bar{\bar{V}}\right)=\delta\frac{1}{2}\left(\bar{\bar{U}}_{en1}+\bar{\bar{U}}_{es1}+\bar{\bar{U}}_{en3}+\bar{\bar{U}}_{es3}+\bar{\bar{U}}_{ezn2}+\bar{\bar{U}}_{esn2}+\bar{\bar{U}}_{esz2}+\bar{\bar{V}}_{gN_1}\right.$$
$$\left.+\bar{\bar{V}}_{g\bar{M}_x}+\bar{\bar{V}}_{g\bar{\bar{M}}_s}+\bar{\bar{V}}_{gQ_1}+\bar{\bar{V}}_{gQ2}+\bar{\bar{V}}_{gqy}+\bar{\bar{V}}_{gP_{yi}}+\bar{\bar{V}}_{gqz}+\bar{\bar{V}}_{gP_{zi}}\right)=0 \tag{4.38}$$

in which $\bar{\bar{U}}_{en1}$ is the second variation of elastic strain energy contributed by the longitudinal normal strain within the wide flange beam (Appendix 4.1) and can be evaluated over the steel section as

$$\bar{\bar{U}}_{en1}=E_1\int_0^L\left\langle\bar{u}''_{1b}\quad\bar{\theta}'_{y1b}\quad\bar{\theta}''_{zb}\quad\bar{\psi}'_{1b}\right\rangle\begin{bmatrix}I_{yyw}&0&0&0\\0&2I_{yyf}&0&0\\0&0&I_{\omega\omega l}&0\\0&0&0&I_{\omega\omega g}\end{bmatrix}\begin{Bmatrix}\bar{u}''_{1b}\\\bar{\theta}'_{y1b}\\\bar{\theta}''_{zb}\\\bar{\psi}'_{1b}\end{Bmatrix}dz \tag{4.39}$$

in which $I_{yyw}=h_w t_w^3/12;\ I_{yyf}=tb^3/12;\ I_{\omega\omega l}=2b^3t^3/144+h_w^3t_w^3/144;\ I_{\omega\omega gs}=h_b^2b^3t/24$ are defined. Also, $\bar{\bar{U}}_{es1}$ is the second variation of the elastic strain energy contributed by the transverse shear strain within the steel beam (Appendix 4.1) and can be is evaluated over the steel section as

$$\bar{\bar{U}}_{es1}=G_1\int_0^L\left\langle\bar{u}'_{1b}\quad\bar{\theta}_{y1b}\quad\bar{\theta}'_{zb}\quad\bar{\psi}_{1b}\right\rangle\begin{bmatrix}2A_f&-2A_f&0&0\\-2A_f&2A_f&0&0\\0&0&J_1&-h_b^2A_f/2\\0&0&-h_b^2A_f/2&h_b^2A_f/2\end{bmatrix}\begin{Bmatrix}\bar{u}'_{1b}\\\bar{\theta}_{y1b}\\\bar{\theta}'_{zb}\\\bar{\psi}_{1b}\end{Bmatrix}dz \tag{4.40}$$

in which $A_f=bt;\ J_1=h_b^2A_f/2+2bt^3/3+h_wt_w^3/3$ are defined and $\bar{\bar{U}}_{en3}$ and $\bar{\bar{U}}_{es3}$ are the second variation of the elastic strain energies contributed by the longitudinal normal strain and shear strain within the GFRP plate (Appendix 4.1) and are expressed as

$$\bar{\bar{U}}_{en3}=E_3\int_0^L\left\langle\bar{\theta}'_{y3b}\quad\bar{\theta}''_{zb}\right\rangle\begin{bmatrix}I_{yyg}&0\\0&I_{\omega\omega g}\end{bmatrix}\begin{Bmatrix}\bar{\theta}'_{y3b}\\\bar{\theta}''_{zb}\end{Bmatrix}dz$$

$$\bar{\bar{U}}_{es3}=G_3\int_0^L\left\langle\bar{u}'_{3b}\quad\bar{\theta}_{y3b}\quad\bar{\theta}'_{zb}\right\rangle\begin{bmatrix}A_3&-A_3&0\\-A_3&A_3&0\\0&0&J_3\end{bmatrix}\begin{Bmatrix}\bar{u}'_{3b}\\\bar{\theta}_{y3b}\\\bar{\theta}'_{zb}\end{Bmatrix}dz \tag{4.41)a-b}$$

in which the section properties $I_{yyg}=t_gb^3/12,\ I_{\omega\omega g}=t_g^3b^3/144,\ A_3=bt_g$ and $J_3=bt_g^3/3$ are defined and $\bar{\bar{U}}_{ezn2}$, $\bar{\bar{U}}_{esn2}$ and $\bar{\bar{U}}_{esz2}$ are the second variations of the internal strain energies within the adhesive layer (Appendix 4.1) and are expressed as

$$\bar{\bar{U}}_{ezn2} = G_2 I_{yya} \int_0^L \left\langle \bar{\theta}_{y1b} \quad \bar{\theta}_{y3b} \quad \bar{\theta}'_{zb} \quad \bar{\psi}_{1b} \right\rangle \times$$

$$\begin{bmatrix} c_5^2 & -c_5^2 & -c_5(1+c_6) & c_5^2 c_7 \\ -c_5^2 & c_5^2 & c_5(1+c_6) & -c_5^2 c_7 \\ -c_5(1+c_6) & c_5(1+c_6) & (1+c_6)^2 & -c_5 c_7 (1+c_6) \\ c_5^2 c_7 & -c_5^2 c_7 & -c_5 c_7 (1+c_6) & c_5^2 c_7^2 \end{bmatrix} \begin{Bmatrix} \bar{\theta}_{y1b} \\ \bar{\theta}_{y3b} \\ \bar{\theta}'_{zb} \\ \bar{\psi}_{1b} \end{Bmatrix} dz$$

$$\bar{\bar{U}}_{esn2} = G_2 A_a \int_0^L \left\langle \bar{u}_{1b} \quad \bar{u}_{3b} \quad \bar{\theta}_{zb} \right\rangle \times$$

$$\begin{bmatrix} c_5^2 & -c_5^2 & c_5(1+c_6+c_5c_7) \\ -c_5^2 & c_5^2 & -c_5(1+c_6+c_5c_7) \\ c_5(1+c_6+c_5c_7) & -c_5(1+c_6+c_5c_7) & (1+c_6+c_5c_7)^2 \end{bmatrix} \begin{Bmatrix} \bar{u}_{1b} \\ \bar{u}_{3b} \\ \bar{\theta}_{zb} \end{Bmatrix} dz$$

$$\bar{\bar{U}}_{esz2} = \frac{1}{12} G_2 A_a \int_0^L \left\langle \bar{u}'_{1b} \quad \bar{\theta}_{y1b} \quad \bar{u}'_{3b} \quad \bar{\theta}_{y3b} \quad \bar{\theta}'_{zb} \quad \bar{\psi}_{1b} \right\rangle \times$$

$$\begin{bmatrix} 4 & -4 & 2 & -2 & 2c_8 & -4c_7 \\ -4 & 4 & -2 & 2 & -2c_8 & 4c_7 \\ 2 & -2 & 4 & -4 & c_9 & -2c_7 \\ -2 & 2 & -4 & 4 & -c_9 & 2c_7 \\ 2c_8 & -2c_8 & c_9 & -c_9 & c_{10} & -2c_7c_8 \\ -4c_7 & 4c_7 & -2c_7 & 2c_7 & -2c_7c_8 & 4c_7^2 \end{bmatrix} \begin{Bmatrix} \bar{u}'_{1b} \\ \bar{\theta}_{y1b} \\ \bar{u}'_{3b} \\ \bar{\theta}_{y3b} \\ \bar{\theta}'_{zb} \\ \bar{\psi}_{1b} \end{Bmatrix} dz \qquad (4.42)\text{a-c}$$

in which $I_{yya} = \int_{A_2} x^2(s)\, dA_2 = t_a b^3/12$ $c_5 = 1/t_a$; $c_6 = (t+t_g)/2t_a$; $c_7 = h_b/2$; ; $c_5 c_7 = h_b/2t_a$; $c_6 + c_5 c_7 = (h+t_g)/2t_a$; $c_8 = h+t-t_g$; $c_9 = h+t-4t_g$; $c_{10} = h^2 + t^2 + 4{t_g}^2 + 2ht - 2ht_g - 2tt_g$. Also, $\bar{\bar{V}}_{gN_1}$ is the second variation of the load potential energy contributed by pre-buckling axial force $\lambda N_{1p}(z)$ (Appendix 4.1) and takes the form

$$\bar{\bar{V}}_{gN_1} = \lambda \int_0^L N_{1p}(z) \left[\left(\bar{u}'_{1b}\right)^2 + \frac{\left(I_{xxs} + I_{yys}\right)}{A_s} \left(\bar{\theta}'_{zb}\right)^2 \right] dz \qquad (4.43)$$

in which $I_{xxs} = h_b^2 bt/2 + t_w h_w^3/12 + 2bt^3/12$; $I_{yys} = 2tb^3/12 + h_w t_w^3/12$; $\bar{\bar{V}}_{gM_x}$ is the second variation of the geometric potential energies contributed by pre-buckling bending moment M_{xp} of the steel beam (Appendix 4.1) and can be evaluated as

$$\bar{\bar{V}}_{gM_x} = 2\lambda \int_0^L M_{xp}(z)\,\bar{u}'_{1b}\bar{\theta}'_{zb}\,dz \tag{4.44}$$

$\bar{\bar{V}}_{gM_s}$ is the second variation of the geometric potential energies contributed by pre-buckling bending moment M_{sp} of the steel beam (Appendix 4.1) and can be evaluated as

$$\bar{\bar{V}}_{gM_s} = 2\frac{2I_{ssf}}{\bar{I}_{xx}}\lambda \int_0^L M_{sp}(z)\,\bar{u}'_{1b}\bar{\theta}'_{zb}\,dz + 2\frac{I_{ssg}}{\bar{I}_{xx}}\lambda \int_0^L M_{sp}(z)\,\bar{u}'_{3b}\delta\bar{\theta}'_{zb}\,dz \tag{4.45}$$

where $I_{ssf} = bt^3/12;\quad I_{ssg} = bt_g^3/12$. Also, the second variation of the pre-buckling shear force potential energy $\bar{\bar{V}}_{gQ_1}$ within the steel beam (Appendix 4.1) can be evaluated as

$$\bar{\bar{V}}_{gQ_1} = -2\lambda \int_0^L Q_{1p}(z)\left(\bar{u}'_{1b}\bar{\theta}_{zb} + \frac{I_{yyw}}{A_w}\bar{u}''_{1b}\bar{\theta}'_{zb}\right)dz \tag{4.46}$$

in which $I_{yyw} = h_w t_w^3/12$ is defined. For the GFRP plate, the second variation of the potential energies contributed by axial force $\lambda N_{3p}(z)$ (Appendix 4.1) can be evaluated as

$$\bar{\bar{V}}_{gN_3} = \lambda \int_0^L N_{3p}(z)\left[\left(\bar{u}'_{3b}\right)^2 + \frac{I_{xxg} + I_{yyg}}{A_g}\left(\bar{\theta}'_{zb}\right)^2\right]dz \tag{4.47}$$

in which $I_{xxg} = bt_g^3/12, I_{yyg} = t_g b^3/12$ are defined. Also, the second variation of the potential energy contributed by shear force $\lambda Q_{2p}(z)$ (Appendix 4.1) can be evaluated as

$$\bar{\bar{V}}_{gQ2} = \lambda \int_0^L Q_{2p}(z)\left\{\left\langle \bar{u}_{1b} \mid \bar{\theta}_{y1b} \mid \bar{u}_{3b} \mid \bar{\theta}_{y3b} \mid \bar{\theta}_{zb} \mid \bar{\theta}'_{zb} \mid \bar{\psi}_{1b} \right\rangle \times\right.$$

$$\times\left.\begin{bmatrix} -c_5 & 0 & -c_5 & 0 & -c_5c_{12} & 0 & 0 \\ 0 & -c_5\alpha_a & 0 & -c_5\alpha_a & 0 & c_5c_{11}\alpha_a & -c_5c_7\alpha_a \\ c_5 & 0 & c_5 & 0 & c_5c_{12} & 0 & 0 \\ 0 & c_5\alpha_a & 0 & c_5\alpha_a & 0 & -c_5c_{11}\alpha_a & c_5c_7\alpha_a \\ -(c_6+c_5c_7) & 0 & -(c_6+c_5c_7) & 0 & -(c_6+c_5c_7)c_{12} & 0 & 0 \\ 0 & c_6\alpha_a & 0 & c_6\alpha_a & 0 & -c_6c_{11}\alpha_a & c_6c_7\alpha_a \\ 0 & -c_5c_7\alpha_a & 0 & -c_5c_7\alpha_a & 0 & c_5c_7c_{11}\alpha_a & -c_5c_7^2\alpha_a \end{bmatrix}\begin{Bmatrix} \bar{u}'_{1b} \\ \bar{\theta}'_{y1b} \\ \bar{u}'_{3b} \\ \bar{\theta}'_{y3b} \\ \bar{\theta}'_{zb} \\ \bar{\theta}''_{zb} \\ \bar{\psi}'_{1b} \end{Bmatrix}\right\}dz \tag{4.48}$$

in which $c_{11} = (t - t_g)/2;\quad c_{12} = (h - t_g)/2;\quad I_{yya} = \alpha_a A_a$ are defined.

4.12. Finite Element Formulation

4.12.1. Interpolation of pre-buckling stress resultants

The pre-buckling stress resultants $N_{1p}(z), Q_{1p}(z), M_{1p}(z), N_{3p}(z), M_{3p}(z)$ and $Q_{2p}(z)$ are related to nodal stress resultants obtained from the pre-buckling analysis by adopting linear interpolation functions $\langle \mathbf{L}(\mathbf{z}) \rangle_{1\times 2}^{\mathbf{T}} = \langle L_1(z) \quad L_2(z) \rangle$ with $L_1(z) = 1 - z/L$ and $L_2(z) = z/L$:

$$\begin{aligned}
N_{1p}(z) &= \langle \mathbf{L}(\mathbf{z}) \rangle_{1\times 2}^{\mathbf{T}} \{\mathbf{N_{1p}}\}_{2\times 1}, \quad \langle \mathbf{N_{1p}} \rangle_{1\times 2}^{\mathbf{T}} = \langle N_{1p}(0) \mid -N_{1p}(L) \rangle \\
Q_{1p}(z) &= \langle \mathbf{L}(\mathbf{z}) \rangle_{1\times 2}^{\mathbf{T}} \{\mathbf{Q_{1p}}\}_{2\times 1}, \quad \langle \mathbf{Q_{1p}} \rangle_{1\times 2}^{\mathbf{T}} = \langle Q_{1p}(0) \mid -Q_{1p}(L) \rangle \\
M_{sp}(z) &= \langle \mathbf{L}(\mathbf{z}) \rangle_{1\times 2}^{\mathbf{T}} \{\mathbf{M_{sp}}\}_{2\times 1}, \quad \langle \mathbf{M_{sp}} \rangle_{1\times 2}^{\mathbf{T}} = \langle M_{sp}(0) \mid -M_{sp}(L) \rangle \\
M_{xp}(z) &= \langle \mathbf{L}(\mathbf{z}) \rangle_{1\times 2}^{\mathbf{T}} \{\mathbf{M_{xp}}\}_{2\times 1}, \quad \langle \mathbf{M_{xp}} \rangle_{1\times 2}^{\mathbf{T}} = \langle M_{xp}(0) \mid -M_{xp}(L) \rangle \\
N_{3p}(z) &= \langle \mathbf{L}(\mathbf{z}) \rangle_{1\times 2}^{\mathbf{T}} \{\mathbf{N_{3p}}\}_{2\times 1}, \quad \langle \mathbf{N_{3p}} \rangle_{1\times 2}^{\mathbf{T}} = \langle N_{3p}(0) \mid -N_{3p}(L) \rangle \\
Q_{2p}(z) &= \langle \mathbf{L}(\mathbf{z}) \rangle_{1\times 2}^{\mathbf{T}} \{\mathbf{Q_{2p}}\}_{2\times 1}, \quad \langle \mathbf{Q_{2p}} \rangle_{1\times 2}^{\mathbf{T}} = \langle Q_{2p}(0) \mid -Q_{2p}(L) \rangle
\end{aligned} \tag{4.49}$$

4.12.2. Displacement Interpolation

Two finite elements are developed for the problem, a two-node element and a three-node element. The relevant nodal degrees of freedom are depicted in Fig. 4.4. When interpolating the displacement fields $\overline{u}_{1b}(z)$ and $\overline{\theta}_{zb}(z)$, cubic Hermitian shape functions are adopted in the case of the two-node element and quadratic Lagrange interpolation functions are used in the case of the three-node element. For the remaining displacement fields $\overline{\theta}_{y1b}(z), \overline{u}_{3b}(z), \overline{\theta}_{y3b}(z)$ and $\overline{\psi}_{1b}(z)$, linear interpolation is adopted in both elements. The two-node element possesses 16 degrees of freedom (DOFs), while the three-node has 14 DOFs.

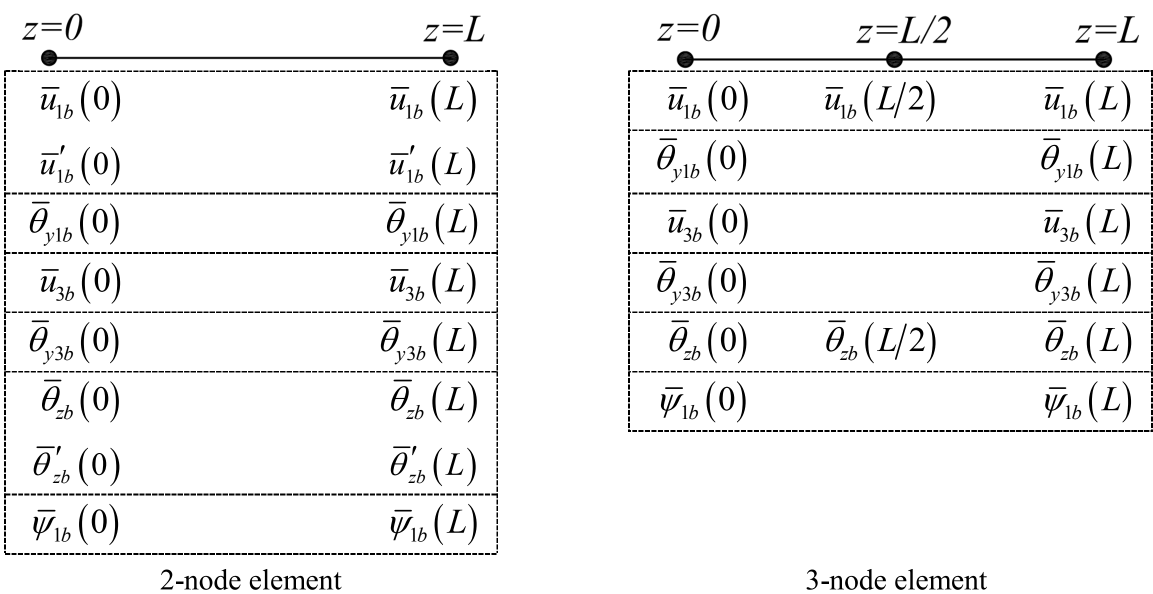

Figure 4.4. DOFs for Two and Three-node elements

4.12.2.1. Two-node element

The displacement fields $\bar{u}_{1b}(z),\bar{\theta}_{y1b}(z),\bar{u}_{3b}(z),\bar{\theta}_{y3b}(z),\bar{\theta}_{zb}(z),\bar{\psi}_{1b}(z)$ are related to the nodal displacement vector $\langle\bar{\boldsymbol{\Delta}}\rangle^{\mathbf{T}}_{1\times16}=\langle\bar{\mathbf{d}}(0)^{\mathbf{T}}_{1\times8}\mid\bar{\mathbf{d}}(L)^{\mathbf{T}}_{1\times8}\rangle$ where

$\bar{\mathbf{d}}(z_i)^{\mathbf{T}}_{1\times8}=\langle\bar{u}_{1b}(z_i)\quad\bar{u}'_{1b}(z_i)\mid\bar{\theta}_{y1b}(z_i)\mid\bar{u}_{3b}(z_i)\mid\bar{\theta}_{y3b}(z_i)\mid\bar{\theta}_{zb}(z_i)\quad\bar{\theta}'_{zb}(z_i)\mid\bar{\psi}_{1b}(z_i)\rangle$, and

$z_i=0$ or L through

$$\begin{aligned}&\langle\bar{u}_{1b}(z),\bar{\theta}_{y1b}(z),\bar{u}_{3b}(z),\bar{\theta}_{y3b}(z),\bar{\theta}_{zb}(z),\bar{\psi}_{1b}(z)\rangle^{T}\\&\qquad=\langle\bar{\boldsymbol{\Delta}}\rangle^{T}_{1\times16}\left(\{\mathbf{S_{u1}}\}_{16\times1},\{\mathbf{S}_{\theta\mathbf{1}}\}_{16\times1},\{\mathbf{S_{u3}}\}_{16\times1},\{\mathbf{S}_{\theta3}\}_{16\times1},\{\mathbf{S}_{\theta z}\}_{16\times1},\{\mathbf{S}_{\psi\mathbf{1}}\}_{16\times1}\right)\end{aligned}\tag{4.50}$$

in which the shape function vectors are defined as

$$\begin{aligned}\langle\mathbf{S_{u1}}\rangle_{1\times16}&=\langle H_1(z)\quad H_2(z)\quad 0\quad 0\quad 0\quad 0\quad 0\quad 0\mid H_3(z)\quad H_4(z)\quad 0\quad 0\quad 0\quad 0\quad 0\quad 0\rangle\\\langle\mathbf{S}_{\theta\mathbf{1}}\rangle_{1\times16}&=\langle 0\quad 0\quad L_1(z)\quad 0\quad 0\quad 0\quad 0\quad 0\mid 0\quad 0\quad L_2(z)\quad 0\quad 0\quad 0\quad 0\quad 0\rangle\\\langle\mathbf{S_{u3}}\rangle_{1\times16}&=\langle 0\quad 0\quad 0\quad L_1(z)\quad 0\quad 0\quad 0\quad 0\mid 0\quad 0\quad 0\quad L_2(z)\quad 0\quad 0\quad 0\quad 0\rangle\\\langle\mathbf{S}_{\theta3}\rangle_{1\times16}&=\langle 0\quad 0\quad 0\quad 0\quad L_1(z)\quad 0\quad 0\quad 0\mid 0\quad 0\quad 0\quad 0\quad L_2(z)\quad 0\quad 0\quad 0\rangle\\\langle\mathbf{S}_{\theta z}\rangle_{1\times16}&=\langle 0\quad 0\quad 0\quad 0\quad 0\quad H_1(z)\quad H_2(z)\quad 0\mid 0\quad 0\quad 0\quad 0\quad 0\quad H_3(z)\quad H_4(z)\quad 0\rangle\\\langle\mathbf{S}_{\psi\mathbf{1}}\rangle_{1\times16}&=\langle 0\quad 0\quad 0\quad 0\quad 0\quad 0\quad 0\quad L_1(z)\mid 0\quad 0\quad 0\quad 0\quad 0\quad 0\quad 0\quad L_2(z)\rangle\end{aligned}\tag{4.51}$$

and $H_1(z)=1-3(z/L)^2+2(z/L)^3$, $H_2(z)=z-2(z^2/L)+(z^3/L^2)$, $H_3(z)=3(z/L)^2-2(z/L)^3$, $H_4(z)=z^3/L^2-z^2/L$. From Eqs.(4.50), by substituting into Eqs. (4.39) through (4.42)a-c, and from Eqs. (4.49) and (4.50) by substituting into Eqs. (4.43)-(4.48) and (4.34), the second variation of the total potential energy in Eq. (4.38) is obtained as

$$\delta\frac{1}{2}\bar{\bar{\pi}}=\delta\frac{1}{2}\langle\bar{\boldsymbol{\Delta}}\rangle^{\mathbf{T}}_{1\times16}\left([\mathbf{K_e}]_{16\times16}+\lambda[\mathbf{K_g}]_{16\times16}\right)\{\bar{\boldsymbol{\Delta}}\}_{16\times1}=0\tag{4.52}$$

in which $[\mathbf{K_e}]_{16\times16}$ and $[\mathbf{K_g}]_{16\times16}$ are elastic and geometric stiffness matrices, respectively as defined in Appendix 4.2. A non-trivial solution of Eq. (4.52) leads to the eigenvalue solution $\left\{[\mathbf{K_e}]_{16\times16}+\lambda[\mathbf{K_g}]_{16\times16}\right\}\{\bar{\boldsymbol{\Delta}}\}_{16\times1}=\{\mathbf{0}\}_{16\times1}$ which is solved for the critical load multiplier λ and the corresponding buckling mode $\{\bar{\boldsymbol{\Delta}}\}_{16\times1}$.

4.12.2.2. Three-node element

The displacement fields $\bar{u}_{1b}(z), \bar{\theta}_{y1b}(z), \bar{u}_{3b}(z), \bar{\theta}_{y3b}(z), \bar{\theta}_{zb}(z), \bar{\psi}_{1b}(z)$ are related to the nodal displacement vector $\left\langle \hat{\mathbf{\Delta}} \right\rangle_{1\times14}^{\mathbf{T}} = \left\langle \hat{\mathbf{d}}(0)_{1\times6}^{\mathbf{T}} \;\middle|\; \hat{\hat{\mathbf{d}}}(L/2)_{1\times2}^{\mathbf{T}} \;\middle|\; \hat{\mathbf{d}}(L)_{1\times6}^{\mathbf{T}} \right\rangle$ where $\hat{\mathbf{d}}(z_i)_{1\times6}^{\mathbf{T}} = \left\langle \bar{u}_{1b}(z_i) \quad \bar{\theta}_{y1b}(z_i) \;\middle|\; \bar{u}_{3b}(z_i) \quad \bar{\theta}_{y3b}(z_i) \;\middle|\; \bar{\theta}_{zb}(z_i) \quad \bar{\psi}_{1b}(z_i) \right\rangle$, and $z_i = 0 \text{ or } L$ and $\hat{\hat{\mathbf{d}}}(L/2)_{1\times2}^{\mathbf{T}} = \left\langle \bar{u}_{1b}(L/2) \quad \bar{\theta}_{zb}(L/2) \right\rangle$ through

$$\begin{aligned} &\left\langle \bar{u}_{1b}(z), \bar{\theta}_{y1b}(z), \bar{u}_{3b}(z), \bar{\theta}_{y3b}(z), \bar{\theta}_{zb}(z), \bar{\psi}_{1b}(z) \right\rangle^T \\ &\quad = \left\langle \hat{\mathbf{\Delta}} \right\rangle_{1\times14}^{T} \left(\left\{ \hat{\mathbf{S}}_{\mathbf{u1}} \right\}_{14\times1}, \left\{ \hat{\mathbf{S}}_{\theta\mathbf{1}} \right\}_{14\times1}, \left\{ \hat{\mathbf{S}}_{\mathbf{u}3} \right\}_{14\times1}, \left\{ \hat{\mathbf{S}}_{\theta3} \right\}_{14\times1}, \left\{ \hat{\mathbf{S}}_{\theta z} \right\}_{14\times1}, \left\{ \hat{\mathbf{S}}_{\psi\mathbf{1}} \right\}_{14\times1} \right) \end{aligned} \tag{4.53}$$

in which the shape function vectors are defined as

$$\begin{aligned} \left\langle \hat{\mathbf{S}}_{\mathbf{u1}} \right\rangle_{1\times14} &= \left\langle R_1(z) \quad 0 \quad 0 \quad 0 \quad 0 \quad 0 \;\middle|\; R_2(z) \quad 0 \;\middle|\; R_3(z) \quad 0 \quad 0 \quad 0 \quad 0 \quad 0 \right\rangle \\ \left\langle \hat{\mathbf{S}}_{\theta\mathbf{1}} \right\rangle_{1\times14} &= \left\langle 0 \quad L_1(z) \quad 0 \quad 0 \quad 0 \quad 0 \;\middle|\; 0 \quad 0 \;\middle|\; 0 \quad L_2(z) \quad 0 \quad 0 \quad 0 \quad 0 \right\rangle \\ \left\langle \hat{\mathbf{S}}_{\mathbf{u}3} \right\rangle_{1\times14} &= \left\langle 0 \quad 0 \quad L_1(z) \quad 0 \quad 0 \quad 0 \;\middle|\; 0 \quad 0 \;\middle|\; 0 \quad 0 \quad L_2(z) \quad 0 \quad 0 \quad 0 \right\rangle \\ \left\langle \hat{\mathbf{S}}_{\theta3} \right\rangle_{1\times14} &= \left\langle 0 \quad 0 \quad 0 \quad L_1(z) \quad 0 \quad 0 \;\middle|\; 0 \quad 0 \;\middle|\; 0 \quad 0 \quad 0 \quad L_2(z) \quad 0 \quad 0 \right\rangle \\ \left\langle \hat{\mathbf{S}}_{\theta z} \right\rangle_{1\times14} &= \left\langle 0 \quad 0 \quad 0 \quad 0 \quad R_1(z) \quad 0 \;\middle|\; 0 \quad R_2(z) \;\middle|\; 0 \quad 0 \quad 0 \quad 0 \quad R_3(z) \quad 0 \right\rangle \\ \left\langle \hat{\mathbf{S}}_{\psi\mathbf{1}} \right\rangle_{1\times14} &= \left\langle 0 \quad 0 \quad 0 \quad 0 \quad 0 \quad L_1(z) \;\middle|\; 0 \quad 0 \;\middle|\; 0 \quad 0 \quad 0 \quad 0 \quad 0 \quad L_2(z) \right\rangle \end{aligned} \tag{4.54}$$

with $R_1(z) = (z/L - 1)(2z/L - 1)$, $R_2(z) = (4z/L)(1 - z/L)$, and $R_3(z) = (z/L)(2z/L - 1)$. From Eqs. (4.53), by substituting into Eqs. (4.39) through (4.42)a-c, and from Eqs. (4.49) and (4.53) by substituting into Eqs. (4.43)-(4.48) and (4.34), the second variation of the total potential energy in Eq. (4.38) is obtained as

$$\delta \frac{1}{2} \bar{\bar{\pi}} = \delta \frac{1}{2} \left\langle \hat{\mathbf{\Delta}} \right\rangle_{1\times14}^{\mathbf{T}} \left(\left[\hat{\mathbf{K}}_{\mathbf{e}} \right]_{14\times14} + \lambda \left[\hat{\mathbf{K}}_{\mathbf{g}} \right]_{14\times14} \right) \left\{ \hat{\mathbf{\Delta}} \right\}_{14\times1} = 0 \tag{4.55}$$

in which $\left[\hat{\mathbf{K}}_{\mathbf{e}} \right]_{14\times14}$ and $\left[\hat{\mathbf{K}}_{\mathbf{g}} \right]_{14\times14}$ are elastic and geometric stiffness matrices, respectively as defined in Appendix 4.3. A non-trivial solution of Eq. (4.55) leads to the eigenvalue solution $\left\{ \left[\hat{\mathbf{K}}_{\mathbf{e}} \right]_{14\times14} + \lambda \left[\hat{\mathbf{K}}_{\mathbf{g}} \right]_{14\times14} \right\} \left\{ \hat{\mathbf{\Delta}} \right\}_{14\times1} = \{\mathbf{0}\}_{14\times1}$.

4.13. Validation and Examples

The elements developed in the present study are adopted to predict the buckling capacities of beams and columns and validated through comparisons with 3-dimentional finite element analyses (3D FEA) under ABAQUS software (and classical solutions for the degenerate case of no GFRP). Although these formulations are developed to apply for GFRP-strengthened beams, they can be also applied for steel beams alone by setting to zero the mechanical properties and/or dimensions of GFRP and adhesive materials.

4.13.1. Example 1 – Simply supported composite beam under a mid-span point load

A simply supported steel beam is subjected to a point load P applied at mid-span (Fig. 4.5a). The beam cross-section is W250x45 with the dimensions shown in Fig. 4.5b. One flange (i.e., compression flange or tension flange) is bonded to a 19mm-thick GFRP plate through a 1-mm thick layer of adhesive. Three spans are considered; 4.0, 6.0 and 8.0m. Elasticity modulus of steel is 200GPa, that of GFRP is 17.2 GPa (Siddique and El Damatty 2013) and that of adhesive are 3.18 GPa (Shaat and Fam 2009). Poisson's ratio for all materials is taken as 0.3 and the yield strength of steel is selected as 350 MPa. The buckling load P_{cr} and corresponding mode shapes for both the strengthened beam and the bare steel beam are determined from the present model and comparisons are made to 3D FEA results based on ABAQUS and standard equations based on the Eurocode Guide moment gradient factor (Gardner and Nethercot 2011).

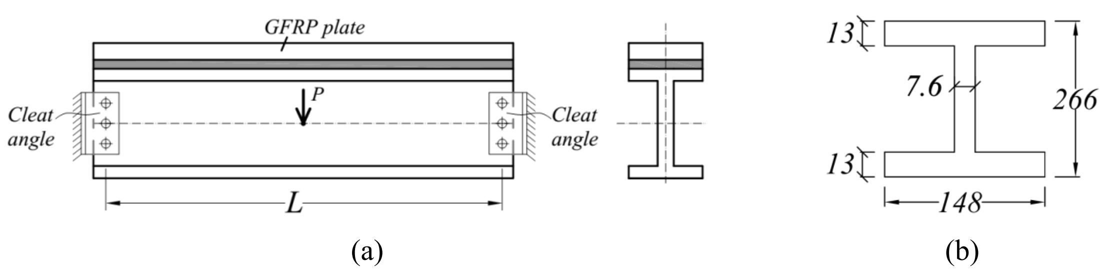

Figure 4.5. Simply supported beams under a point load (a) beam profile and cross-section and (b) dimensions of W250x45 section

Based the given yield strength, the bare beam is found to meet Class 1 requirements of CAN-CSA S16 (2016). The corresponding plastic moment is $M_p = Z_x F_y = 210.7kNm$. Also, the nominal elastic buckling moment is $M_u = \left(C_b \pi / L\right)\sqrt{GJEI_{yy} + I_{yy} I_{\omega\omega}\left(\pi E / L\right)^2}$ where the moment gradient C_b

depends on the standards adopted and ranges from 1.265 in CAN-CSA S16 (2016) to 1.388 in the Australian code AS4100 (1998) and takes the value of 1.365 in the Eurocode guide (2011) which is closest to FEA predictions (Hassan and Mohareb 2015). In CAN-CSA S16 (2016), when $M_u \leq 0.67 M_p$, the elastic LTB resistance is deemed to govern the resistance and the nominal resistance is $M_n = M_u$, while when $M_u > 0.67 M_p$ the inelastic LTB capacity is $M_{in} = 1.15 M_p \left(1 - 0.28 M_p / M_u\right)$ and is deemed to govern the design $M_n = M_{in}$ when $M_{in} < M_p$. Otherwise, the plastic resistance is concluded to govern the design and the beam nominal resistance is governed by its plastic resistance, i.e., $M_n = M_p$. For the present section, the plastic resistance is found to govern the resistance of the beam when $L \leq 2580mm$, the elastic LTB capacity to govern the resistance when $L > 5490mm$, while the inelastic LTB buckling governs the resistance when $2580 \leq L \leq 5490mm$. For the present example, three spans are selected; L=4.0, 6.0, and 8.0m so that the smaller value lies in the inelastic LTB range, while the other two spans correspond to the elastic LTB failure mode.

<u>Mesh study for present element:</u> A mesh study is conducted by modeling the 6m span beam using both elements developed in the present study. Meshes consisting of 16, 32, 40, 80, 160 and 320 elements were considered (Fig. 4.6). For the three-node element, when adopting coarser meshes involving 16-40 elements, the critical loads predicted are found to decrease with the number of elements, afterward the solution stabilizes as meshes with 80- 320 elements provide identical buckling load predictions of 127.0 kN, suggesting that convergence is achieved when 80 elements are taken. The buckling load of 127.0 kN is taken as a reference value for comparison with solutions based on the two-node element. For the two-node element, the buckling loads based on 16, 32, 40, 80, 160, and 320 elements of the two-node elements are 409, 159, 142, 129, 127.9 and 127.5 kN, respectively and the corresponding differences from the reference critical load are 222%, 159%, 11.6%, 1.7%, 0.7% and 0.4%. The results suggest that the convergence rate is somewhat slower than that of the three-node element and hence the three-node element will be adopted in subsequent analyses.

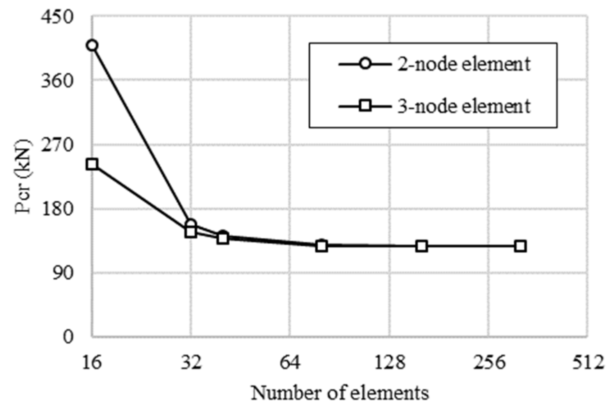

Figure 4.6. Mesh study of the present finite element formulation

Mesh study for the 3D FEA: The 3D FEA is conducted as a benchmark solution against which the results of the present theory are compared. The 8-node brick element C3D8R is selected from the ABAQUS library. The element has 8 nodes with three translations at each node, totaling 24 DOFs. The element uses reduced integration to avoid volumetric locking, and thus has a single integration point located at the centroid. A mesh study is performed to determine the mesh beyond which no improvement is attained in the solution. The mesh is fully characterized by seven parameters $n_1,\ldots,n_7$ as shown in Fig. 4.7. For the 6m span, the study showed that convergence is attained when a mesh with $n_1 = 12, n_2 = n_4 = n_5 = n_6/2 = 4; n_3 = 60; n_7 = 600$ is taken, corresponding to 1,682,199 DOFs. Initially, the 3D FEA model exhibited web distortion and hence under-predicted the critical moments. To control distortional effects, transverse stiffeners were added to the model. Three stiffening arrangements were considered; (a) two stiffeners at both ends of the beam, (b) three stiffeners (two at the ends and one at mid-span), and (c) five stiffeners along the span L (at 0, L/4, L/2, 3L/4, and L) (Appendix 4.4). A comparison of the buckling loads for spans L=4.0, 6.0 and 8.0m are shown in Table 4.1. The addition of more web stiffeners is found to increase the buckling loads, and make the 3D FEA solutions approach the predictions of the present model. The beam with five-stiffener arrangement is found to yield the closest predictions to those of the present study.
The three-stiffener arrangement is adopted in subsequent runs.

Table 4.1. Comparison of buckling load (kN) for different stiffener arrangements

Span (m)	Number of stiffeners adopted:			Present study (*d*)	(*d*) / (*a*)	(*d*) / (*b*)	(*d*) / (*c*)
	2 (*a*)	3 (*b*)	5 (*c*)				
4	271	296	305	314	1.16	1.06	1.03
6	117	121	125.2	127	1.09	1.05	1.01
8	65.3	65.4	67.6	68.5	1.05	1.05	1.01

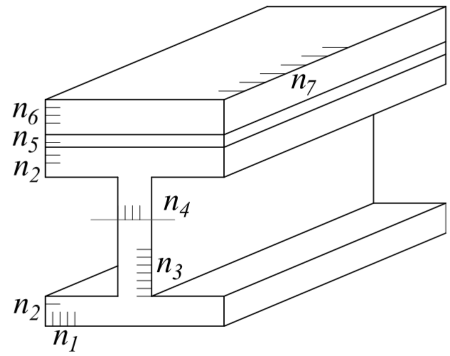

Figure 4.7. Number of elements defining the 3D FEA mesh

Verification of buckling loads: Table 4.2 presents the buckling loads as predicted by the present model, the 3D FEA, and the critical moment based on the Eurocode guide moment gradient factor. For the bare steel beam, the present model respectively predicts buckling loads of 227, 89.0 and 47.8 kN, for the 4, 6 and 8m spans. These values compare to 3D FEA predictions of 223, 87.1 and 46.7 kN which correspond to 2.0%, 2.1 % and 2.3% differences. In comparison, the solution based on the critical moment gradient based on the Eurocode moment gradient factor overestimates the buckling loads by 4.1%, 3.5% and 2.9%.

For the case where the compression flange is strengthened, the buckling loads based on the present solution are 314, 127 and 68.5 kN for 4, 6, and 8m spans, respectively, while those based on the 3D FEA predictions are 296, 121 and 65.4 kN, corresponding to 5.9%, 4.9% and 4.5% differences (Table 4.2). For the case where the tension flange is strengthened, the buckling loads predicted by the present solution are 291, 121 and 66.0 kN for 4, 6, and 8m spans, respectively while those predicted by the 3D FEA solution are 274, 114, 62.6 kN, corresponding to 6.1%, 5.5% and 5.2% differences. The difference between the predictions of both models is attributed to minor web distortions between the stiffeners, which are captured in the 3D FEA solution but not in the present model. The differences between the non-distortional solution in the present model and the 3D FEA solution based on the Abaqus model is slightly larger than the bare beam results. The observation is qualitatively consistent with past research on bare steel beams sections (e.g., Hassan and Mohareb 2015) which suggest that webs for sections with thicker flanges exhibit more pronounced distortional effects. In this respect, the GFRP plate can be conceived to "thicken" the compression flange.

For the 6m span beam with the compression flange strengthened, when the load is moved to the top flange, the present model was found to predict a buckling load of 102 kN, which compares to 96.8 kN as predicted by the 3D FEA model, a 5.1% difference. Also, when the load is moved to the bottom flange, the present model predicted a buckling load of 154 kN which compares to150 kN as predicted by the 3D FEA, a 2.7% difference.

Table 4.2. Buckling loads P_{cr} (kN) for bare and strengthened W250x45 simply supported beam

Span (m)	Bare steel beam					Compression Flange Strengthened			Tension Flange Strengthened		
	PS (1)	E^{+} (2)	3D FEA (3)	(1)/(3)	(2)/(3)	PS (4)	3D FEA (5)	(4)/(5)	PS (6)	3D FEA (7)	(6)/(7)
4	227	232	223	1.02	1.04	314	296	1.06	291	274	1.06
6	89	90.3	87.1	1.02	1.04	127	121	1.05	121	114	1.06
8	47.8	48.1	46.7	1.02	1.03	68.5	65.4	1.05	66.0	62.6	1.05

* PS=Present study, $^{+}$E= classical solution based on moment gradient factor of Eurocode Guide (2011)

Verification of buckling mode: The buckling configuration for the 6m span beam as predicted by the present solution are found to nearly overlap on that predicted by the 3D FEA in Figs. 4.8a-f which depicts the buckling displacements $u_{1b}, u_{3b}, \theta_{zb}, \theta_{y1b}, \theta_{y3b}$ and ψ_{1b}. In a strict sense, owing to cross-sectional distortion, the angle of twist θ_{zb} in the 3D FEA would slightly vary within a given cross-section z. Thus, a representative angle of twist was computed based on the lateral displacements extracted from the buckled configuration of the 3D FEA model at the web-to-flange junctions. In a similar manner, an estimate of the weak axis rotation θ_{y3b} for GFRP is computed from the longitudinal displacements at the plate ends, as extracted from the buckled FEA configuration.

Also, at a given section z, in order to characterize the weak axis rotation θ_{y1b}, and warping deformation , ψ_{1b} as predicted by the 3D FEA model, the longitudinal displacements are extracted at four sampling points within the cross-section and the procedure introduced in Xiao and Doudak 2014 and Hjaji and Mohareb 2015 was adopted to estimate the weak axis rotation, warping deformation, (along with the longitudinal displacement at the section centroid, and strong axis as a by-product) Again, the predicted values would slightly vary within a cross-section depending on selection of the sampling points. In the present study, the four sampling points were selected at the tips of the flanges and the details are provided in Appendix 4.5.

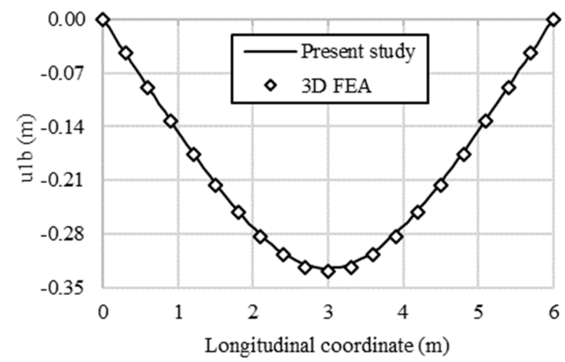

(a) $u_{1b}(z)$

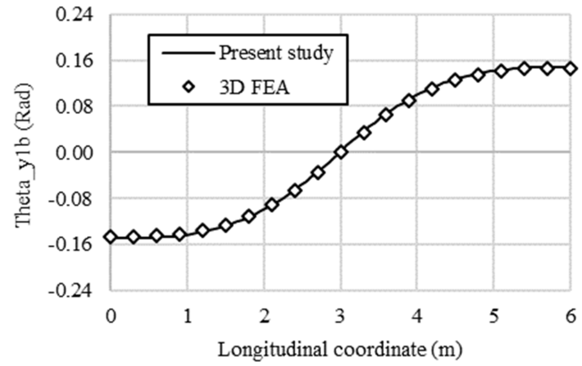

(b) $\theta_{y1b}(z)$

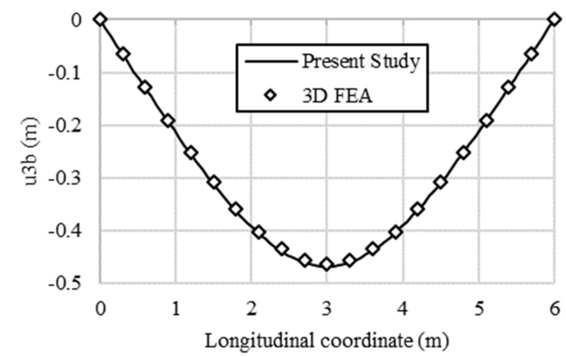

(c) $u_{3b}(z)$

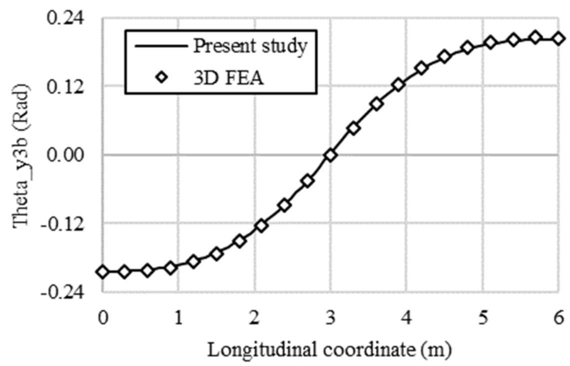

(d) $\theta_{y3b}(z)$

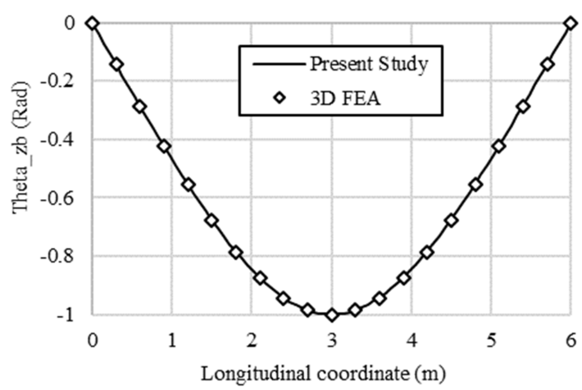

(e) $\theta_{zb}(z)$

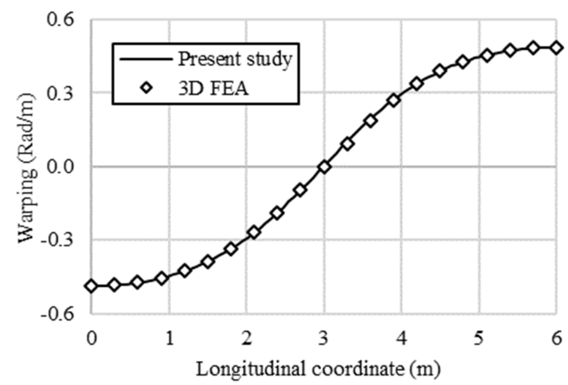

(f) $\psi_{1b}(z)$

Figure 4.8. Comparison of mode shape for span L=6m between present study and 3D FEA solutions

Effectiveness of strengthening: When the compression flange of the present problem is strengthened, the present model predicts respective increases in the elastic critical loads of 38.4%, 42.8%, and 43.3%, for the 4, 6, and 8m spans, above the corresponding elastic critical loads of the bare beams. As expected, strengthening the tension flange leads to less gains in the elastic critical load of 28.2%, 36% and 38.1%, respectively.

Investigating the possibility of material failure prior to buckling: A common concern in beams strengthened with GFRP plates is the possible delamination induced by peeling and/or shear stresses near bond ends. For the 4, 6 and 8m spans investigated, the 3D FEA solution predicts peak peeling stresses near beam ends of 1.3, 0.52, and 0.24 MPa and peak shear stresses of 1.6, 0.67, and 0.37 MPa, respectively. These stresses are significantly smaller than typical adhesive and shear strengths of 33 MPa and 15 MPa, respectively (Shaat and Fam 2009). Also, the peak longitudinal compressive stresses within the GFRP plates occur at mid-span and take the values 57.6, 34.8, and 24.4 MPa for 4, 6 and 8m spans. These values are much smaller than typical GFRP longitudinal strengths of 207 MPa (Siddique and El Damatty 2013). The analysis suggests that material failure of GFRP and adhesive do not govern the capacity of the beams in a manner consistent with assumption ix.

Effect of the load position: Table 4.3 shows the predicted critical loads when the load position is moved to the top and bottom flanges of the 6m and 8m span beams. The percentage gains/reductions due to the effect of load position are compared to the case of shear center loading for each span and each strengthening arrangement (i.e., bare beam, strengthened beams). When applying the load at the top flange of the 6m span bare beam, the buckling load is 75.4% of that of the shear center loading. For the beam strengthened at the compression flange, the buckling load for top flange loading is 80.3% of that of shear center loading. A comparable fraction of 80.4% is attained for tension flange strengthening. When applying the load at the bottom flange of the bare beam, the buckling load was found to increase to 132% of that of the shear center loading. For the strengthened beams, the buckling load increases to 123% for top flange strengthening, and 124% for bottom flange strengthening. Similar results are observed for the 8m span beam.

The limited set of results investigated herein suggests that adopting the load height reduction factors for top flange loading of the bare beam consistently yield conservative buckling strength predictions in the case of strengthened beams. Conversely, adopting load height gain factors for bottom flange loading for the bare beam would consistently lead to un-conservative buckling load predictions.

Table 4.3. Effect of load height and Load height factors for W250x45 beams

Span (m)	Load position	Bare steel beam		Compression Flange Strengthened		Tension Flange Strengthened	
		Critical load (kN)	Load height factor*	Critical load (kN)	Load height factor	Critical load (kN)	Load height factor
6	Top	67.1	75.4%	102	80.3%	97.3	80.4%
	Shear center	89.0	100%	127	100%	121	100%
	Bottom	117	132%	157	123%	150	124%
8	Top	37.2	77.8%	57.5	83.9%	55.3	83.8%
	Shear center	47.8	100%	68.5	100%	66.0	100%
	Bottom	59.4	124%	80.5	118%	77.7	118%

*: Load height factor =buckling load for the given load position/ buckling load for shear center loading for the specified span and strengthening arrangement as applicable

Effect of GFRP and adhesive thicknesses on buckling strength: The 6m-span steel beam with the compression flange strengthened is considered under the effect of a mid-span point load acting at the shear center. The thickness of the GFRP plate first is varied from 0.0 to 30mm while keeping the adhesive layer thickness as 1.0mm and then thickness of the adhesive is varied from 0.5 to 4.0mm while keeping the GFRP plate thickness as 19mm. As observed in Fig. 4.9a, the buckling load increases in a nonlinear fashion with the GFRP thickness. While the buckling load for the bare beam is 89 kN, that corresponding to a 30mm thick plate is significantly increased to 173 kN, a 94.4% difference. In contrast, Fig. 4.9b shows that the buckling load increases only marginally with the thickness of the adhesive. The increase is attributed to the slightly deeper overall cross-section in the case of a thicker adhesive. While the buckling load for the 0.5mm thick adhesive is 126.9 kN, that corresponding to 4.0mm is marginally increased to 133 kN, a 4.6% difference.

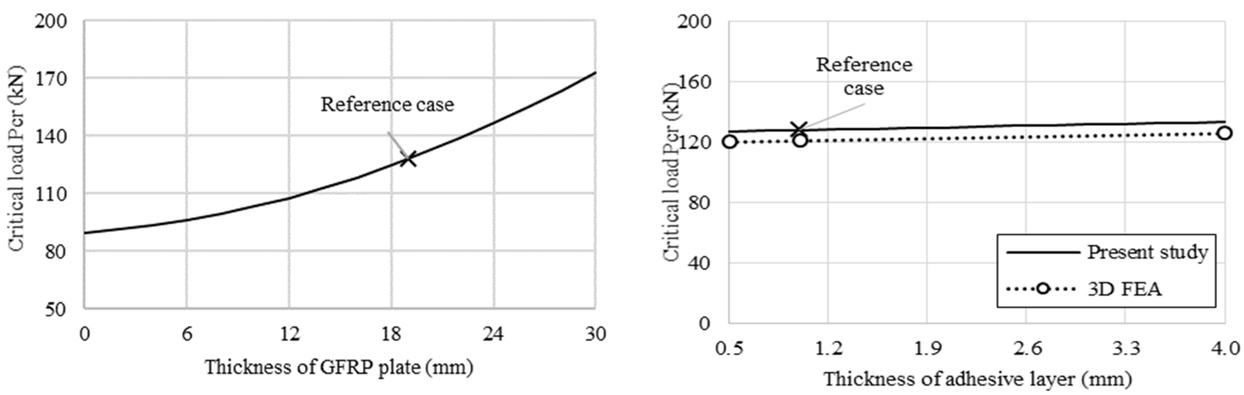

(a) (b)

Figure 4.9. Critical loads P_{cr} (kN) against (a) GFRP plate thickness and (b) adhesive layer thickness

Effect of the steel section dimensions on buckling strength: The steel beam with the compression flange strengthened considered in Example 1 is re-considered while keeping all geometric parameters, material properties, boundary conditions, and loading unchanged. The W250x45 cross-section with dimensions (h_r, b_r, t_r, w_r) is taken as a reference case. Only one of the cross-sectional parameters (h, b, t, w) is varied one at a time in the ranges $0.5 \le R_h = (h/h_r) \le 1.5$; $0.5 \le R_b = (b/b_r) \le 1.5$; $0.5 \le R_w = (w/w_r) \le 1.5$; and $0.5 \le R_t = (t/t_r) \le 1.5$, while keeping the three remaining parameters unchanged from the reference values. The critical loads were extracted for all the cases (Fig. 4.10). It is observed that the flange width b is the most influential on the predicted critical load. The buckling load corresponding to $R_b = 0.5$ is 30 kN while that corresponding to $R_b = 1.5$ is 314 kN, a tenfold increase. The flange thickness is also observed to have a significant influence on the critical load while the section depth and the web thickness are found are less influencial. This finding is consistent with the CAN-CSA S16 (2016) solution for steel sections in which the critical load is largely dependent on the moment of inertial I_{yy} about the weak axis and the warping constant $I_{\omega\omega}$.

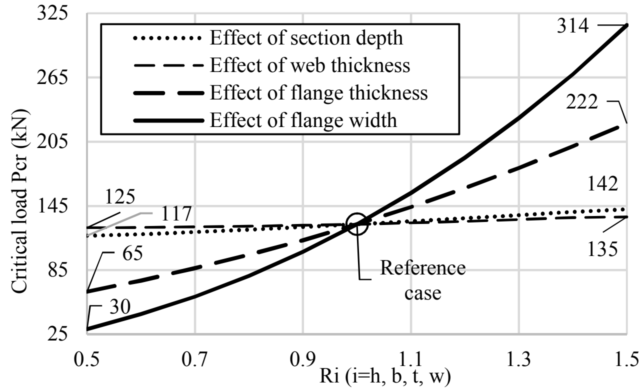

Figure 4.10. Critical loads P_{cr} (kN) against the changed dimensions of the reference section W250x45

4.13.2. Example 2 – Simply supported beam under linear bending moments

The steel beam with top flange strengthening in Example 1 is re-visited here under the action of strong axis linear bending moments induced by two end moments $M_x, \kappa M_x$ with $-1 \le \kappa \le 1$, where $\kappa = -1$ indicates uniform moments and $\kappa = 1$ denotes full reversed moments (Table 4.4). Span is taken as 5m. The end moments were applied as two equal and opposite axial unit forces acting at the flange-web junctions.

Critical moments: Table 4.4 provides the buckling loads for loading cases $\kappa = -1.0, -0.5, 0.0, 0.5, \text{and } 1.0$. For the bare beam, differences within 0.6% are observed between predictions of the present model and the 3D FEA solutions. For the strengthened beam, the differences between both solutions are found to lie within 5.7%. As discussed in previous examples, the difference is attributed to web distortion. A comparison between the critical moments (Table 4.4) for the bare and strengthened beams shows an effectiveness of strengthening of 38.9%, 36.5%, 38.2%, 35.7% and 35.5%, for loading Cases 1 through 5, respectively.

Moment gradient effect: For a given loading case κ, the moment gradient factor C_b evaluated from a buckling analysis can be obtained by dividing the predicted critical moment $M_{cr}(\kappa)$ by the critical uniform moment $M_{cr}(-1)$. Adopting this definition, one can obtain the moment gradient factors based on either the 3D FEA analysis, the present model, or the beam buckling element of Barsoum and Gallagher (1970) and comparisons are made against moment gradients provided in various standards. The relevant equations are $C_b(CAN) = 4M_{\max} \Big/ \sqrt{M_{\max}^2 + 4M_a^2 + 7M_b^2 + 4M_c^2} \le 2.5$ based on the Canadian Standards CAN CSA S16 (2016), $C_b(AISC) = 12.5M_{\max} / (2.5M_{\max} + 3M_a + 4M_b + 3M_c)$ based on American standards AISC (2016), and $C_b(AUS) = 1.7M_{\max} \Big/ \sqrt{M_a^2 + M_b^2 + M_c^2} \le 2.5$ based on the Australian standards AS4100 (1998), and those based on Eurocode Guide (Gardner and Nethercot 2011) (Table 4.4).

The 3D FEA results are taken as a benchmark solution against which other solutions are compared. As observed in Fig. 4.11a, the present solution is in excellent agreement with the predictions of the 3D FEA model with the differences between both solutions within 0.6%. The Barsoum and Gallagher (1970) and Eurocode Guide solutions slightly overestimate the moment gradient factors, while the CSA, AISC and AS solutions under-predict the results. For instance of the case of fully reversed moments $\kappa = 1$, the BG and EG solutions overestimate the moment gradients by 1.7% and 2.8%, while the CSA, AISC and AS underestimate the moment gradients by 14%, 15% and 9.1%, respectively. For the strengthened beam (Table 4.4 and Fig. 4.11b), the moment gradient factors are provided based on the present study and 3D FEA. As observed, the present study and the 3D FEA solutions are in close agreement. The maximum difference between the two solutions is 2.4% for the case of fully reversed moments $\kappa = 1$. Also shown on Fig. 4.11b is a comparison of the moment gradient factor for the strengthened beam overlaid on that of the bare beam. The moment gradients for the bare beam are observed to be marginally lower than those of the strengthened beam in the case double curvature. Otherwise, the moment gradients of both beams nearly coincide for single curvature. The results suggest that moment gradients for bare beams can safely be applied to the design of strengthened beams.

Table 4.4. Comparison of buckling moments and moment gradient factors for beam W250x45

Cross-section		Loading Case	Buckling moment (kNm) PS	3D FEA	% Diff.	C_b of 3DFEA	Ratio of Moment Gradient Factor PS / 3DFEA	BG / 3DFEA	CSA / 3DFEA	EG / 3DFEA	AISC / 3DFEA	AS / 3DFEA
Bare beam	1	M_x $-M_x$	126	126	0.00	1.000	1.000	1.000	1.000	1.000	1.000	0.982
	2	M_x $-0.5M_x$	167	166	0.60	1.318	1.006	1.007	0.981	1.004	0.948	0.984
	3	M_x 0	228	227	0.44	1.802	1.004	1.029	0.969	1.043	0.925	1.009
	4	M_x $0.5M_x$	317	316	0.32	2.508	1.003	1.019	0.912	1.078	0.867	0.990
	5	M_x M_x	338	337	0.30	2.675	1.003	1.017	0.863	1.028	0.850	0.899
GFRP-strengthened beam	1	M_x $-M_x$	175	169	3.4	1.000	1.000	N/A				
	2	M_x $-0.5M_x$	228	221	3.1	1.308	1.000					
	3	M_x 0	315	303	3.8	1.793	1.004					
	4	M_x $0.5M_x$	430	411	4.4	2.432	1.010					
	5	M_x M_x	457	431	5.7	2.550	1.024					

PS=Present study, BG= Barsoum and Gallagher, CSA=Canadian code, EG=Eurocode guide, AISC=American code, AS=Australian code.

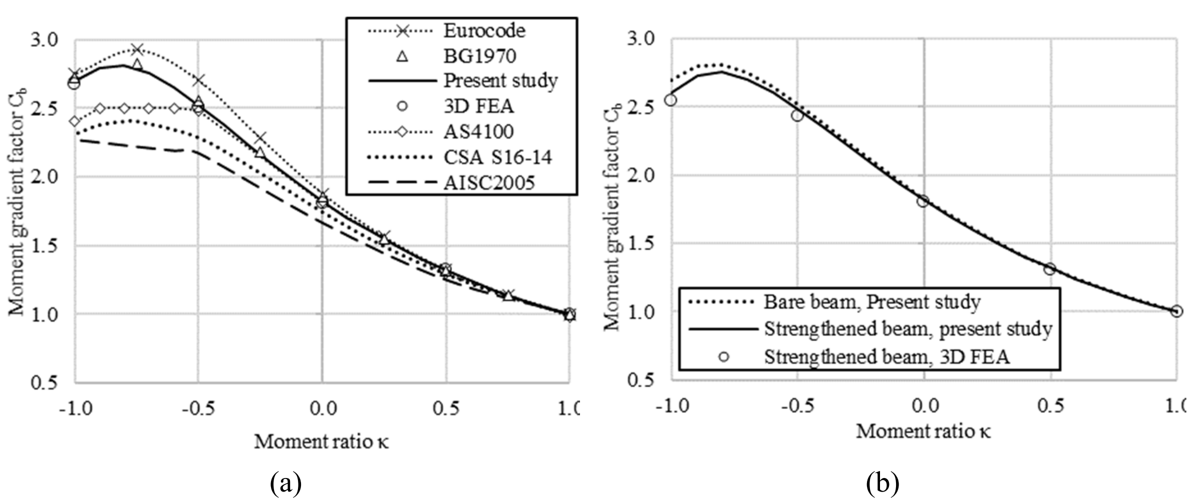

Figure 4.11. Moment gradient factor against moment ratio κ for (a) bare steel beam and (b) strengthened steel beam with comparison to bare beam results

4.13.3. Example 3 – Fixed-free column

A fixed-free column is subjected to a compression force P acting at the steel section centroid. The column cross-section and the specifics of the strengthening GFRP and adhesive are identical to those in Example 1. The span is taken as 3m and 5m.

Table 4.5 presents the buckling loads for the bare columns and strengthened columns based on the present solution, the 3D FEA and the classical solution. The buckling load predictions for the bare column by the present solution are in nearly perfect agreement with the classical solution $P_{cr} = \pi^2 EI/4L^2$ and 3D FEA solution. Also, excellent agreement is obtained between the present solution and the 3D FEA solution for the strengthened column. Small differences (i.e., less than 0.7%) between two solutions are observed, showing the validity of the solution and correctness of implementation. A comparison of the critical loads of the bare and strengthened columns shows a minor increase in buckling strength of 6.8% for the 3m span and 6.5% for the 5m span. The strengthening effectiveness for the present column is significantly lower than that attained for beams in Examples 1 and 2.

Table 4.5. Comparison of critical buckling load P_{cr} for columns

Span (m)	Bare steel column					GFRP-strengthened column		
	Buckling load (kN)			Buckling load ratio		Buckling load (kN)		Buckling load ratio
	PS (1)	CS (2)	3D FEA (3)	(1)/(3)	(2)/(3)	PS (4)	3D FEA (5)	(4)/(5)
3	385	386	384	1.003	1.005	411	408	1.007
5	139	139	139	1.000	1.000	148	147	1.007

* PS=Present study, CS=Classical Solution

4.13.4. Example 4 – Simply supported beam-column

The W250x58 4m span steel beam-column in Wu and Mohareb (2011b) is re-visited. In the present paper, in addition to the steel section, one of the flanges is bonded to a 19mm-thick GFRP plate through a 1-mm thick adhesive layer. Two scenarios are considered, where the strengthening is provided to the top flange (Fig. 4.12a) and to the bottom flange (Fig. 4.12b). The member is subjected to a compressive force P and a uniform strong axis bending moment M. Material properties for steel, GFRP, and adhesive are identical to those of Example 1.

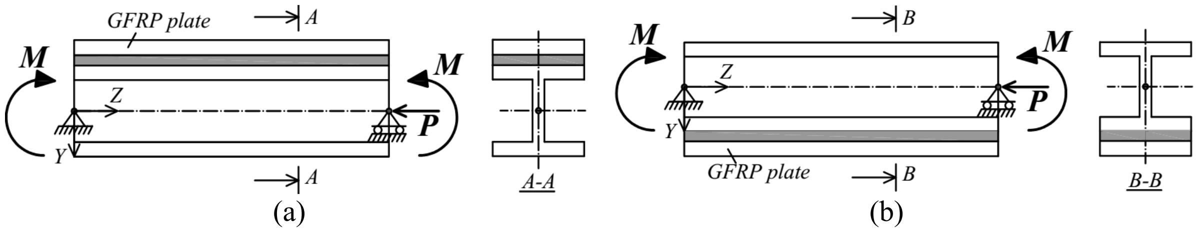

Figure 4.12. Simply supported beam column (a) top flange strengthened (b) bottom flange strengthened

Table 4.6 presents the critical force P_0 in the absence of bending moments M and the critical moment M_0 in the absence of axial force P as predicted by Wu and Mohareb (2011b) (subsequently referenced as WM2011b), 3D FEA and by the present study. The critical loads for the bare beams as predicted by the present solution are nearly identical to those of WM2011b solution. For the strengthened beams, the critical load P_0 as predicted by the present solution nearly coincides with the 3D FEA prediction while the critical moment M_0 predictions differ by about 3%.

Table 4.6. Critical buckling loads P_0 (kN) and M_0 (kNm) for the beam-column in Example 5

Critical buckling load	Bare steel beam			Top Flange Strengthened with GFRP			Bottom Flange Strengthened with GFRP		
	WM2011b (1)	PS (2)	(1)/(2)	3D FEA (3)	PS (4)	(3)/(4)	3D FEA (5)	PS (6)	(5)/(6)
P_0 (kN)	2311	2321	1.00	2440	2475	0.99	2440	2475	0.99
M_0 (kNm)	378	377	1.00	477	486	0.98	448	460	0.97

* PS=Present study, WM2011b=Wu and Mohareb (2011b)

The critical load combinations $\lambda(P,M)$ were sought for different eccentricities M/P to generate the interaction diagrams. The results for the bare and strengthened beams were then normalized by dividing the obtained compressive force λP and moments λM respectively by P_0 and M_0 of the bare beam (Fig. 4.13). For the bare beam, the normalized interaction diagram obtained from the WM2011b solution essentially coincides with that based on the present study. For the strengthened beams (with top or bottom flange strengthening), the interaction diagrams based on the present study are found nearly identical to those based on 3D FEA solution. As expected, strengthening of the compressive flange is observed to be more effective in increasing the lateral torsional buckling strength than does the strengthening of the tension flange. For instance, at a compressive force ratio of 0.557, the critical moment ratio predicted by the present study is 0.557 while that predicted for the case of compression flange strengthening is 0.801, a 43.8% increase. This compares to a ratio of 0.719 when the tension flange is strengthened, a 29.1% increase.

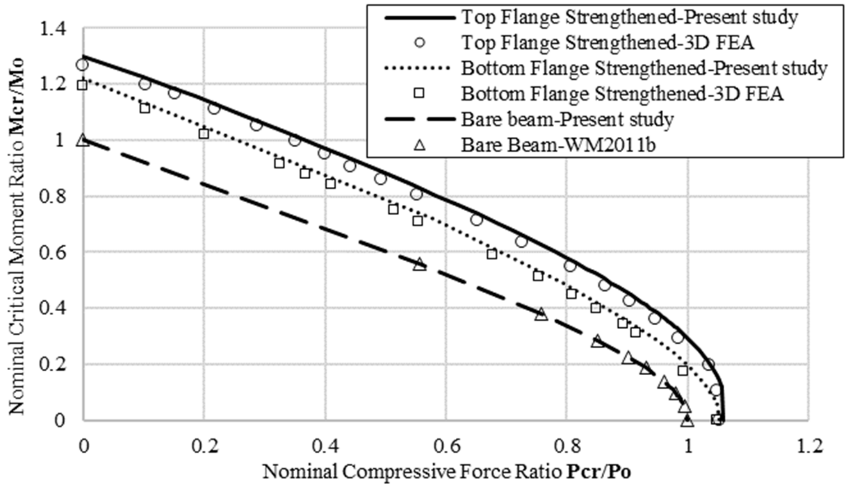

Figure 4.13. Normalized interaction diagram of a beam-column

4.14. Summary and Conclusions

The present study has successfully developed a shear deformable beam theory for the buckling analysis of GFRP-strengthened beam-columns. The principle of total stationary buckling energy was adopted to formulate a two-node finite element based on Hermitian shape functions and a three-node element based on Lagrangian shape functions. The three-node element is more favorable regarding shear-locking effects and possesses fewer degrees of freedom than the two-node elements. It is found to converge faster to the solution while involving less computational effort than the two-node element.

The following conclusions can be drawn from the examples investigated.

(1) The present study is able to reliably predict the buckling loads of GFRP-strengthened beam/column subjected to general load/boundary conditions, load height effects, moment gradient predictions and it accurately predicts mode shapes. Also, the buckling strength predictions of the present model for bare beams were shown to be consistent with other established solutions and equations in various standards (Eurocode guide (Gardner and Nethercot 2011, CSA S16-2016, AS4100-1998, and ANSI/AISC-360-2016).

(2) Examples 1 and 2 suggest that GFRP strengthening is most effective in increasing the LTB strength of a beam when applied to strength compression flanges of laterally unsupported flexural members and moderately effective when strengthening their tension flange. For W250x45 beams strengthened with a 19-mm thick GFRP plate in Examples 1-2, the buckling loads were found to increase by 35.5%-43.3% when the compression flange was strengthened and by 28.2%-38.1% when the tension flange was strengthened. In contrast, the effectiveness for a strengthened column, as evidenced in Example 3, is found small (i.e., 6.8%) as the gain in the flexural stiffness about weak axis is negligible.

(3) Example 1 suggests that the effectiveness of strengthening on lateral torsional buckling strength significantly depends on the GFRP plate thickness but is nearly independent of the adhesive thickness. The findings apply only to combinations of thicknesses and material properties of the adhesive investigated in this example and do not necessarily apply to other thicknesses and material properties.

(4) Example 1 suggests that load height factors for bare beams consistently yield conservative buckling strength predictions for strengthened beams. Conversely, adopting load height factors of bare beams to cases of bottom flange loading for the bare beam would consistently overestimate buckling load predictions. The observations are valid both for compression or tension flange strengthening.

(5) Example 2 suggests the possibility of adopting moment gradient factors for bare beams when designing strengthened beams subjected to linear moment gradients.

(6) The present solution is capable to generate moment-axial force interaction diagrams for beam-columns that account for beam and column stability effects. Example 4 shows that the interaction diagrams are non-linear. The size of the interaction diagrams was found to grow beyond that of the bare beam when the steel beam is strengthened by GFRP at the tension flange and to further grow when GFRP strengthening is applied at the compression flange.

(7) The computational effort involved in the present solution is orders of magnitudes less than that of 3D FEA analysis, particularly for the analysis of GFRP-strengthened beams. The present solutions, implemented in non-compiled MATLAB script files, typically took 40 seconds per run for examples 1-4 on a computer with two Intel(R) Xeon(R) CPU E5-2430 processors at 2.20 GHz and 2.2 GHz speeds, and 64.0 GB memory RAM. In comparison, the 3D FEA under ABAQUS took about 1.2 - 3.9 hours per run on the same computer. The present solution also involves less effort in modelling and post-processing compared to the 3D FEA solutions.

Appendix 4.1: Second variations of total potential energy expressed in Eq. 4.38

The elastic strain energies are defined as

$$\bar{\bar{U}}_{en1}=\int_0^L\int_{A_1}E_1\left[-n_1\sin\alpha\left(s_1\right)\bar{u}''_{1b}-x_1\left(s_1\right)\bar{\theta}'_{y1b}+n_1q\left(s_1\right)\bar{\theta}''_{zb}-\omega\left(s_1\right)\bar{\psi}'_{1b}\right]^2dA_1dz$$

$$\bar{\bar{U}}_{es1}=\int_0^L\int_{A_1}G_1\left[\cos\alpha\left(s_1\right)\bar{u}'_{1b}-\cos\alpha\left(s_1\right)\bar{\theta}_{y1b}+\left\{r\left(s_1\right)+2n_1\right\}\bar{\theta}'_{zb}-r\left(s_1\right)\bar{\psi}_{1b}\right]^2dA_1dz$$

$$\bar{\bar{U}}_{en3}=\int_0^L\int_{A_3}E_3\left[-x_2\left(s_2\right)\bar{\theta}'_{y3b}+n_3x_2\left(s_2\right)\bar{\theta}''_{zb}\right]^2dA_3dz$$

$$\bar{\bar{U}}_{es3}=\int_0^L\int_{A_3}G_3\left(\bar{u}'_{3b}-\bar{\theta}_{y3b}+2n_3\bar{\theta}'_{zb}\right)^2dA_3dz$$

$$\bar{\bar{U}}_{ezn2}=\int_0^L\int_{A_2}G_2\left[c_5x\left(s\right)\bar{\theta}_{y1b}-c_5x\left(s\right)\bar{\theta}_{y3b}-\left(1+c_6\right)x\left(s\right)\bar{\theta}'_{zb}+c_5c_7x\left(s\right)\bar{\psi}_{1b}\right]^2dA_2dz$$

$$\bar{\bar{U}}_{esn2}=\int_0^L\int_{A_2}G_2\left[-c_5\bar{u}_{1b}+c_5\bar{u}_{3b}-\left(1+c_6+c_5c_7\right)\bar{\theta}_{zb}\right]^2dA_2dz+$$

$$\bar{\bar{U}}_{esz2}=\int_0^L\int_{A_2}G_2\Big[c_1\left(n_2\right)\bar{u}'_{1b}-c_1\left(n_2\right)\bar{\theta}_{y1b}+c_2\left(n_2\right)\bar{u}'_{3b}-c_2\left(n_2\right)\bar{\theta}_{y3b}+$$
$$+\left[c_3\left(n_2\right)+c_4\left(n_2\right)\right]\bar{\theta}'_{zb}-c_7c_1\left(n_2\right)\bar{\psi}_{1b}\Big]^2dA_2dz$$

Also, the geometric potential energies are defined as

$$\bar{\bar{V}}_{gN_1}=\lambda\int_0^L\int_{A_1}\frac{N_{1p}\left(z\right)}{A_s}\left\{\left(\bar{u}'_{1b}\right)^2+2\left[n_1\cos\alpha\left(s_1\right)-y_1\left(s_1\right)\right]\bar{u}'_{1b}\bar{\theta}'_{zb}+\left[q^2+r^2+2rn_1+n_1^2\right]\left(\bar{\theta}'_{zb}\right)^2\right\}dA_1dz;$$

$$\bar{\bar{V}}_{gM_s}=\lambda\int_0^L\int_{A_1}\left[\frac{n_1\cos\alpha\left(s_1\right)}{I_{ss}}M_{sp}\left(z\right)\right]\left\{\left(\bar{u}'_{1b}\right)^2+2\left[n_1\cos\alpha\left(s_1\right)-y_1\left(s_1\right)\right]\bar{u}'_{1b}\bar{\theta}'_{zb}+\left(q^2+r^2+2rn_1+n_1^2\right)\left(\bar{\theta}'_{zb}\right)^2\right\}dA_1dz+$$
$$+\lambda\int_0^L\int_{A_3}\left[\frac{n_3}{I_{xxg}}M_{sp}\left(z\right)\right]\left\{\left(\bar{u}'_{3b}\right)^2+2n_3\bar{u}'_{3b}\bar{\theta}'_{zb}+\left[n_3^2+x_3^2\left(s_3\right)\right]\left(\bar{\theta}'_{zb}\right)^2\right\}dA_3dz;$$

$$\bar{\bar{V}}_{gM_x}=\lambda\int_0^L\int_{A_1}\left[-\frac{y_1\left(s_1\right)}{I_{xx}}M_{xp}\left(z\right)\right]\left\{\left(\bar{u}'_{1b}\right)^2+2\left[n_1\cos\alpha\left(s_1\right)-y_1\left(s_1\right)\right]\bar{u}'_{1b}\bar{\theta}'_{zb}+\left(q^2+r^2+2rn_1+n_1^2\right)\left(\bar{\theta}'_{zb}\right)^2\right\}dA_1dz;$$

$$\bar{\bar{V}}_{gQ_1}=\lambda\int_0^L\int_{A_1}\frac{Q_{1p}}{A_s}\sin\alpha\left(s_1\right)\Big\{-2\sin\alpha\left(s_1\right)\bar{u}'_{1b}\bar{\theta}_{zb}-2n_1^2\sin\alpha\left(s_1\right)\bar{u}''_{1b}\bar{\theta}'_{zb}+2n_1r\left(s_1\right)\sin\alpha\left(s_1\right)\bar{u}''_{1b}\bar{\psi}_{1b}+$$
$$+2x\left(s_1\right)\cos\alpha\left(s_1\right)\bar{\theta}_{y1b}\bar{\theta}'_{y1b}-2n_1q\left(s_1\right)\cos\alpha\left(s_1\right)\bar{\theta}_{y1b}\bar{\theta}''_{zb}+2\omega\left(s_1\right)\cos\alpha\left(s_1\right)\bar{\theta}_{y1b}\bar{\psi}'_{1b}+2q\left(s_1\right)\bar{\theta}_{zb}\bar{\theta}'_{zb}+$$
$$-2x\left(s_1\right)n_1\bar{\theta}'_{y1b}\bar{\theta}'_{zb}+2x\left(s_1\right)r\left(s_1\right)\bar{\theta}'_{y1b}\bar{\psi}_{1b}+2n_1^2q\left(s_1\right)\bar{\theta}'_{zb}\bar{\theta}''_{zb}-2\omega\left(s_1\right)n_1\bar{\theta}'_{zb}\bar{\psi}'_{1b}-2r\left(s_1\right)n_1q\left(s_1\right)\bar{\theta}''_{zb}\bar{\psi}_{1b}+$$
$$+2\omega\left(s_1\right)r\left(s_1\right)\bar{\psi}'_{1b}\bar{\psi}_{1b}\Big\}dA_1dz;$$

$$\bar{\bar{V}}_{gN_3}=\lambda\int_0^L\int_{A_3}\frac{N_{3p}\left(z\right)}{A_g}\left\{\left(\bar{u}'_{3b}\right)^2+2n_3\bar{u}'_{3b}\bar{\theta}'_{zb}+\left[n_3^2+x_3^2\left(s_3\right)\right]\left(\bar{\theta}'_{zb}\right)^2\right\}dA_3dz;$$

$$\bar{\bar{V}}_{gQ2} = \lambda \int_0^L \int_{A_2} \frac{Q_{2p}(z)}{A_a} \left\{ -2c_5 c_1(n_2) x^2(s) \bar{\theta}'_{y1b} \bar{\theta}_{y1b} - 2c_5 c_2(n_2) x^2(s) \bar{\theta}_{y1b} \bar{\theta}'_{y3b} + 2c_5 c_3(n_2) x^2(s) \bar{\theta}''_{zb} \bar{\theta}_{y1b} + \right.$$

$$-2c_5 c_7 c_1(n_2) x^2(s) \bar{\psi}'_{1b} \bar{\theta}_{y1b} + 2c_5 c_1(n_2) x^2(s) \bar{\theta}'_{y1b} \bar{\theta}_{y3b} + 2c_5 c_2(n_2) x^2(s) \bar{\theta}'_{y3b} \theta'_{y3b} +$$

$$-2c_5 c_3(n_2) x^2(s) \bar{\theta}''_{zb} \bar{\theta}_{y3b} + 2c_5 c_7 c_1(n_2) x^2(s) \bar{\psi}'_{1b} \bar{\theta}_{y3b} + 2c_6 c_1(n_2) x^2(s) \bar{\theta}'_{y1b} \bar{\theta}'_{zb} +$$

$$+2c_6 c_2(n_2) x^2(s) \bar{\theta}'_{y3b} \bar{\theta}'_{zb} - 2c_6 c_3(n_2) x^2(s) \bar{\theta}''_{zb} \bar{\theta}'_{zb} + 2c_6 c_7 c_1(n_2) x^2 \bar{\psi}'_{1b} \bar{\theta}'_{zb} +$$

$$-2c_5 c_7 c_1(n_2) x^2(s) \bar{\theta}'_{y1b} \bar{\psi}_{1b} - 2c_5 c_7 c_2(n_2) x^2(s) \bar{\theta}'_{y3b} \bar{\psi}_{1b} + 2c_5 c_7 c_3(n_2) x^2(s) \bar{\theta}''_{zb} \bar{\psi}_{1b} +$$

$$-2c_5 c_7^2 c_1(n_2) x^2(s) \bar{\psi}'_{1b} \bar{\psi}_{1b} - 2c_5 c_1(n_2) \bar{u}_{1b} \bar{u}'_{1b} - 2c_5 c_2(n_2) \bar{u}_{1b} \bar{u}'_{3b} - 2c_5 c_4(n_2) \bar{u}_{1b} \bar{\theta}'_{zb} +$$

$$+2c_5 c_1(n_2) \bar{u}'_{1b} \bar{u}_{3b} + 2c_5 c_2(n_2) \bar{u}_{3b} \bar{u}'_{3b} + 2c_5 c_4(n_2) \bar{u}_{3b} \bar{\theta}'_{zb} - 2(c_6 + c_5 c_7) c_1(n_2) \bar{u}'_{1b} \bar{\theta}_{zb} +$$

$$\left. -2(c_6 + c_5 c_7) c_2(n_2) \bar{u}'_{3b} \bar{\theta}_{zb} - 2(c_6 + c_5 c_7) c_4(n_2) \bar{\theta}_{zb} \bar{\theta}'_{zb} \right\} dA_2 dz;$$

$$\bar{\bar{V}}_{gqy} = -\frac{1}{2} \lambda \int_0^L q_y(z) y_{q_y}(z) \left(\bar{\theta}_{zb}\right)^2 dz; \qquad \bar{\bar{V}}_{gqz} = -\frac{1}{2} \lambda \int_0^L q_z(z) y_{q_z}(z) \bar{\theta}_{zb} \bar{\theta}_{y1b} dz;$$

$$\bar{\bar{V}}_{gP_{yi}} = -\frac{1}{2} \lambda \sum_{z_i = 0, L} P_{yi} y_{Pyi}(z) \left[\bar{\theta}_{zb}(z_i)\right]^2; \qquad \bar{\bar{V}}_{gP_{zi}} = -\frac{1}{2} \lambda \sum_{z_i = 0, L} P_{zi} y_{Pzi}(z) \bar{\theta}_{zb}(z_i) \bar{\theta}_{y1b}(z_i);$$

Appendix 4.2: Elastic and geometric stiffness matrices of the two-node element

The elastic and geometric stiffness matrices are defined as

$$[\mathbf{K_e}]_{16\times16} = [\mathbf{K_{en1}} + \mathbf{K_{es1}} + \mathbf{K_{en3}} + \mathbf{K_{es3}} + \mathbf{K_{ezn2}} + \mathbf{K_{esn2}} + \mathbf{K_{esz2}}]_{16\times16}$$

$$[\mathbf{K_g}]_{16\times16} = [\mathbf{K}_{\mathbf{gN_1}} + \mathbf{K}_{\mathbf{gM}_x} + \mathbf{K}_{\mathbf{gM}_s} + \mathbf{K}_{\mathbf{gQ_1}} + \mathbf{K}_{\mathbf{gN}_3} + \mathbf{K}_{\mathbf{gQ_2}} - \mathbf{K}_{gqy} - \mathbf{K}_{gqz} - \mathbf{K}_{gP_{yi}} - \mathbf{K}_{gP_{zi}}]_{16\times16}$$

in which elastic matrices are

$$[\mathbf{K_{en1}}]_{16\times16} = E_1 \int_0^L \left[\{\mathbf{S''_{u1}}\}^{\mathbf{T}}_{16\times1} \quad \{\mathbf{S}'_{\theta\mathbf{1}}\}^{\mathbf{T}}_{16\times1} \quad \{\mathbf{S}''_{\theta z}\}^{\mathbf{T}}_{16\times1} \quad \{\mathbf{S}'_{\psi\mathbf{1}}\}^{\mathbf{T}}_{16\times1} \right] \begin{bmatrix} I_{yyw} & 0 & 0 & 0 \\ 0 & 2I_{yyf} & 0 & 0 \\ 0 & 0 & I_{\omega\omega l} & 0 \\ 0 & 0 & 0 & I_{\omega\omega gs} \end{bmatrix} \begin{bmatrix} \langle \mathbf{S''_{u1}} \rangle_{1\times16} \\ \langle \mathbf{S}'_{\theta\mathbf{1}} \rangle_{1\times16} \\ \langle \mathbf{S}''_{\theta z} \rangle_{1\times16} \\ \langle \mathbf{S}'_{\psi\mathbf{1}} \rangle_{1\times16} \end{bmatrix} dz$$

$$[\mathbf{K_{es1}}]_{16\times16}$$

$$= G_1 \int_0^L \left[\{\mathbf{S'_{u1}}\}^{\mathbf{T}}_{16\times1} \quad \{\mathbf{S}_{\theta\mathbf{1}}\}^{\mathbf{T}}_{16\times1} \quad \{\mathbf{S}'_{\theta z}\}^{\mathbf{T}}_{16\times1} \quad \{\mathbf{S}_{\psi\mathbf{1}}\}^{\mathbf{T}}_{16\times1} \right] \begin{bmatrix} 2A_f & -2A_f & 0 & 0 \\ -2A_f & 2A_f & 0 & 0 \\ 0 & 0 & J_1 & -h_b^2 A_f/2 \\ 0 & 0 & -h_b^2 A_f/2 & h_b^2 A_f/2 \end{bmatrix} \begin{bmatrix} \langle \mathbf{S'_{u1}} \rangle_{1\times16} \\ \langle \mathbf{S}_{\theta\mathbf{1}} \rangle_{1\times16} \\ \langle \mathbf{S}'_{\theta z} \rangle_{1\times16} \\ \langle \mathbf{S}_{\psi\mathbf{1}} \rangle_{1\times16} \end{bmatrix} dz$$

$$[\mathbf{K_{en3}}]_{16\times16} = E_3 \int_0^L \left[\{\mathbf{S}'_{\theta 3}\}^{\mathbf{T}}_{16\times1} \quad \{\mathbf{S}''_{\theta z}\}^{\mathbf{T}}_{16\times1} \right] \begin{bmatrix} I_{yyg} & 0 \\ 0 & I_{\omega\omega g} \end{bmatrix} \begin{bmatrix} \langle \mathbf{S}'_{\theta 3} \rangle_{1\times16} \\ \langle \mathbf{S}''_{\theta z} \rangle_{1\times16} \end{bmatrix} dz$$

$$\left[\mathbf{K_{es3}}\right]_{16\times16}=G_3\int_0^L\left\langle\left\{\mathbf{S}'_{\mathbf{u}3}\right\}^{\mathbf{T}}_{16\times1}\quad\left\{\mathbf{S}_{\theta3}\right\}^{\mathbf{T}}_{16\times1}\quad\left\{\mathbf{S}'_{\theta z}\right\}^{\mathbf{T}}_{16\times1}\right\rangle\begin{bmatrix}A_3 & -A_3 & 0\\ -A_3 & A_3 & 0\\ 0 & 0 & J_3\end{bmatrix}\begin{bmatrix}\left\langle\mathbf{S}'_{\mathbf{u}3}\right\rangle_{1\times16}\\ \left\langle\mathbf{S}_{\theta3}\right\rangle_{1\times16}\\ \left\langle\mathbf{S}'_{\theta z}\right\rangle_{1\times16}\end{bmatrix}dz$$

$$\left[\mathbf{K_{ezn2}}\right]_{16\times16}=G_2I_{yya}\int_0^L\left[\left\{\mathbf{S}_{\theta\mathbf{1}}\right\}_{16\times1}\quad\left\{\mathbf{S}_{\theta3}\right\}_{16\times1}\quad\left\{\mathbf{S}'_{\theta z}\right\}_{16\times1}\quad\left\{\mathbf{S}_{\psi\mathbf{1}}\right\}_{16\times1}\right]\times$$

$$\times\begin{bmatrix}c_5^2 & -c_5^2 & -c_5\left(1+c_6\right) & c_5^2c_7\\ -c_5^2 & c_5^2 & c_5\left(1+c_6\right) & -c_5^2c_7\\ -c_5\left(1+c_6\right) & c_5\left(1+c_6\right) & \left(1+c_6\right)^2 & -c_5c_7\left(1+c_6\right)\\ c_5^2c_7 & -c_5^2c_7 & -c_5c_7\left(1+c_6\right) & c_5^2c_7^2\end{bmatrix}\begin{bmatrix}\left\langle\mathbf{S}_{\theta\mathbf{1}}\right\rangle_{1\times16}\\ \left\langle\mathbf{S}_{\theta3}\right\rangle_{1\times16}\\ \left\langle\mathbf{S}'_{\theta z}\right\rangle_{1\times16}\\ \left\langle\mathbf{S}_{\psi\mathbf{1}}\right\rangle_{1\times16}\end{bmatrix}dz$$

$$\left[\mathbf{K_{esn2}}\right]_{16\times16}=G_2A_a\int_0^L\left[\left\{\mathbf{S_{u1}}\right\}^{\mathbf{T}}_{16\times1}\quad\left\{\mathbf{S_{u3}}\right\}^{\mathbf{T}}_{16\times1}\quad\left\{\mathbf{S}_{\theta z}\right\}^{\mathbf{T}}_{16\times1}\right]\times$$

$$\times\begin{bmatrix}c_5^2 & -c_5^2 & c_5\left(1+c_6+c_5c_7\right)\\ -c_5^2 & c_5^2 & -c_5\left(1+c_6+c_5c_7\right)\\ c_5\left(1+c_6+c_5c_7\right) & -c_5\left(1+c_6+c_5c_7\right) & \left(1+c_6+c_5c_7\right)^2\end{bmatrix}\begin{bmatrix}\left\langle\mathbf{S_{u1}}\right\rangle_{1\times16}\\ \left\langle\mathbf{S_{u3}}\right\rangle_{1\times16}\\ \left\langle\mathbf{S}_{\theta z}\right\rangle_{1\times16}\end{bmatrix}dz$$

$$\left[\mathbf{K_{esz2}}\right]_{16\times16}=\frac{G_2A_a}{12}\int_0^L\left[\left\{\mathbf{S}'_{\mathbf{u1}}\right\}^{\mathbf{T}}_{16\times1}\quad\left\{\mathbf{S}_{\theta\mathbf{1}}\right\}^{\mathbf{T}}_{16\times1}\quad\left\{\mathbf{S}'_{\mathbf{u}3}\right\}^{\mathbf{T}}_{16\times1}\quad\left\{\mathbf{S}_{\theta3}\right\}^{\mathbf{T}}_{16\times1}\quad\left\{\mathbf{S}'_{\theta z}\right\}^{\mathbf{T}}_{16\times1}\quad\left\{\mathbf{S}_{\psi\mathbf{1}}\right\}^{\mathbf{T}}_{16\times1}\right]\times$$

$$\times\begin{bmatrix}4 & -4 & 2 & -2 & 2c_8 & -4c_7\\ -4 & 4 & -2 & 2 & -2c_8 & 4c_7\\ 2 & -2 & 4 & -4 & c_9 & -2c_7\\ -2 & 2 & -4 & 4 & -c_9 & 2c_7\\ 2c_8 & -2c_8 & c_9 & -c_9 & c_{10} & -2c_7c_8\\ -4c_7 & 4c_7 & -2c_7 & 2c_7 & -2c_7c_8 & 4c_7^2\end{bmatrix}\begin{bmatrix}\left\langle\mathbf{S}'_{\mathbf{u1}}\right\rangle_{1\times16}\\ \left\langle\mathbf{S}_{\theta\mathbf{1}}\right\rangle_{1\times16}\\ \left\langle\mathbf{S}'_{\mathbf{u}3}\right\rangle_{1\times16}\\ \left\langle\mathbf{S}_{\theta3}\right\rangle_{1\times16}\\ \left\langle\mathbf{S}'_{\theta z}\right\rangle_{1\times16}\\ \left\langle\mathbf{S}_{\psi\mathbf{1}}\right\rangle_{1\times16}\end{bmatrix}dz$$

and geometric matrices are

$$\left[\mathbf{K_{gN_1}}\right]_{16\times16}=\int_0^L\left\langle\mathbf{L}\left(\mathbf{z}\right)\right\rangle^{\mathbf{T}}_{1\times2}\left\{\mathbf{N_{1p}}\right\}_{2\times1}\left[\left\{\mathbf{S}'_{\mathbf{u1}}\right\}^{\mathbf{T}}_{16\times1}\left\langle\mathbf{S}'_{\mathbf{u1}}\right\rangle_{1\times16}+\frac{\left(I_{xxs}+I_{yys}\right)}{A_s}\left\{\mathbf{S}'_{\theta z}\right\}^{\mathbf{T}}_{16\times1}\left\langle\mathbf{S}'_{\theta z}\right\rangle_{1\times16}\right]dz$$

$$\left[\mathbf{K}_{\mathbf{gM}_x}\right]_{16\times16}=\int_0^L\left\langle\mathbf{L}\left(\mathbf{z}\right)\right\rangle^{\mathbf{T}}_{1\times2}\left\{\mathbf{M}_{x\mathbf{p}}\right\}_{2\times1}\left[\left\langle\mathbf{S}'_{\mathbf{u1}}\right\rangle^{\mathbf{T}}_{16\times1}\left\langle\mathbf{S}'_{\theta z}\right\rangle_{1\times16}+\left\langle\mathbf{S}'_{\theta z}\right\rangle^{\mathbf{T}}_{16\times1}\left\langle\mathbf{S}'_{\mathbf{u1}}\right\rangle_{1\times16}\right]dz$$

$$\left[\mathbf{K}_{\mathbf{gM}_s}\right]_{16\times16}=\frac{2I_{ssf}}{I_{ss}}\int_0^L\left\langle\mathbf{L}\left(\mathbf{z}\right)\right\rangle^{\mathbf{T}}_{1\times2}\left\{\mathbf{M}_{s\mathbf{p}}\right\}_{2\times1}\left[\left\langle\mathbf{S}'_{\mathbf{u1}}\right\rangle^{\mathbf{T}}_{16\times1}\left\langle\mathbf{S}'_{\theta z}\right\rangle_{1\times16}+\left\langle\mathbf{S}'_{\theta z}\right\rangle^{\mathbf{T}}_{16\times1}\left\langle\mathbf{S}'_{\mathbf{u1}}\right\rangle_{1\times16}\right]dz$$

$$+\frac{I_{ssg}}{I_{xxg}}\int_0^L\left\langle\mathbf{L}\left(\mathbf{z}\right)\right\rangle^{\mathbf{T}}_{1\times2}\left\{\mathbf{M}_{s\mathbf{p}}\right\}_{2\times1}\left[\left\langle\mathbf{S}'_{\mathbf{u}3}\right\rangle^{\mathbf{T}}_{16\times1}\left\langle\mathbf{S}'_{\theta z}\right\rangle_{1\times16}+\left\langle\mathbf{S}'_{\theta z}\right\rangle^{\mathbf{T}}_{16\times1}\left\langle\mathbf{S}'_{\mathbf{u}3}\right\rangle_{1\times16}\right]dz$$

$$\left[\mathbf{K}_{\mathbf{gQ_1}}\right]_{16\times16} = -\int_0^L \left\langle \mathbf{L}(\mathbf{z})\right\rangle_{1\times2}^{\mathbf{T}} \left\{\mathbf{Q_{1p}}\right\}_{2\times1} \left[\left\{\mathbf{S}'_{\mathbf{u1}}\right\}_{16\times1}^{\mathbf{T}} \left\langle \mathbf{S}_{\theta z}\right\rangle_{1\times16} + \frac{I_{yyw}}{A_w} \left\{\mathbf{S}''_{\mathbf{u1}}\right\}_{16\times1}^{\mathbf{T}} \left\langle \mathbf{S}'_{\theta z}\right\rangle_{1\times16} \right] dz$$

$$-\int_0^L \left\langle \mathbf{L}(\mathbf{z})\right\rangle_{1\times2}^{\mathbf{T}} \left\{\mathbf{Q_{1p}}\right\}_{2\times1} \left[\left\{\mathbf{S}_{\theta z}\right\}_{16\times1}^{\mathbf{T}} \left\langle \mathbf{S}'_{\mathbf{u1}}\right\rangle_{1\times16} + \frac{I_{yyw}}{A_w} \left\{\mathbf{S}'_{\theta z}\right\}_{16\times1}^{\mathbf{T}} \left\langle \mathbf{S}''_{\mathbf{u1}}\right\rangle_{1\times16} \right] dz$$

$$\left[\mathbf{K}_{\mathbf{gN_3}}\right]_{16\times16} = \int_0^L \left\langle \mathbf{L}(\mathbf{z})\right\rangle_{1\times2}^{\mathbf{T}} \left\{\mathbf{N_{3p}}\right\}_{2\times1} \left[\left\{\mathbf{S}'_{\mathbf{u3}}\right\}_{16\times1}^{\mathbf{T}} \left\langle \mathbf{S}'_{\mathbf{u3}}\right\rangle_{1\times16} + \frac{I_{xxg}+I_{yyg}}{A_g} \left\{\mathbf{S}'_{\theta z}\right\}_{16\times1}^{\mathbf{T}} \left\langle \mathbf{S}'_{\theta z}\right\rangle_{1\times16} \right] dz$$

$$\left[\mathbf{K}_{\mathbf{gQ_2}}\right]_{16\times16} = \frac{\lambda}{2}\int_0^L \left\langle \mathbf{L}(\mathbf{z})\right\rangle_{1\times2}^{\mathbf{T}} \left\{\mathbf{Q_{2p}}\right\}_{2\times1} \left\{ \left[\left\{\mathbf{S_{u1}}\right\}_{16\times1}^{\mathbf{T}} \middle| \left\{\mathbf{S}_{\theta\mathbf{1}}\right\}_{16\times1}^{\mathbf{T}} \middle| \left\{\mathbf{S_{u3}}\right\}_{16\times1}^{\mathbf{T}} \middle| \left\{\mathbf{S}_{\theta 3}\right\}_{16\times1}^{\mathbf{T}} \middle| \left\{\mathbf{S}_{\theta z}\right\}_{16\times1}^{\mathbf{T}} \middle| \left\{\mathbf{S}'_{\theta z}\right\}_{16\times1}^{\mathbf{T}} \middle| \left\{\mathbf{S}_{\psi\mathbf{1}}\right\}_{16\times1}^{\mathbf{T}} \right] \times \right.$$

$$\times \begin{bmatrix} -c_5 & 0 & -c_5 & 0 & -c_5c_{12} & 0 & 0 \\ 0 & -c_5\alpha_a & 0 & -c_5\alpha_a & 0 & c_5c_{11}\alpha_a & -c_5c_7\alpha_a \\ c_5 & 0 & c_5 & 0 & c_5c_{12} & 0 & 0 \\ 0 & c_5\alpha_a & 0 & c_5\alpha_a & 0 & -c_5c_{11}\alpha_a & c_5c_7\alpha_a \\ -(c_6+c_5c_7) & 0 & -(c_6+c_5c_7) & 0 & -(c_6+c_5c_7)c_{12} & 0 & 0 \\ 0 & c_6\alpha_a & 0 & c_6\alpha_a & 0 & -c_6c_{11}\alpha_a & c_6c_7\alpha_a \\ 0 & -c_5c_7\alpha_a & 0 & -c_5c_7\alpha_a & 0 & c_5c_7c_{11}\alpha_a & -c_5c_7^2\alpha_a \end{bmatrix} \begin{bmatrix} \left\langle \mathbf{S}'_{\mathbf{u1}}\right\rangle_{1\times16} \\ \left\langle \mathbf{S}'_{\theta\mathbf{1}}\right\rangle_{1\times16} \\ \left\langle \mathbf{S}'_{\mathbf{u3}}\right\rangle_{1\times16} \\ \left\langle \mathbf{S}'_{\theta 3}\right\rangle_{1\times16} \\ \left\langle \mathbf{S}'_{\theta z}\right\rangle_{1\times16} \\ \left\langle \mathbf{S}''_{\theta z}\right\rangle_{1\times16} \\ \left\langle \mathbf{S}'_{\psi\mathbf{1}}\right\rangle_{1\times16} \end{bmatrix} +$$

$$+\left\langle \mathbf{L}(\mathbf{z})\right\rangle_{1\times2}^{\mathbf{T}} \left\{\mathbf{Q_{2p}}\right\}_{2\times1} \left\{ \left[\left\{\mathbf{S}'_{\mathbf{u1}}\right\}_{16\times1}^{\mathbf{T}} \middle| \left\{\mathbf{S}'_{\theta\mathbf{1}}\right\}_{16\times1}^{\mathbf{T}} \middle| \left\{\mathbf{S}'_{\mathbf{u3}}\right\}_{16\times1}^{\mathbf{T}} \middle| \left\{\mathbf{S}'_{\theta 3}\right\}_{16\times1}^{\mathbf{T}} \middle| \left\{\mathbf{S}'_{\theta z}\right\}_{16\times1}^{\mathbf{T}} \middle| \left\{\mathbf{S}''_{\theta z}\right\}_{16\times1}^{\mathbf{T}} \middle| \left\{\mathbf{S}'_{\psi\mathbf{1}}\right\}_{16\times1}^{\mathbf{T}} \right] \times \right.$$

$$\times \begin{bmatrix} -c_5 & 0 & c_5 & 0 & -(c_6+c_5c_7) & 0 & 0 \\ 0 & -c_5\alpha_a & 0 & c_5\alpha_a & 0 & c_6\alpha_a & -c_5c_7\alpha_a \\ -c_5 & 0 & c_5 & 0 & -(c_6+c_5c_7) & 0 & 0 \\ 0 & -c_5\alpha_a & 0 & c_5\alpha_a & 0 & c_6\alpha_a & -c_5c_7\alpha_a \\ -c_5c_{12} & 0 & c_5c_{12} & 0 & -(c_6+c_5c_7)c_{12} & 0 & 0 \\ 0 & c_5c_{11}\alpha_a & 0 & -c_5c_{11}\alpha_a & 0 & -c_6c_{11}\alpha_a & c_5c_7c_{11}\alpha_a \\ 0 & -c_5c_7\alpha_a & 0 & c_5c_7\alpha_a & 0 & c_6c_7\alpha_a & -c_5c_7^2\alpha_a \end{bmatrix} \begin{bmatrix} \left\langle \mathbf{S_{u1}}\right\rangle_{1\times16} \\ \left\langle \mathbf{S}_{\theta\mathbf{1}}\right\rangle_{1\times16} \\ \left\langle \mathbf{S_{u3}}\right\rangle_{1\times16} \\ \left\langle \mathbf{S}_{\theta 3}\right\rangle_{1\times16} \\ \left\langle \mathbf{S}_{\theta z}\right\rangle_{1\times16} \\ \left\langle \mathbf{S}'_{\theta z}\right\rangle_{1\times16} \\ \left\langle \mathbf{S}_{\psi\mathbf{1}}\right\rangle_{1\times16} \end{bmatrix} dz$$

$$\left[\mathbf{K}_{gqy}\right]_{16\times16} = \frac{1}{2}\int_0^L q_y(z)\, y_{q_y}(z) \left\{\mathbf{S}_{\theta z}\right\}_{16\times1}^{\mathbf{T}} \left\langle \mathbf{S}_{\theta z}\right\rangle_{1\times16} dz; \left[\mathbf{K}_{gP_{yi}}\right]_{16\times16} = \frac{1}{2}\sum_{z_i=0,L} P_{yi}\, y_i(z_i) \left\{\mathbf{S}_{\theta z}(z_i)\right\}_{16\times1}^{\mathbf{T}} \left\langle \mathbf{S}_{\theta z}(z_i)\right\rangle_{1\times16};$$

$$\left[\mathbf{K}_{gqz}\right]_{16\times16} = \frac{1}{4}\int_0^L q_z(z)\, y_{q_z}(z) \left\{\mathbf{S}_{\theta z}\right\}_{16\times1}^{\mathbf{T}} \left\langle \mathbf{S}_{\theta 1}\right\rangle_{1\times16} dz + \frac{1}{4}\int_0^L q_z(z)\, y_{q_z}(z) \left\{\mathbf{S}_{\theta 1}\right\}_{16\times1}^{\mathbf{T}} \left\langle \mathbf{S}_{\theta z}\right\rangle_{1\times16} dz;$$

and

$$\left[\mathbf{K}_{gP_{zi}}\right]_{16\times16} = \frac{1}{4}\sum_{z_i=0,L} P_{zi}\, y_i(z_i) \left\{\mathbf{S}_{\theta z}(z_i)\right\}_{16\times1}^{\mathbf{T}} \left\langle \mathbf{S}_{\theta 1}(z_i)\right\rangle_{1\times16} + \frac{1}{4}\sum_{z_i=0,L} P_{zi}\, y_i(z_i) \left\{\mathbf{S}_{\theta 1}(z_i)\right\}_{16\times1}^{\mathbf{T}} \left\langle \mathbf{S}_{\theta z}(z_i)\right\rangle_{1\times16};$$

Appendix 4.3: Elastic and geometric stiffness matrices of the three-node element

The elastic and geometric stiffness matrices are given by

$$\left[\hat{\mathbf{K}}_{\mathbf{e}}\right]_{14\times 14}=\left[\hat{\mathbf{K}}_{\mathbf{en1}}+\hat{\mathbf{K}}_{\mathbf{es1}}+\hat{\mathbf{K}}_{\mathbf{en3}}+\hat{\mathbf{K}}_{\mathbf{es3}}+\hat{\mathbf{K}}_{\mathbf{ezn2}}+\hat{\mathbf{K}}_{\mathbf{esn2}}+\hat{\mathbf{K}}_{\mathbf{esz2}}\right]_{14\times 14}$$

$$\left[\hat{\mathbf{K}}_{\mathbf{g}}\right]_{14\times 14}=\left[\hat{\mathbf{K}}_{\mathbf{gN_1}}+\hat{\mathbf{K}}_{\mathbf{gM}_x}+\hat{\mathbf{K}}_{\mathbf{gM}_s}+\hat{\mathbf{K}}_{\mathbf{gQ_1}}+\hat{\mathbf{K}}_{\mathbf{gN}_3}+\hat{\mathbf{K}}_{\mathbf{gQ_2}}-\hat{\mathbf{K}}_{gqy}-\hat{\mathbf{K}}_{gqz}-\hat{\mathbf{K}}_{gP_{yi}}-\hat{\mathbf{K}}_{gP_{zi}}\right]_{14\times 14}$$

in which the elastic stiffness matrices are

$$\left[\hat{\mathbf{K}}_{\mathbf{en1}}\right]_{14\times 14}=E_1\int_0^L\left[\left\{\hat{\mathbf{S}}''_{\mathbf{u1}}\right\}^{\mathbf{T}}_{14\times 1}\quad\left\{\hat{\mathbf{S}}'_{\theta\mathbf{1}}\right\}^{\mathbf{T}}_{14\times 1}\quad\left\{\hat{\mathbf{S}}''_{\theta z}\right\}^{\mathbf{T}}_{14\times 1}\quad\left\{\hat{\mathbf{S}}'_{\psi\mathbf{1}}\right\}^{\mathbf{T}}_{14\times 1}\right]\begin{bmatrix} I_{yyw} & 0 & 0 & 0\\ 0 & 2I_{yyf} & 0 & 0\\ 0 & 0 & I_{\omega\omega l} & 0\\ 0 & 0 & 0 & I_{\omega\omega gs}\end{bmatrix}\begin{bmatrix}\left\langle\hat{\mathbf{S}}''_{\mathbf{u1}}\right\rangle_{1\times 14}\\ \left\langle\hat{\mathbf{S}}'_{\theta\mathbf{1}}\right\rangle_{1\times 14}\\ \left\langle\hat{\mathbf{S}}''_{\theta z}\right\rangle_{1\times 14}\\ \left\langle\hat{\mathbf{S}}'_{\psi\mathbf{1}}\right\rangle_{1\times 14}\end{bmatrix}dz$$

$$\left[\hat{\mathbf{K}}_{\mathbf{es1}}\right]_{14\times 14}=$$

$$G_1\int_0^L\left[\left\{\hat{\mathbf{S}}'_{\mathbf{u1}}\right\}^{\mathbf{T}}_{14\times 1}\quad\left\{\hat{\mathbf{S}}_{\theta\mathbf{1}}\right\}^{\mathbf{T}}_{14\times 1}\quad\left\{\hat{\mathbf{S}}'_{\theta z}\right\}^{\mathbf{T}}_{14\times 1}\quad\left\{\hat{\mathbf{S}}_{\psi\mathbf{1}}\right\}^{\mathbf{T}}_{14\times 1}\right]\begin{bmatrix} 2A_f & -2A_f & 0 & 0\\ -2A_f & 2A_f & 0 & 0\\ 0 & 0 & J_1 & -h_b^2A_f/2\\ 0 & 0 & -h_b^2A_f/2 & h_b^2A_f/2\end{bmatrix}\begin{bmatrix}\left\langle\hat{\mathbf{S}}'_{\mathbf{u1}}\right\rangle_{1\times 14}\\ \left\langle\hat{\mathbf{S}}_{\theta\mathbf{1}}\right\rangle_{1\times 14}\\ \left\langle\hat{\mathbf{S}}'_{\theta z}\right\rangle_{1\times 14}\\ \left\langle\hat{\mathbf{S}}_{\psi\mathbf{1}}\right\rangle_{1\times 14}\end{bmatrix}dz$$

$$\left[\hat{\mathbf{K}}_{\mathbf{en3}}\right]_{14\times 14}=E_3\int_0^L\left[\left\{\hat{\mathbf{S}}'_{\theta 3}\right\}^{\mathbf{T}}_{14\times 1}\quad\left\{\hat{\mathbf{S}}''_{\theta z}\right\}^{\mathbf{T}}_{14\times 1}\right]\begin{bmatrix} I_{yyg} & 0\\ 0 & I_{\omega\omega g}\end{bmatrix}\begin{bmatrix}\left\langle\hat{\mathbf{S}}'_{\theta 3}\right\rangle_{1\times 14}\\ \left\langle\hat{\mathbf{S}}''_{\theta z}\right\rangle_{1\times 14}\end{bmatrix}dz$$

$$\left[\hat{\mathbf{K}}_{\mathbf{es3}}\right]_{14\times 14}=G_3\int_0^L\left\langle\left\{\hat{\mathbf{S}}'_{\mathbf{u}3}\right\}^{\mathbf{T}}_{14\times 1}\quad\left\{\hat{\mathbf{S}}_{\theta 3}\right\}^{\mathbf{T}}_{14\times 1}\quad\left\{\hat{\mathbf{S}}'_{\theta z}\right\}^{\mathbf{T}}_{14\times 1}\right\rangle\begin{bmatrix} A_3 & -A_3 & 0\\ -A_3 & A_3 & 0\\ 0 & 0 & J_3\end{bmatrix}\begin{bmatrix}\left\langle\hat{\mathbf{S}}'_{\mathbf{u}3}\right\rangle_{1\times 14}\\ \left\langle\hat{\mathbf{S}}_{\theta 3}\right\rangle_{1\times 14}\\ \left\langle\hat{\mathbf{S}}'_{\theta z}\right\rangle_{1\times 14}\end{bmatrix}dz$$

$$\left[\hat{\mathbf{K}}_{\mathbf{ezn2}}\right]_{14\times 14}=G_2I_{yya}\int_0^L\left[\left\{\hat{\mathbf{S}}_{\theta\mathbf{1}}\right\}_{14\times 1}\quad\left\{\hat{\mathbf{S}}_{\theta 3}\right\}_{14\times 1}\quad\left\{\hat{\mathbf{S}}'_{\theta z}\right\}_{14\times 1}\quad\left\{\hat{\mathbf{S}}_{\psi\mathbf{1}}\right\}_{14\times 1}\right]$$

$$\times\begin{bmatrix} c_5^2 & -c_5^2 & -c_5\left(1+c_6\right) & c_5^2c_7\\ -c_5^2 & c_5^2 & c_5\left(1+c_6\right) & -c_5^2c_7\\ -c_5\left(1+c_6\right) & c_5\left(1+c_6\right) & \left(1+c_6\right)^2 & -c_5c_7\left(1+c_6\right)\\ c_5^2c_7 & -c_5^2c_7 & -c_5c_7\left(1+c_6\right) & c_5^2c_7^2\end{bmatrix}\begin{bmatrix}\left\langle\hat{\mathbf{S}}_{\theta\mathbf{1}}\right\rangle_{1\times 14}\\ \left\langle\hat{\mathbf{S}}_{\theta 3}\right\rangle_{1\times 14}\\ \left\langle\hat{\mathbf{S}}'_{\theta z}\right\rangle_{1\times 14}\\ \left\langle\hat{\mathbf{S}}_{\psi\mathbf{1}}\right\rangle_{1\times 14}\end{bmatrix}dz$$

$$\left[\hat{\mathbf{K}}_{\mathbf{esn2}}\right]_{14\times 14} = G_2 A_a \int_0^L \left[\left\{\hat{\mathbf{S}}_{\mathbf{u1}}\right\}_{14\times 1}^{\mathbf{T}} \quad \left\{\hat{\mathbf{S}}_{\mathbf{u}3}\right\}_{14\times 1}^{\mathbf{T}} \quad \left\{\hat{\mathbf{S}}_{\theta z}\right\}_{14\times 1}^{\mathbf{T}} \right]$$

$$\times \begin{bmatrix} c_5^2 & -c_5^2 & c_5\left(1+c_6+c_5c_7\right) \\ -c_5^2 & c_5^2 & -c_5\left(1+c_6+c_5c_7\right) \\ c_5\left(1+c_6+c_5c_7\right) & -c_5\left(1+c_6+c_5c_7\right) & \left(1+c_6+c_5c_7\right)^2 \end{bmatrix} \begin{bmatrix} \left\langle\hat{\mathbf{S}}_{\mathbf{u1}}\right\rangle_{1\times 14} \\ \left\langle\hat{\mathbf{S}}_{\mathbf{u}3}\right\rangle_{1\times 14} \\ \left\langle\hat{\mathbf{S}}_{\theta z}\right\rangle_{1\times 14} \end{bmatrix} dz$$

$$\left[\hat{\mathbf{K}}_{\mathbf{esz2}}\right]_{14\times 14} = \frac{G_2 A_a}{12} \int_0^L \left[\left\{\hat{\mathbf{S}}'_{\mathbf{u1}}\right\}_{14\times 1}^{\mathbf{T}} \quad \left\{\hat{\mathbf{S}}_{\theta\mathbf{1}}\right\}_{14\times 1}^{\mathbf{T}} \quad \left\{\hat{\mathbf{S}}'_{\mathbf{u}3}\right\}_{14\times 1}^{\mathbf{T}} \quad \left\{\hat{\mathbf{S}}_{\theta 3}\right\}_{14\times 1}^{\mathbf{T}} \quad \left\{\hat{\mathbf{S}}'_{\theta z}\right\}_{14\times 1}^{\mathbf{T}} \quad \left\{\hat{\mathbf{S}}_{\psi\mathbf{1}}\right\}_{14\times 1}^{\mathbf{T}} \right]$$

$$\times \begin{bmatrix} 4 & -4 & 2 & -2 & 2c_8 & -4c_7 \\ -4 & 4 & -2 & 2 & -2c_8 & 4c_7 \\ 2 & -2 & 4 & -4 & c_9 & -2c_7 \\ -2 & 2 & -4 & 4 & -c_9 & 2c_7 \\ 2c_8 & -2c_8 & c_9 & -c_9 & c_{10} & -2c_7c_8 \\ -4c_7 & 4c_7 & -2c_7 & 2c_7 & -2c_7c_8 & 4c_7^2 \end{bmatrix} \begin{bmatrix} \left\langle\hat{\mathbf{S}}'_{\mathbf{u1}}\right\rangle_{1\times 14} \\ \left\langle\hat{\mathbf{S}}_{\theta\mathbf{1}}\right\rangle_{1\times 14} \\ \left\langle\hat{\mathbf{S}}'_{\mathbf{u}3}\right\rangle_{1\times 14} \\ \left\langle\hat{\mathbf{S}}_{\theta 3}\right\rangle_{1\times 14} \\ \left\langle\hat{\mathbf{S}}'_{\theta z}\right\rangle_{1\times 14} \\ \left\langle\hat{\mathbf{S}}_{\psi\mathbf{1}}\right\rangle_{1\times 14} \end{bmatrix} dz$$

and the geometric stiffness matrices include

$$\left[\hat{\mathbf{K}}_{\mathbf{gN_1}}\right]_{14\times 14} = \int_0^L \left\langle\mathbf{L}(\mathbf{z})\right\rangle_{1\times 2}^{\mathbf{T}} \left\{\mathbf{N}_{\mathbf{1p}}\right\}_{2\times 1} \left[\left\{\hat{\mathbf{S}}'_{\mathbf{u1}}\right\}_{14\times 1}^{\mathbf{T}} \left\langle\hat{\mathbf{S}}'_{\mathbf{u1}}\right\rangle_{1\times 14} + \frac{\left(I_{xxs}+I_{yys}\right)}{A_s} \left\{\hat{\mathbf{S}}'_{\theta z}\right\}_{14\times 1}^{\mathbf{T}} \left\langle\hat{\mathbf{S}}'_{\theta z}\right\rangle_{1\times 14} \right] dz$$

$$\left[\hat{\mathbf{K}}_{\mathbf{gQ_2}}\right]_{14\times 14}=\frac{\lambda}{2}\int_0^L\left\langle\mathbf{L}(\mathbf{z})\right\rangle_{1\times 2}^{\mathbf{T}}\left\{\mathbf{Q_{2p}}\right\}_{2\times 1}\left\{\left[\left\{\hat{\mathbf{S}}_{\mathbf{u1}}\right\}_{14\times 1}^{\mathbf{T}}\;\middle|\;\left\{\hat{\mathbf{S}}_{\theta\mathbf{1}}\right\}_{14\times 1}^{\mathbf{T}}\;\middle|\;\left\{\hat{\mathbf{S}}_{\mathbf{u}3}\right\}_{14\times 1}^{\mathbf{T}}\;\middle|\;\left\{\hat{\mathbf{S}}_{\theta 3}\right\}_{14\times 1}^{\mathbf{T}}\;\middle|\;\left\{\mathbf{S}_{\theta z}\right\}_{14\times 1}^{\mathbf{T}}\;\middle|\;\left\{\hat{\mathbf{S}}'_{\theta z}\right\}_{14\times 1}^{\mathbf{T}}\;\middle|\;\left\{\hat{\mathbf{S}}_{\psi\mathbf{1}}\right\}_{14\times 1}^{\mathbf{T}}\right]\times\right.$$

$$\times\begin{bmatrix} -c_5 & 0 & -c_5 & 0 & -c_5c_{12} & 0 & 0\\ 0 & -c_5\alpha_a & 0 & -c_5\alpha_a & 0 & c_5c_{11}\alpha_a & -c_5c_7\alpha_a\\ c_5 & 0 & c_5 & 0 & c_5c_{12} & 0 & 0\\ 0 & c_5\alpha_a & 0 & c_5\alpha_a & 0 & -c_5c_{11}\alpha_a & c_5c_7\alpha_a\\ -(c_6+c_5c_7) & 0 & -(c_6+c_5c_7) & 0 & -(c_6+c_5c_7)c_{12} & 0 & 0\\ 0 & c_6\alpha_a & 0 & c_6\alpha_a & 0 & -c_6c_{11}\alpha_a & c_6c_7\alpha_a\\ 0 & -c_5c_7\alpha_a & 0 & -c_5c_7\alpha_a & 0 & c_5c_7c_{11}\alpha_a & -c_5c_7^2\alpha_a \end{bmatrix}\begin{bmatrix}\left\langle\hat{\mathbf{S}}'_{\mathbf{u1}}\right\rangle_{1\times 14}\\ \hline \left\langle\hat{\mathbf{S}}'_{\theta\mathbf{1}}\right\rangle_{1\times 14}\\ \hline \left\langle\hat{\mathbf{S}}'_{\mathbf{u}3}\right\rangle_{1\times 14}\\ \hline \left\langle\hat{\mathbf{S}}'_{\theta 3}\right\rangle_{1\times 14}\\ \hline \left\langle\hat{\mathbf{S}}'_{\theta z}\right\rangle_{1\times 14}\\ \hline \left\langle\hat{\mathbf{S}}''_{\theta z}\right\rangle_{1\times 14}\\ \hline \left\langle\hat{\mathbf{S}}'_{\psi\mathbf{1}}\right\rangle_{1\times 14}\end{bmatrix}+$$

$$+\left\langle\mathbf{L}(\mathbf{z})\right\rangle_{1\times 2}^{\mathbf{T}}\left\{\mathbf{Q_{2p}}\right\}_{2\times 1}\left\{\left[\left\{\hat{\mathbf{S}}'_{\mathbf{u1}}\right\}_{14\times 1}^{\mathbf{T}}\;\middle|\;\left\{\hat{\mathbf{S}}'_{\theta\mathbf{1}}\right\}_{14\times 1}^{\mathbf{T}}\;\middle|\;\left\{\hat{\mathbf{S}}'_{\mathbf{u}3}\right\}_{14\times 1}^{\mathbf{T}}\;\middle|\;\left\{\hat{\mathbf{S}}'_{\theta 3}\right\}_{14\times 1}^{\mathbf{T}}\;\middle|\;\left\{\hat{\mathbf{S}}'_{\theta z}\right\}_{14\times 1}^{\mathbf{T}}\;\middle|\;\left\{\hat{\mathbf{S}}''_{\theta z}\right\}_{14\times 1}^{\mathbf{T}}\;\middle|\;\left\{\mathbf{S}'_{\psi\mathbf{1}}\right\}_{14\times 1}^{\mathbf{T}}\right]\times\right.$$

$$\times\begin{bmatrix} -c_5 & 0 & c_5 & 0 & -(c_6+c_5c_7) & 0 & 0\\ 0 & -c_5\alpha_a & 0 & c_5\alpha_a & 0 & c_6\alpha_a & -c_5c_7\alpha_a\\ -c_5 & 0 & c_5 & 0 & -(c_6+c_5c_7) & 0 & 0\\ 0 & -c_5\alpha_a & 0 & c_5\alpha_a & 0 & c_6\alpha_a & -c_5c_7\alpha_a\\ -c_5c_{12} & 0 & c_5c_{12} & 0 & -(c_6+c_5c_7)c_{12} & 0 & 0\\ 0 & c_5c_{11}\alpha_a & 0 & -c_5c_{11}\alpha_a & 0 & -c_6c_{11}\alpha_a & c_5c_7c_{11}\alpha_a\\ 0 & -c_5c_7\alpha_a & 0 & c_5c_7\alpha_a & 0 & c_6c_7\alpha_a & -c_5c_7^2\alpha_a \end{bmatrix}\begin{bmatrix}\left\langle\hat{\mathbf{S}}_{\mathbf{u1}}\right\rangle_{1\times 14}\\ \hline \left\langle\hat{\mathbf{S}}_{\theta\mathbf{1}}\right\rangle_{1\times 14}\\ \hline \left\langle\hat{\mathbf{S}}_{\mathbf{u}3}\right\rangle_{1\times 14}\\ \hline \left\langle\hat{\mathbf{S}}_{\theta 3}\right\rangle_{1\times 14}\\ \hline \left\langle\hat{\mathbf{S}}_{\theta z}\right\rangle_{1\times 14}\\ \hline \left\langle\hat{\mathbf{S}}'_{\theta z}\right\rangle_{1\times 14}\\ \hline \left\langle\hat{\mathbf{S}}_{\psi\mathbf{1}}\right\rangle_{1\times 14}\end{bmatrix}dz$$

$$\left[\hat{\mathbf{K}}_{\mathbf{gM}_x}\right]_{14\times 14}=\int_0^L\left\langle\mathbf{L}(\mathbf{z})\right\rangle_{1\times 2}^{\mathbf{T}}\left\{\mathbf{M}_{x\mathbf{p}}\right\}_{2\times 1}\left[\left\langle\hat{\mathbf{S}}'_{\mathbf{u1}}\right\rangle_{14\times 1}^{\mathbf{T}}\left\langle\hat{\mathbf{S}}'_{\theta z}\right\rangle_{1\times 14}+\left\langle\hat{\mathbf{S}}'_{\theta z}\right\rangle_{14\times 1}^{\mathbf{T}}\left\langle\hat{\mathbf{S}}'_{\mathbf{u1}}\right\rangle_{1\times 14}\right]dz$$

$$\left[\hat{\mathbf{K}}_{\mathbf{gM}_s}\right]_{14\times 14}=\frac{2I_{ssf}}{I_{ss}}\int_0^L\left\langle\mathbf{L}(\mathbf{z})\right\rangle_{1\times 2}^{\mathbf{T}}\left\{\mathbf{M}_{s\mathbf{p}}\right\}_{2\times 1}\left[\left\langle\hat{\mathbf{S}}'_{\mathbf{u1}}\right\rangle_{14\times 1}^{\mathbf{T}}\left\langle\hat{\mathbf{S}}'_{\theta z}\right\rangle_{1\times 14}+\left\langle\hat{\mathbf{S}}'_{\theta z}\right\rangle_{14\times 1}^{\mathbf{T}}\left\langle\hat{\mathbf{S}}'_{\mathbf{u1}}\right\rangle_{1\times 14}\right]dz$$

$$+\frac{I_{ssg}}{I_{xxg}}\int_0^L\left\langle\mathbf{L}(\mathbf{z})\right\rangle_{1\times 2}^{\mathbf{T}}\left\{\mathbf{M}_{s\mathbf{p}}\right\}_{2\times 1}\left[\left\langle\hat{\mathbf{S}}'_{\mathbf{u}3}\right\rangle_{14\times 1}^{\mathbf{T}}\left\langle\hat{\mathbf{S}}'_{\theta z}\right\rangle_{1\times 14}+\left\langle\hat{\mathbf{S}}'_{\theta z}\right\rangle_{14\times 1}^{\mathbf{T}}\left\langle\hat{\mathbf{S}}'_{\mathbf{u}3}\right\rangle_{1\times 14}\right]dz$$

$$\left[\hat{\mathbf{K}}_{\mathbf{gQ_1}}\right]_{14\times 14}=-\int_0^L\left\langle\mathbf{L}(\mathbf{z})\right\rangle_{1\times 2}^{\mathbf{T}}\left\{\mathbf{Q_{1p}}\right\}_{2\times 1}\left[\left\{\hat{\mathbf{S}}'_{\mathbf{u1}}\right\}_{14\times 1}^{\mathbf{T}}\left\langle\hat{\mathbf{S}}_{\theta z}\right\rangle_{1\times 14}+\frac{I_{yyw}}{A_w}\left\{\hat{\mathbf{S}}''_{\mathbf{u1}}\right\}_{14\times 1}^{\mathbf{T}}\left\langle\hat{\mathbf{S}}'_{\theta z}\right\rangle_{1\times 14}\right]dz$$

$$-\int_0^L\left\langle\mathbf{L}(\mathbf{z})\right\rangle_{1\times 2}^{\mathbf{T}}\left\{\mathbf{Q_{1p}}\right\}_{2\times 1}\left[\left\{\hat{\mathbf{S}}_{\theta z}\right\}_{14\times 1}^{\mathbf{T}}\left\langle\hat{\mathbf{S}}'_{\mathbf{u1}}\right\rangle_{1\times 14}+\frac{I_{yyw}}{A_w}\left\{\hat{\mathbf{S}}'_{\theta z}\right\}_{14\times 1}^{\mathbf{T}}\left\langle\hat{\mathbf{S}}''_{\mathbf{u1}}\right\rangle_{1\times 14}\right]dz$$

$$\left[\hat{\mathbf{K}}_{\mathbf{gN_3}}\right]_{14\times 14}=\int_0^L\left\langle\mathbf{L}(\mathbf{z})\right\rangle_{1\times 2}^{\mathbf{T}}\left\{\mathbf{N_{3p}}\right\}_{2\times 1}\left[\left\{\hat{\mathbf{S}}'_{\mathbf{u}3}\right\}_{14\times 1}^{\mathbf{T}}\left\langle\hat{\mathbf{S}}'_{\mathbf{u}3}\right\rangle_{1\times 14}+\frac{I_{xxg}+I_{yyg}}{A_g}\left\{\hat{\mathbf{S}}'_{\theta z}\right\}_{14\times 1}^{\mathbf{T}}\left\langle\hat{\mathbf{S}}'_{\theta z}\right\rangle_{1\times 14}\right]dz$$

$$\left[\hat{\mathbf{K}}_{gqy}\right]_{14\times 14} =$$

$$\frac{1}{2}\int_0^L q_y(z)\, y_{q_y}(z)\left\{\hat{\mathbf{S}}_{\theta z}\right\}_{14\times 1}^{\mathbf{T}}\left\langle\hat{\mathbf{S}}_{\theta z}\right\rangle_{1\times 14} dz; \left[\hat{\mathbf{K}}_{gP_{yi}}\right]_{16\times 16} = \frac{1}{2}\sum_{z_i=0,L} P_{yi}\, y_i(z_i)\left\{\hat{\mathbf{S}}_{\theta z}(z_i)\right\}_{14\times 1}^{\mathbf{T}}\left\langle\hat{\mathbf{S}}_{\theta z}(z_i)\right\rangle_{1\times 14};$$

$$\left[\hat{\mathbf{K}}_{gqz}\right]_{14\times 14} = \frac{1}{4}\int_0^L q_z(z)\, y_{q_z}(z)\left\{\hat{\mathbf{S}}_{\theta z}\right\}_{14\times 1}^{\mathbf{T}}\left\langle\hat{\mathbf{S}}_{\theta 1}\right\rangle_{1\times 14} dz + \frac{1}{4}\int_0^L q_z(z)\, y_{q_z}(z)\left\{\hat{\mathbf{S}}_{\theta 1}\right\}_{14\times 1}^{\mathbf{T}}\left\langle\hat{\mathbf{S}}_{\theta z}\right\rangle_{1\times 14} dz;$$

and

$$\left[\hat{\mathbf{K}}_{gP_{zi}}\right]_{14\times 14} = \frac{1}{4}\sum_{z_i=0,L} P_{zi}\, y_i(z_i)\left\{\hat{\mathbf{S}}_{\theta z}(z_i)\right\}_{14\times 1}^{\mathbf{T}}\left\langle\hat{\mathbf{S}}_{\theta 1}(z_i)\right\rangle_{1\times 14} + \frac{1}{4}\sum_{z_i=0,L} P_{zi}\, y_i(z_i)\left\{\hat{\mathbf{S}}_{\theta 1}(z_i)\right\}_{14\times 1}^{\mathbf{T}}\left\langle\hat{\mathbf{S}}_{\theta z}(z_i)\right\rangle_{1\times 14};$$

Appendix 4.4: Web stiffeners in the 3D FEA solution in Example 1

At buckling, the web was observed to considerably distort near beam ends and at mid-span (e.g., Figs. A4.4.2a and A4.4.3a). To control distortion, three stiffener arrangements were considered involving two, three, and five stiffeners (Figs. A4.4.1). Each stiffener was taken as 8mm thick and were connected to the web, the top and bottom flanges directly. The two-stiffener arrangement (Figs. A4.4.2a, A4.4.3a) depicts more distortion than the three-stiffener arrangement (Figs. A4.4.2b, A4.4.3b) but the five-stiffener arrangement (Figs. A4.4.2c, A4.4.3c) involves marginally less distortion than the three-stiffener arrangement.

A comparison of the buckling loads for spans L=4.0m, 6.0m and 8.0m are shown in Table 1. The addition of more web stiffeners is found to increase the buckling loads, and make the 3D FEA solutions closer to the predictions of the present study. The beam with five-stiffener arrangement is found to yield the closest predictions to those of the present study.

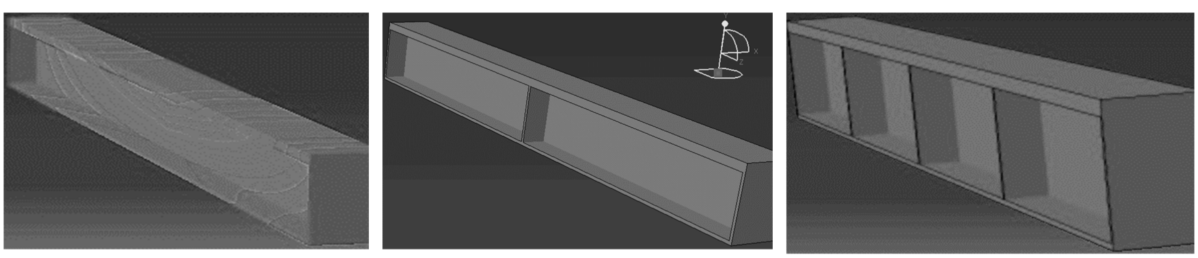

(a) (b) (c)

Figure A4.4.1. Simply supported composite beam with web stiffeners (a) two stiffeners at the beam ends, (b) three stiffeners, and (c) five stiffeners.

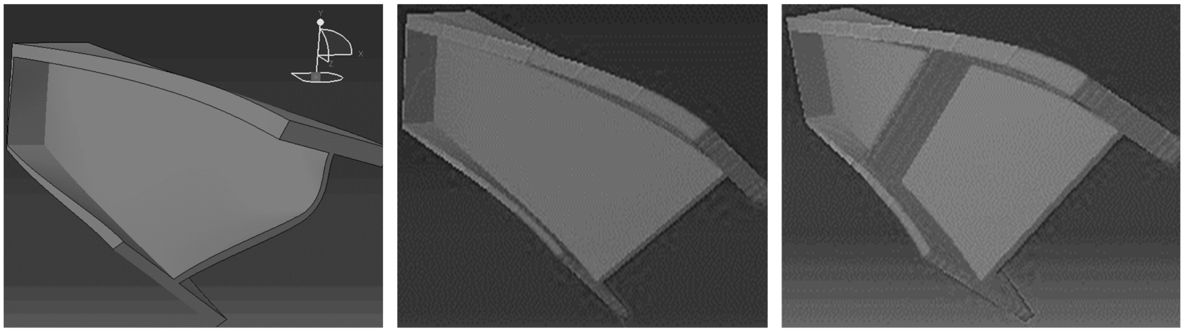

(a) (b) (c)

Figure A4.4.2. Web deformation –only half of the span is shown (a) beam stiffened at the supports, (b) beam stiffened at both ends and mid-span (mid-span stiffeners not shown for clarity) and (3) beam stiffened with five stiffeners (mid-span stiffeners not shown for clarity)

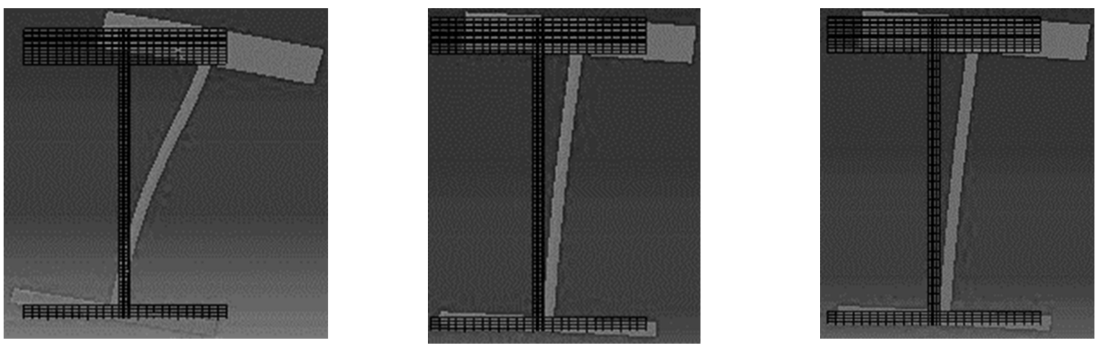

(a) (b) (c)

Figure A4.4.3. Unreformed and deformed cross-section at z=300mm from the end supports in (a) 2-stiffener beam, (b) 3-stiffener beam and (3) 5-stiffener beam

Appendix 4.5: Estimating buckling displacements $\theta_{y1b}, \theta_{y3b}, \theta_{zb}, \psi_{1b}$ from 3D FEA solution in Example 1

The displacements in the 3D FEA solution are obtained in a similar way as conducted in Xiao et al. 2014. At a section $z_0 \left(0 \le z_0 \le L\right)$, the lateral displacements η_1 at Points 5 and 6 (Fig. A4.5.1) at the top and bottom of the web are extracted from the buckled configuration of the 3D FEA model and are denoted as $\left\langle \eta_{1,5}, \eta_{1,6} \right\rangle^T$. Using Eq. (4.5b), and setting $\alpha\left(s_1\right) = 90^o, n_1 = 0$, one can relate the displacements $\left\langle \eta_{1,5}, \eta_{1,6} \right\rangle^T$ to the lateral displacement at the centroid u_{1b} and the angle of twist of θ_{zb} for the line connecting 5 and 6:

$$\begin{Bmatrix} \eta_{1,5} \\ \eta_{1,6} \end{Bmatrix}_{FEA} = \left[\begin{array}{c|c} 1 & h_b/2 \\ \hline 1 & -h_b/2 \end{array}\right] \begin{Bmatrix} u_{1b} \\ \theta_{zb} \end{Bmatrix} \tag{A4.5.1}$$

Equations (A4.5.1) are solved for u_{1b}, θ_{zb} at section z_0 and the procedures is repeated for all sections $(0 \leq z_0 \leq L)$. Similarly, the longitudinal displacements $\zeta_{1,FEA}$ at Points 1- 4 with coordinates $(x, y, \omega) = (\pm b/2, \pm h_b/2, \pm bh_b/4)$ (Fig. A4.5.1) are extracted from the buckled configuration of the 3D FEA model and are denoted as $\langle \zeta_{1,1}, \zeta_{1,2}, \zeta_{1,3}, \zeta_{1,4} \rangle^T$. Using Eq. (4.5c) and setting $n_1 = 0$, one can relate the displacements $\langle \zeta_{1,1}, \zeta_{1,2}, \zeta_{1,3}, \zeta_{1,4} \rangle^T_{FEA}$ to the displacements $\lambda w_{1p}(z_0)$, $\lambda \theta_{xp}(z_0), \theta_{y1b}(z_0), \psi_{1b}(z_0)$ through:

$$\begin{Bmatrix} \zeta_{1,1} \\ \zeta_{1,2} \\ \zeta_{1,3} \\ \zeta_{1,4} \end{Bmatrix}_{FEA} = \begin{bmatrix} 1 & h_b/2 & b/2 & h_b b/4 \\ 1 & h_b/2 & -b/2 & -h_b b/4 \\ 1 & -h_b/2 & b/2 & -h_b b/4 \\ 1 & -h_b/2 & -b/2 & h_b b/4 \end{bmatrix} \begin{Bmatrix} \lambda w_{1p} \\ \lambda \theta_{xp} \\ \theta_{y1b} \\ \psi_{1b} \end{Bmatrix} \tag{A4.5.2}$$

Equations (A4.5.2) are solved for buckling deformations $\theta_{y1b}(z)$ and $\psi_{1b}(z)$. By adopting Eq. (4.6c) for Points 7 and 8 and applying the same procedure as above, rotation angle $\theta_{y3b}(z)$ is obtained for the 3D FEA solution.

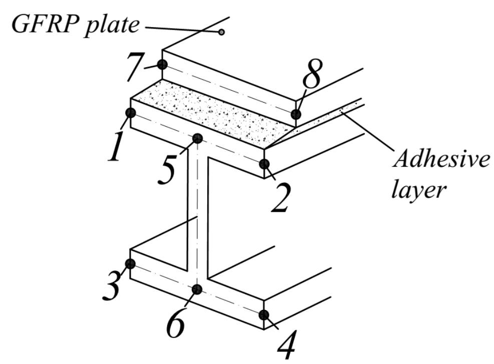

Figure A4.5.1. Points lie on the composite cross-section

References

[4-1] Accord, E., and Earls, C.J., (2006), Use of fiber-reinforced polymer composite elements to enhance structural steel member ductility, Journal of composites for construction ASCE, 10, 337-344.

[4-2] Aguilera, J. and Fam, A., (2013), Bonded FRP plates for strengthening rectangular hollow steel section T-joints against web buckling induced by transverse compression, Journal of composites for constructions ASCE, 17, 421-432.

[4-3] ANSI/AISC 360-16, Specification for structural steel buildings, American Institute of Steel Construction (AISC), Chicago, IL (2016).

[4-4] Aydin E. and Aktas, M. (2015), Obtaining a permanent repair by using GFRP in steel plates reformed by heat-treatment, Thin-Walled Structures, 94, 13-22.

[4-5] Barsoum, R. S., and Gallagher, R. H., (1970), Finite element analysis of torsional and torsional–flexural stability problems, Int. Journal for Numerical Methods in Engineering, 2, 335-352.

[4-6] CSA, Limit states design of steel structures, Standard CAN/CSA-S16-14, Canadian Standards Association, Mississauga, Ontario (2014).

[4-7] Challamel, N. and Girhammar, U.A., (2012), Lateral-torsional buckling of vertically layered composite beams with interlayer slip under uniform moment, Eng. Structures, 34, 505-513.

[4-8] Du, Y., Mohareb, M., and Doudak, G., (2016), Nonsway model for lateral torsional buckling of wooden beams under wind uplift, J. Engineering Mechanics ASCE, 142, 04016104.

[4-9] El Damatty, A., Abushagur, M. and Youssef, M. A., (2003), Experimental and analytical investigation of steel beams rehabilitated using GFRP sheets, J. Steel & Comp. Str. 3, 421-438.

[4-10] Erkmen, R.E., and Mohareb, M., (2008), Buckling analysis of thin-walled open structures – A finite element formulation, Thin-walled structures, 46,618-636.

[4-11] Gara, F., Ranzi, G. and Leoni, G., (2006), Displacement-based formulations for composite beams with longitudinal slip and vertical uplift, Int. J. Num. Methods in Eng., 65, 1197-1220.

[4-12] Gardner, L., and Nethercot (2011), D. A., designers' guide to EUROCODE 3: Design of steel buildings, Imperial College London, UK.

[4-13] Girhammar, U.A. and Pan, D.H., (2007), Exact static analysis of partially composite beams and beam-columns, International Journal of Mechanical Sciences, 49, 239-255.

[4-14] Gjelsvik A., (1981), The Theory of Thin Walled Bars, 1st Edition, New York, et al., John Wiley & Sons publishing Incorporation.

[4-15] Harries, K.A., Peck A.J., Abraham, E.J., (2009), Enhancing stability of structural steel sections using FRP, Thin-walled structures, 47, 2092-1101.

[4-16] Hassan, R. and Mohareb, M., (2015), Distortional lateral torsional buckling for simply supported beams with web cleats, Canadian journal of civil engineering, 42, 1091-1103.

[4-17] Hjaji, M.A. and Mohareb, M., (2015) Finite-element formulation for the linear steady-state response of asymmetric thin-walled members under harmonic forces, Engineering Mechanics ASCE, 141, 04014126.

[4-18] Hu, Y., Mohareb, M., and Doudak, G., Lateral torsional buckling of wooden beams with midspan lateral bracing offset from section midheight, Eng. Mechanics, 143 (2017) 04017134.

[4-19] Liu, Y. and Gannon, L., (2009), Finite element study of steel beam reinforced while under load, Engineering Structures, 31, 2630-2642.

[4-20] Miller, C.T., Chajes J.M. and Hastings N.J., (2001), Strengthening of a steel bridge girder using CFRP plates, Journal of Bridge Engineering 6, 514-522.

[4-21] Pham, V. P, (2013), Stress-deformation theories for the analysis of steel beams reinforced with GFRP plates, Master of Science thesis, Dept. of Civil Engineering, Univ. of Ottawa, Ottawa.

[4-22] Pham, P.V. and Mohareb, M., (2014), A shear deformable theory for the analysis of steel beams reinforced with GFRP plates, Thin-Walled Structures, 85, 165-182.

[4-23] Pham, P.V. and Mohareb, M., (2015a), Finite-Element Formulations for the Spatial Static Response of Steel Beams Bonded to a GFRP Plate, J. Eng. Mechanics, ASCE, 141, 04014143.

[4-24] Pham, P.V and Mohareb, M., (2015b), Nonshear Deformable Theory for Analysis of Steel Beams Reinforced with GFRP Plate Closed-Form Solution, J. Struct. Eng., ASCE, 141, 04015063.

[4-25] Shaat, A., and Fam, A., (2009), Slender Steel Columns Strengthened Using High Modulus CFRP Plates for Buckling Control, Journal of Composites for Construction, 13, 2-12.

[4-26] Sahraei, A., Wu, L., and Mohareb, M., (2015), Finite element formulation for lateral torsional buckling analysis of shear deformable mono-symmetric thin-walled members, Thin-walled structures, 89, 212-226.

[4-27] Sahraei, A., and Mohareb, M., (2016), Upper and lower bound solutions for lateral-torsional buckling of double symmetric members, Thin-walled structures, 102, 180-196.

[4-28] Siddique, M.A.A. and El Damatty, A.A. (2013), Improvement of local buckling behaviour of steel beams through bonding GFRP plates, Composite Structures, 96, 44-56.

[4-29] Standards Association of Australia (SAA), Steel Structures, AS4100-1998, SAA, Australian Institute of Steel Construction, Sydney, Australia (1998).

[4-30] Trahair, N.S., (1993), Flexual torsional buckling of structures, CRC Press, USA.

[4-31] Vlasov, V. Z., (1961), Thin-walled elastic beams, 2nd Ed., Israel Program for Scientific Translations, Jerusalem.

[4-32] Wu, L., and Mohareb, M., (2011a), Buckling of shear deformable thin-walled members —I. Variational principle and analytical solutions. Thin-walled Structures, 49, 197 –207.

[4-33] Wu, L., and Mohareb, M., (2011b), Buckling formulation for shear deformable thin-walled members—II. Finite element formulation. Thin-walled Structures, 49, 208 –222.

[4-34] Wenwei, W. and Guo, L., (2006), Experimental study and analysis of RC beams strengthened with CFRP laminates under sustaining load, Int. J. of solids and structures, 43, 1372-1387.

[4-35] Xiao, Q., Doudak, G, and Mohareb, M., (2014), Lateral torsional buckling of wood beams: FEA-modelling and sensitivity analysis, World conference on Timber Engineering, Montreal.

[4-36] Xu, R., and Wu Y., (2007), Static, dynamic, and buckling analysis of partial interaction composite members using Timoshenko's beam theory, Int. J. of mech. sciences, 49, 1139-1155.

[4-37] Youssef, M., (2006), Analytical Prediction of the Linear and Nonlinear Behaviour of Steel Beams Rehabilitated using FRP Sheets. Engineering Structures, 28, 903-911.

[4-38] Zaghian, S., (2015), Buckling analysis of steel plates reinforced with GFRP, Master of Science thesis, University of Ottawa.

Chapter 5: Analytical and Numerical Study for Ultimate Capacity of Steel Beams Strengthened with GFRP Plates

Abstract

The present study develops a simplified design-oriented model to determine the ultimate moment capacity for compact wide flange steel sections strengthened with a GFRP plate bonded to one of the flanges. The model accounts for the elasto-plastic behaviour of steel, the shear capacity of the adhesive at the steel-GFRP interfaces, and the rupture strength of the GFRP. Considerations are given to local buckling classification rules for the strengthened steel section. In order to assess the validity of analytical models, developed are a series of 3D finite element analysis models that account for material and geometric nonlinear effects, initial out of straightness, and residual stresses. The ultimate moments and modes of failure predicted by the proposed analytical solutions are shown to agree well with the finite element solutions for beams strengthened with GFRP plates on the tension side. Additional comparisons with experimentally verified shell solutions by others suggest the simplified model is equally applicable to steel beams strengthened with GFRP plates on the compression side.

Keywords: Ultimate moment capacity, structural steel, adhesive, GFRP, compact sections, finite element analysis

List of symbols:

C_s = total internal compressive force acting on the steel section above the PNA,

C_{s1} = internal compressive force acting on the plastified portion of the steel section.

C_{s2} = internal compressive force acting on the elastic core of the steel section.

T_a = internal tensile force acting on the adhesive,

T_g = internal tensile force acting on the GFRP plate

T_{g1}, T_{g2} = components of T_g acting on the GFRP plate, defined in Eq. (9).

T_s = total internal force acting on the steel section below the PNA,

T_{s1} = internal tensile force acting on the elastic core of the steel section.

T_{s2} = internal tensile force acting on the plastified portion of the steel section.

Q_{at} , Q_{ab} = horizontal shear stress resultant at the adhesive/steel and adhesive/GFRP interfaces,

F_g = rupture strength of the GFRP plate, F_y = yielding strength of the steel,

A_{sc1}, A_{sc} = Cross-sectional steel area under compression plastic stresses,

A_{sc2} = Cross-sectional steel area under compression elastic stresses,

A_{st1} = Cross-sectional steel area under tension elastic stresses,

A_{st2}, A_{st} = Cross-sectional steel area under tension plastic stresses,

L_e = distance between the sections of zero moment and maximum moment,

d_{NA} = distance from the neutral axis to the bottom fiber of steel,

d_y = distance from the neutral axis to the end of the elastic core

y_c = distance from the centroid of the compressive plastic stress block to the top steel fiber,

y_t = distance from the centroid of the tensile plastic stress block to the bottom steel fiber,

e_1 = distance between the points of action of C_{s1} and C_{s2},

e_2 = distance between the points of actions of C_{s1} and T_{s1},

e = distance between the points of action of C_{s1} and T_{s2},

e_g, e_{g1}, or e_{g2} = distance between the point of action C_{s1} and that of T_g, T_{g1}, or T_{g2}, respectively,

t_f, t_a, t_g, t_w, d, b = Cross-sectional dimensions defined in Fig. 5.1b,

ε_g = rupture strain of GFRP plate, ε_y = yielding strain of the steel,

E_s = Elastic modulus of steel, G_a = Shear modulus of adhesive layer,

E_p = Elastic modulus of the GFRP plate in the longitudinal direction,

5.1. Introduction

Glass Fiber-Reinforce Polymer (GFRP) plates offer a viable option to strengthen steel members. GFRP can be manufactured in relatively thick plates. The main advantages include low cost and ease and quick installation to steel surfaces through adhesive layers. Much of the work on strengthening steel structures has been focused on using Carbon-FRP (CFRP) laminates. However, studies presented in the following section have shown that a thicker GFRP plate can in fact compensate for the lower Young's modulus of GFRP and provide a strengthening effectiveness similar to that of CFRP, at a lower cost. Additionally, when in contact with steel, GFRP plates do not induce galvanic corrosion. As such, they are gaining momentum as means of strengthening steel members.

Relevant studies using GFRP plates include the work of El Damatty and Abushagur (2003) and El Damatty et al. (2005) who reported experimental and numerical studies for shear and peel behavior of adhesives used to bond GFRP plates to steel bridge beams. Accord and Earls (2006) conducted numerical studies for wide flange steel beams strengthened by four GFRP plates to the compression flange. Youssef (2006) conducted an experimental study on a wide flange steel beam strengthened with GFRP plates bonded to the top and bottom flanges. The author also developed an analytical model to estimate the ultimate load capacity of steel beams strengthened with two identical GFRP plates by assuming a constant longitudinal stress across the GFRP plate thickness. Harries et al. (2009) reported an experimental study in which they strengthened WT steel columns by bonding GFRP plates to the web to delay their local buckling. Aguilera and Fam (2013) reported an increase in strength up to 53% for rectangular hollow steel section (HSS) T-joints experimentally strengthened with GFRP plates bonded to the face of the HSS. Siddique and El Damatty (2012, 2013) developed a finite element formulation for the local buckling analysis of steel beams strengthened with GFRP plates. The authors identified three possible failure modes; (1) local buckling of the flanges, (2) adhesive shear failure and (3) GFRP plate tension failure. Aydin and Aktas (2015) reported an experimental study where cruciform steel plates under compression were strengthened with GFRP plates. Siddique et al. (2013) investigated the seismic response and ductility of steel frames strengthened with GFRP plates. Zaghian (2015) developed a finite shell element for the buckling analysis of steel plates symmetrically strengthened with two GFRP plates. Pham and Mohareb (2014, 2015a,b) developed analytical solutions and finite element formulations for the analysis wide flange steel beams strengthened with a single GFRP plate under longitudinal-transverse and lateral-torsional loading conditions. The comparison of shear deformable and non-shear deformable solutions showcased the importance of shear deformation. Pham et al. (2017) developed a solution to characterize the effects of pre-existing loads on the response and strength of steel beams strengthened with GFRP plates. Based on the principle of stationary complementary energy, Pham et al. (2018) developed a family of high-order beam finite elements that capture the shear and peeling stresses at the GFRP-adhesive and steel-adhesive interfaces.

Among the previous studies, only the study by Youssef (2006) provided an ultimate moment solution for steel beams strengthened with GFRP plates. Unlike the study by Youssef (2006) which focused on simply supported steel beams strengthened at both flanges, the present study develops expressions for the ultimate moment of beams strengthened with a single GFRP plate bonded to a single flange. Other features of the model include its applicability for general boundary conditions. Also, unlike the bilinear material model with strain hardening adopted in Youssef (2006), a linear perfectly plastic idealization is adopted in the analytical models of the present study. The results are then compared to those predicted by 3D FEA that captures material and geometric nonlinearity, strain hardening, initial out-of-straightness, and residual stresses.

5.2. Statement of the problem

A steel beam of compact (class 1 or 2) wide flange cross-section is strengthened with a GFRP plate bonded to the bottom flange through an adhesive layer. It is required to determine the ultimate capacity of the strengthened section based on a material mode of failure (plastification of steel, attainment of shear strength by the adhesive, and/or attainment of rupture strength by the GFRP). Another potential mode of failure involving the attainment of peeling strength of the adhesive have been investigated in a separate model (Pham et al. 2018) and hence is outside the scope of the present investigation. In line with limit state design methodology, the strength based on the models developed in the present study and the peeling mode of failure in Pham et al. (2018) need to be determined, and the capacity of the strengthened system would be governed by the smaller of both strengths.

5.3. Assumptions

The following assumptions are made regarding the material behavior in the analytical model:

(i) Steel is assumed to behave as an elastic perfectly plastic material (i.e., strain hardening is neglected),

(ii) The GFRP and adhesive materials are linearly elastic. This assumption is experimentally substantiated for GFRP and adhesives at room temperature. Adhesives under higher temperature show signs of yielding (Sahin and Dawood 2016). For such cases, the present solution can still be applied while adopting linear secant approximation of the adhesive stress-strain behavior.

5.4. Equilibrium Conditions

Consider a GFRP-strengthened steel beam under load applications. A typical bending moment diagram for the loaded beam is schematically illustrated in Figure. 5.1a. The beam segment between the sections of zero and maximum moments is assumed to have a length L_e. A free body diagram for segment L_e is depicted in Figure. 5.1b and a cross-sectional view with dimension notation is shown on Figure. 5.1c. The following formulation assumes that the steel section is strengthened on the tension side. However, as will be shown in the example section, the solution developed is equally valid for compression side strengthening.

The longitudinal internal resultant forces C_s, T_s, T_a and T_g within the three materials are shown for the case where the plastic neutral axis (PNA) is assumed to lie in the steel section. Separate free body diagrams for each of the three materials are depicted in

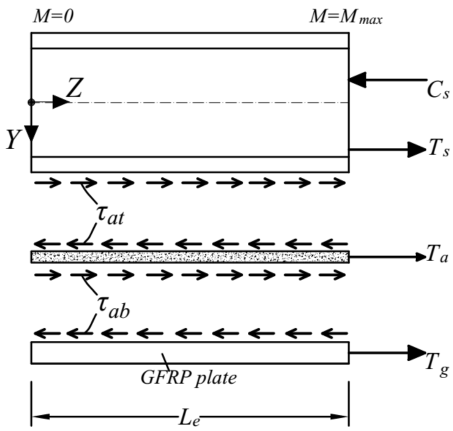

Figure. 5.2. The figures depict the internal horizontal forces acting on a segment of length L_e between the sections of zero and maximum moments. Irrespective of the material model adopted for the adhesive, the shear stresses at the interface of steel-adhesive is assumed to be $\tau_{at}(z)$ and those at the adhesive-GFRP interface are denoted as $\tau_{ab}(z)$.

The equilibrium condition for the horizontal forces acting on the steel segment are

$$C_s - T_s + Q_{at} = 0, \qquad Q_{at} = \int_0^{L_e} \tau_{at}(z)\, b dz \tag{5.1)a-b}$$

For the adhesive layer, the horizontal equilibrium force is

$$Q_{at} - Q_{ab} - T_a = 0 \qquad Q_{ab} = \int_0^{L_e} \tau_{ab}(z)\, b dz \tag{5.2)a-b}$$

Because the thickness and tensile strength of the adhesive layer are small relative to those of the steel and the GFRP, one has $T_a << T_g, T_s$ and thus T_a can be neglected in Eq. (5.2)a and one has

$$Q_{at} \approx Q_{ab} = Q_a \tag{5.3}$$

For GFRP, the horizontal force equilibrium condition plate yields

$$T_g - Q_a = 0 \tag{5.4}$$

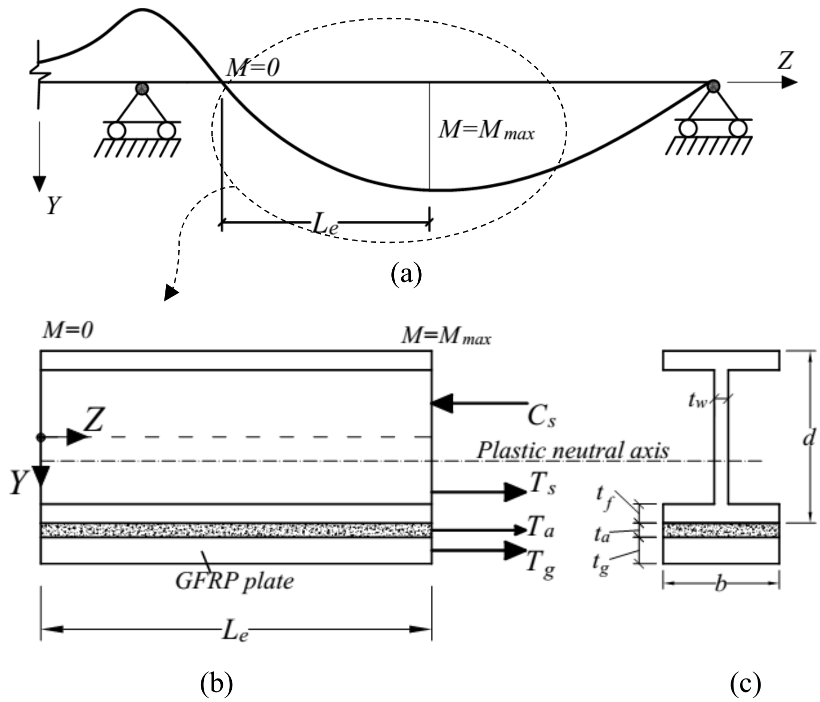

Figure. 5.1. (a) Bending moment diagram, (b) free body diagram of segment Le, (c) cross-section view

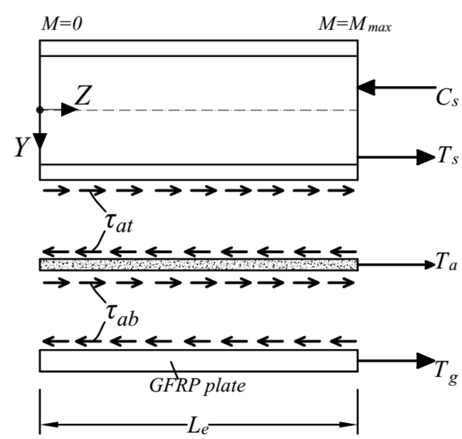

Figure. 5.2. Internal horizontal forces and stresses acting on free body diagrams

5.5. Capacities of individual components

The maximum compressive capacity of the steel beam $C_{s,\max}$ is obtained when the full steel cross-section is subjected to compressive stresses and is given by

$$C_{s,\max} = A_s F_y \tag{5.5}$$

in which A_s is the steel section area. The maximum tensile capacity $T_{g,\max}$ of the GFRP plate is given by

$$T_{g,\max} = A_g F_g \tag{5.6}$$

in which A_g is the GFRP cross-sectional area. For adhesives, and for the sake of simplified integrations, it is assumed that the shear stress distribution is linearly distributed along the length L_e where the maximum value $\tau = \tau_u$ takes place at section of zero moment and the τ vanishes at the section of maximum moment (Fig.5.3). The validity of this assumption will be verified against 3D finite element results. In such a case, the maximum horizontal shear capacity at the adhesive interfaces for the strong adhesives is given by

$$Q_{a,\max} = \tau_u b L_e / 2 \tag{5.7}$$

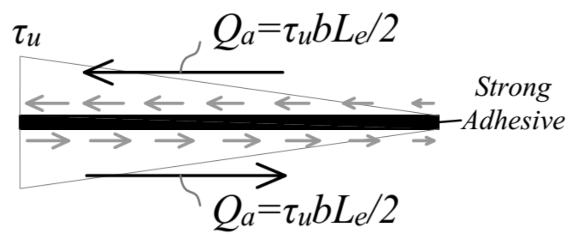

Figure. 5.3. Shear stresses and stress resultants for both strong and weak adhesives

5.6. Possible modes of failure

Based on the calculated capacities $C_{s,\max}, Q_{a,\max}$ and $T_{g,\max}$, the ultimate strength of the strengthened section can be associated with one of three failure modes;

(1) When $T_{g,\max} \le C_{s,\max}$ and $T_{g,\max} \le Q_{a,\max}$, the tensile strength of the GFRP is the weakest link, and thus governs the capacity of the system. In this case, satisfying the equilibrium conditions in Eqs. (5.1) a, (5.3), (5.4) necessitates that the plastic neutral axis lies in steel. This condition is realized in most common steel sections and material properties.

(2) When $Q_{a,\max} \le C_{s,\max}$ and $Q_{a,\max} \le T_{g,\max}$, the shear capacity of the adhesive becomes the weakest link and thus governs the capacity of the composite system as the adhesive provides only partial interaction and there exists significant slip at the interface between the steel section and GFRP. Satisfying the equilibrium conditions Eqs.(5.1), (5.3), (5.4) signifies that the GFRP cannot fully

develop its tensile strength. This failure mode would occur when the steel beam is strengthened with a relatively short GFRP plate bonded to steel by a weak adhesive.

(3) A third mode of failure can conceptually take place if $C_{s,\max} \le Q_{a,\max}$ and $C_{s,\max} \le T_{g,\max}$ where equilibrium would necessitate a neutral axis to lie in the GFRP plate. However, practical geometric dimensions and material properties make this possibility highly unlikely and will thus not be considered.

5.7. Case 1 -Capacity based on the GFRP tensile failure

The present section develops two models to characterize the strength of the GFRP-strengthened steel sections based on Failure Mode 1. These are (1) a detailed model based on an elasto-plastic idealization for the stress profile within the steel and (2) a simplified model based on an assumed fully plastified stress profile within the steel section.

5.7.1. Detailed Model

When $T_{g,\max} \le C_{s,\max}$ and $T_{g,\max} \le Q_{a,\max}$, the neutral axis lies in the steel section as discussed and the failure is induced by GFRP rupture. Because the rupture strength $T_{g,\max}$ for the GFRP is smaller than the yielding strength $C_{s,\max}$ for the steel, the steel section will not fully plastify and thus will consist of an elastic core in the central portion of the section and two plastified regions near the extreme fibers at the onset of GFRP rupture. Also, as the GFRP does not possess a yielding plateau, the stress profile is linear across the GFRP thickness. The following additional assumptions are made

(i) The elastic core for the steel entirely lies within the web. The conditions that ensure this requirement will be given below and the assumption will be shown to be non-restrictive for most sections and material properties.

(ii) The slope of the strain profile within the steel elastic core equals that within the GFRP plate (Figure. 5.4b). Outside the elastic core, 3D FEA suggests that the strain profile is slightly nonlinear as schematically illustrated in Fig. 4b. However, the nonlinear distribution of the strain profile has no influence on the stress distribution in the plastified portion of the steel section.

The stress distributions and corresponding internal forces consistent with the previous assumptions are provided in Figure. 5.4c. The internal resultant forces are C_{s1}, C_{s2}, T_{s1}, T_{s2}, and $T_g = F_g t_g b - E_g t_g \varepsilon_y t_g b / 2\,d_y$ as depicted in Figure. 5.4. The condition $0 < d_y \le \left(d - 2t_f\right)/2$ must be satisfied to conform to assumption (i).

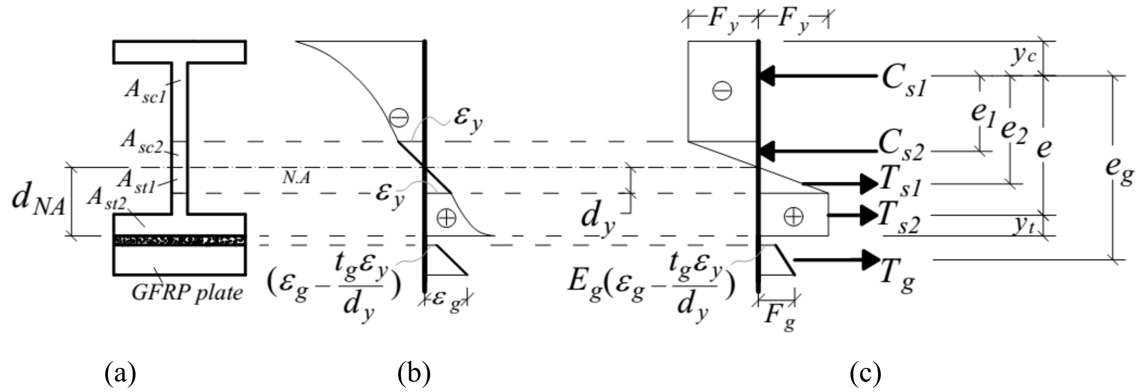

Figure. 5.4. Modified resulting forces at cross-section $M = M_{\max}$ in failure case 1a

For a pure flexural member, the sum of the horizontal internal forces vanish, i.e.,

$$T_{s1} + T_{s2} + T_{g1} - T_{g2} - C_{s1} - C_{s2} = 0 \tag{5.8}$$

in which the internal forces are expressed in term of the depth d_y of the elastic core as

$$\begin{aligned}
&C_{s1}\left(d_y\right) = bt_f F_y + \left(d - d_{NA} - t_f - d_y\right) t_w F_y; && C_{s2}\left(d_y\right) = t_w d_y F_y / 2; \\
&T_{s1}\left(d_y\right) = t_w d_y F_y / 2; && T_{s2}\left(d_y\right) = bt_f F_y + \left(d_{NA} - t_f - d_y\right) t_w F_y; \\
&T_g\left(d_y\right) = T_{g1} - T_{g2}; \quad \text{where } T_{g1} = F_g t_g b; && T_{g2}\left(d_y\right) = \left(E_g t_g \varepsilon_y / d_y\right) t_g b / 2
\end{aligned} \tag{5.9}$$

From Eqs. (5.9), by substituting into Eq. (5.8), the neutral axis depth d_{NA} can be expressed in term of d_y as

$$d_{NA}\left(d_y\right) = \frac{bt_g^2 E_g}{4t_w E_s} \frac{1}{d_y} + \frac{d}{2} - \frac{t_g b F_g}{2t_w F_y} \tag{5.10}$$

where condition $t_f < d_{NA} < d - t_f$ must be satisfied. Also, the moment arms are expressed in terms of d_{NA} and d_y as

$$\begin{aligned}
&y_c\left(d_y\right) = \left[bt_f^2/2 + \left(d - d_{NA} - d_y - t_f\right) t_w \left(d - d_{NA} - d_y + t_f\right)/2\right] \Big/ \left[bt_f + \left(d - d_{NA} - d_y - t_f\right) t_w\right]; \\
&y_t\left(d_y\right) = \left[bt_f^2/2 + \left(d_{NA} - d_y - t_f\right) t_w \left(d_{NA} - d_y + t_f\right)/2\right] \Big/ \left[bt_f + \left(d_{NA} - d_y - t_f\right) t_w\right]; \\
&e_1\left(d_y\right) = d - d_{NA} - 2d_y/3 - y_c; \qquad e_2\left(d_y\right) = e_1 + 4d_y/3; \qquad e\left(d_y\right) = d - y_t - y_c; \\
&e_{g1}\left(d_y\right) = e + y_t + t_a + t_g/2; \qquad e_{g2}\left(d_y\right) = e + y_t + t_a + t_g/3
\end{aligned} \tag{5.11}$$

The moment capacity of the strengthened beam is then evaluated by summing moments of internal forces, i.e.,

$$M_p = T_{s1} e_2 + T_{s2} e + T_{g1} e_{g1} - T_{g2} e_{g2} - C_{s2} e_1 \tag{5.12}$$

From Eqs. (5.9)-(5.11), by substituting into Eq. (5.12), one recovers an expression for the moment $M_p = M_p\left(d_y\right)$ as a nonlinear function of d_y. The ultimate moment is then obtained by selecting the value of $d_{y,\max}$ which maximizes the moment $M_p\left(d_y\right)$ and corresponds to the condition

$$\left.\frac{\partial M_p\left(d_y\right)}{\partial d_y}\right|_{d_{y\max}} = 0 \tag{5.13}$$

which is solved for the possible values for d_y. The corresponding values of $d_{NA}\left(d_y\right)$ are determined from Eq. (5.10). The admissible values of d_y and d_{NA} must satisfy conditions

$$0 < d_y \leq \left(d - 2t_f\right)/2, \qquad t_f < d_{NA} < d - t_f \tag{5.14)a-b}$$

which will yield only a single admissible value of $d_y = d_{y\max}$ and a corresponding $d_{NA}\left(d_{y\max}\right)$. The corresponding internal forces $C_{s1}\left(d_{y\max}\right), C_{s2}\left(d_{y\max}\right), T_{s1}\left(d_{y\max}\right), T_{s2}\left(d_{y\max}\right)$ and $T_g\left(d_{y\max}\right)$ are then determined from Eq. (5.9). Also, moment arms $y_c\left(d_{y\max}\right)$, $y_t\left(d_{y\max}\right)$, $e_1\left(d_{y\max}\right), e_2\left(d_{y\max}\right), e\left(d_{y\max}\right), e_{g1}\left(d_{y\max}\right)$ and $e_{g2}\left(d_{y\max}\right)$ are obtained from Eq. (5.11) and the ultimate moment $M_p\left(d_{y\max}\right)$ by substitution into Equation (5.12).

5.7.2. Simplified Model

The detailed solution above requires an iterative solution when solving equation (13). Therefore, a more simplified solution that eliminates the need for iteration is developed by introducing two additional simplifying assumptions i.e.,

(i) Steel fully yields either in compression or tension at the onset of GFRP failure,

(ii) Given that GFRP plate is relatively thin, the stresses across its thickness are assumed uniform and equal to the material strength F_g.

The stress distributions and corresponding internal resultant forces consistent with the previous assumptions are depicted in Figure. 5.5. The internal resultant forces are $C_{s1} = A_{sc}F_y, T_{s2} = A_{st}F_y$, and $T_g = A_g F_g$.

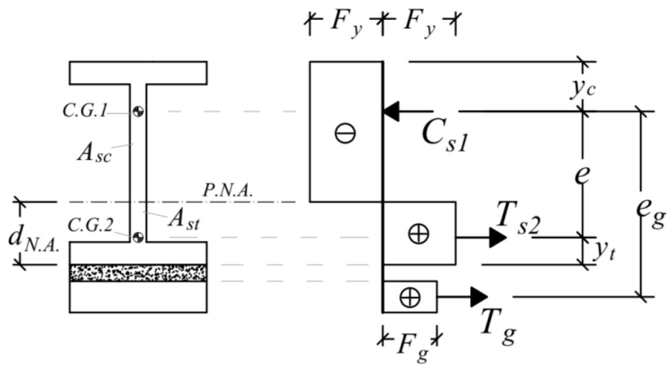

Figure. 5.5. Resulting forces at cross-section $M = M_{\max}$ in failure case 1

For a pure flexural member, the sum of internal forces in the horizontal direction must vanish, i.e.,

$$T_{s2} + T_g - C_{s1} = 0 \tag{5.15}$$

Starting with identity $A_{sc} + A_{st} = A_s$ and multiplying both sides by F_y, one obtains $C_{s1} = A_s F_y - T_{s2}$. By substituting into Eq. (5.15) and solving for the tensile force, one obtains

$$T_{s2} = \left(A_s F_y - A_g F_g \right) / 2 \tag{5.16}$$

If the maximum tensile resistance of the top flange $T_{bf,\max} = F_y b t_f$ is less than the tensile force as determined from Eq. (5.16), i.e., $T_{bf,\max} < T_{s2}$, the PNA must lie in the web. This will be the case for practical dimensions and material properties and hence the case $T_{bf,\max} > T_{s2}$ is only hypothetical and will not be considered. In this case, the total tensile stress resultant in the steel is given by $T_{s2} = T_{bf,\max} + \left(d_{NA} - t_f \right) t_w F_y$, which when equated to Eq. (5.16), yields the following expression for the plastic neutral axis d_{NA}

$$d_{NA} = \left(T_{s2} - T_{bf,\max} + t_f t_w F_y \right) / t_w F_y \tag{5.17}$$

Given d_{NA}, the centroidal distances y_c and y_t can be determined from $y_c = \left[A_s d / 2 - A_{st} \left(d - y_t \right) \right] / \left(A_s - A_{st} \right)$, $y_t = \left[b t_f^2 / 2 + \left(d_{NA} - t_f \right) t_w \left(d_{NA} + t_f \right) / 2 \right] / A_{st}$ where $A_{st} = t_f b + \left(d_{NA} - t_f \right) t_w$, and moment arms are $e = d - y_t - y_c$ and $e_g = d + t_a + t_g / 2 - y_c$. By summing moments about the point of action of the stress resultant C_s, one obtains the ultimate moment of the strengthened section as

$$M_p = T_{s2} e + T_g e_g \tag{5.18}$$

5.8. Case 2 - Capacity based on adhesive shear failure

When $Q_{a,\max} \le C_{s,\max}$ and $Q_{a,\max} \le T_{g,\max}$, the system capacity is dictated by the adhesive shear failure and, in principle, the GFRP cannot fully develop its tensile strength. In order to devise a simple solution for the adhesive shear failure mode, the following assumptions are made: (1) The steel section is assumed to be fully plastified, (2) The GFRP is subjected solely to tensile stresses (no compression), and (3) the stress profile in the GFRP is considered constant with $\bar{\sigma}_g < F_g$. As will be subsequently shown, experimentation with 3D FEA finite element modelling on practical section dimensions and material properties supports the validity of assumptions (1) and (2), while assumption (3) is an approximation leading to moment capacity predictions in close agreement with finite element results. The stress distribution and corresponding internal resultant forces based on above assumptions are depicted on Figs. 5.6a,b. The internal forces are $C_{s1} = A_{sc}F_y$, $T_{s2} = A_{st}F_y$, and $T_g = \bar{\sigma}_g A_g$. At the adhesive-steel and adhesive-GFRP interfaces, the internal shear forces are $Q_{a,\max}$ (Figure. 5.6b). From the equilibrium condition in the horizontal direction; $T_g - Q_{a,\max} = 0$ for the GFRP plate (Figure. 5.6b), in which $T_g = \bar{\sigma}_g bt_g$ and $Q_{a,\max} = \tau_u bL_e/2$, the stress in the GFRP plate can be obtained as $\bar{\sigma}_g = Q_{a,\max}/bt_g$. Also, the equilibrium of internal forces acting on the steel in the horizontal direction yields

$$T_{s1} + Q_{a,\max} - C_{s2} = 0 \tag{5.19}$$

Starting with identity $A_{sc} + A_{st} = A_s$ and multiplying both sides by F_y, one obtains $C_{s1} = A_sF_y - T_{s2}$. By substituting into Eq. (5.19) and solving for the tensile force, one obtains

$$T_{s2} = \left(A_sF_y - Q_{a,\max}\right)/2 \tag{5.20}$$

If the maximum tensile resistance of the top flange $T_{bf,\max} = F_ybt_f$ is less than the tensile force as calculated by Eq.(5.20), i.e., $T_{bf,\max} < T_{s2}$, the steel PNA must lie in the web. Again, the case $T_{bf,\max} > T_{s2}$ is hypothetical for practical geometries and material properties and will not be considered. In this case, the total tensile stress resultant in the steel is given by $T_{s2} = T_{bf,\max} + \left(d_{NA} - t_f\right)t_wF_y$, which when equated to Eq. (5.20) yields

$$d_{NA} = \left(T_{s2} - T_{bf,\max} + t_ft_wF_y\right)/t_wF_y \tag{5.21}$$

Given d_{NA}, the centroidal distances y_c and y_t can be determined from the relations $y_c = \left[A_s d/2 - A_{st}\left(d - y_t\right)\right] / \left(A_s - A_{st}\right)$, $y_t = \left[bt_f^2/2 + \left(d_{NA} - t_f\right)t_w\left(d_{NA} + t_f\right)/2\right] / A_{st}$ where $A_{st} = t_f b + \left(d_{NA} - t_f\right)t_w$. The moment arms e, e_g between the internal forces are determined from $e = d - y_t - y_c$ and $e_g = d + t_a + t_g/2 - y_c$. By summing moments about the point of action of the stress resultant C_s, one obtains the ultimate moment capacity of the strengthened section as

$$M_p = T_{s2}e + T_g e_g \tag{5.22}$$

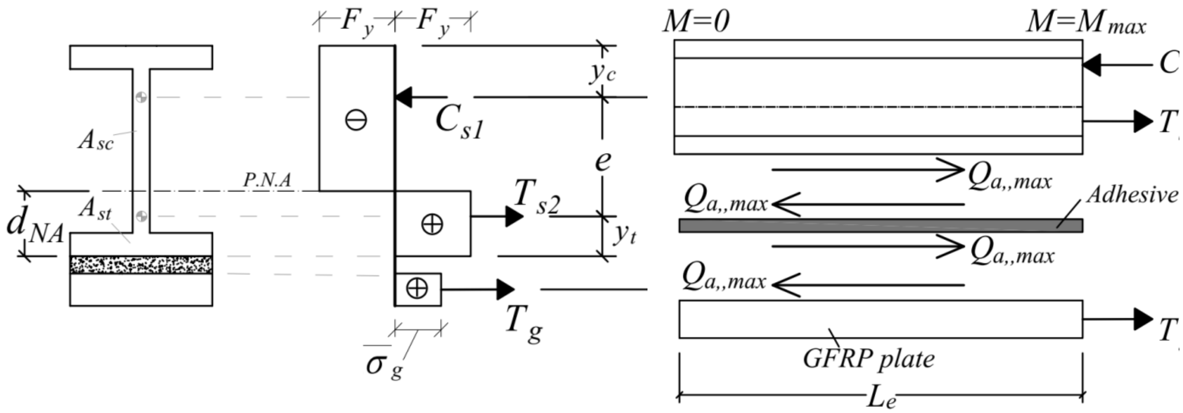

(a) (b)

Figure. 5.6. Resulting forces in failure cases 2a (a) Cross-section and horizontal internal forces (b) Free body diagrams for the steel, adhesive and GFRP plate

5.9. Validation

In the following sections, Examples 1, 2 and 3 are intended to assess the validity of the detailed and simplified models developed for the case of GFRP tensile failure mode (Mode 1) while Example 4 is intended to assess the validity of the analytical solution for the case of adhesive failure (Mode 2). The moment capacity predicted by the analytical solutions are compared to those predicted by the 3D Finite Element Analyses (FEA) under ABAQUS and an experimentally verified shell finite element reported in Siddique and El Damatty (2012, 2013).

While the material properties in the analytical models were idealized as elastic-perfectly plastic for simplification, those adopted in the FEA models included strain hardening (Fig. 5.7a) to replicate more closely the expected stress-strain curves for structural steel. In all cases, GFRP is modelled as a linearly elastic material up to a specified rupture strength in tension (Fig. 5.7b). Adhesive properties were taken from Shaat and Fam 2007 with an elastic modulus $E_s = 3.18\ GPa$, a shear modulus $G = 1.22\ GPa$

and a rupture strength $\sigma_u = 72.4\ MPa$. The study of Kadam (2014) investigated several failure criteria to characterize the adhesive constitutive behavior of adhesives, including the von-Mises, Drucker Prager, maximum principal stress, maximum shear stress, maximum peel stress, in-plane shear stresses, mean stress, fracture stress, and Mohr-Coulomb models. Among these models, the Drucker Prager criterion was found to yield the closest representation of the adhesive constitutive behavior as observed in shear lap experiments. In the absence of experimental characterization of the internal friction angle for specific type of adhesive used in bonding steel to GFRP, the present study assumes that the internal angle of friction to vanish, leading to a simple and conservative solution. In this case, the Drucker-Prager model degenerates to the von-Mises failure criterion and corresponding rupture strength in shear is $\tau_u = \sigma_u / \sqrt{3} = 41.8\ MPa$ as depicted in Fig. 5.3.

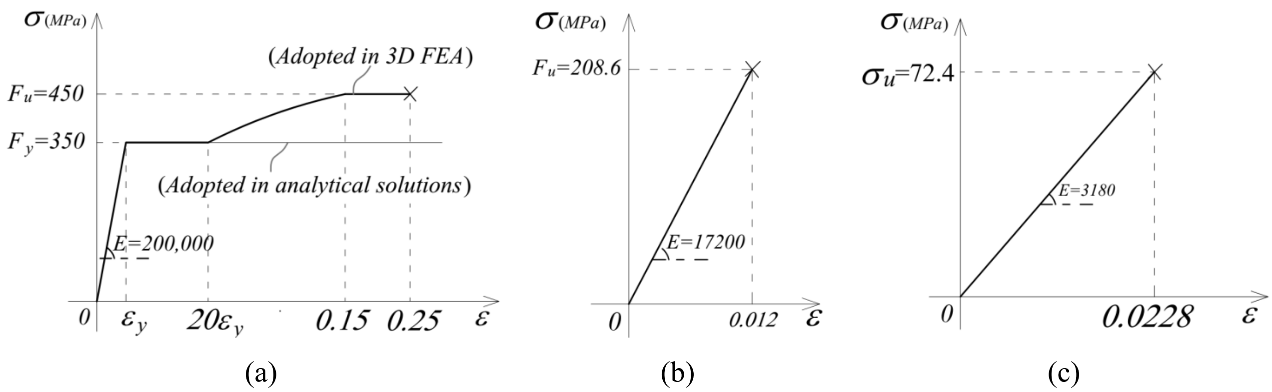

Figure. 5.7. Tensile stress-strain relationships for (a) steel, (b) GFRP, and (c) weak and strong adhesives

5.9.1. Example 1: Beam under uniformly distributed load

Statement of the problem:

Consider a simply supported steel beam with a W250x45 cross-section (meets class 2/compactness requirement) and a span $L = 4m$. The beam is strengthened with a 15.5 mm-thick GFRP plate over the entire span through a 1.0 mm-thick adhesive. The beam is subjected to a uniformly distributed load q (Fig. 5.8). It is required to determine the moment capacity and longitudinal stress profiles for the cases of weak and strong adhesives.

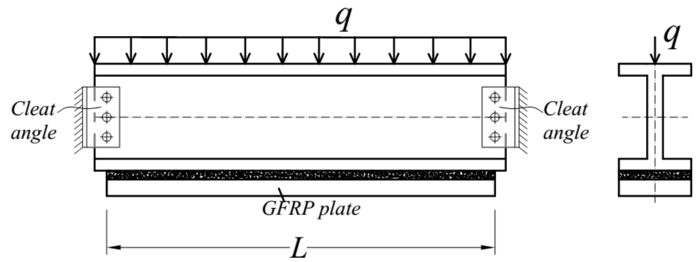

Figure. 5.8. 4m-span beams strengthened with GFRP plate

Solution based on the Detailed Model:

From Eqs. (5.5)-(5.7), the maximum values for the compressive force in the steel, tensile force in GFRP, and the interfacial shear forces are obtained as $C_{s,\max} = 1990\,kN$, $T_{g,\max} = 479\,kN$, $Q_{a,\max} = 1660\,kN$ (for the weak adhesive) and $Q_{a,\max} = 6100\,kN$ (for the strong adhesive). For both types of adhesives, the conditions $T_{g,\max} < C_{s,\max}$ and $T_{g,\max} < Q_{a,\max}$ are satisfied, suggesting that a GFRP tensile failure mode is expected. Hence the procedure associated with Case 1 is applied.

By solving Eq. (5.13) for d_y, one obtains the five roots $d_y = -11.6$, -2.04, 0.217, 25.2 and $463\,mm$. The only admissible solution is $d_{y\max} = d_y = 25.2$ satisfies conditions stipulated in Eqs. (5.14)a-b (i.e., $0 < d_y \le \left(d - 2t_f\right)/2 = 120\,mm$ and $13mm = t_f < d_{NA} < d - t_f = 253mm$). The corresponding depth of the neutral axis d_{NA} as determined from Eq. (10) is $47.1\,mm$ and the maximum moment capacity of the strengthened section is $M_p = 253\,kNm$. This compares to a plastic moment resistance for the bare section of $209\,kNm$, i.e., in the present problem, the addition of GFRP plate increased the capacity of the section by 21.0%.

Classification considerations: Under AISC-ANSI 360 (2016) and AS4100 (1998) the interaction equations for members under combined flexure (beam-columns) take the generic form $C_f/C_r + \alpha M_f/M_r = 1$ where C_r and M_r are the axial and flexural resistances based on the relevant section class, C_f and M_f are internal axial force and moments acting on the section, and α is a section-dependent and (standard-dependent) constant. Web classification thresholds for beam-column with compact are $h_w/t_w \le 3.76\sqrt{E_s/F_y}$ in AISC-ANSI 360 (2016) and $h_w/t_w < 82\sqrt{250/F_y}$ in AS4100 (1998). In both cases, classification limits solely depend upon the slenderness of the web. These thresholds remain applicable for the strengthened section, owing to the similarity of the stress profile in the steel section (Fig. 5.4) to that of a beam column.

For the present example, the web slenderness $h_w/t_w = 31.6$ is less than the compactness threshold $3.76\sqrt{E_s/F_y} = 3.76\sqrt{200,000/350} = 89.9$ as defined in ANSI-AISC 360 (2016), and $\lambda_{ep}\sqrt{250/F_y} = 82\sqrt{250/350} = 69.3$ as defined in AS4100 (1998).

Under CAN-CSA S16 (2014), web classification rules are based on web slenderness (in a manner similar to AISC-ANSI 360 (2016) and AS4100-(1998)) and also on the level of internal compressive force C_f acting on the section, i.e., $h_w/t_w \le 1700\left(1-0.61C_f/\phi C_y\right)/\sqrt{F_y}$ for class 2 (compact) sections, where $\phi = 0.90$ is a resistance factor $C_y = AF_y$ is the yield compressive load. Under CAN-CSA S16 (2014), for a strengthened steel member under pure bending, the net compressive force C_f acting on the steel section alone can be obtained by summing the internal forces acting on the steel section, i.e., in the elasto-plastic stress profile in Fig. 5.4, one has $C_f = C_{s1} + C_{s2} - T_{s1} - T_{s2}$ while in the fully plastic profile in Fig. 5.5, one has $C_f = C_{s1} - T_{s2}$. For the web of the strengthened beam section, the net compressive force acting on the section is $C_f = C_{s1} + C_{s2} - T_{s1} - T_{s2} = 457kN$. Also, one has $\phi C_y = \phi A_s F_y = 0.9 \times 5720 \times 350 = 1802\,kN$, In this case, the web slenderness $h_w/t_w = 31.6 < 1700\left(1-0.61\times 457/1802\right)/\sqrt{350} = 76.8$ and thus the web is found to also meet Class 2 (i.e., compactness) requirements. Under all three standards, the web is judged to be thick enough to develop the full plastic resistance as depicted in Fig. 5.4.

For the flange, irrespective of the magnitude of C_f, the flange threshold for classification requirements in AISC-ANSI 360 (2016), AS4100 (1998), and CAN-CSA (2014) remain valid given that the stress profile in flange remain identical to that of members under pure flexure. For the present example, the flange slenderness $b/2t_f = 148/(2\times 13) = 5.7$ is less than the compactness threshold $0.56\sqrt{E_s/F_y} = 0.56\sqrt{200,000/350} = 13.4$ based on AISC-ANSI 360 (2016) and $170/\sqrt{F_y} = 170/\sqrt{350} = 9.1$ based on CAN-CSA (2014). Also, based on AS4100 (1998), the flange slenderness $(b-t_w)/2t_f = (148-7.6)/(2\times 13) = 5.4$ is less than the compactness threshold $\lambda_{ep} = 8$.

Solution based on the Simplified Model:

From Eq. (5.16), T_{s2} is evaluated as $753\,kN$, which is greater than $T_{bf,\max} = 673\,kN$ and thus the neutral axis lies in the steel section web. The value of d_{NA} as evaluated from Eq. (5.17) is $43.1\,mm$ and the corresponding plastic moment is determined from Eq. (5.18) as $255\,kNm$ which is 1.0% higher than that predicted by the detailed procedure. In order to check the section class based on the CAN-CSA S16 (2014) for the strengthened section based on the simplified solution, the total compressive force is $C_f = C_{s1} - T_{s2} = 1232 - 753 = 479\,kN$ and the compressive load at yield resistance is $\phi C_y = \phi A_s F_y = 0.9 \times 5720 \times 350 = 1802\,kN$, which satisfies the condition $h_w/t_w = 31.58 < 1700\left(1 - 0.61 \times 479/1802\right)/\sqrt{350} = 89.4$ and thus the web was found to also meet Class 2 requirements. Section class based on the AISC-ANSI 360 (2016) or AS4100 (1998) is remains compact as shown in the detailed model solution.

Description of the finite element analysis:

Nonlinear 3D FEAs are conducted as benchmarks to assess the validity of the present analytical model. The FEA models are based on brick element C3D8R in the ABAQUS library. The element has 8 nodes with three translations per node, totaling 24 DOFs and adopts reduced integration to avoid volumetric locking, and thus has a single integration point located at the element centroid. A line load is applied at the centerline of the top flange. Four analyses are conducted that incorporate material nonlinearity of the steel. The analyses varied the combinations of features included (geometric nonlinearity, residual stresses, and/or initial imperfections). The specifics of each type of analysis are provided in Table 5.1.

Table 5.1. FEA models in Example 1

FEA models	Geometric nonlinearity	Residual stresses	Initial imperfections	
			Amplitude=2mm	Amplitude=4mm
FEA-NG	-	-	-	-
FEA-G	✓	-	-	-
FEA-GR	✓	✓	-	-
FEA-GRI2	✓	✓	✓	-
FEA-GRI4	✓	✓	-	✓

✓ = captured in the analysis, - = not captured in the analysis

In runs FEA-GR, FEA-GRI2, and FEA-GRI4, residual stresses have been modelled according to the stress distribution pattern in Figure. 5.9a (Hasham and Rasmussen 1998). The residual stresses were assumed constant throughout the section thickness and were incorporated into the ABAQUS models through the *INITIAL CONDITIONS, TYPE=STRESS keyword. A blank *STEP is then set to balance stresses in the steel, before the loading step is evoked. In runs FEA-GRI2 and FEA-GRI4, geometric initial imperfections have been modelled by introducing a transverse sinusoidal initial crookedness $y_i(x,z)$ to the compression flange of the form $y_i(x,z) = A(2x/b)\sin(2\pi z/a)$ (Niu et al. 2015), where $-b/2 \le x \le b/2$ is the lateral coordinate, $0 \le z \le L$ is the longitudinal coordinate, a is the length of the sine wave (Fig. 5.9b) taken as 200mm in the present study, and A is the imperfection amplitude assumed not to exceed $L/1000$ in a manner consistent with the out-of-straightness tolerances provided in CISC Handbook of Steel Construction (2016). For the present problem, two amplitudes have been considered: $A = L/1000 = 4mm$ (in run FEA GRI4) and $A = 2mm$ (in run FEA GRI2).

The load application scheme follows the arc length control scheme using the Ritz method. A mesh study is performed to determine the mesh beyond which no improvement is attained in the solution. The mesh is fully characterized by seven parameters $n_1,...,n_7$ as shown in Fig. 5.10. For the 4m span considered, the study showed that convergence is attained for a mesh with $n_1 = 20, n_2 = 8; n_3 = n_4 = n_6 = 4; n_5 = 40; n_7 = 500$, corresponding to over $1,7 \times 10^6$ DOFs.

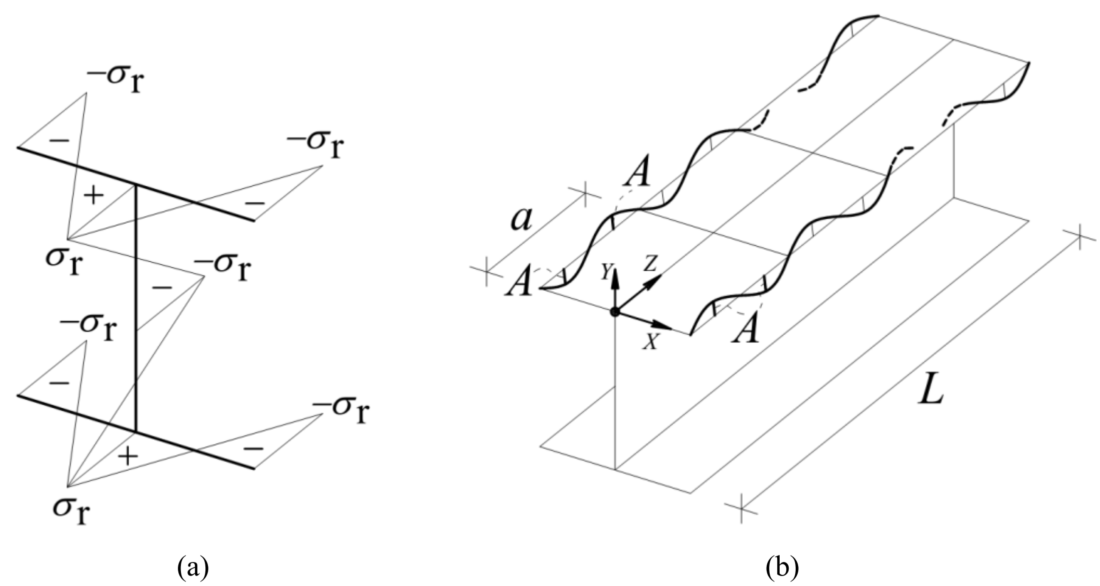

Figure. 5.9. (a) Residual stresses for the steel section and (b) Initial imperfection for the top flange

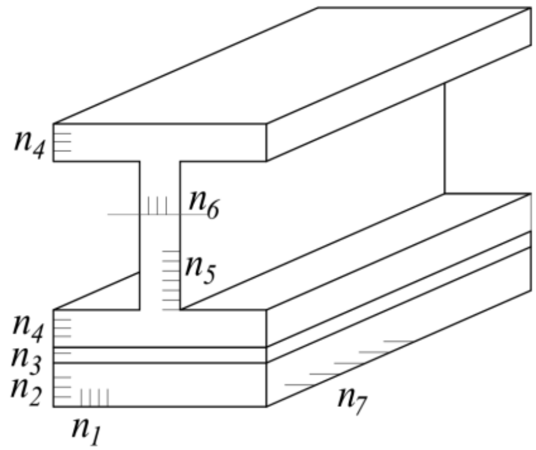

Figure. 5.10. Parameters defining the FE mesh

Results:

Moment deflection relationship: Figures 5.11a,b present the moment versus mid-span deflection for the bare beam and GFRP-strengthened beam as predicted by the 3D FEA. Overlaid on the figure is the plastic moment capacity $M = Z_x F_y$, where Z_x is the plastic section modulus. Also, overlaid on Fig.5.11a are the moment capacities as predicted by the detailed and simplified analytical models. The plastic moment capacity for the bare beam is $209\ kNm$. This value is asymptotically approached by the moment deflection curves predicted by the FEA-NG, FEA-G and FEA-GRI2 analyses. The imperfection in the FEA-GRI2 run initiates local buckling as manifested by the descending branch on Fig.5.11a.

For the strengthened beam (Figure. 5.11b), the points of failure at the end of each curve correspond to the point at which the GFRP plate attains the rupture strain. The peak moments predicted by FEA-NG, FEA-G, FEA-GR analyses are 254, 266, $266 kNm$, which are respectively 0.4%, 5.1%, 5.1% higher than the $253 kNm$ value predicted by the detailed analytical solution. When the geometric imperfections are included (in FEA-GRI2 and FEA-GRI4), the predicted peak moments drop to 230 and $225\ kNm$, respectively, which are 9.1% and 11.1% smaller than the predicted analytical solution. The above observations show that the moment capacity predicted by the detailed model is very close to that based on FEA-NG analysis (both analyses neglected the effect of geometric nonlinearity). The proximity of predictions of the FEA-G and FEA-GR suggest that residual stresses have a minor effect in a manner consistent with past studies (e.g., Nowzartash and Mohareb (2011), Siddique and El Damatty (2013). Thus, in the following examples, the effect of residual stresses will be omitted. Of interest is to note that the inclusion of geometric nonlinear effects in the analysis increases the peak moment predicted as evidenced by comparing the results of FEA-NG and FEA-G.

This increase in the observed FEA capacity is due to the action of the adhesive on the underside of the steel beam which tends to stretch the bottom flange. When the geometric nonlinear effects are omitted from the analysis in FEA-NG, the large rotation effect is not captured in the analysis, and the stretching action induced by the adhesive remains perfectly horizontal in the model. Thus, it does not contribute to the vertical load-carrying capacity. In contrast, when geometrically nonlinear effects are included in FEA-G, such shear stresses follow the deformed configuration of the beam and will have a vertical component (similar to a catenary action) with an upward component that tends to resist part of the vertical loads, thus causing a slight increase in the predicted moment capacity. A comparison of FEA-GR and FEA-GRI2 results indicates that initial imperfections have a slight detrimental effect and, as expected, this detrimental effect tends to grow as the amplitude of the initial imperfection increases (as evidenced by comparing the results of FEA-GRI2 and FEA-GRI4).

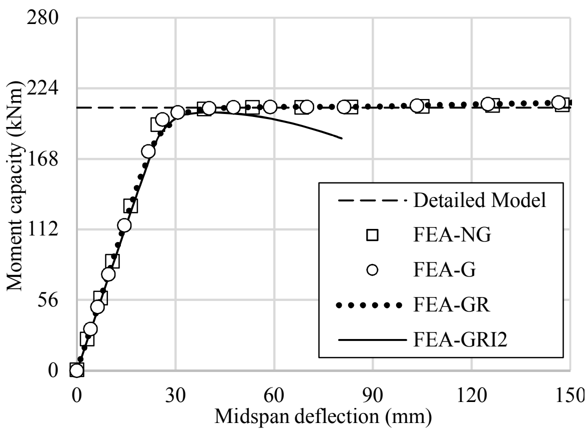

(a)

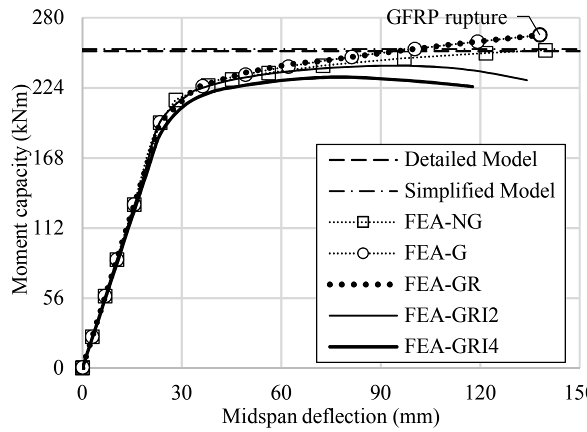

(b)

Figure. 5.11. Moment versus mid-span displacement (a) for the bare beam and (b) for the strengthened beam

<u>Stress profiles</u>: Figure. 5.12a-b provides the longitudinal normal stress and von Mises stress profiles at mid-span for the GFRP-strengthened as predicted by the FEA-G and FEA-NG. Overlaid on the figures are the stress profiles associated with the detailed and simplified models for comparison. Close proximity is observed between the profiles of FEA-NG and the detailed model. The inclusion of geometric nonlinearity in FEA-G is found to raise upward the neutral axis owing to the catenary action of the shear stresses acting at the underside of the bottom flange which tends to resist part of the transverse loads applied as discussed previously. This upward neutral axis shift causes a slight reduction in the net internal compressive force acting on the steel section alone, and a corresponding slight increase in the flexural resistance provided by the steel section. Figure 5.12a indicates that the

compressive stresses near the top of the steel section slightly exceed the yield strength F_y while the tensile stresses near the bottom are slightly lower than F_y . This is attributed to the presence of minor vertical stresses induced by the line load applied at the top flange which induces a biaxial compression state in the top of the section (which increases the admissible compressive yield stress limit according to the von-Mises yield criterion) and a biaxial tension/compression state in the bottom part (which reduces the admissible tensile yield stress limit). As expected, Figure 5.12b shows that the von-Mises stress is less than F_y as long as long as the beam does not deform into the strain hardening range.

The 3D FEA shows that the stresses $\tau_{xy}, \tau_{yz}, \tau_{xz}, \sigma_{xx}$ (XYZ coordinates are defined in Figure 5.9b) are negligible compared to the longitudinal and transverse normal stresses σ_{zz} and σ_{yy} . In such as case, the von Mises criterion yields the expression $\sigma_{zz} = \left[\sigma_{yy} \pm \sqrt{4F_y - 3\sigma_{yy}^2} \right] / 2$ for the maximal longitudinal stress attainable. The mid-span transverse normal stress σ_{yy} profiles predicted from FEA-G and FEA-NG (Fig. 5.12c) shown that σ_{yy} are generally compressive stresses, apart from a localized spike near the bottom edge. Thus, the magnitude of the peak longitudinal compressive stress attainable σ_{zz}^- is larger than that of the peak longitudinal tensile stress σ_{zz}^+ as evidenced by the inequality $\left|\sigma_{zz}^-\right| = 0.5\left|\sigma_{yy} - \sqrt{4F_y - 3\sigma_{yy}^2}\right| > \left|\sigma_{zz}^+\right| = 0.5\left|\sigma_{yy} + \sqrt{4F_y - 3\sigma_{yy}^2}\right|$ (Fig.5.12a). The inclusion of geometric nonlinear effects in FEA-G leads to higher transverse stresses $\sigma_{yy,G}$ compared to those based on FEA-NG $\sigma_{yy,NG}$, given that the catenary action is captured only in the geometric nonlinear analysis as previously discussed. If σ_{yy} is assumed to be negligible, one has $\sigma_{zz} \approx \pm F_y$ and one recovers a solution akin to that of present analytical model. The longitudinal stress based FEA-NG is $\sigma_{zz,NG} = 0.5\left(\sigma_{yy,NG} \pm \sqrt{4F_y - 3\sigma_{yy,NG}^2}\right)$ and that based on FEA-G is $\sigma_{zz,G} = 0.5\left(\sigma_{yy,G} \pm \sqrt{4F_y - 3\sigma_{yy,G}^2}\right)$. These equations in general satisfy the relations $\left|\sigma_{yy,G}\right| > \left|\sigma_{yy,NG}\right| > 0$ and one has $\left|\sigma_{zz,G}^-\right| > \left|\sigma_{zz,NG}^-\right| > \left|\sigma_{zz}^-\right|$, and $\left|\sigma_{zz,G}^+\right| < \left|\sigma_{zz,NG}^+\right| < \left|\sigma_{zz}^+\right|$ as depicted in Fig.5.12a.

The fact that the magnitude of the attainable modified compressive yield stress is higher than that of the modified tensile yield stress raises upwards the location of the neutral axis for a given bending moment as shown in Figs. 5.12a, b.

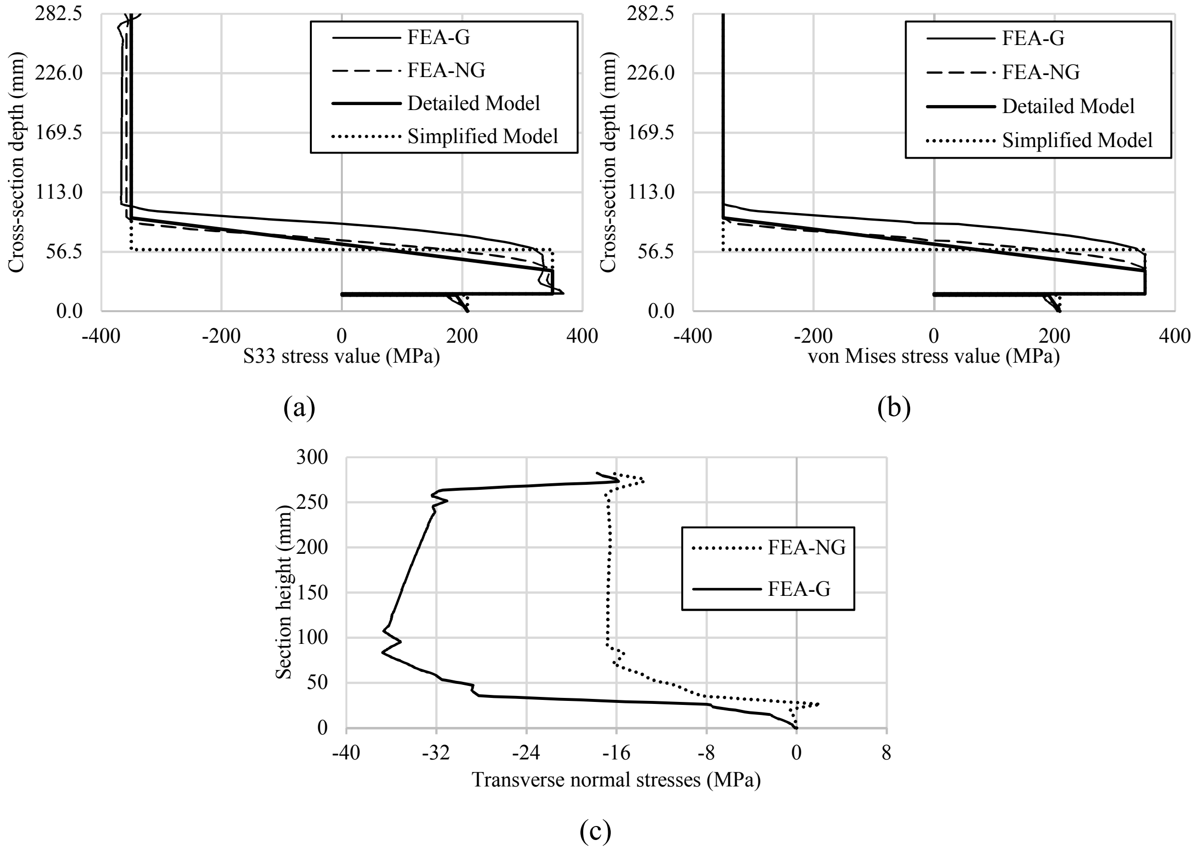

Figure. 5.12. (a) Longitudinal stresses and (b) von Mises stresses profiles at mid-span cross-section based on FEA analyses and present study, and (c) transverse normal stress profiles based on FEA analyses.

<u>Effect of beam spans:</u> To investigate the effect of the attained ultimate moments, two additional spans $L=3$ and $5\,m$ are investigated using the FEA-G solution and the detailed and simplified models. Negligible changes are attained in the ultimate moments predicted (Table 5.2, Fig.5.13).

Table 5.2. Ultimate load capacities of the strengthened beams with spans 3, 4 and 5m

Span (m)	FEA-G (2)	Detailed solution (3)	Simplified solution (4)	% difference (3-2)/2	% difference (4-2)/(2)

3.0	264	253	255	4.2	3.4
4.0	266	253	255	4.9	4.1
5.0	267	253	255	5.2	4.5

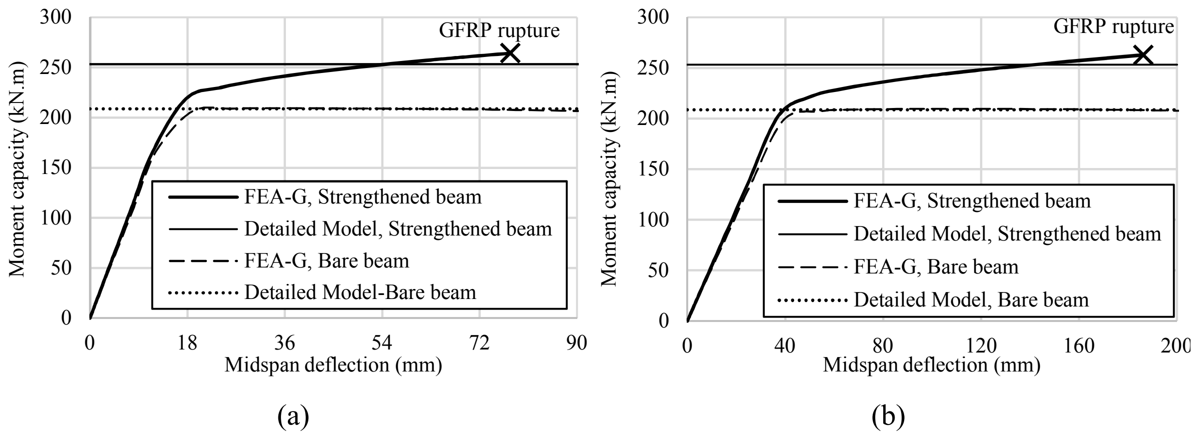

Figure. 5.13. Load displacement relationship for spans (a) L=3m and (b) L=5m

5.9.2. Example 2: Beam under a mid-span point load

The steel beam in Example 1 is reconsidered under the action of a mid-span point load (Fig. 5.14a). The beam is strengthened with a 19.0 mm-thick GFRP plate through a 1.0 mm-thick adhesive layer. Two beam spans are considered; 3m and 5m. The moment capacity versus mid-span deflection predicted by the detailed model are evaluated and compared to the FEA-G solution. A mesh study for the FEA-G model lead to a mesh similar to that in Example 1. The maximum capacities as determined from the detailed solution are $C_{s,\max} = 1990\,kN$,$T_{g,\max} = 586kN$, $Q_{a,\max} = 4570\,kN$ (for L=3m) and $Q_{a,\max} = 15,200kN$ (for L=5m). Both spans satisfy the conditions $T_{g,\max} < C_{s,\max}$ and $T_{g,\max} < Q_{a,\max}$, and thus the ultimate moment capacity is governed by GFRP rupture (Case 1). Figure 5.14b presents the moment capacity versus mid-span deflection as predicted by the FEA-G analysis for both spans. Overlaid on the Figure is the moment capacity predicted by the detailed solution (identical for both spans). As observed at the onset of GFRP rupture, the moment capacity predicted by the FEA-G solution for spans L=3 and 5m are 266 and 270 kNm, respectively, which are 1.9% and 3.3% higher than the moment capacity of 261 kNm as predicted by the detailed solution.

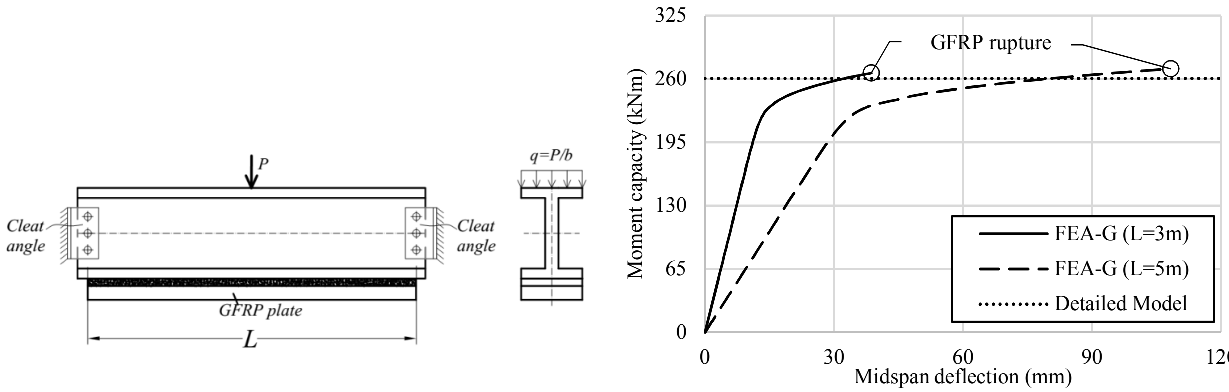

(a) (b)

Figure. 5.14. (a) Steel beams strengthened with GFRP plate, and (b) Load-deflection relationships

5.9.3. Example 3: Steel sections strengthened on the compression side:

Siddique and El Damatty (2013) reported the ultimate loads for beams with cross-section dimensions ($b = 150mm$, $t_f = 7.5mm$, $h_w = 150mm$, $t_w = 7.5mm$) with the compression flange strengthened by a GFRP plate as predicted by a shell element FEA model modified for the presence of GFRP (Siddique and El Damatty 2012). GFRP plate thicknesses ranged from 0 to 19mm. The validity of the model was assessed against experimental results (Siddique and El Damatty 2012, 2013) for steel beams strengthened with GFRP plates on both flanges. Span was taken as $L = 2.0m$. Two types of problems were solved; a cantilever with a tip load and a simply supported beam with two-point loads acting at third points. Steel had a yield strength of 350 MPa and an elastic modulus of 200 GPa, GFRP had a rupture strength 206.8 MPa and an elastic modulus 17.2 GPa while the adhesive shear strength was 35 MPa. The section meets compactness requirements as defined in ANSI AISC 360 (2016) (i.e., $h_w/t_w = 20 < 3.76\sqrt{E_s/F_y} = 89.9$ for the web and $b/2t_f = 10 < 0.56\sqrt{E_s/F_y} = 13.4$ for the flange) suggesting that the section is able to develop its fully plastic strength.

The maximum tensile force capacity in the steel is $T_{s,\max} = 1181\,kN$, the maximum shear capacity of the adhesive $Q_{a,\max} = 5250\,kN$ for the cantilever ($L_e = L$) and $1750\,kN$ for the simply supported beam ($L_e = L/3$), the largest compressive capacity in the GFRP (corresponding to 19mm plate) is $C_{g,\max} = 589.4\,kN$. In all cases, the conditions $C_{g,\max} < T_{s,\max}$ and $C_{g,\max} < Q_{a,\max}$ are satisfied, suggesting that the GFRP is the weakest link. Thus, GFRP failure governs the capacity of the strengthened system, which is consistent with the failure mode reported in Siddique and El Damatty

(2013) in all cases. As shown in Table 5.3, the present simplified model is found to slightly under-predict (i.e., within 2.6%) the ultimate capacities when compared to the experimentally verified finite element predictions of Siddique and El Damatty (2013). The results suggest (a) the validity of the present model, and (b) the possibility of applying the model to cases where the compression flange is strengthened.

Table 5.3. Comparison of ultimate load (kN) between present study and Siddique and El Damatty (2013)

Boundary condition [1]	GFRP plate thickness (mm) [2]	Simplified model [3]	Siddique and El Damatty (2013) [4]	(%) difference [4-3]/ [4]
Cantilever	0	41.0	41.0(1)	0.0
	6.35	45.1	46.3(1)	2.6
	19	50.9	52.1(1)	2.3
Simply supported	0	230.3	230.3(2)	0.0
	6.35	270.3	273.8(2)	1.3
	19	305.5	308.6(2)	1.0

(1) is based on Fig. 8a and (2) is based on Fig. 9a of Siddique and El Damatty (2013).

5.9.4. Example 4: Beam strengthened with a short GFRP plate

Statement of the problem:

The 4m span W250x45 steel beam in Example 1 is re-visited. Instead to the full-length GFRP adopted in Example 1, a shorter GFRP plate length is considered (Figure. 5.15). Two plate lengths are considered; $2L_e = 1.3m$ and $1.6m$. Also, a flexible adhesive is adopted, characteristic of adhesive behavior at high temperatures. Properties taken from Sahin and Dawood (2016): Young modulus $E_a = 472MPa$, a shear modulus $G_a = 182MPa$, an average rupture stress $\sigma_u \approx 9.7\,MPa$. The corresponding ultimate averaged-shear stress is thus $\tau_u = \sigma_u / \sqrt{3} = 5.6\ MPa$ (Pham 2018). The adhesive is assumed to attain failure when longitudinal strain attains 0.4 (Sahin and Dawood 2016). Two types of analyses are conducted FEA-NG and FEA-G.

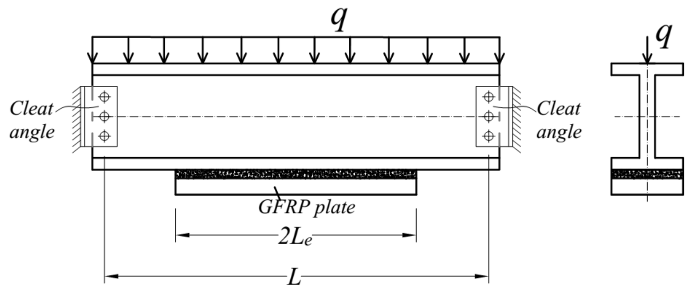

Figure. 5.15. Steel beam strengthened with a short GFRP plate under a line load

Description of the Simplified Model:

From Eqs. (5.5)-(5.7), the maximum net compressive forces in the steel, tensile force in the GFRP, and interfacial adhesive shear forces are obtained as $C_{s,\max} = 1990\,kN$, $T_{g,\max} = 479\,kN$, and $Q_{a,\max} = 269\ kN$ (for $L_e = 0.65m$) and $Q_{a,\max} = 332\,kN$ (for $L_e = 0.8m$). For both L_e values, the conditions $Q_{a,\max} < C_{s,\max}$ and $Q_{a,\max} < T_{g,\max}$ are satisfied. An adhesive shear failure mode is then expected (Case 2). From Eq. (5.16), one obtains $T_{s2} = 827\,kN$, which is greater than $T_{bf,\max} = 673\ kN$ and thus the neutral axis lies in the web. The value of d_{NA} is evaluated from Eq. (5.17) as $71\,mm$ and the capacity moment is determined from Eq. (5.18) as $245\ kNm$.

Results:

Moment capacity: Figure. 5.16a,b present the moment capacity versus mid-span deflection of beams for L_e =0.65m and 0.8m as obtained from the FEA-G, FEA-NG solutions and the analytical model for Case 2. For L_e =0.65m (Figure. 5.16a), the moment capacities predicted by FEA-NG, FEA-G are 233 and $234\ kNm$, respectively, while those based of the analytical model is $240\ kNm$, corresponding to differences of 2.9% and 2.5%. The slight overestimation of the simplified model is attributed in part to the assumption of a constant stress profile for the GFRP plate. As a result, the peak stress at the bottom GFRP fiber is overestimated by the simplified model as shown in Figure. 5.17a. For $L_e = 0.8\ m$ (Figure. 5.16b), the moment capacity obtained from the FEA-G is $248\,kNm$, while that based on FEA-NG $245\,kNm$. The later value coincides with that predicted by the present analytical model. The excellent agreement is consistent with the agreement of stresses in the GFRP between all three solutions (Figure. 5.17b) as will be discussed in the following section.

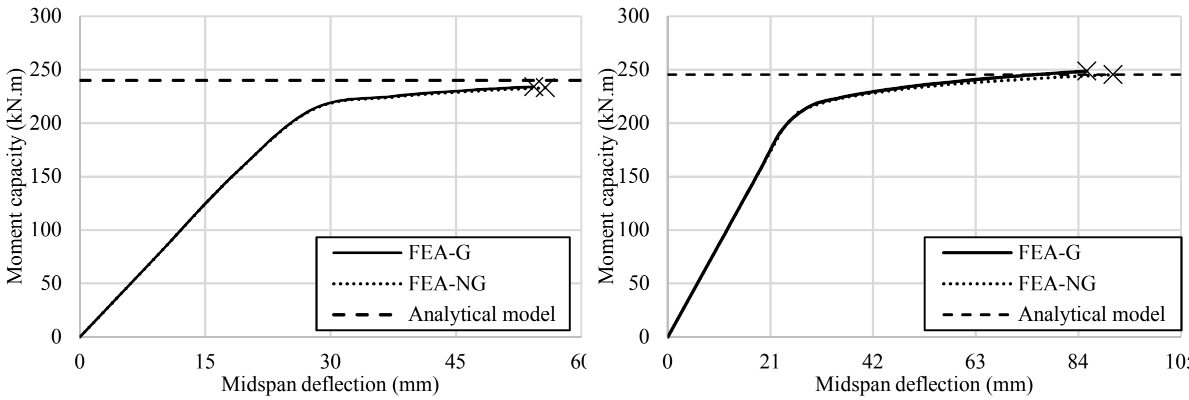

(a) (b)

Figure. 5.16. Moment versus mid-span deflection for (a) Le=0.65m and (b) Le=0.8m

Stress profiles: Figures 5.17a,b present the longitudinal normal stress and von Mises stress profiles for the mid-span section for the beams with $L_e = 0.65$m and 0.8m, as obtained from the FEA-NG, FEA-G and simplified solutions. For the stresses in steel, the plastified stresses at the top and bottom fibers predicted by all three solutions are in nearly perfect agreement. However, both FEA solutions predicted an elastic core in steel which is omitted by the simplified model. For $L_e = 0.65$m, the simplified model predicted a peak stress in the GFRP of 118 MPa while both FEA solutions predicted a value of 93 MPa, corresponding to a difference of 21%. For $L_e = 0.8$m, the simplified model predicted a peak stress in the GFRP of 145 MPa while the FEA solutions provided a value of 150 MPa, a 3.3% difference.

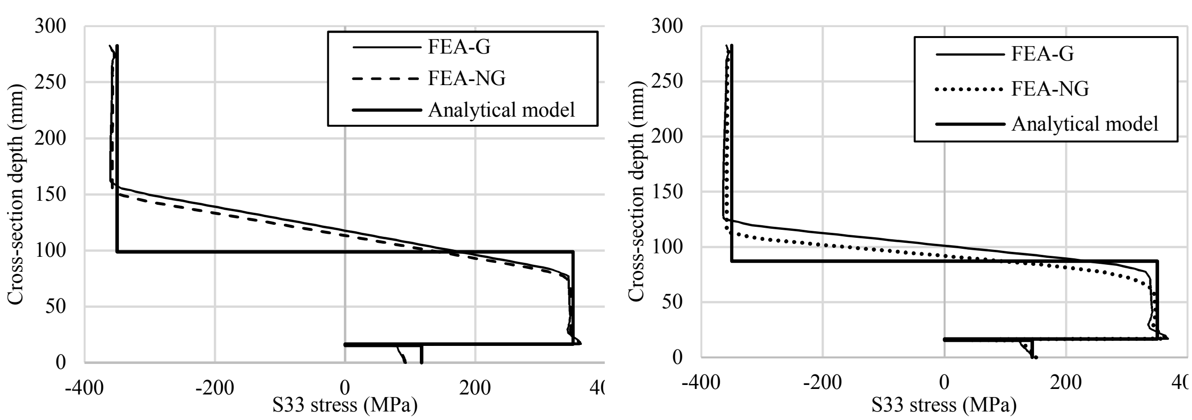

(a) (b)

Figure. 5.17. Longitudinal stress profiles at the onset of adhesive failure model (a) Le=0.65m and (b) Le=0.8m

Adhesive shear stress distribution: Figures 5.18a,b present the adhesive shear stress distribution along the left half of the adhesive bond line for $L_e = 0.65$m and 0.8m, respectively, as predicted from the FEA-NG, FEA-G models. Also, the idealized linear shear stress distribution with a peak value $\tau_u = 5.6\ MPa$ as postulated in Fig. 5.3 is overlaid on the figure for comparison. Peak shear stresses at the bond end and zero at mid-span are observed in all solutions. However, unlike the present idealized shear stress distribution, the FEA solutions predict nonlinear shear stress distributions those are attributed to the relatively high and localized peeling stress distributions along the beam span particularly near the bond ends. In spite of the significant difference observed between the stress distributions predicted by the FEA and the idealized linear shear stress distribution, the areas under both curves maybe approximately equivalent. Hence the assumption of $Q_{a,\max} = \tau_u b L_e / 2$ in Eq. (5.7) , though approximate, still provides a good estimate of the horizontal shear capacity of the adhesive.

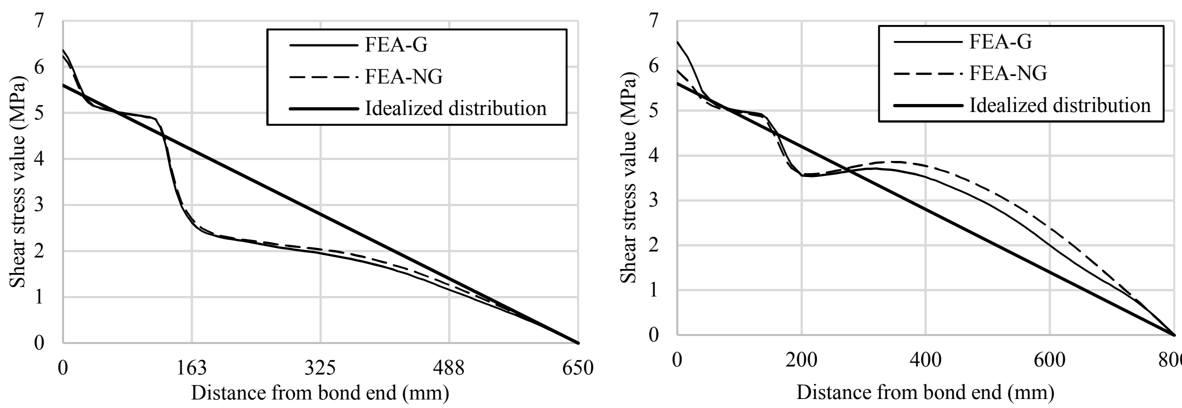

(a) (b)

Figure. 5.18. Shear stress distribution along the bond line for (a) Le=0.65m and (b) Le=0.8m

5.10. Summary and Conclusions

The main findings of the research are summarized in the following:

(1) The present study developed analytical solutions to predict the ultimate load capacity of compact wide flange steel beams strengthened with GFRP plates. Depending on the beam geometry and material properties of the adhesive and GFRP, three possible failure modes are identified; (1) GFRP rupture mode, (2) adhesive shear failure, or (3) full plastification of the steel section. The proposed analytical solutions provide a systematic methodology to identify the governing mode of failure and develop separate analytical expressions to quantify the ultimate moment based on each mode of failure.

(2) The examples investigated suggest that the GFRP rupture mode of failure is likely to govern the ultimate moment capacity of steel members strengthened by full-length GFRP plates. For this

particular mode of failure, two analytical techniques were developed (detailed and simplified) to predict the ultimate moment capacity. When the strengthening GFRP plates do not entirely cover the beam span and/or when the adhesive utilized is weak, a shear failure in the adhesive is conceivable. Practical section dimensions, GFRP thicknesses, and material properties would likely prevent steel section failure from governing the design.

(3) Consideration has been given to local buckling classification rules to ensure that the steel section develops its fully plastic strength prior to undergoing local buckling. The present web compactness requirements for flexural members remain valid for the strengthened steel sections under the ANSI AISC 360 (2016) and AS4100 (1998) design philosophy. In contrast, under the CAN-CSA S16 (2014) design philosophy, classification rules analogous to those of Class 2 beam-columns were advocated for strengthened steel sections.

(4) Strengthening a W250x45 steel cross-section by 15.5-mm thick GFRP plate with a rupture strength of 208.6 MPa was found increase ultimate moment capacity by 21%.

(5) Nonlinear 3D FEA analyses that incorporate material and geometric nonlinear effects, residual stresses and initial imperfections conducted under ABAQUS indicate that the incorporation of geometric nonlinear effects is beneficial for tension side strengthening as it captures the catenary action when the GFRP plate is in tension. The ultimate moment capacity predicted by the FEA were shown to be significantly influenced by initial out-of-straightness of the compression flange. In contrast, residual stresses were shown to have a rather minor influence on the ultimate moment capacity.

(6) The analytical predictions of the mode of failure and ultimate moment capacity were found to be in close agreement with 3D finite element predictions for cases where the tension flange is strengthened.

(7) Comparisons with experimentally verified shell FEA analyses by others showcase the validity of the analytical solutions for the cases where the compression flange is strengthened.

References

[5-1] ANSI/AISC 360-16, (2016), Specification for structural steel buildings, American Institute of Steel Construction (AISC), Chicago, IL.

[5-2] CSA, (2014), Limit states design of steel structures, Standard CAN/CSA-S16-14, Canadian Standards Association, Mississauga, Ontario.

[5-3] CISC Steel Construction Handbook, 11th Edition (2016), Canada Institute of Steel Construction.

[5-4] El Damatty, A.A. and Abushagur, M. (2003), Testing and modeling of shear and peel behavior for bonded steel/FRP connections, Thin-Walled Structures, 41(11), 987-1003

[5-5] El Damatty, A., Abushagur, M. and Youssef, M. A. (2005), Experimental and analytical investigation of steel beams rehabilitated using GFRP sheets, Steel&Comp.Str., 3(6),421-438.

[5-6] Hasham, A.S., and Rasmussen, K.J.R., (1998), Section capacity of thin-walled I-section beam columns, Journal of Structural Engineering, ASCE, 124(4), 351–359.

[5-7] Kadam, S., (2014), Failure criteria for evaluating Strength of Adhesive joints, Master thesis, Technische University Delft.

[5-8] Niu, S, Rasmussen, K.J.R., Fan, F., (2015), Local-global interaction buckling of stainless steel I-beams. II: Numerical study and design, J. Structural Eng., ASCE, 141(8), 04014195.

[5-9] Sahin, M.U., and Dawood, M., (2016), Experimental investigation of bond between high-modulus CFRP and steel at moderately elevated temperatures, Journal of Composites for Construction ASCE, 20 (6), 04016049.

[5-10] Shaat, A., and Fam, A., (2007), Fiber-element model for slender HSS columns retrofitted with bonded high-modulus composites, Journal of Structural Engineering, 133(1), 85-95.

[5-11] Siddique, M.A.A. and El Damatty, A.A. (2012), Enhancement of buckling capacity of steel plates strengthened with GFRP plates, Thin-Walled Structures, 60(16), 154-162.

[5-12] Siddique, M.A.A. and El Damatty, A.A. (2013), Improvement of local buckling behaviour of steel beams through bonding GFRP plates, Composite Structures, 96(6), 44-56.

[5-13] Standards Association of Australia (SAA), Steel Structures, AS4100-1998, SAA, Australian Institute of Steel Construction, Sydney, Australia (1998).

[5-14] Pham, P.V. and Mohareb, M. (2014), A shear deformable theory for the analysis of steel beams reinforced with GFRP plates, Thin-Walled Structures, 85, 165-182.

[5-15] Pham, P.V and Mohareb, M. (2015), Nonshear Deformable Theory for Analysis of Steel Beams Reinforced with GFRP Plate Closed-Form Solution, J. Str. Eng., ASCE, 141(12), 04015063.

[5-16] Pham, P.V and Mohareb, M., and Fam, A., (2017), Elastic Analysis of Steel Beams Strengthened with GFRP Plates Including Preexisting Loading Effects, Journal of Structural Engineering ASCE, 143(12), 04017163.

[5-17] Pham, P.V., (2018), Analysis of Steel Beams Strengthened with Adhesively-bonded GFRP Plates, Ph.D. thesis, Dept. of Civil Engineering, University of Ottawa, Ottawa, ON, Canada.

[5-18] Pham, P.V., Mohareb, M., and Fam, A., (2018), Finite element formulation for the analysis of multilayered beams based on the principle of stationary complementary strain energy, Engineering Structures, 167C, 287-307.

[5-19] Youssef, M. (2006), Analytical Prediction of the Linear and Nonlinear Behaviour of Steel Beams Rehabilitated using FRP Sheets. Engineering Structures, 28(6), 903-911.

Chapter 6: Elastic Analysis of Steel Beams Strengthened with GFRP Plates Including Pre-existing Loading Effects

Abstract

The present study develops a theory for the elastic analysis of a pre-loaded wide flange steel beam, strengthened with two Glass Fiber Reinforced Polymer (GFRP) plates bonded to both flanges, then subjected to additional loads. Starting with the principle of stationary potential energy, the governing equilibrium equations and corresponding boundary conditions are formulated prior to and after GFRP strengthening. The resulting theory involves four coupled equilibrium equations and 10 boundary conditions. A general closed form solution is then provided for general loading and boundary conditions. Detailed comparisons with three-dimensional finite element solutions show that the theory provides reliable predictions for the displacements and stresses. A parametric study is then developed to quantify the effects of strengthening, GFRP plate thicknesses, and pre-existing loads, on the capacity of the strengthened beam.

Key words: steel beam, GFRP, strengthening, closed form solution, loading history

6.1. Introduction and Background

Strengthening steel structures using adhesively bonded FRP plates has been extensively studied in recent years due to the advantages this method offers; primarily the ease and speed of installation, and lightweight, compared to welded or bolted steel plates. The majority of studies focused on the use of carbon-FRP (CFRP) plates because of their higher Young modulus which can approach or exceed that of steel (Miller et al. 2001, Zhao and Zhang 2007, Harris and El-Tawil 2008, and Fam et al. 2009). GFRP plates, on the other hand, are considerably lower in cost than CFRP plates and their lower elasticity modulus can be compensated for by the fact that GFRP plates are typically thicker (El Damatty and Abushagur 2003 and El Damatty et al. 2003) than CFRP sheets. Thick GFRP plates with low elasticity modulus typically offer a higher flexural stiffness compared to thin CFRP plates and thus can be advantageous in strengthening thin compression flanges against local buckling (Aguilera and Fam 2013). Additionally, when in contact with steel, GFRP does not induce galvanic corrosion.

The beneficial effect of strengthening the tensile flanges of the W-steel beam sections is widely reported in the literature. Siddique and El Damatty (2013) reported a load capacity increase of 15% whereas deflection at failure increased by 99% for cantilevers. The beneficial effect of GFRP was observed in experiments by El Damatty and Abushagur (2003), Holloway et al. (2006), Teng and Hu (2007), Correia et al. (2011), Siddique and Damatty (2012, 2013), Aguilera and Fam (2013), and

Torabizaheh (2013). By using a single 19mm thick-GFRP plate on the tension side of a W150x13 cantilever, Pham and Mohareb (2015b) predicted a reduction in deflection and stresses of about 29% and 11%, respectively.

As indicated, GFRP plates can be relatively thick and are thus potentially effective on the compression side of a steel beam. Accord and Earl (2006) used four 6.35mm-thick GFRP plates to strengthen the compressive flange of a W-steel beam. The GFRP plates had an elasticity modulus in compression of 27.6 GPa. El Damatty and Abushagur (2003) tested 19mm-thick GFRP plates in shear lap tests. The plates had a compressive strength of $207\ MPa$ and a modulus of elasticity in compression of 17 GPa

Strengthening of the compression zone of steel beams using GFRP plates was also reported in Westover (1998), Correia et al. (2011), and Elchalakani and Fernando (2012). Compressive failures of GFRP plates were observed to be associated with layer delamination (Westover, 1998). Correia et al. (2011) provided a review of the compressive properties of pultruded GFRP composites and indicated that the compressive strength ranges from 20% to 80% of the tensile strength. Also, in Correia et al. (2011), the GFRP modulus of elasticity in compression was reported to be 80% of the tensile modulus.

A few studies analyzed beams strengthened with GFRP plates (El Damatty and Abushagur 2003, Linghoff et al. 2010a, 2010b, and Pham and Mohareb 2014, 2015a, 2015b). These studies focus on the response of steel beams strengthened with a single GFRP plate, either on the tensile or the compressive side. Another common theme among the above studies is the fact that they do not capture the loading history nor do they capture initial stresses that may exist in the beam prior to and during strengthening.

In some beam strengthening applications, it is possible to fully unload an existing beam before retrofitting. In other cases, the existing loads cannot be fully removed, i.e., initial stresses and strains may exist in the steel beam at the time of strengthening. The effect of preloading on the strength of the retrofitted beam has been experimentally investigated for concrete beams strengthened with CFRP (Bonacci and Maalej 2000, Wenwei and Guo 2006, Wu et al. 2007, Kim and Shin 2011, and Richardson and Fam 2014). In some cases, the presence of preloading was shown to lower the capacity of the strengthened beam. Experimental investigations of preloaded I-section steel beams were also reported by Liu and Gannon (2009) and Qing et al. (2015) and showed a reduction in strength.

Analytical models for concrete beams strengthened with FRP plates which incorporate the effect of initial stresses/strains were reported in Wenwei and Guo (2006) and GangaRao et al. (2007). However, both studies adopted the transformed section method and are applicable for the case of full interaction. In the present study, given the large difference between the elastic moduli of the adhesive, GFRP and steel, only partial interaction is typically achieved and the transformed section solutions typically overestimates the strength and stiffness of the composite system. Ghafoori and Motavalli (2013) developed analytical models for the analysis of wide flange steel beams strengthened by a single pre-tensioned CFRP plate at the tensile flange, but did not capture the effect of preloading in the steel beam.

When both sides of a steel beam are accessible, as may be the case in open industrial structures or pipe racks, it may be beneficial to strengthen steel beams by bonding GFRP plates to both flanges (e.g., Youssef 2006, Shaat and Fam 2009, Elchalakani and Fernando 2012, Quin et al. 2015). For situations where only a single flange is accessible from the outside, the present model is able to determine the response of the beam by assigning low thicknesses and elastic constants to the absent GFRP and adhesive layer.

To the author's knowledge, no model is available for predicting the response of such systems. The present study aims to fill this gap by developing a theory for steel beams strengthened by two GFRP plates. The theory also captures the effects of partial interaction and pre-existing loads that may exist at the time of strengthening. The analysis is restricted to the elastic response of the strengthened system. As such, failure modes, whether by steel yielding, local buckling, GFRP plate through-thickness delamination, or plate de-bonding from steel, are beyond the scope of the present work.

When such modes are not critical, the present solution is expected to provide means to quantify the capacity of beams with non-compact (class 3) cross-sections strengthened with GFRP plates. When used for compact sections (classes 1 and 2), the theory is expected to predict only a conservative lower bound of the strength since it does not account for material plastic effects. From a serviceability viewpoint, the present model is expected to predict deflections at service load levels for beams with compact and non-compact sections as the strengthened system is expected to deform within the elastic range.

6.2. Sequence of Loading and Strengthening

The loading and strengthening history for a steel beam are shown in Fig.6.1a through configurations 1 to 6. Four deformation steps A-D are identified:

Throughout Step A, the steel beam, referred to here as element *c*, is subjected to a gradually changing load from $q_{c,1}(z)=0$ to $q_{c,2}(z)$, where z is a longitudinal coordinate along the beam axis. Under the applied load, the beam deforms from Configuration 1 and attains equilibrium at Configuration 2 through a transverse deflection $v_2(z)$.

Throughout Step B (from Configurations 2 to 4), two longitudinally-straight GFRP plates a and e are added for strengthening (Configuration 3). The difference in curvature between the straight GFRP plates and bent steel beam means that they are not in full contact along the span of the beam, causing gaps $\Delta_a(z)$ and $\Delta_e(z)$. To eliminate these gaps, adhesive layers b and d are first applied, and plates a and e are strapped to beam c and are thus forced to bend through additional temporarily loads $q_{a,4}(z)$ and $q_{e,4}(z)$ (Configuration 4 and Fig. 6.1b). Loads $q_{a,4}(z)$ and $q_{e,4}(z)$ are intended to close the gaps $\Delta_a(z)$ and $\Delta_e(z)$, and are kept until bonding is fully developed between the steel flanges and GFRP.

Throughout Step C (from Configurations 4 to 5), external loads $q_{a,4}(z)$ and $q_{e,4}(z)$ due to strapping forces are removed (i.e., $q_{a,5}(z)=q_{e,5}(z)=0$) while the original external load acting on the steel beam is assumed to remain (i.e., $q_{c,5}(z)=q_{c,2}(z)$). The composite system then moves to a new equilibrium position (Configuration 5) characterized by four displacement fields; namely the total longitudinal displacement at the centroid of the top GFRP plate $w_{a,5}(z)$, that of the steel beam centroid $w_{c,5}(z)$, that of the bottom GFRP plate centroid $w_{e,5}(z)$ and the transverse deflection $v_5(z)$ of the system, which is assumed equal to that of the steel beam (Fig. 6.2 where step i is set to 5). In the general case where the GFRP plates have different geometries and/or material properties, the internal axial forces in both plates have different magnitudes and an internal force must be induced in the steel beam to enforce the internal axial force equilibrium condition, and hence the presence of displacement $w_{c,5}(z)$. Because the adhesive layers provide partial interaction between the GFRP plates and the steel beam, a section initially plane for the composite system exhibits a kink at the adhesive locations.

In Step D (from Configurations 5 to 6), an additional operating external load $q_6(z)$ is applied to the strengthened beam. Under the new load, the composite beam attains equilibrium at Configuration 6 through total displacements $w_{a,6}(z)$, $w_{c,6}(z)$, $w_{e,6}(z)$ and $v_6(z)$ (Fig. 6.2 in which the configuration $i=5$ and configuration $j=i+1=6$). The loads and displacements corresponding to each configuration are summarized in Table 6.1.

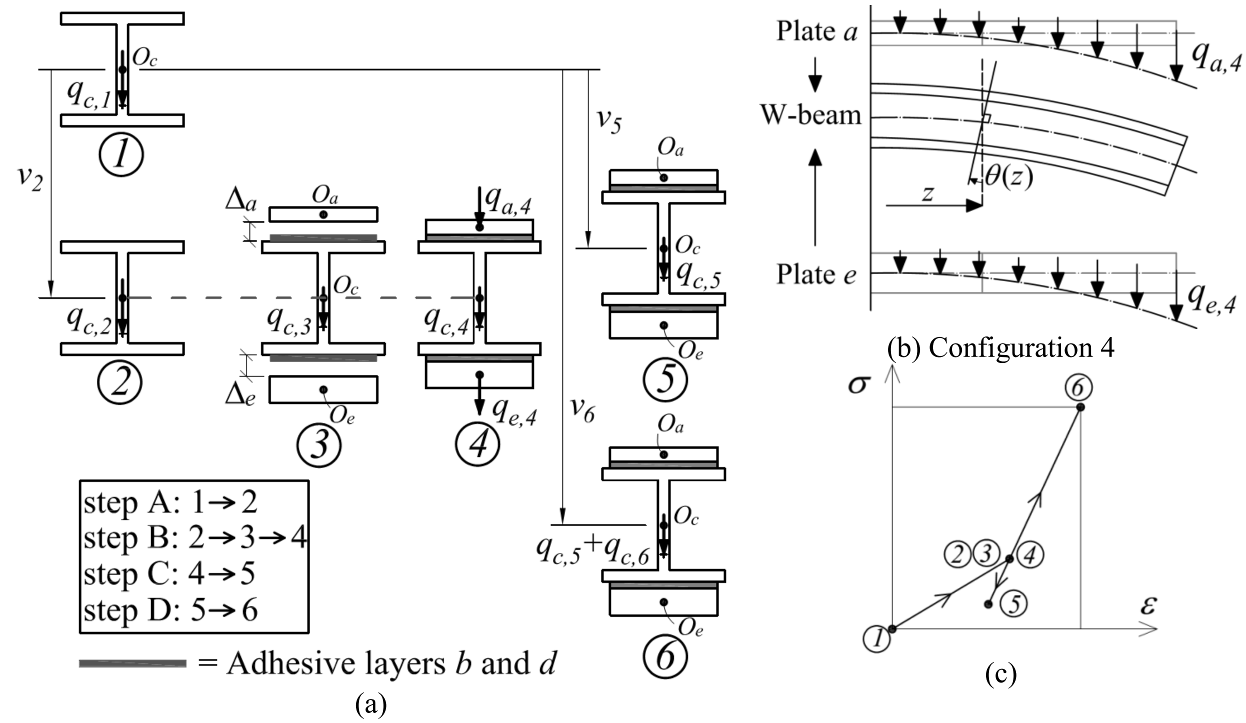

Figure 6.1. Strengthening and Loading History (a) Configurations, (b) Shaping GFRP plates and bonding them to W-beam (Step B), and (c) Stress path of a point within the steel beam

Table 6.1. Summary of loads and displacements in configurations 1-6

	Step A		**Step B**		**Step C**	**Step D**
Configuration	**1**	**2**	**3**	**4**	**5**	**6**
Total Loads						
GFRP plate a	-	-	0	$q_{a,4}$	0	0
Steel beam c	$q_{c,1}=0$	$q_{c,2}$	$q_{c,3}=q_{c,2}$	$q_{c,4}=q_{c,2}$	$q_{c,5}=q_{c,2}$	$q_{c,2}+q_{c,6}$
GFRP plate e	-	-	0	$q_{e,4}$	0	0
Sum	0	$q_{c,2}$	$q_{c,2}$	$q_{a,4}+q_{c,2}+q_{e,4}$	$q_{c,2}$	$q_{c,2}+q_{c,6}$
Total Transverse Displacements (measured relative to configuration 1)						
GFRP plate a	-	-	0			
Steel beam c	0	v_2	$v_3=v_2$	$v_4=v_2$	v_5	v_6
GFRP plate e	-	-	0			
Total Longitudinal Displacement (measured relative to configuration (1) for steel beam or relative to configuration (4) for GFRP plates)						
GFRP plate a	-	-	0	0	$w_{a,5}$	$w_{a,6}$
Steel beam c	0	0	0	0	$w_{c,5}$	$w_{c,6}$
GFRP plate e	-	-	0	0	$w_{e,5}$	$w_{e,6}$

6.3. General Model and Special Cases

The aim is to develop a generic model to trace the entire equilibrium path of the loading and strengthening history described in the previous section. At a given equilibrium point i of the trajectory 1-2-3-4-5-6, the composite system is assumed to be in equilibrium under a transverse load $\overline{q}_i\left(z\right)$. The equilibrium configuration for the system (denoted as Configuration i) is assumed to be known and fully characterized by the known displacement fields $\overline{w}_{a,i}\left(z\right)$, $\overline{w}_{c,i}\left(z\right)$, $\overline{w}_{e,i}\left(z\right)$, $\overline{v}_i\left(z\right)$ (Fig.6.2a). The system is then assumed to be subjected to an additional transverse load $\overline{q}_j\left(z\right)$. Under the new load, the system reaches a new equilibrium configuration (denoted as Configuration $j=i+1$). The system is assumed to undergo additional displacements $\overline{w}_{a,j}\left(z\right)$, $\overline{w}_{c,j}\left(z\right)$, $\overline{w}_{e,j}\left(z\right)$, $\overline{v}_j\left(z\right)$ (Fig.6.2). Given $\overline{q}_i\left(z\right)$, $\overline{q}_j\left(z\right)$, $\overline{w}_{a,i}\left(z\right)$, $\overline{w}_{c,i}\left(z\right)$, $\overline{w}_{e,i}\left(z\right)$, and $\overline{v}_i\left(z\right)$, it is required to determine the $\overline{w}_{a,j}\left(z\right)$, $\overline{w}_{c,j}\left(z\right)$, $\overline{w}_{e,j}\left(z\right)$, $\overline{v}_j\left(z\right)$.

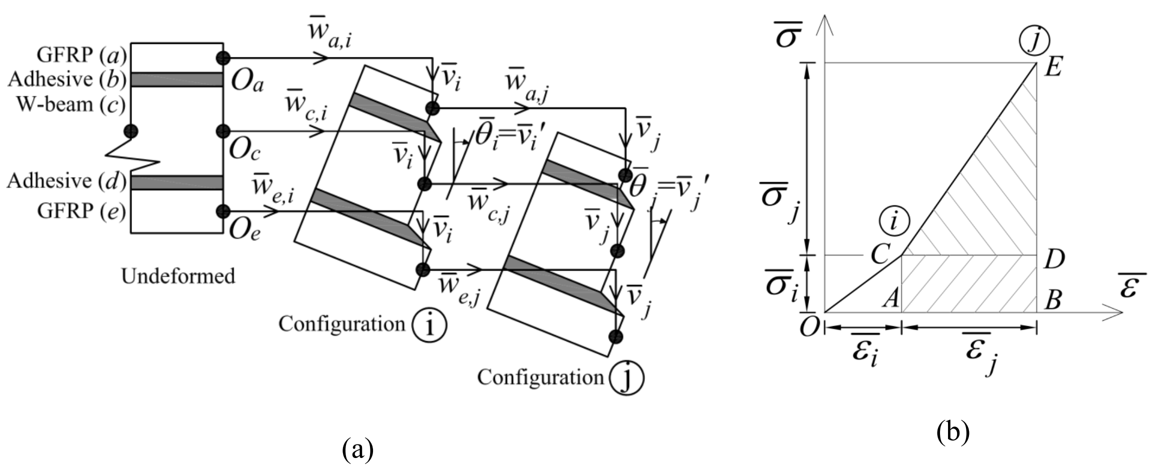

Figure 6.2. General model of the composite beam in going from Stage *i* to Stage *j* (a) Kinematics, and (b) Stress-strain schematic

The deformations of step A can be obtained as special case of the general model by entirely eliminating the GFRP plates and adhesive layers from the composite section and setting loads $\overline{q}_i=q_{c,1}=0$ and $\overline{q}_j=q_{c,2}$. Displacement fields $\overline{w}_{c,i}\left(z\right)$ and $\overline{v}_i\left(z\right)$ at Configuration i are set to zero, while displacement fields $\overline{w}_{c,j}\left(z\right)$ and $\overline{v}_j\left(z\right)$ at Configuration j are set to 0 and v_2, respectively.

Also, the deformations of step B can be obtained from the general model by entirely eliminating the adhesive layers (i.e., GFRP plates and W-beam works independently) and setting loads $\overline{q}_i = q_{c,2}$. Also, because the transverse displacements of both GFRP plates and W-beam are assumed equal, load potential energy gains of forces $q_{a,4}$ and $q_{e,4}$ are assumed to undergo the same transverse displacement as that of $q_{c,2}$ and thus $\overline{q}_j = q_{a,4} + q_{e,4}$. Longitudinal displacement fields $\overline{w}_{a,i}(z)$, $\overline{w}_{c,i}(z)$, $\overline{w}_{e,i}(z)$, $\overline{w}_{a,j}(z)$, $\overline{w}_{c,j}(z)$, $\overline{w}_{e,j}(z)$ at both Configurations i and j are set to be zero, while transverse displacement fields $\overline{v}_i(z)$ and $\overline{v}_j(z)$ are set to be v_2.

Also, from the general model, by eliminating adhesive layers in only Configuration i and setting loads $\overline{q}_i = q_{a,4} + q_{c,4} + q_{e,4}$ and $\overline{q}_j = -q_{a,4} - q_{e,4}$, the displacements throughout Step C can be recovered. Longitudinal displacements $\overline{w}_{a,i}(z)$, $\overline{w}_{c,i}(z)$ and $\overline{w}_{e,i}(z)$ in Configuration i are set to zero while transverse displacement $\overline{v}_i(z)$ is set to v_2. Also, longitudinal displacements $\overline{w}_{a,j}(z)$, $\overline{w}_{c,j}(z)$ and $\overline{w}_{e,j}(z)$ in Configuration j are respectively set to $w_{a,5}$, $w_{c,5}$ and $w_{e,5}$, while transverse displacement $\overline{v}_j(z)$ is set equal to $(v_5 - v_2)$.

Finally, Step D can be considered as the general case when loads $\overline{q}_i = q_{c,5}$ and $\overline{q}_j = q_{c,6}$ are set. Also, displacement fields $\overline{w}_{a,i}(z)$, $\overline{w}_{c,i}(z)$, $\overline{w}_{e,i}(z)$ and $\overline{v}_i(z)$ in Configuration i are respectively taken as $w_{a,5}$, $w_{c,5}$, $w_{e,5}$ and v_5 while displacement fields $\overline{w}_{a,j}(z)$, $\overline{w}_{c,j}(z)$, $\overline{w}_{e,j}(z)$, $\overline{v}_j(z)$ in Configuration j are taken as $(w_{a,6} - w_{a,5})$, $(w_{c,6} - w_{c,5})$, $(w_{e,6} - w_{e,5})$ and $(v_6 - v_5)$.

6.4. Dimensions and Coordinates

The dimensions of the five-layer cross-section are shown in Fig. 6.3. The thicknesses of GFRP plate a and adhesive layer b are t_a and t_b while their width b_a is identical. Also, the thicknesses of GFRP plate e and adhesive layer d are t_e and t_d, and their width b_e is also identical. Wide flange beam c has a depth h_c, a flange width b_c, a flange thickness t_c, and a web thickness w_c. A global right-hand coordinate system $OXYZ$ is selected as shown. Local coordinates (s_k, n_k) where $k = a, b, c, d, e$ are also selected for each layer in which s_k is oriented in the tangential direction to the contour, and n_k is oriented in the normal direction to the contour.

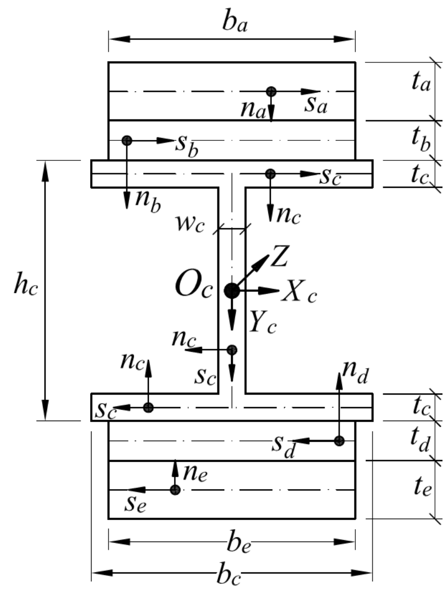

Figure 6.3. Geometric designations and global and local coordinates for wide flange beam, GFRP plates *a* and *e*, and adhesive layers *b* and *d*

6.5. Assumptions

The steel beam and GFRP plates are considered as three Gjelsvik beams (Gjelsvik 1981). For each of the two components, the following assumptions are made:

(i) The shear strain γ_{sz} of the middle surface is assumed to vanish,

(ii) The middle surface contours of all three sections do not deform in their own plane,

(iii) Each component behaves as a thin shell, in line with the Kirchhoff assumption that straight lines remain normal to the middle surface during deformation,

(iv) Forces applied by the straps to bring the intially straight GFRP plates into contact with the curved steel beam are assumed to preserve the initial curvature of the steel beams.

The following additional assumptions are made regarding the adhesive material:

(v) Perfect bond is assumed at the adhesive-GFRP and adhesive-steel interfaces,

(vi) The adhesive is treated as an elastic material with a small modulus of elasticity compared to those of the steel and GFRP. Thus, adhesive normal stresses in the longitudinal direction are considered negligible compared to those of the GFRP and steel,

(vii) The thickness of the adhesive is assumed to remain constant throughout deformation,

(viii) Within the steel and GFRP, only the normal stresses in the longitudinal direction and the shear stresses in the tangential plane are assumed to contribute to the internal strain energy while contributions of other stresses are assumed to be comparatively negligible,

(ix) Displacement fields at a point within the adhesive, are linearly interpolated from those at the steel-adhesive and GFRP-adhesive interfaces.

The following assumption is made regarding the constitutive behavior of the materials:

(x) Steel is assumed is assumed to remain in the elastic range. The model is not intended to capture the post-yield response of the steel. In a strict sense, GFRP can exhibit orthotropic properties. However, given that only the longitudinal normal stresses and the shear stresses in the tangential plane are assumed to contribute to the internal strain energy (assumption viii), its relevant constitutive properties are fully characterized through only two constitutive constants; the longitudinal elastic modulus and a single shear modulus, in a manner similar to linearly elastic isotropic material. Thus, it is common to treat GFRP and CFRP as an isotropic material (e.g., Miller et al. 2001, El Damatty and Abushagur 2003, and Deng et al. 2004).

The following assumption is made regarding the nature of analysis:

(xi) Geometric and material non-linear and inertial effects as well as failure modes including yielding, buckling, delamination, and de-bonding are beyond the scope of the model.

6.6. Formulation

6.6.1. Kinematic Relations

The transverse and longitudinal displacements of a generic point within each layer are respectively denoted as $\bar{v}_k(z)$ and $\tilde{w}_k^*(s,n,z)$. These displacements are expressed in terms of centroidal displacement fields, coordinate $y_c(s)$ and tangential angle $\alpha(s_c)$ to the section contour:

$$\tilde{w}_k^* = \begin{cases} \bar{w}_{a,k}(z) - n_a \bar{v}_k'(z) & (n_a, z) \in \Omega_a \\ \bar{w}_{c,k}(z) - \left[y(s_c) + n_c \cos\alpha(s_c)\right]\bar{v}_k'(z) & (s_c, n_c, z) \in \Omega_c \\ \bar{w}_{e,k}(z) + n_e \bar{v}_k'(z) & (n_e, z) \in \Omega_e \end{cases} \qquad (k = i \text{ or } j) \tag{6.1}$$

where k denotes configurations "i" or "j" as defined in Fig. 6.2 and Ω_l denotes the volumes of components $l = a, c, e$. The longitudinal displacement within adhesive layers b and d are linearly interpolated from the displacements at the interfaces with GFRP and steel, i.e.,

$$\begin{Bmatrix} \tilde{w}_k^*(n_b,z) \\ \tilde{w}_k^*(n_d,z) \end{Bmatrix} = \left(\frac{1}{2}-\frac{n_b}{t_b}\right)\begin{Bmatrix} \overline{w}_{a,k}(z)-\dfrac{t_a}{2}\overline{v}_k'(z) \\ \overline{w}_{e,k}(z)+\dfrac{t_e}{2}\overline{v}_k'(z) \end{Bmatrix} + \left(\frac{1}{2}+\frac{n_b}{t_b}\right)\begin{Bmatrix} \overline{w}_{c,k}(z)+\dfrac{h_c}{2}\overline{v}_k'(z) \\ \overline{w}_{c,k}(z)-\dfrac{h_c}{2}\overline{v}_k'(z) \end{Bmatrix} \tag{6.2}$$

6.6.2. Strain-displacement relations

Longitudinal strains $\varepsilon = \partial \tilde{w}^* / \partial z$ is provided for each component as

$$\varepsilon_k = \begin{cases} \overline{w}_{a,k}'(z) - n_a \overline{v}_k''(z) & (n_a, z) \in \Omega_a \\ \overline{w}_{c,k}'(z) - \left[y(s_c) + n_c \cos\alpha(s_c) \right] \overline{v}_k''(z) & (s_c, n_c, z) \in \Omega_c \\ \overline{w}_{e,k}'(z) + n_e \overline{v}_k''(z) & (n_e, z) \in \Omega_e \end{cases} \tag{6.3}$$

Also, the transverse shear strains within adhesive layers is given by $\gamma = \partial \tilde{w}^* / \partial n + \partial \overline{v} / \partial z$, i.e.,

$$\begin{aligned} \gamma_k(n_b,z) &= -\frac{1}{t_b}\overline{w}_{a,k}(z) + \frac{1}{t_b}\overline{w}_{c,k}(z) + \frac{t_a + h_c + 2t_b}{2t_b}\overline{v}_k'(z); \quad n_b \in \Omega_b \\ \gamma_k(n_d,z) &= -\frac{1}{t_d}\overline{w}_{e,k}(z) + \frac{1}{t_d}\overline{w}_{c,k}(z) - \frac{t_e + h_c - 2t_d}{2t_d}\overline{v}_k'(z); \quad n_d \in \Omega_d \end{aligned} \tag{6.4}$$

6.6.3. Stress-displacement relations

Assuming linear isotropic material responses, the longitudinal stresses are related to the longitudinal normal strain through:

$$\sigma_k = \begin{cases} E_a \left[\overline{w}_{a,k}'(z) - n_a \overline{v}_k''(z) \right] & n_a \in \Omega_a \\ E_c \left[\overline{w}_{c,k}'(z) - \left[y(s_c) + n_c \cos\alpha(s_c) \right] \overline{v}_k''(z) \right] & s_c \in \Omega_c \\ E_e \left[\overline{w}_{e,k}'(z) + n_e \overline{v}_k''(z) \right] & n_e \in \Omega_e \end{cases} \tag{6.5}$$

and shear stresses within the adhesive layers are:

$$\begin{aligned} \tau_k(n_b,z) &= G_b\left[-\frac{1}{t_b}\overline{w}_{a,k}(z) + \frac{1}{t_b}\overline{w}_{c,k}(z) + \frac{t_a + h_c + 2t_b}{2t_b}\overline{v}_k'(z) \right]; \quad n_b \in \Omega_b \\ \tau_k(n_d,z) &= G_d\left[-\frac{1}{t_d}\overline{w}_{e,k}(z) + \frac{1}{t_d}\overline{w}_{c,k}(z) - \frac{t_e + h_c - 2t_d}{2t_d}\overline{v}_k'(z) \right]; \quad n_d \in \Omega_d \end{aligned} \tag{6.6}$$

where E_l are the moduli of elasticity of layers $l = a, c, e$, and G_l are shear moduli of layers b, d

6.6.4. Total Potential Energy

Under pre-existing loads $\overline{q}_i(z)$, equilibrium configuration i, as characterized by displacement fields $\overline{w}_{a,i}(z), \overline{w}_{e,i}(z), \overline{v}_i(z)$, corresponding to the initial stresses $\overline{\sigma}_i$ and strains $\overline{\varepsilon}_i$, is assumed to be known. The system is then subjected to additional loads $\overline{q}_j(z)$. In going from configuration i to j, the potential energy loss consists of two components: (1) Component $\overline{V}_j$ caused by load $\overline{q}_i(z)+\overline{q}_j(z)$ undergoing transverse displacement $\overline{v}_j(z)$, and (2) Components caused by axial forces $\overline{N}_{\alpha,i}(z_0)+\overline{N}_{\alpha,j}(z_0)$ undergoing displacement $\overline{w}_{\alpha,j}(z_0)$, shear forces $\overline{Q}_{\alpha,i}(z_0)+\overline{Q}_{\alpha,j}(z_0)$ undergoing displacement $\overline{v}_j(z_0)$, and bending moment $\overline{M}_{\alpha,i}(z_0)+\overline{M}_{\alpha,j}(z_0)$ undergoing rotations $\overline{v}_j'(z_0)$, in which z_0 denotes the ends $z=0$ or $z=L$. Under the additional load $q_j(z)$, additional strains $\overline{\varepsilon}_j$ and stresses $\overline{\sigma}_j$ take place within the system. The total strain energy consists of two components; the first is induced by the initial stresses $\overline{\sigma}_i$ undergoing strains $\overline{\varepsilon}_i$ and is depicted by the rectangular area $ABCD$ (Fig.6.2b). This component gives rise to the internal strain energy terms $\left(\overline{U}_a,\overline{U}_b,\overline{U}_c,\overline{U}_d,\overline{U}_e\right)_{i,j}$. The second component is induced by stresses $\overline{\sigma}_j$ undergoing strains $\overline{\varepsilon}_j$ and is depicted by the triangular area CDE. This gives rise to the internal strain energy terms $\left(\overline{U}_a,\overline{U}_b,\overline{U}_c,\overline{U}_d,\overline{U}_e\right)_j$. As a result, the total potential energy can be expressed as:

$$
\begin{aligned}
\pi_{ij} &= \left(\overline{U}_a+\overline{U}_b+\overline{U}_c+\overline{U}_d+\overline{U}_e\right)_{i,j}+\left(\overline{U}_a+\overline{U}_b+\overline{U}_c+\overline{U}_d+\overline{U}_e\right)_j-\overline{V}_j \\
&-\left[\overline{N}_{a,i}(z)+\overline{N}_{a,j}(z)\right]\overline{w}_{a,j}(z)\Big|_0^L-\left[\overline{Q}_{a,i}(z)+\overline{Q}_{a,j}(z)\right]\overline{v}_j(z)\Big|_0^L-\left[\overline{M}_{a,i}(z)+\overline{M}_{a,j}(z)\right]\overline{v}_j'(z)\Big|_0^L \\
&-\left[\overline{N}_{c,i}(z)+\overline{N}_{c,j}(z)\right]\overline{w}_{c,j}(z)\Big|_0^L-\left[\overline{Q}_{c,i}(z)+\overline{Q}_{c,j}(z)\right]\overline{v}_j(z)\Big|_0^L-\left[\overline{M}_{c,i}(z)+\overline{M}_{c,j}(z)\right]\overline{v}_j'(z)\Big|_0^L \\
&-\left[\overline{N}_{e,i}(z)+\overline{N}_{e,j}(z)\right]\overline{w}_{e,j}(z)\Big|_0^L-\left[\overline{Q}_{e,i}(z)+\overline{Q}_{e,j}(z)\right]\overline{v}_j(z)\Big|_0^L-\left[\overline{M}_{e,i}(z)+\overline{M}_{e,j}(z)\right]\overline{v}_j'(z)\Big|_0^L
\end{aligned}
\tag{6.7}
$$

Equation (6.7) can be expressed in terms of stress and strain fields as:

$$\pi_{ij}=\left(\int_L\int_{A_a}\bar{\sigma}_i\bar{\varepsilon}_j dA_a dz+\int_L\int_{A_b}\bar{\tau}_i\bar{\gamma}_j dA_b dz+\int_L\int_{A_c}\bar{\sigma}_i\bar{\varepsilon}_j dA_c dz+\int_L\int_{A_d}\bar{\tau}_i\bar{\gamma}_j dA_d dz+\int_L\int_{A_e}\bar{\sigma}_i\bar{\varepsilon}_j dA_e dz\right)+$$
$$+\frac{1}{2}\left(\int_L\int_{A_a}\bar{\sigma}_j\bar{\varepsilon}_j dA_a dz+\int_L\int_{A_b}\bar{\tau}_j\bar{\gamma}_j dA_b dz+\int_L\int_{A_c}\bar{\sigma}_j\bar{\varepsilon}_j dA_c dz+\int_L\int_{A_d}\bar{\tau}_j\bar{\gamma}_j dA_d dz+\int_L\int_{A_e}\bar{\sigma}_j\bar{\varepsilon}_j dA_e dz\right)+$$
$$-\int_L\left[\bar{q}_i(z)+\bar{q}_j(z)\right]v_j(z)dz-\left[\bar{N}_{a,i}(z)+\bar{N}_{a,j}(z)\right]\bar{w}_{a,j}(z)\Big|_0^L-\left[\bar{Q}_{a,i}(z)+\bar{Q}_{a,j}(z)\right]\bar{v}_j(z)\Big|_0^L \tag{6.8}$$
$$-\left[\bar{M}_{a,i}(z)+\bar{M}_{a,j}(z)\right]\bar{v}_j'(z)\Big|_0^L-\left[\bar{N}_{c,i}(z)+\bar{N}_{c,j}(z)\right]\bar{w}_{c,j}(z)\Big|_0^L-\left[\bar{Q}_{c,i}(z)+\bar{Q}_{c,j}(z)\right]\bar{v}_j(z)\Big|_0^L$$
$$-\left[\bar{M}_{c,i}(z)+\bar{M}_{c,j}(z)\right]\bar{v}_j'(z)\Big|_0^L-\left[\bar{N}_{e,i}(z)+\bar{N}_{e,j}(z)\right]\bar{w}_{e,j}(z)\Big|_0^L-\left[\bar{Q}_{e,i}(z)+\bar{Q}_{e,j}(z)\right]\bar{v}_j(z)\Big|_0^L$$
$$-\left[\bar{M}_{e,i}(z)+\bar{M}_{e,j}(z)\right]\bar{v}_j'(z)\Big|_0^L$$

in which the following energy contributions have been defined

$$\left(\bar{U}_a,\bar{U}_b,\bar{U}_c,\bar{U}_d,\bar{U}_e\right)_{i,j}=\int_L\left(\int_{A_a}\bar{\sigma}_i\bar{\varepsilon}_j dA_a,\int_{A_b}\bar{\tau}_i\bar{\gamma}_j dA_b,\int_{A_c}\bar{\sigma}_i\bar{\varepsilon}_j dA_c,\int_{A_d}\bar{\tau}_i\bar{\gamma}_j dA_d,\int_{A_e}\bar{\sigma}_i\bar{\varepsilon}_j dA_e\right)dz$$
$$\left(\bar{U}_a,\bar{U}_b,\bar{U}_c,\bar{U}_d,\bar{U}_e\right)_{j}=\frac{1}{2}\int_L\left(\int_{A_a}\bar{\sigma}_j\bar{\varepsilon}_j dA_a,\int_{A_b}\bar{\tau}_j\bar{\gamma}_j dA_b,\int_{A_c}\bar{\sigma}_j\bar{\varepsilon}_j dA_c,\int_{A_d}\bar{\tau}_j\bar{\gamma}_j dA_d,\int_{A_e}\bar{\sigma}_j\bar{\varepsilon}_j dA_e\right)dz \tag{6.9}$$
$$\bar{V}_j=\int_L\left[\bar{q}_i(z)+\bar{q}_j(z)\right]v_j(z)dz$$

From Eqs. (6.3)-(6.4), by substituting into Eq.(6.9), the variation of the total potential energy can be expressed as:

$$\delta\pi=\int_L\left\langle\delta\mathbf{\Delta}_j'(z)\right\rangle_{1\times4}^{\mathbf{T}}\left[\mathbf{H}_1\right]_{4\times4}\left\{\mathbf{\Delta}_i'(z)\right\}_{4\times1}dz+\int_L\left\langle\delta\mathbf{\Delta}_j'(z)\right\rangle_{1\times4}^{\mathbf{T}}\left[\mathbf{H}_1\right]_{4\times4}\left\{\mathbf{\Delta}_j'(z)\right\}_{4\times1}dz+$$
$$+\int_L\left\langle\delta\mathbf{\Delta}_j(z)\right\rangle_{1\times4}^{\mathbf{T}}\left[\mathbf{H}_2\right]_{4\times4}\left\{\mathbf{\Delta}_i(z)\right\}_{4\times1}dz+\int_L\left\langle\delta\mathbf{\Delta}_j(z)\right\rangle_{1\times4}^{\mathbf{T}}\left[\mathbf{H}_2\right]_{4\times4}\left\{\mathbf{\Delta}_j(z)\right\}_{4\times1}dz$$
$$-\left(\int_L\left[q_i(z)+q_j(z)\right]v_j(z)dz\right)-\left[\bar{N}_{a,i}(z)+\bar{N}_{a,j}(z)\right]\bar{w}_{a,j}(z)\Big|_0^L-\left[\bar{Q}_{a,i}(z)+\bar{Q}_{a,j}(z)\right]\bar{v}_j(z)\Big|_0^L \tag{6.10}$$
$$-\left[\bar{M}_{a,i}(z)+\bar{M}_{a,j}(z)\right]\bar{v}_j'(z)\Big|_0^L-\left[\bar{N}_{c,i}(z)+\bar{N}_{c,j}(z)\right]\bar{w}_{c,j}(z)\Big|_0^L-\left[\bar{Q}_{c,i}(z)+\bar{Q}_{c,j}(z)\right]\bar{v}_j(z)\Big|_0^L$$
$$-\left[\bar{M}_{c,i}(z)+\bar{M}_{c,j}(z)\right]\bar{v}_j'(z)\Big|_0^L-\left[\bar{N}_{e,i}(z)+\bar{N}_{e,j}(z)\right]\bar{w}_{e,j}(z)\Big|_0^L-\left[\bar{Q}_{e,i}(z)+\bar{Q}_{e,j}(z)\right]\bar{v}_j(z)\Big|_0^L$$
$$-\left[\bar{M}_{e,i}(z)+\bar{M}_{e,j}(z)\right]\bar{v}_j'(z)\Big|_0^L$$

in which

$$\left\langle \mathbf{\Delta}_j(z) \right\rangle_{1\times4}^{\mathrm{T}} = \left\langle \bar{w}_{a,j}(z) \quad \bar{w}_{e,j}(z) \quad \bar{w}_{c,j} \quad \bar{v}_j'(z) \right\rangle; \quad \left\langle \mathbf{\Delta}_i(z) \right\rangle_{1\times4}^{\mathrm{T}} = \left\langle \bar{w}_{a,i}(z) \quad \bar{w}_{e,i}(z) \quad \bar{w}_{c,i} \quad \bar{v}_i'(z) \right\rangle;$$

$$[\mathbf{H_1}]_{4\times4} = \begin{bmatrix} E_a A_a & 0 & 0 & 0 \\ 0 & E_e A_e & 0 & 0 \\ 0 & 0 & E_c A_c & 0 \\ 0 & 0 & 0 & \alpha_1 \end{bmatrix};$$

$$[\mathbf{H}_2]_{4\times4} = \left[\begin{array}{c:c:c:c} G_b b_b/t_b & 0 & -G_b b_b/t_b & -c_b\, G_b b_b/t_b \\ \hdashline 0 & G_d b_d/t_d & -G_d b_d/t_d & -c_d\, G_d b_d/t_d \\ \hdashline -G_b b_b/t_b & -G_d b_d/t_d & G_b b_b/t_b + G_d b_d/t_d & c_b\, G_b b_b/t_b + c_d\, G_d b_d/t_d \\ \hdashline -c_b\, G_b b_b/t_b & -c_d\, G_d b_d/t_d & c_b\, G_b b_b/t_b + c_d\, G_d b_d/t_d & c_b^2\, G_b b_b/t_b + c_d^2\, G_d b_d/t_d \end{array}\right]$$

with $\alpha_1 = E_c I_{xxc} + E_a I_{xxa} + E_e I_{xxe}; \quad 2c_b = 2t_b + h_c + t_a; \quad 2c_d = 2t_d - h_c - t_e$.

6.6.5. Equilibrium equations and boundary conditions

From Eq.(6.10), through integration by parts setting the variation of the potential energy to zero, one recovers the equilibrium equations. Expressed in a non-dimensional form, they take the form

$$\left[\begin{array}{c:c:c:c} \left(r_a \dfrac{\partial^2}{\partial \xi^2} - 1\right) & 0 & 1 & \alpha_b \dfrac{\partial}{\partial \xi} \\ \hdashline 0 & \left(r_e \dfrac{\partial^2}{\partial \xi^2} - r_d\right) & r_d & \alpha_d r_d \dfrac{\partial}{\partial \xi} \\ \hdashline 1 & r_d & r_c \dfrac{\partial^2}{\partial \xi^2} - 1 - r_d & -(\alpha_b + r_d \alpha_d) \dfrac{\partial}{\partial \xi} \\ \hdashline \alpha_b \dfrac{\partial}{\partial \xi} & \alpha_d r_d \dfrac{\partial}{\partial \xi} & -(\alpha_b + \alpha_d r_d) \dfrac{\partial}{\partial \xi} & r_f \dfrac{\partial^4}{\partial \xi^4} - \left(\alpha_b^2 + r_d \alpha_d^2\right) \dfrac{\partial^2}{\partial \xi^2} \end{array}\right] \begin{Bmatrix} \tilde{w}_a \\ \tilde{w}_e \\ \tilde{w}_c \\ \tilde{v} \end{Bmatrix} = \begin{Bmatrix} 0 \\ 0 \\ 0 \\ \alpha_q(\xi) \end{Bmatrix} \quad (6.11)$$

where $\xi = z/L$ is the non-dimensional longitudinal coordinate, $\tilde{w}_a = \left(\bar{w}_{a,j} + \bar{w}_{a,i}\right)/L$ $\tilde{w}_c = \left(\bar{w}_{c,j} + \bar{w}_{c,i}\right)/L$, $\tilde{w}_e = \left(\bar{w}_{e,j} + \bar{w}_{e,i}\right)/L$, and $\tilde{v} = \left(\bar{v}_j + \bar{v}_i\right)/L$ are non-dimensional displacements, and following parameters have been introduced:

$$r_a = \left(\frac{E_a A_a}{L^2}\right)\left(\frac{t_b}{G_b b_b}\right); \quad r_e = \left(\frac{E_e A_e}{L^2}\right)\left(\frac{t_b}{G_b b_b}\right); \quad r_c = \left(\frac{E_c A_c}{L^2}\right)\left(\frac{t_b}{G_b b_b}\right); \quad r_d = \left(\frac{G_d b_d}{t_d}\right)\left(\frac{t_b}{G_b b_b}\right);$$

$$r_f = \frac{1}{L^4}\left(E_c I_{xxc} + E_a I_{xxa} + E_e I_{xxe}\right)\left(\frac{t_b}{G_b b_b}\right); \quad \alpha_b = \frac{2t_b + h_c + t_a}{2L}; \quad \alpha_d = \frac{2t_d - h_c - t_e}{2L}; \quad \alpha_q(\xi) = \frac{t_b\left(q_i + q_j\right)}{LG_b b_b};$$

Ten boundary conditions arise from the boundary terms. These are:

$$\begin{gathered}
\delta\overline{w}_{a,j}(\xi)\left[r_a \tilde{w}_a{}'(\xi) - \frac{t_b}{G_b b_b L^2}\left(\overline{N}_{a,i}(\xi) + \overline{N}_{a,j}(\xi)\right)\right]\Bigg|_0^1 = 0 \\
\delta\overline{w}_{e,j}(\xi)\left[r_e \tilde{w}_e{}'(\xi) - \frac{t_b}{G_b b_b L^2}\left(\overline{N}_{e,i}(\xi) + \overline{N}_{e,j}(\xi)\right)\right]\Bigg|_0^1 = 0 \\
\delta\overline{w}_{c,j}(\xi)\left[r_c \tilde{w}_c{}'(\xi) - \frac{t_b}{G_b b_b L^2}\left(\overline{N}_{c,i}(\xi) + \overline{N}_{c,j}(\xi)\right)\right]\Bigg|_0^1 = 0 \\
\delta\overline{v}_j{}'(\xi)\left[r_f \tilde{v}''(\xi) - \frac{t_b}{G_b b_b L^3}\left[\overline{M}_{c,i}(\xi) + \overline{M}_{a,i}(\xi) + \overline{M}_{e,i}(\xi) + \overline{M}_{c,j}(\xi) + \overline{M}_{a,j}(\xi) + \overline{M}_{e,j}(\xi)\right]\right]\Bigg|_0^1 = 0 \\
-\left\{\begin{aligned}
&\delta\overline{v}_1(\xi)\Big[r_f \tilde{v}'''(\xi) - \left(\alpha_b^2 + r_d\alpha_d^2\right)\tilde{v}'(\xi) + \alpha_b \tilde{w}_a(\xi) + \alpha_d r_d \tilde{w}_e(\xi) - \left(\alpha_b + \alpha_d r_d\right)\tilde{w}_c(\xi) \\
&- \frac{t_b}{G_b b_b L^2}\left[\overline{Q}_{c,i}(\xi) + \overline{Q}_{a,i}(\xi) + \overline{Q}_{e,i}(\xi) + \overline{Q}_{c,j}(\xi) + \overline{Q}_{a,j}(\xi) + \overline{Q}_{e,j}(\xi)\right]\Big]
\end{aligned}\right\}\Bigg|_0^1 = 0
\end{gathered} \tag{6.12}$$

6.7. General Solution

The general solution is the sum of homogeneous and particular solutions, i.e.,

$$\begin{Bmatrix} \tilde{w}_a(\xi) \\ \tilde{w}_e(\xi) \\ \tilde{w}_c(\xi) \\ \tilde{v}(\xi) \end{Bmatrix} = \begin{Bmatrix} \tilde{w}_a(\xi) \\ \tilde{w}_e(\xi) \\ \tilde{w}_c(\xi) \\ \tilde{v}(\xi) \end{Bmatrix}_H + \begin{Bmatrix} \tilde{w}_a(\xi) \\ \tilde{w}_e(\xi) \\ \tilde{w}_c(\xi) \\ \tilde{v}(\xi) \end{Bmatrix}_P \tag{6.13}$$

The homogeneous solution is recovered by setting the right hand side of Eqs. (6.11) to zero (Appendix 6.1), yielding

$$\begin{Bmatrix} \tilde{w}_a(\xi) \\ \tilde{w}_e(\xi) \\ \tilde{w}_c(\xi) \\ \tilde{v}(\xi) \end{Bmatrix}_H = \begin{bmatrix} 1 & \xi & \xi^2 & \xi^3 & e^{m_5\xi} & e^{m_6\xi} & e^{m_7\xi} & e^{m_8\xi} & 0 & 0 \\ 0 & 0 & 0 & -3L_1\xi^2 & R_5 e^{m_5\xi} & R_6 e^{m_6\xi} & R_7 e^{m_7\xi} & R_8 e^{m_8\xi} & 1 & \xi \\ 0 & \alpha_b & 2\alpha_b\xi & 3L_2\left(2r_a + \xi^2\right) & S_5 e^{m_5\xi} & S_6 e^{m_6\xi} & S_7 e^{m_7\xi} & S_8 e^{m_8\xi} & 1 & \xi \\ 0 & \alpha_d & 2\alpha_d\xi & 3L_3\left(2\frac{r_e}{r_d} + \xi^2\right) & T_5 e^{m_5\xi} & T_6 e^{m_6\xi} & T_7 e^{m_7\xi} & T_8 e^{m_8\xi} & 1 & \xi \end{bmatrix}\{\mathbf{D}\}_{10\times 1} \tag{6.14}$$

in which $\langle \mathbf{D} \rangle_{1\times 10}^{\mathbf{T}} = \langle D_1 \quad D_2 \quad ... \quad D_{10} \rangle$ is the vector of integration constants,

$L_1 = (\alpha_b r_a + \alpha_d r_e)/(r_a + r_e + r_c)$, $L_2 = (\alpha_b r_e - \alpha_d r_e + \alpha_b r_c)/(r_a + r_e + r_c)$,

$L_3 = (-\alpha_b r_a + \alpha_d r_a + \alpha_d r_c)/(r_a + r_e + r_c)$, and

$$R_k = \frac{r_a r_c r_e r_f (\alpha_b r_e - \alpha_d r_a r_d)}{\left[\alpha_b \alpha_d r_c (r_a r_d - r_e) + r_a r_e (\alpha_b - \alpha_d)(\alpha_b + \alpha_d r_d)\right] r_d (r_a + r_e + r_c)} m_k^5 - \frac{(\alpha_b r_a + \alpha_d r_e)}{(r_a + r_e + r_c)} m_k$$
$$+ \frac{(\alpha_d r_a^2 r_d^2 - \alpha_b r_e^2) r_c r_f + (\alpha_b + \alpha_d r_d)(r_d r_a - r_e) r_a r_e r_f + (\alpha_d r_a r_d - \alpha_b r_e)(\alpha_b^2 + \alpha_d^2 r_d) r_a r_c r_e}{\left[\alpha_b \alpha_d r_c (r_a r_d - r_e) + r_a r_e (\alpha_b - \alpha_d)(\alpha_b + \alpha_d r_d)\right] r_d (r_a + r_e + r_c)} m_k^3;$$

$$S_k = R_k + \alpha_b m_k + \frac{r_a (\alpha_b r_e + \alpha_d r_d r_e + \alpha_d r_c r_d)}{(\alpha_b r_e - \alpha_d r_a r_d)} R_k m_k^2 + \frac{(\alpha_b^2 r_a r_e + \alpha_d^2 r_a r_d r_e)}{(\alpha_b r_e - \alpha_d r_a r_d)} m_k^3 - \frac{r_a r_e r_f}{(\alpha_b r_e - \alpha_d r_a r_d)} m_k^5;$$

$$T_k = R_k + \alpha_d m_k - \frac{\alpha_b r_c r_e + \alpha_b r_a r_e + \alpha_d r_a r_d r_e}{r_d (\alpha_b r_e - \alpha_d r_a r_d)} R_k m_k^2 - \frac{\alpha_b^2 r_a r_e + \alpha_d^2 r_a r_d r_e}{r_d (\alpha_b r_e - \alpha_d r_a r_d)} m_k^3 + \frac{r_a r_e r_f}{r_d (\alpha_b r_e - \alpha_d r_a r_d)} m_k^5;$$

$k = 5, \ldots, 8$

Parameters $m_k \, (k = 5, \ldots, 8)$ appearing in Eq. (6.14) are four roots of the characteristic equation $A m_k{}^4 + B m_k{}^2 + C = 0$ where,

$$A = \frac{r_a r_c r_e r_f (\alpha_b r_e - \alpha_d r_a r_d)}{\{\alpha_b \alpha_d r_c (r_a r_d - r_e) + r_a r_e (\alpha_b - \alpha_d)(\alpha_b + \alpha_d r_d)\} r_d (r_a + r_e + r_c)};$$

$$B = \frac{(\alpha_d r_a^2 r_d^2 - \alpha_b r_e^2) r_c r_f + \left[\alpha_d r_d (r_a r_d + r_a + r_c) - \alpha_b (r_e r_d + r_e + r_c r_d)\right] r_a r_e r_f + (\alpha_d r_a r_d - \alpha_b r_e)(\alpha_b^2 + \alpha_d^2 r_d) r_a r_c r_e}{\{\alpha_b \alpha_d r_c (r_a r_d - r_e) + r_a r_e (\alpha_b - \alpha_d)(\alpha_b + \alpha_d r_d)\} r_d (r_a + r_e + r_c)};$$

$$C = -\left[\frac{(\alpha_b r_a + \alpha_d r_e)}{(r_a + r_e + r_c)} + \frac{(\alpha_d r_a r_d - \alpha_b r_e) r_f + r_a r_e (\alpha_d - \alpha_b)(\alpha_b^2 + \alpha_d^2 r_d)}{\alpha_b \alpha_d r_c (r_a r_d - r_e) + r_a r_e (\alpha_b - \alpha_d)(\alpha_b + \alpha_d r_d)}\right];$$

For the particular solution, it is expedient to expand the load function $\alpha_q(\xi)$, in Eqs. (6.11) using a Fourier series decomposition in the domain $0 \le \xi \le 1$, yielding

$$\alpha_q(\xi) = \sum_{n=1}^{n=n_{\max}} \alpha_{nq} \sin(n\pi\xi) \tag{6.15}$$

where n is a positive integer ranging from $n = 1, 2 ... n_{\max}$. In theory, an exact solution is obtained when $n_{\max} \to \infty$ but practically, convergence is attained by taking a finite number of terms. Also, α_{nq} is defined as

$$\alpha_{nq} = 2\int_0^1 \alpha_q(\xi)\sin(n\pi\xi)d\xi \tag{6.16}$$

The particular solution is then assumed to take the form

$$\begin{Bmatrix} \tilde{w}_a(\xi) \\ \tilde{w}_e(\xi) \\ \tilde{w}_c(\xi) \\ \tilde{v}(\xi) \end{Bmatrix}_P = \sum_{n=1}^{m} \begin{Bmatrix} a^*_{n\tilde{w}a} \\ a^*_{n\tilde{w}e} \\ a^*_{n\tilde{w}c} \\ a^*_{n\tilde{v}} \end{Bmatrix} \sin(n\pi\xi) + \sum_{n=1}^{m} \begin{Bmatrix} b^*_{n\tilde{w}a} \\ b^*_{n\tilde{w}e} \\ b^*_{n\tilde{w}c} \\ b^*_{n\tilde{v}} \end{Bmatrix} \cos(n\pi\xi) \tag{6.17}$$

From Eqs. (6.17), by substituting into Eqs. (6.11) and noting that ξ is arbitrary, one obtains

$$\begin{bmatrix} \eta_1(n) & 0 & 0 & 0 & 1 & 0 & 0 & -\eta_2(n) \\ 0 & \eta_1(n) & 0 & 0 & 0 & 1 & \eta_2(n) & 0 \\ 0 & 0 & \eta_3(n) & 0 & r_d & 0 & 0 & -\eta_4(n) \\ 0 & 0 & 0 & \eta_3(n) & 0 & r_d & \eta_4(n) & 0 \\ 1 & 0 & r_d & 0 & \eta_5(n) & 0 & 0 & \eta_6(n) \\ 0 & 1 & 0 & r_d & 0 & \eta_5(n) & -\eta_6(n) & 0 \\ 0 & -\eta_2(n) & 0 & -\eta_4(n) & 0 & \eta_6(n) & \eta_7(n) & 0 \\ \eta_2(n) & 0 & \eta_4(n) & 0 & -\eta_6(n) & 0 & 0 & \eta_7(n) \end{bmatrix}_n \begin{Bmatrix} a^*_{n\tilde{w}a} \\ b^*_{n\tilde{w}a} \\ a^*_{n\tilde{w}e} \\ b^*_{n\tilde{w}e} \\ a^*_{n\tilde{w}c} \\ b^*_{n\tilde{w}c} \\ a^*_{n\tilde{v}} \\ b^*_{n\tilde{v}} \end{Bmatrix} = \begin{Bmatrix} 0 \\ 0 \\ 0 \\ 0 \\ 0 \\ 0 \\ \alpha_{nq} \\ 0 \end{Bmatrix} \tag{6.18}$$

where

$$\eta_1(n) = -\left[r_a(n\pi)^2 + 1\right];\ \eta_2(n) = \alpha_b(n\pi);\ \eta_3(n) = -\left[r_e(n\pi)^2 + r_d\right];\ \eta_4(n) = \alpha_d r_d(n\pi);$$

$$\eta_5(n) = -\left[r_c(n\pi)^2 + 1 + r_d\right];\ \eta_6(n) = (n\pi)(\alpha_b + r_d\alpha_d);\ \eta_7(n) = r_f(n\pi)^4 + \left(\alpha_b^2 + r_d\alpha_d^2\right)(n\pi)^2$$

By solving Eqs. (6.18), coefficients $a^*_{n\tilde{w}a}, b^*_{n\tilde{w}a}, a^*_{n\tilde{w}e}, b^*_{n\tilde{w}e}, a^*_{n\tilde{w}c}, b^*_{n\tilde{w}c}, a^*_{n\tilde{v}}, b^*_{n\tilde{v}}$ are determined and substituted into Eqs. (6.17) to yield the particular solution.

6.8. Model Verification

The validity of the results based on the present formulation will be assessed through comparison with Finite Element Analysis (FEA) using the ABAQUS program. Also, 3D analyses based on the C3D8R element within the ABAQUS library will be used for verification. The C3D8R element is a 3D eight-node brick element with reduced integration. A mesh sensitivity study was conducted for similar problems and the details and specifics of the converged mesh have been reported in (Pham and Mohareb 2015b).

A 3.0m span simply supported beam consists of a W150x13 steel beam (flange width $= 100mm$, flange thickness $= 4.9mm$, depth $= 148mm$ and web thickness $= 4.3mm$) is preloaded by a transversely uniform line load $q_{c,2} = 6.0\ kN/m$ acting at the steel section centroidal axis (Step B). Strengthening is contemplated by bonding two originally straight GFRP plates to the top and bottom flanges of the steel beam over the whole span (Step C). Both GFRP plates have identical thicknesses and widths ($t_a = t_e = 19mm$, $b_a = b_e = 100mm$) and are bonded to the steel beam through two identical adhesive layers with the thickness $t_b = t_d = 1.0mm$ (Fig. 6.3). Steel modulus of elasticity is taken as $200\ GPa$, that of GFRP is assumed as $E_a = E_e = 42\ GPa$, and the shear modulus of the adhesive is $G_b = G_d = 0.4\ GPa$. Poisson's ratio μ for all three materials is taken as 0.3. The yielding strength of steel is $350MPa$, the rupture strength of GFRP plates is $896MPa$, and the shear strength of adhesive is $9.0MPa$.

After strengthening, the composite beam is subjected to additional uniform transverse line load $q_{c,6} = 6.0\ kN/m$ (Step D). It is required to compare (i) the transverse displacement and maximum longitudinal normal stresses for the wide flange beam and GFRP plates, and (ii) the transverse shear stresses within the adhesive layers as predicted by the present closed form solution and the 3D FEA under ABAQUS.

The applicable boundary conditions are $\tilde{w}_a'(0) = \tilde{w}_e'(0) = \tilde{w}_c'(0) = \bar{v}_j(0) = \tilde{v}''(0) = \tilde{w}_a'(1)$ $= \tilde{w}_e'(1) = \overline{w}_{c,j}(1) = \bar{v}_j(1) = \tilde{v}''(1) = 0$. A mesh study indicated that convergence is attained when n=10 is taken. Also, a mesh sensitivity study on the 3D FEA model indicated that convergence is attained by taking 20 elements along each flange overhang, four elements across the flange thickness, 70 elements along the web height, four elements across the web thickness, four elements across each adhesive thickness, eight elements across each GFRP thickness, and 750 elements in the longitudinal direction. In step A, the steel beam is first activated and bent while GFRP plates are deactivated. Then, in step B, GFRP plates are activated and prescribed to take the curvature of the farthermost fibers of the steel beam (i.e., top and bottom fibers). Also, adhesive layers are activated using the free strain option. In step C, the displacements applied to GFRP plates in step B are released. Finally, in step D, the steel is exposed to additional loading.

Displacements:

Figure 6.4a depicts the transverse displacements in Steps B and D. Maximum displacements at mid-span in Step B and Step D obtained from the present study are $5.3\ mm$ and $8.1\ mm$, respectively, while those predicted by the 3D FEA are $5.5\ mm$ and $8.3\ mm$, corresponding to 1.9 % and 2.4% differences. The differences are attributed to neglecting the effect of transverse shear (Pham and Mohareb 2015b). The additional deflection in going from configuration 4 to 5 (Step C) is only $-0.011\ mm$, corresponding to 0.1% of the displacement in Step D. This negligible displacement is attributed to the fact that loads $q_{a,4}(z)$ and $q_{e,4}(z)$ needed to bend the GFRP plates are rather small compared to $q_{c,2}(z)$.

Longitudinal normal stresses:

Figures 6.4b,c provide the maximum tensile stresses at the bottom fiber of the wide flange beam and at the bottom of GFRP plate e. Maximum stresses in Steps B and D in the steel provided by the present study are $83.7\ MPa$ and $127\ MPa$, respectively, and those provided by the 3D FEA model are $83.2\ MPa$ and $126.9\ MPa$, which correspond to 0.6% and 0.1% differences. Also, the maximum tensile stress induced in Step D in GFRP a based on the present study is $13.54\ MPa$ while that based on the 3D-FEA is $13.55\ MPa$, a 0.1% difference. The additional longitudinal stress within the steel in Step C is only $-0.19\ MPa$ and is thus are negligible.

Shear stresses in adhesive layers:

Figure 6.4d shows the 3D FEA transverse shear stresses τ_{nz} along the left edge of the beam and at the center line (both lines are shown on the plan view provided in Fig. 6.6d). The shear stress averaged over the width of the adhesive is also depicted. At $z = 500\ mm$, the maximum difference between the present solution and that based on 3D-FEA is 2.3%. Near beam ends, i.e. at $z = 30\ mm$, the 3D-FEA model predicts maximum shear stresses of $0.57MPa$ at the center fibers and peeling stresses of $0.13MPa$. Both stresses correspond to an effective Mises stress of $0.59MPa$ and are significantly less than the experimentally determined in El Damatty and Abushagur (2003). (In the later study, shear strength ranged from $20.9\ MPa$ to $34.3\ MPa$ while the peeling strength ranged from $0.95\ MPa$ to $6.01\ MPa$). Also, the strains predicted by the present model and ABAQUS were observed to be nearly constant across the adhesive depth in a manner consistent with Pham (2013).

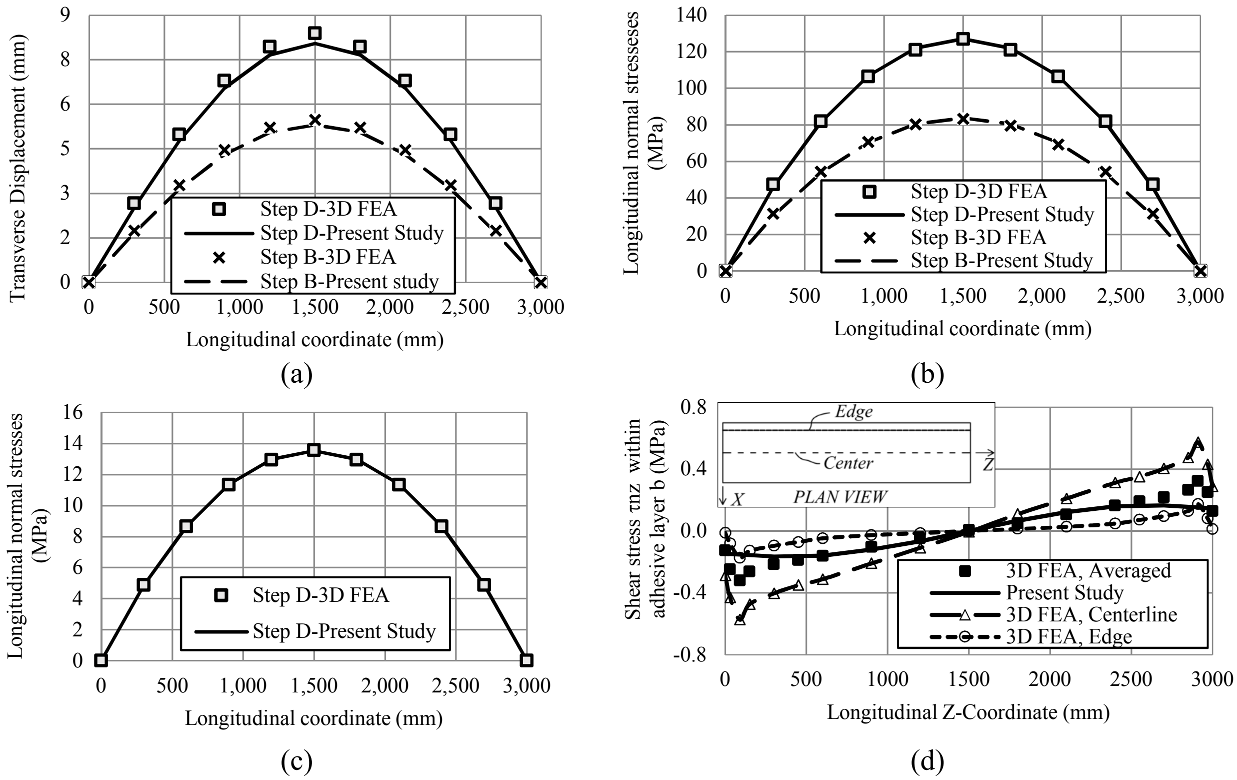

Figure 6.4. Response of simply supported reinforced W130x15 beam (a) Transverse deflection, (b) Longitudinal normal stresses in W-steel beam, (c) Longitudinal normal stresses within GFRP plate *a* (or plate *e*), (d) Shear stresses within adhesive layer *b*

Validation for different GFRP thicknesses:

The validation is also extended for three pairs of GFRP plate thicknesses $(t_a, t_e) = (9,29), (19,19)$, and $(29,9)\,mm$ (Table 6.2), while all other dimension parameters are kept identical. For all three cases, the transverse displacements in step C and D based on the present solution are observed to remain almost unchanged at $5.3\,mm$ and $8.1\,mm$, respectively, while those based on the 3D FEA solution were $5.5\,mm$ and $8.3\,mm$. The peak compressive and tensile stresses in the wide flange beam and GFRP plates are observed to change considerably (Table 6.2). The maximum difference between both solutions is 0.4% for the compression flange of the wide flange beam when $(t_a, t_e) = (29,9)\,mm$ and 1.1% for GFRP plate e when $(t_a, t_e) = (19,19)\,mm$.

Table 6.2. Maximum and minimum longitudinal normal stresses (*MPa*)

t_a (mm)	t_e (mm)	Wide Flange Steel Beam						GFRP plate					
		Compression			Tension			*a*			*e*		
		Present Study	3D-FEA	% Diff.*	Present Study	3D-FEA	% Diff.	Present Study	3D-FEA	% Diff.	Present Study	3D-FEA	% Diff.
9	29	-137	-138	0.3	119	119	0.0	-13.5	-13.4	0.7	14.2	14.3	0.7
19	19	-127	-127	0.0	127	127	0.0	-13.7	-13.5	1.0	13.7	13.5	1.1
29	9	-118	-118	0.4	137	138	0.3	-14.2	-14.4	1.0	13.3	13.4	1.1

* % difference = (3DFEA -Present study)*100/3DFEA

Comparison with Transformed Section Method:

The transformed section method is based on the assumption that plane section for the strengthened system remains plane throughout deformation. It is expected that the plane section condition is approached when the elastic properties of the materials involved do not vary significantly. Depending on the type of adhesive selected, the elastic properties significantly vary at room temperature from as low as 0.7MPa for polyurethane (e.g., Huveners et al. 2007) to 3.5 GPa for stiff epoxies (e.g., Hall, J. 2002). Further, for a given type of epoxy, the elastic properties have been reported to drop by orders of magnitudes when temperature rises from 20^0C to 50^0C (Sahin and Dawood 2016). It is thus of interest to quantify the adhesive shear modulus values needed to approach the plane section condition (i.e., full interaction).

Three adhesive shear moduli are selected for the comparison. These are Polyvinyl Butyral with $G_d = G_d = 1.3$ MPa (Asik and Tezcan 2005), Cyanoacrylates with $G_d = G_d =$ 0.4 GPa (Hall 2002) and SP Spabond two part epoxy with $G_d = G_d = 1.3$ GPa as estimated from the Young modulus and Poisson's ratio reported in Dawood (2008).

For the two stiffer cases $G_d = G_d = 0.4\,GPa$ and $G_d = G_d = 1.3\,GPa$, the present model predicts identical deflections of 8.1 mm (Table 6.3). When the shear moduli are reduced to $G_d = G_d = 1.3\,MPa$, the present model predicts a deflection of 8.9mm. Nearly identical predictions are obtained by ABAQUS in all cases. When adopting the transformed section method, the moment of inertia I of the composite section is found to be negligibly affected by the modulus of the adhesive. When $G_d = G_d = 1.3\,GPa$, the moment of inertia is $I = 1.1700e+07\,mm^4$ and when $G_d = G_d = 0.4\,GPa$, the moment of inertia is $I = 1.1693e+07\,mm^4$. These value compare to $I = 1.1687e+07\,mm^4$ when $G_d = G_d = 1.3\,MPa$, a mere 0.11% and 0.05% difference. Thus, the large difference in adhesive elasticity and shear moduli in all three cases results in essentially in the same predicted deflection of 8.0mm. For the cases of stiff adhesive shear moduli (i.e., 1.3 GPa and 0.4 GPa), the transformed section method under-predicts the deflection by 1.2%. However, for the weak adhesive, the method is found to underpredict the displacement by 10.1%. For the steel section, stress perdictions based on the transformed section agree with the present solution and 3D FEA within 0.4% for the stiff adhesives. However, the difference between predictions grows to 9.0% for the weak adhesive. For the GFRP, the present solution and ABAQUS predict a maximum normal stress of 13.5 MPa in the case stiff adhesives. This compares to 11.4MPa as predicted by the transformed section method. In the present example, the transformed section method underpredicts the GFRP stresses by a 15.5% difference for the case of stiff adhesive. The percentage difference improves to 5.6% for the case of the weak adhesive. Also, the present study and 3D FEA solutions show that for practical purposes the deflection and normal stresses in the steel and GFRP do not change for adhesive shear modulus values larger than 0.4GPa.

Table 6.3. Comparison of results based on 3D FEA, present study and transformed section

Solution:	Present study			3D FEA			% difference[1]			***TS*** [2]	*% difference*[3]		
Gb, Gd (MPa):	1300	400	1.3	1300	400	1.3	1300	400	1.3		*1300*	*400*	*1.3*
Peak deflection (mm)	8.1	8.1	8.9	8.3	8.3	9.1	2.4	2.4	2.2	***8.0***	*1.2*	*1.2*	*10.1*
Normal stress in Steel (MPa)	127	127	139	127	127	138	0.0	0.0	0.7	***126.5***	*0.4*	*0.4*	*9.0*
Normal stress in GFRP (MPa)	13.5	13.5	10.8	13.5	13.5	10.8	0.1	0.1	0.0	***11.4***	*15.5*	*15.5*	*5.6*

[1] % difference = % difference between the present solution and 3D FEA;

[2] TS = Transformed Section Method;

[3] % difference =% difference between the transformed section method and 3D FEA;

6.9. Effectiveness of Strengthening

As discussed in the previous example, the normal stresses in the GFRP plates and the shearing stresses in the adhesive layers were rather small compared to their respective material strengths. As a result, the effectiveness of strengthening can be assessed by comparing the peak displacements and normal stresses of the un-strengthened and strengthened steel beam. We recall that the beam was under a pre-existing load of $q_{c,2} = 6\ kN/m$. The corresponding peak deflection and stresses are $5.5\ mm$ and $84\ MPa$. If the un-strengthened beam is subjected to an additional load $q_{c,5} = 6\ kN/m$, the peak deflection would be $11\ mm$ and the corresponding peak longitudinal normal stresses would increase to $168\ MPa$. If the beam is strengthened with FRP plates of equal thicknesses, the peak deflection is observed to drop by $27.3\,\%$ to $8\ mm$. The corresponding stress drops by $24.2\,\%$ to $127\ MPa$. Also, as shown in Table 6.2, when the thickness of GFRP plates a and e are taken unequal, i.e., $(t_a, t_e) = (29,9)\,mm$, the peak normal stresses are found to increase from $127\ MPa$ to $137\ MPa$, a $7.3\,\%$ difference.

6.10. Parametric Study

6.10.1. Effect of GFRP Elastic Modulus

In the cases where the modulus of elasticity for both GFRP plates are taken equal in compression and tension, the previous section has shown that strengthening is most effective when both GFRP plate thicknesses are equal, resulting in the lowest normal stresses in the steel. This section explores the case where both GFRP plates have different elastic moduli as reported in Correia et al. (2011) where the GFRP compressive elastic modulus is reported to be 80% of that in tension. In such cases, the optimum thickness ratio t_a/t_e needs to be established. Towards this goal, the simply supported composite beam as presented in Example 1 is re-considered, while changing the modulus of elasticity for the GFRP plate a from $42.0\ GPa$ to $33.6\ GPa$. The thickness of GFRP plate a is assumed to range from $1.0\ mm$ to approximately $30\,mm$ while that of GFRP plate e is varied from $37.0\ mm$ to approximately $8.0mm$ such that the total thickness $t_a + t_e = 38mm$, resulting in a constant volume of GFRP material in all cases. Figure 6.5 shows the deflection at mid-span and maximum longitudinal normal stresses at top and bottom fibers of the wide flange beam under the application of additional load $q_{c,6}(z)$ in Step D versus the thickness ratio t_a/t_e. For $t_a/t_e = 0.027$, corresponding to $(t_a, t_e) = (1.0, 37)\ mm$, the deflection is $8.1\ mm$. The deflection is observed to mildly increase to a peak value of $8.3\ mm$ when $t_a/t_e = 4$ corresponding to $(t_a, t_e) = (30.4, 7.6)\ mm$. Based on a minimum deflection criterion, the solution $t_a/t_e = 0.027$ or $(t_a, t_e) = (1.0, 37)\ mm$ provides the optimum design. Also shown are the peak compressive stresses at the top fiber of the steel section. The peak compressive stress is $149\ MPa$ and occurs at $t_a/t_e = 0.027$ and is found to decrease as the ratio t_a/t_e increases. A reverse trend is observed for the peak tensile stresses in the steel where they have a minimal value at stress of $t_a/t_e = 0.027$ and monotonically increase to $140MPa$ when $t_a/t_e = 4$. The optimum t_a/t_e ratio is that at which the peak tensile stress in the steel is equal to that of the peak compressive stresses. This condition is realized at a t_a/t_e ratio of 1.22. The corresponding deflection value is $8.2\ mm$ which is marginally higher than the minimum deflection of $8.1\ mm$ while the corresponding stress is $129\ MPa$.

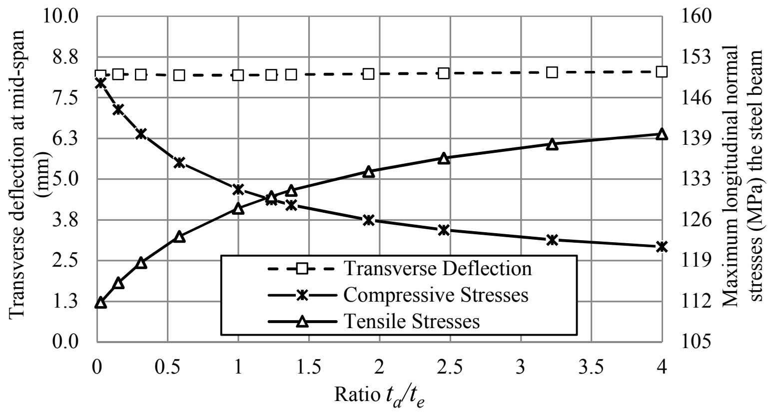

Figure 6.5. Effect of the GFRP thicknesses on stresses in steel and deflection ($t_a + t_e = 38mm$)

6.10.2. Effect of GFRP Plate Thickness

The previous case is revisited while keeping all parameters unchanged except that both GFRP plate thicknesses are varied. Unlike the previous case where the sum of plate thicknesses was kept constant, the present example investigates other cases where the sum of plate thicknesses is variable. Two thicknesses are considered for the GFRP plate: $t_e = 19\ mm$ and $t_e = 30\ mm$. For both cases, the thickness of GFRP plate a is increased from $t_a = 0.2t_e$ to $t_a = 4t_e$. For $t_e = 19\ mm$, the mid-span deflection is observed to decrease from $8.9\ mm$ at $t_a = 0.2t_e$ to $6.8\ mm$ at $t_a = 4t_e$ (Fig. 6.6a). Also, for $t_e = 30\ mm$ the mid-span deflection decreases from $8.2\ mm$ at $t_a = 0.2t_e$ to $6.1\ mm$ at $t_a = 4t_e$ (Fig. 6.6b).

Also depicted in the figure are the peak compressive and tensile stresses in the steel. Of particular interest is to note that both curves intersect at a thickness ratio $t_a/t_e = 1.22$, which exactly coincides with the optimum thickness ratio obtained in the previous case. However, unlike the previous case, as t_a/t_e exceeds 1.22, both compressive and tensile stresses are observed to decrease. This is a natural outcome of the fact that thicknesses of both GFRP plates increase. As expected, the larger plate thicknesses are observed to correspond to a lower deflection.

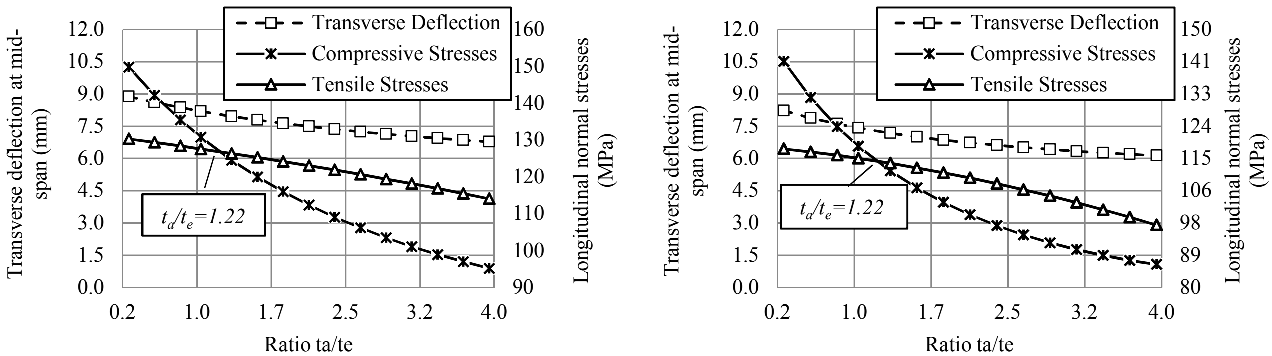

(a) (b)

Figure 6.6. Effect of GFRP plate thicknesses on the stresses in steel and deflection (a) $t_e = 19mm$ and (b) $t_e = 30mm$

6.10.3. Effect of Pre-existing Load and Stresses

The present example investigates the effect of initial stresses/strains state induced by the pre-existing loads on the capacity of the strengthened beam. A 3m-span W150x13 cantilever steel beam is considered. All dimensions and material parameters are identical to those in Example 1. During strengthening, the beam is assumed to be under a pre-existing point load $P_{c,2}$. The load can be acting downward (Fig. 6.7a.1) in cases where an existing structure cannot be fully unloaded prior to strengthening, or can vanish in cases where the structure is fully unloaded prior to strengthening (Fig. 6.7a.2). Alternatively, a hydraulic jack can be used to temporarily prop up the beam prior to and during strengthening (Fig. 6.7a.3) inducing a beneficial pre-stressing effect. For the problem under investigation, the load corresponding to the first yield of $\sigma_y = 350\ MPa$ is $P_{c,2} = \pm 9.4\ kN$ which defines the practical range of interest of pre-existing loading.

The total applied load versus the tip deflection is depicted in Fig. 6.7b and the total applied load versus the peak normal stress is provided in Fig. 6.7c. Three cases corresponding to different pre-existing load levels $P_{c,2} = 4.7\ kN$ (downward), $P_{c,2} = 0$ and $P_{c,2} = -9.4\ kN$ (i.e., upward pre-stressing load) are depicted by the loading path 1-2a-6a,1-6b, and 1-2c-6c, respectively. Also, depicted as a reference is the loading path for the case for the un-strengthened beam. As marked on the figures, without strengthening, the beam is able to withstand a load of $9.4\ kN$, which corresponds to a peak stress of $350MPa$ in the steel (Fig. 6.7c). When the beam is under a pre-existing gravity load of $4.7kN$ during strengthening (Path 1-2a-6a), the strengthening allows the beam to reach a load of $13.8kN$, a 47% increase over the un-strengthened case. If the beam is fully unloaded prior to strengthening (Path 1-

6b), it can sustain a load of $18.1kN$, a 93% increase over the strengthened case. The most beneficial strengthening scenario is the case where a pre-stressing load $P_{c,2}$ is $=-9.4\,kN$ (i.e. upward force) is applied. For this case, the beam is able to attain a gravity load of $26.8\,kN$ which corresponds to 185% increase in capacity over the un-strengthened beam. The last scenario corresponds to the highest shear stresses in the adhesive and the highest normal stresses in the GFRP. Under this scenario, the stresses in the adhesive and GFRP are observed to remain significantly smaller than the respective material strengths. Thus, the capacity of the strengthened system solely depends on the peak stresses in the steel. Figure 6.7d depicts the relationship between applied load ($P_{c,2}+P_{c,6}$) the strengthened beam can withstand versus the peak stress in the steel. Also, shown on the top horizontal axis is the value of the pre-existing load $P_{c,2}$. The total applied load ($P_{c,2}+P_{c,6}$) is linearly related to the pre-existing load $P_{c,2}$.

6.10.4. Effect of Adhesive Shear Modulus

In the previous example, the effect of the adhesive shear modulus on the total load is presented in Fig. 6.7d comparing the results for two shear moduli and $G_b = G_d = 0.4GPa$ (Cyanoacrylates, Polyurhetane) and $G_b = G_d = 1.3MPa$ (Polyvinyl Butyral). The slope of the total load to pre-stressing for the system with weaker shear modulus is milder than that with a stiffer adhesive, leading to a lower peak total load. At a pre-existing load $P_{c,2} = -9.4\,kN$, a significant reduction of the adhesive shear modulus from $0.4GPa$ to $1.3MPa$ causes a relatively mild reduction of the peak load reduction from $26.8kN$ to $21.7kN$.

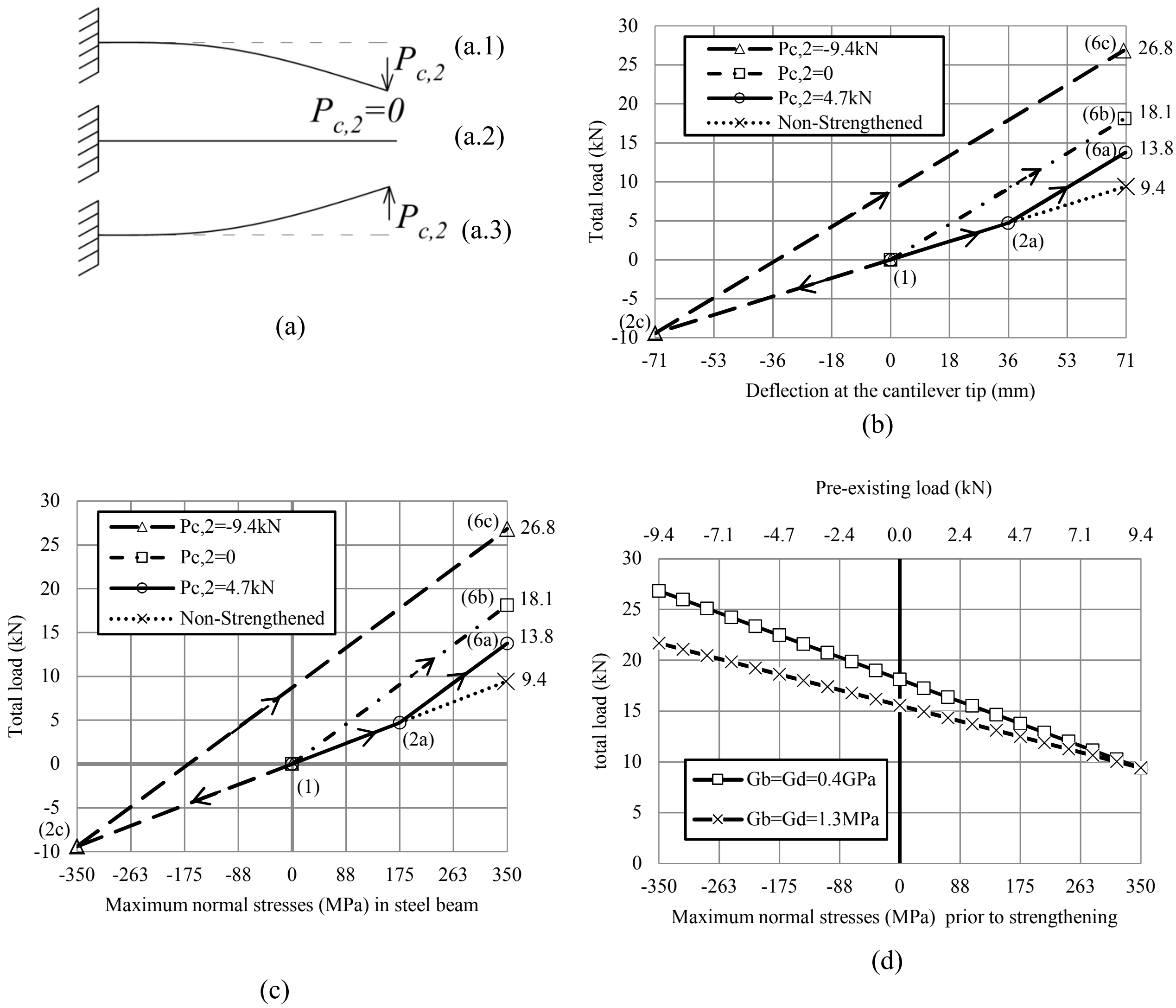

Figure 6.7. Effect of pre-existing load on the capacity of a strengthened beam: (a) Cases of pre-existing load applied to the wide flange beam in Step B, (b) Load versus deflection, (c) Load versus maximum normal stress, and (d) Total load versus Pre-existing load.

6.11. Summary and Conclusions

(1) A theory was developed for the analysis of preloaded/pre-stressed wide flange beams strengthened with GFRP plates bonded to both flanges through adhesive layers providing partial interaction. The theory results in four coupled differential equations of equilibrium and 10 boundary conditions.

(2) A closed form solution was developed for general loading and boundary conditions.

(3) For the examples investigated, the present theory provides stress and displacement predictions in the steel and GFRP in excellent agreement with those based on 3D FEA results. The maximum

difference between both solutions is 2.4% for deflection and 1.1% for stresses. For the adhesive, the shear stress obtained from the present study agrees well with the average shear stress obtained from 3D FEA results (i.e., the maximum difference between two solutions is about 2.3%), except at the points of singularity, where the present theory, like other beam theories, does not capture localized stress concentrations.

(3) The present solution is computationally efficient when compared to ABAQUS 3D FEA solutions. For example, when the present analysis, when implemented under MATLAB R2011b, it was completed in 45 seconds on a computer with two Intel(R) Xeon(R) CPU E5-24300 processors at 2.2 GHz and 2.21 GHz speeds and 64.0 GB of RAM. On the same computer, the run time of the 3D FEA ABAQUS model for the same problem, based on 2,243,000 C3H8R elements, was 5.43 hours.

(4) For the case where the elasticity moduli of both GFRP plates are identical, plates of equal thickness were found to optimize the design based on a stress in the steel criterion. For example, a 3m-span W130x15 simply supported beam strengthened with two $19mm-$ thick GFRP plates has a peak normal stress that is 7.9% smaller than that in the wide flange beam strengthened with $9mm$ and $29mm-$ thick GFRP plates, of a similar total volume of GFRP.

(5) For the same problem, when the elasticity modulus of the compressive GFRP plate is taken as a 80% of that of the tensile GFRP plate, the most effective thickness ratio of the compressive plate to that of the tensile plate for strengthening is found to be 1.22 when the sum of the thicknesses of both GFRP plates is kept constant.

(6) Pre-existing loads acting on the beam during strengthening are shown to significantly affect the capacity of the system. Pre-stressing is found to be particularly beneficial in this respect.

(7) The examples investigated in the present study suggest that the strengthened system is only mildly sensitive to the shear modulus of the adhesive.

Appendix 6.1: Homogeneous Solution of the Equilibrium Equations

From expressing Eqs. (6.11) in an explicit form, introducing the non-dimensional coordinate $\xi = z/L$ and dividing all equation by $G_b b_b / t_b$, one obtains

$$
\begin{aligned}
&r_a D^2 \tilde{w}_a - \tilde{w}_a + \tilde{w}_c + \alpha_b D\tilde{v} = 0 \\
&r_e D^2 \tilde{w}_e - r_d \tilde{w}_e + r_d \tilde{w}_c + \alpha_d r_d D\tilde{v} = 0 \\
&\tilde{w}_a + r_d \tilde{w}_e + r_c D^2 \tilde{w}_c - \tilde{w}_c - r_d \tilde{w}_c - \left(\alpha_b + r_d \alpha_d\right) D\tilde{v} = 0 \\
&\alpha_b D\tilde{w}_a + \alpha_d r_d D\tilde{w}_e - \left(\alpha_b + \alpha_d r_d\right) D\tilde{w}_c + r_f D^4 \bar{v} - \left(\alpha_b^2 + r_d \alpha_d^2\right) D^2 \tilde{v} = 0
\end{aligned}
\qquad (6.19)\text{a-d}
$$

in which D denotes the differential operator. From Eq. (6.19)a-d, by adding equations (6.19)a, b to Eq. (6.19)c, one obtains

$$\begin{aligned}
&r_a D^2 \tilde{w}_a - \tilde{w}_a + \tilde{w}_c + \alpha_b D\tilde{v} = 0\\
&r_e D^2 \tilde{w}_e - r_d \tilde{w}_e + r_d \tilde{w}_c + \alpha_d r_d D\tilde{v} = 0\\
&r_a D^2 \tilde{w}_a + r_e D^2 \tilde{w}_e + r_c D^2 \tilde{w}_c = 0\\
&\alpha_b D\tilde{w}_a + \alpha_d r_d D\tilde{w}_e - \left(\alpha_b + \alpha_d r_d\right) D\tilde{w}_c + r_f D^4 \bar{v} - \left(\alpha_b^2 + r_d \alpha_d^2\right) D^2 \tilde{v} = 0
\end{aligned} \tag{6.20)a-d$$

From Eqs. (6.20)a-b, one has

$$\begin{aligned}
\tilde{w}_a &= r_a D^2 \tilde{w}_a + \tilde{w}_c + \alpha_b D\tilde{v}\\
\tilde{w}_e &= \frac{r_e}{r_d} D^2 \tilde{w}_e + \tilde{w}_c + \alpha_d D\tilde{v}
\end{aligned} \tag{6.21)a-b$$

and from Eqs.(6.20)c-d, by taking the derivative of Eq. (6.20)d with respect to ξ , one obtains

$$\begin{aligned}
D^2 \tilde{w}_a &= \frac{\alpha_b r_e + \alpha_d r_d r_e + \alpha_d r_c r_d}{\alpha_b r_e - \alpha_d r_a r_d} D^2 \tilde{w}_c - \frac{r_e r_f}{\alpha_b r_e - \alpha_d r_a r_d} D^5 \tilde{v} + \frac{\alpha_b^2 r_e + \alpha_d^2 r_d r_e}{\alpha_b r_e - \alpha_d r_a r_d} D^3 \tilde{v}\\
D^2 \tilde{w}_e &= -\frac{\alpha_b r_c + \alpha_b r_a + \alpha_d r_a r_d}{\alpha_b r_e - \alpha_d r_a r_d} D^2 \tilde{w}_c + \frac{r_a r_f}{\alpha_b r_e - \alpha_d r_a r_d} D^5 \tilde{v} - \left(\frac{\alpha_b^2 r_a + \alpha_d^2 r_a r_d}{\alpha_b r_e - \alpha_d r_a r_d}\right) D^3 \tilde{v}
\end{aligned} \tag{6.22)a-b$$

From Eqs. (6.22)a-b and(6.21)a-b, by eliminating $\tilde{w}_a$ and $\tilde{w}_e$, one obtains

$$\begin{aligned}
&\left(\alpha_b r_e + \alpha_d r_d r_e + \alpha_d r_c r_d\right) r_a D^4 \tilde{w}_c - \left(r_a + r_e + r_c\right) r_d \alpha_d D^2 \tilde{w}_c\\
&= r_a r_e r_f D^7 \tilde{v} - \left(r_f + \alpha_b^2 r_a + \alpha_d^2 r_a r_d\right) r_e D^5 \tilde{v} + \left(\alpha_d r_e + \alpha_b r_a\right) r_d \alpha_d D^3 \tilde{v}\\
&\left(\alpha_b r_c + \alpha_b r_a + \alpha_d r_a r_d\right) r_e D^4 \tilde{w}_c - \left(r_a + r_e + r_c\right) r_d \alpha_b D^2 \tilde{w}_c\\
&= r_a r_e r_f D^7 \tilde{v} - \left(r_d r_f + \alpha_b^2 r_e + \alpha_d^2 r_d r_e\right) r_a D^5 \tilde{v} + \left(\alpha_b r_a + \alpha_d r_e\right) r_d \alpha_b D^3 \tilde{v}
\end{aligned} \tag{6.23)a-b$$

From Equations (6.23)a-b, by solving for fourth and second order derivatives of $\bar{w}_c$ and eliminating $\bar{w}_c$, one obtains an equation of only transverse displacement $\tilde{v}$. By assuming that the solution of displacement $\tilde{v}$ takes an exponential form $\tilde{v} = Ce^{m\xi}$ and substituting into the resulting equation, one obtains

$$m^5\left(Am^4 + Bm^2 + C\right) = 0 \tag{6.24}$$

Equation (6.24) has five zero roots and four non-zero inter-different roots, by solving the differential equation, the closed form solution for $\tilde{v}$ can be obtained as

$$\tilde{v} = C_1 + C_2\xi + C_3\xi^2 + C_4\xi^3 + C_5\xi^4 + \sum_{k=6}^{9} C_k e^{m_k\xi} \tag{6.25}$$

where $C_1, \cdots, C_9$ are unknown integration constants and $m_k\left(k=6,...,9\right)$ are non-zero distinct roots of Eq. (6.24). The integration can be determined based on boundary conditions. From Eq.(6.25), the closed form solutions for $\tilde{w}_c, \tilde{w}_a, \tilde{w}_e$ can be also obtained based on Eqs. (6.23)a-b and (6.21)a-b as

$$\begin{aligned}
\tilde{v} &= C_1 + C_2\xi + C_3\xi^2 + C_4\xi^3 + C_5\xi^4 + \sum_{k=6}^{9} C_k e^{m_k\xi} \\
\tilde{w}_c &= -3L_1C_4\xi^2 - 4L_1\xi^3C_5 + \sum_{k=6}^{9} R_k e^{m_k\xi}C_t + C_{10} + C_{11}\xi \\
\tilde{w}_a &= \alpha_b C_2 + 2\alpha_b\xi C_3 + 3L_2\left(2r_a + \xi^2\right)C_4 + 4L_2\left(6r_a\xi + \xi^3\right)C_5 + \sum_{k=6}^{9} S_k e^{m_k\xi}C_t + C_{10} + C_{11}\xi \\
\tilde{w}_e &= \alpha_d C_2 + 2\alpha_d\xi C_3 + 3L_3\left(2\frac{r_e}{r_d} + \xi^2\right)C_4 + 4L_3\left(6\frac{r_e}{r_d}\xi + \xi^3\right)C_5 + \sum_{k=6}^{9} T_k e^{m_k\xi}C_t + C_{10} + C_{11}\xi
\end{aligned} \tag{6.26}$$

in which

$$L_1 = \frac{\left(\alpha_b r_a + \alpha_d r_e\right)}{\left(r_a + r_e + r_c\right)}; \quad L_2 = \frac{\left(\alpha_b r_e - \alpha_d r_e + \alpha_b r_c\right)}{\left(r_a + r_e + r_c\right)}; \quad L_3 = \frac{\left(-\alpha_b r_a + \alpha_d r_a + \alpha_d r_c\right)}{\left(r_a + r_e + r_c\right)};$$

$$\begin{aligned}
R_k &= \frac{r_a r_c r_e r_f\left(\alpha_b r_e - \alpha_d r_a r_d\right)}{\left\{\alpha_b\alpha_d r_c\left(r_a r_d - r_e\right) + r_a r_e\left(\alpha_b - \alpha_d\right)\left(\alpha_b + \alpha_d r_d\right)\right\} r_d\left(r_a + r_e + r_c\right)} m_k^5 - \frac{\left(\alpha_b r_a + \alpha_d r_e\right)}{\left(r_a + r_e + r_c\right)} m_k \\
&+ \frac{\left(\alpha_d r_a^2 r_d^2 - \alpha_b r_e^2\right) r_c r_f + \left(\alpha_b + \alpha_d r_d\right)\left(r_d r_a - r_e\right) r_a r_e r_f + \left(\alpha_d r_a r_d - \alpha_b r_e\right)\left(\alpha_b^2 + \alpha_d^2 r_d\right) r_a r_c r_e}{\left\{\alpha_b\alpha_d r_c\left(r_a r_d - r_e\right) + r_a r_e\left(\alpha_b - \alpha_d\right)\left(\alpha_b + \alpha_d r_d\right)\right\} r_d\left(r_a + r_e + r_c\right)} m_k^3;
\end{aligned}$$

$$S_k = R_k + \alpha_b m_k + \frac{r_a\left(\alpha_b r_e + \alpha_d r_d r_e + \alpha_d r_c r_d\right)}{\left(\alpha_b r_e - \alpha_d r_a r_d\right)} R_k m_k^2 + \frac{\left(\alpha_b^2 r_a r_e + \alpha_d^2 r_a r_d r_e\right)}{\left(\alpha_b r_e - \alpha_d r_a r_d\right)} m_k^3 - \frac{r_a r_e r_f}{\left(\alpha_b r_e - \alpha_d r_a r_d\right)} m_k^5;$$

$$T_k = R_k + \alpha_d m_k - \frac{\alpha_b r_c r_e + \alpha_b r_a r_e + \alpha_d r_a r_d r_e}{r_d\left(\alpha_b r_e - \alpha_d r_a r_d\right)} R_k m_k^2 - \frac{\alpha_b^2 r_a r_e + \alpha_d^2 r_a r_d r_e}{r_d\left(\alpha_b r_e - \alpha_d r_a r_d\right)} m_k^3 + \frac{r_a r_e r_f}{r_d\left(\alpha_b r_e - \alpha_d r_a r_d\right)} m_k^5;$$

Equations (6.26) involve 11 unknown integration constants $C_1,...,C_{11}$ while we have only ten boundary conditions. This is a result of the fact that, during the solution procedure, we have taken a derivative of Eq. (6.20)-d with respect to ξ, i.e., Eq.(6.22)-b. Therefore, from Eqs. (6.26), by substituting into Eq. (6.20)-d, it can be shown that constant C_5 vanishes. By setting constants C_1, C_2, C_3, C_4 equal to D_1, D_2, D_3, D_4, and $C_6, C_7, C_8, C_9, C_{10}, C_{11}$ equal to $D_5, D_6, D_7, D_8, D_9, D_{10}$, respectively, on recovers the solution in Eqs. (6.14).

References

[6-1] Accord, N.B. and Earls, C. J. (2006), Use of Fiber-Reinforced Polymer Composite Elements to Enhance Structural Steel Member Ductility, J. of Composites for Construction, 10(4), 337-344.

[6-2] Aguilera, J. and Fam, A. (2013), Bonded FRP Plates for Strengthening Rectangular Hollow Steel Section T-Joints against Web Buckling Induced by Transverse Compression, Journal of Composites for Construction, ASCE, 17(4), 421-432.

[6-3] Asik, M.Z. and Tezcan, S. (2005), A mathematical model for the behavior of laminated glass beams, Computers and Structures, 83 (21-22), 1742-1753.

[6-4] Bonacci, J.F. and Maalej, M. (2000), Externally bonded fiber-reinforced polymer for rehabilitation of corrosion damaged concrete beams, ACI Structural Journal, 97(5), 703-711.

[6-5] Correia, J.R., Branco, F.A., Silva, N.M.F, Camotim, D. and Silvestre, N. (2011), First-order, buckling and post-buckling behaviour of GFRP pultruded beams. Part 1: Experimental study, Computers and Structures, 89(21-22), 2052-2064.

[6-6] Dawood, M.M.R., (2008), Bond characteristics and environmental durability of CFRP materials for strengthening steel bridges and structures, Ph.D. thesis, North Carolina State University.

[6-7] Elchalakani, M. and Fernando, D. (2012), Plastic mechanism analysis of unstiffened steel I-section beams strengthened with CFRP under 3-point bending, Thin-Walled Structs., 53, 58-71.

[6-8] El Damatty, A.A. and Abushagur, M. (2003), Testing and modeling of shear and peel behavior for bonded steel/FRP connections, Thin-Walled Structures, 41(11), 987-1003

[6-9] El Damatty, A., Abushagur, M. and Youssef, M. A. (2003), Experimental and analytical investigation of steel beams rehabilitated using GFRP sheets, Journal of Steel & Composite Structures 3(6), 421-438.

[6-10] Fam, A., MacDougall and Shaat, A. (2009) "Upgrading Steel-Concrete Composite Girders and Repair of Damaged Steel Beams using Bonded CFRP Laminates", Thin-Walled Structures, 47(10):1122-1135.

[6-11] Ganga, H.V.S., Taly, N., and Vijay, P.V., (2007), Reinforce Concrete Design, Taylor and Francis Group publisher.

[6-12] Gjelsvik A. (1981), The Theory of Thin Walled Bars, 1st Edition, New York, et al., John Wiley & Sons publishing Incorporation.

[6-13] Ghafoori, E, Motavalli, M., (2013) Flexural and interfacial behavior of metallic beams strengthened by prestressed bonded plates, Journal of composite structures, 101, 22-34.

[6-14] Kim, H.,S. and Shi, S., Y., (2011), Flexural behaviour of reinforced concrete (RC) beams retrofitted with hybrid fiber reinforced polymers (FRPs) under sustaining loads, Journal of Composite Structures, 93(2), 802-811.

[6-15] Hall, J., (2002), Adhesives-Section B15 Kempe's Engineers Year-Book. Adhesive Design Toolkit: http://www.adhesivestoolkit.com/Toolkits/DesignGuidance/AdhesiveType.xtp.

[6-16] Harries, A. K. and El-Tawil, S. (2008) Steel-FRP composite structural systems. " Int. Conf. on Composite Construction in Steel and Concrete 2008, Composite Construction in Steel and Concrete VI, ASCE, Reston, VA, 703 –716

[6-17] Hollaway, L.C., Zhang, L., Photiou, N.K., Teng, J.G. and Zhang, S.S. (2006). Advances in Adhesive Joining of Carbon Fiber/Polymer Composites to Steel Members for Repair and Rehabilitation of Bridge Structures. Advances in Structural Engineering, 9(6), 791-803.

[6-18] Huveners, E.M.P, Gerwijnen, F.V., Soetens, F., Hofmeyer, H. (2007), Mechanical shear properties of adhesives, Proceedings of the 10th International Conference on Architectural and Automotive Glass, Tampere, Finland: Glass Performance Days, Tamglass Ltd. Oy, 367-370.

[6-19] Narmashiri, K., Ramli Sulong, N.H. and Jumaat, M.Z. (2012), Failure analysis and structural behaviour of CFRP strengthened steel I-beams, Construction and Building Materials, 30, 1 -9.

[6-20] Mallick, P., K., (1988), Fiber Reinforced Composites: Materials, Manufacturing, and Design, Third Edition, Taylor and Francis Group publisher.

[6-21] Miller, C.T., Chajes J.M. and Hastings N.J. (2001), Strengthening of a steel bridge girder using CFRP plates, Journal of Bridge Engineering 6(6), 514-522.

[6-22] Linghoff, D. and Al-Emrani, M. (2010), Performance of steel beams strengthened with CFRP laminate – Part 2: Laboratory tests, Composites Part B, 41(7), 516-522

[6-23] Linghoff, D., Al-Emrani and Kliger, M. R. (2010), Performance of steel beams strengthened with CFRP laminate – Part 1: Laboratory tests, Composites Part B, 41(7), 509-515.

[6-24] Liu, P., Zhao, Q., Li, F, Liu, J, Chen, H., (2014), Research on the Mechanical Properties of a Glass Fiber Reinforced Polymer-Steel Combined Truss Structure, The Scientific World Journal, 2014, 309872.

[6-25] Liu, Y. and Gannon, L., (2009), Finite element study of steel beams reinforced while under load, Journal of Engineering Structures, 31(11), 2630-2642.

[6-26] Pham, P.V., (2013), Stress-Deformation Theories for the Analysis of Steel Beams Reinforced with GFRP Plates, Master of Science Thesis, Department of Civil Engineering, University of Ottawa, Ottawa, ON, Canada.

[6-27] Pham, P.V. and Mohareb, M. (2014), A shear deformable theory for the analysis of steel beams reinforced with GFRP plates, Thin-Walled Structures, 85, 165-182.

[6-28] Pham, P.V. and Mohareb, M. (2015a), Finite-Element Formulations for the Spatial Static Response of Steel Beams Bonded to a GFRP Plate, Journal of Engineering Mechanics, ASCE, 141(4), 04014143.

[6-29] Pham, P.V and Mohareb, M. (2015b), Nonshear Deformable Theory for Analysis of Steel Beams Reinforced with GFRP Plate Closed-Form Solution, Journal of Structural Engineering, ASCE, 141(12), 04015063.

[6-30] Richardson, T. and Fam, A. (2014) "Modulus Effect of Bonded CFRP Laminates used for Repairing Pre- and Post-Yield Cracked Concrete Beams", ASCE Journal of Composites for Construction, 18(4), 04013054.

[6-31] Sahin, M., U. and Dawood, M., (2016), Experimental investigation of bond between High-Modulus CFRP and Steel at moderately elevated temperatures, Journal of composites for constructions, ASCE, 10.1061/ (ASCE) CC.1943-5614.0000702, 04016049.

[6-32] Shaat, A., and Fam, A. (2009), Slender steel columns strengthened using high modulus CFRP plates for buckling control, Journal of Composites for construction, 13(1), 2-12.

[6-33] Siddique, M.A.A. and El Damatty, A.A. (2012), Enhancement of buckling capacity of steel plates strengthened with GFRP plates, Thin-Walled Structures, 60(16), 154-162

[6-34] Siddique, M.A.A. and El Damatty, A.A. (2013), Improvement of local buckling behaviour of steel beams through bonding GFRP plates, Composite Structures, 96(6), 44-56

[6-35] Quin, W. Y., Liang, Z., Xiang, Z.R., Yue, L.X., and Jiu, S.Y., (2015), Behaviour of I-section steel beam welding reinforced while under load, Constructional Steel Research, 106, 278-288.

[6-36] Teng, J.G., and Hu, Y.M. (2007). Behaviour of FRP-jacketed circular steel tubes and cylindrical shells under axial compression. Construction and Building Materials, *21*(4), 827-838.

[6-37] Tomblin, J., Seneviratne, W., Escobar, P., and Khian, Y., Y., (2002), Shear stress-strain data for structural adhesives, Technical Report, National Technical Information Service (NTIS), Springfield, Virginia, 22161.

[6-38] Torabizaheh, M.A., (2013), Tensile, compressive and shear properties of unidirectional glass/epoxy composites subjected to mechanical loading and low temperature services, Indian Journal of Engineering & Materials Sciences, 20(4), 299-309.

[6-39] Wenwei, W. and Guo, L.(2006), Experimental study and analysis of RC beams strengthened with CFRP laminates under sustaining load, Int. J. of solids and structures, 43(6), 1372-1387.

[6-40] Westover, C.M., (1998), The compressive behaviour of Glass Reinforced Composite subjected to local Thermal Loading, Master thesis of Engineering, University of California, Berkeley.

[6-41] Wu, Z., Shao, Y., Iwashita, K., and Sakamoto, K., (2007), Strengthening of Preloaded RC Beams using Hybrid Carbon Sheets, J. of composites for construction, ASCE, 11(3), 299-307.

[6-42] Youssef, M. (2006). Analytical Prediction of the Linear and Nonlinear Behaviour of Steel Beams Rehabilitated using FRP Sheets, Engineering Structures*,* 28(6), 903-911.

[6-43] Zhao, X.-L. and Zhang, L. (2007), State-of-the-art review on FRP strengthened steel structures, Engineering Structures, 29(8), 1808-1823.

Chapter 7: High-order theory for the static analysis of beams with mono-symmetric cross-sections

Abstract

A family of high order beam solutions is developed for the analysis of beams with general mono-symmetric cross-sections. The nonlinear distribution of the longitudinal normal stress across the depth is represented by a polynomial series expansion up to any order, and the corresponding transverse shear and transverse normal stresses are obtained by satisfying the 2D infinitesimal stress equilibrium conditions. The resulting statically admissible stress fields are applied in conjunction with the principle of stationary complementary strain energy to formulate the compatibility equations and boundary conditions. Closed form solutions are then developed for general loading and boundary conditions. Comparisons with results based on the theory of elasticity and 3D finite element analyses showcase the ability of the present theory to naturally capture shear deformation effects, transverse normal stress effects, nonlinear longitudinal normal stress distributions in beams with intermediate and short spans, and the effect of support height. Unlike conventional beam solutions based on postulated kinematic assumptions, which tend to converge to the displacement response from below, the present theory avoids any kinematic assumptions and is shown to converge to the solution from above.

Keywords: High order beam theory, principle of stationary complementary energy, shear deformation, deep beams, and orthotropic material.

7.1. Introduction and Literature Review

The conventional Euler Bernoulli beam is based on the assumption that plane sections remain plane after deformation and normal to the beam axis. The normality condition implies omission of shear deformation. Thus, the theory is able to reliably predict the response of long-span beams where shear deformations are negligible, but underestimates deflections for short-span beams where shear deformation are known to be influential. The Timoshenko beam theory, where the plane section assumption is retained but the normality to the beam axis is relaxed, is an improvement over the Euler-Bernoulli beam theory in that it accounts for shear deformation effects. However, the plane section assumption creates a non-zero shear strain, and hence a non-zero shear stress, at the outermost fibers, which violates the traction boundary conditions as the externally applied shear traction typically vanishes at the outermost fibers of the beam. As a result, the Timoshenko theory tends to overestimate the stiffness of the beam (Mucichescu 1984). Other variations of the Timoshenko beam theory involve shear modification factors that depend on the cross-section shape (e. g., Timoshenko 1921, Cowper 1966, Stephen 1980) and the type of analysis, whether static or dynamic (Mindlin 1953, Heyliger and

Reddy 1988). Another limitation of the Timoshenko beam theory is the fact it omits the normal stresses in the transverse direction. As a result, while it satisfies the vertical equilibrium condition for the whole cross-section in a global integral sense, it violates the vertical equilibrium requirement in an infinitesimal sense. Also, both the Euler Bernoulli and Timoshenko beam theories predict linear stress profiles, which are appropriate approximations for long-span beams but are inconsistent with elasticity solutions for deep beams (e.g., Timoshenko and Goodier 1970) and more advanced beam theories (e.g., Carrera and Guinta 2010). Also, conventional beam theories adopt the centroidal axis as a reference. By default, such solutions locate transverse restraints at the section centroid. As such, the modelling of supports that are offset from the centroid requires special considerations (Wight and Parra (2002), Erkmen and Mohareb (2006a,b), Wu and Mohareb (2011).

To remedy the limitations of the conventional beam theories, higher order theories for beams with rectangular cross-sections were developed based on the principle of stationary potential strain energy. This includes the work of Stephen and Levinson (1979), Levinson (1981), Reddy (1984), Heyliger and Reddy (1988), Shu and Sun (1994), and Jha et al (2013), all assumed a cubic distribution of the longitudinal displacement along the height. Further advancements were proposed in the work of Carrera and Guinta (2010), Carrera et al (2015), and Groh and Weaver (2015) where the longitudinal displacement field was assumed to follow higher order polynomials. A common theme in the above high-order theories is that they postulate kinematic assumptions satisfying compatibility in an exact point-wise sense, and then use the principle of stationary potential energy to formulate approximate equilibrium equations. The approach contrasts with that based on the principle of stationary complementary strain energy, whereby stress fields that exactly satisfy the infinitesimal stress equilibrium conditions are postulated and then used with the stationary complementary energy principle to formulate approximate compatibility equations. Examples of such developments include the work of Chen and Cheng (1983) on adhesive bonded shear laps, Ekmen and Mohareb (2008) on torsional analysis of thin-walled members, and Zhao et al. (2014) for lap joints.

Within the above context, the present study adopts the principle of stationary complementary energy to develop a high-order beam theory that captures the nonlinear distribution for the stress fields. The solution sought is intended for beams with general mono-symmetric cross-sections, loading, and boundary conditions, with orthotropic material properties. The solution sought is able to seamlessly model supports that are offset from the section centroid.

7.2. Statement of the Problem

A prismatic homogeneous beam with an arbitrary mono-symmetric cross-section is loaded by transverse and longitudinal body forces $p_y(y,z)$ and $p_z(y,z)$ and surface tractions $\sigma_y(h_1,z), \tau(h_1,z), \sigma_y(h_2,z), \tau(h_2,z)$ (Figure 7.1a,b). Ends $z_e = 0, L$ are assumed to have general boundary conditions where longitudinal traction $\sigma_z(z_e,y)$ and transverse shear traction $\tau(z_e,y)$ are specified on part of the cross-sections $A_{0\sigma}, A_{0\tau}$ while longitudinal displacement $w(z_e,y)$ and transverse displacement $v(z_e,y)$ are specified on the remaining part of the cross-section (i.e., A_{0w}, A_{0v}). A high order beam theory is sought for the problem based on the principle of stationary complementary energy.

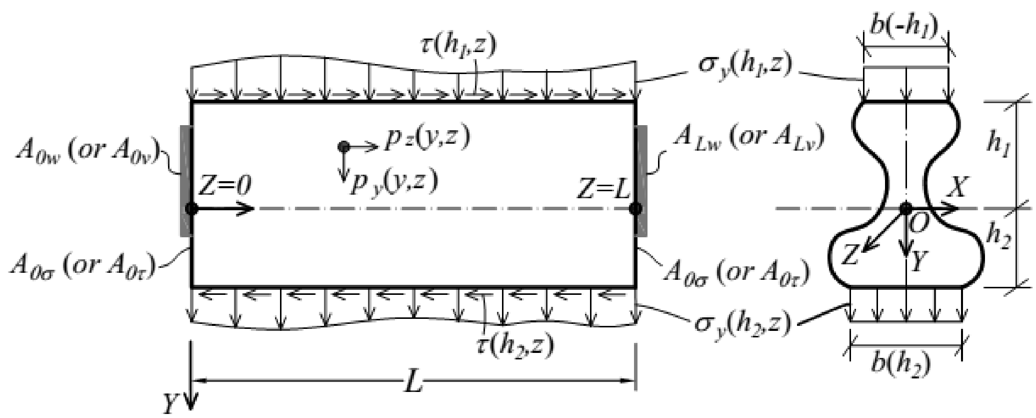

(a) Profile view (b) Mono-symmetric cross-section

Figure 7.1. Beam Tractions and body forces

7.3. Assumptions

The formulation is based on the following assumptions: (a) Material is linearly elastic orthotropic, (b) Strains are assumed to be small, and (c) The longitudinal normal stress field is assumed to take the form $\sigma_z(y,z) = \sum_{i=1}^{n} y^{i-1} F_i(z)$ where $F_i(z)$ are unknown functions of longitudinal z-coordinate, y is the transverse coordinate and n is a positive integer.

7.4. Expressions for Statically Admissible Stress Fields

The longitudinal normal stresses $\sigma_z(y,z)$ are postulated to take the form

$$\sigma_z(y,z) = \sum_{i=1}^{n} y^{i-1} F_i(z) \tag{7.1}$$

in which the contribution of each terms is shown in Figure 7.2. Traditional treatments only adopted the first two terms, which provides linear stress profiles. In fact, the stress profile may not be linear for beams with short spans (Carrera and Guinta 2010) and thus the assumption of a number of stress terms n introduced in Eq. (7.1) can capture the nonlinear response.

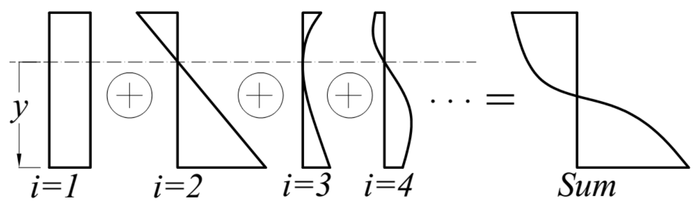

Figure 7.2. Normal longitudinal stress profiles

For the stress field postulated in Eq. (7.1) to be statically admissible, it needs to satisfy the shear flow equilibrium conditions

$$\begin{aligned} \partial\left[b(y)\sigma_y(y,z)\right]/\partial y + \partial\left[b(y)\tau(y,z)\right]/\partial z = b(y)\,p_y(y,z) \\ \partial\left[b(y)\tau(y,z)\right]/\partial y + \partial\left[b(y)\sigma_z(y,z)\right]/\partial z = b(y)\,p_z(y,z) \end{aligned} \tag{7.2a-b}$$

in which τ is used to represent for τ_{zy}, $b(y)$ is the section width at height y. The stress components expressed in the equilibrium equations are depicted in Figure 7.3.

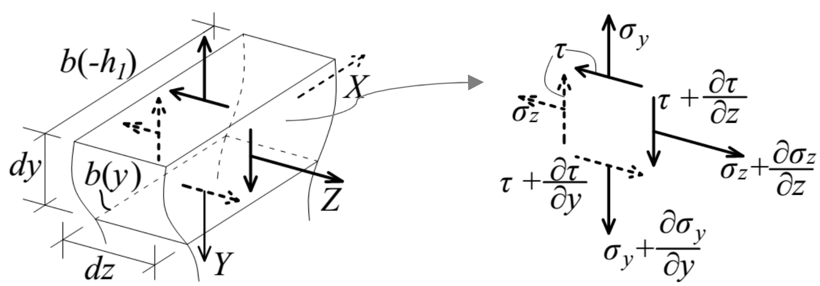

(a) (b)

Figure 7.3. (a) Infinitesimal beam element (b) stress state acting on element

From Eq. (7.1), by substituting into Eq. (7.2b), and integrating from $-h_1$ to y, one recovers the expression of shear stresses $\tau(y,z)$. Also, given the expression for $\tau(y,z)$, by substituting into Eq.

(7.2a) and integrating from $-h_1$ to y, the transversal normal stresses $\sigma_y\left(y,z\right)$ is obtained. The resulting equations take the form

$$\tau\left(y,z\right)=\bar{\tau}\left(y,z\right)-\sum_{i=1}^{n}\alpha_i\left(y\right)F_i'\left(z\right),\qquad \sigma_y\left(y,z\right)=\bar{\sigma}_y\left(y,z\right)+\sum_{i=1}^{n}\beta_i\left(y\right)F_i''\left(z\right) \tag{7.3a-b}$$

in which functions $\bar{\tau}\left(y,z\right)$ and $\bar{\sigma}_y\left(y,z\right)$ depend on surface tractions $\tau\left(-h_1,z\right)$ and $\sigma_y\left(-h_1,z\right)$, and body forces $p_z\left(y,z\right)$ and $p_y\left(y,z\right)$, and are defined as

$$\begin{aligned}
\bar{\tau}\left(y,z\right)&=\left[1/b\left(y\right)\right]\left\{b\left(-h_1\right)\tau\left(-h_1,z\right)+\int_{-h_1}^{y}b\left(\xi\right)p_z\left(\xi,z\right)d\xi\right\}\\
\bar{\sigma}_y\left(y,z\right)&=\left[1/b\left(y\right)\right]\left\{b\left(-h_1\right)\sigma_y\left(-h_1,z\right)+\int_{-h_1}^{y}b\left(\xi\right)p_y\left(\xi,z\right)d\xi-b\left(-h_1\right)\partial\left[\tau\left(-h_1,z\right)\right]/\partial z\right.\\
&\qquad\left.-\int_{-h_1}^{y}\int_{-h_1}^{\eta}b\left(\xi\right)\left[\partial p_z\left(\xi,z\right)/\partial z\right]d\xi d\eta\right\}
\end{aligned} \tag{7.4}$$

while $\alpha_i\left(y\right)$ and $\beta_i\left(y\right)$ are distribution functions depending on the section geometry and defined as

$$\alpha_i\left(y\right)=\left[1/b\left(y\right)\right]\int_{-h_1}^{y}b\left(\xi\right)\xi^{i-1}d\xi;\qquad \beta_i\left(y\right)=\left[1/b\left(y\right)\right]\int_{-h_1}^{y}\int_{-h_1}^{\eta}b\left(\xi\right)\xi^{i-1}d\xi d\eta \tag{7.5a-b}$$

Equations (7.1) and (7.3a-b) satisfy the traction boundary condition at the top face, but not the boundary conditions at bottom face $y=h_2$. By equating the stresses in Eqs. (7.3a-b) to the specified traction $\tau\left(h_2,z\right)$ and $\sigma_y\left(h_2,z\right)$), functions $F_{n-1}(z)$ and $F_n(z)$ are related to the remaining functions $F_i(z)$ where $i=1,\ldots,n-2$. By substituting into Eq. (7.1) (Appendix 7.1), one obtains

$$\begin{aligned}
\sigma_z\left(y,z\right)&=\hat{\boldsymbol{\chi}}\left(y\right)\hat{\mathbf{F}}\left(z\right)+\sigma_z^*\left(y,z\right)\\
\tau\left(y,z\right)&=\tilde{\boldsymbol{\chi}}\left(y\right)\tilde{\mathbf{F}}\left(z\right)+\tau^*\left(y,z\right)\\
\sigma_y\left(y,z\right)&=\boldsymbol{\xi}_3\left(y\right)\mathbf{F}''\left(z\right)+\sigma_y^*\left(y,z\right)
\end{aligned} \tag{7.6a-c}$$

in which unknown vectors $\mathbf{F}\left(z\right),\hat{\mathbf{F}}\left(z\right),\tilde{\mathbf{F}}\left(z\right)$ are given by

$$\begin{aligned}
\mathbf{F}\left(z\right)_{1\times m}^{\mathbf{T}}&=\left\langle F_1\left(z\right)\quad F_2\left(z\right)\quad\ldots\quad F_m\left(z\right)\right\rangle,\qquad m=n-2\\
\hat{\mathbf{F}}\left(z\right)_{1\times 3(m+1)}^{\mathbf{T}}&=\left\langle \mathbf{F}\left(z\right)_{1\times m}^{\mathbf{T}}\;\vdots\;\mathbf{F}\left(0\right)_{1\times m}^{\mathbf{T}}\quad z\mathbf{F}'\left(0\right)_{1\times m}^{\mathbf{T}}\;\vdots\;N\left(0\right)\quad zQ\left(0\right)\quad M\left(0\right)\right\rangle\\
\tilde{\mathbf{F}}\left(z\right)_{1\times(2m+1)}^{\mathbf{T}}&=\left\langle \mathbf{F}'\left(z\right)_{1\times m}^{\mathbf{T}}\;\vdots\;\mathbf{F}'\left(0\right)_{1\times m}^{\mathbf{T}}\;\vdots\;Q\left(0\right)\right\rangle
\end{aligned}$$

and stress resultants at $z_i = 0$ (Figure 7.4a) are defined as

$$N(z_i) = \int_{A_{iw}} \sigma_z(y, z_i)\, dA; \quad Q(z_i) = \int_{A_{i\tau}} \tau(y, z_i)\, dA; \quad M(z_i) = \int_{A_{iw}} y\sigma_z(y, z_i)\, dA \tag{7.7}$$

In Eqs. (7.6a-c), vectors $\hat{\boldsymbol{\chi}}(y)$, $\tilde{\boldsymbol{\chi}}(y)$, $\boldsymbol{\xi}_3(y)$ are known functions of y that depend upon the cross-section geometry and applied tractions and defined in Appendix 7.1. Also, in Equations 6-c, the load dependent terms are

$$\begin{aligned}
&\sigma_z^*(y,z) = \int_0^z \int_0^z \left[y^{n-2}\rho_1(z) + y^{n-1}\rho_2(z) \right] dz dz + z\left(y^{n-2}\varsigma_{11} + y^{n-1}\varsigma_{21} \right); \\
&\tau^*(y,z) = \bar{\tau}(y,z) - \int_0^z \left[\alpha_{n-1}(y)\rho_1(z) + \alpha_n(y)\rho_2(z) \right] dz - \alpha_{n-1}(y)\varsigma_{11} - \alpha_n(y)\varsigma_{21}; \\
&\sigma_y^*(y,z) = \bar{\sigma}_y(y,z) + \beta_{n-1}(y)\rho_1(z) + \beta_n(y)\rho_2(z);
\end{aligned} \tag{7.8a-c}$$

where $\rho_1(z)$, $\rho_2(z)$, and ς_{11} and ς_{21} depend on applied loads and are defined in Appendix 7.2.

7.5. Variational principle

The total complementary energy $\pi^* = U^* + V^*$ is the sum of the total complementary internal strain energy U^* and the load potential energy V^* gained by the end forces within the composite system.

7.5.1. Complementary internal strain energy

Total complementary strain energy U^* is contributed by longitudinal and transversal normal and transverse shear stresses and is expressed as

$$U^* = (1/2)\int_L \int_A \left(\sigma_z \varepsilon_z + \sigma_y \varepsilon_y + \tau\gamma \right) dA dz \tag{7.9}$$

The strains are related to stresses through the orthotropic constitutive relations, i.e.,

$$\varepsilon_z = (1/E_z)\sigma_z - (\mu_{yz}/E_y)\sigma_y; \qquad \varepsilon_y = (1/E_y)\sigma_y - (\mu_{zy}/E_z)\sigma_z; \qquad \gamma = \tau/G \tag{7.10}$$

where E_z, E_y are the longitudinal and transverse elasticity moduli, respectively, G is the shear modulus, and μ_{zy} and μ_{yz} are Poisson's ratios which satisfy the condition $\mu_{yz}/E_y = \mu_{zy}/E_z$. From Eqs.(7.10), by substituting into Eq.(7.9), one obtains

$$U^* = (1/2)\int_L \int_A \left(\sigma_z^2/E_z + \sigma_y^2/E_y - 2\mu_{zy}\sigma_z\sigma_y/E_z + \tau^2/G \right) dA dz \tag{7.11}$$

Also, from Eqs. (7.6), by substituting into Eq.(7.11), one obtains

$$U^*=\int_L \frac{1}{2}\left\langle \hat{\mathbf{F}}(z) \quad \mathbf{F}''(z) \quad \tilde{\mathbf{F}}(z)\right\rangle^{\mathbf{T}} \begin{bmatrix} \mathbf{C}_{11} & -\mathbf{C}_{12} & \mathbf{0} \\ -\mathbf{C}_{12}^{\mathbf{T}} & \mathbf{C}_{22} & \mathbf{0} \\ \mathbf{0} & \mathbf{0} & \mathbf{C}_{33} \end{bmatrix} \begin{Bmatrix} \hat{\mathbf{F}}(z) \\ \mathbf{F}''(z) \\ \tilde{\mathbf{F}}(z) \end{Bmatrix} + \left\langle \hat{\mathbf{F}}(z) \quad \mathbf{F}''(z) \quad \tilde{\mathbf{F}}(z)\right\rangle^{\mathbf{T}} \begin{Bmatrix} \mathbf{d}_1(z) \\ \mathbf{d}_2(z) \\ \mathbf{d}_3(z) \end{Bmatrix} dz + D_1 \quad (7.12)$$

in which the following matrices of cross-sectional properties have been defined

$$\begin{aligned} &[\mathbf{C_{11}}]_{3(m+1)\times 3(m+1)} = (1/E_z)\int_A \hat{\boldsymbol{\chi}}(y)_{3(m+1)\times 1}\, \hat{\boldsymbol{\chi}}(y)^{\mathbf{T}}_{1\times 3(m+1)}\, dA;\; [\mathbf{C_{22}}]_{m\times m} = (1/E_y)\int_A \boldsymbol{\xi}_3(y)_{m\times 1}\, \boldsymbol{\xi}_3(y)^{\mathbf{T}}_{1\times m}\, dA; \\ &[\mathbf{C_{12}}]_{3(m+1)\times m} = (\mu_{zy}/E_z)\int_A \hat{\boldsymbol{\chi}}(y)_{3(m+1)\times 1}\, \boldsymbol{\xi}_3(y)^{\mathbf{T}}_{1\times m}\, dA; [\mathbf{C_{33}}]_{(2m+1)\times(2m+1)} = (1/G)\int_A \tilde{\boldsymbol{\chi}}(y)_{(2m+1)\times 1}\, \tilde{\boldsymbol{\chi}}(y)^{\mathbf{T}}_{1\times(2m+1)}\, dA; \end{aligned} \quad (7.13)$$

In Eq. (7.12), the term $D_1 = \int_L \int_A \left(\sigma_z^{*2}/2E_z + \sigma_y^{*2}/2E_y - \mu_{yz}\sigma_z^*\sigma_y^*/E_z + \tau^{*2}/2G \right) dA\,dz$ will vanish after taking the variation of the expression, and the traction-dependent displacement vectors are defined as

$$\begin{aligned} \mathbf{d_1}(z)_{3(m+1)\times 1} &= (1/E_z)\int_A \hat{\boldsymbol{\chi}}(y)_{3(m+1)\times 1}\left[\sigma_z^*(y,z) - \mu_{zy}\sigma_y^*(y,z)\right] dA; \\ \mathbf{d_2}(z)_{m\times 1} &= (1/E_y)\int_A \boldsymbol{\xi}_3(y)_{m\times 1}\left[\sigma_y^*(y,z) - \mu_{yz}\sigma_z^*(y,z)\right] dA; \\ \mathbf{d_3}(z)_{(2m+1)\times 1} &= (1/G)\int_A \tilde{\boldsymbol{\chi}}(y)_{(2m+1)\times 1}\, \tau^*(y,z)\, dA; \end{aligned} \quad (7.14a\text{-}c)$$

7.5.2. Load potential energy

The load potential energy is the surface integral of the tractions and line loads by the corresponding displacements and is given by

$$\begin{aligned} V^* = \; & \int_{A_{0\sigma}} w(y,0)\,\overline{\sigma}_z(y,0)\,dA + \int_{A_{0w}} \overline{w}(y,0)\,\sigma_z(y,0)\,dA + \int_{A_{0\tau}} v(y,0)\,\overline{\tau}(y,0)\,dA \\ & + \int_{A_{0v}} \overline{v}(y,0)\,\tau(y,0)\,dA - \int_{A_{L\sigma}} w(y,L)\,\overline{\sigma}_z(y,L)\,dA - \int_{A_{Lw}} \overline{w}(y,L)\,\sigma_z(y,L)\,dA \\ & - \int_{A_{L\tau}} v(y,L)\,\overline{\tau}(y,L)\,dA_s - \int_{A_{Lv}} \overline{v}(y,L)\,\tau(y,L)\,dA - \int_L q_y(z) v(z)\,dz - \int_L q_z(z) w(z)\,dz \end{aligned} \quad (7.15)$$

where all bars denote specified quantities. For example, for end $z_e = 0$, $\overline{\sigma}_z(y,0)$ is the specified longitudinal traction acting on area $A_{0\sigma}$ (Figure 7.1) and $\overline{w}(y,0)$ is the specified longitudinal displacement acting on area $A_{0w} = A - A_{0\sigma}$. Also, $\overline{\tau}(y,0)$ is the specified shear traction acting on area $A_{0\tau}$ and $\overline{v}(y,0)$ is the specified transverse displacement acting on $A_{0v} = A - A_{0\tau}$, and similar notation is adopted for end $z_e = L$. In the last two terms of Eq. (7.15), $q_y(z)$ and $q_z(z)$ are line loads in the transverse and longitudinal directions acting at height $y = a$ (Figure 7.4).They can be expressed as body forces $p_y(y,z)$ and $p_z(y,z)$ through the Dirac delta function as

$q_y(z) = Ap_y(y,z)Dirac(y-a)$ and $q_z(z) = Ap_z(y,z)Dirac(y-a)$ where A is the cross-section area of the beam.

7.5.3. Variation of total complementary strain energy

By taking the variation of the total complementary internal strain energy in Eq. (7.12) and integrating by parts (Appendix 7.3), one obtains

$$
\begin{aligned}
&\delta U^* = \\
&= \int_L \delta\mathbf{F}(z)^{\mathrm{T}} \left\{ \hat{\mathbf{I}}_1 \left[\mathbf{C}_{11}\hat{\mathbf{F}}(z) - \mathbf{C}_{12}\mathbf{F}''(z) + \mathbf{d}_1(\mathbf{z}) \right] - \mathbf{C}_{12}^{\mathrm{T}}\hat{\mathbf{F}}''(z) + \mathbf{C}_{22}\mathbf{F}''''(z) + \mathbf{d}_2''(\mathbf{z}) - \tilde{\mathbf{I}}_1\mathbf{C}_{33}\tilde{\mathbf{F}}'(z) - \tilde{\mathbf{I}}_1\mathbf{d}_3'(\mathbf{z}) \right\} dz \\
&+\delta\mathbf{F}(0)^{\mathrm{T}} \left\{ \int_L \hat{\mathbf{I}}_2 \left[\mathbf{C}_{11}\hat{\mathbf{F}}(z) - \mathbf{C}_{12}\mathbf{F}''(z) + \mathbf{d}_1(\mathbf{z}) \right] dz - \mathbf{C}_{12}^{\mathrm{T}}\hat{\mathbf{F}}'(0) + \mathbf{C}_{22}\mathbf{F}'''(0) + \mathbf{d}_2'(0) - \tilde{\mathbf{I}}_1\mathbf{C}_{33}\tilde{\mathbf{F}}(0) - \tilde{\mathbf{I}}_1\mathbf{d}_3(0) \right\} \\
&+\delta\mathbf{F}'(0)^{\mathrm{T}} \left\{ \int_L z\hat{\mathbf{I}}_3 \left[\mathbf{C}_{11}\hat{\mathbf{F}}(z) - \mathbf{C}_{12}\mathbf{F}''(z) + \mathbf{d}_1(\mathbf{z}) \right] dz - \left[-\mathbf{C}_{12}^{\mathrm{T}}\hat{\mathbf{F}}(0) + \mathbf{C}_{22}\mathbf{F}''(0) + \mathbf{d}_2(0) \right] + \int_L \tilde{\mathbf{I}}_2 \left[\mathbf{C}_{33}\tilde{\mathbf{F}}(z) + \mathbf{d}_3(\mathbf{z}) \right] dz \right\} \\
&-\delta\mathbf{F}(L)^{\mathrm{T}} \left\{ -\mathbf{C}_{12}^{\mathrm{T}}\hat{\mathbf{F}}'(L) + \mathbf{C}_{22}\mathbf{F}'''(L) - \tilde{\mathbf{I}}_1\mathbf{C}_{33}\tilde{\mathbf{F}}(L) + \mathbf{d}_2'(L) - \tilde{\mathbf{I}}_1\mathbf{d}_3(L) \right\} + \delta\mathbf{F}'(L)^{\mathrm{T}} \left\{ -\mathbf{C}_{12}^{\mathrm{T}}\hat{\mathbf{F}}(L) + \mathbf{C}_{22}\mathbf{F}''(L) + \mathbf{d}_2(L) \right\} \\
&+\delta N(0)\int_L \hat{\mathbf{I}}_4 \left[\mathbf{C}_{11}\hat{\mathbf{F}}(z) - \mathbf{C}_{12}\mathbf{F}''(z) + \mathbf{d}_1(\mathbf{z}) \right] dz + \delta M(0)\int_L \hat{\mathbf{I}}_6 \left[\mathbf{C}_{11}\hat{\mathbf{F}}(z) - \mathbf{C}_{12}\mathbf{F}''(z) + \mathbf{d}_1(\mathbf{z}) \right] dz + \\
&+\delta Q(0)\int_L \left[z\hat{\mathbf{I}}_5\mathbf{C}_{11}\hat{\mathbf{F}}(z) - z\hat{\mathbf{I}}_5\mathbf{C}_{12}\mathbf{F}''(z) + \tilde{\mathbf{I}}_3\mathbf{C}_{33}\tilde{\mathbf{F}}(z) + z\hat{\mathbf{I}}_5\mathbf{d}_1(\mathbf{z}) + \tilde{\mathbf{I}}_3\mathbf{d}_3(\mathbf{z}) \right] dz
\end{aligned}
\tag{7.16}
$$

in which the following matrices have been introduced

$$
\begin{aligned}
&\left[\hat{\mathbf{I}}_1\right]_{m\times 3(m+1)} = \left[[\mathbf{I}]_{m\times m} \mid \mathbf{0}_{m\times m} \mid \mathbf{0}_{m\times m} \mid \mathbf{0}_{m\times 1} \mid \mathbf{0}_{m\times 1} \mid \mathbf{0}_{m\times 1} \right]; \quad \left[\hat{\mathbf{I}}_2\right]_{m\times 3(m+1)} = \left[\mathbf{0}_{m\times m} \mid [\mathbf{I}]_{m\times m} \mid \mathbf{0}_{m\times m} \mid \mathbf{0}_{m\times 1} \mid \mathbf{0}_{m\times 1} \mid \mathbf{0}_{m\times 1} \right]; \\
&\left[\hat{\mathbf{I}}_3\right]_{m\times 3(m+1)} = \left[\mathbf{0}_{m\times m} \mid \mathbf{0}_{m\times m} \mid [\mathbf{I}]_{m\times m} \mid \mathbf{0}_{m\times 1} \mid \mathbf{0}_{m\times 1} \mid \mathbf{0}_{m\times 1} \right]; \quad \left[\hat{\mathbf{I}}_4\right]_{1\times 3(m+1)} = \left[\mathbf{0}_{1\times m} \mid \mathbf{0}_{1\times m} \mid \mathbf{0}_{1\times m} \mid 1 \mid 0 \mid 0 \right]; \\
&\left[\hat{\mathbf{I}}_5\right]_{1\times 3(m+1)} = \left[\mathbf{0}_{1\times m} \mid \mathbf{0}_{1\times m} \mid \mathbf{0}_{1\times m} \mid 0 \mid 1 \mid 0 \right]; \quad \left[\hat{\mathbf{I}}_6\right]_{1\times 3(m+1)} = \left[\mathbf{0}_{1\times m} \mid \mathbf{0}_{1\times m} \mid \mathbf{0}_{1\times m} \mid 0 \mid 0 \mid 1 \right]; \\
&\left[\tilde{\mathbf{I}}_1\right]_{m\times(2m+1)} = \left[\mathbf{I}_{m\times m} \quad \mathbf{0}_{m\times m} \quad \mathbf{0}_{m\times 1} \right]; \quad \left[\tilde{\mathbf{I}}_2\right]_{m\times(2m+1)} = \left[\mathbf{0}_{m\times m} \quad \mathbf{I}_{m\times m} \quad \mathbf{0}_{m\times 1} \right]; \quad \left[\tilde{\mathbf{I}}_3\right]_{1\times(2m+1)} = \left[\mathbf{0}_{1\times m} \quad \mathbf{0}_{1\times m} \quad 1 \right]
\end{aligned}
\tag{7.17}
$$

where $[\mathbf{I}]$ are the identity matrices. By taking the variation of Eq. (7.15) and noting that the variation of specified tractions and loads vanish, one obtains

$$
\delta V^* = \int_{A_{0w}} \bar{w}(y,0)\delta\sigma_z(y,0)\,dA + \int_{A_{0v}} \bar{v}(y,0)\delta\tau(y,0)\,dA - \int_{A_{Lw}} \bar{w}(y,L)\delta\sigma_z(y,L)\,dA - \int_{A_{Lv}} \bar{v}(y,L)\delta\tau(y,L)\,dA
\tag{7.18}
$$

Specified displacements $\bar{w}(y,z_e)$ and $\bar{v}(y,z_e)$ at member ends $z_e = 0, L$ are assumed to follow the distributions $\bar{w}(z_e,y) = \bar{W}(z_e) + \bar{\theta}(z_e)y$ and $\bar{v}(z_e,y) = \bar{V}(z_e)$ in which $\bar{W}(z_e), \bar{V}(z_e)$ are the specified longitudinal and transverse displacements and $\overline{\theta}(z_e)$ is the specified rotation (Figure 7.4) at both beam ends $(z_e = 0, L)$. By substitution into Eq. (7.18), one obtains

$$\delta V^* = \overline{W}(0)\delta N(0) + \overline{V}(0)\delta Q(0) + \overline{\theta}(0)\delta M(0) - \overline{W}(L)\delta N(L) - \overline{V}(L)\delta Q(L) - \overline{\theta}(L)\delta M(L) \tag{7.19}$$

in which stress resultants $N(z_e), Q(z_e), M(z_e)$ have been defined in Eq. (7.7).

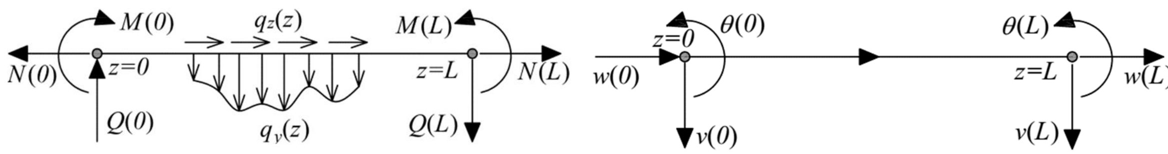

(a) (b)

Figure 7.4. Sign convention for (a) Resultant line loads and stress resultants and (b) End displacements

From Eqs. (7.6a-b), by substituting into Eq.(7.7), and setting $z = L$, one has

$$\begin{aligned} N(L) &= \left[\int_{A_{Lw}} \hat{\boldsymbol{\chi}}(y)^{\mathbf{T}}_{1\times 3(m+1)}\, dA\right]\hat{\mathbf{F}}(L)_{3(m+1)\times 1} + \int_{A_{Lw}} \sigma_z^*(y,L)\, dA \\ M(L) &= \left[\int_{A_{Lw}} y\hat{\boldsymbol{\chi}}(y)^{\mathbf{T}}_{1\times 3(m+1)}\, dA\right]\hat{\mathbf{F}}(L)_{3(m+1)\times 1} + \int_{A_{Lw}} y\sigma_z^*(y,L)\, dA \\ Q(L) &= \left[\int_{A_{L\tau}} \tilde{\boldsymbol{\chi}}(y)^{\mathbf{T}}_{1\times(2m+1)}\, dA\right]\tilde{\mathbf{F}}(L)_{(2m+1)\times 1} + \int_{A_{L\tau}} \tau^*(y,L)\, dA \end{aligned} \tag{7.20}$$

By the taking variation of Eq.(7.20), substituting into Eq.(7.19) (Appendix 7.4), and noting that the variations of the specified tractions and loads vanish, one obtains

$$\begin{aligned} \delta V^* &= -\delta\mathbf{F}(0)^{\mathbf{T}}\left[\{\mathbf{a}_1\}_{m\times 1}\overline{W}(L) + \{\mathbf{a}_2\}_{m\times 1}\overline{\theta}(L)\right] \\ &-\delta\mathbf{F}'(0)^{\mathbf{T}}\left[\{\mathbf{a}_3\}_{m\times 1}\overline{W}(L) + \{\mathbf{a}_4\}_{m\times 1}\overline{V}(L) + \{\mathbf{a}_5\}_{m\times 1}\overline{\theta}(L)\right] \\ &-\delta\mathbf{F}(L)^{\mathbf{T}}\left[\{\mathbf{a}_6\}_{m\times 1}\overline{W}(L) + \{\mathbf{a}_7\}_{m\times 1}\overline{\theta}(L)\right] - \delta\mathbf{F}'(L)^{\mathbf{T}}\{\mathbf{a}_8\}_{m\times 1}\overline{V}(L) \\ &-\delta N(0)\left[-\overline{W}(0) + a_9\overline{W}(L) + a_{10}\overline{\theta}(L)\right] \\ &-\delta Q(0)\left[-\overline{V}(0) + a_{11}(L)\overline{W}(L) + a_{12}(L)\overline{V}(L) + a_{13}(L)\overline{\theta}(L)\right] \\ &-\delta M(0)\left[-\overline{\theta}(0) + a_{14}\overline{W}(L) + a_{15}\overline{\theta}(L)\right] \end{aligned} \tag{7.21}$$

in which

$$\{\mathbf{a}_1\}_{m\times1}=\int_{A_{Lw}}\langle\boldsymbol{\psi}_2(y)\rangle_{1\times m}^T\,dA;\ \{\mathbf{a}_2\}_{m\times1}=\int_{A_{Lw}}y\langle\boldsymbol{\psi}_2(y)\rangle_{1\times m}^T\,dA;\ \{\mathbf{a}_3\}_{m\times1}=L\int_{A_{Lw}}\langle\boldsymbol{\psi}_1(y)\rangle_{1\times m}^T\,dA;$$

$$\{\mathbf{a}_4\}_{m\times1}=\int_{A_{L\tau}}\langle\boldsymbol{\psi}_3(y)\rangle_{1\times m}^T\,dA;\quad \{\mathbf{a}_5\}_{m\times1}=L\int_{A_{Lw}}y\langle\boldsymbol{\psi}_1(y)\rangle_{1\times m}^T\,dA;$$

$$\{\mathbf{a}_6\}_{m\times1}=\int_{A_{Lw}}\langle\boldsymbol{\xi}_1(y)\rangle_{1\times m}^T\,dA;\ \{\mathbf{a}_7\}_{m\times1}=\int_{A_{Lw}}y\langle\boldsymbol{\xi}_1(y)\rangle_{1\times m}^T\,dA;\ \{\mathbf{a}_8\}_{m\times1}=\int_{A_{L\tau}}\langle\boldsymbol{\xi}_2(y)\rangle_{1\times m}^T\,dA;$$

$$a_9=\int_{A_{Lw}}\eta_{12}(y)\,dA=1;\qquad a_{10}=\int_{A_{Lw}}y\eta_{12}(y)\,dA=0;\qquad a_{11}(L)=\int_{A_{Lw}}L\eta_{13}(y)\,dA=0;$$

$$a_{12}(L)=\int_{A_{L\tau}}\eta_{22}(y,L)\,dA=1;\quad a_{14}=\int_{A_{Lw}}\eta_{14}(y)\,dA=0;\qquad a_{15}=\int_{A_{Lw}}y\eta_{14}(y)\,dA=1;$$

$$a_{13}(L)=\left[L/b(h_2)\right]\left\{\left[\int_{-h_1}^{h_2}b(y)\,y^{n-1}dy\right]^2-\left[\int_{-h_1}^{h_2}b(y)\,y^{n}dy\right]\left[\int_{-h_1}^{h_2}b(y)y^{n-2}dy\right]\right\}\tag{7.22}$$

7.5.4. Compatibility equations and boundary conditions

From Eqs. (7.16) and (7.21), by substituting into the stationarity condition $\delta\pi^*=\delta U^*+\delta V^*=0$, one obtains m compatibility equations:

$$\mathbf{C_{22}F''''}(z)-\left[\hat{\mathbf{I}}_1\mathbf{C_{12}}+\mathbf{C_{12}^T}\hat{\mathbf{I}}_1^{\mathbf{T}}+\tilde{\mathbf{I}}_1\mathbf{C_{33}}\tilde{\mathbf{I}}_1^{\mathbf{T}}\right]\mathbf{F}''(z)+\hat{\mathbf{I}}_1\mathbf{C_{11}}\hat{\mathbf{I}}_1^{\mathbf{T}}\mathbf{F}(z)=\mathbf{R_{p1}}(z)+\mathbf{R_{p2}}(z)\tag{7.23}$$

In which $\mathbf{R_{p1}}(z)=-\hat{\mathbf{I}}_1\mathbf{C_{11}}\hat{\mathbf{I}}_2^{\mathbf{T}}\mathbf{F}(0)-z\hat{\mathbf{I}}_1\mathbf{C_{11}}\hat{\mathbf{I}}_3^{\mathbf{T}}\mathbf{F}'(0)-\hat{\mathbf{I}}_1\mathbf{C_{11}}\hat{\mathbf{I}}_4^{\mathbf{T}}N(0)-z\hat{\mathbf{I}}_1\mathbf{C_{11}}\hat{\mathbf{I}}_5^{\mathbf{T}}Q(0)-\hat{\mathbf{I}}_1\mathbf{C_{11}}\hat{\mathbf{I}}_6^{\mathbf{T}}M(0)$ and $\mathbf{R_{p2}}(z)=-\hat{\mathbf{I}}_1\mathbf{d_1}(z)-\mathbf{d_2}''(z)+\tilde{\mathbf{I}}_1\mathbf{d_3}'(z)=0$. The corresponding $4m+3$ boundary conditions are obtained as

$$\begin{aligned}\delta\mathbf{F}(0)^{\mathbf{T}}\Big\{&\int_0^L\left[\hat{\mathbf{I}}_2\mathbf{C_{11}}\hat{\mathbf{I}}_1^{\mathbf{T}}\mathbf{F}(z)-\hat{\mathbf{I}}_2\mathbf{C_{12}}\mathbf{F}''(z)\right]dz+\int_0^L dz\left[\hat{\mathbf{I}}_2\mathbf{C_{11}}\hat{\mathbf{I}}_2^{\mathbf{T}}\mathbf{F}(0)+\hat{\mathbf{I}}_2\mathbf{C_{11}}\hat{\mathbf{I}}_3^{\mathbf{T}}z\mathbf{F}'(0)\right]\\&+\mathbf{C_{22}F'''}(0)-\mathbf{C_{12}^T}\hat{\mathbf{I}}_1^{\mathbf{T}}\mathbf{F}'(0)-\mathbf{C_{12}^T}\hat{\mathbf{I}}_3^{\mathbf{T}}\mathbf{F}'(0)-\tilde{\mathbf{I}}_1\mathbf{C_{33}}\tilde{\mathbf{I}}_1^{\mathbf{T}}\mathbf{F}'(0)-\tilde{\mathbf{I}}_1\mathbf{C_{33}}\tilde{\mathbf{I}}_2^{\mathbf{T}}\mathbf{F}'(0)\\&+\int_0^L\hat{\mathbf{I}}_2\mathbf{C_{11}}\hat{\mathbf{I}}_4^{\mathbf{T}}N(0)dz+\left[\int_0^L\hat{\mathbf{I}}_2\mathbf{C_{11}}\hat{\mathbf{I}}_5^{\mathbf{T}}z\,dz-\mathbf{C_{12}^T}\hat{\mathbf{I}}_5^{\mathbf{T}}-\tilde{\mathbf{I}}_1\mathbf{C_{33}}\tilde{\mathbf{I}}_3^{\mathbf{T}}\right]Q(0)+\int_0^L\hat{\mathbf{I}}_2\mathbf{C_{11}}\hat{\mathbf{I}}_6^{\mathbf{T}}M(0)dz\\&+\int_0^L\hat{\mathbf{I}}_2\mathbf{d_1}(\mathbf{z})\,dz+\mathbf{d_2}'(0)-\tilde{\mathbf{I}}_1\mathbf{d_3}(0)-\left[\{\mathbf{a}_1\}W(L)+\{\mathbf{a}_2\}\theta(L)\right]\Big\}=0\end{aligned}\tag{7.24}$$

$$\begin{aligned}\delta\mathbf{F}'(0)^{\mathbf{T}}\Big\{&\int_0^L\left[z\hat{\mathbf{I}}_3\mathbf{C_{11}}\hat{\mathbf{I}}_1^{\mathbf{T}}\mathbf{F}(z)+\tilde{\mathbf{I}}_2\mathbf{C_{33}}\tilde{\mathbf{I}}_1^{\mathbf{T}}\mathbf{F}'(z)-z\hat{\mathbf{I}}_3\mathbf{C_{12}}\mathbf{F}''(z)\right]dz-\mathbf{C_{22}F''}(0)+\int_0^L z\hat{\mathbf{I}}_3\mathbf{C_{11}}\hat{\mathbf{I}}_2^{\mathbf{T}}\mathbf{F}(0)\,dz\\&+\mathbf{C_{12}^T}\hat{\mathbf{I}}_1^{\mathbf{T}}\mathbf{F}(0)+\mathbf{C_{12}^T}\hat{\mathbf{I}}_2^{\mathbf{T}}\mathbf{F}(0)+\int_0^L\left[z^2\hat{\mathbf{I}}_3\mathbf{C_{11}}\hat{\mathbf{I}}_3^{\mathbf{T}}\mathbf{F}'(0)+\tilde{\mathbf{I}}_2\mathbf{C_{33}}\tilde{\mathbf{I}}_2^{\mathbf{T}}\mathbf{F}'(0)\right]dz+\int_0^L z\hat{\mathbf{I}}_3\mathbf{C_{11}}\hat{\mathbf{I}}_4^{\mathbf{T}}N(0)\,dz\\&+\mathbf{C_{12}^T}\hat{\mathbf{I}}_4^{\mathbf{T}}N(0)+\int_0^L\left[z^2\hat{\mathbf{I}}_3\mathbf{C_{11}}\hat{\mathbf{I}}_5^{\mathbf{T}}+\tilde{\mathbf{I}}_2\mathbf{C_{33}}\tilde{\mathbf{I}}_3^{\mathbf{T}}\right]Q(0)\,dz+\int_0^L z\hat{\mathbf{I}}_3\mathbf{C_{11}}\hat{\mathbf{I}}_6^{\mathbf{T}}M(0)\,dz+\mathbf{C_{12}^T}\hat{\mathbf{I}}_6^{\mathbf{T}}M(0)\\&+\int_0^L z\hat{\mathbf{I}}_3\mathbf{d_1}(\mathbf{z})\,dz-\mathbf{d_2}(0)+\int_0^L\tilde{\mathbf{I}}_2\mathbf{d_3}(\mathbf{z})\,dz-\left[\{\mathbf{a}_3\}W(L)+\{\mathbf{a}_4\}V(L)+\{\mathbf{a}_5\}\theta(L)\right]\Big\}=0\end{aligned}\tag{7.25}$$

$$\delta\mathbf{F}(L)^{\mathrm{T}}\Big\{-\mathbf{C}_{12}^{\mathrm{T}}\hat{\mathbf{I}}_1^{\mathrm{T}}\mathbf{F}'(L)-\tilde{\mathbf{I}}_1\mathbf{C}_{33}\tilde{\mathbf{I}}_1^{\mathrm{T}}\mathbf{F}'(L)+\mathbf{C}_{22}\mathbf{F}'''(L)-\mathbf{C}_{12}^{\mathrm{T}}\hat{\mathbf{I}}_3^{\mathrm{T}}\mathbf{F}'(0)-\tilde{\mathbf{I}}_1\mathbf{C}_{33}\tilde{\mathbf{I}}_2^{\mathrm{T}}\mathbf{F}'(0)$$
$$-\mathbf{C}_{12}^{\mathrm{T}}\hat{\mathbf{I}}_5^{\mathrm{T}}Q(0)-\tilde{\mathbf{I}}_1\mathbf{C}_{33}\tilde{\mathbf{I}}_3^{\mathrm{T}}Q(0)+\mathbf{d}_2'(L)-\tilde{\mathbf{I}}_1\mathbf{d}_3(L)+\Big[\{\mathbf{a}_6\}_{n-2,1}W(L)+\{\mathbf{a}_7\}_{n-2,1}\theta(L)\Big]\Big\}=0 \tag{7.26}$$

$$\delta\mathbf{F}'(L)^{\mathrm{T}}\Big\{-\mathbf{C}_{12}^{\mathrm{T}}\hat{\mathbf{I}}_1^{\mathrm{T}}\mathbf{F}(L)+\mathbf{C}_{22}\mathbf{F}''(L)-\mathbf{C}_{12}^{\mathrm{T}}\hat{\mathbf{I}}_2^{\mathrm{T}}\mathbf{F}(0)-L\mathbf{C}_{12}^{\mathrm{T}}\hat{\mathbf{I}}_3^{\mathrm{T}}\mathbf{F}'(0)-\mathbf{C}_{12}^{\mathrm{T}}\hat{\mathbf{I}}_4^{\mathrm{T}}N(0)$$
$$-L\mathbf{C}_{12}^{\mathrm{T}}\hat{\mathbf{I}}_5^{\mathrm{T}}Q(0)-\mathbf{C}_{12}^{\mathrm{T}}\hat{\mathbf{I}}_6^{\mathrm{T}}M(0)+\mathbf{d}_2(L)-\{\mathbf{a}_8\}_{n-2,1}V(L)\Big\}=0 \tag{7.27}$$

$$\delta N(0)\Big\{\int_0^L\Big\{\Big[\hat{\mathbf{I}}_4\mathbf{C}_{11}\hat{\mathbf{I}}_1^{\mathrm{T}}\mathbf{F}(z)-\hat{\mathbf{I}}_4\mathbf{C}_{12}\mathbf{F}''(z)\Big]+\hat{\mathbf{I}}_4\mathbf{C}_{11}\hat{\mathbf{I}}_2^{\mathrm{T}}\mathbf{F}(0)+\hat{\mathbf{I}}_4\mathbf{C}_{11}\hat{\mathbf{I}}_3^{\mathrm{T}}z\mathbf{F}'(0)+\hat{\mathbf{I}}_4\mathbf{C}_{11}\hat{\mathbf{I}}_4^{\mathrm{T}}N(0)+$$
$$+\hat{\mathbf{I}}_4\mathbf{C}_{11}\hat{\mathbf{I}}_5^{\mathrm{T}}zQ(0)+\hat{\mathbf{I}}_4\mathbf{C}_{11}\hat{\mathbf{I}}_6^{\mathrm{T}}M(0)+\hat{\mathbf{I}}_4\mathbf{d}_1(\mathbf{z})\Big\}dz-\Big[W(0)+W(L)\Big]\Big\}=0 \tag{7.28}$$

$$\delta Q(0)\Big\{\int_0^L\Big[z\hat{\mathbf{I}}_5\mathbf{C}_{11}\hat{\mathbf{I}}_1^{\mathrm{T}}\mathbf{F}(z)+\tilde{\mathbf{I}}_3\mathbf{C}_{33}\tilde{\mathbf{I}}_1^{\mathrm{T}}\mathbf{F}'(z)-z\hat{\mathbf{I}}_5\mathbf{C}_{12}\mathbf{F}''(z)+z\hat{\mathbf{I}}_5\mathbf{C}_{11}\hat{\mathbf{I}}_2^{\mathrm{T}}\mathbf{F}(0)+z^2\hat{\mathbf{I}}_5\mathbf{C}_{11}\hat{\mathbf{I}}_3^{\mathrm{T}}\mathbf{F}'(0)+\tilde{\mathbf{I}}_3\mathbf{C}_{33}\tilde{\mathbf{I}}_2^{\mathrm{T}}\mathbf{F}'(0)$$
$$+z\hat{\mathbf{I}}_5\mathbf{C}_{11}\hat{\mathbf{I}}_4^{\mathrm{T}}N(0)+z^2\hat{\mathbf{I}}_5\mathbf{C}_{11}\hat{\mathbf{I}}_5^{\mathrm{T}}Q(0)+\tilde{\mathbf{I}}_3\mathbf{C}_{33}\tilde{\mathbf{I}}_3^{\mathrm{T}}Q(0)+z\hat{\mathbf{I}}_5\mathbf{C}_{11}\hat{\mathbf{I}}_6^{\mathrm{T}}M(0)+z\hat{\mathbf{I}}_5\mathbf{d}_1(\mathbf{z})+\tilde{\mathbf{I}}_3\mathbf{d}_3(\mathbf{z})\Big]dz \tag{7.29}$$
$$-\Big[V(0)+V(L)+a_{13}\theta(L)\Big]\Big\}=0$$

$$\delta M(0)\Big\{\int_0^L\Big[\hat{\mathbf{I}}_6\mathbf{C}_{11}\hat{\mathbf{I}}_1^{\mathrm{T}}\mathbf{F}(z)-\hat{\mathbf{I}}_6\mathbf{C}_{12}\mathbf{F}''(z)+\hat{\mathbf{I}}_6\mathbf{C}_{11}\hat{\mathbf{I}}_2^{\mathrm{T}}\mathbf{F}(0)+z\hat{\mathbf{I}}_6\mathbf{C}_{11}\hat{\mathbf{I}}_3^{\mathrm{T}}\mathbf{F}'(0)+\hat{\mathbf{I}}_6\mathbf{C}_{11}\hat{\mathbf{I}}_4^{\mathrm{T}}N(0)$$
$$+z\hat{\mathbf{I}}_6\mathbf{C}_{11}\hat{\mathbf{I}}_5^{\mathrm{T}}Q(0)+\hat{\mathbf{I}}_6\mathbf{C}_{11}\hat{\mathbf{I}}_6^{\mathrm{T}}M(0)+\hat{\mathbf{I}}_6\mathbf{d}_1(\mathbf{z})\Big]dz-\Big[-\theta(0)+\theta(L)\Big]\Big\}=0 \tag{7.30}$$

The m compatibility equations in Eq. (7.23) are of the fourth order and their integration leads to $4m$ unknown integration constants. The boundary conditions (7.24)-(7.30) involve nine end variables $W(0),V(0),\theta(0),W(L),V(L),\theta(L),N(0),Q(0),M(0)$ of which six will be known a-priori in a given problem. Thus, the total number of unknown constants is $4m+3$. In Eq. (7.24)-(7.30), either the variations $\delta\mathbf{F}(0)^{\mathrm{T}}$, $\delta\mathbf{F}'(0)^{\mathrm{T}}$, $\delta\mathbf{F}(L)^{\mathrm{T}}$ and $\delta\mathbf{F}'(L)^{\mathrm{T}}$ or the corresponding bracketed terms will vanish, leading to $4m$ boundary equations. It is always possible to select the z orientation so that either $\delta N(0)$, $\delta Q(0)$ or $\delta M(0)$ vanish or corresponding bracketed terms will vanish, leading to three additional equations, bringing the total number of boundary equations to $4m+3$. Explicit expressions of the stresses, governing equations, boundary conditions equations, and solutions for simple beams are provided in Appendix 7.5.

7.6. Closed form Solution

The homogeneous solution of the system is obtained by setting $\mathbf{R_{p1}}(z)+\mathbf{R_{p2}}(z)=\mathbf{0}$ in Eqs. (7.23) and is assumed to take the form $\{\mathbf{F}_H(z)\}_{m\times 1}=\sum\{\mathbf{F}_{Hi}(z)\}_{m\times 1}$ where $\{\mathbf{F}_{Hi}(z)\}_{m\times 1}=\{\phi_i\}_{m\times 1}e^{c_i z}A_i$, $\{\phi_i\}=\langle 1 \quad \phi_{2,i} \quad \ldots \quad \phi_{m,i}\rangle$, A_i are unknown constants and the value of i depends on the eigenvalue problem of the given compatibility equations. By substituting $\{\mathbf{F}_{Hi}(z)\}_{m\times 1}$ into Eq. (7.23), one obtains $\left[c_i^4\mathbf{C_{22}}-\left(\hat{\mathbf{I}}_1\mathbf{C_{12}}+\mathbf{C_{12}^T}\hat{\mathbf{I}}_1^{\mathbf{T}}+\tilde{\mathbf{I}}_1\mathbf{C_{33}}\tilde{\mathbf{I}}_1^{\mathbf{T}}\right)c_i^2+\hat{\mathbf{I}}_1\mathbf{C_{11}}\hat{\mathbf{I}}_1^{\mathbf{T}}\right]_{m\times m}\{\phi_i\}_{m\times 1}A_i=0$. For a non-trivial solution, the determinant of the matrix of coefficients vanishes. Given that the resulting eigenvalue problem is quartic in constant c_i, one obtains $4m$ eigen-pairs and the resulting solution takes the form

$$\{\mathbf{F_H}(z)\}_{m\times 1}=\{\mathbf{f}\}_{m\times 4m}\left[\mathbf{e}(z)\right]_{4m\times 4m}\{\mathbf{A}\}_{4m\times 1} \tag{7.31}$$

in which

$$\{\mathbf{f}\}_{m\times 4m}=\begin{bmatrix}1 & 1 & \ldots & 1\\ \phi_{2,1} & \phi_{2,2} & \ldots & \phi_{2,4m}\\ \vdots & \vdots & \ddots & \vdots\\ \phi_{m,1} & \phi_{m,2} & \ldots & \phi_{m,4m}\end{bmatrix};\quad \left[\mathbf{e}(z)\right]_{4m\times 4m}=\begin{Bmatrix}e^{c_1 z} & 0 & \ldots & 0\\ 0 & e^{c_2 z} & \ldots & 0\\ \vdots & \vdots & \ddots & \vdots\\ 0 & 0 & \ldots & e^{c_{4m}z}\end{Bmatrix};\quad \{\mathbf{A}\}_{4m\times 1}=\begin{Bmatrix}A_1\\ A_2\\ \vdots\\ A_{4m}\end{Bmatrix} \tag{7.32}$$

The particular solution $\{\mathbf{F_{P1}}(z)\}_{m\times 1}$ corresponding to $\mathbf{R_{p1}}(z)$ as given in Eq. (7.23) is assumed to take the form

$$\begin{aligned}\{\mathbf{F}_{P1}(z)\}_{m\times 1}=&\left[\overline{\mathbf{C}}_1\right]_{m\times m}\{\mathbf{F}(0)\}_{m\times 1}+z\left[\overline{\mathbf{C}}_2\right]_{m\times m}\{\mathbf{F}'(0)\}_{m\times 1}+\{\overline{\mathbf{C}}_3\}_{m\times 1}N(0)+z\{\overline{\mathbf{C}}_4\}_{m\times 1}Q(0)\\ &+\{\overline{\mathbf{C}}_5\}_{m\times 1}M(0)\end{aligned} \tag{7.33}$$

From Eq. (7.33), by substituting into Eq. (7.23), matrices and vectors $\overline{\mathbf{C}}_1,\ldots,\overline{\mathbf{C}}_5$ are determined as

$$\left[\overline{\mathbf{C}}_1\right]_{m\times m}=-\left(\hat{\mathbf{I}}_1\mathbf{C_{11}}\hat{\mathbf{I}}_1^{\mathbf{T}}\right)^{-1}\hat{\mathbf{I}}_1\mathbf{C_{11}}\hat{\mathbf{I}}_2^{\mathbf{T}};\left[\overline{\mathbf{C}}_2\right]_{m\times m}=-\left(\hat{\mathbf{I}}_1\mathbf{C_{11}}\hat{\mathbf{I}}_1^{\mathbf{T}}\right)^{-1}\hat{\mathbf{I}}_1\mathbf{C_{11}}\hat{\mathbf{I}}_3^{\mathbf{T}};\{\overline{\mathbf{C}}_3\}_{m\times 1}=-\left(\hat{\mathbf{I}}_1\mathbf{C_{11}}\hat{\mathbf{I}}_1^{\mathbf{T}}\right)^{-1}\hat{\mathbf{I}}_1\mathbf{C_{11}}\hat{\mathbf{I}}_4^{\mathbf{T}};$$
$$\{\overline{\mathbf{C}}_4\}_{m\times 1}=-\left(\hat{\mathbf{I}}_1\mathbf{C_{11}}\hat{\mathbf{I}}_1^{\mathbf{T}}\right)^{-1}\hat{\mathbf{I}}_1\mathbf{C_{11}}\hat{\mathbf{I}}_5^{\mathbf{T}};\{\overline{\mathbf{C}}_5\}_{m\times 1}=-\left(\hat{\mathbf{I}}_1\mathbf{C_{11}}\hat{\mathbf{I}}_1^{\mathbf{T}}\right)^{-1}\hat{\mathbf{I}}_1\mathbf{C_{11}}\hat{\mathbf{I}}_6^{\mathbf{T}}$$

Vector $\mathbf{R_{p2}}(z)$ in Eq. (7.23) depends upon the applied tractions $\sigma_y(h_1,z),\tau(h_1,z),\sigma_y(h_2,z)$, $\tau(h_2,z)$ The tractions are assumed as a power series with $u+1$ terms, i.e.,

$$\left\langle \sigma_y\left(h_1,z\right),\tau\left(h_1,z\right),\sigma_y\left(h_2,z\right),\tau\left(h_2,z\right)\right\rangle=\left\langle \sum_{i=0}^{u}\bar{a}_i z^i,\sum_{i=0}^{u}\bar{b}_i z^i,\sum_{i=0}^{u}\bar{c}_i z^i,\sum_{i=0}^{u}\bar{d}_i z^i\right\rangle \tag{7.34}$$

where u is the highest power of the series, and $\bar{a}_i,\bar{b}_i,\bar{c}_i$, $\bar{d}_i$ are known constants. Vector $\mathbf{R_{p2}}\left(z\right)$ can be evaluated from the tractions as given in Eq.(7.34) through the following 4-step procedure: (1) Substitute the tractions expressions in Eq. (7.34) into Eq.(7.4) to obtain $\bar{\tau}\left(y,z\right)$ and $\bar{\sigma}_y\left(y,z\right)$. (2) Given the traction expression in Eq. (7.34) and the expressions for $\bar{\tau}\left(y,z\right)$ and $\bar{\sigma}_y\left(y,z\right)$, substitute into Eq. (A1.4) to obtain $\rho_1\left(z\right)$ and $\rho_2\left(z\right)$. (3) Given ς_{11} and ς_{21} as determined from Eq. (A1.2) and $\rho_1\left(z\right)$, $\rho_2\left(z\right)$ as determined from step 2, determine the load dependent terms $\sigma_z^*\left(y,z\right),\tau^*\left(y,z\right)$ and $\sigma_y^*\left(y,z\right)$ from Eqs.(7.8)a-c. If the power series in Eq. (7.34) consists of $u+1$ terms, the double integration with respect to z of Eq. (7.8)a, increases the power series of $\sigma_z^*\left(y,z\right)$ to $u+3$ terms. (4) The expressions for $\sigma_z^*\left(y,z\right),\tau^*\left(y,z\right)$ and $\sigma_y^*\left(y,z\right)$ given in step 4 are substituted into Eq. (7.14) to determine $\mathbf{d_1}\left(z\right),\mathbf{d_2}\left(z\right),\mathbf{d_3}\left(z\right)$, and hence vector $\left\{\mathbf{R_{p2}}\left(z\right)\right\}$ can be expressed as

$$\left\{\mathbf{R_{p2}}\left(z\right)\right\}_{m\times1}=\left[\mathbf{g}\right]_{m\times(u+3)}\left\{\mathbf{Z}\left(z\right)\right\}_{(u+3)\times1} \tag{7.35}$$

where matrix $\left[\mathbf{g}\right]_{m\times(u+3)}$ is known and vector $\left\langle\mathbf{Z}\right\rangle^{\mathbf{T}}_{1\times(u+3)}=\left\langle 1 \quad z \quad \ldots \quad z^{u+2}\right\rangle$ has been defined. The particular solution $\left\{\mathbf{F_{P2}}\left(z\right)\right\}_{m\times1}$ corresponding to $\mathbf{R_{p2}}\left(z\right)$ can be assumed to take the form

$$\left\{\mathbf{F_{P2}}\left(z\right)\right\}_{m\times1}=\left[\overline{\mathbf{C}}\right]_{m\times(u+3)}\left\{\mathbf{Z}(z)\right\}_{(u+3)\times1} \tag{7.36}$$

where $\left[\overline{\mathbf{C}}\right]$ is an unknown matrix. From Eqs. (7.35), (7.36), by substituting into Eq. (7.23), one obtains

$$\begin{gathered}\mathbf{C_{22}}\left[\overline{\mathbf{C}}\right]_{m\times(u+3)}\left\{\mathbf{Z}_1\left(z\right)\right\}''''_{(u+3)\times1}-\left[\hat{\mathbf{I}}_1\mathbf{C_{12}}+\mathbf{C_{12}^T}\hat{\mathbf{I}}_1^{\mathbf{T}}+\tilde{\mathbf{I}}_1\mathbf{C_{33}}\tilde{\mathbf{I}}_1^{\mathbf{T}}\right]\left[\overline{\mathbf{C}}\right]_{m\times(u+3)}\left\{\mathbf{Z}_1\left(z\right)\right\}''_{(u+3)\times1}+\\+\hat{\mathbf{I}}_1\mathbf{C_{11}}\hat{\mathbf{I}}_1^{\mathbf{T}}\left[\overline{\mathbf{C}}\right]_{m\times(u+3)}\left\{\mathbf{Z}_1\left(z\right)\right\}_{(u+3)\times1}=\left[\overline{\mathbf{A}}\right]_{m\times(u+3)}\left\{\mathbf{Z}(z)\right\}_{(u+3)\times1}\end{gathered} \tag{7.37}$$

From Eq.(7.37), by equating the coefficients of z^i on both sides, one recovers the $m\times\left(u+3\right)$ equations that relate the coefficients of matrix $\left[\mathbf{g}\right]$ to those of the of unknown matrix $\left[\overline{\mathbf{C}}\right]$.

The general solution of Eqs. (7.23) is obtained by summing Eq. (7.31), (7.33) and (7.36) yielding

$$\left\{\mathbf{F}(z)\right\}_{m\times 1}=\left\{\mathbf{f}\right\}_{m\times 4m}\left[\mathbf{e}(z)\right]_{4m\times 4m}\left\{\mathbf{A}\right\}_{4m\times 1}+\left[\overline{\mathbf{C}}_1\right]_{m\times m}\left\{\mathbf{F}(\mathbf{0})\right\}_{m\times 1}+z\left[\overline{\mathbf{C}}_2\right]_{m\times m}\left\{\mathbf{F}'(\mathbf{0})\right\}_{m\times 1}+$$
$$+\left\{\overline{\mathbf{C}}_3\right\}_{m\times 1}N(0)+z\left\{\overline{\mathbf{C}}_4\right\}_{m\times 1}Q(0)+\left\{\overline{\mathbf{C}}_5\right\}_{m\times 1}M(0)+\left[\overline{\mathbf{C}}\right]_{m\times(u+3)}\left\{\mathbf{Z}(z)\right\}_{(u+3)\times 1} \quad (7.38)$$

Vector $\left\{\mathbf{F}(\mathbf{0})\right\}_{m\times 1}$ is determined by setting $z=0$ in Eq. (7.38) and $\left\{\mathbf{F}'(\mathbf{0})\right\}_{m\times 1}$ is obtained by differentiating Eqs. (7.38), and then setting $z=0$ (Appendix 7.6). The expressions of $\left\{\mathbf{F}(\mathbf{0})\right\}_{m\times 1}$ and $\left\{\mathbf{F}'(\mathbf{0})\right\}_{m\times 1}$ are then substituted into Eq. (7.38) yielding

$$\left\{\mathbf{F}(z)\right\}_{m\times 1}=\left[\mathbf{H_1}(z)\right]_{m\times 4m}\left\{\mathbf{A}\right\}_{4m\times 1}+\left\{\mathbf{H_2}\right\}_{m\times 1}N(0)+z\left\{\mathbf{H}_3\right\}_{m\times 1}Q(0)+\left\{\mathbf{H}_4\right\}_{m\times 1}M(0)+\left\{\mathbf{H}_5(z)\right\}_{m\times 1} \quad (7.39)$$

in which the following matrices have been defined.

$$\begin{aligned}
\left[\mathbf{H_1}(z)\right]_{m\times 4m}&=\left\{\mathbf{f}\right\}_{m\times 4m}\left[\mathbf{e}(z)\right]_{4m\times 4m}+z\left[\overline{\mathbf{C}}_2\right]_{m\times m}\left[\bar{\mathbf{I}}-\overline{\mathbf{C}}_1\right]_{m\times m}^{-1}\left\{\mathbf{f}\right\}_{m\times 4m}\left[\mathbf{e}'(0)\right]_{4m\times 4m}\\
&+\left[\overline{\mathbf{C}}_1\right]_{m\times m}\left[\bar{\mathbf{I}}-\overline{\mathbf{C}}_1\right]_{m\times m}^{-1}\left\{\mathbf{f}\right\}_{m\times 4m}\\
\left\{\mathbf{H_2}\right\}_{m\times 1}&=\left[\bar{\mathbf{I}}-\overline{\mathbf{C}}_1\right]_{m\times m}^{-1}\left\{\overline{\mathbf{C}}_3\right\}_{m\times 1},\left\{\mathbf{H}_3\right\}_{m\times 1}=\left[\bar{\mathbf{I}}-\overline{\mathbf{C}}_2\right]_{m\times m}^{-1}\left\{\overline{\mathbf{C}}_4\right\}_{m\times 1},\left\{\mathbf{H}_4\right\}_{m\times 1}=\left[\bar{\mathbf{I}}-\overline{\mathbf{C}}_1\right]_{m\times m}^{-1}\left\{\overline{\mathbf{C}}_5\right\}_{m\times 1},\\
\left\{\mathbf{H}_5(z)\right\}_{m\times 1}&=\left[\overline{\mathbf{C}}\right]_{m\times(u+3)}\left\{\mathbf{Z}(z)\right\}_{(u+3)\times 1}+z\left[\overline{\mathbf{C}}_2\right]_{m\times m}\left[\bar{\mathbf{I}}-\overline{\mathbf{C}}_2\right]_{m\times m}^{-1}\left[\overline{\mathbf{C}}\right]_{m\times(u+3)}\left\{\mathbf{Z}'(0)\right\}_{(u+3)\times 1}\\
&+\left[\overline{\mathbf{C}}_1\right]_{m\times m}\left[\bar{\mathbf{I}}-\overline{\mathbf{C}}_1\right]_{m\times m}^{-1}\left[\overline{\mathbf{C}}\right]_{m\times(u+3)}\left\{\mathbf{Z}(0)\right\}_{(u+3)\times 1}
\end{aligned} \quad (7.40)$$

From Eqs. (7.39), by substituting into the $4m+3$ boundary condition in Eq. (7.24)-(7.30), one obtains

$$\begin{aligned}
&\delta\mathbf{F}(0)^{\mathbf{T}}\left\{\left[\mathbf{b_{11}}\right]_{m\times 4m}\left\{\mathbf{A}\right\}_{4m\times 1}+\left\{\mathbf{b}_{12}\right\}_{m\times 1}N(0)+\left\{\mathbf{b}_{13}\right\}_{m\times 1}Q(0)+\left\{\mathbf{b}_{14}\right\}_{m\times 1}M(0)+\left[\mathbf{L_1}\right]_{m\times 1}\right.\\
&\left.-\left[\left\{\mathbf{a}_1\right\}_{m\times 1}\overline{W}(L)+\left\{\mathbf{a}_2\right\}_{m\times 1}\bar{\theta}(L)\right]\right\}=0
\end{aligned} \quad (7.41)$$

$$\begin{aligned}
&\delta\mathbf{F}'(0)^{\mathbf{T}}\left\{\left[\mathbf{b}_{21}\right]_{m\times 4m}\left\{\mathbf{A}\right\}_{4m\times 1}+\left\{\mathbf{b}_{22}\right\}_{m\times 1}N(0)+\left\{\mathbf{b}_{23}\right\}_{m\times 1}Q(0)+\left\{\mathbf{b}_{24}\right\}_{m\times 1}M(0)\right.\\
&\left.+\left\{\mathbf{L_2}\right\}_{m\times 1}-\left[\left\{\mathbf{a}_3\right\}_{n-2,1}\overline{W}(L)+\left\{\mathbf{a}_4\right\}_{n-2,1}\overline{V}(L)+\left\{\mathbf{a}_5\right\}_{n-2,1}\bar{\theta}(L)\right]\right\}=0
\end{aligned} \quad (7.42)$$

$$\delta\mathbf{F}(L)^{\mathbf{T}}\left\{\left[\mathbf{b}_{31}\right]_{m\times 4m}\left\{\mathbf{A}\right\}_{4m\times 1}+\left\{\mathbf{b}_{32}\right\}_{m\times 1}Q(0)+\left\{\mathbf{L_3}\right\}_{m\times 1}+\left[\left\{\mathbf{a}_6\right\}_{n-2,1}\overline{W}(L)+\left\{\mathbf{a}_7\right\}_{n-2,1}\bar{\theta}(L)\right]\right\}=0 \quad (7.43)$$

$$\begin{aligned}
&\delta\mathbf{F}'(L)^{\mathbf{T}}\left\{\left[\mathbf{b}_{41}\right]_{m\times 4m}\left\{\mathbf{A}\right\}_{4m\times 1}+\left\{\mathbf{b}_{42}\right\}_{m\times 1}N(0)+\left\{\mathbf{b}_{43}\right\}_{m\times 1}Q(0)+\left\{\mathbf{b}_{44}\right\}_{m\times 1}M(0)\right.\\
&\left.+\left\{\mathbf{L_4}\right\}_{m\times 1}-\left\{\mathbf{a}_8\right\}_{n-2,1}\overline{V}(L)\right\}=0
\end{aligned}$$

$$\delta N(0)\left\{\left[\mathbf{b}_{51}\right]_{m\times 4m}\left\{\mathbf{A}\right\}_{4m\times 1}+\left\{\mathbf{b}_{52}\right\}_{m\times 1}N(0)+\left\{\mathbf{b}_{53}\right\}_{m\times 1}Q(0)+\left\{\mathbf{b}_{54}\right\}_{m\times 1}M(0)+\left\{\mathbf{L_5}\right\}_{m\times 1}\right.$$
$$\left.-\left[-\overline{W}(0)+\overline{W}(L)\right]\right\}=0 \tag{7.44}$$

$$\delta Q(0)\left\{\left[\left[\mathbf{b}_{61}\right]_{m\times 4m}\left\{\mathbf{A}\right\}_{4m\times 1}+\left\{\mathbf{b}_{62}\right\}_{m\times 1}N(0)+\left\{\mathbf{b}_{63}\right\}_{m\times 1}Q(0)+\left\{\mathbf{b}_{64}\right\}_{m\times 1}M(0)+\left\{\mathbf{L_6}\right\}_{m\times 1}\right]\right.$$
$$\left.-\left[-\overline{V}(0)+\overline{V}(L)+a_{13}\overline{\theta}(L)\right]\right\}=0 \tag{7.45}$$

$$\delta M(0)\left\{\left[\left[\mathbf{b}_{71}\right]_{m\times 4m}\left\{\mathbf{A}\right\}_{4m\times 1}+\left\{\mathbf{b}_{72}\right\}_{m\times 1}N(0)+\left\{\mathbf{b}_{73}\right\}_{m\times 1}Q(0)+\left\{\mathbf{b}_{74}\right\}_{m\times 1}M(0)+\left\{\mathbf{L_7}\right\}_{m\times 1}\right]\right.$$
$$\left.-\left[-\overline{\theta}(0)+\overline{\theta}(L)\right]\right\}=0 \tag{7.46}$$

in which matrices $\left[\mathbf{b_{ij}}\right]$, ($i=1,\ldots,7$ and $j=1,2,\ldots,4$) depend solely on mechanical properties and beam cross-section, load vectors $\left\{\mathbf{L}_i\right\}_{m\times 1}$ are defined in Appendix 7.7, and one recalls that vectors $\left\{\mathbf{a_i}\right\}_{m\times 1}$ have been defined in Eqs. (7.22).

7.7. Verification and Applications

Example 1: Deflection of steel beams with W and WT cross-sections

A cantilever is subjected to a point load P acting at the tip (Figure 7.5a). Material is steel with a modulus of elasticity of 200 GPa and a Poisson ratio of 0.3. The span is taken as $L=4h$ in which h is the cross-sectional depth. Two cross-sections are considered (1) a W250x45 section (Figure 7.5b) and a WT250x200 (Figure 7.5c) according to ASTM A36. The cantilever is subjected to a load P acting at the tip with $P=18.2\ kN$ for the W-section and $P=23.4\ kN$ for the WT-section. The load levels were chosen to correspond to the same shear traction of $0.01MPa$ to the web of the cantilever tip, preventing stress localizations in the 3-D Finite Element Analysis (3D FEA). The deflections of the beam obtained from the present solutions are compared to those based as 3D FEA solution.

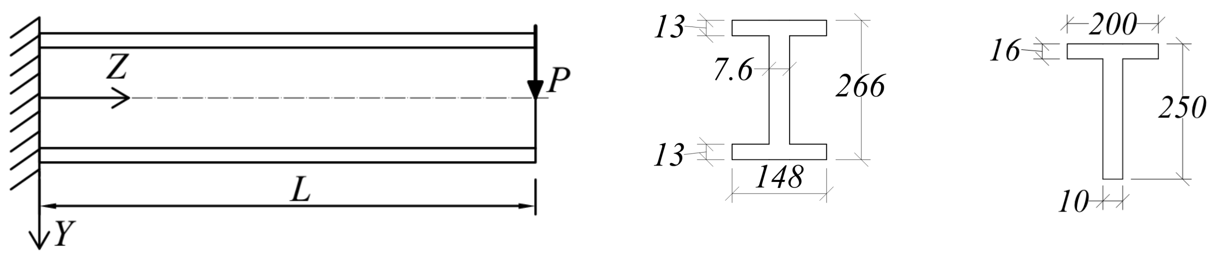

(a) (b) (c)

Figure 7.5. Cantilever steel beams under point load at the tip (a) Elevation, (b) cross-sectional dimensions for W250x45 (mm) and (c) cross-sectional dimensions for WT250x200 (mm)

Specifics of present closed form solution: In Eqs.(7.41)-(7.46), the natural boundary conditions of the problem correspond to $\delta\mathbf{F}(L)=\delta\mathbf{F}'(L)=0$, $\delta\mathbf{F}(0)\neq\mathbf{0}$, $\delta\mathbf{F}'(0)\neq\mathbf{0}$, $\delta N(0)\neq 0$, $\delta Q(0)\neq 0$, $\delta M(0)\neq 0$. Also, the essential boundary conditions are $V(0)=\theta(0)=W(0)=0$, $V(L)\neq 0$, $\theta(L)\neq 0$ and $W(L)\neq 0$. The internal forces $N(0)=0$, $Q(0)=P$, $M(0)=-PL$ are obtained from equilibrium. By applying the natural and essential boundary conditions in Eq. (7.41)-(7.46), $4m+3$ boundary equations are obtained for the $4m+3$ variables $\{\mathbf{A}\}_{4m\times 1}$, $V(L)$, $\theta(L)$ and $W(L)$. Expressions for $V(z)$, $\theta(z)$ and $W(z)$ are obtained by replacing symbol L in Eqs. (7.41)-(7.46) by coordinate z .

Description of the 3D FEA: The C3D8R element in the ABAQUS library is adopted for the 3D FEA solution. The element is an 8-node brick element with 3 translational degrees of freedom per node with reduced integration. A mesh sensitivity study was conducted to obtain the number of elements necessary to achieve convergence and the final mesh selected comprised 20 elements along the flange width overhang, 40 elements along the web height, 4 elements along the flange thickness, and 4 elements along the web thickness.

Deflections: Figure 7.6a-b present the deflection as a function of the longitudinal coordinate obtained from the present solution with n=3, 4, the Euler Bernoulli beam theory and the 3D FEA for W250x45 and WT250x200 sections. Compared to the 3D FEA solution, the Euler Bernoulli beam solution is observed to considerably underestimate beam deflections since it neglects shear deformation. In contrast, the present solutions with n=3 and 4 are found to be in excellent agreement with the 3D FEA results. Table 7.1 presents a comparison of the peak deflections as predicted by all four solutions. The

3D FEA solution is taken as a reference against which other solutions are compared. The Euler Bernoulli beam solution under-predicts the peak deflections by 18.1% and 9.0% for W250x45 and WT250x200 sections. In contrast, the present solution with n=3 over-predicts the peak deflection by 0.6% for the W250x45 and by 0.3% for the WT250x200. For n=4, the over-prediction reduces to 0.1% in both cases. It is also observed that the predictions of the present solutions match the Timoshenko beam solution (nearly coincident with the Euler Bernoulli beam but not shown for clarity).

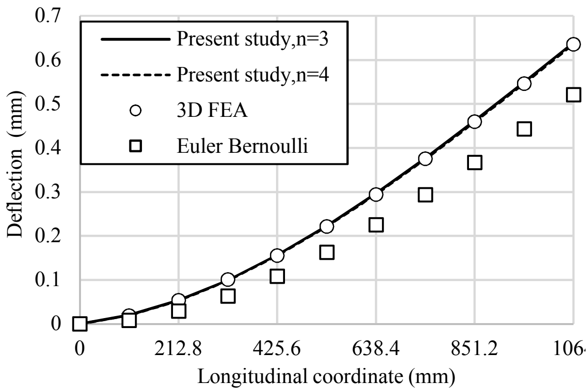

(a)

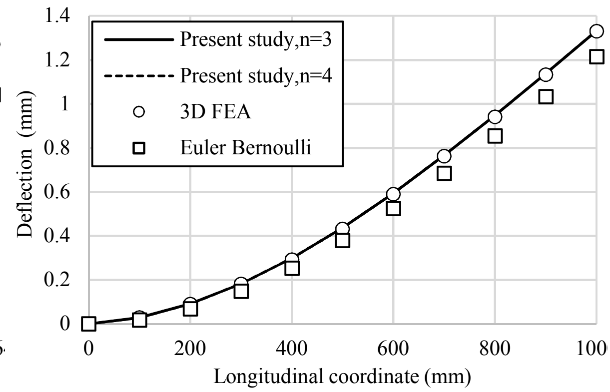

(b)

Figure 7.6. Deflection distributions against the longitudinal coordinate for (a) W250x45 section and (b) WT250x200 section

Table 7.1. Comparison of the peak deflections at the cantilever tips between three solutions

Solution	W250x45 section		T section	
	Value (mm)	% difference	Value (mm)	% difference
Euler Bernoulli beam	0.520	18.1	1.21	9.0
Present study, n=3	0.639	0.6	1.333	0.3
Present study, n=4	0.636	0.1	1.330	0.1
3D FEA	0.635	0.0	1.329	0.0

% difference of a solution is compared to the 3D FEA solution

Example 2: Simply supported wooden beam under uniform traction

A simply supported rectangular wooden beam is considered (Figure 7.7). Cross-section dimensions are $b \times h$ $=100 \times 200 mm$. Wood is assumed to have a longitudinal modulus of elasticity E_z = 11.4

GPa, a transverse modulus of elasticity E_y =1.48 GPa, a shear modulus G =1.24 GPa, and a Poisson's ratio $\mu_{zy} = 0.35$. The span L is taken as $3h$ and $10h$ to investigate the cases of deep and shallow beams. The uniform traction σ applied to span $L = 3h$ is 4.0 MPa while that applied to span $L = 10h$ is 0.4 MPa. Load magnitudes were selected to induce longitudinal stress levels at the extreme fiber that are comparable for both cases as predicted by the Euler-Bernoulli theory. The stress fields obtained from the present solution are compared to those based on the Euler-Bernoulli beam, the Timoshenko beam and the 3D FEA under ABAQUS.

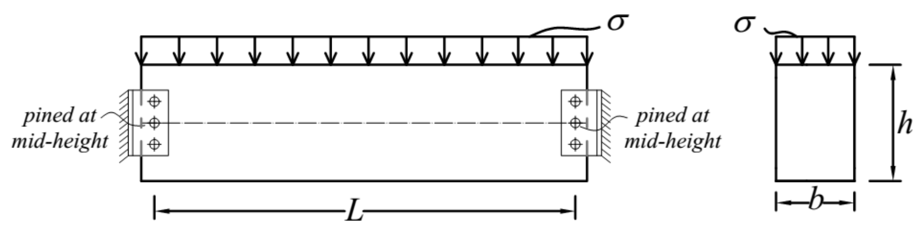

Figure 7.7. Simply supported beam under a uniform traction

Longitudinal normal stresses: Figure 7.8a-b depicts the mid-span longitudinal normal stress profiles for spans L=3h and L=10h as predicted by the present study with n=3 and 4, the Timoshenko beam solution, and the 3D FEA. For the short span L=3h, the stress profile predicted by the present solution with n=4 shows a slightly nonlinear distribution in a manner consistent with the 3D FEA solution. In slight contrast, the solutions based on the Timoshenko and present solution with n=3 show a linear stress profile. The peak stress at the top and bottom fibers predicted by the present solution with n=4 and the 3D FEA solution is 30.4 MPa, while that predicted by the Timoshenko and present solution with n=3 is 27.0 MPa, a 12.6% difference from the 3D FEA. For the longer span L=10h, the stress profiles predicted by all solutions are linear and essentially coincide.

Transverse shear stress profile: Figure 7.9a-b provide a comparison of the transverse shear stress profiles at end cross-sections for L=3h and L=10h. As observed, the present solutions with n=3, 4 predict identical stress profiles for both spans. The 3D FEA solution predicts a slightly smaller peak shear stress at mid-height fibers and non-zero stresses at the top and bottom fibers, especially in the span L=3h. Because no external shear tractions are applied to the top and bottom faces of the beam, the 3D FEA violates the traction boundary condition at both faces. This finding is characteristic of displacement based finite element formulations which interpolate displacement fields and contrasts with the present solution. In the contrast, the present solution which is based on statically admissible stress fields is able to satisfy the horizontal traction boundary conditions at the top and bottom faces in an exact sense.

Transverse normal stress profiles at mid-span: Figure 7.10a-b present the transverse normal stress profiles at mid-span section obtained from the present solution with n=3, 4 and the 3D FEA solution for L=3h and L=10h. As observed, all solutions are in excellent agreement. Both solutions contrast with conventional Euler-Bernoulli and Timoshenko beam solutions which cannot capture the transverse normal stresses.

Transverse normal stress profiles at support section: Figure 7.11a depicts the transverse normal stress profile at the support section as obtained from the present study with n=3-13 and the 3D FEA solution. The present solutions is observed to converge when n=9 as further increase in n does not cause a change in the stress profile. The 3D FEA predicted stress profile has a similar trend but different values from those of the present solution. Unlike the present solution which exactly satisfies the vertical traction boundary conditions at the top and bottom faces, the 3D FEA solution violates the vertical traction conditions at both faces.

Transverse normal stress profiles along the span: Figure 7.11b depicts the transverse normal stress profiles based on the present solution with n=9 for sections at z = 0, 0.1L-0.5L. Except for the stresses at z = 0 where significant localizations occur at the support, all stress profiles are nearly identical.

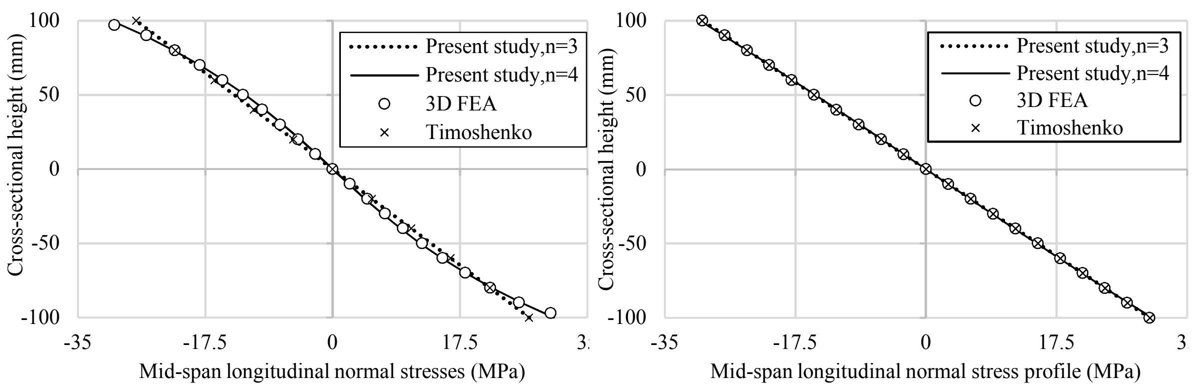

(a) (b)

Figure 7.8. Longitudinal stress profiles at mid-span cross-section for spans (a) L=3h and (b) L=10h

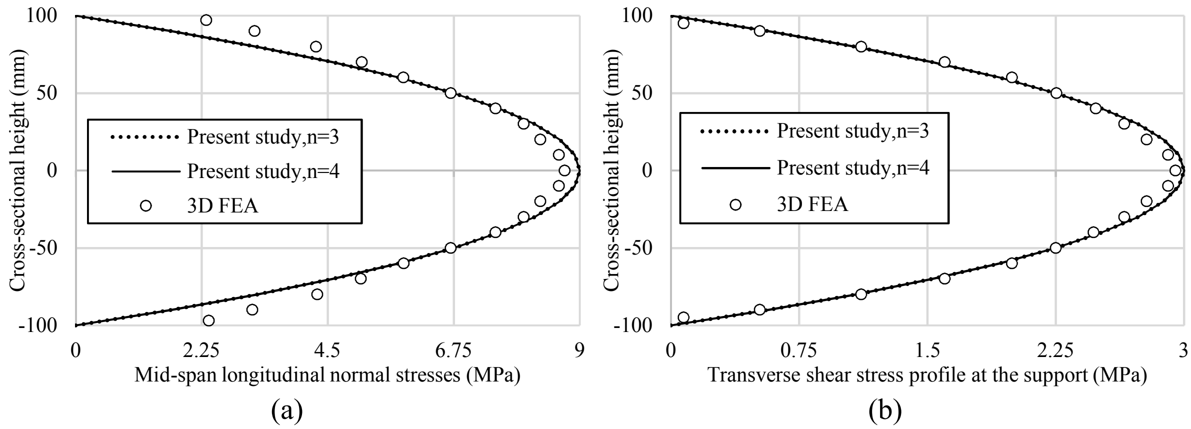

Figure 7.9. Transverse shear stress profiles at support cross-sections for spans (a) L=3h, (b) L=10h

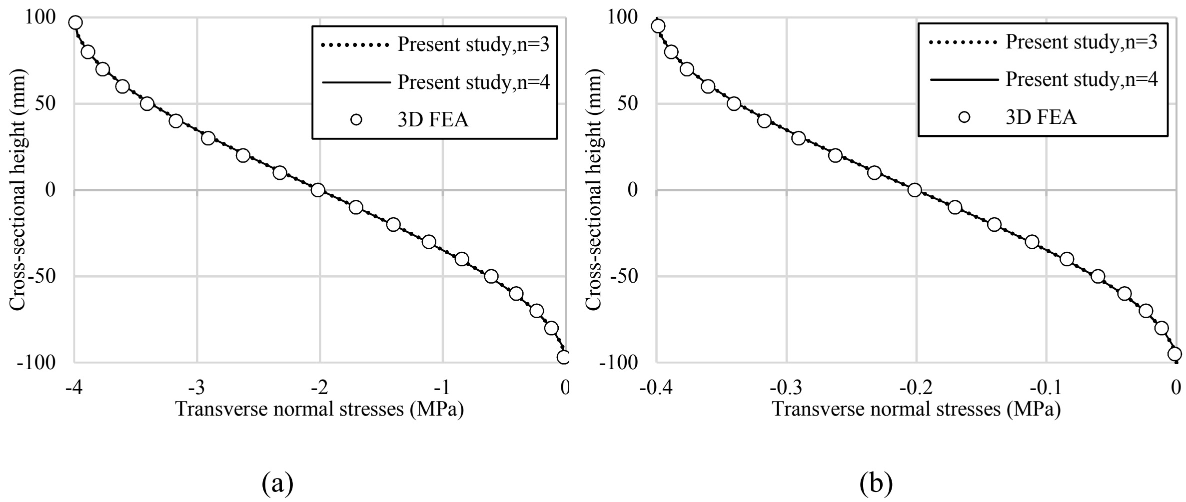

Figure 7.10. Transverse normal stress profiles at mid-span cross-sections for spans (a) L=3h, (b) L=10h (positive stresses denote tension)

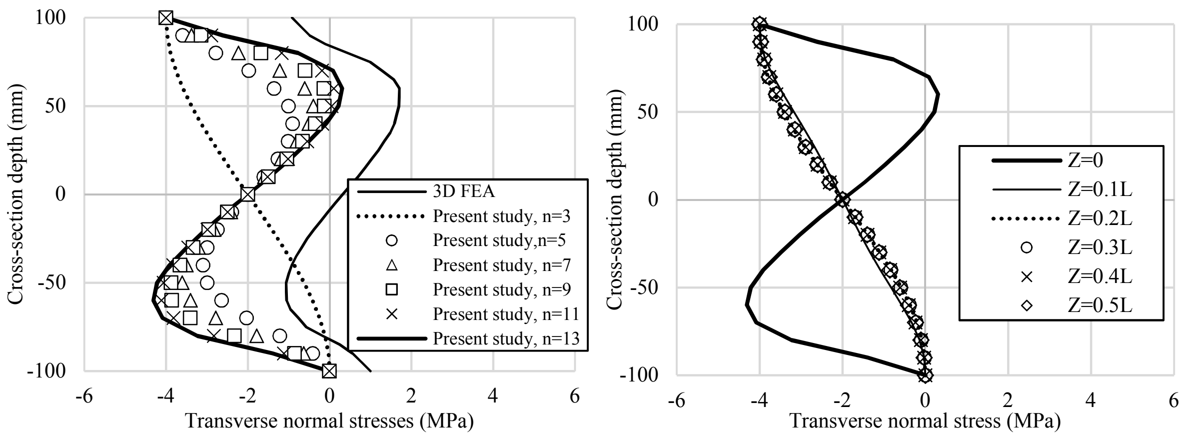

(a) (b)

Figure 7.11. Transverse normal stress profiles for L=3h (a) Effect of the number of terms n (z=0) , and (b) Effect of cross-section location Z (n=9)

<u>Effect of shear and transverse normal stresses</u>: In order to investigate the effect of shear deformation and transverse stresses on the mid-span deflection, the beam depth is kept constant and the span is changed so that the span-to-depth ratio is varied from 2 to 14. The ratio PS/EB of the peak deflection based present solution (PS) to that based on the Euler-Bernoulli beam solution (EB) is plotted as a function of the L/h ratio. Overlaid on the figure is the ratio PS/TB of the peak deflection based present solution (PS) to that based on the Timoshenko beam (TB) solution. Since the Timoshenko and present solutions capture the effects of longitudinal normal and shear stresses, but only the present solution captures the effect of normal transverse stress, the PS/TB ratio is indicative of transverse deformation effect on the deflection. Also, since the shear and the transverse stress effects are captured by the present theory but not in the Euler-Bernoulli beam, the ratio PS/EB can be considered to reflect the combined effect of shear and transverse normal stresses. Finally, the vertical distance in Fig. (7.12) between both curves reflect the effect of shear stresses alone. As expected, shear deformation effects are significant for short spans (e.g., PS/EB-PS/TB=3.17-1.12=2.05 at L/h=2) and reduces with higher L/h. The effect of transverse deformation is also observed to gain significance for shorter spans, albeit it is less influential than shear stresses. The PS/TB ratio is 1.12 at L/h=2 and reduces to 1.007 when L/h=14, suggesting it is negligible for long span beams.

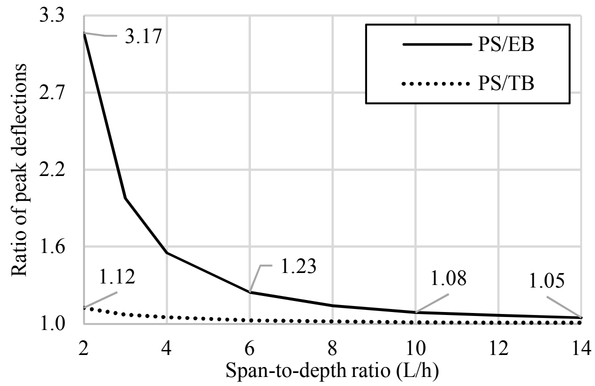

Figure 7.12. Effect of the shear deformation on the prediction of the peak deflection

Example 3. Effect of support height

In the present formulation, origin O in Figure 7.1 does not necessarily need to coincide with the cross-sectional centroid. This feature is used in the present example to model supports that are offset from the centroid. In Example 2, the end supports were assumed to be located at the section mid-height by locating origin O at the mid-height. We deviate from this convention in the present example, where origin O is moved to the bottom face of the beam (Figure 7.13). Figure 7.14a-b provides a comparison of the longitudinal normal stress distribution at the top and bottom fibers against the longitudinal coordinate for a span L=3h. Unlike the Timoshenko beam theory whereby the longitudinal stresses at the extreme fibers have a parabolic distribution with the longitudinal coordinate, those predicted by the 3D FEA solution exhibit a more complex shape. In comparison to the 3D FEA, the present solution with n=3 underestimates the stress distributions along both top and bottom faces. As the number of terms n increases to 5 and 7, the stress distributions along the top fiber predicted by the present solution approach that of the of the 3D FEA solution (Figure 7.14a). More terms are found necessary to attain convergence for the stresses on the bottom (Figure 7.14b) where convergence is attained for n=9 in excellent agreement with the 3D FEA predictions and no further change is observed for n=10. Similar findings are observed for L=10h (Figure 7.14c-d) where the solution with n=9 is observed to successfully capture the stress localization near the bottom supports. The longitudinal stress distribution for the case of mid-height support (as obtained from Example 2) based on the present solution with n=9 is overlaid on Figs.7.14a-d. Stress distributions at the top fibers for mid-height and bottom supports are comparable for the short-span beam (Fig. 7.14a) and nearly identical for the long-span beam, but considerable difference is observed between the stress distributions at bottom fiber between the bottom and mid-height support cases (Figs. 7.14b and 7.14d).

Figure 7.15a-b depicts the stress profiles at the mid-span cross-section predicted for L=3h and L=10h, respectively. For the short span L=3h, the linear stress profile predicted by the present solution with n=3 slightly differs from the slightly nonlinear stress profile predicted by the present study with n=5, which is observed to nearly coincide with the 3D FEA. It of interest to note that the neutral axis in the latter two solutions is slightly shifted downwards from the section mid-height since the high transverse stresses provided by the end supports at the bottom slightly enlarge the section width based on the Poisson's ratio effect, which causes a downward shift of the deformed section centroid. This phenomenon has not been observed in Example 2 where the end supports were located at mid-height. For L/h=10 (Fig. 7.15b), the downward shift of the neutral axis becomes negligible since the width enlargement is localized at the supports and is far from mid-span.

Figure 7.16 depicts the transverse normal stress profiles at sections z=0.1L-0.5L as obtained from the present solution with n=9 for a span L=3h. Overlaid on the figure is the stress profile at z=0.1L as obtained from the 3D FEA. Close agreement is observed between the present solution and 3D FEA predictions. Unlike the case of mid-height support in Example 2, stresses near the bottom face are significant. The stress profiles at sections from z=0.3L-0.5L are found almost identical. However, the stresses significantly increase as one approaches the support location.

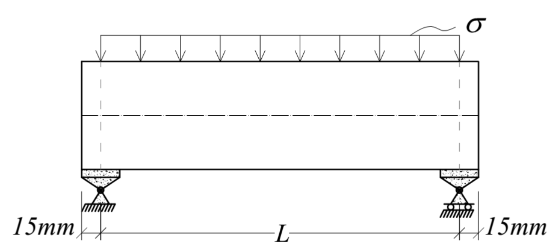

Figure 7.13. Beams simply supported at the bottom fibers

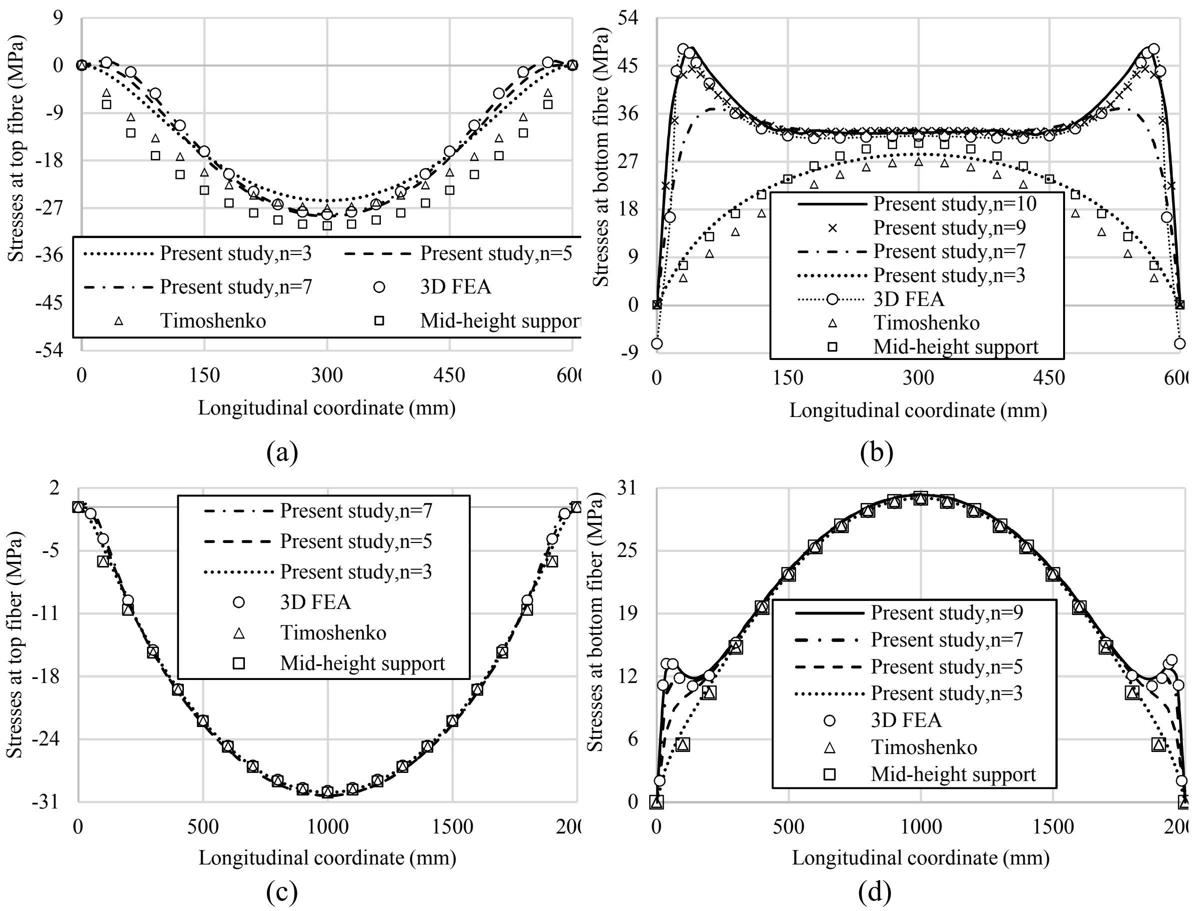

Figure 7.14. Longitudinal normal stresses for (a) At top fiber L=3h (b) At bottom fiber L-3h, (c) at top fiber L=10h, and b) at bottom fiber L=10h

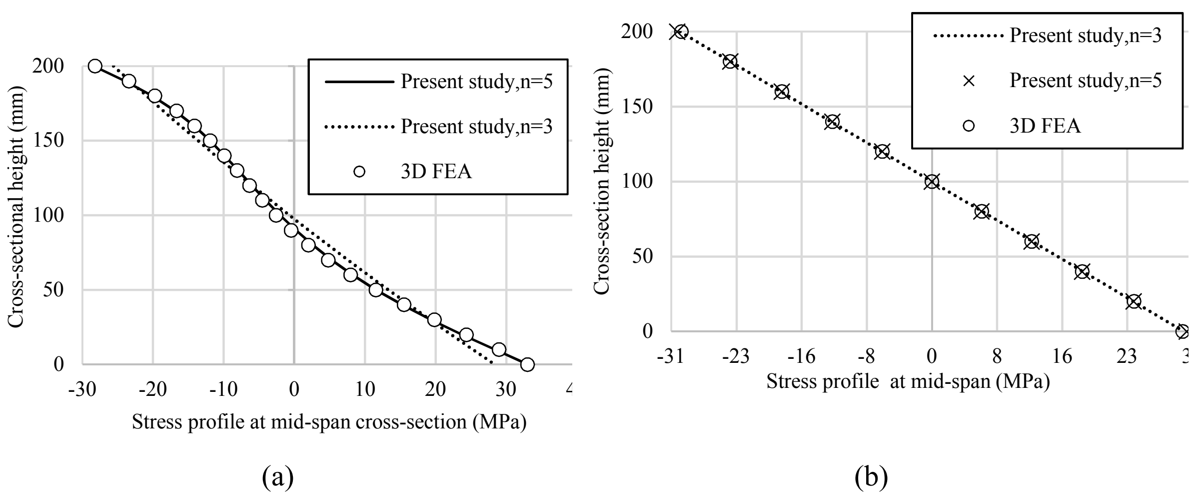

Figure 7.15. Longitudinal stress profiles at mid-span cross-section for spans (a) L=3h, (b) L=10h

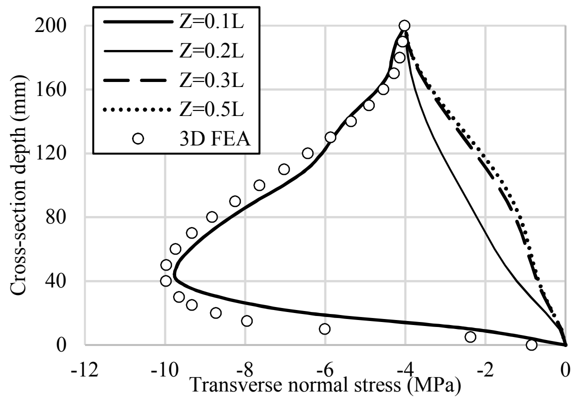

Figure 7.16. Transverse normal stress profiles at sections z=0.1L, 0.2L, 0.3L, and 0.5L

Example 4. Longitudinal stress profiles in deep beams:

Carrera and Guita (2010) and Patel et al. (2014) showed that the nonlinear distribution of the longitudinal normal stress across the section depth is significant for beams with very short spans (e.g., $L/h = 2$). As observed in Example 3, the longitudinal normal stress profile at mid-span is slightly nonlinear for the span-to-depth ratio $L = 3h$. The present solution is thus conducted to investigate the nonlinear stress profiles for the beam given in Example 3 with span-to-depth ratio L/h=1 and 2 and subjected to a downward traction $\sigma_y = 10MPa$ on the top face. Figure 7.17a,b) depicts the stress profiles at the mid-span section obtained from the present solution with n=4, 5, 7, 8 and 9 for L/h=1 and 2, respectively. When $n = 3$ (not shown on the figure for clarity), the present solution coincides with Euler-Bernoulli profile and as n increases, the predicted profiles become highly nonlinear and convergence is attained when $n = 8$. Further increase of n is shown not to influence the predicted stress profile. The converged stress profiles are clearly nonlinear across the depth.

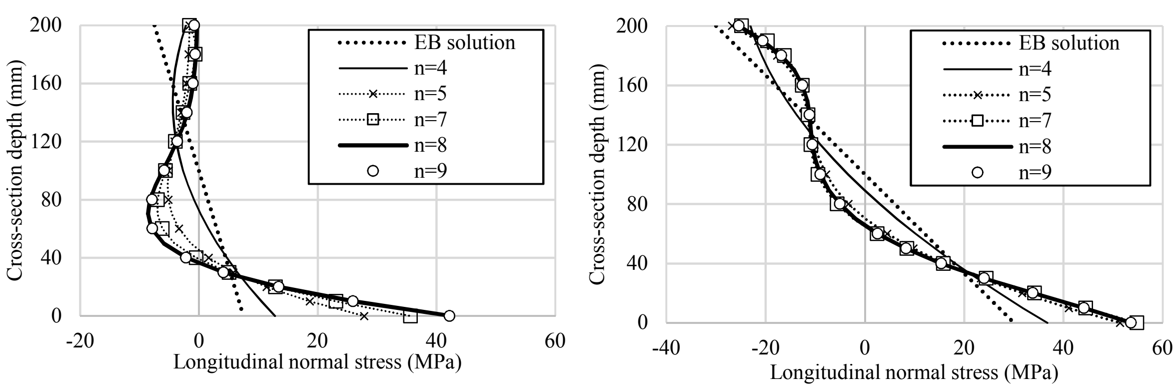

(a) L/h=1 (b) L/h=2

Figure 7.17. Longitudinal stress profiles at mid-span for spans (a) L=h and (b) L=2h

7.8. Summary and Conclusions

The main contributions of the study are summarized in the following:

(1) A high-order beam theory was developed for the static analysis of beams. The longitudinal normal stress field was assumed as a series of power functions in the transverse coordinate $y^{i-1}\left(i=1,2...,n\right)$ multiplied by unknown functions $F_i\left(z\right)$ of the longitudinal coordinate z. The corresponding shear and transverse normal stress fields were then derived from the infinitesimal 2D equilibrium conditions and the traction boundary conditions were satisfied in an infinitesimal exact sense. The resulting stress fields were used in conjunction with the principle of stationary complementary strain energy to express the compatibility conditions in terms of the unknown functions $F_i\left(z\right)$ and the possible essential and natural boundary conditions. The differential equations of compatibility were found to be coupled and a general solution was developed for the system.

(2) The theory was shown to successfully capture the longitudinal and transverse normal stresses, shear stresses, material orthotropy, and nonlinear stress profiles. It was shown to reliably predict the response of beams with monosymmetric cross-sections, with supports that are offset from the section centroid, and with short or long spans.

(3) Unlike conventional beam theories (e.g., Euler-Bernoulli, Timoshenko, etc.), the present solution avoids postulating any kinematic assumptions. As a result, the solution was shown to consistently converge to the displacements from above, in the sense that lower order stress polynomial solutions (i.e., small n) tend to overestimate the predicted deformations (i.e., underestimate the stiffness). As the polynomial order increases, the predicted displacements tend to reduce and approach those based on the 3D FEA in all cases examined.

(4) The assumed stress fields satisfy the traction boundary conditions at the top and bottom faces of the beam in an exact sense, a feature that is un-attainable under displacement-based 3D FEA solutions (e.g, Example 2) where equilibrium is satisfied only in an average integral sense.

(5) Within the family of solution developed, when the number of stress terms is $n=3$, the resulting longitudinal normal stress has a linear solution and the present theory provides results that are close, but not identical, to the Timoshenko beam theory predictions. The predictions of both theories do not exactly coincide since the present theory captures the transverse stresses while the Timoshenko beam omits the presence of transverse stresses. When the number of stress terms is $n \geq 4$ the stress profiles based on the present theory enable the solution to model nonlinear stress profiles that may arise in

deep beams and/or beams with supports that are offset from the section centroid. In such cases, the conventional Euler Bernoulli and Timoshenko beam theories were shown to yield unreliable predictions for the examples examined in the present study. The number of stress terms required to attain convergence depends on the beam span.

(6) The examples investigated in the present study showed that stress distribution near the end support highly depends on the support location relative to the section centroid. While supports at the centroid were associated with little nonlinearity of the stress profiles, bottom supports were associated with highly nonlinear stress distributions as predicted by the present solution and the 3D FEA.

(7) For the case of bottom supports, the present theory and the 3D FEA predict significant transverse normal stresses near the supports.

Appendix 7.1: Background for Developing Equations (7.6)a-c

This appendix presents the procedure to turn Eqs. (7.1) and (7.3a-b) into Eqs. (7.6a-c).

A7.1.1. Reducing the Number of Unknown Functions $F_i(z)$

From Equations (7.3a-b), by expressing functions F_{n-1} and F_n in terms of others $F_i(z)$ $i=1,\ldots,n-2$ one obtains

$$\begin{aligned}
&\alpha_{n-1}(h_2)F_{n-1}{}'(z)+\alpha_n(h_2)F_n'(z)=\bar{\tau}(h_2,z)-\tau(h_2,z)-\sum_{i=1}^{n-2}\alpha_i(h_2)F_i'(z)\\
&\beta_{n-1}(h_2)F_{n-1}{}''(z)+\beta_n(h_2)F_n''(z)=\sigma_y(h_2,z)-\bar{\sigma}_y(h_2,z)-\sum_{i=1}^{n-2}\beta_i(h_2)F_i''(z)
\end{aligned}\tag{7.47a-b}$$

From Eq. (7.47a), by differentiation with respect to z, combining with Eq. (7.47b) and solving for F''_{n-1} and F''_n, one obtains

$$\begin{aligned}
&F_{n-1}{}''(z)=\rho_1(z)-\sum_{i=1}^{n-2}\lambda_{1i}F_i''(z)\\
&F_n''(z)=\rho_2(z)-\sum_{i=1}^{n-2}\lambda_{2i}F_i''(z)
\end{aligned}\tag{7.48a-b}$$

Where the following symbols have been defined

$$\rho_1(z)=\frac{\alpha_n(h_2)\left[\sigma_y(h_2,z)-\bar{\sigma}_y(h_2,z)\right]-\beta_n(h_2)\left[\bar{\tau}'(h_2,z)-\tau'(h_2,z)\right]}{\alpha_n(h_2)\beta_{n-1}(h_2)-\alpha_{n-1}(h_2)\beta_n(h_2)};$$
$$\rho_2(z)=-\frac{\alpha_{n-1}(h_2)\left[\sigma_y(h_2,z)-\bar{\sigma}_y(h_2,z)\right]-\beta_{n-1}(h_2)\left[\bar{\tau}'(h_2,z)-\tau'(h_2,z)\right]}{\alpha_n(h_2)\beta_{n-1}(h_2)-\alpha_{n-1}(h_2)\beta_n(h_2)}; \qquad (7.49a\text{-}d)$$
$$\lambda_{1i}=\frac{\alpha_n(h_2)\beta_i(h_2)-\beta_n(h_2)\alpha_i(h_2)}{\alpha_n(h_2)\beta_{n-1}(h_2)-\alpha_{n-1}(h_2)\beta_n(h_2)};\quad \lambda_{2i}=-\frac{\alpha_{n-1}(h_2)\beta_i(h_2)-\beta_{n-1}(h_2)\alpha_i(h_2)}{\alpha_n(h_2)\beta_{n-1}(h_2)-\alpha_{n-1}(h_2)\beta_n(h_2)};$$

Traction equilibrium requires that stress fields $\sigma_y(y,z)$ and $\tau(y,z)$ at the top and faces $z=-h_1$ and $z=h_2$ be equal to the externally applied surface tractions. Therefore, all factors in Eqs. (7.49a-d) are known. By integrating Eqs. (7.48a-b) twice from 0 to z, functions $F_{n-1}(z)$ and $F_n(z)$ are obtained as

$$\begin{aligned}F_{n-1}(z)&=\int_0^z\int_0^z\rho_{11}(z)dz-\sum_{i=1}^{n-2}\lambda_{1i}F_i(z)+\sum_{i=1}^{n-2}\lambda_{1i}F_i(0)+z\sum_{i=1}^{n-2}\lambda_{1i}F_i'(0)+F_{n-1}(0)+zF_{n-1}'(0)\\ F_n(z)&=\int_0^z\int_0^z\rho_{21}(z)dzdz-\sum_{i=1}^{n-2}\lambda_{2i}F_i(z)+\sum_{i=1}^{n-2}\lambda_{2i}F_i(0)+z\sum_{i=1}^{n-2}\lambda_{2i}F_i'(0)+F_n(0)+zF_n'(0)\end{aligned} \qquad (7.50a\text{-}b)$$

A7.1.2. Expressing Constants in terms of Stress Resultants

Constants $F_{n-1}(0)$, $F_{n-1}'(0)$, $F_n(0)$, and $F_n'(0)$ appearing in Eqs. (7.50a-b) are then eliminated by using four equations; the first one is obtained by differentiating Eqs. (7.50a-b) with respect to z and substituting $F_{n-1}{}'$ and $F_{n-1}{}''$ into Eq. (7.47a), yielding

$$\begin{aligned}&\left\{\alpha_{n-1}(h_2)\int_0^z\rho_{11}(z)dz+\alpha_n(h_2)\int_0^z\rho_{21}(z)dz-\left[\bar{\tau}(h_2,z)-\tau(h_2,z)\right]\right\}+\\ &+\left\{-\alpha_{n-1}(h_2)\sum_{i=1}^{n-2}\lambda_{1i}F_i'(z)-\alpha_n(h_2)\sum_{i=1}^{n-2}\lambda_{2i}F_i'(z)+\sum_{i=1}^{n-2}\alpha_i(h_2)F_i'(z)\right\}+\\ &+\alpha_{n-1}(h_2)F_{n-1}'(0)+\alpha_n(h_2)F_n'(0)=-\alpha_{n-1}(h_2)\sum_{i=1}^{n-2}\lambda_{1i}F_i'(0)-\alpha_n(h_2)\sum_{i=1}^{n-2}\lambda_{2i}F_i'(0)\end{aligned} \qquad (7.51)$$

From Eqs. (7.49a-b), by substituting into Eq.(7.51), one obtains

$$\begin{aligned}&-\bar{\tau}(h_2,0)+\tau(h_2,0)+\left[-\sum_{i=1}^{n-2}\left[\alpha_{n-1}(h_2)\lambda_{1i}+\alpha_n(h_2)\lambda_{2i}+\alpha_i(h_2)\right]F_i'(z)\right]+\\ &+\alpha_{n-1}(h_2)F_{n-1}'(0)+\alpha_n(h_2)F_n'(0)=-\alpha_{n-1}(h_2)\sum_{i=1}^{n-2}\lambda_{1i}F_i'(0)-\alpha_n(h_2)\sum_{i=1}^{n-2}\lambda_{2i}F_i'(0)\end{aligned} \qquad (7.52)$$

From Eq. (7.52), by noting the identity $\alpha_{n-1}(h_2)\lambda_{1i}+\alpha_n(h_2)\lambda_{2i}+\alpha_i(h_2)=0$, one obtains

$$\alpha_{n-1}(h_2)F'_{n-1}(0)+\alpha_n(h_2)F'_n(0)=\left[\bar{\tau}(h_2,0)-\tau(h_2,0)\right]-\sum_{i=1}^{n-2}\alpha_i(h_2)F'_i(0) \tag{7.53}$$

The other three equations are recovered by introducing the stress resultant

$$\int_{A_{0w}}\sigma_z(y,0)dA=N(0);\quad \int_{A_{0\tau}}\tau(y,0)dA=Q(0);\quad \int_{A_{0w}}y\sigma_z(y,0)dA=M(0) \tag{7.54a-c}$$

Where A_{0w} and $A_{0\tau}$ are area parts of member cross-section at $z=0$ where prescribed longitudinal and transverse displacements, respectively are applied as boundary conditions. These stress resultants can be balanced to reaction forces at the boundary. From Eqs. (7.1) and (7.3a-b), one obtains

$$\begin{aligned}
\sigma_z(y,0)&=y^{n-2}F_{n-1}(0)+y^{n-1}F_n(0)+\sum_{i=1}^{n-2}y^{i-1}F_i(0)\\
\tau(y,0)&=\bar{\tau}(y,0)-\alpha_{n-1}(y)F_{n-1}{}'(0)-\alpha_n(y)F_n{}'(0)-\sum_{i=1}^{n-2}\alpha_i(y)F'_i(0)
\end{aligned} \tag{7.55a-b}$$

From Eqs. (7.55a-b), by substituting into Eqs. (7.54a-c), one obtains

$$\begin{aligned}
&\bar{\alpha}_{n-2}F_{n-1}(0)+\bar{\alpha}_{n-1}F_n(0)=N(0)-\sum_{i=1}^{n-2}\bar{\alpha}_{i-1}F_i(0)\\
&\hat{\alpha}_{n-1}F'_{n-1}(0)+\hat{\alpha}_nF'_n(0)=-Q(0)+\int_A\bar{\tau}(y,0)dA-\sum_{i=1}^{n-2}\hat{\alpha}_iF'_i(0)\\
&\bar{\alpha}_{n-1}F_{n-1}(0)+\bar{\alpha}_nF_n(0)=M(0)-\sum_{i=1}^{n-2}\bar{\alpha}_iF_i(0)
\end{aligned} \tag{7.56a-c}$$

in which sectional properties $\bar{\alpha}_i=\int_{A_{0w}}y^idA$ and $\hat{\alpha}_i=\int_{A_{0\tau}}\alpha_i(y)dA$ have been defined. From Eq. (7.53) and Eqs. (7.56a-c), functions $F'_{n-1}(0),F'_n(0),F_{n-1}(0),F_n(0)$ can be expressed as

$$\begin{aligned}
F'_{n-1}(0)&=\varsigma_{11}+\varsigma_{12}Q(0)+\sum_{i=1}^{n-2}\varsigma_{13i}F'_i(0)\\
F'_n(0)&=\varsigma_{21}+\varsigma_{22}Q(0)+\sum_{i=1}^{n-2}\varsigma_{23i}F'_i(0)\\
F_{n-1}(0)&=\varsigma_{31}N(0)+\varsigma_{32}M(0)+\sum_{i=1}^{n-2}\varsigma_{33i}F_i(0)\\
F_n(0)&=\varsigma_{41}N(0)+\varsigma_{42}M(0)+\sum_{i=1}^{n-2}\varsigma_{43i}F_i(0)
\end{aligned} \tag{7.57a-d}$$

in which the coefficients ς_{ij} are defined in Appendix 2. From Eqs. (7.50a-b), by substituting into Eqs. (7.1) and (7.3a-b), one obtains

$$\sigma_z(y,z)=\int_0^z\int_0^z\left(y^{n-2}\rho_1(z)+y^{n-1}\rho_2(z)\right)dzdz+\left(y^{n-2}F_{n-1}(0)+zy^{n-2}F'_{n-1}(0)+y^{n-1}F_n(0)+zy^{n-1}F'_n(0)\right)$$
$$+\sum_{i=1}^{n-2}\left(y^{n-2}\lambda_{1i}+y^{n-1}\lambda_{2i}\right)F_i(0)+\sum_{i=1}^{n-2}\left(y^{n-2}\lambda_{1i}+y^{n-1}\lambda_{2i}\right)zF'_i(0)-\sum_{i=1}^{n-2}\left(y^{n-2}\lambda_{1i}+y^{n-1}\lambda_{2i}-y^{i-1}\right)F_i(z)$$
$$\tau(y,z)=\bar{\tau}(y,z)-\int_0^z\left[\alpha_{n-1}(y)\rho_1(z)+\alpha_n(y)\rho_2(z)\right]dz-\alpha_{n-1}(y)F'_{n-1}(0)-\alpha_n(y)F'_n(0)$$
$$-\sum_{i=1}^{n-2}\left[\alpha_{n-1}(y)\lambda_{1i}+\alpha_n(y)\lambda_{2i}\right]F'_i(0)+\sum_{i=1}^{n-2}\left[\alpha_{n-1}(y)\lambda_{1i}+\alpha_n(y)\lambda_{2i}-\alpha_i(y)\right]F'_i(z)$$
$$\sigma_y(y,z)=\bar{\sigma}_y(y,z)+\beta_{n-1}(y)\rho_1(z)+\beta_n(y)\rho_2(z)+\sum_{i=1}^{n-2}\left[\beta_i(y)-\beta_{n-1}(y)\lambda_{1i}-\beta_n(y)\lambda_{2i}\right]F''_i(z)$$

(7.58a-c)

Also, from Eqs. (7.57a-d), by substituting into Eqs. (7.58a-c) and introducing $m=n-2$, one obtains Eqs. (7.6)a-c.

Appendix 7.2: Definition of Terms appearing the stress expressions

This appendix provides the steps for characterizing the terms appearing in Eqs. (7.6) and (7.8).

(1) Determine the constants:

$$\bar{\alpha}_i=\int_{A_{0w}}y^i dA,\quad \hat{\alpha}_i=\int_{A_{0\tau}}\alpha_i(y)\,dA \tag{7.59}$$

where i ranges from 1 to $m=n-2$.

(2) Given $\alpha_i(y)$ in Eq. 7.5a, $\bar{\alpha}_i$ and $\hat{\alpha}_i$ in Eqs. (7.59) and the applied tractions, determine:

$$\varsigma_{11}=-\frac{\alpha_n(h_2)\int_A\bar{\tau}(y,0)\,dA-\hat{\alpha}_n\left[\bar{\tau}(h_2,0)-\tau(h_2,0)\right]}{\hat{\alpha}_n\alpha_{n-1}(h_2)-\hat{\alpha}_{n-1}\alpha_n(h_2)};\qquad \varsigma_{12}=\frac{\alpha_n(h_2)}{\hat{\alpha}_n\alpha_{n-1}(h_2)-\hat{\alpha}_{n-1}\alpha_n(h_2)};$$
$$\varsigma_{21}=\frac{\alpha_{n-1}(h_2)\int_A\bar{\tau}(y,0)\,dA-\hat{\alpha}_{n-1}\left[\bar{\tau}(h_2,0)-\tau(h_2,0)\right]}{\hat{\alpha}_n\alpha_{n-1}(h_2)-\hat{\alpha}_{n-1}\alpha_n(h_2)};\varsigma_{22}=-\frac{\alpha_{n-1}(h_2)}{\hat{\alpha}_n\alpha_{n-1}(h_2)-\hat{\alpha}_{n-1}\alpha_n(h_2)};$$
$$\varsigma_{31}=\frac{\bar{\alpha}_n}{\bar{\alpha}_n\bar{\alpha}_{n-2}-\bar{\alpha}_{n-1}\bar{\alpha}_{n-1}};\qquad \varsigma_{32}=-\frac{\bar{\alpha}_{n-1}}{\bar{\alpha}_n\bar{\alpha}_{n-2}-\bar{\alpha}_{n-1}\bar{\alpha}_{n-1}};$$
$$\varsigma_{41}=-\frac{\bar{\alpha}_{n-1}}{\bar{\alpha}_n\bar{\alpha}_{n-2}-\bar{\alpha}_{n-1}\bar{\alpha}_{n-1}};\qquad \varsigma_{42}=\frac{\bar{\alpha}_{n-2}}{\bar{\alpha}_n\bar{\alpha}_{n-2}-\bar{\alpha}_{n-1}\bar{\alpha}_{n-1}}; \tag{7.60}$$
$$\varsigma_{13i}=\frac{\alpha_n(h_2)\hat{\alpha}_i-\hat{\alpha}_n\alpha_i(h_2)}{\hat{\alpha}_n\alpha_{n-1}(h_2)-\hat{\alpha}_{n-1}\alpha_n(h_2)};\qquad \varsigma_{23i}=-\frac{\alpha_{n-1}(h_2)\hat{\alpha}_i-\hat{\alpha}_{n-1}\alpha_i(h_2)}{\hat{\alpha}_n\alpha_{n-1}(h_2)-\hat{\alpha}_{n-1}\alpha_n(h_2)};$$
$$\varsigma_{33i}=-\frac{\bar{\alpha}_n\bar{\alpha}_{i-1}-\bar{\alpha}_{n-1}\bar{\alpha}_i}{\bar{\alpha}_n\bar{\alpha}_{n-2}-\bar{\alpha}_{n-1}\bar{\alpha}_{n-1}};\qquad \varsigma_{43i}=\frac{\bar{\alpha}_{n-1}\bar{\alpha}_{i-1}-\bar{\alpha}_{n-2}\bar{\alpha}_i}{\bar{\alpha}_n\bar{\alpha}_{n-2}-\bar{\alpha}_{n-1}\bar{\alpha}_{n-1}};$$

(3) Starting from the definitions of $\alpha_i(y), \beta_i(y)$ as provided in Eqs. 7.5a-b, determine the following constants

$$\lambda_{1i} = \frac{\alpha_n(h_2)\beta_i(h_2) - \beta_n(h_2)\alpha_i(h_2)}{\alpha_n(h_2)\beta_{n-1}(h_2) - \alpha_{n-1}(h_2)\beta_n(h_2)}; \qquad \lambda_{2i} = -\frac{\alpha_{n-1}(h_2)\beta_i(h_2) - \beta_{n-1}(h_2)\alpha_i(h_2)}{\alpha_n(h_2)\beta_{n-1}(h_2) - \alpha_{n-1}(h_2)\beta_n(h_2)}; \quad (7.61)$$

(4) Also, starting from the definitions of $\alpha_i(y), \beta_i(y)$ as provided in Eqs. (7.5a-b) and the applied traction (i.e, $\sigma_y(h_1,z)$, $\tau(h_1,z)$, $\sigma_y(h_2,z)$, $\tau(h_2,z)$), determine the following constants

$$\begin{aligned}
\rho_1(z) &= \frac{\alpha_n(h_2)\left[\sigma_y(h_2,z) - \overline{\sigma}_y(h_2,z)\right] - \beta_n(h_2)\left[\overline{\tau}'(h_2,z) - \tau'(h_2,z)\right]}{\alpha_n(h_2)\beta_{n-1}(h_2) - \alpha_{n-1}(h_2)\beta_n(h_2)}, \\
\rho_2(z) &= -\frac{\alpha_{n-1}(h_2)\left[\sigma_y(h_2,z) - \overline{\sigma}_y(h_2,z)\right] - \beta_{n-1}(h_2)\left[\overline{\tau}'(h_2,z) - \tau'(h_2,z)\right]}{\alpha_n(h_2)\beta_{n-1}(h_2) - \alpha_{n-1}(h_2)\beta_n(h_2)}
\end{aligned} \quad (7.62)$$

(5) Given ς_{ij} as obtained in Eq. (7.60), λ_{ij} as given in Eq. (7.61) and $\alpha_i(y)$ in Eqs. (7.5a), the following distribution functions of the $y-$ coordinated are defined:

$$\begin{aligned}
&\eta_{12}(y) = y^{n-2}\varsigma_{31} + y^{n-1}\varsigma_{41}; \qquad \eta_{13}(y) = y^{n-2}\varsigma_{12} + y^{n-1}\varsigma_{22}; \\
&\eta_{14}(y) = y^{n-2}\varsigma_{32} + y^{n-1}\varsigma_{42}; \qquad \eta_{22}(y) = -\left[\alpha_{n-1}(y)\varsigma_{12} + \alpha_n(y)\varsigma_{22}\right]; \\
&\xi_{1i}(y) = y^{i-1} - y^{n-2}\lambda_{1i} - y^{n-1}\lambda_{2i}; \qquad \xi_{2i}(y) = \alpha_{n-1}(y)\lambda_{1i} + \alpha_n(y)\lambda_{2i} - \alpha_i(y); \\
&\xi_{3i}(y) = \beta_i(y) - \beta_{n-1}(y)\lambda_{1i} - \beta_n(y)\lambda_{2i}; \\
&\psi_{1i}(y) = y^{n-2}\varsigma_{13i} + y^{n-1}\varsigma_{23i} + y^{n-2}\lambda_{1i} + y^{n-1}\lambda_{2i}; \\
&\psi_{2i}(y) = y^{n-2}\varsigma_{33i} + y^{n-1}\varsigma_{43i} + y^{n-2}\lambda_{1i} + y^{n-1}\lambda_{2i}; \\
&\psi_{3i}(y) = -\alpha_{n-1}(y)\varsigma_{13i} - \alpha_n(y)\varsigma_{23i} - \alpha_{n-1}(y)\lambda_{1i} - \alpha_n(y)\lambda_{2i}; \qquad i = 1,\ldots,m
\end{aligned} \quad (7.63)$$

(6) Given functions $\psi_{1i}(y)$, $\psi_{2i}(y)$ and $\psi_{3i}(y)$ from Eqs. (7.63), the following vector functions of the $y-$coordinates are defined:

$$\begin{aligned}
\boldsymbol{\psi}_1(y)^{\mathbf{T}}_{1\times m} &= \langle \psi_{11}(y) \quad \ldots \quad \psi_{1i}(y) \quad \ldots \quad \psi_{1m}(y) \rangle; \\
\boldsymbol{\psi}_2(y)^{\mathbf{T}}_{1\times m} &= \langle \psi_{21}(y) \quad \ldots \quad \psi_{2i}(y) \quad \ldots \quad \psi_{2m}(y) \rangle; \\
\boldsymbol{\psi}_3(y)^{\mathbf{T}}_{1\times m} &= \langle \psi_{31}(y) \quad \ldots \quad \psi_{3i}(y) \quad \ldots \quad \psi_{3m}(y) \rangle;
\end{aligned} \quad (7.64)$$

(7) Given Eqs. (7.63) and (7.64), the vectors of Eqs. (7.6) are determined from

$$
\begin{aligned}
\hat{\boldsymbol{\chi}}(y)^{\mathbf{T}}_{1\times 3(m+1)} &= \left\langle \boldsymbol{\xi}_1(y)^{\mathbf{T}}_{1\times m} \;\vdots\; \boldsymbol{\psi}_2(y)^{\mathbf{T}}_{1\times m} \quad \boldsymbol{\psi}_1(y)^{\mathbf{T}}_{1\times m} \;\vdots\; \eta_{12}(y) \quad \eta_{13}(y) \quad \eta_{14}(y) \right\rangle \\
\tilde{\boldsymbol{\chi}}(y)^{\mathbf{T}}_{1\times(2m+1)} &= \left\langle \boldsymbol{\xi}_2(y)^{\mathbf{T}}_{1\times m} \;\vdots\; \boldsymbol{\psi}_3(y)^{\mathbf{T}}_{1\times m} \;\vdots\; \eta_{22}(y) \right\rangle \\
\boldsymbol{\xi}_3(y)^{\mathbf{T}}_{1\times m} &= \left\langle \xi_{31}(y) \quad \dots \quad \xi_{3i}(y) \quad \dots \quad \xi_{3m}(y) \right\rangle
\end{aligned}
\tag{7.65}
$$

(8) Given terms $\rho_1(z)$, $\rho_2(z)$ from Eqs. (7.62), ς_{11} and ς_{21} from Eq. (7.60), and $\bar{\tau}(y,z)$, $\bar{\sigma}_y(y,z)$ from Eq. (7.4), one recovers the expressions for $\sigma_z^*(y,z), \tau^*(y,z).\sigma_y^*(y,z)$ in Eq. (7.8).

Appendix 7.3: Explicit Expression for Total Complementary Energy Variation in Eq.(7.12)

Variation of total complimentary strain energy δU^* as shown in Eq. (7.12) is expressed in a matrix form of composed vectors $\delta\hat{\mathbf{F}}(z), \delta\tilde{\mathbf{F}}(z)$ which have been defined in Eqs.(7.6). The expression is complicated and thus it needs to be expanded to have an explicit expression in terms of variables $\delta\mathbf{F}(z)^{\mathbf{T}}_{1\times m}$, $\delta\mathbf{F}(0)^{\mathbf{T}}_{1\times m}$, $\delta\mathbf{F}'(0)^{\mathbf{T}}_{1\times m}$, $\delta N(0)$, $\delta Q(0)$, $\delta M(0)$. Also, some integrations by parts are performed in Eqs. (7.12) to obtain a new expression of variational of total complementary energy as shown in Eqs. (7.16).

From Eq. (7.12), by taking the variation and expanding all terms from matrix expression forms, one has

$$
\begin{aligned}
\delta U^* &= \int_L \delta\hat{\mathbf{F}}(z)^{\mathbf{T}}\left[\mathbf{C}_{11}\hat{\mathbf{F}}(z) - \mathbf{C}_{12}\mathbf{F}''(z) + \mathbf{d}_1(\mathbf{z})\right]dz + \int_L \delta\mathbf{F}''(z)^{\mathbf{T}}\left[-\mathbf{C}_{12}^{\mathbf{T}}\hat{\mathbf{F}}(z) + \mathbf{C}_{22}\mathbf{F}''(z) + \mathbf{d}_2(\mathbf{z})\right]dz \\
&\quad + \int_L \delta\tilde{\mathbf{F}}(z)^{\mathbf{T}}\left[\mathbf{C}_{33}\tilde{\mathbf{F}}(z) + \mathbf{d}_3(\mathbf{z})\right]dz
\end{aligned}
\tag{7.66}
$$

From Eq.(7.66), by decomposing vector $\delta\tilde{\mathbf{F}}(z)^{\mathbf{T}}$ using identity matrices $\tilde{\mathbf{I}}_1, \tilde{\mathbf{I}}_2, \tilde{\mathbf{I}}_3$ defined in Eqs.(7.17), performing integration by parts the coefficients of $\delta\mathbf{F}''(z)^{\mathbf{T}}$ and $\delta\mathbf{F}'(z)^{\mathbf{T}}$, one obtains

$$\delta U^{*}=\int_{L}\delta\widehat{\mathbf{F}}(z)^{\mathbf{T}}\left[\mathbf{C}_{11}\widehat{\mathbf{F}}(z)-\mathbf{C}_{12}\mathbf{F}''(z)+\mathbf{d}_{1}(\mathbf{z})\right]dz+\int_{L}\delta\mathbf{F}(z)^{\mathbf{T}}\left[-\mathbf{C}_{12}^{\mathbf{T}}\widehat{\mathbf{F}}''(z)+\mathbf{C}_{22}\mathbf{F}''''(z)+\mathbf{d}_{2}''(\mathbf{z})\right]dz+$$
$$+\left\{\delta\mathbf{F}'(z)^{\mathbf{T}}\left[-\mathbf{C}_{12}^{\mathbf{T}}\widehat{\mathbf{F}}(z)+\mathbf{C}_{22}\mathbf{F}''(z)+\mathbf{d}_{2}(\mathbf{z})\right]\right\}\Big|_{0}^{L}-\left\{\delta\mathbf{F}(z)^{\mathbf{T}}\left[-\mathbf{C}_{12}^{\mathbf{T}}\widehat{\mathbf{F}}'(z)+\mathbf{C}_{22}\mathbf{F}'''(z)+\mathbf{d}_{2}'(\mathbf{z})\right]\right\}\Big|_{0}^{L}+$$
$$-\int_{L}\delta\mathbf{F}(z)^{\mathbf{T}}\tilde{\mathbf{I}}_{1}\left[\mathbf{C}_{33}\widetilde{\mathbf{F}}'(z)+\mathbf{d}_{3}'(\mathbf{z})\right]dz+\left\{\delta\mathbf{F}(z)^{\mathbf{T}}\tilde{\mathbf{I}}_{1}\left[\mathbf{C}_{33}\widetilde{\mathbf{F}}(z)+\mathbf{d}_{3}(\mathbf{z})\right]\right\}\Big|_{0}^{L}$$
$$+\int_{L}\delta\mathbf{F}'(0)^{\mathbf{T}}\tilde{\mathbf{I}}_{2}\left[\mathbf{C}_{33}\widetilde{\mathbf{F}}(z)+\mathbf{d}_{3}(\mathbf{z})\right]dz+\int_{L}\delta Q(0)^{\mathbf{T}}\tilde{\mathbf{I}}_{3}\left[\mathbf{C}_{33}\widetilde{\mathbf{F}}(z)+\mathbf{d}_{3}(\mathbf{z})\right]dz$$

(7.67)

From Eq.(7.67), by re-arranging the terms, one obtains

$$\delta U^{*}=\int_{L}\delta\widehat{\mathbf{F}}(z)^{\mathbf{T}}\left[\mathbf{C}_{11}\widehat{\mathbf{F}}(z)-\mathbf{C}_{12}\mathbf{F}''(z)+\mathbf{d}_{1}(\mathbf{z})\right]dz+\int_{L}\delta\mathbf{F}(z)^{\mathbf{T}}\left[-\mathbf{C}_{12}^{\mathbf{T}}\widehat{\mathbf{F}}''(z)+\mathbf{C}_{22}\mathbf{F}''''(z)+\mathbf{d}_{2}''(\mathbf{z})\right]dz+$$
$$-\int_{L}\delta\mathbf{F}(z)^{\mathbf{T}}\tilde{\mathbf{I}}_{1}\left[\mathbf{C}_{33}\widetilde{\mathbf{F}}'(z)+\mathbf{d}_{3}'(\mathbf{z})\right]dz+\int_{L}\delta\mathbf{F}'(0)^{\mathbf{T}}\tilde{\mathbf{I}}_{2}\left[\mathbf{C}_{33}\widetilde{\mathbf{F}}(z)+\mathbf{d}_{3}(\mathbf{z})\right]dz+$$
$$+\int_{L}\delta Q(0)^{\mathbf{T}}\tilde{\mathbf{I}}_{3}\left[\mathbf{C}_{33}\widetilde{\mathbf{F}}(z)+\mathbf{d}_{3}(\mathbf{z})\right]dz+\left\{\delta\mathbf{F}'(z)^{\mathbf{T}}\left[-\mathbf{C}_{12}^{\mathbf{T}}\widehat{\mathbf{F}}(z)+\mathbf{C}_{22}\mathbf{F}''(z)+\mathbf{d}_{2}(\mathbf{z})\right]\right\}\Big|_{0}^{L}$$
$$-\left\{\delta\mathbf{F}(z)^{\mathbf{T}}\left[-\mathbf{C}_{12}^{\mathbf{T}}\widehat{\mathbf{F}}'(z)+\mathbf{C}_{22}\mathbf{F}'''(z)+\mathbf{d}_{2}'(\mathbf{z})\right]\right\}\Big|_{0}^{L}+\left\{\delta\mathbf{F}(z)^{\mathbf{T}}\tilde{\mathbf{I}}_{1}\left[\mathbf{C}_{33}\widetilde{\mathbf{F}}(z)+\mathbf{d}_{3}(\mathbf{z})\right]\right\}\Big|_{0}^{L}$$

(7.68)

From Eq. (7.68), by decomposing vector $\delta\widehat{\mathbf{F}}(z)^{\mathbf{T}}$ using identity matrices $\hat{\mathbf{I}}_1,\hat{\mathbf{I}}_2,\hat{\mathbf{I}}_3,\hat{\mathbf{I}}_4,\hat{\mathbf{I}}_5,\hat{\mathbf{I}}_6$, which were defined in Eqs.(7.17), the final expression of variational of total complimentary strain energy is obtained as shown in Eq. (7.16).

Appendix 7.4: Variation of the total potential energy

Starting with Eq.(7.15), (7.19), (7.20), this appendix shows the steps for obtaining Eq. (7.21). The expressions for $N(L)$, $Q(L)$ and $M(L)$ as obtained in Eqs. (7.20) are substituted into Eq. (7.15) to express the total load potential energy in terms of the independent variables $\mathbf{F}(0)^{\mathbf{T}}$, $\mathbf{F}'(0)^{\mathbf{T}}$, $\mathbf{F}(L)^{\mathbf{T}}$, $\mathbf{F}'(L)^{\mathbf{T}}$, $N(0)$, $Q(0)$, $M(0)$. From Eq.(7.20), by substituting into Eq.(7.19), one obtains

$$
\begin{aligned}
\delta V^{*} &= \delta N(0)\overline{W}(0)+\delta Q(0)\overline{V}(0)+\delta M(0)\overline{\theta}(0)-\delta\hat{\mathbf{F}}(L)^{\mathbf{T}}_{1\times 3(m+1)}\left[\int_A \hat{\boldsymbol{\chi}}(y)_{3(m+1)\times 1}\, dA\right]\overline{W}(L) \\
&\quad -\delta\hat{\mathbf{F}}(L)^{\mathbf{T}}_{1\times 3(m+1)}\left[\int_A y\hat{\boldsymbol{\chi}}(y)_{3(m+1)\times 1}\, dA\right]\overline{\theta}(L)-\delta\tilde{\mathbf{F}}(L)^{\mathbf{T}}_{1\times(2m+1)}\left[\int_A \tilde{\boldsymbol{\chi}}(y)_{(2m+1)\times 1}\, dA\right]\overline{V}(L)
\end{aligned} \tag{7.69}
$$

From Eq.(7.69), by adopting the definitions of $\hat{\mathbf{F}}(L)$ and $\tilde{\mathbf{F}}(L)$ as given after Eq. (7.6), one obtains

$$
\begin{aligned}
\delta V^{*} &= \delta N(0)\overline{W}(0)+\delta Q(0)\overline{V}(0)+\delta M(0)\overline{\theta}(0)-\delta\mathbf{F}(L)^{\mathbf{T}}_{1\times m}\left[\int_A \boldsymbol{\xi}_1(y)^{\mathbf{T}}_{1\times m}\, dA\right]\overline{W}(L)+ \\
&\quad -\delta\mathbf{F}(0)^{\mathbf{T}}_{1\times m}\left[\int_A \boldsymbol{\psi}_2(y)^{\mathbf{T}}_{1\times m}\, dA\right]\overline{W}(L)-\delta\mathbf{F}'(0)^{\mathbf{T}}_{1\times m}\left[L\int_A \boldsymbol{\psi}_1(y)^{\mathbf{T}}_{1\times m}\, dA\right]\overline{W}(L)-\delta N(0)\left[\int_A \eta_{12}(y)\,dA\right]\overline{W}(L)+ \\
&\quad -\delta Q(0)\left[L\int_A \eta_{13}(y)\,dA\right]\overline{W}(L)-\delta M(0)\left[\int_A \eta_{14}(y)\,dA\right]\overline{W}(L)-\delta\mathbf{F}(L)^{\mathbf{T}}_{1\times m}\left[\int_A y\boldsymbol{\xi}_1(y)^{\mathbf{T}}_{1\times m}\, dA\right]\overline{\theta}(L) \\
&\quad -\delta\mathbf{F}(0)^{\mathbf{T}}_{1\times m}\left[\int_A y\boldsymbol{\psi}_2(y)^{\mathbf{T}}_{1\times m}\, dA\right]\overline{\theta}(L)-\delta\mathbf{F}'(0)^{\mathbf{T}}_{1\times m}\left[L\int_A y\boldsymbol{\psi}_1(y)^{\mathbf{T}}_{1\times m}\, dA\right]\overline{\theta}(L) \\
&\quad -\delta N(0)\left[\int_A y\eta_{12}(y)\,dA\right]\overline{\theta}(L)-\delta Q(0)\left[L\int_A y\eta_{13}(y)\,dA\right]\overline{\theta}(L)-\delta M(0)\left[\int_A y\eta_{14}(y)\,dA\right]\overline{\theta}(L)+ \\
&\quad -\delta\mathbf{F}'(L)^{\mathbf{T}}_{1\times m}\left[\int_A \boldsymbol{\xi}_2(y)^{\mathbf{T}}_{1\times m}\, dA\right]\overline{V}(L)-\delta\mathbf{F}'(0)^{\mathbf{T}}_{1\times m}\left[\int_A \boldsymbol{\psi}_3(y)^{\mathbf{T}}_{1\times m}\, dA\right]\overline{V}(L)-\delta Q(0)\left[\int_A \eta_{22}(y)\,dA\right]\overline{V}(L)
\end{aligned} \tag{7.70}
$$

From Eq. (7.70), by taking the variation of the total load potential energy, one recovers Eq. (7.21).

Appendix 7.5: Illustrative examples

A7.5.1. Beam under uniform traction when the number of terms = 3

This section illustrates the applicability of the present theory for a beam of length L. The beam has a rectangular cross-section $b\times h$ and is subjected to a uniform traction $\sigma(h_1,z)=\sigma_0$ acting at the top surface while other tractions vanish, i.e., $\tau(h_1,z)=\ \sigma(h_2,z)=\tau(h_2,z)=0$. Two solutions are provided for a cantilever and for a simply supported beam. The number of stress terms is taken as n =3.

Stress fields and governing equations:

The expressions for the stress fields as given by Eq. (7.6) take the form

$$\sigma_z(y,z)=\left(1-\frac{12y^2}{h^2}\right)F_1(z)+\frac{12y}{bh^3}\left[yN(0)+zQ(0)+M(0)\right]+\frac{6yz^2}{h^3}\sigma_0$$

$$\tau_{yz}(y,z)=\left(-y+\frac{4y^3}{h^2}\right)F_1'(z)+6\sigma z\left(\frac{1}{4h}-\frac{y^2}{h^3}\right)+6Q(0)\left(\frac{1}{4bh}-\frac{y^2}{bh^3}\right) \tag{7.71}$$

$$\sigma_y(y,z)=\left(-\frac{h^2}{16}+\frac{y^2}{2}-\frac{y^4}{h^2}\right)F_1''(z)+\frac{1}{2}\left(1-\frac{3y}{h}+\frac{4y^3}{h^3}\right)\sigma_0$$

In this case, the number of compatibility equations is $m=n-2=1$ and the corresponding differential equation of compatibility as given by Eq.(7.23) takes the form

$$\frac{bh^5}{630E_y}F_1''''(z)+\left(\frac{4\mu_{zy}bh^3}{105E_z}-\frac{2bh^3}{105G}\right)F_1''(z)+\frac{4bh}{5E_z}F_1(z)-\frac{4}{5E_z}N(0)=0 \tag{7.72}$$

The integration of Eq. (7.72) gives four unknown constants. Also, equations(7.24)-(7.30) give $4m+3=7$ boundary conditions, which take the form

$$\delta F_1(0)\left[\frac{bh^5}{630E_y}F_1'''(0)+\left(\frac{2\mu_{zy}bh^3}{105E_z}-\frac{2bh^3}{105G}\right)F_1'(0)\right]=0$$

$$\delta F_1'(0)\left[-\frac{bh^5}{630E_y}F_1''(0)-\frac{2\mu_{zy}bh^3}{105G}F_1(0)-\frac{\mu_{zy}h^2}{70E_z}N(0)+\frac{\sigma_0bh^3}{60E_y}\right]=0$$

$$\delta F_1(L)\left[\left(\frac{2\mu_{yz}bh^3}{105E_y}-\frac{2bh^3}{105G}\right)F_1'(L)+\frac{bh^5}{630E_y}F_1'''(L)\right]=0$$

$$\delta F_1'(L)\left[\frac{2\mu_{zy}bh^3}{105E_z}F_1(L)+\frac{bh^5}{630E_y}F_1''(L)+\frac{\mu_{zy}h^2}{70E_z}N(0)-\frac{\sigma_0bh^3}{60E_y}\right]=0$$

$$\delta N(0)\left\{\int_0^L\left[\frac{4F_1(L)}{5E_z}+\frac{\mu_{zy}h^2}{70E_z}F_1''(L)+\frac{9N(0)}{5E_zhb}-\frac{\mu_{zy}\sigma_0}{2E_z}\right]dz-W(0)-W(L)\right\}=0$$

$$\delta Q(0)\left\{\int_0^L\left[\left(\frac{12z^2}{E_zbh^3}+\frac{6}{5Ghb}\right)Q(0)+\frac{12zM(0)}{E_zbh^3}+\frac{6\sigma_0z^3}{E_zh^3}-\frac{6\mu_{zy}\sigma_0z}{5E_zh}+\frac{6\sigma_0z}{5Gh}\right]dz\right.$$
$$\left.-V(0)-V(L)-L\theta(L)\right\}=0$$

$$\delta M(0)\left\{\int_0^L\left[\frac{12zQ(0)}{E_zbh^3}+\frac{12M(0)}{E_zbh^3}+\frac{6\sigma_0z^2}{E_zh^3}+\frac{6\mu_{zy}\sigma_0}{5E_zh}\right]dz+\theta(0)-\theta(L)\right\}=0 \tag{7.73a-g}$$

In Eq.(7.73), depending on the boundary conditions, either the bracketed expression or its variational coefficient will vanish. It is emphasized that Eqs.(7.74)-(7.73) are applicable for general boundary conditions.

Case 1: Cantilever

For a cantilever fixed at $z=0$ and free at $z=L$, one has $V(0)=W(0)=\theta(0)=0$. Since the cantilever is not subjected to axial forces, one has $N(0)=0$. By substituting $N(0)=0$ into Eq.(7.72), enforcing the boundary conditions $\delta F_1(0)\neq 0$, $\delta F_1'(0)\neq 0$, $\delta F_1(L)=0, \delta F_1'(L)=0$, $\delta N(0)\neq 0, \delta Q(0)\neq 0, \delta M(0)\neq 0$ in Eqs. (7.73a,g) and solving for the four integration constants and the three unknown displacements $W(L), V(L), \theta(L)$, one obtains $F_1(z)$ which contributes to a nonlinear distribution of the longitudinal normal stresses across the section depth as evidenced in Eq. (7.71). Boundary equations (7.73f-g) are found independent of $F_1(z)$. Thus, the angle of rotation $\theta(L)$ and deflection $V(L)$ at the free end can then be evaluated by setting $Q(0)=-\sigma_0 bL$ and $M(0)=\sigma_0 bL^2/2$ leading to

$$\theta(L)=\frac{\sigma_0 bL^3}{6E_zI}+\frac{6\sigma_0\mu_{zy}L}{5hE_z};\qquad V(L)=-\left(\frac{\sigma_0 bL^4}{8E_zI}+\frac{3\sigma_0 L^2}{5hG}+\frac{9\sigma_0\mu_{zy}L^2}{5hE_z}\right) \qquad (7.75)\text{a,b}$$

The first term of the right hand side of Eq. (7.75a) and the first two terms of Eq. (7.75b) coincide with those of the Timoshenko beam solution. Thus, the present study is found to provide higher predictions of beam deflections than does Timoshenko beam theory.

Case 2: Simply supported beam

If the beam is simply supported at both ends, the normal force vanishes within the member given there no axial forces applied. By substituting $N(0)=0$ into Eq. (7.72) and applying the boundary conditions $\delta F_1(0)\neq 0$, $\delta F_1'(0)\neq 0$, $\delta F_1(L)\neq 0, \delta F_1'(L)\neq 0, \delta N(0)\neq 0, \delta Q(0)\neq 0$ and solving, four unknown constants of the closed form solution and two displacements $W(L), \theta(L)$ are determined. Also by setting $Q(0)=-\sigma_0 bL/2$ and $M(0)=0$, the mid-span deflection $V(L/2)$ can be obtained by integrating Eq. (7.73f) over a half span while the end rotation $\theta(L)$ can be also obtained by integrating Eq. (7.73f) over the whole span to yield

$$\theta(L)=\frac{\sigma_0 L^3}{2E_z h^3}+\frac{3\mu_{zy}\sigma_0 L}{5E_z h};\qquad V(L/2)=\frac{5\sigma_0 L^4}{32E_z h^3}+\frac{3\sigma_0 L^2}{20hG}+\frac{3\mu_{zy}\sigma_0 L^2}{20E_z h}\qquad \text{(7.76)a,b}$$

From Eq.(7.76)b and assuming that $G=E_z/2(1+\mu_{zy})$, the deflection becomes $V(L/2)=5\sigma_0 L^4/32E_z h^3+3\sigma_0 L^2/10E_z h+9\mu_{zy}\sigma_0 L^2/20E_z h$. This deflection is observed to be higher than the elasticity theory solution developed by Timoshenko and Goodier (1970), which is $V(L/2)=5\sigma_0 L^4/32E_z h^3+3\sigma_0 L^2/10E_z h+3\mu_{zy}\sigma_0 L^2/16E_z h$.

A7.5.2 Stress Fields and Compatibility Equations when the number of stress terms = 4

The expressions for the stress fields are:

$$\begin{aligned}
\sigma_z(y,z)&=\left(1-\frac{12y^2}{h^2}\right)F_1(z)+\left(y-\frac{20y^3}{3h^2}\right)F_2(z)+\frac{12y^2}{bh^3}N(0)+\frac{80y^3z}{bh^5}Q(0)+\frac{80y^3}{bh^5}M(0)+\frac{40y^3z^2}{h^5}\sigma_0\\
\tau(y,z)&=\left(-y+\frac{4y^3}{h^2}\right)F_1'(z)+\left(\frac{5y^4}{3h^2}-\frac{y^2}{2}+\frac{h^2}{48}\right)F_2'(z)+\left(\frac{5}{4bh}-\frac{20y^4}{bh^5}\right)Q(0)+\left(\frac{5}{4h}-\frac{20y^4}{h^5}\right)z\sigma_0\\
\sigma_y(y,z)&=\left(-\frac{y^4}{h^2}+\frac{y^2}{2}-\frac{h^2}{16}\right)F_1''(z)+\left(-\frac{y^5}{3h^2}+\frac{y^3}{6}-\frac{h^2}{48}y\right)F_2''(z)+\left(\frac{4y^5}{h^5}-\frac{5y}{4h}+\frac{1}{2}\right)\sigma_0
\end{aligned}\qquad (7.77)$$

The highest order of y in the longitudinal normal stress field is 3, which is higher than that when $n=3$. Also, the compatibility equations as obtained from Eq.(7.23) take the form

$$\begin{aligned}
&\frac{bh^5}{249480E_y}\begin{bmatrix}396&0\\0&h^2\end{bmatrix}\mathbf{F}''''(z)+\frac{2bh^3}{11340}\begin{bmatrix}108&0\\0&h^2\end{bmatrix}\left(\frac{2\mu_{yz}}{E_z}-\frac{1}{G}\right)\mathbf{F}''(z)+\frac{bh}{315E_z}\begin{bmatrix}252&0\\0&5h^2\end{bmatrix}\mathbf{F}(z)\\
&-\frac{4}{5E_z}\begin{Bmatrix}1\\0\end{Bmatrix}N(0)-\frac{4z}{21E_z}\begin{Bmatrix}0\\1\end{Bmatrix}Q(0)-\frac{4}{21E_z}\begin{Bmatrix}0\\1\end{Bmatrix}M(0)+\frac{\sigma_0 b}{378}\left(\frac{h^2}{G}-\frac{\mu_{zy}h^2}{E_y}-\frac{\mu_{yz}h^2}{E_z}+\frac{36z^2}{E_z}\right)\begin{Bmatrix}0\\1\end{Bmatrix}=0
\end{aligned}\qquad (7.78)$$

In this case, the two compatibility equations $F_1(z)$ and $F_z(z)$ are found uncoupled as the off-diagonal terms vanish. This will generally not be the case. For instance for $n\geq 5$, all compatibility equations happen to be coupled. Also, for a T-section, the equations are coupled for $n\geq 4$.

Appendix 7.6: Details related to the Closed Form Solution

By setting $z=0$ in Eq. (7.38), and noting that $[\mathbf{e}(0)]=[\mathbf{I}]$, one obtains

$$\{\mathbf{F}(0)\}_{m,1}=\{\mathbf{f}\}_{m\times 4m}\{\mathbf{A}\}_{4m\times 1}+\left[\overline{\mathbf{C}}_1\right]_{m,m}\{\mathbf{F}(\mathbf{0})\}_{m,1}+\left\{\overline{\mathbf{C}}_3\right\}_{m,1}N(0)+\left\{\overline{\mathbf{C}}_5\right\}_{m,1}M(0)+\left[\overline{\mathbf{C}}\right]_{m,u}\{\mathbf{Z}(0)\}_{u,1}\qquad (7.79)$$

By solving for $\{\mathbf{F}(\mathbf{0})\}$, one obtains

$$\left\{\mathbf{F}(\mathbf{0})\right\}_{m\times1}=\left[\bar{I}-\bar{\mathbf{C}}_1\right]_{m\times m}^{-1}\left\{\{\mathbf{f}\}_{m\times4m}\left[\mathbf{e}(0)\right]_{4m\times4m}\{\mathbf{A}\}_{4m\times1}+N(0)\left\{\bar{\mathbf{C}}_3\right\}_{m\times1}+M(0)\left\{\bar{\mathbf{C}}_5\right\}_{m\times1}+\left[\bar{\mathbf{C}}\right]_{m\times(u+3)}\{\mathbf{Z}(0)\}_{(u+3)\times1}\right\} \quad (7.80)$$

Also, from Eq.(7.38), by taking the first derivative of both sides with respect to z, setting $z=0$ and solving for $\left\{\mathbf{F}'(0)\right\}_{m\times1}$, one obtains

$$\left\{\mathbf{F}'(0)\right\}_{m\times1}=\left[\bar{I}-\bar{\mathbf{C}}_2\right]_{m\times m}^{-1}\times\left(\{\mathbf{f}\}_{m\times4m}\left[\mathbf{e}'(0)\right]_{4m\times4m}\{\mathbf{A}\}_{4m\times1}+Q(0)\left\{\bar{\mathbf{C}}_4\right\}_{m\times1}+\left[\bar{\mathbf{C}}\right]_{m\times(u+3)}\left\{\mathbf{Z}'(0)\right\}_{(u+3)\times1}\right) \quad (7.81)$$

Finally, from Eqs.(7.80) and(7.81), by substituting into Eqs. (7.38), one obtains the general solution given in Eq.(7.39).

Appendix 7.7: Vectors and Matrices appearing in boundary equations

The boundary conditions Eqs. (7.41)-(7.46) were expressed in terms of matrices $\mathbf{b_{ij}}$ defined as

$$\begin{aligned}
\left[\mathbf{b}_{11}\right]_{m\times4m}&=\int_0^L\left\{\hat{\mathbf{I}}_2\mathbf{C}_{11}\hat{\mathbf{I}}_1^{\mathbf{T}}\left[\mathbf{H}_1(z)\right]_{m\times4m}-\hat{\mathbf{I}}_2\mathbf{C}_{12}\left[\mathbf{H}_1''(z)\right]_{m\times4m}+\hat{\mathbf{I}}_2\mathbf{C}_{11}\hat{\mathbf{I}}_2^{\mathbf{T}}\left[\mathbf{H}_1(0)\right]_{m\times4m}\right\}+\mathbf{C}_{22}\left[\mathbf{H}_1'''(0)\right]_{m\times4m}\\
&+\left(\int_0^L\hat{\mathbf{I}}_2\mathbf{C}_{11}\hat{\mathbf{I}}_3^{\mathbf{T}}z\,dz-\mathbf{C}_{12}^{\mathbf{T}}\hat{\mathbf{I}}_1^{\mathbf{T}}-\mathbf{C}_{12}^{\mathbf{T}}\hat{\mathbf{I}}_3^{\mathbf{T}}-\tilde{\mathbf{I}}_1\mathbf{C}_{33}\tilde{\mathbf{I}}_1^{\mathbf{T}}-\tilde{\mathbf{I}}_1\mathbf{C}_{33}\tilde{\mathbf{I}}_2^{\mathbf{T}}\right)\left[\mathbf{H}_1'(0)\right]_{m\times4m},
\end{aligned}$$

$$\left\{\mathbf{b}_{12}\right\}_{m\times1}=\int_0^L\left\{\hat{\mathbf{I}}_2\mathbf{C}_{11}\hat{\mathbf{I}}_1^{\mathbf{T}}\{\mathbf{H}_2\}_{m\times1}+\hat{\mathbf{I}}_2\mathbf{C}_{11}\hat{\mathbf{I}}_2^{\mathbf{T}}\{\mathbf{H}_2\}_{m\times1}+\hat{\mathbf{I}}_2\mathbf{C}_{11}\hat{\mathbf{I}}_4^{\mathbf{T}}\right\}dz,$$

$$\begin{aligned}
\left\{\mathbf{b}_{13}\right\}_{m\times1}&=\int_0^L\hat{\mathbf{I}}_2\mathbf{C}_{11}\hat{\mathbf{I}}_1^{\mathbf{T}}z\{\mathbf{H}_3\}_{m\times1}dz+\left(\int_0^L z\hat{\mathbf{I}}_2\mathbf{C}_{11}\hat{\mathbf{I}}_3^{\mathbf{T}}dz-\mathbf{C}_{12}^{\mathbf{T}}\hat{\mathbf{I}}_1^{\mathbf{T}}-\mathbf{C}_{12}^{\mathbf{T}}\hat{\mathbf{I}}_3^{\mathbf{T}}-\tilde{\mathbf{I}}_1\mathbf{C}_{33}\tilde{\mathbf{I}}_1^{\mathbf{T}}-\tilde{\mathbf{I}}_1\mathbf{C}_{33}\tilde{\mathbf{I}}_2^{\mathbf{T}}\right)\{\mathbf{H}_3\}_{m\times1}+\\
&+\left(\int_0^L z\hat{\mathbf{I}}_2\mathbf{C}_{11}\hat{\mathbf{I}}_5^{\mathbf{T}}dz-\mathbf{C}_{12}^{\mathbf{T}}\hat{\mathbf{I}}_5^{\mathbf{T}}-\tilde{\mathbf{I}}_1\mathbf{C}_{33}\tilde{\mathbf{I}}_3^{\mathbf{T}}\right),
\end{aligned}$$

$$\left\{\mathbf{b}_{14}\right\}_{m\times1}=\int_0^L\hat{\mathbf{I}}_2\mathbf{C}_{11}\hat{\mathbf{I}}_1^{\mathbf{T}}\{\mathbf{H}_4\}_{m\times1}dz+\int_0^L\hat{\mathbf{I}}_2\mathbf{C}_{11}\hat{\mathbf{I}}_2^{\mathbf{T}}\{\mathbf{H}_4\}_{m\times1}dz+\int_0^L\hat{\mathbf{I}}_2\mathbf{C}_{11}\hat{\mathbf{I}}_6^{\mathbf{T}}dz,$$

$$\begin{aligned}
\left[\mathbf{b}_{21}\right]_{m\times4m}&=\int_0^L\left\{z\hat{\mathbf{I}}_3\mathbf{C}_{11}\hat{\mathbf{I}}_1^{\mathbf{T}}\left[\mathbf{H}_1(z)\right]_{m\times4m}+\tilde{\mathbf{I}}_2\mathbf{C}_{33}\tilde{\mathbf{I}}_1^{\mathbf{T}}\left[\mathbf{H}_1'(z)\right]_{m\times4m}-z\hat{\mathbf{I}}_3\mathbf{C}_{12}\left[\mathbf{H}_1''(z)\right]_{m\times4m}\right\}dz\\
&-\mathbf{C}_{22}\left[\mathbf{H}_1''(0)\right]_{m\times4m}+\left(\int_0^L z\hat{\mathbf{I}}_3\mathbf{C}_{11}\hat{\mathbf{I}}_2^{\mathbf{T}}dz+\mathbf{C}_{12}^{\mathbf{T}}\hat{\mathbf{I}}_1^{\mathbf{T}}+\mathbf{C}_{12}^{\mathbf{T}}\hat{\mathbf{I}}_2^{\mathbf{T}}\right)\left[\mathbf{H}_1(0)\right]_{m\times4m}+\\
&+\left(\int_0^L z^2\hat{\mathbf{I}}_3\mathbf{C}_{11}\hat{\mathbf{I}}_3^{\mathbf{T}}dz+\int_0^L\tilde{\mathbf{I}}_2\mathbf{C}_{33}\tilde{\mathbf{I}}_2^{\mathbf{T}}dz\right)\left[\mathbf{H}_1'(0)\right]_{m\times4m},
\end{aligned}$$

$$\left\{\mathbf{b}_{22}\right\}_{m\times1}=\int_0^L z\hat{\mathbf{I}}_3\mathbf{C}_{11}\hat{\mathbf{I}}_1^{\mathbf{T}}\{\mathbf{H}_2\}_{m\times1}dz+\left(\int_0^L z\hat{\mathbf{I}}_3\mathbf{C}_{11}\hat{\mathbf{I}}_2^{\mathbf{T}}dz+\mathbf{C}_{12}^{\mathbf{T}}\hat{\mathbf{I}}_1^{\mathbf{T}}+\mathbf{C}_{12}^{\mathbf{T}}\hat{\mathbf{I}}_2^{\mathbf{T}}\right)\{\mathbf{H}_2\}_{m\times1}+\int_0^L z\hat{\mathbf{I}}_3\mathbf{C}_{11}\hat{\mathbf{I}}_4^{\mathbf{T}}dz+\mathbf{C}_{12}^{\mathbf{T}}\hat{\mathbf{I}}_4^{\mathbf{T}},$$

$$\left\{\mathbf{b}_{23}\right\}_{m\times1}=\int_0^L\left\{\left[z\hat{\mathbf{I}}_3\mathbf{C}_{11}\hat{\mathbf{I}}_1^{\mathbf{T}}z+\tilde{\mathbf{I}}_2\mathbf{C}_{33}\tilde{\mathbf{I}}_1^{\mathbf{T}}+z^2\hat{\mathbf{I}}_3\mathbf{C}_{11}\hat{\mathbf{I}}_3^{\mathbf{T}}+\tilde{\mathbf{I}}_2\mathbf{C}_{33}\tilde{\mathbf{I}}_2^{\mathbf{T}}dz\right]\{\mathbf{H}_3\}_{m\times1}+z^2\hat{\mathbf{I}}_3\mathbf{C}_{11}\hat{\mathbf{I}}_5^{\mathbf{T}}+\tilde{\mathbf{I}}_2\mathbf{C}_{33}\tilde{\mathbf{I}}_3^{\mathbf{T}}\right\}dz,$$

$$\left\{\mathbf{b}_{24}\right\}_{m\times1}=\int_0^L z\left\{\hat{\mathbf{I}}_3\mathbf{C}_{11}\hat{\mathbf{I}}_1^{\mathbf{T}}\{\mathbf{H}_4\}_{m\times1}+\hat{\mathbf{I}}_3\mathbf{C}_{11}\hat{\mathbf{I}}_6^{\mathbf{T}}\right\}dz+\left(\int_0^L z\hat{\mathbf{I}}_3\mathbf{C}_{11}\hat{\mathbf{I}}_2^{\mathbf{T}}dz+\mathbf{C}_{12}^{\mathbf{T}}\hat{\mathbf{I}}_1^{\mathbf{T}}+\mathbf{C}_{12}^{\mathbf{T}}\hat{\mathbf{I}}_2^{\mathbf{T}}\right)\{\mathbf{H}_4\}_{m\times1}+\mathbf{C}_{12}^{\mathbf{T}}\hat{\mathbf{I}}_6^{\mathbf{T}},$$

$$\left[\mathbf{b}_{31}\right]_{m\times4m}=\left(-\mathbf{C}_{12}^{\mathbf{T}}\hat{\mathbf{I}}_1^{\mathbf{T}}-\tilde{\mathbf{I}}_1\mathbf{C}_{33}\tilde{\mathbf{I}}_1^{\mathbf{T}}\right)\left[\mathbf{H}_1'(L)\right]_{m\times4m}+\mathbf{C}_{22}\left[\mathbf{H}_1'''(L)\right]_{m\times4m}+\left(-\mathbf{C}_{12}^{\mathbf{T}}\hat{\mathbf{I}}_3^{\mathbf{T}}-\tilde{\mathbf{I}}_1\mathbf{C}_{33}\tilde{\mathbf{I}}_2^{\mathbf{T}}\right)\left[\mathbf{H}_1'(0)\right]_{m\times4m},$$

$$\left\{\mathbf{b}_{32}\right\}_{m\times1}=\left(-\mathbf{C}_{12}^{\mathbf{T}}\hat{\mathbf{I}}_1^{\mathbf{T}}-\tilde{\mathbf{I}}_1\mathbf{C}_{33}\tilde{\mathbf{I}}_1^{\mathbf{T}}\right)\{\mathbf{H}_3\}_{m\times1}+\left(-\mathbf{C}_{12}^{\mathbf{T}}\hat{\mathbf{I}}_3^{\mathbf{T}}-\tilde{\mathbf{I}}_1\mathbf{C}_{33}\tilde{\mathbf{I}}_2^{\mathbf{T}}\right)\{\mathbf{H}_3\}_{m\times1}-\mathbf{C}_{12}^{\mathbf{T}}\hat{\mathbf{I}}_5^{\mathbf{T}}-\tilde{\mathbf{I}}_1\mathbf{C}_{33}\tilde{\mathbf{I}}_3^{\mathbf{T}},$$

$$\left[\mathbf{b}_{41}\right]_{m\times4m}=-\mathbf{C}_{12}^{\mathbf{T}}\hat{\mathbf{I}}_1^{\mathbf{T}}\left[\mathbf{H}_1(L)\right]_{m\times4m}+\mathbf{C}_{22}\left[\mathbf{H}_1''(L)\right]_{m\times4m}-L\mathbf{C}_{12}^{\mathbf{T}}\hat{\mathbf{I}}_3^{\mathbf{T}}\left[\mathbf{H}_1'(0)\right]_{m\times4m}-\mathbf{C}_{12}^{\mathbf{T}}\hat{\mathbf{I}}_2^{\mathbf{T}}\left[\mathbf{H}_1(0)\right]_{m\times4m},$$

$$\left\{\mathbf{b}_{42}\right\}_{m\times1}=-\mathbf{C}_{12}^{\mathrm{T}}\hat{\mathbf{I}}_1^{\mathrm{T}}\left\{\mathbf{H}_2\right\}_{m\times1}-\mathbf{C}_{12}^{\mathrm{T}}\hat{\mathbf{I}}_2^{\mathrm{T}}\left\{\mathbf{H}_2\right\}_{m\times1}-\mathbf{C}_{12}^{\mathrm{T}}\hat{\mathbf{I}}_4^{\mathrm{T}},$$

$$\left\{\mathbf{b}_{43}\right\}_{m\times1}=-\mathbf{C}_{12}^{\mathrm{T}}\hat{\mathbf{I}}_1^{\mathrm{T}}L\left\{\mathbf{H}_3\right\}_{m\times1}-L\mathbf{C}_{12}^{\mathrm{T}}\hat{\mathbf{I}}_3^{\mathrm{T}}\left\{\mathbf{H}_3\right\}_{m\times1}-L\mathbf{C}_{12}^{\mathrm{T}}\hat{\mathbf{I}}_5^{\mathrm{T}},$$

$$\left\{\mathbf{b}_{44}\right\}_{m\times1}=-\mathbf{C}_{12}^{\mathrm{T}}\hat{\mathbf{I}}_1^{\mathrm{T}}\left\{\mathbf{H}_4\right\}_{m\times1}-\mathbf{C}_{12}^{\mathrm{T}}\hat{\mathbf{I}}_2^{\mathrm{T}}\left\{\mathbf{H}_4\right\}_{m\times1}-\mathbf{C}_{12}^{\mathrm{T}}\hat{\mathbf{I}}_6^{\mathrm{T}},$$

$$\left[\mathbf{b}_{51}\right]_{m\times4m}=\int_0^L\left\{\hat{\mathbf{I}}_4\mathbf{C}_{11}\hat{\mathbf{I}}_1^{\mathrm{T}}\left[\mathbf{H}_1(z)\right]_{m\times4m}-\hat{\mathbf{I}}_4\mathbf{C}_{12}\left[\mathbf{H}_1''(z)\right]_{m\times4m}+\hat{\mathbf{I}}_4\mathbf{C}_{11}\hat{\mathbf{I}}_2^{\mathrm{T}}\left[\mathbf{H}_1(0)\right]_{m\times4m}+\hat{\mathbf{I}}_4\mathbf{C}_{11}\hat{\mathbf{I}}_3^{\mathrm{T}}z\left[\mathbf{H}_1'(0)\right]_{m\times4m}\right\}dz,$$

$$\left\{\mathbf{b}_{52}\right\}_{m\times1}=\int_0^L\left\{\hat{\mathbf{I}}_4\mathbf{C}_{11}\hat{\mathbf{I}}_1^{\mathrm{T}}\left\{\mathbf{H}_2\right\}_{m\times1}+\hat{\mathbf{I}}_4\mathbf{C}_{11}\hat{\mathbf{I}}_2^{\mathrm{T}}\left\{\mathbf{H}_2\right\}_{m\times1}+\hat{\mathbf{I}}_4\mathbf{C}_{11}\hat{\mathbf{I}}_4^{\mathrm{T}}\right\}dz,$$

$$\left\{\mathbf{b}_{53}\right\}_{m\times1}=\int_0^L\left\{\hat{\mathbf{I}}_4\mathbf{C}_{11}\hat{\mathbf{I}}_1^{\mathrm{T}}z\left\{\mathbf{H}_3\right\}_{m\times1}+\hat{\mathbf{I}}_4\mathbf{C}_{11}\hat{\mathbf{I}}_3^{\mathrm{T}}z\left\{\mathbf{H}_3\right\}_{m\times1}+\hat{\mathbf{I}}_4\mathbf{C}_{11}\hat{\mathbf{I}}_5^{\mathrm{T}}z\right\}dz,$$

$$\left\{\mathbf{b}_{54}\right\}_{m\times1}=\int_0^L\left\{\hat{\mathbf{I}}_4\mathbf{C}_{11}\hat{\mathbf{I}}_1^{\mathrm{T}}\left\{\mathbf{H}_4\right\}_{m\times1}+\hat{\mathbf{I}}_4\mathbf{C}_{11}\hat{\mathbf{I}}_2^{\mathrm{T}}\left\{\mathbf{H}_4\right\}_{m\times1}+\hat{\mathbf{I}}_4\mathbf{C}_{11}\hat{\mathbf{I}}_6^{\mathrm{T}}\right\}dz,$$

$$\left[\mathbf{b}_{61}\right]_{m\times4m}=\int_0^L\left\{z\hat{\mathbf{I}}_5\mathbf{C}_{11}\hat{\mathbf{I}}_1^{\mathrm{T}}\left[\mathbf{H}_1(z)\right]_{m\times4m}+\tilde{\mathbf{I}}_3\mathbf{C}_{33}\tilde{\mathbf{I}}_1^{\mathrm{T}}\left[\mathbf{H}_1'(z)\right]_{m\times4m}-z\hat{\mathbf{I}}_5\mathbf{C}_{12}\left[\mathbf{H}_1''(z)\right]_{m\times4m}+\right.$$

$$\left.+z\hat{\mathbf{I}}_5\mathbf{C}_{11}\hat{\mathbf{I}}_2^{\mathrm{T}}\left[\mathbf{H}_1(0)\right]_{m\times4m}+\left(z^2\hat{\mathbf{I}}_5\mathbf{C}_{11}\hat{\mathbf{I}}_3^{\mathrm{T}}+\tilde{\mathbf{I}}_3\mathbf{C}_{33}\tilde{\mathbf{I}}_2^{\mathrm{T}}\right)\left[\mathbf{H}_1'(0)\right]_{m\times4m}\right\}dz,$$

$$\left\{\mathbf{b}_{62}\right\}_{m\times1}=\int_0^L\left(z\hat{\mathbf{I}}_5\mathbf{C}_{11}\hat{\mathbf{I}}_1^{\mathrm{T}}\left\{\mathbf{H}_2\right\}_{m\times1}+z\hat{\mathbf{I}}_5\mathbf{C}_{11}\hat{\mathbf{I}}_2^{\mathrm{T}}\left\{\mathbf{H}_2\right\}_{m\times1}+z\hat{\mathbf{I}}_5\mathbf{C}_{11}\hat{\mathbf{I}}_4^{\mathrm{T}}\right)dz,$$

$$\left\{\mathbf{b}_{63}\right\}_{m\times1}=\int_0^L\left(z\hat{\mathbf{I}}_5\mathbf{C}_{11}\hat{\mathbf{I}}_1^{\mathrm{T}}z\left\{\mathbf{H}_3\right\}_{m\times1}+\tilde{\mathbf{I}}_3\mathbf{C}_{33}\tilde{\mathbf{I}}_1^{\mathrm{T}}\left\{\mathbf{H}_3\right\}_{m\times1}+z^2\hat{\mathbf{I}}_5\mathbf{C}_{11}\hat{\mathbf{I}}_5^{\mathrm{T}}+\tilde{\mathbf{I}}_3\mathbf{C}_{33}\tilde{\mathbf{I}}_3^{\mathrm{T}}+\left(z^2\hat{\mathbf{I}}_5\mathbf{C}_{11}\hat{\mathbf{I}}_3^{\mathrm{T}}+\tilde{\mathbf{I}}_3\mathbf{C}_{33}\tilde{\mathbf{I}}_2^{\mathrm{T}}\right)\left\{\mathbf{H}_3\right\}_{m\times1}\right)dz,$$

$$\left\{\mathbf{b}_{64}(z)\right\}_{m\times1}=\int_0^L\left(z\hat{\mathbf{I}}_5\mathbf{C}_{11}\hat{\mathbf{I}}_1^{\mathrm{T}}\left\{\mathbf{H}_4\right\}_{m\times1}+z\hat{\mathbf{I}}_5\mathbf{C}_{11}\hat{\mathbf{I}}_2^{\mathrm{T}}\left\{\mathbf{H}_4\right\}_{m\times1}+z\hat{\mathbf{I}}_5\mathbf{C}_{11}\hat{\mathbf{I}}_6^{\mathrm{T}}\right)dz,$$

$$\left[\mathbf{b}_{71}\right]_{m\times4m}=\int_0^L\left\{\hat{\mathbf{I}}_6\mathbf{C}_{11}\hat{\mathbf{I}}_1^{\mathrm{T}}\left[\mathbf{H}_1(z)\right]_{m\times4m}-\hat{\mathbf{I}}_6\mathbf{C}_{12}\left[\mathbf{H}_1''(z)\right]_{m\times4m}+\hat{\mathbf{I}}_6\mathbf{C}_{11}\hat{\mathbf{I}}_2^{\mathrm{T}}\left[\mathbf{H}_1(0)\right]_{m\times4m}+z\hat{\mathbf{I}}_6\mathbf{C}_{11}\hat{\mathbf{I}}_3^{\mathrm{T}}\left[\mathbf{H}_1'(0)\right]_{m\times4m}\right\}dz,$$

$$\left\{\mathbf{b}_{72}\right\}_{m\times1}=\int_0^L\left(\hat{\mathbf{I}}_6\mathbf{C}_{11}\hat{\mathbf{I}}_1^{\mathrm{T}}\left\{\mathbf{H}_2\right\}_{m\times1}+\hat{\mathbf{I}}_6\mathbf{C}_{11}\hat{\mathbf{I}}_2^{\mathrm{T}}\left\{\mathbf{H}_2\right\}_{m\times1}+\hat{\mathbf{I}}_6\mathbf{C}_{11}\hat{\mathbf{I}}_4^{\mathrm{T}}\right)dz,$$

$$\left\{\mathbf{b}_{73}\right\}_{m\times1}=\int_0^L\left(\hat{\mathbf{I}}_6\mathbf{C}_{11}\hat{\mathbf{I}}_1^{\mathrm{T}}z\left\{\mathbf{H}_3\right\}_{m\times1}+z\hat{\mathbf{I}}_6\mathbf{C}_{11}\hat{\mathbf{I}}_3^{\mathrm{T}}\left\{\mathbf{H}_3\right\}_{m\times1}+z\hat{\mathbf{I}}_6\mathbf{C}_{11}\hat{\mathbf{I}}_5^{\mathrm{T}}\right)dz,$$

$$\left\{\mathbf{b}_{74}\right\}_{m\times1}=\int_0^L\left(\hat{\mathbf{I}}_6\mathbf{C}_{11}\hat{\mathbf{I}}_1^{\mathrm{T}}\left\{\mathbf{H}_4\right\}_{m\times1}+\hat{\mathbf{I}}_6\mathbf{C}_{11}\hat{\mathbf{I}}_2^{\mathrm{T}}\left\{\mathbf{H}_4\right\}_{m\times1}+\hat{\mathbf{I}}_6\mathbf{C}_{11}\hat{\mathbf{I}}_6^{\mathrm{T}}\right)dz.$$

Also, Eqs. (7.41)-(7.46) were expressed in terms of the following load vectors $\left\{\mathbf{L}_i\right\}_{m\times1}$

$$\left\{\mathbf{L}_1\right\}_{m\times1}=\int_0^L\left\{\hat{\mathbf{I}}_2\mathbf{C}_{11}\hat{\mathbf{I}}_1^{\mathrm{T}}\left\{\mathbf{H}_5(z)\right\}_{m\times1}-\hat{\mathbf{I}}_2\mathbf{C}_{12}\left\{\mathbf{H}_5''(z)\right\}_{m\times1}+\hat{\mathbf{I}}_2\mathbf{C}_{11}\hat{\mathbf{I}}_2^{\mathrm{T}}\left\{\mathbf{H}_5(0)\right\}_{m\times1}+\hat{\mathbf{I}}_2\mathbf{C}_{11}\hat{\mathbf{I}}_3^{\mathrm{T}}z+\hat{\mathbf{I}}_2\mathbf{d}_1(\mathbf{z})\right\}dz$$

$$+\mathbf{C}_{22}\left\{\mathbf{H}_5'''(0)\right\}_{m\times1}-\left(\mathbf{C}_{12}^{\mathrm{T}}\hat{\mathbf{I}}_1^{\mathrm{T}}+\mathbf{C}_{12}^{\mathrm{T}}\hat{\mathbf{I}}_3^{\mathrm{T}}+\tilde{\mathbf{I}}_1\mathbf{C}_{33}\tilde{\mathbf{I}}_1^{\mathrm{T}}+\tilde{\mathbf{I}}_1\mathbf{C}_{33}\tilde{\mathbf{I}}_2^{\mathrm{T}}\right)\left\{\mathbf{H}_5'(0)\right\}_{m\times1}+\mathbf{d}_2'(0)+\tilde{\mathbf{I}}_1\mathbf{d}_3(0),$$

$$\left\{\mathbf{L}_2\right\}_{m\times1}=\int_0^L\left\{z\hat{\mathbf{I}}_3\mathbf{C}_{11}\hat{\mathbf{I}}_1^{\mathrm{T}}\left\{\mathbf{H}_5(z)\right\}_{m\times1}+\tilde{\mathbf{I}}_2\mathbf{C}_{33}\tilde{\mathbf{I}}_1^{\mathrm{T}}\left\{\mathbf{H}_5'(z)\right\}_{m\times1}-z\hat{\mathbf{I}}_3\mathbf{C}_{12}\left\{\mathbf{H}_5''(z)\right\}_{m\times1}\right\}dz-\mathbf{C}_{22}\left\{\mathbf{H}_5''(0)\right\}_{m\times1}$$

$$+\left(\int_0^L z\hat{\mathbf{I}}_3\mathbf{C}_{11}\hat{\mathbf{I}}_2^{\mathrm{T}}dz+\mathbf{C}_{12}^{\mathrm{T}}\hat{\mathbf{I}}_1^{\mathrm{T}}+\mathbf{C}_{12}^{\mathrm{T}}\hat{\mathbf{I}}_2^{\mathrm{T}}\right)\left\{\mathbf{H}_5(0)\right\}_{m\times1}+\left(\int_0^L z^2\hat{\mathbf{I}}_3\mathbf{C}_{11}\hat{\mathbf{I}}_3^{\mathrm{T}}dz+\int_0^L\tilde{\mathbf{I}}_2\mathbf{C}_{33}\tilde{\mathbf{I}}_2^{\mathrm{T}}dz\right)\left\{\mathbf{H}_5'(0)\right\}_{m\times1}+$$

$$+\int_0^L z\hat{\mathbf{I}}_3\mathbf{d}_1(\mathbf{z})dz-\mathbf{d}_2(0)+\int_0^L\tilde{\mathbf{I}}_2\mathbf{d}_3(\mathbf{z})dz,$$

$$\left\{\mathbf{L_3}\right\}_{m\times1}=\left(-\mathbf{C}_{12}^{\mathbf{T}}\hat{\mathbf{I}}_1^{\mathbf{T}}-\tilde{\mathbf{I}}_1\mathbf{C}_{33}\tilde{\mathbf{I}}_1^{\mathbf{T}}\right)\left\{\mathbf{H}_5'\left(L\right)\right\}_{m\times1}+\mathbf{C}_{22}\left\{\mathbf{H}_5'''\left(L\right)\right\}_{m\times1}+\left(-\mathbf{C}_{12}^{\mathbf{T}}\hat{\mathbf{I}}_3^{\mathbf{T}}-\tilde{\mathbf{I}}_1\mathbf{C}_{33}\tilde{\mathbf{I}}_2^{\mathbf{T}}\right)\left\{\mathbf{H}_5'\left(0\right)\right\}_{m\times1}$$

$$+\mathbf{d_2}'\left(L\right)-\tilde{\mathbf{I}}_1\mathbf{d_3}\left(L\right),$$

$$\left\{\mathbf{L_4}\right\}_{m\times1}=-\mathbf{C}_{12}^{\mathbf{T}}\hat{\mathbf{I}}_1^{\mathbf{T}}\left\{\mathbf{H}_5\left(L\right)\right\}_{m\times1}+\mathbf{C}_{22}\left\{\mathbf{H}_5''\left(L\right)\right\}_{m\times1}-L\mathbf{C}_{12}^{\mathbf{T}}\hat{\mathbf{I}}_3^{\mathbf{T}}\left\{\mathbf{H}_5'\left(0\right)\right\}_{m\times1}-\mathbf{C}_{12}^{\mathbf{T}}\hat{\mathbf{I}}_2^{\mathbf{T}}\left\{\mathbf{H}_5\left(0\right)\right\}_{m\times1}+\mathbf{d_2}\left(L\right),$$

$$\left\{\mathbf{L_5}\right\}_{m\times1}=\int_0^L\left\{\hat{\mathbf{I}}_4\mathbf{C}_{11}\hat{\mathbf{I}}_1^{\mathbf{T}}\left\{\mathbf{H}_5\left(z\right)\right\}-\hat{\mathbf{I}}_4\mathbf{C}_{12}\left\{\mathbf{H}_5''\left(z\right)\right\}+\hat{\mathbf{I}}_4\mathbf{C}_{11}\hat{\mathbf{I}}_2^{\mathbf{T}}\left\{\mathbf{H}_5\left(0\right)\right\}_{m\times1}+\hat{\mathbf{I}}_4\mathbf{C}_{11}\hat{\mathbf{I}}_3^{\mathbf{T}}z\left\{\mathbf{H}_5'\left(0\right)\right\}+\hat{\mathbf{I}}_4\mathbf{d_1}\left(\mathbf{z}\right)\right\}dz,$$

$$\left\{\mathbf{L_6}\right\}_{m\times1}=\int_0^L\left\{z\hat{\mathbf{I}}_5\mathbf{C}_{11}\hat{\mathbf{I}}_1^{\mathbf{T}}\left\{\mathbf{H}_5\left(z\right)\right\}_{m\times1}+\tilde{\mathbf{I}}_3\mathbf{C}_{33}\tilde{\mathbf{I}}_1^{\mathbf{T}}\left\{\mathbf{H}_5'\left(z\right)\right\}_{m\times1}-z\hat{\mathbf{I}}_5\mathbf{C}_{12}\left\{\mathbf{H}_5''\left(z\right)\right\}_{m\times1}+z\hat{\mathbf{I}}_5\mathbf{C}_{11}\hat{\mathbf{I}}_2^{\mathbf{T}}\left\{\mathbf{H}_5\left(0\right)\right\}_{m\times1}+\right.$$

$$\left.+\left(z^2\hat{\mathbf{I}}_5\mathbf{C}_{11}\hat{\mathbf{I}}_3^{\mathbf{T}}+\tilde{\mathbf{I}}_3\mathbf{C}_{33}\tilde{\mathbf{I}}_2^{\mathbf{T}}\right)\left\{\mathbf{H}_5'\left(0\right)\right\}_{m\times1}+z\hat{\mathbf{I}}_5\mathbf{d_1}\left(\mathbf{z}\right)+\tilde{\mathbf{I}}_3\mathbf{d_3}\left(\mathbf{z}\right)\right\}dz,$$

$$\left\{\mathbf{L_7}\right\}_{m\times1}=\int_0^L\left(\hat{\mathbf{I}}_6\mathbf{C}_{11}\hat{\mathbf{I}}_1^{\mathbf{T}}\left\{\mathbf{H}_5\left(z\right)\right\}_{m\times1}-\hat{\mathbf{I}}_6\mathbf{C}_{12}\left\{\mathbf{H}_5''\left(z\right)\right\}_{m\times1}+\hat{\mathbf{I}}_6\mathbf{C}_{11}\hat{\mathbf{I}}_2^{\mathbf{T}}\left\{\mathbf{H}_5\left(0\right)\right\}_{m\times1}+z\hat{\mathbf{I}}_6\mathbf{C}_{11}\hat{\mathbf{I}}_3^{\mathbf{T}}\left\{\mathbf{H}_5'\left(0\right)\right\}_{m\times1}+\hat{\mathbf{I}}_6\mathbf{d_1}\left(\mathbf{z}\right)\right)dz$$

References

[7-1] Carrena, E., and Guinta, G., (2010), Refined beam theories based on a unified formulation, International journal of applied mechanics, 2(1), 117-143.

[7-2] Chen, D., and Cheng, S., (1983), An analysis of adhesive bonded single-lap joints, Journal of applied mechanics, 50(1), 109-115.

[7-3] Erkmen, R.E., and Mohareb, M. (2006a), Nonorthogonal solution for thin-walled members- A finite element formulation, Canadian Journal of Civil Engineering, 33(4), 421-439.

[7-4] Erkmen, R.E., and Mohareb, M. (2006b), Nonorthogonal solution for thin-walled members-applications and modelling considerations, Canadian J. of Civil Engineering, 33(4), 440-450.

[7-5] Erkmen, R.E., and Mohareb, M. (2008a), Buckling analysis of thin-walled open members – A complementary energy variational principle, Thin Walled Structures, 46(6), 602-617.

[7-6] Erkmen, R.E., and Mohareb, M. (2008b), Buckling analysis of thin-walled open members – A finite element formulation, Thin Walled Structures, 46(6), 602-617.

[7-7] Groh,R.M., and Weaver, P.M., (2015), Static inconsistencies in certain axiomatic higher-order shear deformation theories for beams, plates and shells, Composite structures, 120, 231-245.

[7-8] Jha,D.K., Kant,T. and Singh,R.K.,(2013), Stress analysis of transversely loaded functionally graded plates with a higher order shear and normal deformation theory, J. of engineering mechanics, 139(12), 1663-1680.

[7-9] Heyliger, P. R. and Reddy, J. N., (1988), A higher order beam finite element for bending and vibration problems, Journal of Sound and Vibration, 126(2), 309-326.

[7-10] Levinson, M., (1981), A new rectangular beam theory, J. Sound and Vibration, 74 (1), 81-87.

[7-11] Mucichescu, D.T. (1984), Bounds for stiffness for prismatic beams, Journal of Structural Engineering, 110(6), 1410–1414.

[7-12] Parra, G.J. and Wight J.K. (2002), Prediction of Shear Strength and Shear Distortion in R/C Beam-Column Joints, American Concrete Institute, Michigan, SP197-10.

[7-13] Patel, R., Dubey, S. K., and Pathak, K.K. (2014), Effect of depth span ratio on the behaviour of beams, International Journal of Advanced Structural Engineering, 56(6), 1-7.

[7-14] Pham, P.V. and Mohareb, M. (2014), A shear deformable theory for the analysis of steel beams reinforced with GFRP plates, Thin-Walled Structures, 85, 165-182.

[7-15] Pham, P.V and Mohareb, M. (2015), Nonshear Deformable Theory for Analysis of Steel Beams Reinforced with GFRP Plate Closed-Form Solution, J. Struct. Eng., ASCE, 141(12),04015063.

[7-16] Timoshenko, S. P. (1921), On the corrections for shear of the differential equation for transverse vibrations of prismatic bars, Philosophical Magazine, 41, 744-746.

[7-17] Timoshenko, S. P. and Goodier, J., N. (1970), theory of elasticity (McGwaw-Hill, New York).

[7-1] Santos,H.A..F.A. (2012a), A complementary-energy based criterion for the stability analysis of geometrically exact framed structures, Computers & Structures, 106-107, 196-203

[7-18] Santos,H.A..F.A. (2012b), Variationally consistent force-based finite element method for the geometrically non-linear analysis of Euler-Bernoulli framed structures, Finite Elements in Analysis and Design, 53, 24-36

[7-19] Stephen, N. G. and Levinson, M. (1979), A second order beam theory, Journal of Sound and Vibration, 67 (3), 293-305.

[7-20] Shu, X., and Sun, L., (1994), An improved simply higher order theory for laminated composite plates, Journal of computers and Structures, 50(2), 231-236.

[7-21] Reddy, J. (1984), Energy and variational methods in applied mechanics, John Wiley & Sons.

[7-22] Zhao, B., Lu, Z.H., and Lu, Y., N., (2014), 2D analytical solution of elastic stresses for balanced single-lap joints-Variational method, Int. J. of Adhesion & Adhesives, 49, 115-126.

Chapter 8: Finite element formulation for the analysis of multilayered beams based on the principle of stationary complementary strain energy

Abstract

A family of finite elements for the analysis of orthotropic multilayered beams with mono-symmetric cross-sections is developed based on the principle of stationary complementary energy. The longitudinal normal stress field is postulated as polynomial and Heaviside step function series and substituted into the infinitesimal equilibrium conditions to develop expressions for the shear and transverse stress fields. The statically admissible stress fields thus derived are then adopted within the complementary energy variational principle framework to develop a family of finite elements. The distinguishing features of the solution are: (i) it captures the nonlinear distribution of the stress fields along the section depth and steep stress gradients typically occurring near bondline ends of multilayer beams, (ii) unlike conventional solutions based on the principle of stationary potential energy which predict jumps in the shear and peeling stresses at interfaces of adjacent layers, the present solution satisfies equilibrium in an exact infinitesimal sense at layer interfaces and thus ensures continuity of the stress fields across the interface, (iii) it naturally captures the effects of transverse shear and transverse normal stresses, and (iv) it consistently converges to the displacements from above, in contrast to conventional finite element solutions where convergence is typically from below. The versatility of the solution is then illustrated in applications involving wood beams and steel beams strengthened with GFRP plates and sandwich beams with soft cores.

Keywords: High order beam theory, complementary strain energy, variational principle, finite element, orthotropic materials, layered beams, sandwich beams, GFRP, beam strengthening.

8.1. Motivation and Literature review

The adoption of conventional beam theories (e.g., the Euler-Bernouilli or Timoshenko theories) in the analysis of multilayered beams is associated with inconsistencies and limitations. The Euler-Bernoulli beam kinematic assumption postulating that plane section remains plane and normal to the beam axis throughout deformation, implies the neglect of shear deformation effects and thus tends to grossly over-predict the stiffness of short-span composite beams. An improved solution accounting for shear deformation is the Timoshenko beam assumption which retains the plane section assumption but relaxes the normality condition between the cross-section plane and the beam axis. The Timoshenko beam kinematics however introduce non-zero shear strains (and hence stresses) at the extreme fibers of the cross-section and thus violate the traction boundary conditions at extreme fibers where externally applied shear stresses typically vanish. To remedy such contradictions, various researchers have formulated correction shear coefficients (e.g., Timoshenko 1921, Cowper 1966, Stephen 1980, Kaneko 1975, Blevins 2015) that depend on whether the analysis is static or dynamic (e.g., Timoshenko 1922, Mindlin 1953, Hutchinson 1981, Heyliger and Ready 1988) and are section dependent.

Higher order beam theories with improved kinematic assumptions include the work of Stephen and Levinson (1979), Reddy (1984), Heyliger and Reddy (1988), Shu and Sun (1994), Jha et al (2013), Kant and Manjunatha (1990), Zhang et al (2016) where the longitudinal displacement field is assumed as a third order polynomial. Such studies are however limited to rectangular cross-sections (Wu and Jensen 2011, 2014). Another class of solutions based on assumed higher order polynomials for the longitudinal displacements were developed by Carrera and Giunta (2010), Carrera et al. (2015), and Groh and Weaver (2015). Such theories have the advantage of capturing shear deformation effects without the need of introducing shear modification factors. Some of these theories (Carrera and Guinta 2010, Carrera et al. 2015) have additionally captured the effect of transverse normal stresses.

Irrespective of the kinematic assumptions made in the above studies, when used in conjunction with the principle of minimum potential energy (referred to as the conventional treatment subsequently), they lead to approximate differential equations of equilibrium providing a stiffer representation of the structure compared to that based on the exact infinitesimal equilibrium conditions (e.g., solutions based on the theory of elasticity). Another characteristic observed when applying the conventional treatment to composite beams with layers of different materials is that the postulation of continuous displacement fields (either linear, cubic, or higher order), while ensuring continuity of strains at the interfaces of adjoining materials, lead to discontinuous stresses at the interfaces when such strains are multiplied by the different constitutive properties of the interfaces of adjoining materials. Such stress discontinuities violate the local shear and transverse equilibrium conditions at the interface. This disadvantage is observed not only in analytical solutions but also in finite element solutions based on the principle of stationary potential energy. In 3D finite element solutions, such discrepancies can be minimized, but not eliminated, by adopting a fine mesh in the transverse direction, albeit such a measure results in an undesirable computational expense. Within this context, the present study contributes to remedy the limitations of the conventional treatment by adopting the principle of complementary potential energy in conjunction with statically admissible high-order stress fields to develop an improved finite element solution that satisfies continuity of shear and transverse stress fields at layer interfaces.

A comparison between the conventional treatment and the complementary energy solution is depicted in Figure 8.1. Under the conventional stationary potential energy principle, displacement fields are initially postulated, hence satisfying compatibility of strains in an exact pointwise sense. The stationarity condition of the total potential energy functional is then evoked to yield approximate equilibrium equations which tend to overestimate the stiffness of the structure. In contrast, under the principle of stationary total complementary strain energy, stress fields exactly satisfying the equilibrium conditions in an exact pointwise sense are postulated and the complementary strain energy principle is then expressed in terms of the unknown stress fields. The condition of stationarity of the complementary strain energy functional then yields approximate compatibility equations in terms of the stress fields, which lead to a solution that tends to underestimate the stiffness of the structure. Recently, Groh and Tessler (2017) developed a refined zigzag theory for the analysis for multi-layered beam with doubly symmetric cross-sections based on the Reissner variational principle.

A comparatively limited number of finite element solutions have adopted the principle of stationary complementary energy. Wunderlich and Pilkey (2003) developed complementary strain energy solutions for plane stress problems by postulating a longitudinal stress field that varies linearly across the section height. Erkmen and Mohareb (2006) derived a complementary energy solution for the torsional analysis of thin-walled beams. Erkmen and Mohareb (2008) developed a complementary energy variational principle for the buckling analysis of thin-walled open members based on the principle of stationary complementary energy. Zhao et al. (2014) adopted a two-dimensional elasticity theory solution in conjunction with the principle of stationary complementary energy for the analysis of adhesive-bonded single-lap joints. By adopting longitudinal normal stress fields that linearly vary in the transverse direction, and incorporating shear stresses, Wu and Jensen (2011) developed a solution for layered beams to predict interfacial shear and normal stresses. However, discrepancies between their solutions and two-dimensional finite element analyses under ANSYS were observed near the bond ends and were attributed to the postulated approximate linear distribution for longitudinal normal stresses.

Within the above context, the present study develops a higher order beam theory that naturally incorporates shear and normal transverse stresses. Since the theory aims at the accurate predictions of interfacial stresses, the longitudinal normal stresses are assumed to have a general non-linear distribution along the section height. In order to adopt the jumps of the longitudinal stresses at layer interfaces, Heaviside step functions are introduced in the characterization of the longitudinal stress field.

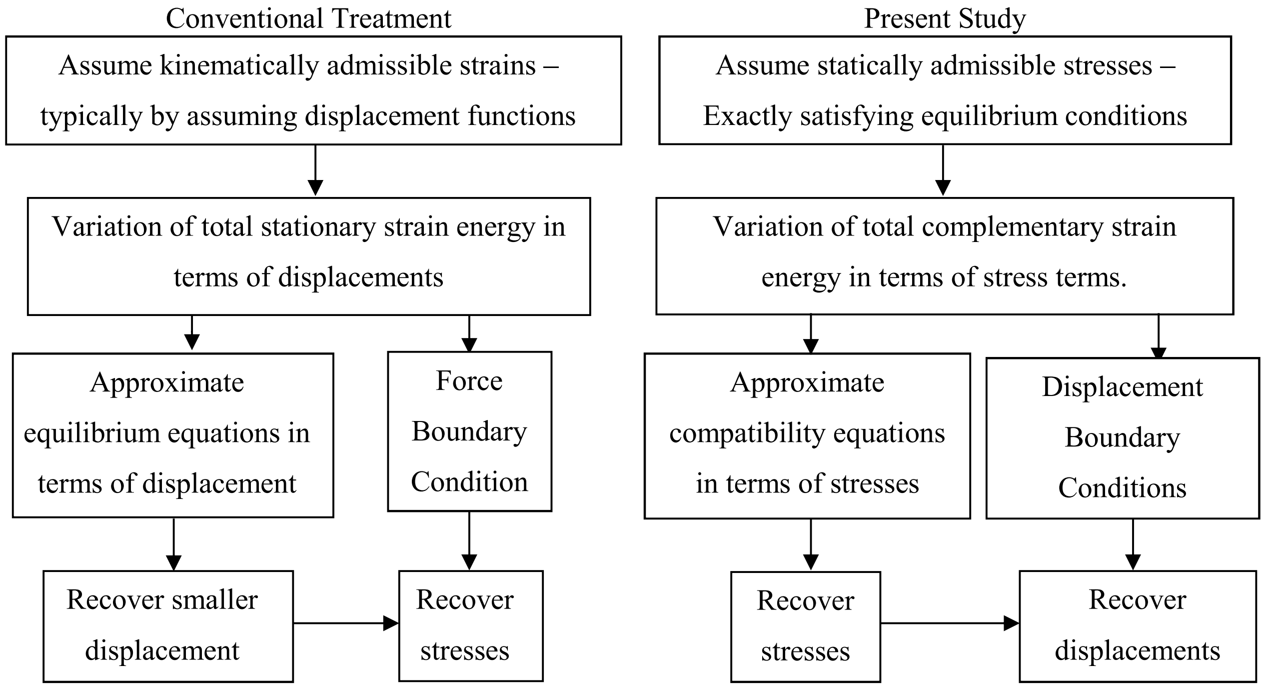

Figure 8.1. Conventional solutions versus present complementary energy solution

8.2. Statement of the Problem

A prismatic multi-layer beam with an arbitrary mono-symmetric cross-section is subjected to general body forces $p_y(y,z)$ and $p_z(y,z)$ in the transverse and longitudinal directions. Externally applied surface tractions $\sigma(-h_1,z),\tau(-h_1,z),\sigma(h_2,z),\tau(h_2,z)$ are applied to the top and bottom faces (Fig.8.2a). It is required to formulate a finite element formulation for the problem. The coordinate system $OXYZ$ is adopted, in which origin O is an arbitrary point on the cross-section (

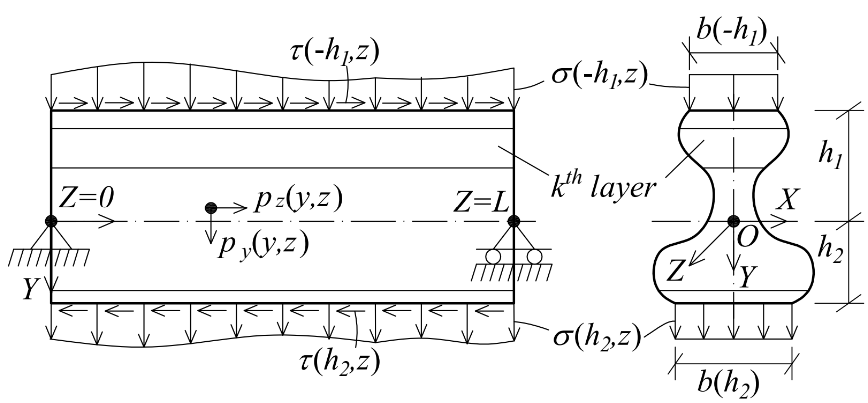

(a) (b)

Figure 8.2a and b). Cross-sectional dimension notations are depicted on

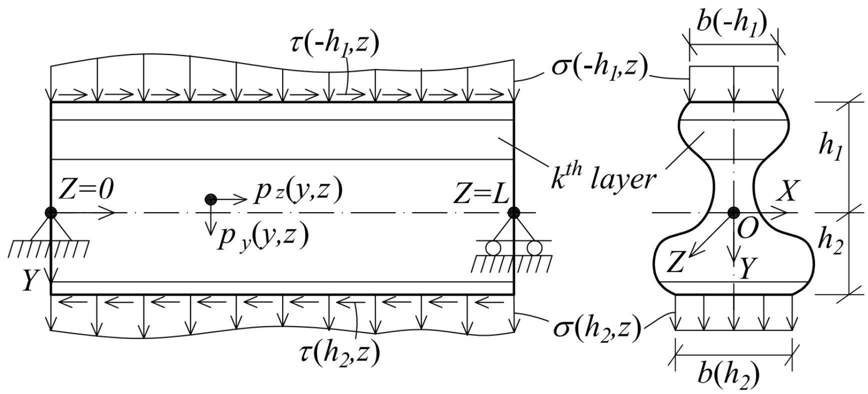

(a) (b)

Figure 8.2b in which h_1 and h_2 respectively denote the distances from top and bottom fibers and $b(y)$ is the cross-section width as a function of the coordinate y ($-h_1 \le y \le h_2$).

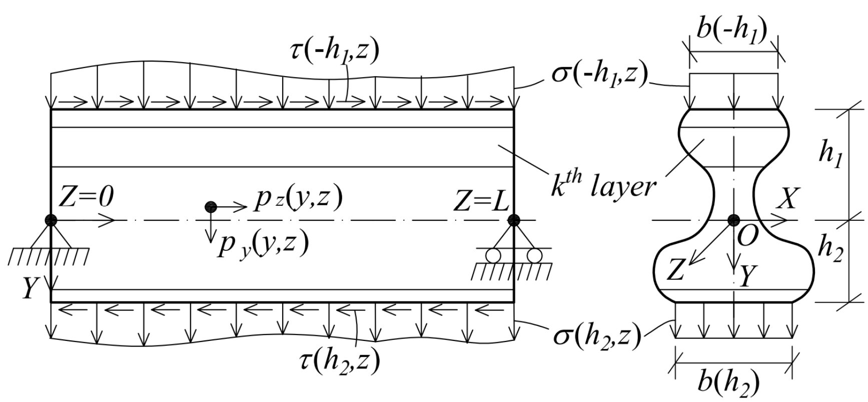

(a) (b)

Figure 8.2. Tractions and body forces applied to the beam (a) Profile view and (b) Cross-section view

8.3. Assumptions

The following assumptions are made:

a) The beam is prismatic and subjected to longitudinal and transverse loads,

b) The beam consists of p layers with $p-1$ interfaces.

c) All materials are linearly elastic orthotropic,

d) Perfect bonding is assumed between the various layers,

e) The longitudinal normal stresses take the form $\sigma_z(y,z)=\sum_{i=1}^{n} y^{i-1}F_i(z)+\sum_{k=1}^{p-1} H(y-y_k)J_k(z)$ where $F_i(z)$ are unknown functions of longitudinal coordinate z, y is the transverse coordinate and n is a positive integer. The second summation is on the number of interfaces $k=1,2,\ldots,p-1$ and $J_k(z)$ are unknown functions. The term $H(y-y_k)$ is the Heaviside step function defined as $H(y-y_k)=0$ when $y<y_k$ and $H(y-y_k)=1.0$ when $y>y_k$. While the Heaviside step function is discontinuous at the interface $y=y_k$ (and hence accurately represents the stress jumps expected at the layer interfaces), its first integral $\int_{-h_1}^{y} H(y-y_k)\,dy$ and second integral $\int_{-h_1}^{y}\int_{-h_1}^{y} H(y-y_k)\,dydy$ are continuous functions at interfaces $y=y_k$, and thus emulate the expected continuous shear and transverse stress fields across the interfaces. Also, the transverse normal stresses $\sigma_y(y,z)$ and shear stresses $\tau(y,z)$ (Figure 8.3) are to be determined from infinitesimal equilibrium conditions. Other out-of-plane stress components are assumed negligible.

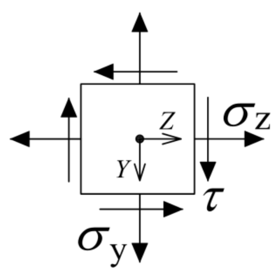

Figure 8.3. Stresses components considered in the present theory

8.4. Formulation

8.4.1. Statically Admissible Stress Fields

As discussed in the assumption, the longitudinal stresses $\sigma_z(y,z)$ are postulated to take the form

$$\sigma_z(y,z)=\sum_{i=1}^{n} y^{i-1}F_i(z)+\sum_{k=1}^{p-1} H(y-y_k)J_k(z) \tag{8.1}$$

For the stress fields to be statically admissible, the stress fields $\sigma_y(y,z)$ and $\tau(y,z)$ (Figure 8.4) need to satisfy the equilibrium conditions in an exact pointwise sense. The equilibrium conditions take the form

$$\frac{\partial}{\partial y}\left[b(y)\sigma_y(y,z)\right]+\frac{\partial}{\partial z}\left[b(y)\tau(y,z)\right]=b(y)\,p_y(y,z)$$
$$\frac{\partial}{\partial y}\left[b(y)\tau(y,z)\right]+\frac{\partial}{\partial z}\left[b(y)\sigma_z(y,z)\right]=b(y)\,p_z(y,z) \tag{8.2a-b}$$

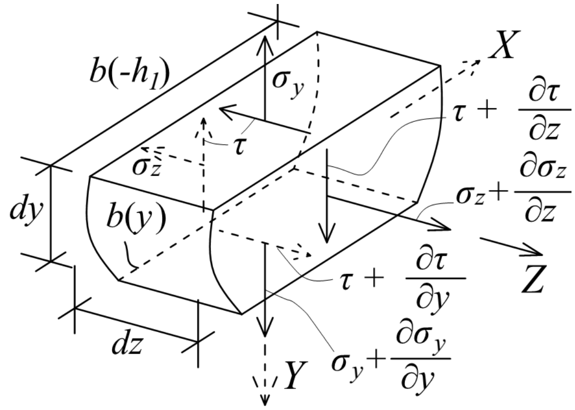

Figure 8.4. Infinitesimal element in equilibrium

From Eq.(8.1), by substituting into Eq. (8.2b), and integrating both sides with respect to y from the top fiber at height $-h_1$ to an arbitrary height y, one recovers the expression of shear stresses $\tau(y,z)$. Next, given the expression for $\tau(y,z)$, by substituting into Eq. (8.2a) and integrating with respect to y from $-h_1$ to y, one recovers an expression for the transverse normal stress $\sigma_y(y,z)$. The resulting stress fields take the form

$$\begin{aligned}
\tau(y,z)=&\frac{1}{b(y)}b(-h_1)\tau(-h_1,z)+\frac{1}{b(y)}\int_{-h_1}^{y}b(y)\,p_z(y,z)\,dy-\sum_{i=1}^{n}\left(\frac{1}{b(y)}\int_{-h_1}^{y}b(y)y^{i-1}dy\right)F_i'(z)\\
&-\left[\frac{1}{b(y)}\sum_{k=1}^{p-1}\int_{-h_1}^{y}b(y)H(y-y_k)\,dy\right]J_k'(z)\\
\sigma_y(y,z)=&\frac{1}{b(y)}b(-h_1)\sigma_y(-h_1,z)+\frac{1}{b(y)}\int_{-h_1}^{y}b(y)\,p_y(y,z)\,dy-\frac{1}{b(y)}b(-h_1)\frac{\partial\tau(-h_1,z)}{\partial z}\\
&-\frac{1}{b(y)}\int_{-h_1}^{y}\int_{-h_1}^{y}b(y)\frac{\partial p_z(y,z)}{\partial z}dydy+\sum_{i=1}^{n}\left(\frac{1}{b(y)}\int_{-h_1}^{y}\int_{-h_1}^{y}b(y)y^{i-1}dydy\right)F_i''(z)\\
&+\left[\frac{1}{b(y)}\sum_{k=1}^{p-1}\int_{-h_1}^{y}\int_{-h_1}^{y}b(y)H(y-y_k)\,dy\right]J_k''(z)
\end{aligned} \tag{8.3a-b}$$

Equations (8.3a-b) can be re-written in the form

$$\tau(y,z)=\bar{\tau}(y,z)-\sum_{i=1}^{n}\alpha_i(y)F_i'(z)-\sum_{k=1}^{p-1}a_k(y)J_k'(z)$$
$$\sigma_y(y,z)=\bar{\sigma}_y(y,z)+\sum_{i=1}^{n}\beta_i(y)F_i''(z)+\sum_{k=1}^{p-1}c_k(y)J_k''(z) \qquad (8.4a\text{-}b)$$

in which functions

$$\bar{\tau}(y,z)=\frac{1}{b(y)}b(-h_1)\tau(-h_1,z)+\frac{1}{b(y)}\int_{-h_1}^{y}b(\xi)p_z(\xi,z)d\xi;$$
$$\bar{\sigma}_y(y,z)=\frac{1}{b(y)}b(-h_1)\sigma_y(-h_1,z)+\frac{1}{b(y)}\int_{-h_1}^{y}b(\xi)p_y(\xi,z)d\xi-\frac{1}{b(y)}b(-h_1)\frac{\partial\tau(-h_1,z)}{\partial z} \qquad (8.5a\text{-}b)$$
$$-\frac{1}{b(y)}\int_{-h_1}^{y}\int_{-h_1}^{\eta}b(\xi)\frac{\partial p_z(\xi,z)}{\partial z}d\xi d\eta$$

depend on surface tractions $\tau(-h_1,z)$ and $\sigma_y(-h_1,z)$, and body forces $p_z(y,z)$ and $p_y(y,z)$. Also, in Eq. (8.4a-b), $\alpha_i(y)$, $\beta_i(y)$, $a_k(y)$ and $c_k(y)$ are cross-section functions of coordinate y along the height given by

$$\alpha_i(y)=\frac{1}{b(y)}\int_{-h_1}^{y}b(\xi)\xi^{i-1}d\xi; \qquad \beta_i(y)=\frac{1}{b(y)}\int_{-h_1}^{y}\int_{-h_1}^{\eta}b(\xi)\xi^{i-1}d\xi d\eta$$
$$a_k(y)=\frac{1}{b(y)}\int_{-h_1}^{y}b(y)H(y-y_k)dy; \qquad c_k(y)=\frac{1}{b(y)}\int_{-h_1}^{y}\int_{-h_1}^{y}b(y)H(y-y_k)dydy \qquad (8.6a\text{-}b)$$

From Eqs. (8.4a-b), by setting $y=h_2$, the stresses at the bottom fiber (Fig. 8.1) are obtained as

$$\tau(h_2,z)=\bar{\tau}(h_2,z)-\sum_{i=1}^{n}\alpha_i(h_2)F_i'(z)-\sum_{k=1}^{p-1}a_k(h_2)J_k'(z)$$
$$\sigma_y(h_2,z)=\bar{\sigma}_y(h_2,z)+\sum_{i=1}^{n}\beta_i(h_2)F_i''(z)+\sum_{k=1}^{p-1}c_k(h_2)J_k''(z) \qquad (8.7a\text{-}b)$$

8.4.2. Reducing the Number of Unknown Functions $F_i(z)$

From Equations (8.7a-b), by expressing functions F_{n-1} and F_n in terms of other functions $F_i(z)$ ($i=1,\ldots,n-2$), one obtains

$$\alpha_{n-1}(h_2)F_{n-1}'(z)+\alpha_n(h_2)F_n'(z)=\bar{\tau}(h_2,z)-\tau(h_2,z)-\sum_{i=1}^{n-2}\alpha_i(h_2)F_i'(z)-\sum_{k=1}^{p-1}a_k(h_2)J_k'(z)$$
$$\beta_{n-1}(h_2)F_{n-1}''(z)+\beta_n(h_2)F_n''(z)=\sigma_y(h_2,z)-\bar{\sigma}_y(h_2,z)-\sum_{i=1}^{n-2}\beta_i(h_2)F_i''(z)-\sum_{k=1}^{p-1}c_k(h_2)J_k''(z) \quad (8.8\text{a-b})$$

From Eq. (8.8a), by differentiation with respect to z, combining with Eq. (8.8b) and solving for F''_{n-1} and F''_n, one obtains

$$F_{n-1}''(z)=\rho_1(z)-\sum_{i=1}^{n-2}\lambda_{1i}F_i''(z)-\sum_{k=1}^{p-1}\xi_{1k}J_k''(z)$$
$$F_n''(z)=\rho_2(z)-\sum_{i=1}^{n-2}\lambda_{2i}F_i''(z)-\sum_{k=1}^{p-1}\xi_{2k}J_k''(z) \quad (8.9\text{a-b})$$

where the following function of the longitudinal coordinate z have been defined

$$\rho_1(z)=\frac{\alpha_n(h_2)\left[\sigma_y(h_2,z)-\bar{\sigma}_y(h_2,z)\right]-\beta_n(h_2)\left[\bar{\tau}'(h_2,z)-\tau'(h_2,z)\right]}{\alpha_n(h_2)\beta_{n-1}(h_2)-\alpha_{n-1}(h_2)\beta_n(h_2)};$$
$$\rho_2(z)=-\frac{\alpha_{n-1}(h_2)\left[\sigma_y(h_2,z)-\bar{\sigma}_y(h_2,z)\right]-\beta_{n-1}(h_2)\left[\bar{\tau}'(h_2,z)-\tau'(h_2,z)\right]}{\alpha_n(h_2)\beta_{n-1}(h_2)-\alpha_{n-1}(h_2)\beta_n(h_2)}; \quad (8.10\text{a-d})$$
$$\lambda_{1i}=\frac{\alpha_n(h_2)\beta_i(h_2)-\beta_n(h_2)\alpha_i(h_2)}{\alpha_n(h_2)\beta_{n-1}(h_2)-\alpha_{n-1}(h_2)\beta_n(h_2)};\quad \lambda_{2i}=-\frac{\alpha_{n-1}(h_2)\beta_i(h_2)-\beta_{n-1}(h_2)\alpha_i(h_2)}{\alpha_n(h_2)\beta_{n-1}(h_2)-\alpha_{n-1}(h_2)\beta_n(h_2)};$$
$$\xi_{1k}=\frac{\alpha_n(h_2)c_k(h_2)-\beta_n(h_2)a_k(h_2)}{\alpha_n(h_2)\beta_{n-1}(h_2)-\alpha_{n-1}(h_2)\beta_n(h_2)};\ \xi_{2k}=-\frac{\alpha_{n-1}(h_2)c_k(h_2)-\beta_{n-1}(h_2)a_k(h_2)}{\alpha_n(h_2)\beta_{n-1}(h_2)-\alpha_{n-1}(h_2)\beta_n(h_2)};$$

Traction equilibrium requires the stress fields $\sigma_y(y,z)$ and $\tau(y,z)$ at the extreme faces $z=-h_1$ and $z=h_2$ to be equal to the externally applied surface tractions. Therefore, all terms in the right hand side of Eqs. (8.10a-d) are known. By integrating Eqs. (8.9a-b) twice from 0 to z, functions $F_{n-1}(z)$ and $F_n(z)$ are obtained as

$$F_{n-1}(z)=\int_0^z\int_0^z \rho_{11}(z)dz-\sum_{i=1}^{n-2}\lambda_{1i}F_i(z)+\sum_{i=1}^{n-2}\lambda_{1i}F_i(0)+z\sum_{i=1}^{n-2}\lambda_{1i}F_i'(0)+F_{n-1}(0)+zF_{n-1}'(0)$$
$$-\sum_{k=1}^{p-1}\xi_{1k}J_k(z)+\sum_{k=1}^{p-1}\xi_{1k}J_k(0)+z\sum_{k=1}^{p-1}\xi_{1k}J_k{}'(0)$$
$$F_n(z)=\int_0^z\int_0^z \rho_{21}(z)dzdz-\sum_{i=1}^{n-2}\lambda_{2i}F_i(z)+\sum_{i=1}^{n-2}\lambda_{2i}F_i(0)+z\sum_{i=1}^{n-2}\lambda_{2i}F_i'(0)+F_n(0)+zF_n'(0)$$
$$-\sum_{k=1}^{p-1}\xi_{2k}J_k(z)+\sum_{k=1}^{p-1}\xi_{2k}J_k(0)+z\sum_{k=1}^{p-1}\xi_{2k}J_k{}'(0) \qquad (8.11a\text{-}b)$$

8.4.3. Expressing Stress Constants in terms of Stress Resultants

Constants $F_{n-1}(0)$, $F_{n-1}'(0)$, $F_n(0)$ and $F_n'(0)$ appearing in Eqs. (8.11a-b) are then eliminated by using four equations: the first one is obtained by differentiating Eqs. (8.11a-b) with respect to z, substituting $F_{n-1}{}'$ and $F_n{}'$ into Eq. (8.8a), and performing simplifications as detailed in Appendix 8.1, leading to

$$\alpha_{n-1}(h_2)F_{n-1}'(0)+\alpha_n(h_2)F_n'(0)=\left[\bar{\tau}(h_2,0)-\tau(h_2,0)\right]-\sum_{i=1}^{n-2}\alpha_i(h_2)F_i'(0)-\sum_{k=1}^{p-1}a_k(h_2)J_k{}'(0) \qquad (8.12)$$

The other three equations are recovered by introducing the stress resultants at $z=0$ where boundary conditions are applied

$$\int_A \sigma_z(y,0)dA=N(0);\quad \int_A \tau(y,0)dA=Q(0);\quad \int_A y\sigma_z(y,0)dA=M(0) \qquad (8.13a\text{-}c)$$

in which A is the cross-sectional area. From Eqs. (8.1) and (8.4a-b), one can obtain the stress fields at $z=0$, yielding

$$\sigma_z(y,0)=y^{n-2}F_{n-1}(0)+y^{n-1}F_n(0)+\sum_{i=1}^{n-2}y^{i-1}F_i(0)+\sum_{k=1}^{p-1}H(y-y_k)J_k(z)$$
$$\tau(y,0)=\bar{\tau}(y,0)-\alpha_{n-1}(y)F_{n-1}{}'(0)-\alpha_n(y)F_n{}'(0)-\sum_{i=1}^{n-2}\alpha_i(y)F_i'(0)-\sum_{k=1}^{p-1}a_k(y)J_k{}'(z) \qquad (8.14a\text{-}b)$$

From Eqs. (8.14a-b), by substituting into Eqs. (8.13a-c), one obtains

$$\overline{\alpha}_{n-2}F_{n-1}\left(0\right)+\overline{\alpha}_{n-1}F_{n}\left(0\right)=N\left(0\right)-\sum_{i=1}^{n-2}\overline{\alpha}_{i-1}F_{i}\left(0\right)-\sum_{k=1}^{p-1}\int_{A}H\left(y-y_{k}\right)dAJ_{k}\left(0\right)$$

$$\widehat{\alpha}_{n-1}F_{n-1}'\left(0\right)+\widehat{\alpha}_{n}F_{n}'\left(0\right)=-Q\left(0\right)+\int_{A}\overline{\tau}\left(y,0\right)dA-\sum_{i=1}^{n-2}\widehat{\alpha}_{i}F_{i}'\left(0\right)-\sum_{k=1}^{p-1}\int_{A}a_{k}\left(y\right)dAJ_{k}'\left(0\right) \qquad (8.15a-c)$$

$$\overline{\alpha}_{n-1}F_{n-1}\left(0\right)+\overline{\alpha}_{n}F_{n}\left(0\right)=M\left(0\right)-\sum_{i=1}^{n-2}\overline{\alpha}_{i}F_{i}\left(0\right)-\sum_{k=1}^{p-1}\int_{A}yH\left(y-y_{k}\right)dAJ_{k}\left(0\right)$$

in which sectional properties $\overline{\alpha}_{i}=\int_{A}y^{i}dA$ and $\widehat{\alpha}_{i}=\int_{A}\alpha_{i}\left(y\right)dA$ have been defined. From Eq. (8.12) and Eqs. (8.15a-c), one can recover the following expressions for functions $F_{n-1}'\left(0\right),F_{n}'\left(0\right),F_{n-1}\left(0\right)$ and $F_{n}\left(0\right)$

$$\begin{aligned}
F_{n-1}'\left(0\right)&=\varsigma_{11}+\varsigma_{12}Q\left(0\right)+\sum_{i=1}^{n-2}\varsigma_{13i}F_{i}'\left(0\right)+\sum_{k=1}^{p-1}\varsigma_{14k}J_{k}'\left(0\right)\\
F_{n}'\left(0\right)&=\varsigma_{21}+\varsigma_{22}Q\left(0\right)+\sum_{i=1}^{n-2}\varsigma_{23i}F_{i}'\left(0\right)+\sum_{k=1}^{p-1}\varsigma_{24k}J_{k}'\left(0\right)\\
F_{n-1}\left(0\right)&=\varsigma_{31}N\left(0\right)+\varsigma_{32}M\left(0\right)+\sum_{i=1}^{n-2}\varsigma_{33i}F_{i}\left(0\right)+\sum_{k=1}^{p-1}\varsigma_{34k}J_{k}\left(0\right)\\
F_{n}\left(0\right)&=\varsigma_{41}N\left(0\right)+\varsigma_{42}M\left(0\right)+\sum_{i=1}^{n-2}\varsigma_{43i}F_{i}\left(0\right)+\sum_{k=1}^{p-1}\varsigma_{44k}J_{k}\left(0\right)
\end{aligned} \qquad (8.16a-d)$$

in which coefficients ς_{ij} depend on the cross-section geometry and are defined in Appendix 8.2. From Eqs. (8.11a-b), by substituting into Eqs. (8.1) and (8.4a-b), one obtains

$$\begin{aligned}
\sigma_{z}\left(y,z\right)=&\int_{0}^{z}\int_{0}^{z}\left(y^{n-2}\rho_{1}\left(z\right)+y^{n-1}\rho_{2}\left(z\right)\right)dzdz+\left(y^{n-2}F_{n-1}\left(0\right)+zy^{n-2}F_{n-1}'\left(0\right)+y^{n-1}F_{n}\left(0\right)+zy^{n-1}F_{n}'\left(0\right)\right)\\
&+\sum_{i=1}^{n-2}\left(y^{n-2}\lambda_{1i}+y^{n-1}\lambda_{2i}\right)F_{i}\left(0\right)+\sum_{i=1}^{n-2}\left(y^{n-2}\lambda_{1i}+y^{n-1}\lambda_{2i}\right)zF_{i}'\left(0\right)-\sum_{i=1}^{n-2}\left(y^{n-2}\lambda_{1i}+y^{n-1}\lambda_{2i}-y^{i-1}\right)F_{i}\left(z\right)\\
&+\sum_{k=1}^{p-1}\left(y^{n-2}\xi_{1k}+y^{n-1}\xi_{2k}\right)J_{k}\left(0\right)+\sum_{k=1}^{p-1}\left(y^{n-2}\xi_{1k}+y^{n-1}\xi_{2k}\right)zJ_{k}'\left(0\right)-\sum_{k=1}^{p-1}\left[y^{n-2}\xi_{1k}+y^{n-1}\xi_{2k}-H\left(y-y_{k}\right)\right]J_{k}\left(z\right)\\
\tau\left(y,z\right)=&\overline{\tau}\left(y,z\right)-\int_{0}^{z}\left[\alpha_{n-1}\left(y\right)\rho_{1}\left(z\right)+\alpha_{n}\left(y\right)\rho_{2}\left(z\right)\right]dz-\alpha_{n-1}\left(y\right)F_{n-1}'\left(0\right)-\alpha_{n}\left(y\right)F_{n}'\left(0\right)\\
&-\sum_{i=1}^{n-2}\left[\alpha_{n-1}\left(y\right)\lambda_{1i}+\alpha_{n}\left(y\right)\lambda_{2i}\right]F_{i}'\left(0\right)+\sum_{i=1}^{n-2}\left[\alpha_{n-1}\left(y\right)\lambda_{1i}+\alpha_{n}\left(y\right)\lambda_{2i}-\alpha_{i}\left(y\right)\right]F_{i}'\left(z\right)\\
&-\sum_{k=1}^{p-1}\left[\alpha_{n-1}\left(y\right)\xi_{1k}+\alpha_{n}\left(y\right)\xi_{2k}\right]J_{k}'\left(0\right)+\sum_{k=1}^{p-1}\left[\alpha_{n-1}\left(y\right)\xi_{1k}+\alpha_{n}\left(y\right)\xi_{2k}-a_{k}\left(y\right)\right]J_{k}'\left(z\right) \qquad (8.17a-c)\\
\sigma_{y}\left(y,z\right)=&\overline{\sigma}_{y}\left(y,z\right)+\beta_{n-1}\left(y\right)\rho_{1}\left(z\right)+\beta_{n}\left(y\right)\rho_{2}\left(z\right)+\sum_{i=1}^{n-2}\left[\beta_{i}\left(y\right)-\beta_{n-1}\left(y\right)\lambda_{1i}-\beta_{n}\left(y\right)\lambda_{2i}\right]F_{i}''\left(z\right)\\
&+\sum_{k=1}^{p-1}\left[c_{k}\left(y\right)-\beta_{n-1}\left(y\right)\xi_{1k}-\beta_{n}\left(y\right)\xi_{2k}\right]J_{k}''\left(z\right)
\end{aligned}$$

By introducing $m=n-2$. From Eqs. (8.16a-d), by substituting into Eqs. (8.17a-c), one obtains

$$\sigma_z(y,z)=\mathbf{a_1}(y)^T\,\mathbf{F}(z)+\mathbf{a_2}(y)^T\,\mathbf{F}(0)+\mathbf{a_3}(y,z)^T\,\mathbf{F}'(0)+\mathbf{b_1}(y,z)^T\,\mathbf{R}(0)+\sigma_z^*(y,z);$$
$$\tau(y,z)=\mathbf{a_4}(y)^T\,\mathbf{F}'(z)+\mathbf{a_5}(y)^T\,\mathbf{F}'(0)+\mathbf{b_2}(y)^T\,\mathbf{R}(0)+\tau^*(y,z); \tag{8.18}$$
$$\sigma_y(y,z)=\mathbf{a_6}(y)^T\,\mathbf{F}''(z)+\sigma_y^*(y,z);$$

where functions $F_i(z), J_p(z)$, and stress results, have been grouped into the following vectors:

$$\begin{aligned}&\mathbf{F}(z)^T=\langle F_1(z)\quad F_1(z)\quad \ldots\quad F_i(z)\ldots\quad F_m(z)\mid J_1(z)\quad J_2(z)\quad \ldots\quad J_k(z)\ldots\quad J_{p-1}(z)\rangle;\\&\mathbf{R}(0)^T=\langle N(0)\quad Q(0)\quad M(0)\rangle;\end{aligned} \tag{8.19}$$

and the contribution of applied loads are defined as

$$\begin{aligned}&\sigma_z^*(y,z)=\int_0^z\!\!\int_0^z\left[y^{n-2}\rho_1(z)+y^{n-1}\rho_2(z)\right]dzdz+z\left(y^{n-2}\varsigma_{11}+y^{n-1}\varsigma_{21}\right)\\&\tau^*(y,z)=\bar{\tau}(y,z)-\int_0^z\left[\alpha_{n-1}(y)\rho_1(z)+\alpha_n(y)\rho_2(z)\right]dz-\alpha_{n-1}(y)\varsigma_{11}-\alpha_n(y)\varsigma_{21};\\&\sigma_y^*(y,z)=\bar{\sigma}_y(y,z)+\beta_{n-1}(y)\rho_1(z)+\beta_n(y)\rho_2(z);\end{aligned} \tag{8.20a-c}$$

In Eq. (18), the following vectors of cross-sectional parameters have been introduced

$$\begin{aligned}
&\mathbf{a_1}(y)^T=\langle a_{11}(y)\quad a_{12}(y)\quad \ldots a_{1i}(y)\ldots\quad a_{1m}(y)\mid g_{11}(y)\quad g_{12}(y)\quad \ldots g_{1k}(y)\ldots\quad g_{1p-1}(y)\rangle,\\
&\mathbf{a_2}(y)^T=\langle a_{21}(y)\quad a_{22}(y)\quad \ldots a_{2i}(y)\ldots\quad a_{2m}(y)\mid g_{21}(y)\quad g_{22}(y)\quad \ldots g_{2k}(y)\ldots\quad g_{2p-1}(y)\rangle,\\
&\mathbf{a_3}(y,z)^T=z\langle a_{31}(y)\quad a_{32}(y)\quad \ldots a_{3i}(y)\ldots\quad a_{3m}(y)\mid g_{31}(y)\quad g_{32}(y)\quad \ldots g_{3k}(y)\ldots\quad g_{3p-1}(y)\rangle,\\
&\mathbf{a_4}(y)^T=\langle a_{41}(y)\quad a_{42}(y)\quad \ldots a_{4i}(y)\ldots\quad a_{4m}(y)\mid g_{41}(y)\quad g_{42}(y)\quad \ldots g_{4p}(y)\ldots\quad g_{4k}(y)\rangle,\\
&\mathbf{a_5}(y)^T=\langle a_{51}(y)\quad a_{52}(y)\quad \ldots a_{5i}(y)\ldots\quad a_{5m}(y)\mid g_{51}(y)\quad g_{52}(y)\quad \ldots g_{5p}(y)\ldots\quad g_{5k}(y)\rangle,\\
&\mathbf{a_6}(y)^T=\langle a_{61}(y)\quad a_{62}(y)\quad \ldots a_{6i}(y)\ldots\quad a_{6m}(y)\mid g_{61}(y)\quad g_{62}(y)\quad \ldots g_{6p}(y)\ldots\quad g_{6k}(y)\rangle,\\
&\mathbf{b_1}(y,z)^T=\langle b_{11}(y)\quad zb_{12}(y)\quad b_{13}(y)\rangle,\qquad \mathbf{b_2}(y)=\langle 0\quad b_{22}(y)\quad 0\rangle,\\
&a_{1i}(y)=y^{i-1}-y^{n-2}\lambda_{1i}-y^{n-1}\lambda_{2i};\qquad g_{1k}(y)=H(y-y_k)-y^{n-2}\xi_{1k}-y^{n-1}\xi_{2k};\\
&a_{2i}(y)=y^{n-2}\varsigma_{33i}+y^{n-1}\varsigma_{43i}+y^{n-2}\lambda_{1i}+y^{n-1}\lambda_{2i};\qquad g_{2k}(y)=y^{n-2}\varsigma_{34k}+y^{n-1}\varsigma_{44k}+y^{n-2}\xi_{1k}+y^{n-1}\xi_{2k};\\
&a_{3i}(y)=y^{n-2}\varsigma_{13i}+y^{n-1}\varsigma_{23i}+y^{n-2}\lambda_{1i}+y^{n-1}\lambda_{2i};\qquad g_{3k}(y)=y^{n-2}\varsigma_{14k}+y^{n-1}\varsigma_{24k}+y^{n-2}\xi_{1k}+y^{n-1}\xi_{2k};\\
&a_{4i}(y)=\alpha_{n-1}(y)\lambda_{1i}+\alpha_n(y)\lambda_{2i}-\alpha_i(y);\qquad g_{4k}(y)=\alpha_{n-1}(y)\xi_{1k}+\alpha_n(y)\xi_{2k}-a_k(y);\\
&a_{5i}(y)=-\alpha_{n-1}(y)\varsigma_{13i}-\alpha_n(y)\varsigma_{23i}-\alpha_{n-1}(y)\lambda_{1i}-\alpha_n(y)\lambda_{2i};\\
&g_{5k}(y)=-\alpha_{n-1}(y)\varsigma_{14k}-\alpha_n(y)\varsigma_{24k}-\alpha_{n-1}(y)\xi_{1k}-\alpha_n(y)\xi_{2k};\\
&a_{6i}(y)=\beta_i(y)-\beta_{n-1}(y)\lambda_{1i}-\beta_n(y)\lambda_{2i};\qquad g_{6k}(y)=c_k(y)-\beta_{n-1}(y)\xi_{1k}-\beta_n(y)\xi_{2k};\\
&b_{11}(y)=y^{n-2}\varsigma_{31}+y^{n-1}\varsigma_{41},\qquad b_{12}(y)=y^{n-2}\varsigma_{12}+y^{n-1}\varsigma_{22},\\
&b_{13}(y)=y^{n-2}\varsigma_{32}+y^{n-1}\varsigma_{42},\qquad b_{22}(y)=-\left[\alpha_{n-1}(y)\varsigma_{12}+\alpha_n(y)\varsigma_{22}\right];
\end{aligned} \tag{8.21}$$

8.4.4. Interpolation of stress fields

Functions $F_i(z),\ i=1,2,\ldots,m$ and $J_k,\ k=1,2,...,p-1$ are assumed to follow a cubic distribution in coordinate z. One can express each stress function $F_i(z), J_k(z)$ in terms of the nodal values as

$$\begin{aligned} F_i(z) &= \overline{\mathbf{S}}^T_{1\times2}\left\{\overline{\mathbf{F}}_{\mathbf{N}i}\right\}_{2\times1} + \overline{\overline{\mathbf{S}}}^T_{1\times2}\left\{\overline{\overline{\mathbf{F}}}_{\mathbf{N}i}\right\}_{2\times1} \\ J_i(z) &= \overline{\mathbf{S}}^T_{1\times2}\left\{\overline{\mathbf{J}}_{\mathbf{N}i}\right\}_{2\times1} + \overline{\overline{\mathbf{S}}}^T_{1\times2}\left\{\overline{\overline{\mathbf{J}}}_{\mathbf{N}i}\right\}_{2\times1} \end{aligned} \tag{8.22}$$

in which $\overline{\mathbf{S}}^T_{1\times2}, \overline{\overline{\mathbf{S}}}^T_{1\times2}$ are the vectors of interpolation functions and defined as

$$\overline{\mathbf{S}}^T_{1\times2} = \frac{1}{L^3}\left\langle 2z^3 - 3z^2L + L^3 \ \middle|\ z^3L - 2z^2L^2 + zL^3 \right\rangle; \quad \overline{\overline{\mathbf{S}}}^T_{1\times2} = \frac{1}{L^3}\left\langle -2z^3 + 3z^2L \ \middle|\ z^3L - z^2L^2 \right\rangle \tag{8.23}$$

and

$$\begin{aligned} \left\langle \overline{\mathbf{F}}_{\mathbf{N}i} \right\rangle^T_{1\times2} &= \left\langle F_i(0) \ \middle|\ F_i'(0) \right\rangle; \qquad \left\langle \overline{\overline{\mathbf{F}}}_{\mathbf{N}i} \right\rangle^T_{1\times2} = \left\langle F_i(L) \ \middle|\ F_i'(L) \right\rangle; \\ \left\langle \overline{\mathbf{J}}_{\mathbf{N}i} \right\rangle^T_{1\times2} &= \left\langle J_i(0) \ \middle|\ J_i'(0) \right\rangle; \qquad \left\langle \overline{\overline{\mathbf{J}}}_{\mathbf{N}i} \right\rangle^T_{1\times2} = \left\langle J_i(L) \ \middle|\ J_i'(L) \right\rangle; \end{aligned} \tag{8.24}$$

are the vectors of nodal forces. It is convenient to express the nodal force functions $\{\mathbf{F}(z)\}$ as

$$\{\mathbf{F}(z)\}_{(m+p-1)\times1} = \left[\mathbf{\Lambda}_{\mathbf{F}}(\mathbf{z})\right]\left\{\overline{\mathbf{P}}\right\} \tag{8.25}$$

in which the interpolation function matrix $\left[\mathbf{\Lambda}_{\mathbf{F}}(\mathbf{z})\right]$ is defined as

$$\mathbf{\Lambda}_{\mathbf{F}}(\mathbf{z})_{(m+p-1)\times(4m+4p-4+3)} = \left[\begin{array}{c|c|c|c|c} -\overline{\mathbf{\Lambda}}_{\mathbf{FF}(m\times2m)} & \mathbf{0}^T_{m\times(2p-2)} & \mathbf{0}^T_{m\times3} & \overline{\overline{\mathbf{\Lambda}}}_{\mathbf{FF}(m\times2m)} & \mathbf{0}^T_{m\times(2p-2)} \\ \hline \mathbf{0}^T_{(p-1)\times2m} & -\overline{\mathbf{\Lambda}}_{\mathbf{FJ}(p-1)\times(2p-2)} & \mathbf{0}^T_{(p-1)\times3} & \mathbf{0}^T_{(p-1)\times2m} & \overline{\overline{\mathbf{\Lambda}}}_{\mathbf{FJ}(p-1)\times(2p-2)} \end{array}\right] \tag{8.26}$$

where

$$\overline{\mathbf{\Lambda}}_{\mathbf{FF}(m\times2m)} = \underbrace{\begin{bmatrix} \overline{\mathbf{S}}^T_{1\times2} & \mathbf{0}^T_{1\times2} & \ldots & \mathbf{0}^T_{1\times2} \\ \mathbf{0}^T_{1\times2} & \overline{\mathbf{S}}^T_{1\times2} & \ldots & \mathbf{0}^T_{1\times2} \\ \vdots & \vdots & \ddots & \vdots \\ \mathbf{0}^T_{1\times2} & \mathbf{0}^T_{1\times2} & \ldots & \overline{\mathbf{S}}^T_{1\times2} \end{bmatrix}}_{m\times2m}; \qquad \overline{\overline{\mathbf{\Lambda}}}_{\mathbf{FJ}(p-1)\times(2p-2)} = \underbrace{\begin{bmatrix} \overline{\overline{\mathbf{S}}}^T_{1\times2} & \mathbf{0}^T_{1\times2} & \ldots & \mathbf{0}^T_{1\times2} \\ \mathbf{0}^T_{1\times2} & \overline{\overline{\mathbf{S}}}^T_{1\times2} & \ldots & \mathbf{0}^T_{1\times2} \\ \vdots & \vdots & \ddots & \vdots \\ \mathbf{0}^T_{1\times2} & \mathbf{0}^T_{1\times2} & \ldots & \overline{\overline{\mathbf{S}}}^T_{1\times2} \end{bmatrix}}_{(p-1)\times(2p-2)};$$

and the nodal force vector $\left\{\overline{\mathbf{P}}\right\}$ is given by

$$\left\langle\overline{\mathbf{P}}\right\rangle^{T}_{1\times(4m+4p-4+3)}=\left\langle-\left\langle\tilde{\mathbf{F}}(0)\right\rangle^{T}_{1\times(2m+2p-2)}\;\vdots\;-\left\langle\mathbf{R}(0)\right\rangle^{T}_{1\times3}\;\vdots\;\left\langle\tilde{\mathbf{F}}(\mathbf{L})\right\rangle^{T}_{1\times(2m+2p-2)}\right\rangle \tag{8.27}$$

and

$$\begin{aligned}\tilde{\mathbf{F}}(\mathbf{0})^{T}&=\left\langle F_1(0)\quad F_1'(0)\;\middle|\;\dots\quad\dots\;\middle|\;F_m(0)\quad F_m{}'(0)\;\middle|\;J_1(0)\quad J_1'(0)\;\middle|\;\dots\quad\dots\;\middle|\;J_{p-1}(0)\quad J_{p-1}{}'(0)\right\rangle;\\ \tilde{\mathbf{F}}(L)^{T}&=\left\langle F_1(L)\quad F_1'(L)\;\middle|\;\dots\quad\dots\;\middle|\;F_m(L)\quad F_m{}'(L)\;\middle|\;J_1(L)\quad J_1'(L)\;\middle|\;\dots\quad\dots\;\middle|\;J_{p-1}(L)\quad J_{p-1}{}'(L)\right\rangle\end{aligned} \tag{8.28}$$

It is possible to express vector $\mathbf{R}(0)_{3\times1}$ in terms of the nodal force vector $\left\{\overline{\mathbf{P}}\right\}$ as

$$\mathbf{R}(0)_{3\times1}=\Lambda_{\mathbf{R}3\times(4m+4p-4+3)}\left\{\overline{\mathbf{P}}\right\}_{(4m+4p-4+3)\times1} \tag{8.29}$$

where $\Lambda_{\mathbf{R}3\times(4m+4p-4+3)}=\left[\mathbf{0}_{3\times(2m+2p-2)}\quad \mathbf{-I}_{3\times3}\quad \mathbf{0}_{3\times(2m+2p-2)}\right]$ and $\mathbf{I}$ is the identity matrix. From Eqs. (8.25) and (8.29), by substituting into Eqs. (8.18), one obtains

$$\begin{aligned}\sigma_z(y,z)&=\overline{\mathbf{P}}^{T}\mathbf{X}_{\sigma z}+\sigma_z^{*}(y,z);\\ \tau(y,z)&=\overline{\mathbf{P}}^{T}\mathbf{X}_{\tau}+\tau^{*}(y,z);\\ \sigma_y(y,z)&=\overline{\mathbf{P}}^{T}\mathbf{X}_{\sigma y}+\sigma_y^{*}(y,z);\end{aligned} \tag{8.30}$$

in which the vectors $\{\mathbf{X}_{\sigma z}\}=\mathbf{\Lambda_F}(\mathbf{z})^{T}\mathbf{a_1}(y)+\mathbf{\Lambda_F}(0)^{T}\mathbf{a}_2(y)+\mathbf{\Lambda_F}'(0)^{T}\mathbf{a_3}(y,z)+\Lambda_{\mathbf{R}}\mathbf{b_1}(y,z)$,

$\left\{\mathbf{X}_{\sigma y}\right\}=\mathbf{\Lambda_F}''(\mathbf{z})^{T}\mathbf{a_6}(y)$ and $\{\mathbf{X}_{\tau}\}=\mathbf{\Lambda_F}'(\mathbf{z})^{T}\mathbf{a_4}(y)+\mathbf{\Lambda_F}'(0)^{T}\mathbf{a_5}(y)+\Lambda_{\mathbf{R}}\mathbf{b_2}(y)^{T}$ have been defined.

8.4.5. Variational Principle

The total complementary energy π^{*} is the sum of the total complementary strain energy U^{*} and the load potential V^{*} gained by the external forces and tractions, i.e.,

$$\pi^{*}=U^{*}+V^{*} \tag{8.31}$$

8.4.5.1. Complementary strain energy

The total complementary strain energy $U^{*}\left(\sigma_z,\sigma_y,\tau\right)$ is contributed by longitudinal normal stresses, transversal normal stresses, and transverse shear stresses which can be expressed as

$$U^* = \sum_{j=1}^{p} \frac{1}{2} \int_L \int_{A_j} \left\langle \varepsilon_z \quad \varepsilon_y \quad \gamma \right\rangle_j \begin{Bmatrix} \sigma_z \\ \sigma_y \\ \tau \end{Bmatrix} dA_j dz \tag{8.32}$$

where $j = 1, 2..., p$ denotes the j^{th} layer of the material. For each material, the strains are related to stresses via the generalized 2D Hooke's law, i.e.,

$$\begin{Bmatrix} \varepsilon_z \\ \varepsilon_y \\ \gamma \end{Bmatrix}_j = \begin{bmatrix} 1/E_z & -\mu_y/E_y & 0 \\ -\mu_z/E_z & 1/E_y & 0 \\ 0 & 0 & 1/G \end{bmatrix}_j \begin{Bmatrix} \sigma_z \\ \sigma_y \\ \tau \end{Bmatrix} \tag{8.33}$$

It is noted that for orthotropic materials, the condition $\mu_{zy}/E_z = \mu_{yz}/E_y$ must be satisfied, i.e., μ_{zy} and μ_{yz} are dependent parameters (e.g., Wu and Jensen 2011). From Eqs. (8.33), by substituting into Eq.(8.32), one obtains

$$U^* = \sum_{j=1}^{p} \frac{1}{2} \int_L \int_{A_j} \left\langle \sigma_z \quad \sigma_y \quad \tau \right\rangle [\mathbf{D}]_j \begin{Bmatrix} \sigma_z \\ \sigma_y \\ \tau \end{Bmatrix} dA_j dz \tag{8.34}$$

in which

$$[\mathbf{D}]_j = \begin{bmatrix} 1/E_z & -\mu_{zy}/E_y & 0 \\ -\mu_{yz}/E_z & 1/E_y & 0 \\ 0 & 0 & 1/G \end{bmatrix}_j$$

From Eqs. (8.30), by substituting into Eq. (8.34), the total complementary strain energy is expressed as

$$\begin{aligned} U^* = {} & \sum_{j=1}^{p} \frac{1}{2} \int_L \int_{A_j} \overline{\mathbf{P}}^T \left\langle \mathbf{X}_{\sigma z} \quad \mathbf{X}_{\sigma y} \quad \mathbf{X}_{\tau} \right\rangle [\mathbf{D}]_j \begin{Bmatrix} \mathbf{X}_{\sigma z}^T \\ \mathbf{X}_{\sigma y}^T \\ \mathbf{X}_{\tau}^T \end{Bmatrix} \overline{\mathbf{P}} dA_j dz + \sum_{j=1}^{p} \int_L \int_{A_j} \overline{\mathbf{P}}^T \left\langle \mathbf{X}_{\sigma z} \quad \mathbf{X}_{\sigma y} \quad \mathbf{X}_{\tau} \right\rangle \frac{1}{2} \left[\mathbf{D} + \mathbf{D}^T \right]_j \begin{Bmatrix} \sigma_z^*(y,z) \\ \sigma_y^*(y,z) \\ \tau^*(y,z) \end{Bmatrix} dA_j dz + \\ & + \sum_{j=1}^{p} \frac{1}{2} \int_L \int_{A_j} \left\langle \sigma_z^*(y,z) \quad \sigma_y^*(y,z) \quad \tau^*(y,z) \right\rangle [\mathbf{D}]_j \begin{Bmatrix} \sigma_z^*(y,z) \\ \sigma_y^*(y,z) \\ \tau^*(y,z) \end{Bmatrix} dA_j dz \end{aligned}$$

(8.35)

8.4.5.2. Load potential energy

The load potential gain is the sum of products of stress resultants with corresponding governing displacements, i.e.,

$$V^* = \left\langle \tilde{\mathbf{F}}(\mathbf{0})^T_{1\times(2m+2p-2)} \;\middle|\; \mathbf{R}(0)^T_{1\times 3} \;\middle|\; -\tilde{\mathbf{F}}(L)^T_{1\times(2m+2p-2)} \;\middle|\; -\mathbf{R}(L)^T_{1\times 3} \right\rangle \langle \mathbf{\Delta} \rangle^{\mathbf{T}}_{1\times(4m+4p-4+6)} \tag{8.36}$$

in which

$$\langle \mathbf{\Delta} \rangle^{\mathbf{T}} = \left\langle \langle \tilde{\mathbf{d}}(0) \rangle^{\mathbf{T}}_{1\times(2m+2p-2)} \;\middle|\; W(0) \;\middle|\; V(0) \;\middle|\; \theta(0) \;\middle|\; \langle \tilde{\mathbf{d}}(L) \rangle^{\mathbf{T}}_{1\times(2m+2p-2)} \;\middle|\; W(L) \;\middle|\; V(L) \;\middle|\; \theta(L) \right\rangle \tag{8.37}$$

with

$$\begin{aligned} \tilde{\mathbf{d}}(0)^{\mathbf{T}} &= \langle d_1(0) \quad d_1^*(0) \mid \dots \quad \dots \mid d_m(0) \quad d_m^*(0) \mid w_1(0) \quad w_1^*(0) \mid \dots \quad \dots \mid w_{p-1}(0) \quad w_{p-1}^*(0) \rangle; \\ \tilde{\mathbf{d}}(L)^{\mathbf{T}} &= \langle d_1(L) \quad d_1^*(L) \mid \dots \quad \dots \mid d_m(L) \quad d_m^*(L) \mid w_1(L) \quad w_1^*(L) \mid \dots \quad \dots \mid w_{p-1}(L) \quad w_{p-1}^*(L) \rangle; \end{aligned} \tag{8.38}$$

where $d_i(z_0)$ ($z_0 = 0$ or L and $i = 1, 2, \dots, m$) is the displacement conjugate to $F_i(z_0)$ while $d_i^*(z_0)$ is the displacement conjugate to $F_i'(z_0)$. In Eq. (8.36), the vector of internal forces at end $z = L$ is defined as $\mathbf{R}(L)^T = \langle N(L) \quad Q(L) \quad M(L) \rangle$ (Figure 8.5). By adopting the internal force definitions $\mathbf{R}(L)^T = \langle N(L) \quad Q(L) \quad M(L) \rangle = \int_A \langle \sigma_z(y,L), \tau(y,L), y\sigma_z(y,L) \rangle dA$ and substituting from the statically admissible stress fields in Eq. (8.18) one obtains

$$\begin{aligned} \mathbf{R}(L)^{\mathbf{T}} = &\int_A \langle \mathbf{a}_2(y) \mid 0 \mid y\mathbf{a}_2(y) \rangle dA\, \mathbf{F}(0) + \int_A \langle \mathbf{a}_3(y,L) \mid \mathbf{a}_5(y) \mid y\mathbf{a}_3(y,L) \rangle dA\, \mathbf{F}'(0) + \\ &+ \int_A \langle \mathbf{a}_1(y) \mid 0 \mid y\mathbf{a}_1(y) \rangle dA\, \mathbf{F}(L) + \int_A \langle 0 \mid \mathbf{a}_4(y) \mid 0 \rangle dA\, \mathbf{F}'(L) + \\ &+ \int_A \langle \mathbf{b}_1(y,L) \mid \mathbf{b}_2(y) \mid y\mathbf{b}_1(y,L) \rangle dA\, \mathbf{R}(0) + \int_A \langle \sigma_z^*(y,L) \mid \tau^*(y,L) \mid y\sigma_z^*(y,L) \rangle dA \end{aligned} \tag{8.39}$$

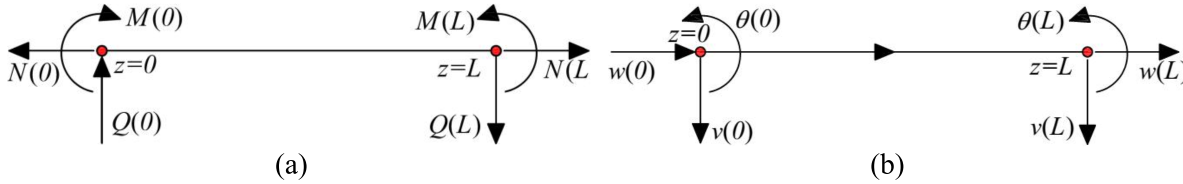

Figure 8.5. Beam sign convention (a) Applied loads and end stress resultants forces and, (b) Energy conjugate end displacements

8.4.5.3. Variation of total complementary strain energy

From Eq.(8.35), the variation of the total complementary strain energy is given by

$$\delta U^* = \delta \overline{\mathbf{P}}^{\mathbf{T}} \left(\mathbf{H}\overline{\mathbf{P}} + \mathbf{d}_0 \right) \tag{8.40}$$

in which $[\mathbf{H}]_{(4m+4p-4+3)\times(4m+4p-4+3)}$ is the flexibility matrix defined as

$$[\mathbf{H}] = \sum_{j=1}^{p} \int_L \int_{A_j} \langle \mathbf{X}_{\sigma z} \quad \mathbf{X}_{\sigma y} \quad \mathbf{X}_{\tau} \rangle [\mathbf{D}]_j \begin{Bmatrix} \mathbf{X}_{\sigma z}^T \\ \mathbf{X}_{\sigma y}^T \\ \mathbf{X}_{\tau}^T \end{Bmatrix} dA_j dz \tag{8.41}$$

and $\mathbf{d}_0$ the energy conjugate generalized displacement vector given by

$$\mathbf{d}_0 = \sum_{j=1}^{p} \int_L \int_{A_j} \langle \mathbf{X}_{\sigma z} \quad \mathbf{X}_{\sigma y} \quad \mathbf{X}_{\tau} \rangle \frac{1}{2} \left[\mathbf{D} + \mathbf{D}^T \right]_j \begin{Bmatrix} \sigma_z^*(y,z) \\ \sigma_y^*(y,z) \\ \tau^*(y,z) \end{Bmatrix} dA_j dz \tag{8.42}$$

8.4.5.4. Variation of load potential energy

From Eq. (8.25), by substituting into Eq. (8.39), one obtains

$$\mathbf{R}(L) = \begin{Bmatrix} N(L) \\ Q(L) \\ M(L) \end{Bmatrix} = \begin{Bmatrix} \overline{\mathbf{P}}^T \mathbf{\Gamma}_N(L) \\ \overline{\mathbf{P}}^T \mathbf{\Gamma}_Q(L) \\ \overline{\mathbf{P}}^T \mathbf{\Gamma}_M(L) \end{Bmatrix} + \int_A \begin{Bmatrix} \sigma_z^*(y,L) \\ \tau^*(y,L) \\ y\sigma_z^*(y,L) \end{Bmatrix} dA \tag{8.43}$$

in which the following vectors are defined

$$\mathbf{\Gamma}_N(L)_{(4m+4p-4+3)\times 1} = \int_A \left[\mathbf{\Lambda_F}(L)^T \mathbf{a_1}(y) + \mathbf{\Lambda_F}(0)^T \mathbf{a_2}(y) + \mathbf{\Lambda_F}'(0)^T \mathbf{a_3}(y,L) + \Lambda_{\mathbf{R}}(0)^T \mathbf{b_1}(y,L) \right] dA$$

$$\mathbf{\Gamma}_Q(L)_{(4m+4p-4+3)\times 1} = \int_A \left[\mathbf{\Lambda_F}'(L)^T \mathbf{a_4}(y) + \mathbf{\Lambda_F}'(0)^T \mathbf{a_5}(y) + \Lambda_{\mathbf{R}}(0)^T \mathbf{b_2}(y) \right] dA$$

$$\mathbf{\Gamma}_M(L)_{(4m+4p-4+3)\times 1} = \int_A y \left[\mathbf{\Lambda_F}(L)^T \mathbf{a_1}(y) + \mathbf{\Lambda_F}(0)^T \mathbf{a_2}(y) + \mathbf{\Lambda_F}'(0)^T \mathbf{a_3}(y,L) + \Lambda_{\mathbf{R}}(0)^T \mathbf{b_1}(y,L) \right] dA$$

Equation (8.43) can be used to eliminate $\mathbf{R}(L)$ from Eq.(8.36) yielding

$$V^{*}=-\overline{\mathbf{P}}^{\mathbf{T}}_{1\times(4m+4p-4+3)}\left[\mathbf{\Gamma}(L)\right]_{(4m+4p-4+3)\times(4m+4p-4+6)}\{\mathbf{\Delta}\}_{(4m+4p-4+6)\times 1}$$
$$-\left\langle \int_A \sigma_z^{*}(y,L)\,dA \;\middle|\; \int_A \tau^{*}(y,L)\,dA \;\middle|\; \int_A y\sigma_z^{*}(y,L)\,dA \right\rangle \begin{Bmatrix} W(L) \\ V(L) \\ \theta(L) \end{Bmatrix} \tag{8.44}$$

in which

$$\mathbf{\Gamma}(L)=\left[\mathbf{I}_{(4m+4p-4+3)\times(4m+4p-4+3)} \quad \mathbf{\Gamma}_N(L)_{(4m+4p-4+3)\times 1} \quad \mathbf{\Gamma}_Q(L)_{(4m+4p-4+3)\times 1} \quad \mathbf{\Gamma}_M(L)_{(4m+4p-4+3)\times 1}\right] \tag{8.45}$$

From Eq. (8.44), by taking variations with respect to the nodal force vector $\overline{\mathbf{P}}^{\mathbf{T}}$, one obtains

$$\delta V^{*}=-\delta\overline{\mathbf{P}}^{T}_{1\times(4m+4p-4+3)}\left[\mathbf{\Gamma}(L)\right]_{(4m+4p-4+3)\times(4m+4p-4+6)}\{\mathbf{\Delta}\}_{(4m+4p-4+6)\times 1} \tag{8.46}$$

In summary, from Eqs. (8.40) and (8.46), the stationarity condition is expressed by setting the variation of total complementary potential energy to zero, yielding

$$\delta\pi^{*}=\delta U^{*}+\delta V^{*}=\delta\overline{\mathbf{P}}^{\mathbf{T}}\left[\left(\mathbf{H}\overline{\mathbf{P}}+\mathbf{d}_0\right)-\mathbf{\Gamma}(L)\mathbf{\Delta}\right]=0 \tag{8.47}$$

8.4.5.5. Augmented form of the finite element formulation

Equation(8.47) is used to solve for the nodal force vector yielding

$$\overline{\mathbf{P}}=\mathbf{H}^{-1}\left[\mathbf{\Gamma}(L)\right]\mathbf{\Delta}-\mathbf{H}^{-1}\mathbf{d}_0 \tag{8.48}$$

It is noted that the size of nodal force vector $\overline{\mathbf{P}}_{(4m+4p-4+3)\times 1}$ is smaller than that of the nodal displacement vector $\mathbf{\Delta}_{(4m+4p-4+6)\times 1}$. It is thus required to augment nodal force vector $\overline{\mathbf{P}}$ by combining it with the vector of internal forces $\mathbf{R}(L)$. From Eq. (8.48), by substituting into Eqs. (8.43), one obtains

$$\mathbf{R}(L)=\begin{Bmatrix} \left\langle \mathbf{\Gamma}_N^T(L)\right\rangle_{1\times(4m+4p-4+3)} \\ \left\langle \mathbf{\Gamma}_Q^T(L)\right\rangle_{1\times(4m+4p-4+3)} \\ \left\langle \mathbf{\Gamma}_M^T(L)\right\rangle_{1\times(4m+4p-4+3)} \end{Bmatrix}\left[\mathbf{H}^{-1}\left\langle \mathbf{\Gamma}(L)\right\rangle\mathbf{\Delta}-\mathbf{H}^{-1}\mathbf{d}_0\right]+\int_A \begin{Bmatrix} \sigma_z^{*}(y,L) \\ \tau^{*}(y,L) \\ y\sigma_z^{*}(y,L) \end{Bmatrix} dA \tag{8.49}$$

From Eq. (8.49), by combining with Eq. (8.48) into a single matrix, the augmented nodal force vector is given as

$$\{\mathbf{P}\}_{(4m+4p-4+6)\times 1}=\left[\mathbf{K}\right]_{(4m+4p-4+6)\times(4m+4p-4+6)}\{\mathbf{\Delta}\}_{(4m+4p-4+6)\times 1}-\{\mathbf{P}_0\}_{(4m+4p-4+6)\times 1} \tag{8.50}$$

in which

$$\{\mathbf{P}\}=\left\{\begin{array}{c}\overline{\mathbf{P}}\\ \hdashline \mathbf{R}(L)\end{array}\right\},\quad [\mathbf{K}]=\mathbf{\Gamma}^{\mathrm{T}}(L)\mathbf{H}^{-1}\mathbf{\Gamma}(L),\quad \{\mathbf{P}_0\}=\mathbf{\Gamma}^{\mathrm{T}}(L)[\mathbf{H}]^{-1}\mathbf{d}_0-\int_A\left[\begin{array}{c}\{\mathbf{0}\}_{(4m+4p-4+3)\times 1}\\ \hdashline \sigma_z^*(y,L)\\ \hdashline \tau^*(y,L)\\ \hdashline y\sigma_z^*(y,L)\end{array}\right]dA$$

where $\{\mathbf{P}\}$ is the augmented nodal force vector, $[\mathbf{K}]$ is the stiffness matrix, and $\{\mathbf{P}_0\}$ is the energy equivalent load vector. The steps for forming $[\mathbf{K}]$ and $\{\mathbf{P}_0\}$ are provided in Appendix 8.3. In general, the size of matrix $[\mathbf{K}]$ and vector $\{\mathbf{P}_0\}$ will depend on the reduced number of stress terms $m=n-2$ and the number of layers p (as defined in Eq. 1). The entries of the matrix depend on the constitutive constants E_z, E_y, G, μ_{zy}, μ_{yz} for each layer. Thus, explicit expressions for the entries of $[\mathbf{K}]$ and $\{\mathbf{P}_0\}$ are too lengthy to provide. Instead, Appendix 8.4 provides, as an illustrative example, the expressions for $[\mathbf{H}]$, $[\mathbf{K}]$ and $\{\mathbf{P}_0\}$ for the special case of a homogeneous beam element with a rectangular cross-section made of an orthotropic material when the number of terms is taken as $n=3$

8.5. Verification and Applications

The present section aims at assessing the validity of the present finite element formulation in predicting deflections and stresses for both homogeneous and multilayer beams and showcasing its applicability to a variety of practical problems. While the formulation is primarily intended for multilayer beams, it can also be applied for homogeneous beams by eliminating all Heaviside Step Functions terms in the second summation of Eq. (8.1) and subsequent equations, by setting $p=1$. The first two examples provide an assessment of the validity of the present theory for the case of homogeneous beams. Examples 3-5 then illustrate the applicability of the theory to multilayer beams including wood beams and steel beams, both strengthened with GFRP plates, and sandwich beams with soft cores. In all cases, three-dimensional finite element analyses under ABAQUS are provided as benchmark solutions to assess the validity of the results.

Verification Example 1. Simply supported homogeneous beam under uniform traction

The example in Carrera and Giunta (2010) is revisited in the present study. A simply supported beam with a slender rectangular cross-section is considered. The beam is subjected to a transversely uniform traction $\sigma_y(-h/2,z)=\sigma=1.0MPa$ acting at the top surface acting at the top surface (Figure 8.6) while other applied tractions $\tau(-h/2,z),\tau(h/2,z),\sigma_y(h/2,z)$ vanish. Material is steel with a modulus of elasticity $E=200,000\ MPa$ and a Poison's ratio $\mu=0.3$. Beam depth is 1.0m. The depth to width ratio h/b of the cross-section is 100 while span to depth L/h is varied from 2 to 50. It is assumed that the beam is laterally restrained to avoid lateral buckling.

Convergence study: A convergence study is conducted for the case $L/h=5$ (Figure 8.7). For a homogeneous beam, the number of layers is set to $p=1$ and the second summation in Eq. (1) vanishes. For $n=3$, Eq. (1) takes the form $\sigma_z(y,z)=F_1(z)+yF_2(z)+y^2F_3(z)$ while for $n=4$, Eq. (1) becomes $\sigma_z(y,z)=F_1(z)+yF_2(z)+y^2F_3(z)+y^3F_4(z)$. Figure 8.7a and Figure 8.7b present the deflection predicted by the present theory when the number of stress terms is taken as $n=3$ and $n=4$, respectively. The number of elements based on the present finite element formulation was varied from 2 to 10. The predicted peak deflection is observed to be independent of the number of elements taken. This is due to the fact that the cubic shape functions assumed to interpolate functions $F_i(z)$ in Eqs. (8.23) are enough to capture the closed form solution of the compatibility equations. Similar observations are made for any number of stress terms n. The peak deflection for $n=3$ is 0.5331 mm while that based on $n=4$ is 0.5328 mm, a negligible 0.1% difference. Further increase in n was found not to change the predicted peak deflection. Of particular interest is to note that the predicted deflection decreases as n increases. Table 8.1 provides the normal stresses ($\sigma_{z,\max}$) at the mid-span extreme fiber and the maximum shear stresses ($\tau_{\max}$) at section mid-height of section at the support. Both stresses are observed to be independent of the number of elements for $n=3$. In contrast, for $n=4$, six elements are needed for the normal stresses to attain convergence, albeit only two elements for the shear stresses to converge. In summary, convergence of displacements is attained when four stress terms and convergence of stresses are attained when six elements are taken.

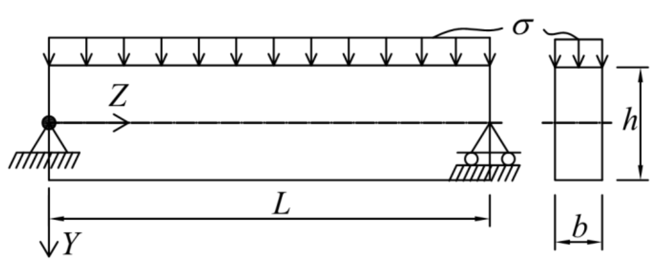

Figure 8.6. Simply supported beam under a uniform traction

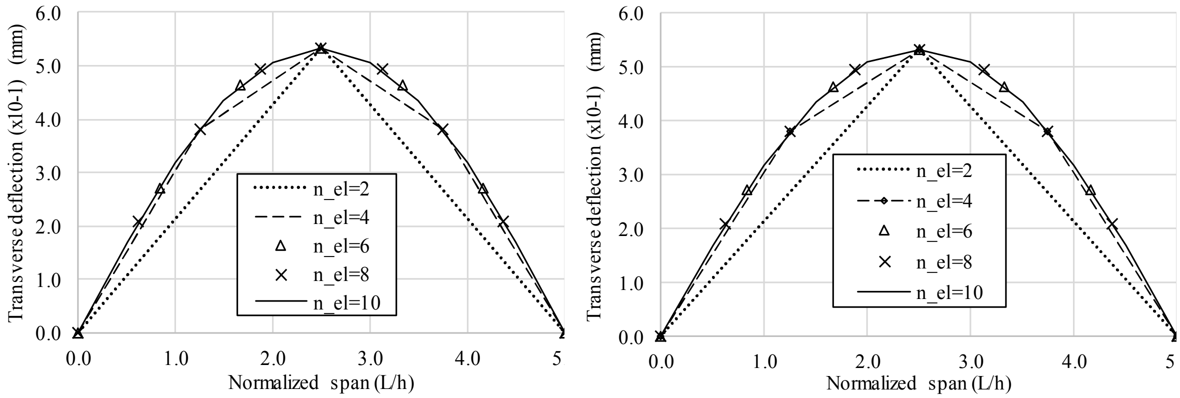

(a) n=3 (b) n=4

Figure 8.7. Mesh sensitivities for deflection obtained from present finite element formulation

Table 8.1. Mesh sensitivity study for peak stresses (MPa)

Number of elements	n=3		n=4	
	$\sigma_{z,\max}$	$\tau_{\max}$	$\sigma_{z,\max}$	$\tau_{\max}$
2	18.75	3.75	16.99	3.71
4	18.75	3.75	18.79	3.71
6	18.75	3.75	18.95	3.71
8	18.75	3.75	18.96	3.71
10	18.75	3.75	18.96	3.71

Comparative study: The peak deflection and stresses based on the present solution (Table 8.2) are compared to the those based on the Euler Bernouilli beam (EB), the Timoshenko beam (TB) solution based on a shear coefficient $\kappa = 0.85$ (Cowper 1966), the high-order solution by Carrera and Giunta (2010), and the elasticity solution in Timoshenko and Goodier (1970), referred to as TG1970. The relevant equations in TG1970 are $v = \left[1+12c^2\left(4/5+\mu/2\right)/5L_t^2\right]5qL_t^4/24EI_t$ $\sigma_z = q\left(L_t^2 - z_t^3\right)y_t/2I_t + q\left(5y_t^3 - 3c^2y_t\right)/15I_t$; $\sigma_y = -q\left(y_t^3/3 - c^2y_t + 2c^3/3\right)/2I_t$; $\tau_{zy} = -q\left(c^2 - y_t^2\right)z_t/2I_t$; in which $L_t = L/2$; $c = h/2$; $q = \sigma b$; and $I_t = bh^3/12$. The TG1970 solution is taken as a reference solution against which all solutions are compared. For the case $L/h = 2$, the solution based on EB grossly underestimates the deflection by 36.2%. The deflection based on TB with $\kappa = 0.85$ is 2.5% higher than that based on the reference solution. The peak deflection predicted based on the present solution with $n = 3$ is only 1.0% larger than that predicted by the reference solution. The present solution with $n = 4$ or 5 is in exact agreement with that based on TG1970 solution for all spans. The solution of Carrera and Giunta (2010) also provides identical predictions to the TG1970 solution for short beams when the number of terms is taken as $n = 6$. In this respect, the present solution attains the solution of TG1970 with fewer terms than that in Carrera and Giunta (2010). As expected, for higher L / h ratios, the effect of transverse shear stresses on the deflection becomes less significant and the difference between all solutions become smaller (Table 8.2).

Table 8.2. Mid-span deflections of the simply supported rectangle beam under the uniform traction

Solution	Order	$L / h = 2$ Deflection (mm)	$L / h = 2$ Difference (%)	$L / h = 5$ Deflection (mm)	$L / h = 5$ Difference (%)	$L / h = 50$ Deflection (m)	$L / h = 50$ Difference (%)
EB	NA	0.0125	36.2	0.4883	8.1	4.88	0.2
TB	NA	0.0201	2.5	0.5360	0.6	4.89	0.0
TG1970	NA	0.0196	0.0	0.5328	0.0	4.89	0.0
Present solution	n=3	0.0198	1.0	0.5331	0.1	4.89	0.0
	n=4	0.0196	0.0	0.5328	0.0	4.89	0.0
	n=5	0.0196	0.0	0.5328	0.0	4.89	0.0

% difference of row i= (deflection at row i-deflection of TG1970 solution)*100/(deflection of TG1970 solution).

Figure 8.8a and 8.8b present the longitudinal normal stress distributions along the section normalized height for span-to-height ratios of $L/h = 2$ and $L/h = 5$ while Figure 8.8c,d present the transverse normal and shear stresses for $L/h = 5$. For $L/h = 2$ (Figure 8.8a), the present solution with $n = 4$ depicts a slightly nonlinear distribution of the longitudinal normal stresses with depth, in a manner consistent with the TG1970 solution. In contrast, both the EB and the present solutions with $n = 3$ predict a linear distribution for the stresses. For the case $L/h = 5$ (Figure 8.8b-d), the longitudinal normal and transverse shear stresses are observed to be identical for the solutions based on EB, TG1970 and present solution (with n=3,4). Contrary to the EB solution, which does not capture the transverse normal stresses, the TG1970 and present solutions depict non-zero transverse normal stresses (Figure 8.8c). Unlike the case $L/h = 2$, excellent stress predictions can be obtained for $L/h = 5$ when the number of terms taken is $n = 3$.

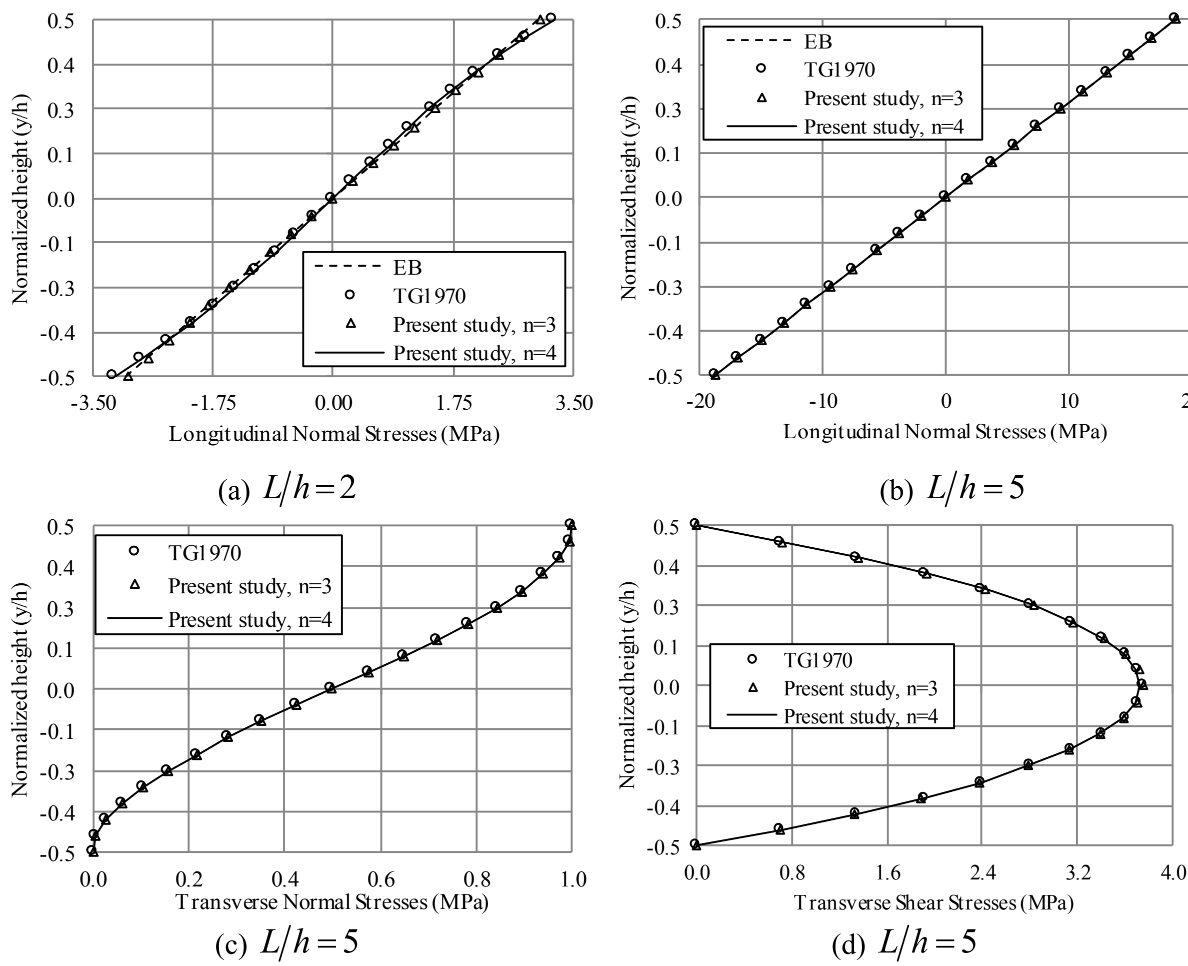

Figure 8.8. Distribution across the normalized cross-section height (y/h) of: (a) Longitudinal normal stresses at $z=L/2$ in case of $L/h=2$. (b) Longitudinal normal stresses at mid-span $z=L/2$, (c) Transverse normal stresses at $z=0$ and (d) Transverse shear stresses at $z=0$ in cases of $L/h=5$.

Verification Example 2. Clamped homogeneous beam with Tee cross-section

While Example 1 focused on a beam with a rectangular cross-section, the present example showcases the ability of the theory to model a mono-symmetrical cross-section. A steel beam is clamped at both ends and subjected to a vertical uniform traction $\sigma = 1.0MPa$ acting on the top surface (Figure 8.9a,b). The beam cross-section is a T-shaped with the dimensions shown in Fig. 8.9b. Three span-to-depth ratios $L/h = 2,5,10$ are considered where h denotes the cross-sectional depth. The modulus of elasticity of steel is $200GPa$ and its Poison's ratio is 0.3. It is required to compare the mid-span deflection predicted by the present solution, the Euler-Bernoulli (EB) beam, Timoshenko beam (TB) and 3D-FEA under Abaqus.

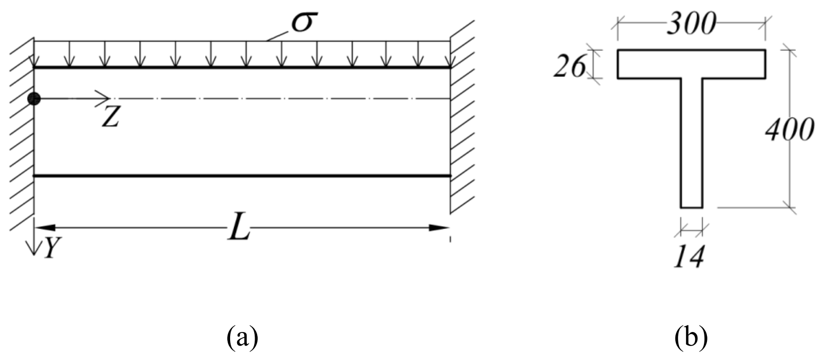

Figure 8.9. (a) fixed-fixed beam under uniform traction (b) cross-section for Example 2

In the present solution, all displacements at member ends are set to vanish to model the fixity conditions of the problem. A mesh sensitivity analysis indicated that 6 elements are enough for the deflections to convergence. The Timoshenko beam solution predicts a peak deflection of $v = \sigma bL^4/384EI_{xx} + \sigma bL^2/8\kappa GA$ in which shear correction factor $\kappa = 0.333$ (Cowper 1966). The Euler-Bernoulli solution is obtained from the Timoshenko solution by omitting the shear deformation term. A 3D FEA is conducted under ABAQUS using the eight-nodded continuum element C3D8R with 3 degrees of freedom per node with reduced integration to avoid shear locking. A mesh sensitivity was conducted and the results reported are based on the converged results. Deflection predictions for $n = 4$ (Table 8.3) are observed to match those based on $n = 5$. Thus, the present solution with $n = 4$ is taken as a reference solution. Compared to the reference solution, for span-to-depth ratios of L/h=2, 5 and 10, the EB solution underestimates the peak deflection by 87.1%, 54.8% and 23.2%, respectively, while the TB solution overestimates it by 18.6%, 5.8% and 2.6%, respectively. The solution based on 3D FEA is only 2.4%, 1.0% and 0.1% lower than the reference solution. Unlike the EB and 3D FEA solutions which under-predict the displacement, the present solution with $n = 3$ is observed to over-predict the deflection by 5.7%, 2.2% and 0% respectively.

Table 8.3. Maximum deflection for clamped homogeneous beams

Solution	Order	$L/h=2$		$L/h=5$		$L/h=10$	
		Deflection (mm)	Difference (%)	Deflection (mm)	Difference (%)	Deflection (mm)	Difference (%)
EB	NA	0.0086	87.1	0.3346	54.8	5.354	23.2
TB	NA	0.0804	18.6	0.7834	5.8	7.149	2.6
3D FEA	NA	0.0652	2.4	0.7327	1.0	6.961	0.1

Present study	n=3	0.0706	5.7	0.7569	2.2	6.971	0.0
	n=4	0.0668	0.0	0.7403	0.0	6.968	0.0
	n=5	0.0668	0.0	0.7403	0.0	6.968	0.0

% difference of row i= (deflection at row i-deflection of present solution,n=5)*100/(deflection of present solution,n=5).

Example 3: Application to Wood beam strengthened with single GFRP plate

A simply supported wood beam with a solid rectangular cross-section ($b \times h = 200 \times 200$ mm) is considered (Figure 8.10). Span to depth ratios L/h of 5, 10 and 20 are investigated. The beam is strengthened with a 9.5 mm-thick GFRP plate through a 1-mm thick adhesive layer (Figure 8.10). Wood and GFRP are treated as orthotropic materials while the adhesive is isotropic (Table 8.4). Top surface traction $\sigma = 0.4 MPa$ is applied to the beam for span ratios L/h = 5 and 10 while the traction value $\sigma = 0.05 MPa$ is applied for L/h=20 (to keep deflections within acceptable limits). It is required to (1) predict the maximum deflection at mid-span, (2) predict the interfacial shear and normal stresses in the adhesive, and (3) obtain the longitudinal normal stress profile at mid-span cross-section based on the present solution and compare results with the 3D FEA solution under ABAQUS.

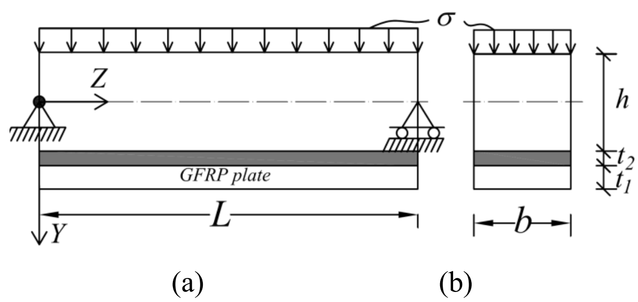

Figure 8.10. Wood beam strengthened with GFRP (a) elevation and (b) cross-section

Table 8.4. Material properties of a wood beam strengthened with a GFRP plate

Material	E_z (GPa)	E_y (GPa)	μ_{zy}	G_{yz} (GPa)
Wood	11.4	1.482	0.35	1.243
Adhesive	3.18	3.18	0.3	1.223
GFRP	19.3	8.873	0.295	2.834

Mesh sensitivity study for the present solution:

The case *L/h*= 10 is taken to perform a mesh study for the present solution and the 3D FEA solutions. The boundary conditions $W(0)=V(0)=V(L)=0$ are enforced in the present solution. For the present three-layer problem, the number of interfaces is $p-1=$ 2. The number of stress terms n introduced in Eq. (8.1) is varied from 3 to 8 and the corresponding longitudinal stresses expression from Eq. (8.1) take the form $\sigma_z(y,z)=\sum_{i=1}^{n} y^{i-1}F_i(z)+H(y-h/2)J_1(z)+H(y-h/2-t_2)J_2(z)$ where $n=3,4,5,6,7,8$. In a manner similar to the mesh study conducted for Example 1, the deflections and interfacial stresses convergence is attained with 6 elements when the number of stress terms is $n=3$, 8 elements when $n=4$, 12 elements when $n=5$, 16 elements when $n=6$, 20 elements when $n=7$, and 20 elements when $n=8$. In order to capture the high gradients for interfacial stresses near the bond ends, 30 elements per meter long were taken for all runs. Figure 8.12a,b respectively depict the interfacial shear and peeling stresses at the adhesive-wood interface based on the present solution. The interfacial stresses based on n=3 are found to be smaller than those based on n=5, 7 and 8. Also, the interfacial stresses are found to converge when n=7.

Mesh sensitivity for 3D FEA solution:

A 3D FEA solution based on ABAQUS was conducted for validation. The 3D mesh adopted is similar to that reported in (Pham and Mohareb 2014, 2015). The eight-node brick elements C3D8R is selected from ABAQUS library. The element has eight nodes with three translations per node. To avoid volumetric locking, the element uses reduced integration and thus has a single integration point at the element centroid. The input material properties in the longitudinal and transverse directions are identical to those in Table 8.5. The elasticity and shear moduli and Poisson's ratio characterizing the material behavior in the lateral direction are taken to conform to those of the transverse direction. Only half of the span is modeled to account for the symmetry of the problem. Three meshes were generated with parameters n_1 through n_5 as listed in Figure 8.11a,b where the number of elements across the cross-sectional width, GFRP plate thickness, adhesive thickness, wood beam depth are n_1 through n_4 respectively and the number of elements along the longitudinal direction is n_5.

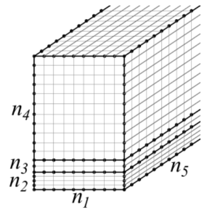

(a)

Mesh	n_1	n_2	n_3	n_4	n_5	#DOF
1	10	10	4	10	150	124,575
2	50	10	4	100	400	2,632,565
3	80	10	4	100	500	4,807,095

(b)

Figure 8.11. Section meshing parameters (a) Meshing parameters and (b) Values of parameters

The mesh study for the predicted interfacial shear and peeling stresses is conducted for Point 1 along the longitudinal z - direction as shown in Figure 8.12b,d. The peak interfacial shear stress based on the coarse 3D FEA mesh is 1.48 MPa (Figure 8.12b) while that based on the medium mesh is 0.98 MPa, and that for the fine mesh is 0.97 MPa, all occurring at a distance of 120mm from the bond end. The interfacial peeling stress distribution based on Mesh 1 exhibits an oscillatory behavior (Figure 8.12d) while those based on Meshes 2 and 3 practically agree with one another. Within the 3D FEA solution, the mesh size is observed to significantly influence the predicted interfacial shear stresses. Also, the above mesh study suggests that convergence is achieved for Mesh 2.

Comparisons of interfacial shear and peeling stresses

The peak shear and peeling stresses based on the predictions of the present solution with a number of stress terms $n = 3$ are 0.80 MPa and 0.09 MPa, respectively, while those based on the 3D FEA solution with Mesh 2 are 0.97 MPa and 0.109 MPa, corresponding to 17.5% and 18.1% differences, respectively. In contrast, the present solution with $n = 7$ predicts a peak shear stress of 0.96 MPa and a peak peeling stress of 0.114 MPa. The converged solutions for n=7 is 1.0% lower than the shear stresses and 4.4% higher than the peeling stresses as predicted by the 3D FEA.

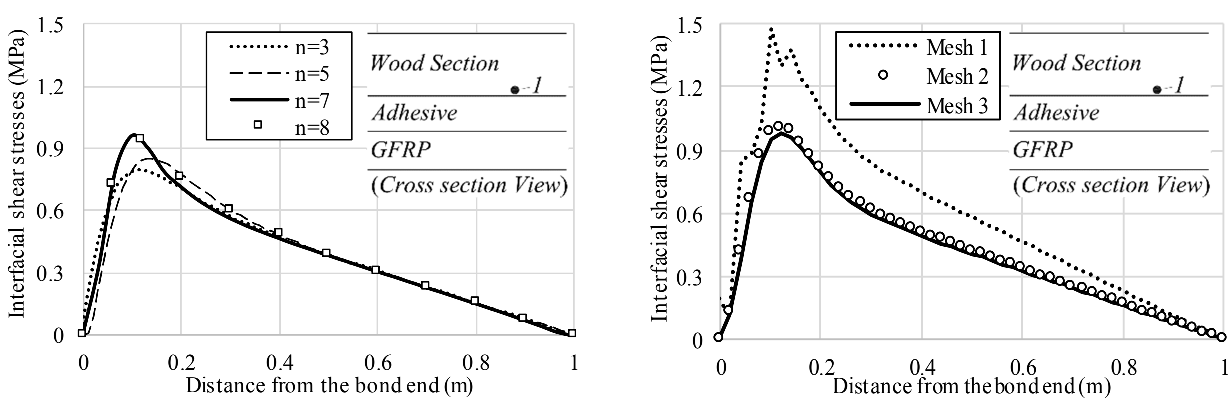

(a) Present solution

(b) 3D FEA

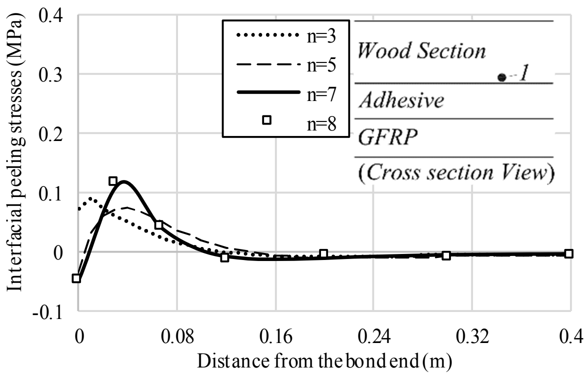

(c) Present solution

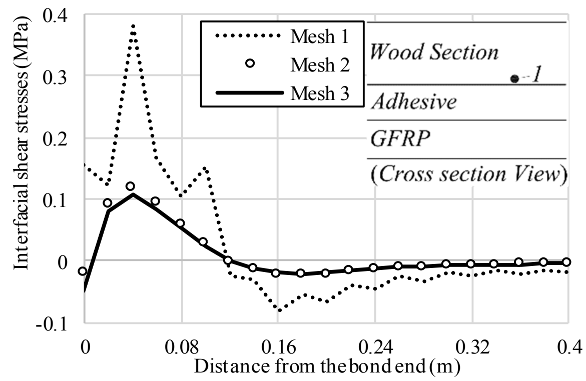

(d) 3D FEA

Figure 8.12. Mesh studies for the interfacial stresses extracted at Point 1 (a) Interfacial shear stresses - Present solution, (b) Interfacial shear stresses - 3D FEA, (c) Interfacial peeling stresses – Present solution, (d) Interfacial peeling stresses- 3D FEA

The previous section focused on the stresses at the upper interface as extracted from the wood section (i.e., point 1 in Figure 8.12). In principle, satisfying the infinitesimal equilibrium condition at the interfaces necessitates that the shear and peeling stresses at points 1 and 2 are equal (Figure 8.13a-d). A similar argument can be made for points 3 and 4. This indeed is the case under the present solution which is based on satisfying the equilibrium conditions in Eqs. 2(a-b), but is not the case for 3D FEA solution which satisfies equilibrium only in an average integral sense. This is illustrated by considering the peeling and shear stresses based from the present solution with n= 7 and the 3D FEA solution based on Mesh 2 (Figure 8.13a-d). It is observed that (1) the 3D FEA solution predicts an artificial jump in the stresses at the interfaces (i.e., between Points 1 and 2 and between Points 3 and 4) in contrast to the present solution which provides a continuous stress distribution at the interface (e.g., exactly identical stresses at points 1 and 2), (2) both solutions predict that the highest stresses take place at Point 1 among points 1-4, and (3) the interfacial shear stresses at Points 2 and 3 are found almost identical. The computational time for the 3D FEA solution based on Mesh 2 was 3.75 hours on a computer with two Intel (R) Xeon (R) CPU E5-24300 processors at 2.20GHz speed and 64 GB of RAM. This compares to 12.2 minutes for the present solution (implemented in a non-compiled MATLAB script file) with $n = 7$ and 60-elements.

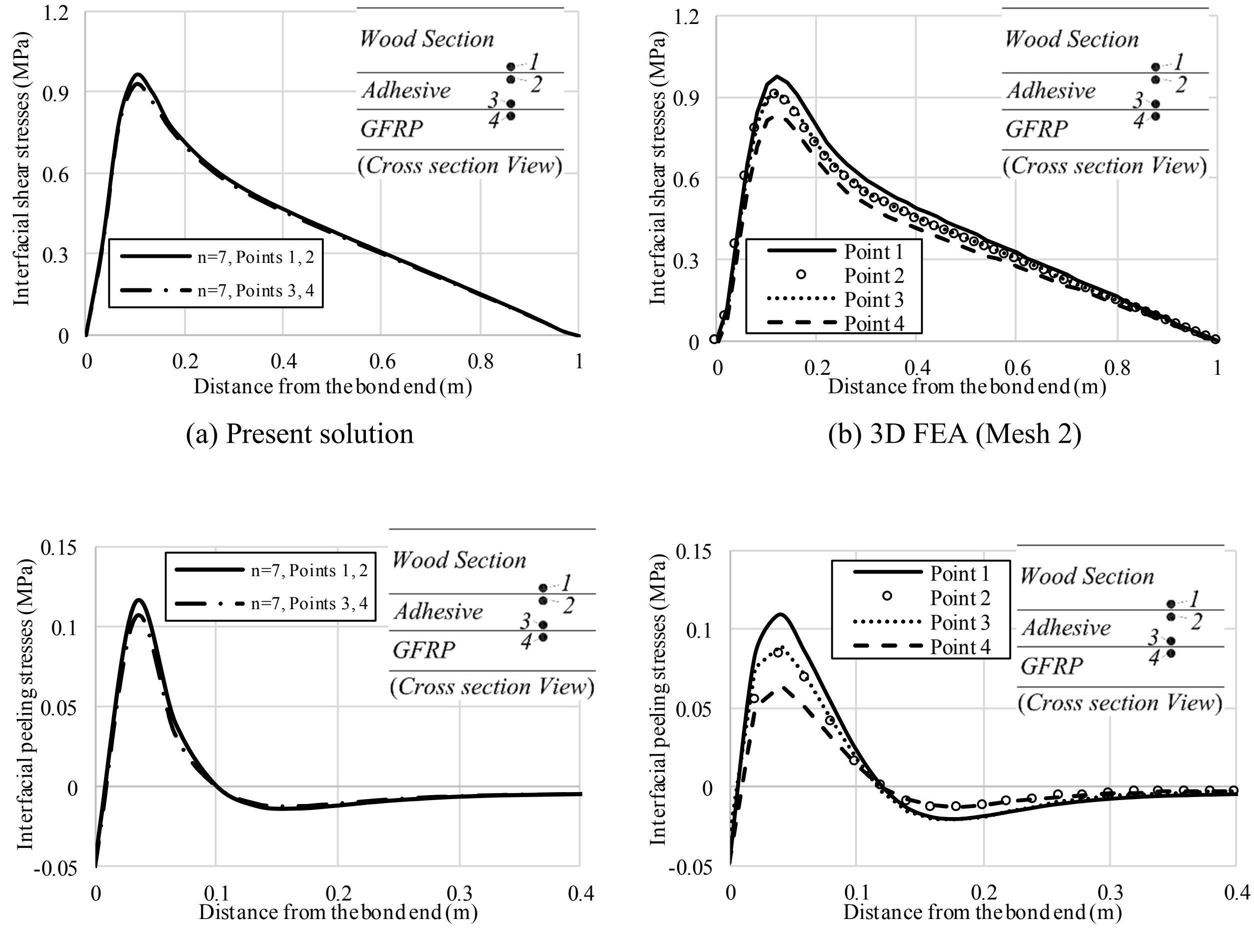

(a) Present solution

(b) 3D FEA (Mesh 2)

(c) Present solution

(d) 3D FEA (Mesh 2)

Figure 8.13. Interfacial shear and peeling stresses extracted at Points 1 through 4 from the present solution with n 7 and the 3D FEA solution based on Mesh 2 (a) Interfacial shear stresses - Present solution, (b) Interfacial shear stresses – 3D FEA, (c) Interfacial peeling stresses – Present solution, (d) Interfacial peeling stresses –3D FEA.

<u>Effect of adhesive elastic modulus</u>

The adhesive elasticity modulus in the above example (i.e., 3.18 GPa) is changed into 0.472 GPa to investigate the effect of the elastic modulus on the peak interfacial shear and peeling stresses. Based on the present solution, the peak shear and peeling stresses at Point 1 are evaluated as 0.82 and 0.091 MPa, respectively. When compared to the peak shear stress 0.96 MPa and peak peeling stress 0.114 MPa in the above example, the peak shear and peeling stresses in the case of using the adhesive elasticity modulus 0.472 GPa drops 14.6% and 20.2%, respectively. Thus, the interfacial shear and peeling stresses in the adhesive layer are observed to decrease for a more flexural adhesive material (i.e., an adhesive with a smaller elastic modulus).

Effect of span-to-depth ratio on Deflections

The effect of span-to-depth ratio on the predicted deflections is examined based on the present solution, a modified Euler-Bernoulli beam (EB) solution with a transformed section to account for the three materials, and the 3D FEA solution. The deflections obtained from the 3D FEA solution are taken as a basis for the comparison in Table 8.5. In contrast to conventional finite elements where a finer mesh is associated with a larger deflection, the present solution is found to converge to the FEA solution based on Mesh 2 from above, i.e., as the number of stress terms n increases, the deflection tends to reduce (Table 8.5). For the short span ($L/h=5$), the present solution with $n=3$ predicts a maximum deflection of $0.84mm$ while that with $n=5$ is $0.81mm$. This value coincides with that based on the 3D FEA solution. The deflection obtained from the EB solution is 0.54mm, which is 33.3% smaller than the 3D FEA solution. The large difference between the EB solution and the FEA is due to the neglect of transverse shear deformation effects. For medium and long spans (i.e., $L/h=10$ and 20), the present solution with $n=3,5$ provides the deflections identical to those of the 3D FEA. In contrast, the EB solution predicts a deflection of 8.6mm for L/h=10 and 17.2mm for L/h=20. These values are 13.1% and 4.4% smaller those based on the 3D FEA solution.

Table 8.5. Maximum deflection (mm) at mid-span

Solution		L/h=6		L/h=10		L/h=20*	
		Deflection	% Diff.**	Deflection	% Diff.	Deflection	% Diff.
EB		0.54	33.3	8.6	13.1	17.2	4.4
3D FEA		0.81	0.0	9.9	0.0	18.0	0.0
Present study	n=3	0.84	3.6	9.9	0.0	18.0	0.0
	n=5	0.81	0.0	9.9	0.0	18.0	0.0

* Applied traction is $\sigma = 0.05MPa$. ** % diff. = (deflection-deflection based on 3D FEA)/ deflection based on 3D FEA

Effect of span-to-depth ratio on interfacial stresses

The mesh study has shown that the peak interfacial shear and peeling stresses take place at Point 1. Therefore, the present parametric study will focus only on the stresses at point 1. The interfacial shear and peeling stresses are obtained from the present solution with n=7 and from the 3D FEA solutions for span-to-depth ratios of 5, 10, and 20. A comparison of the results is shown in Figure 8.14a-b for L/h=5 and Figure 8.14c-d for L/h=20. All shear stresses exhibit high concentrations near the bond ends and gradually drop to zero at mid-span. The peak shear stress predictions based on the present solution are found to be marginally smaller than those based on the 3D FEA solution. This is evidenced by the 2.4%, 1.0%, and 4.2% differences for from 3D FEA for span-to-depth ratios of 5, 10, and 20, respectively(Table 8.6). While the distribution of the shear stresses along the distance from the bond end predicted by the present solution closely match the 3D FEA solution, an even better agreement is obtained for the peeling stresses (Figure 8.14b,d). The maximum peeling stresses predicted from the present solution with $n = 7$ are 0.041MPa for L/h=5, 0.114MPa for L/h=10, and 0.019MPa for L/h=20, while those predicted by the 3D FEA solution at Point 1 are 0.042MPa for L/h=5, 0.109MPa for L/h=10, and 0.019MPa for L/h=20, corresponding to 2.4%, 4.4%, and 0.0% differences, respectively.

<u>Longitudinal stress distribution across section height:</u>

Figure 8.15 provides a comparison for the longitudinal normal stress distribution across the mid-span cross-section as predicted by the present and 3D FEA solutions for L/h=10. In contrast to interfacial shear and peeling stresses which converged for n=7, longitudinal stresses in the wood beam, adhesive, and GFRP are observed to converge for n=3. Excellent agreement is obtained for the stresses in the wood beam, adhesive layer and GFRP plate between the present solution and the 3D FEA solution.

In summary, deflections and longitudinal normal stresses of the strengthened beam were accurately predicted by the present solution with n=3 while the interfacial shear and peeling stresses are found to converge and to essentially coincide with the 3D FEA prediction when n=7 was taken in the present solution.

Table 8.6. Peak shear stresses (MPa) and locations z (mm) between two solutions

Solution	L/h=5			L/h=10			L/h=20		
	Magnitude (MPa)	z* (mm)	% Difference **	Magnitude (MPa)	z* (mm)	% Difference **	Magnitude (MPa)	z* (mm)	% Difference **
Present solution, n=7	0.41	125	2.4	0.96	120	1.0	0.23	140	4.2
3D FEA-Point 1	0.42	110	0.0	0.97	120	0.0	0.24	125	0.0

* z = Distance from bond end to the location of the maximum shear stress.
** % Difference = (Stress based on present solution - Stress based on 3D FEA-Point 1) x 100 / Stress based on 3D FEA-Point 1

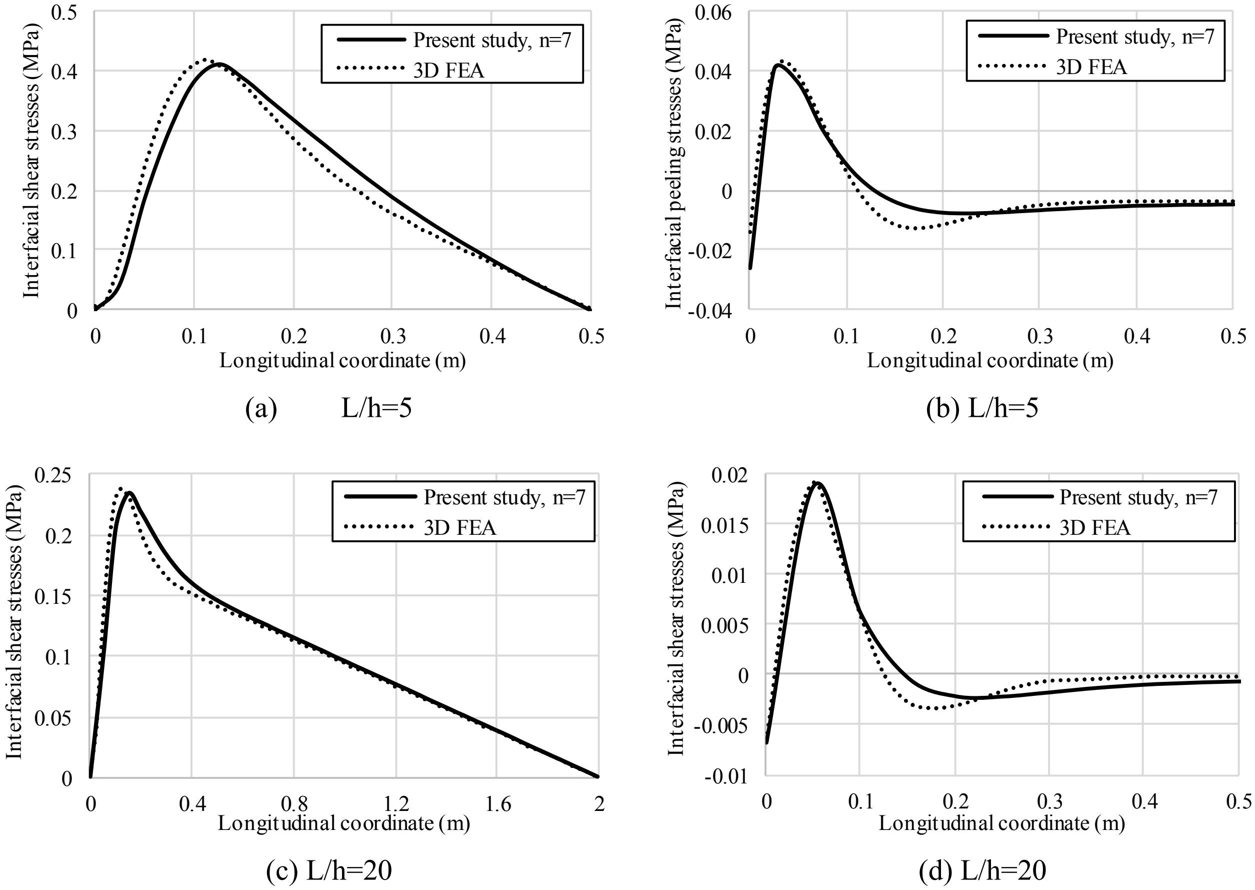

Figure 8.14. Interfacial shear and peeling stresses for a wood beam bonded with a GFRP plate

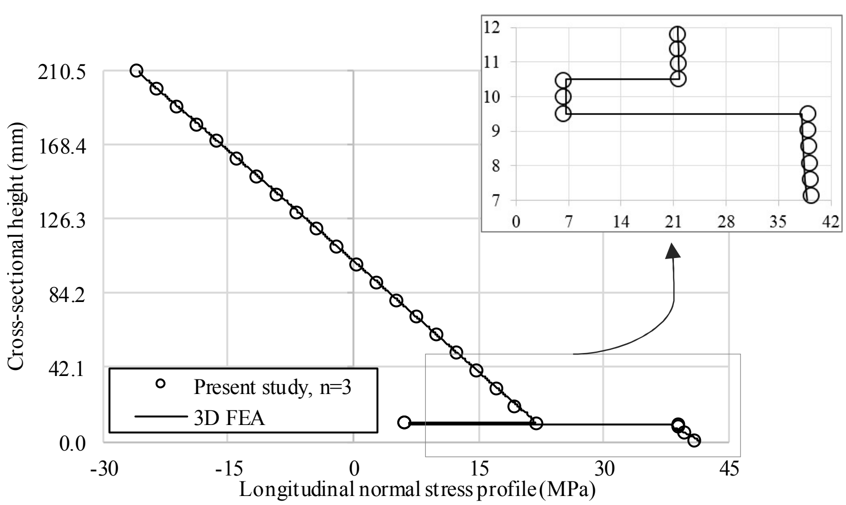

Figure 8.15. Longitudinal normal stresses between 3D FEA and present solution

Example 4: Application to simply supported sandwich beam under line load

The present example is intended in part to illustrate the handling of point loads within the present finite element solution. A standard Hexlite 220 panel (Hexcel Corporation 2000) is considered. The face skins are Alumium 5251 H24 with a thickness of 0.5mm (per each face) with a Young modulus of 70 GPa and a Poisson's ratio of 0.33. The core is 25.4mm thick with a Young modulus of 1.0 GPa, and a shear modulus of 220 MPa. Beam width is taken as 0.5m and the span is 2.0m. The beam is simply supported at both ends (Figure 8.16) and subjected to a mid-span line load $P = 313N$ along the section width. A comparison is sought between deflections and stresses as predicted by the present solution and 3D FEA.

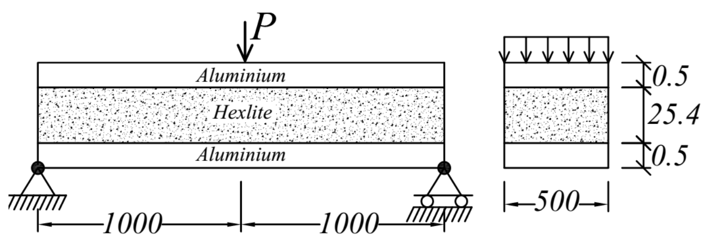

Figure 8.16. A sandwich beam with softcore under a mid-span point load

<u>Description of the solution:</u>

Because stresses are highly concentrated near mid-span where the load is applied, the present finite element formulation adopts more elements near mid-span (Figure 8.17a). A convergence study for the stresses showed that 30 elements are required for the 100mm-long mid-span segment and only 9 elements are enough for each of 900mm-long end segments. The mid-span point load $P = 312\,N$ is assumed to be applied to the left node of element No. 25 depicted in Figure 8.17a and applied at $y = -h/2$ and $z = 0$. The body forces corresponding to the point load are expressed as $p_y = p_y(y,z) = P\mathrm{Dirac}(z)\mathrm{Dirac}(y + h_1), p_z = 0$. Substitution into Eq. (8.5b) yields the expressions $\bar{\tau}(y,z) = 0$ and $\bar{\sigma}_y(y,z) = P\mathrm{Dirac}(z)$. Further substitution into Eq. (8.10a-b) yields $\rho_1(z)$ and $\rho_2(z)$ and subsequent substitution into Eq. (8.20a-c) yields $\sigma_z^*(y,z) = \left[y^{n-2}\rho_1(z) + y^{n-1}\rho_2(z)\right]Pz$, $\sigma_y^*(y,z) = P\mathrm{Dirac}(z)\left[1 + \beta_{n-1}(y)\rho_1(z) + \beta_n(y)\rho_2(z)\right]$, $\tau^*(y,z) = -\left[\alpha_{n-1}(y)\rho_1(z) + \alpha_n(y)\rho_2(z)\right]P$.

The ABAQUS 3D FEA solution is meshed in a manner similar to Example 3. In the 3D model, four elements are taken across the thicknesses of the two faces, 40 elements across the core depth, 120 elements across the section width, and 600 elements across the span. The point load is applied by using a line load across the beam width to avoid the localization of stresses. The pin supports are modelled by applying the multi-point constrain *MPC, type BEAM in the 3D FEA Abaqus model.

<u>Deflections and longitudinal stresses:</u>

Figure 8.17b presents the deflection curve predicted by the present solution with n=3,5 and the 3D FEA solution. Both solutions predict a nearly identical mid-span deflection of 8.0mm. Figure 8.18a,b show the distribution of the longitudinal normal stresses at the bottom fiber of the bottom face and the bottom fiber of the core along the z coordinate as predicted based on the present solution and the 3D FEA solution. The results are also observed to essentially coincide.

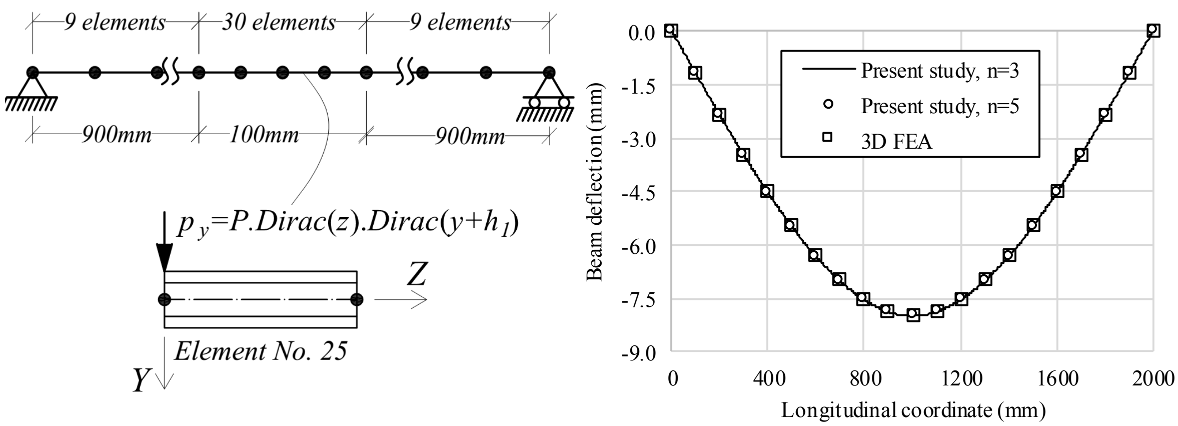

(a) (b)

Figure 8.17. (a) Mesh adopted in present solution and loading and (b) Deflections

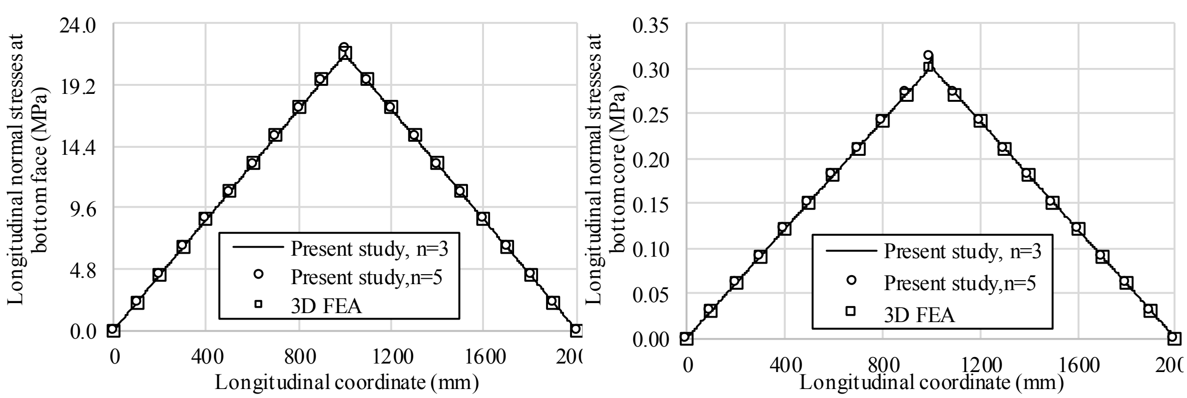

(a) (b)

Figure 8.18. Longitudinal normal stresses for sandwich beam with a soft core at (a) bottom fiber of the bottom face, and (b) bottom fibre of the core

Interfacial shear and peeling stresses: The interfacial shear and peeling stresses at the top interface as predicted by the present solution and the 3D FEA are presented in Figure 8.19a and b, respectively. The shear stress distributions of both solutions (Figure 8.19a) is anti-symmetric about the mid-span point and exhibit larger concentrations near the point of load application at mid-span. Near mid-span, the element length in the 3D FEA mesh is taken as 3.33mm. Thus, the peak shear stress at the integration point located at 1.67mm from the beam mid-span is 164.9 kPa. The present solution with n=3 predicts a peak shear stresses of 112 kPa while those based on n=5 and n=7 are 169.3 kPa and 174.0 kPa, respectively. All peak shear stresses based on the present solution occur at mid-span. Similar observations for peak stress locations was reported for an ANSYS model in Pappada et al. (2009). When compared to the 3D FEA peak shear stress value of 164.9 kPa, the present solution underestimates the peak shear stress by 32.1% when n=3, overestimates it by 2.3% for n=5 and by 5.2% for n=7. The interfacial normal stresses at the top interface obtained from the present solution and the 3D FEA are found to be symmetric about the mid-span (Figure 8.19b). While the peak stress value obtained from the 3D FEA solution is 85.7 kPa, those based on the present solution with n=3, 5 and 7 are 43 kPa, 75 kPa and 80 kPa, respectively, which are 49.8%, 12.5%, and 6.7% lower than the 3D FEA value. The fact that both interfacial shear and peeling stresses peak at mid-span is consistent with the shear failure mode of the core or face delamination mode, both reported in the experimental work of Pappada et al. (2009).

The shear stresses at the bottom interface obtained from the present solutions with n=3 and 5 (Figure 8.19c) are observed to be identical while that based on the 3D FEA is slightly smaller. On the other hand, the peeling stresses at the bottom interface are observed to agree well between both solutions (Figure 8.19d).

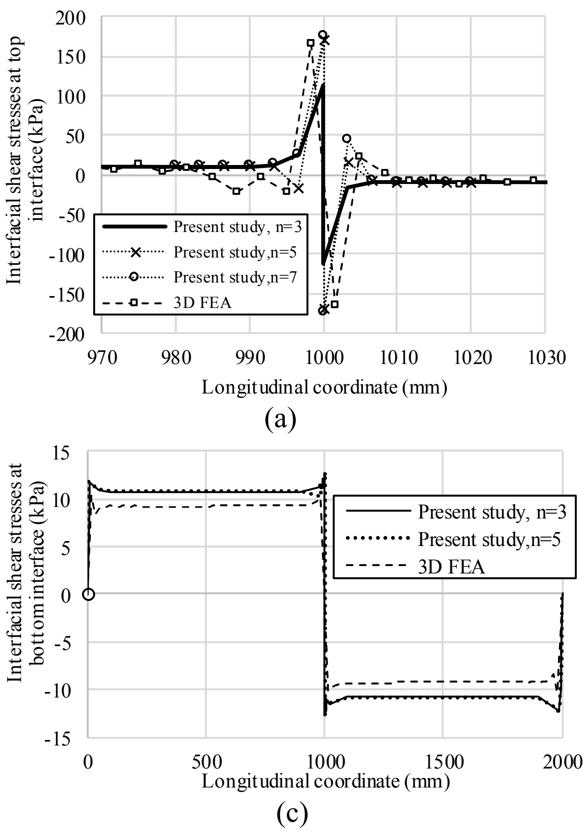

Figure 8.19. Interfacial shear and peeling stresses of sandwich beam: (a) shear stresses at top interface, (b) peeling stresses at top interface, (c) shear stresses at bottom interface, (d) peeling stresses at bottom interface.

Example 5 – Application to wide flange steel beam strengthened with GFRP plate

A W150x13 steel beam (depth = 148mm, flange width = 100mm, flange thickness = 4.9mm, and web thickness = 4.3mm) is strengthened with a 100mm wide x 19mm-thick GFRP plate through a 1-mm thick adhesive layer (Figure 8.20). Moduli of elasticity for steel, GFRP, and adhesive are respectively 200, 17.2, and 3.18 GPa, and Poisson's ratios are taken as 0.3 for all materials. Two spans L=1.5m and 3.0m are considered. The steel beam is supported by two cleat angles which can be idealized as pin supports. A downward traction $\sigma = 0.430 MPa$ is applied to at top face for the 1.5m span while $\sigma = 0.215 MPa$ is applied for the 3.0m span (in order to ensure that peak deflections remain within allowable limits). It is required to compare the mid-span deflection, the longitudinal normal stress profile at mid-span and the interfacial shear and peeling stresses as predicted by the 3D FEA and the present solution.

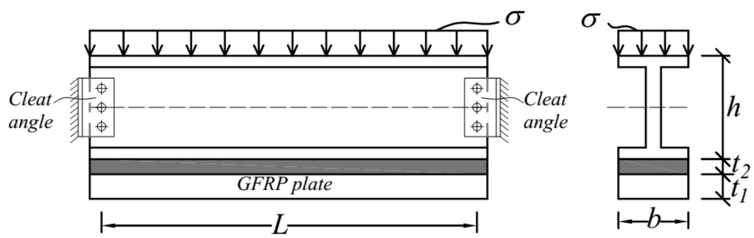

Figure 8.20. Beam elevation and cross-section

Results:

The 3D FEA solution predicts a peak deflection of 2.5mm for span L =1.5m and 16.5mm for span L =3.0m (Table 8.7). In comparison, the present solution over-predicts the deflection for L=1.5m by 4.0% for n=3, and exactly agrees with FEA for n=5 and n=7. For L=3.0m, the present solution over-predicts the deflection by 2.4% for n=3, by 1.2% for n=5, and exactly agrees with the FEA for n=7. Figure 8.21a-b show good agreement between the longitudinal stress profiles predicted by the present theory with n=3 and the 3D FEA. When higher order stress terms are taken (i.e., n=5, 7), the predicted stress profiles are found to nearly coincide with those based on the 3D FEA solution. Figure 8.22a-d present the interfacial stresses obtained from the present solutions with n=3,5,7 and the 3D FEA solutions for spans L=1.5m and L=3.0m, respectively. The stresses in the 3D FEA solution are the average values across the cross-sectional width. The stresses predicted by the present solution with n=3 are found smaller than those based on n=5 or 7 while the predictions of solutions with n= 5 and 7 are nearly identical to the 3D FEA predictions.

Table 8.7. Mid-span deflection (mm) of W-steel beams reinforced with GFRP plates.

Solution		L =1.5m		L=3.0m	
		Deflection	% Difference*	Deflection	% Difference*
Present solution	n=3	2.6	4.0	16.9	2.4
	n=5	2.5	0.0	16.6	1.2
	n=7	2.5	0.0	16.5	0.0
3D FEA		2.5	0.0	16.5	0.0

* % Difference = (stress based on present solution - stress based on 3D FEA) / Stress based on 3D FEA

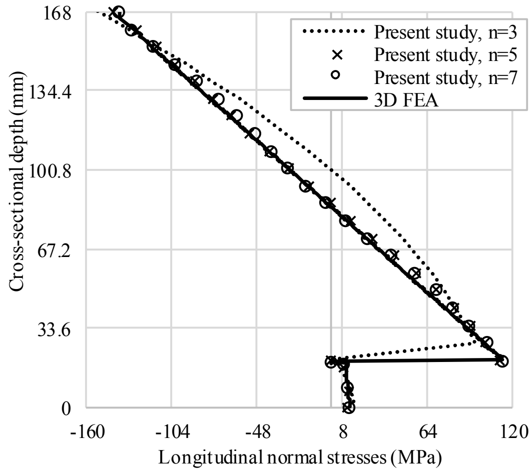

(a) L =1.5m (b) L=3.0m

Figure 8.21. Longitudinal normal stress profiles at mid-span cross-section

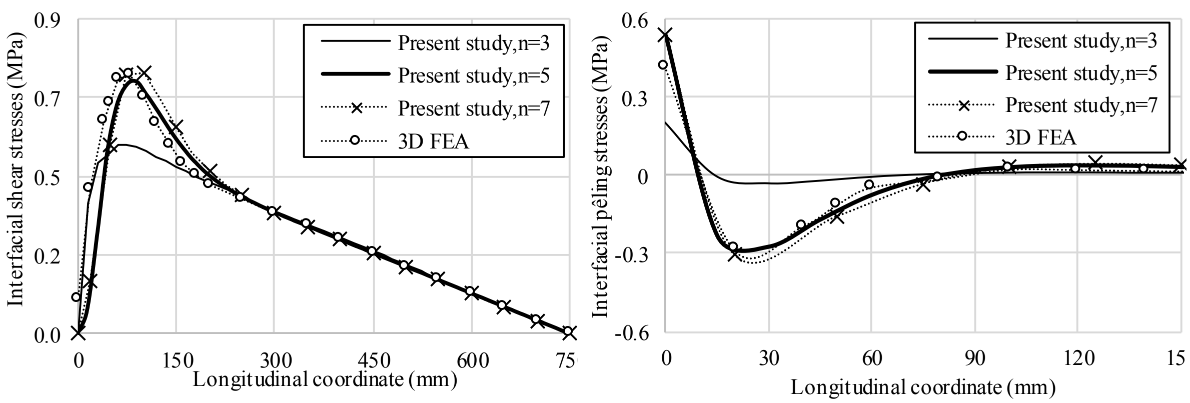

(a) L =1.5m (b) L=1.5m

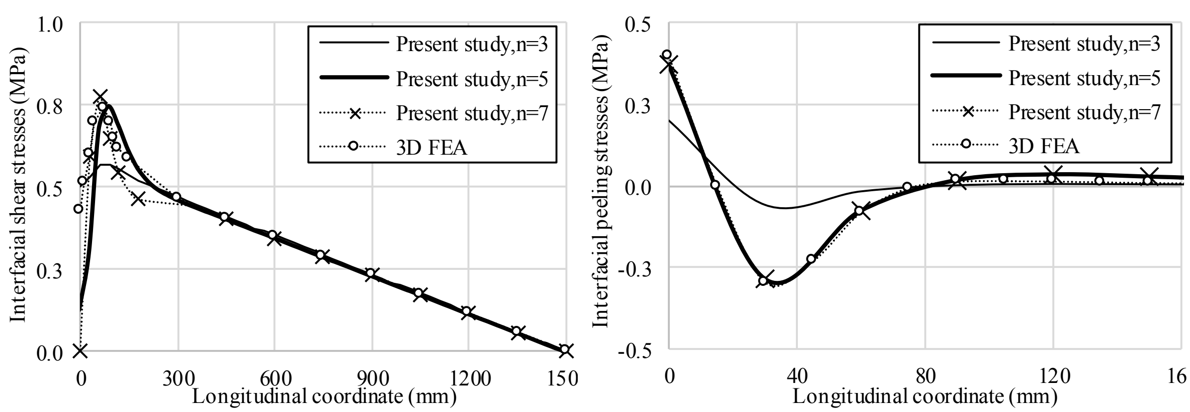

(c) L=3.0m (d) L=3.0m

Figure 8.22. Comparisons of the interfacial shear and peeling stresses obtained from the present solution and the 3D FEA solutions

Example 6 –Sandwich beam with layers of equal thicknesses

A sandwich beam has three layers, each having a $50mm$ thickness. Beam width is $80mm$. The span L is taken as $600mm$ and $1500mm$. The beam is subjected to a transverse uniform traction $\sigma\left(-h_1,z\right)=0.1MPa$ acting on the top face while other tractions vanish, i.e., $\tau\left(-h_1,z\right)=\sigma\left(h_2,z\right)=\tau\left(h_2,z\right)=0$. Material properties of the faces are $E_z=10$, $E_x=E_y=4$, $G_{xy}=G_{xz}=G_{yz}=0.8GPa$, and $\mu_{yz}=\mu_{xy}=\mu_{xz}=0.25$ while the core material properties are $E_z=E_x=E_y=2GPa$, $G_{xy}=G_{xz}=G_{yz}=0.24GPa$, and $\mu_{yz}=\mu_{xy}=\mu_{xz}=0.25$ [31]. Figures 8.23a-b show the longitudinal normal stress profiles at mid-span as predicted from the present solution with $n=3$. The excellent agreement observed with the 3D FEA stress profiles suggests the present solution is able to accurately capture the zigzag stress profiles.

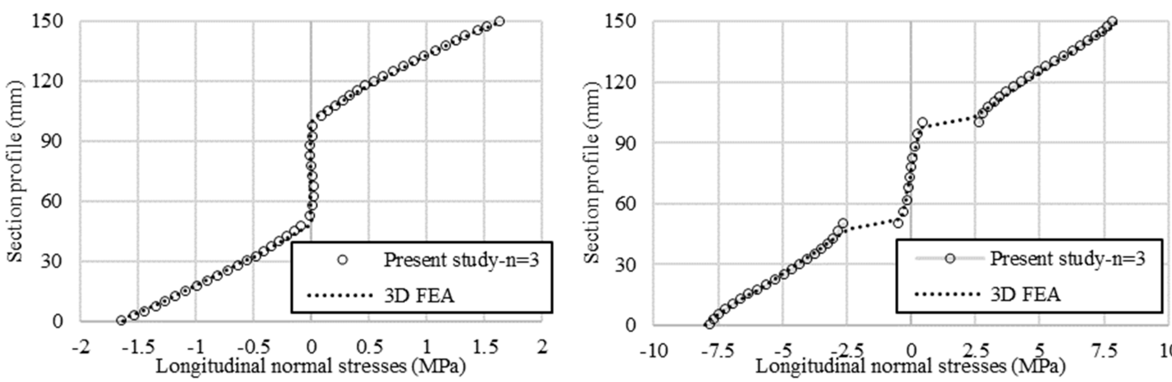

(a) span L=600mm (b) span L=1500mm

Figure 8.23. Longitudinal normal stress profile at midspan for a sandwich beam with equal thickness layers

8.6. Summary and Conclusions

The present study has successfully developed a complementary strain energy variational principle for the analysis of homogeneous and multilayered beams. A finite element formulation was then developed based on the variational principle. The accuracy of the predictions of the present solution was shown to increase with the number of stress terms taken. Comparisons with other beam theories, elasticity theory solution and 3D FEA solutions suggest the validity of the present formulation for homogeneous and layered beams. The main findings of the studies are:

(1) The present solution captures shear deformation effects in a natural way that does not require the introduction of shear modification factors.

(2) The solution converges to the deflections from above in contrast to conventional solutions which tend to converge to the deflections from below.

(3) The present solution captures the nonlinear distribution of the longitudinal normal stress across the cross-section depth for short-span beams. Also, it captures the nonlinear distribution of the transverse normal stresses across the section depth.

(4) Unlike conventional 3D FEA solutions that interpolate the displacement fields, which violate the local equilibrium condition at the interfaces, the present solution satisfies the equilibrium condition at the interface in an exact sense as illustrated in Example 3.

(5) The high interfacial shear and peeling stresses predicted by the present solution agree well with the 3D FEA solution. Examples 3 through 5 suggest that the present solution with $n=7$ provides reliable predictions for the interfacial stresses.

(6) The computational effort involved in the present solution is orders of magnitudes less than that of 3D FEA analysis, particularly for the analysis of layered beams. The present solutions, implemented in non-compiled MATLAB script files, took between 3-15 minutes to conduct the runs in Examples 3-5 on a computer with two Intel(R) Xeon(R) CPU E5-24300 processors at 2.20 GHz speed, and 64.0 GB memory RAM. In comparison, the 3D FEA under ABAQUS took 3.8 - 6.9 hours per run on the same computer. The new solution also involves less effort in modelling and post-processing compared to 3D FEA solutions.

Appendix 8.1: Background for Developing Equation 12

Equations (8.11a-b) are differentiated with respect to z and the result is substituted into the expressions of $F_{n-1}{}'$ and $F_n{}'$ as given by Eq. (8.8a), yielding

$$\begin{aligned}
&\left\{\alpha_{n-1}(h_2)\int_0^z \rho_1(z)dz + \alpha_n(h_2)\int_0^z \rho_2(z)dz - \left[\bar{\tau}(h_2,z) - \tau(h_2,z)\right]\right\} + \\
&+\left\{-\alpha_{n-1}(h_2)\sum_{i=1}^{n-2}\lambda_{1i}F_i'(z) - \alpha_n(h_2)\sum_{i=1}^{n-2}\lambda_{2i}F_i'(z) + \sum_{i=1}^{n-2}\alpha_i(h_2)F_i'(z)\right\} + \\
&+\left\{-\alpha_{n-1}(h_2)\sum_{k=1}^{p-1}\xi_{1k}J_k'(z) - \alpha_n(h_2)\sum_{k=1}^{p-1}\xi_{2k}J_k'(z) + \sum_{k=1}^{p-1}a_k(h_2)J_k{}'(z)\right\} + \\
&+\alpha_{n-1}(h_2)\sum_{k=1}^{p-1}\xi_{1k}J_k{}'(0) + \alpha_n(h_2)\sum_{k=1}^{p-1}\xi_{2k}J_k{}'(0) + \alpha_{n-1}(h_2)\sum_{i=1}^{n-2}\lambda_{1i}F_i'(0) + \\
&+\alpha_n(h_2)\sum_{i=1}^{n-2}\lambda_{2i}F_i'(0) + \alpha_{n-1}(h_2)F_{n-1}'(0) + \alpha_n(h_2)F_n'(0) = 0
\end{aligned} \tag{A.1}$$

From Eqs. (8.10a-b), by substituting into Eq.(A.1), one obtains

$$
\begin{aligned}
&-\overline{\tau}(h_2,0)+\tau(h_2,0)-\sum_{i=1}^{n-2}\left[\alpha_{n-1}(h_2)\lambda_{1i}+\alpha_n(h_2)\lambda_{2i}-\alpha_i(h_2)\right]F_i'(z)+\\
&-\sum_{k=1}^{p-1}\left[\alpha_{n-1}(h_2)\xi_{1k}+\alpha_n(h_2)\xi_{2k}-a_k(h_2)\right]J_k{}'(z)+\alpha_{n-1}(h_2)F_{n-1}'(0)+\alpha_n(h_2)F_n'(0) \qquad \text{(A.2)}\\
&=-\alpha_{n-1}(h_2)\sum_{i=1}^{n-2}\lambda_{1i}F_i'(0)-\alpha_n(h_2)\sum_{i=1}^{n-2}\lambda_{2i}F_i'(0)-\alpha_{n-1}(h_2)\sum_{k=1}^{p-1}\xi_{1k}J_k{}'(0)-\alpha_n(h_2)\sum_{k=1}^{p-1}\xi_{2k}J_k{}'(0)
\end{aligned}
$$

From Eq. (A.2), by noting the identity $\alpha_{n-1}(h_2)\lambda_{1i}+\alpha_n(h_2)\lambda_{2i}-\alpha_i(h_2)=0$ and $\alpha_{n-1}(h_2)\xi_{1k}+\alpha_n(h_2)\xi_{2k}-a_k(h_2)=0$, one obtains

$$
\alpha_{n-1}(h_2)F_{n-1}'(0)+\alpha_n(h_2)F_n'(0)=\left[\overline{\tau}(h_2,0)-\tau(h_2,0)\right]-\sum_{i=1}^{n-2}\alpha_i(h_2)F_i'(0)-\sum_{k=1}^{p-1}a_k(h_2)J_k{}'(0) \qquad \text{(A.3)}
$$

Appendix 8.2: Coefficients introduced in Equations (8.16a-d)

$$
\begin{aligned}
&\varsigma_{11}=-\frac{\alpha_n(h_2)\int_A\overline{\tau}(y,0)dA-\widehat{\alpha}_n\left[\overline{\tau}(h_2,0)-\tau(h_2,0)\right]}{\widehat{\alpha}_n\alpha_{n-1}(h_2)-\widehat{\alpha}_{n-1}\alpha_n(h_2)}; \qquad \varsigma_{12}=\frac{\alpha_n(h_2)}{\widehat{\alpha}_n\alpha_{n-1}(h_2)-\widehat{\alpha}_{n-1}\alpha_n(h_2)};\\
&\varsigma_{13i}=\frac{\alpha_n(h_2)\widehat{\alpha}_i-\widehat{\alpha}_n\alpha_i(h_2)}{\widehat{\alpha}_n\alpha_{n-1}(h_2)-\widehat{\alpha}_{n-1}\alpha_n(h_2)}; \qquad \varsigma_{14k}=\frac{\alpha_n(h_2)\int_A a_k(y)dA-\widehat{\alpha}_n a_k(h_2)}{\widehat{\alpha}_n\alpha_{n-1}(h_2)-\widehat{\alpha}_{n-1}\alpha_n(h_2)};\\
&\varsigma_{21}=\frac{\alpha_{n-1}(h_2)\int_A\overline{\tau}(y,0)dA-\widehat{\alpha}_{n-1}\left[\overline{\tau}(h_2,0)-\tau(h_2,0)\right]}{\widehat{\alpha}_n\alpha_{n-1}(h_2)-\widehat{\alpha}_{n-1}\alpha_n(h_2)}; \qquad \varsigma_{22}=-\frac{\alpha_{n-1}(h_2)}{\widehat{\alpha}_n\alpha_{n-1}(h_2)-\widehat{\alpha}_{n-1}\alpha_n(h_2)};\\
&\varsigma_{23i}=-\frac{\alpha_{n-1}(h_2)\widehat{\alpha}_i-\widehat{\alpha}_{n-1}\alpha_i(h_2)}{\widehat{\alpha}_n\alpha_{n-1}(h_2)-\widehat{\alpha}_{n-1}\alpha_n(h_2)}; \qquad \varsigma_{24k}=-\frac{\alpha_{n-1}(h_2)\int_A a_k(y)dA-\widehat{\alpha}_{n-1}a_k(h_2)}{\widehat{\alpha}_n\alpha_{n-1}(h_2)-\widehat{\alpha}_{n-1}\alpha_n(h_2)}; \qquad \text{(B.1)}\\
&\varsigma_{31}=\frac{\overline{\alpha}_n}{\overline{\alpha}_n\overline{\alpha}_{n-2}-\overline{\alpha}_{n-1}\overline{\alpha}_{n-1}}; \quad \varsigma_{32}=-\frac{\overline{\alpha}_{n-1}}{\overline{\alpha}_n\overline{\alpha}_{n-2}-\overline{\alpha}_{n-1}\overline{\alpha}_{n-1}}; \quad \varsigma_{33i}=-\frac{\overline{\alpha}_n\overline{\alpha}_{i-1}-\overline{\alpha}_{n-1}\overline{\alpha}_i}{\overline{\alpha}_n\overline{\alpha}_{n-2}-\overline{\alpha}_{n-1}\overline{\alpha}_{n-1}};\\
&\varsigma_{41}=-\frac{\overline{\alpha}_{n-1}}{\overline{\alpha}_n\overline{\alpha}_{n-2}-\overline{\alpha}_{n-1}\overline{\alpha}_{n-1}}; \quad \varsigma_{42}=\frac{\overline{\alpha}_{n-2}}{\overline{\alpha}_n\overline{\alpha}_{n-2}-\overline{\alpha}_{n-1}\overline{\alpha}_{n-1}}; \quad \varsigma_{43i}=\frac{\overline{\alpha}_{n-1}\overline{\alpha}_{i-1}-\overline{\alpha}_{n-2}\overline{\alpha}_i}{\overline{\alpha}_n\overline{\alpha}_{n-2}-\overline{\alpha}_{n-1}\overline{\alpha}_{n-1}};\\
&\varsigma_{34k}=\frac{\overline{\alpha}_{n-1}\int_A yH(y-y_k)dA-\overline{\alpha}_n\int_A H(y-y_k)dA}{\overline{\alpha}_{n-2}\overline{\alpha}_n-\overline{\alpha}_{n-1}\overline{\alpha}_{n-1}}; \quad \varsigma_{44k}=\frac{\overline{\alpha}_{n-1}\int_A H(y-y_k)dA-\overline{\alpha}_{n-2}\int_A yH(y-y_k)dA}{\overline{\alpha}_n\overline{\alpha}_{n-2}-\overline{\alpha}_{n-1}\overline{\alpha}_{n-1}}
\end{aligned}
$$

Appendix 8.3- Procedure for developing the finite element formulation

This appendix provides the steps for formulating the finite element solutions:

(1) Determine constants $\overline{\alpha}_i, \widehat{\alpha}_i$ as defined from Eqs. (8.15a-c):

$$
\overline{\alpha}_i=\int_A y^i dA, \quad \widehat{\alpha}_i=\int_A \alpha_i(y)\,dA \qquad (i=1,2,...,m) \qquad \text{(C.1)}
$$

(2) Starting from the definitions of $\alpha_i(y), \beta_i(y),\ c_k(y),\ a_k(y)$ as provided in Eqs. (8.6a-d), determine the following constants according to Eqs. (8.10a-d):

$$\begin{aligned}
\lambda_{1i} &= \frac{\alpha_n(h_2)\beta_i(h_2)-\beta_n(h_2)\alpha_i(h_2)}{\alpha_n(h_2)\beta_{n-1}(h_2)-\alpha_{n-1}(h_2)\beta_n(h_2)}; \qquad &\lambda_{2i} &= -\frac{\alpha_{n-1}(h_2)\beta_i(h_2)-\beta_{n-1}(h_2)\alpha_i(h_2)}{\alpha_n(h_2)\beta_{n-1}(h_2)-\alpha_{n-1}(h_2)\beta_n(h_2)}; \\
\xi_{1k} &= \frac{\alpha_n(h_2)c_k(h_2)-\beta_n(h_2)a_k(h_2)}{\alpha_n(h_2)\beta_{n-1}(h_2)-\alpha_{n-1}(h_2)\beta_n(h_2)}; \qquad &\xi_{2k} &= -\frac{\alpha_{n-1}(h_2)c_k(h_2)-\beta_{n-1}(h_2)a_k(h_2)}{\alpha_n(h_2)\beta_{n-1}(h_2)-\alpha_{n-1}(h_2)\beta_n(h_2)};
\end{aligned} \tag{C.2}$$

(3) Given $\alpha_i(y)$ and $a_k(y)$ as given in Eq. (8.6a,b), $\overline{\alpha}_i$ and $\widehat{\alpha}_i$ in Eqs. (C.1) and the knowing applied tractions, determine the following constants:

$$\varsigma_{11} = -\frac{\alpha_n(h_2)\int_A \overline{\tau}(y,0)\,dA - \widehat{\alpha}_n\left[\overline{\tau}(h_2,0)-\tau(h_2,0)\right]}{\widehat{\alpha}_n\alpha_{n-1}(h_2)-\widehat{\alpha}_{n-1}\alpha_n(h_2)}; \qquad \varsigma_{12} = \frac{\alpha_n(h_2)}{\widehat{\alpha}_n\alpha_{n-1}(h_2)-\widehat{\alpha}_{n-1}\alpha_n(h_2)};$$

$$\varsigma_{13i} = \frac{\alpha_n(h_2)\widehat{\alpha}_i-\widehat{\alpha}_n\alpha_i(h_2)}{\widehat{\alpha}_n\alpha_{n-1}(h_2)-\widehat{\alpha}_{n-1}\alpha_n(h_2)}; \qquad \varsigma_{14k} = \frac{\alpha_n(h_2)\int_A a_k(y)\,dA - \widehat{\alpha}_n a_k(h_2)}{\widehat{\alpha}_n\alpha_{n-1}(h_2)-\widehat{\alpha}_{n-1}\alpha_n(h_2)};$$

$$\varsigma_{21} = \frac{\alpha_{n-1}(h_2)\int_A \overline{\tau}(y,0)\,dA - \widehat{\alpha}_{n-1}\left[\overline{\tau}(h_2,0)-\tau(h_2,0)\right]}{\widehat{\alpha}_n\alpha_{n-1}(h_2)-\widehat{\alpha}_{n-1}\alpha_n(h_2)}; \qquad \varsigma_{22} = -\frac{\alpha_{n-1}(h_2)}{\widehat{\alpha}_n\alpha_{n-1}(h_2)-\widehat{\alpha}_{n-1}\alpha_n(h_2)};$$

$$\varsigma_{23i} = -\frac{\alpha_{n-1}(h_2)\widehat{\alpha}_i-\widehat{\alpha}_{n-1}\alpha_i(h_2)}{\widehat{\alpha}_n\alpha_{n-1}(h_2)-\widehat{\alpha}_{n-1}\alpha_n(h_2)}; \qquad \varsigma_{24k} = -\frac{\alpha_{n-1}(h_2)\int_A a_k(y)\,dA - \widehat{\alpha}_{n-1} a_k(h_2)}{\widehat{\alpha}_n\alpha_{n-1}(h_2)-\widehat{\alpha}_{n-1}\alpha_n(h_2)};$$

$$\varsigma_{31} = \frac{\overline{\alpha}_n}{\overline{\alpha}_n\overline{\alpha}_{n-2}-\overline{\alpha}_{n-1}\overline{\alpha}_{n-1}}; \quad \varsigma_{32} = -\frac{\overline{\alpha}_{n-1}}{\overline{\alpha}_n\overline{\alpha}_{n-2}-\overline{\alpha}_{n-1}\overline{\alpha}_{n-1}}; \quad \varsigma_{33i} = -\frac{\overline{\alpha}_n\overline{\alpha}_{i-1}-\overline{\alpha}_{n-1}\overline{\alpha}_i}{\overline{\alpha}_n\overline{\alpha}_{n-2}-\overline{\alpha}_{n-1}\overline{\alpha}_{n-1}};$$

$$\varsigma_{34k} = \frac{\overline{\alpha}_{n-1}\int_A yH(y-y_k)\,dA - \overline{\alpha}_n\int_A H(y-y_k)\,dA}{\overline{\alpha}_{n-2}\overline{\alpha}_n-\overline{\alpha}_{n-1}\overline{\alpha}_{n-1}}; \quad \varsigma_{44k} = \frac{\overline{\alpha}_{n-1}\int_A H(y-y_k)\,dA - \overline{\alpha}_{n-2}\int_A yH(y-y_k)\,dA}{\overline{\alpha}_n\overline{\alpha}_{n-2}-\overline{\alpha}_{n-1}\overline{\alpha}_{n-1}}$$

$$\varsigma_{41} = -\frac{\overline{\alpha}_{n-1}}{\overline{\alpha}_n\overline{\alpha}_{n-2}-\overline{\alpha}_{n-1}\overline{\alpha}_{n-1}}; \quad \varsigma_{42} = \frac{\overline{\alpha}_{n-2}}{\overline{\alpha}_n\overline{\alpha}_{n-2}-\overline{\alpha}_{n-1}\overline{\alpha}_{n-1}}; \quad \varsigma_{43i} = \frac{\overline{\alpha}_{n-1}\overline{\alpha}_{i-1}-\overline{\alpha}_{n-2}\overline{\alpha}_i}{\overline{\alpha}_n\overline{\alpha}_{n-2}-\overline{\alpha}_{n-1}\overline{\alpha}_{n-1}};$$

(C.3)

(4) Also, starting from the definitions of $\alpha_i(y), \beta_i(y),\ c_k(y),\ a_k(y)$ as provided in Eqs. (8.6a-d) and the applied traction (i.e., $\sigma_y(-h_1,z)$, $\tau(-h_1,z)$, $\sigma_y(h_2,z)$, $\tau(h_2,z)$), determine the following constants according to Eqs. (8.10a-d):

$$\rho_1(z)=\left\{\alpha_n(h_2)\left[\sigma_y(h_2,z)-\overline{\sigma}_y(h_2,z)\right]-\beta_n(h_2)\left[\overline{\tau}'(h_2,z)-\tau'(h_2,z)\right]\right\}\Big/\Lambda,$$

$$\rho_2(z)=-\left\{\alpha_{n-1}(h_2)\left[\sigma_y(h_2,z)-\overline{\sigma}_y(h_2,z)\right]-\beta_{n-1}(h_2)\left[\overline{\tau}'(h_2,z)-\tau'(h_2,z)\right]\right\}\Big/\Lambda \qquad \text{(C.4)}$$

$$\Lambda=\left\{\alpha_n(h_2)\beta_{n-1}(h_2)-\alpha_{n-1}(h_2)\beta_n(h_2)\right\}$$

(5) Given ς_{ij} as given from Eq. (C.3), λ_{ij} and ξ_{ik} as given from Eq. (C.2), and $\alpha_i(y),\beta_i(y)$, $c_k(y)$, $a_k(y)$ as given from Eqs. (8.6a-d), functions $a_{ji}(y),g_{jk}(y),b_{11}(y),b_{12}(y),b_{13}(y),b_{22}(y)$($j=1,2,\ldots,6$) defined in Eq. (8.21) are determined.

(6) Given $\rho_1(z)$, $\rho_2(z)$ from Eqs. (C.4), ς_{11} and ς_{21} from Eq.(C.4), and $\overline{\tau}(y,z)$, $\overline{\sigma}_y(y,z)$ from Eq. (8.5a-b), one recovers the expressions for $\sigma_z^*(y,z),\tau^*(y,z),\sigma_y^*(y,z)$ as defined in Eq.(8.20a-c).

(7) Given $\mathbf{a}_1(y),\mathbf{a}_2(y),\mathbf{a}_3(y,z),\mathbf{a}_4(y),\mathbf{a}_5(y),\mathbf{a}_6(y),\mathbf{b}_1(y,z),\mathbf{b}_2(y)$ as defined in Step 5, $\mathbf{\Lambda_F}(z)$ as defined in Eq. (8.26), $\{\mathbf{X}_{\sigma y}\}$ from Step 7, and the constitutive matrix in Eq. (8.33b), evaluate the flexibility matrix $[\mathbf{H}]$ from Eq. (8.41).

(9) Given $\{\mathbf{X}_{\sigma z}\}$, $\{\mathbf{X}_{\tau}\}$, $\{\mathbf{X}_{\sigma y}\}$ from Step 7 and load terms $\sigma_z^*(y,z),\tau^*(y,z),\sigma_y^*(y,z)$ from Step 6, evaluate the energy conjugate generalized displacement vector $\mathbf{d}_0$ from Eq. (8.42).

(10) Given the flexibility matrix $[\mathbf{H}]$ from Step 8 and $\mathbf{\Gamma}(L)$ from Eq. (8.45), evaluate the element stiffness matrix $[\mathbf{K}]$ from Eq. (8.50).

(11) Given the flexibility matrix $[\mathbf{H}]$ from Step 8, $\mathbf{\Gamma}(L)$ from Eq. (8.45), vector $\mathbf{d}_0$ from Step 9 and the load terms $\sigma_z^*(y,z),\tau^*(y,z),\sigma_y^*(y,z)$ from Step 6, evaluate the energy equivalent load vector $\{\mathbf{P}_0\}$ from Eq. (8.50).

(12) Use the element stiffness matrix and load vector $[\mathbf{K}]$ and $\{\mathbf{P}_0\}$ obtained in Steps 10 and 11 to form the structure stiffness matrix and load vector and solve for nodal displacements.

(13) Given the nodal displacements, evaluate the augmented nodal vector $\{\mathbf{P}\}$ and obtain vector $\{\overline{\mathbf{P}}\}$ from Eq. (8.50).

(14) Given $\{\mathbf{X}_{\sigma z}\}$, $\{\mathbf{X}_{\tau}\}$, $\{\mathbf{X}_{\sigma y}\}$ from Step 7, load terms $\sigma_z^*(y,z),\tau^*(y,z),\sigma_y^*(y,z)$ from Step 6 and $\{\overline{\mathbf{P}}\}$ from Step 13, and setting $z=0,L$, determine the nodal stresses from Eqs. (8.30).

Appendix 8.4- Flexibility and Stiffness matrices and load vector for Special Case

A homogeneous beam element with span L has a rectangular cross-section with dimensions $b \times t$ and is subjected to a uniform traction $\sigma(-h_1, z) = \sigma_0$ acting at the top surface while other tractions vanish, i.e., $\tau(-h_1, z) = \sigma(h_2, z) = \tau(h_2, z) = 0$. Material is orthotropic with a longitudinal elastic modulus E_z, transverse elastic modulus E_y, shear modulus G, and Poisson's ratios μ_{zy} and μ_{yz}. For the homogeneous beam, the number of layers is set to $p = 1$ in Eq. (1). For simplicity, the number of stress terms is taken as $n = 3$. The nodal force vector $\{\overline{\mathbf{P}}\}$ in Eq. (8.48) and the augmented nodal force vector $\{\mathbf{P}\}$ in Eq. (8.50) are

$$\langle \overline{\mathbf{P}} \rangle_{1\times 7}^{T} = \left\langle F_1(0) \quad F_1'(0) \quad N(0) \quad Q(0) \quad M(0) \;\middle|\; F_1(L) \quad F_1'(L) \right\rangle, \text{ and}$$

$$\langle \mathbf{P} \rangle_{1\times 10}^{T} = \left\langle F_1(0) \quad F_1'(0) \quad N(0) \quad Q(0) \quad M(0) \;\middle|\; F_1(L) \quad F_1'(L) \quad N(L) \quad Q(L) \quad M(L) \right\rangle.$$

From Eqs. (8.30), by evaluating $\mathbf{X}_{\sigma z}$, $\mathbf{X}_{\tau}$, and $\mathbf{X}_{\sigma y}$, and substituting into Eq. (8.41), the flexibility matrix $[\mathbf{H}]$ is obtained as

$$[\mathbf{H}]_{7\times 7} = [\mathbf{H}_1] + [\mathbf{H}_2] + [\mathbf{H}_3] + [\mathbf{H}_4]$$

in which matrix $[\mathbf{H}_1]$ provides the contribution of the longitudinal stresses and is given by

$$[\mathbf{H}_1] = \frac{1}{525E_z}\left[\begin{array}{c:c:c:c:c:c:c}
156btL & & & & & & \\ \hdashline
22btL^2 & 4btL^3 & & & & syms & \\ \hdashline
-210L & -35L^2 & 945L/bt & & & & \\ \hdashline
0 & 0 & 0 & 2100L^3/bt^3 & & & \\ \hdashline
0 & 0 & 0 & 3150L^2/bt^3 & 6300L/bt^3 & & \\ \hdashline
-54btL & -13btL^2 & 210L & 0 & 0 & 156btL & \\ \hdashline
13btL^2 & 3btL^3 & -35L^2 & 0 & 0 & -22btL^2 & 4btL^3
\end{array}\right],$$

$[\mathbf{H}_2]$ provides the contribution of the coupling terms μ_{yz}/E_z (or μ_{zy}/E_y) and is given by

$$[\mathbf{H}_2] = \frac{-\mu_{1z}}{1575E_z}\left[\begin{array}{c:c:c:c:c:c:c}
72bt^3/L & & & & & & \\ \hdashline
36bt^3 & 8bt^3L & & & & syms & \\ \hdashline
0 & -45t^2/2 & 0 & & & & \\ \hdashline
0 & 0 & 0 & 0 & & & \\ \hdashline
0 & 0 & 0 & 0 & 0 & & \\ \hdashline
72bt^3/L & 6bt^3 & 0 & 0 & 0 & 72bt^3/L & \\ \hdashline
-6bt^3 & 2bt^3L & 45t^2/2 & 0 & 0 & -36bt^3 & 8bt^3L
\end{array}\right],$$

$\left[\mathbf{H}_3\right]$ provides the contribution of the transverse normal stresses and is given by

$$\left[\mathbf{H}_3\right]=\frac{bt^5}{315E_yL^3}\begin{bmatrix} 6 & & & & & & \\ 3L & 2L^2 & & & & syms & \\ 0 & 0 & 0 & & & & \\ 0 & 0 & 0 & 0 & & & \\ 0 & 0 & 0 & 0 & 0 & & \\ 6 & 3L & 0 & 0 & 0 & 6 & \\ -3L & -L^2 & 0 & 0 & 0 & -3L & 2L^2 \end{bmatrix},$$

and $\left[\mathbf{H}_4\right]$ provides the contribution of the shear stresses and is given by

$$\left[\mathbf{H}_4\right]=\frac{1}{525G}\begin{bmatrix} 12bt^3/L & & & & & & \\ bt^3 & 4bt^3L/3 & & & & syms & \\ 0 & 0 & 0 & & & & \\ 0 & 0 & 0 & 630L/bt & & & \\ 0 & 0 & 0 & 0 & 0 & & \\ 12bt^3/L & bt^3 & 0 & 0 & 0 & 12bt^3/L & \\ -bt^3 & bt^3L/3 & 0 & 0 & 0 & -bt^3 & 4bt^3L/3 \end{bmatrix}.$$

In the present solution, matrices $\left[\mathbf{H}_1\right],\left[\mathbf{H}_2\right],\left[\mathbf{H}_3\right],\left[\mathbf{H}_4\right]$ are added and the resulting flexibility matrix $\left[\mathbf{H}\right]$ is then inverted. The procedure in Appendix B is then followed to recover the stiffness matrix $\left[\mathbf{K}\right]$ and load vector $\left\{\mathbf{P}_0\right\}$.

It is of interest to consider the case where matrices $\left[\mathbf{H}_2\right],\left[\mathbf{H}_3\right],\left[\mathbf{H}_4\right]$ are negligible. This corresponds to omitting the shear and transverse normal stresses and orthotropic coupling effects. In this case, the resulting stiffness matrix takes the form:

$[\mathbf{K}] =$

$$
\left[\begin{array}{ccccc|ccccc}
21E/AL & & & & & & & & & \\
-150E/AL^2 & 1500E/AL^3 & & & & & & & & \\
E/L & 0 & \boxed{EA/L} & & & & & & syms & \\
0 & 0 & \boxed{0} & \boxed{12EI/L^3} & & & & & & \\
0 & 0 & \boxed{0} & \boxed{-6EI/L^2} & \boxed{4EI/L} & & & & & \\
\hline
4E/AL & -75E/AL^2 & -E/L & 0 & 0 & 21E/AL & 150EA/L^2 & & & \\
75E/AL^2 & -1050E/AL^3 & 0 & 0 & 0 & 150E/AL^2 & 1500EA/L^3 & & & \\
-E/L & 0 & \boxed{-EA/L} & \boxed{0} & \boxed{0} & E/L & 0 & \boxed{EA/L} & & \\
0 & 0 & \boxed{0} & \boxed{-12EI/L^3} & \boxed{6EI/L^3} & 0 & 0 & \boxed{0} & \boxed{12EI/L^3} & \\
0 & 0 & \boxed{0} & \boxed{-6EI/L^3} & \boxed{2EI/L} & 0 & 0 & \boxed{0} & \boxed{6EI/L^2} & \boxed{4EI/L}
\end{array}\right]
$$

in which the terms $A = bt$, $I = bt^3/12$ and $E = E_z$ have been introduced. It is of interest to note that the boxed entries match those of the classical Euler Bernoulli beam element. Also, the nodal force vector is found to take the form

$$
\langle \mathbf{P}_0 \rangle_{1\times 10}^T = \left\langle 0 \quad 0 \quad \boxed{0} \quad \boxed{qL/2} \quad \boxed{-qL^2/12} \;\middle|\; 0 \quad 0 \quad \boxed{0} \quad \boxed{qL/2} \quad \boxed{qL^2/12} \right\rangle
$$

with $q = \sigma_0 b$. Again, for the boxed terms correspond to the energy equivalent load vector for an Euler Bernoulli beam element subjected to uniformly distributed load.

References

[8-1] Blevins, R., D., (2015), Formulas for Dynamics, Acoustics and Vibration, Wiley Publisher, ISBN: 978-1-119-03811-5.

[8-2] Carrera, E., and Guinta, G., (2010), Refined beam theories based on a unified formulation, International journal of applied mechanics, 2(1), 117-143.

[8-3] Carrera, E., Pagani, A., and Zangallo, F., (2015), Comparison of various 1D, 2D, and 3D models for the analysis of thin-walled box with transverse ribs subjected to load factors, Journal of finite elements in analysis and design, 95, 1-11.

[8-4] Cowper, G. R., (1966), The Shear Coefficient in Timoshenko's Beam Theory, Journal of applied mechanics, 33(2), 335–340.

[8-5] Erkmen, R., E., and Mohareb, M., (2006), Torsion analysis of thin-walled beams including shear deformation effects, Journal of thin walled structures, 44(10), 1096-1108.

[8-6] Erkmen, R., E., and Mohareb, M., (2008), Buckling analysis of thin-walled open members- A complementary energy variational principle, Journal of thin walled structures, 46(6), 602-617.

[8-7] Groh, R. M. J., and Weaver, P. M., (2015), Static inconsistencies in certain axiomatic higher-order shear deformation theories for beams, plates and shells, Journal of composite structures, 120, 231-245.

[8-8] Groh, R.M., J. and Tessler, A., (2017), Computationally efficient beam elements for accurate stresses in sandwich laminates and laminated composites with delamination, Computer Methods in Applied Mechanics and Engineering, 320 (1), 369-395.

[8-9] Hexcel Corporation, (2000), HexWeb TM Honeycomb Sandwich Design Technology, website: http://www.hexcel.com/Resources/DataSheets/Brochure Data Sheets/ Honeycomb Sandwich Design Technology.pdf.

[8-10] Heyliger, P. R. and Reddy, J. N., (1988), A higher order beam finite element for bending and vibration problems, Journal of sound and vibration,126(2), 309-326.

[8-11] Hutchinson, J. R., (1981), Transverse vibration of beams, exact versus approximate solutions, Journal of applied mechanics, 48(4), 923–928.

[8-12] Jha, D., K., Kant, T., and Singh, R., K., (2013), Stress analysis of transversely loaded functionally graded plates with a higher order shear and normal deformation theory, Journal of engineering mechanics. 139(12), 1663-1680.

[8-13] Kaneko, T., (1975), On Timoshenko's correction for shear in vibrating beams, Journal of physics D: Applied Physics. 8(16), 1927–1936.

[8-14] Kant, T. and Manjunatha, B.S., (1990), Higher-order theories for symmetric and unsymmetric fiber reinforced composite beams with C0 finite elements, Journal of finite elements in analysis and design, 6(4), 303-320.

[8-15] Mindlin, R. D., Deresiewicz, H., (1953), Timoshenko's Shear Coefficient for Flexural Vibrations of Beams, Technical Report No. 10, ONR Project NR064-388, Department of Civil Engineering, Columbia University, New York, N. Y.

[8-16] Stephen, N. G. and Levinson, M., (1979), A second order beam theory, Journal of Sound and Vibration. 67(3), 293-305.

[8-17] Pham, P.V. and Mohareb, M., (2014), A shear deformable theory for the analysis of steel beams reinforced with GFRP plates, Thin-walled structures, 85, 165-182.

[8-18] Pham, P.V. and Mohareb, M., (2015), Finite-Element Formulations for the Spatial Static Response of Steel Beams Bonded to a GFRP Plate, J. Eng. Mechanics, 141(4), 04014143.

[8-19] Pappada, S., Rametta, R., and Lanzilotto, L., (2009), Effect of manufacturing process and skin-core adhesion efficiency on the mechanical properties of a thermoplastic sandwich. In: ICCM 17, Edinburgh, Scottland, 27–31.

Chapter 9: Summary, Conclusions and Recommendations

9.1. Summary

The present thesis focused on the analysis of composite beams consisting of wide flange steel beams strengthened with adhesively-bonded GFRP plates. In addition to the introductory sections in chapters 1 and 2, a series of analytical/numerical solutions were developed to predict the response and quantify the capacity of such system based on a variety of potential modes of failure. The features relevant to design aspects of the GFRP strengthened steel beams are outlined in the following:

Chapter 3 developed a solution for the analysis of steel beams strengthened with a single GFRP plate under the action of transverse loads. The solution accounts for partial interaction between GFRP and steel. The solution provides the pre-buckling response required to conduct lateral torsional buckling analysis (covered in chapter 4), evaluates the elastic flexural resistance of GFRP-strengthened steel beams of class 3 (subcompact) sections, and quantifies the deflection limits.

Chapter 4 developed elastic lateral torsional buckling solutions for steel beams strengthened with a single GFRP plate. The solution captures partial interaction between the steel and GFRP; the destabilizing effects due to strong axis bending moments and axial forces and load height effect are incorporated into the formulation. The solution quantifies the gain in elastic buckling strength achieved by GFRP strengthening, developed moment gradient factors for such sections, and generated elastic buckling interaction diagrams for beam-columns.

Chapter 5 developed analytical solutions to determine the ultimate moment resistance for Class 1 and 2 (compact) sections for steel beams strengthened with a single GFRP plate on the tension side. The solutions take advantage of the plastic deformations in the steel and consider the GFRP tensile failure and/or adhesive shear failure. Attention was given to relatively strong adhesives (e.g., common adhesives at room temperature) and weak adhesives (at elevated temperatures). A methodology was developed for classifying steel beams strengthened with GFRP plates to ensure that local buckling does not occur prior the attainment of the ultimate moment resistance.

Chapter 6 developed a solution for the elastic analysis of steel beams strengthened with one or two GFRP plates bonded to both flanges where practical considerations prevent the complete removal of pre-existing loads prior to strengthening. The solution is intended to capture the detrimental effects of pre-existing loads on the strength gained by GFRP strengthening, provides a basis to quantify the elastic flexural resistance of strengthened beams with class 3 (subcompact) sections, and quantify deflections for such systems.

Chapter 7 developed a high-order beam theory for the analysis of homogeneous beams with mono-symmetrical cross-sections. The theory captures transverse normal stresses commonly omitted in other beam theories. While the innovative features of the theory are not directly related to the GFRP-strengthened steel sections, the development served as an initial step towards developing a more general model in Chapter 8 aimed at analyzing multi-layer beams including (but not limited to) GFRP-strengthened steel beams. A distinguishing feature of the developments of Chapter 8 over previous work is that they capture the localized peeling stresses near bond ends within the adhesive layer, and hence provide a basis to quantify the strength of the system based on an adhesive peeling mode of failure.

9.2. Research relevance to various limit states

Each of the models developed in this thesis is intended to quantify the capacity of the strengthened beam based on one (or more) mode(s) of failure as summarized in Table 9.1. Depending on (a) the section class, (b) whether or not pre-existing loads exist prior to strengthening, and (c) whether the strengthened beam is laterally/torsionally braced, eight possibilities may arise. Four modes of failures are identified in each case. These are: (a) elastic lateral torsional buckling, (b) material failure (either in steel, GFRP, or adhesive), (c) interfacial failure due to peeling, and (d) excessive deflection serviceability failure. For each case, the table refers to the models (by chapter) proposed to quantify the strength corresponding to each mode of failure. As shown in the table, the present study provides solutions for a large number of cases, although in some cases, the present models have limitations. For example, Case 2 laterally unsupported beams with pre-existing loads, the present developments do not provide means to quantify the elastic lateral torsional buckling strength.

Apart from Chapter 6 where a steel beam is assumed to be strengthened with two GFRP plates bonded to both flanges, the remaining chapters tackle steel beams strengthened with a single GFRP plate.

As an initial classification trial, one may adopt the present classification rules for steel beams. However, the addition of GFRP plates alters the stress profiles in the steel section and makes it resemble those of beam columns. Chapters 3 and 5 thus provide means to predict the stress profiles in the strengthened section, while accounting for partial interaction, based on elastic distribution (Class 3 sections) or elasto-plastic or fully plastic distributions (Class 1 and 2 sections). Both chapters proposed means to classify sections that are analogous to the classification requirements for bare beam-columns. The proposed classification methodology is proposed as a check once the stress profile has been determined from the models developed and may serve as a basis to verify whether the trial classification remains valid. A second trial may be needed if the proposed detailed classification check suggests otherwise.

For class 1 and 2 sections, with no pre-existing loads (i.e., Cases 3 and 4), the elastic lateral torsional buckling moment capacity is determined from Chapter 4 and the ultimate moment capacity (based on elasto-plastic deformation) is calculated from Chapter 5. The peak peeling stress is to be computed from Chapter 8 and checked against the threshold peeling stress as determined from material tests (or supplier information). The deflections under service loads are determined from the model in Chapter 3 and are compared to threshold values, similar to those provided in informative Appendix D to CAN-CSA S16 (2016).

Also, for class 3 sections with no-pre-existing loads (i.e., Cases 7 and 8) strengthened with a single plate, the elastic lateral torsional buckling moment capacity is determined from Chapter 4 and the first yield moment capacity is determined from the model in Chapter 3 (or 6 in the case of two GFRP strengthening plates). The rest of the design is similar to that of cases 3 and 4: the peak peeling stress is to then compute from the model in chapter 8 and checked against the threshold peeling stress as determined from material tests. The deflections under service loads are determined from the model in Chapter 3 (or 6) and compared to allowable threshold values.

Table 9.1. Modes of failures and relevant chapters

<table>
<tr><th rowspan="3">Case</th><th colspan="3" rowspan="2">Problem description</th><th colspan="5">Modes of failure</th></tr>
<tr><th rowspan="2">Elastic lateral torsional buckling</th><th colspan="2">Flexural strength based on the material failure</th><th rowspan="2">Interfacial peel stress</th><th rowspan="2">Deflection limit state</th></tr>
<tr><th>Section class</th><th>Pre-existing loads?</th><th>Laterally supported?</th><th>First yield moment</th><th>Ultimate moment</th></tr>
<tr><td>1</td><td>1,2</td><td>Y</td><td>Y</td><td>NA</td><td rowspan="2">NA</td><td rowspan="2">Not covered</td><td rowspan="2">Not covered</td><td rowspan="2">Chapter 6</td></tr>
<tr><td>2</td><td>1,2</td><td>Y</td><td>N</td><td>Not covered</td></tr>
<tr><td>3</td><td>1,2</td><td>N</td><td>Y</td><td>NA</td><td rowspan="2">NA</td><td rowspan="2">Chapter 5</td><td rowspan="2">Chapter 8</td><td rowspan="2">Chapters 3 or 6</td></tr>
<tr><td>4</td><td>1,2</td><td>N</td><td>N</td><td>Chapter 4</td></tr>
<tr><td>5</td><td>3</td><td>Y</td><td>Y</td><td>NA</td><td rowspan="2">Chapter 6</td><td rowspan="2">NA</td><td rowspan="2">Not covered</td><td rowspan="2">Chapter 6</td></tr>
<tr><td>6</td><td>3</td><td>Y</td><td>N</td><td>Not covered</td></tr>
<tr><td>7</td><td>3</td><td>N</td><td>Y</td><td>NA</td><td rowspan="2">Chapter 3</td><td rowspan="2">NA</td><td rowspan="2">Chapter 8</td><td rowspan="2">Chapters 3 or 6</td></tr>
<tr><td>8</td><td>3</td><td>N</td><td>N</td><td>Chapter 4</td></tr>
</table>

Y=yes, N=No, NA=Not applicable.

9.3. Design Considerations

9.3.1. Effectiveness of GFRP strengthening

The present study suggests that GFRP-strengthening for steel beams increases the resistance based on material failure and elastic lateral torsional buckling moment, and reduces deflections as described in the following:

Elastic stresses and first yield moments: In Chapter 3, strengthening the continuous two-span beam (W150x13) with a single 19-mm GFRP plate was found to lower the stresses by 25% compared to the bare steel beam. When the same section and strengthening scheme is adopted for a simply supported beam, the additional gain in strength was only 6% compared to the bare beam, and when two GFRP plates are used to strengthen the section (Chapter 6), the gain in strength increased to 24% for a simply supported beam.

Effect of GFRP strengthening on pre-loaded beams:

(1) Chapter 6 showed that the presence of pre-existing loads before GFRP strengthening has a detrimental effect on the capacity of the section, when compared to the case where all pre-existing loads are removed prior to strengthening. For example, for a 3m-span cantilever with W150x13 section, the presence of a $4.7kN$ pre-existing tip-load (corresponding to a maximum longitudinal normal stress of $F_y/2 = 175MPa$ at the cantilever root) was found to reduce the loading capacity from 18.1 kN for the case of no pre-existing load, to 13.8kN, corresponding to a 24% reduction.

(2) For the case where the elasticity moduli of both GFRP plates are identical, plates of equal thickness were found to optimize the design based on the stresses in the steel (Chapter 6). For example, a 3m-span W130x15 simply supported beam strengthened with two $19mm-$ thick GFRP plates has a peak normal stress that is 7.9% smaller than that in the wide flange beam strengthened with $9mm$ and $29mm-$thick GFRP plates, of a similar total volume of GFRP.

(3) For the same problem as (2), when the elasticity modulus of the compressive GFRP plate is taken as a 80% of that of the tensile GFRP plate, the optimum compressive to tensile GFRP thickness ratio is found to be 1.22, when the sum of the thicknesses of both GFRP plates is kept constant.

Ultimate moment capacity: GFRP strengthening is also found to increase the ultimate moment capacity based on a plastic stress profile. Chapter 5 has shown that the ultimate moment increased by 21% for a 4m-span steel beam with W250x45 section strengthened with a 15.5mm-thick GFRP plate.

Elastic lateral torsional buckling:

(1) GFRP strengthening was observed to significantly increase the elastic lateral-torsional buckling capacity. Chapter 4 reports a 43% increase in the buckling capacity for a 6m-span beam with a W250x45 section strengthened with a 19mm- thick GFRP plate bonded to the compression flange. Strengthening of the tension flange was also found to an increase in the critical moments by 36%. In contrast, GFRP-strengthening for a 5-m span column with a W250x45 section using a 19-mm thick GFRP plate was found to marginally increase the buckling capacity by 6.8% as the gain in the weak axis flexural stiffness is low.

(2) The effectiveness of strengthening on lateral torsional buckling strength significantly depends on the GFRP plate thickness. The 6m-span steel beam with a W250x45 section strengthened with GFRP plates with thicknesses ranging from 0.0 to 30mm was investigated in Chapter 4. The buckling load increases in a nonlinear fashion with the GFRP thickness. While the buckling load for the bare beam is 89 kN, that corresponding to a 30mm thick plate is significantly increased to 173 kN, a 94.4% difference.

(3) Load height factors for bare beams consistently yield conservative buckling strength predictions for strengthened beams. Conversely, adopting load height factors of bare beams to cases of bottom flange loading for the bare beam would consistently overestimate buckling load predictions. The observations are valid both for compression or tension flange strengthening.

(4) It is suggested the possibility of adopting moment gradient factors for bare beams when designing strengthened beams subjected to linear moment gradients.

(5) It was shown that the moment-axial force interaction diagrams are non-linear. The size of the interaction diagrams was found to grow beyond that of the bare beam when the steel beam is strengthened by GFRP at the tension flange and to further grow when GFRP strengthening is applied at the compression flange.

Peak deflections:

(1) Chapter 3 showed that GFRP strengthening for a two-span span continuous beam with a W150x13 cross-section strengthened with a single 19mm thick GFRP plate was observed to lower the peak deflection by 12%. When two 19mm-thick GFRP plates are used for strengthening, Chapter 6 showed a decrease in deflection of 27% for a 3m single span beam (with the same cross-section).

(2) Chapter 3 also showed that shear deformation effects are significantly more important when predicting deflections for the strengthened beams than for the case of homogeneous beams.

(3) Chapter 6 has shown that the transformed section method underestimates the elastic deflection and considerably overestimate the stresses in GFRP plates.

9.3.2. Adhesive Properties

Peak interfacial shear and peeling stresses: The peak interfacial shear and peeling stresses in the adhesive layer were observed to decrease when a more flexible adhesive material was used for the strengthening. Chapter 8 reported a reduction of 20.2% for the peak peeling stress and 14.6% for the peak shear stress when the adhesive elasticity modulus decreases from 3.18 to 0.472 GPa.

Load capacity in linear elastic analyses: Chapter 6 reported that a significant reduction of the adhesive shear modulus (e.g., from $1.3MPa$ to $0.4GPa$) caused a relatively mild reduction of the peak load reduction (e.g., from $21.7kN$ to $26.8kN$).

Ultimate moment capacity: Chapter 5 indicated that the shear strength of the adhesive can strongly influence the ultimate moment capacity (when the shear failure mode of the adhesive governs the design). The weak adhesive (i.e., Spabond 345 at 50^0C with a shear strength 5.6 MPa) was observed to lead to the shear failure mode. In contrast, strong adhesive (i.e., Typo S epoxy at room temperature with a shear strength 42 MPa) was found to avoid the shear failure mode and to lead to a GFRP tension failure mode.

Elastic lateral torsional buckling capacity: Chapter 4 investigated the effect of adhesive thickness on the buckling capacity for a 6m-span beam with a W250x45 section strengthened with a 19mm- thick GFRP plate bonded to the compression flange by using Typo S epoxy (with an elastic modulus of 3.18 GPa). The buckling load increases only marginally with the thickness of the adhesive. The buckling load for the 0.5mm thick adhesive was 126.9 kN, that corresponding to 4.0mm was marginally increased to 133 kN, a 4.6% difference. The increase was attributed to the slightly deeper overall cross-section in the case of a thicker adhesive.

9.3.3. Other considerations

The theory developed in Chapter 7 for the analysis of homogeneous beams successfully captures the effect of pin height on the beam displacement and stress responses. For short span beams, when supports are located at the mid-height, it was observed that the stress distributions differ significantly from those for the case where the supports are located at the underside of the beam. In contrast, the effect of support height was shown to be negligible for beams with long spans.

9.4. Recommendations for future research

Based on the developments conducted in the present thesis, the following recommendations are proposed for future research:

(1) Chapter 4 developed an elastic lateral-torsional buckling solution which tends to govern the capacity of long span laterally unsupported beams. Also, Chapter 5 developed solutions for ultimate moment capacity of GFRP-strengthened steel beams which tends to govern the capacity of short spans of Class 1 and 2 sections. For beams of intermediate spans, inelastic lateral torsional buckling is expected to govern the capacity. The present study has not investigated this mode of failure. It is thus suggested that future research numerically investigate inelastic lateral torsional buckling for GFRP-strengthened steel beams and verify whether the inelastic lateral torsional buckling equation in present design standards, or a modification thereof, can be extended to strengthened beams.

(2) The elastic lateral-torsional buckling solution developed in Chapter 4, while suitable for computational methods, may be challenging to use in a design environment. It is thus recommended to generate a database of runs using the model in Chapter 4, and develop simplified design equations, possibly using regression analysis, to approximately quantify the critical moments given the geometric and mechanical properties of the steel, GFRP, and adhesive.

(3) In the absence of experimental evidence suggesting otherwise, the finite element simulations in Chapter 5 were based on a postulated von-Mises yield criterion for the adhesive. It is required to conduct a material testing experimental program to test adhesives under various combinations of shear and peeling stresses and develop and propose a yield criterion for the adhesive based on experimental evidence.

(4) In the limited study in Chapter 5, a steel beam of a given span, the length of the strengthening GFRP plates was shown to considerably influence the peak shear near the bond ends where a longer GFRP plate was shown to lead to smaller peak shear stresses in the adhesive. It would be of practical interest to conduct a parametric investigation that accounts for other factors (e.g., GFRP and adhesive thicknesses and material properties) on the peak shear stresses developed.

(5) Chapter 6 developed a closed form solution for the analysis of steel beams strengthened with two GFRP plates including the pre-existing loading effects. To generalize the solutions for other loading and boundary conditions, it is proposed to develop finite element solutions based on the variational expressions developed in the study.

(6) As discussed in Cases 2 and 6 of Table 9.1, the lateral torsional buckling solution developed in Chapter 4 was limited to strengthened beams with no pre-existing loads. It is thus recommended

to extend the formulation to include the effect of pre-existing loads on the lateral torsional buckling strength.

(7) The present work has exclusively focused on the modeling aspects of the problem. It is of practical interest to conduct full-scale experimental studies to serve as a basis to assess the validity of the various models developed in the present study.

(8) The present study has focused on a limited number of failure modes; (1) local buckling, (2) elastic lateral torsional buckling, (3) material failure based on elastic or plastic stress profiles, (4) GFRP plate tension failure, (5) shear failure of the adhesive, (6) peeling failure of the adhesive, and (7) deflections. Other modes of failures induced by delamination, fatigue, and thermal effects need to be investigated in future studies.